

RS•C



*inorganic
electrochemistry
theory, practice and application*

PIERO ZANELLO

Inorganic Electrochemistry
Theory, Practice and Application

Inorganic Electrochemistry

Theory, Practice and Application

P. Zanotto

University of Siena, Italy

RS•C

advancing the chemical sciences

ISBN 0-85404-661-5

A catalogue record for this book is available from the British Library

© The Royal Society of Chemistry 2003

All rights reserved

Apart from any fair dealing for the purpose of research or private study, or criticism or review as permitted under the terms of the UK Copyright, Designs and Patents Act, 1988, this publication may not be reproduced, stored or transmitted, in any form or by any means, without the prior permission in writing of The Royal Society of Chemistry, or in the case of reprographic reproduction only in accordance with the terms of the licences issued by the Copyright Licensing Agency in the UK, or in accordance with the terms of the licences issued by the appropriate Reproduction Rights Organization outside the UK. Enquiries concerning reproduction outside the terms stated here should be sent to The Royal Society of Chemistry at the address printed on this page.

Published by The Royal Society of Chemistry,
Thomas Graham House, Science Park, Milton Road, Cambridge CB4 0WF, UK
Registered Charity Number 207890

For further information see our web site at www.rsc.org

Typeset by Alden Bookset, Northampton, UK
Printed by TJ International, Padstow, Cornwall, UK

Preface

The use of electrochemical measurements to determine the ability of inorganic molecules to undergo electron-transfer processes has become a routine tool in synthetic chemistry (just like elemental analysis and spectroscopic techniques). Nevertheless, the first approach of researchers to electrochemistry is often on an approximate basis (it often happens, in quoted journals, that a few cyclic voltammetric runs are assumed to cover all the redox aspects of a molecule) in that electrochemistry books are commonly not easily comprehensible to non-electrochemists and even more rarely deal with ‘inorganic chemistry’ (in contrast with the well-established tradition of ‘organic’ electrochemistry). Thus, the present book (which should be considered more an ‘applied inorganic chemistry’ book than a ‘real electrochemistry’ book) aims to bridge the gap between undergraduate and research level electrochemistry books, in order to initiate inorganic chemists into electrochemical investigations in as straightforward a way as possible, as well as to introduce electrochemists to the opportunities offered by the multiple fields of inorganic chemistry.

Pure electrochemists might disapprove of some oversimplifications (or find a few inaccuracies), but as an inorganic chemist I think that the main targets of an electrochemical investigation are:

- to determine if an inorganic compound is redox active
- to measure the electrode potentials at which eventual redox changes take place
- to state if the redox processes lead to stable species
- in the case of derivatives which undergo degradation as a consequence of electron transfer processes, to measure the rate of such degradation paths, eventually suggesting those techniques which can help the identification of the intermediate products

- to suggest the proper chemical reagents to perform large-scale redox processes
- to throw light onto redox paths through comprehensive electrode mechanisms, the latter having to be always based on well documented experimental evidence (complicated speculative mechanisms are almost always tedious and not useful)
- to point out eventual molecular dynamics triggered by electron-transfer processes.

The selection of the matter treated in the text was dictated by the conflicting requirements of controlling its length and offering a satisfactory survey of the use of electrochemistry in inorganic chemistry (in this connection, I wish to express my gratitude to Jean-Marc Lievens and Emanuela Grigiotti for their invaluable graphic help). It is therefore possible that the text appears incomplete with respect to some important topics. Readers, however, must keep in mind that it simply constitutes a first approach to inorganic electrochemistry targeted at the newcomers, even if we hope that it might be of some help also to the practitioners, in that the different subjects are updated as much as possible.

Unfortunately (or better, fortunately) chemical innovation is very fast and any matter rapidly ages. Perspectively, the dynamic aspects of inorganic compounds (or, ‘molecular machinery’) will become more and more sophisticated (their interpretation thus requiring also more and more sophisticated electrochemical techniques), but the basic equipment to their operation will remain in some ways still valid for a long time (screws, bolts, screwdrivers, pliers and drills are still basic pieces of the actual super-technological assemblies). In this picture, it is expected that the basic approach outlined here, to face with the electrochemical aspects of a number of topics in inorganic chemistry, will (hopefully) maintain its middle-term validity.

Contents

Introduction	1
---------------------	----------

BASIC ASPECTS OF ELECTROCHEMISTRY

Chapter 1 Fundamentals of Electrode Reactions	7
1 Electron Transfer Reactions	7
2 Fundamentals of Electron Transfers at an Electrode	10
2.1 The Electrode/Solution System	11
2.2 The Nature of Electrode Reactions	12
2.3 The Current as a Measurement of the Rate of an Electrode Reaction	14
2.4 The Potential as a Measurement of the Energy of the Electrons Inside the Electrode	15
2.5 The Biunique Relationship Between Current and Potential	16
3 Potential and Electrochemical Cells	16
4 Kinetic Aspects of the Electrode Reactions	22
4.1 Electron Transfer	22
4.1.1 A Deeper Insight into the Meaning of k° and α	26
4.1.2 Verification of the Theory Under Equilibrium Conditions	28
4.1.3 Further Considerations on the Fundamental Equation of the Electron Transfer Process. The Exchange Current	30
4.2 Mass Transport	34
4.2.1 Possible Ways to Move a Species from the Bulk of the Solution to the Electrode Surface	35

4.2.2	Linear Diffusion at a Planar Electrode	36
4.2.3	Spherical Diffusion	38
4.2.4	Concentration Profiles. Cottrell Equation	38
4.3	Influence of Mass Transport on Charge Transfer. Electrochemically 'Reversible' and 'Irreversible' Processes	42
5	Non-Faradaic Processes. Capacitive Currents	43
6	The Electrical Double Layer. A Deeper Examination	45
6.1	The Kinetic Consequences of the Double Layer Composition on the Electron Transfer	46
	References	48
 Chapter 2 Voltammetric Techniques		 49
1	Cyclic Voltammetry	49
1.1	Reversible (Nernstian) Processes	51
1.1.1	Diagnostic Criteria to Identify a Reversible Process	55
1.1.2	The Chemical Meaning of an Electrochemically Reversible Process	57
1.2	Irreversible Processes	59
1.2.1	Diagnostic Criteria to Identify an Irreversible Process	60
1.2.2	The Chemical Meaning of an Electrochemically Irreversible Process	62
1.3	Quasireversible Processes	62
1.3.1	Diagnostic Criteria to Identify a Quasireversible Process	64
1.3.2	The Chemical Meaning of an Electrochemically Quasireversible Process	66
1.4	The Effect of Chemical Reactions Coupled to Electron Transfers	67
1.4.1	Preceding Chemical Reactions	68
1.4.2	Following Chemical Reactions	74
1.4.3	A Chemical Reaction Interposed Between Two Electron Transfers	87
1.4.4	Electrocatalysis	93
1.5	Consecutive Electron Transfer Processes	99

1.5.1	Two Reversible One-electron Transfers	100
1.5.2	Two One-electron Transfers with Different Extents of Reversibility	104
1.6	Adsorption Processes	104
2	Electrochemical Techniques Complementary to Cyclic Voltammetry	110
2.1	Pulsed Voltammetric Techniques	110
2.1.1	Differential Pulse Voltammetry	110
2.1.2	Square Wave Voltammetry	113
2.2	Hydrodynamic Techniques	115
2.3	Controlled Potential Electrolysis	117
2.4	Chronoamperometry	123
2.4.1	Coupled Chemical Reactions	126
2.5	Determination of the Number of Electrons Involved in an Electron Transfer Process from the Correlation Between Cyclic Voltammetry and Chronoamperometry	133
	References	134

PRACTICAL ASPECTS

Chapter 3	Basic Equipment for Electrochemical Measurements	139
1	Electrodes	139
1.1	Indicator Electrodes	139
1.2	Reference Electrodes	141
1.3	Auxiliary Electrodes	141
2	Electrochemical Cells	142
2.1	Cells for Cyclic Voltammetry and Chronoamperometry	146
2.2	Cells for Controlled Potential Electrolysis	147
3	Solutions for Electrochemical Studies. Solvents and Supporting Electrolytes	149
	References	154

APPLICATIVE ASPECTS

Chapter 4	The Electrochemical Behaviour of First Row Transition Metal Metallocenes	159
1	Ferrocenes	160
1.1	Monoferrocenes	160
1.2	Ferrocenophanes	167

1.3	Olygoferrocene Derivatives	171
1.4	Ferrocene Polymers	182
1.4.1	Ferrocene-based Linear Polymers	182
1.4.2	Ferrocene-based Branched Polymers (Dendrimers)	185
1.5	Recent Applications of Ferrocenes	193
1.5.1	Ferrocenes as Electrochemical Sensors	193
1.5.2	Ferrocenes as Materials Displaying 'Non-Linear Optical Properties'	198
2	Vanadocenes	204
3	Chromocenes	205
4	Manganocenes	207
5	Cobaltocenes	208
6	Nickelocenes	210
	References	211

Chapter 5 The Electrochemical Behaviour of Transition

	Metal Complexes	217
1	Vanadium Complexes	219
2	Chromium Complexes	230
3	Manganese Complexes	236
3.1	The Role of Manganese Complexes in Photosynthesis	244
3.2	Tetranuclear Manganese Complexes Modelling the Photosynthetic Water Oxidation Site	251
3.2.1	Derivatives of Diamantoidal Geometry	251
3.2.2	Derivatives of Cuboidal Geometry	252
3.2.3	Derivatives of Planar Geometry	253
3.2.4	Derivatives of Butterfly Geometry	256
3.2.5	Derivatives of Linear Chain Geometry	258
3.2.6	Derivatives of Layered Geometry	260
3.3	The Role of Manganese Complexes in Material Science	262
4	Iron Complexes	263
4.1	Intramolecular Electronic Communication in Polynuclear Iron Complexes	274
5	Cobalt Complexes	276
5.1	Intramolecular Electronic Communication in Polynuclear Cobalt Complexes	288
6	Nickel Complexes	290

7	Copper Complexes	302
8	Zinc Complexes	314
	References	316
Chapter 6	Metal Complexes Containing Redox-active Ligands	325
1	Ferrocenes as Ligands in Metal Complexes	325
2	Fullerenes as Ligands in Metal Complexes	332
2.1	Intramolecular Electronic Communication in Metallo-bis(fullerenes)	346
3	Dioxolenes (and Their Imino Analogues) and Dithiolenes as Ligands in Metal Complexes	348
4	Porphyrins (and Tetraazaporphyrins) as Ligands in Metal Complexes	363
5	Less Known Redox-active Ligands in Metal Complexes	371
	References	374
Chapter 7	Electrochemically Induced Structural Modifications	381
1	Geometrical Isomerization	381
2	Some Examples of Molecular Reorganizations Induced by Deprotonation or Dehydrogenation	392
3	Reversible Migration of a Hydrogen Atom from a Metal Centre to a Peripheral Ligand	397
4	Reversible Orientation from ‘Perpendicular’ to ‘Parallel’ Disposition of an Alkyne Group Bridging Two Metal Centres	399
5	Redox Transformations Following Irreversible Electron-Transfer Pathways	402
6	Redox Transformations Following Quasireversible Electron-Transfer Pathways	404
	References	407
Chapter 8	Transition Metal Clusters	409
1	Metal–Sulfur Clusters	409
1.1	M_3S_n ($n = 2, 4$)	409
1.2	M_4S_n ($n = 3–6$)	414
1.3	M_6S_n ($n = 6, 8, 9$)	419
1.4	M_9S_9	421
2	Metal–Carbonyl Clusters	422
2.1	$M_3(CO)_{12}$, $[M_3(CO)_{11}]^{2-}$ ($M = Fe, Ru, Os$)	422
2.2	$[Fe_4(CO)_{13}]^{2-}$, $M_4(CO)_{12}$ ($M = Co, Rh, Ir$)	425
2.3	$[M_5(CO)_{15}]^{n-}$ ($M = Os, n = 2$; $M = Rh, n = 1$)	426
2.4	$[M_6(CO)_{15}]^{2-}$ ($M = Co, Rh, Ir$), $[M_6(CO)_{18}]^{2-}$ ($M = Ru, Os$)	427

2.5	Clusters of Higher Nuclearity: [Ir ₁₄ (CO) ₂₇] ⁻ , [Pt ₁₉ (CO) ₂₂] ⁴⁻ , [Pt ₂₄ (CO) ₃₀] ²⁻	431
3	Carbonyl Clusters with Interstitial Atoms	432
3.1	[Fe ₄ (CO) ₁₂ C] ²⁻ , [Fe ₄ (CO) ₁₂ N] ⁻	433
3.2	[Fe ₅ (CO) ₁₄ C] ²⁻ , [Fe ₅ (CO) ₁₄ N] ⁻	436
3.3	[Fe ₆ (CO) ₁₆ C] ²⁻ , [Fe ₆ (CO) ₁₅ N] ³⁻ , [Os ₆ (CO) ₁₈ P] ⁻	438
3.4	[Os ₁₀ (CO) ₂₄ C] ²⁻	440
3.5	[Co ₁₃ (CO) ₂₄ (C) ₂] ⁴⁻	440
3.6	[Ni ₃₂ (CO) ₄₂ (C) ₆] ⁶⁻	442
	References	443
Chapter 9	The Reactivity of Transition Metal Complexes with Small Molecules	445
1	The Reactivity of Transition Metal Complexes with Oxygen	445
1.1	Metal Complexes which React Irreversibly with Dioxygen	446
1.2	Metal Complexes which React Reversibly with Dioxygen	449
1.3	Hemoprotein-like Metal Complexes	452
1.4	Hemocyanin-like Metal Complexes	466
1.5	Haemerythrin-like Metal Complexes	467
2	The Reactivity of Transition Metal Complexes with Dinitrogen	469
2.1	Metal Complexes with Terminal Coordination to One Dinitrogen Molecule	474
2.2	Metal Complexes with Bridging Coordination to One Dinitrogen Molecule	476
2.3	Metal Complexes with Terminal Coordination to Two Dinitrogen Molecules	482
3	The Reactivity of Transition Metal Complexes with Dihydrogen	484
	References	491
Chapter 10	Superconductors in Electrochemistry	497
1	General Aspects of Superconductivity	497
1.1	Physical Properties of Superconductors	499
1.1.1	The Loss of Electrical Resistance	499
1.1.2	The Meissner Effect and Levitation	500
1.1.3	The Mechanism of Superconductivity	502
1.2	Chemical Properties of High T_c Superconductors	504
1.2.1	Synthesis and Oxidation States of 1-2-3 Superconductors	504

1.2.2	Molecular Structure of 1-2-3 Superconductors	505
2	Electrochemical Aspects of Superconductors	506
2.1	The Preparation and Use of Electrodes of Superconducting Materials	507
2.2	Study of the Corrosion of Ceramic Superconductors	508
2.3	Electrochemical Synthesis of Superconductors	512
2.4	Electrochemistry Using Electrodes of Superconducting Materials at Temperatures Below T_c	513
	References	514
Chapter 11	Molecular Metal Wires: An Electrochemical Inspection	517
1	Platinum Blues	519
2	Chloride-Bridged Triruthenium Complexes	522
3	Oligo-2-Pyridylamides as Bridging Ligands in Polynuclear Linear Complexes	524
3.1	Trinuclear Complexes	524
3.2	Tetranuclear Complexes	528
3.3	Pentanuclear Complexes	528
3.4	Higher Nuclearity Complexes	530
4	Isocyanides and Nitrile Ligands in Polynuclear Linear Complexes	532
	References	533
Chapter 12	The ‘Direct’ Electrochemistry of Redox-active Proteins	539
1	Introduction	539
2	Electrochemistry of Cytochromes	542
3	Electrochemistry of Iron–Sulfur Proteins	556
4	Electrochemistry of Blue Copper Proteins	567
	References	574
Chapter 13	Linear Correlations Between the Redox Potential and Other Chemical and Physico-chemical Parameters	579
1	Redox Potential and Electronic Effects of the Ligands	579
2	Redox Potential and Solvent Effects	589
3	Redox Potential and Temperature	594
	References	602

Appendices	603
Physical Constants	603
SI Base Units	603
Derived SI Units	603
SI Prefixes	604
Conversion Factors	604
The Greek Alphabet	605
Subject Index	607

Introduction

In order to understand the basic aspects of an electrochemical investigation on inorganic molecules (in its widest meaning, of any molecule which contains at least one metal centre) it must be taken into account that in these molecules the metal–ligand bonds are prevailingly covalent type. Since electrochemical techniques allow one to add or remove electrons in a controlled manner, it is conceivable that the addition or removal of electrons inside these molecules can lead to the formation of new bonds or to the breakage of existing bonds.

The first target of Inorganic Electrochemistry is therefore to study the effects of such electron addition/removal processes on the molecular frames.

As a matter of fact, the structural consequences of the electron exchanges are governed by the bonding, anti-bonding or non-bonding character of the frontier orbitals of the molecule. When one removes an electron from the energetically more easily accessible occupied molecular orbital (HOMO), which for instance possesses bonding character, it is clear that the molecular frame is weakened. The same happens, when one adds an electron to the energetically more easily accessible unoccupied molecular orbital (LUMO), if it possesses anti-bonding character.

For instance let us consider the case of the tetrahedral carbonyl cluster $[\text{Rh}_4(\text{CO})_{12}]$, together with the theoretical analysis of its molecular orbitals, Figure 1.

The lowest energy unoccupied orbital (LUMO – 27e) is *anti-bonding* with respect to the Rh–Rh bonds. As a consequence, the addition of electrons to $[\text{Rh}_4(\text{CO})_{12}]$ would cause destruction of the molecular frame (see Chapter 8, Section 2.2).

Actually, if we look at the cyclic voltammogram of a non-aqueous solution of $[\text{Rh}_4(\text{CO})_{12}]$ shown in Figure 2, we see a reduction profile (peak A) which lacks a directly associated re-oxidation peak in the reverse scan.

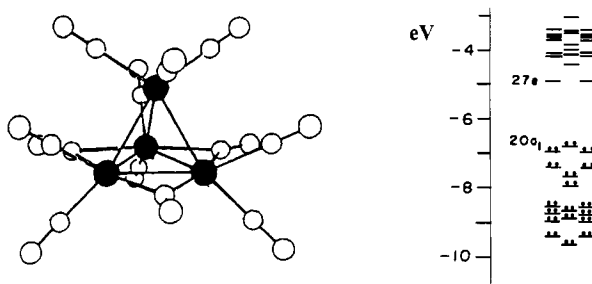


Figure 1 Molecular structure and theoretical analysis of $[Rh_4(CO)_{12}]$

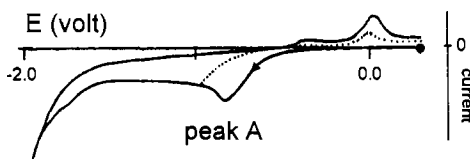


Figure 2 Cyclic voltammogram exhibited by $[Rh_4(CO)_{12}]$ in dichloroethane solution. From hereafter the symbol ● will indicate the starting potential

As we will discuss in Chapter 2, such an ‘unsymmetrical’ pattern foreshadows fragmentation or severe structural reorganization of the original molecular frame.

Obviously, the addition or removal of electrons can also lead to less drastic geometrical effects if the molecular orbitals involved are non-bonding.

Consider, for instance, the case of ferrocene, $[Fe(\eta\text{-C}_5\text{H}_5)_2]$, which, according to the 18-electron rule, is highly stable. As one can deduce from its orbital diagram shown in Figure 3, its highest occupied orbital ($HOMO - a'_1$) possesses a non-bonding character; this means that if we remove one electron from such an orbital, we do not trigger breakage of the molecule.

In agreement with such an electronic distribution, the cyclic voltammogram of ferrocene displays an oxidation profile (peak A) which is accompanied in the reverse scan by a directly associated reduction process (peak B), Figure 4.

As we will discuss, such a ‘symmetric’ profile is typical of an electron removal which does not lead to important structural changes. In fact, the 17-electron ferrocenium ion, $[Fe(C_5H_5)_2]^+$, generated upon oxidation, is a stable species which substantially maintains the original molecular frame (but for the fact that, because of the electron removal, the iron–carbon bonds are slightly weakened and hence elongated by about 0.04 Å with respect to the neutral parent; see Chapter 4, Section 1.1).

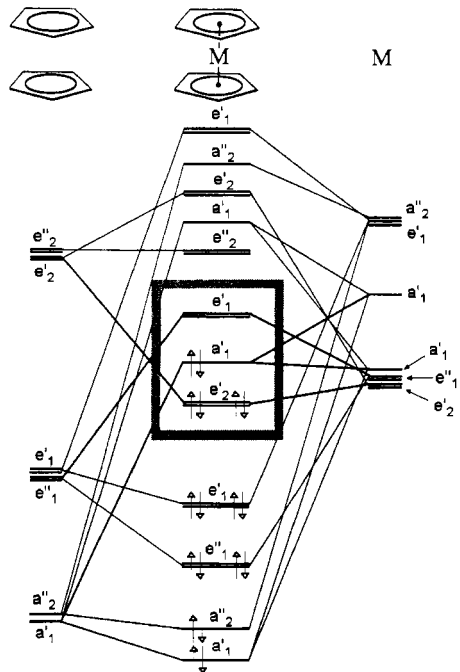


Figure 3 Molecular orbital diagram of ferrocene

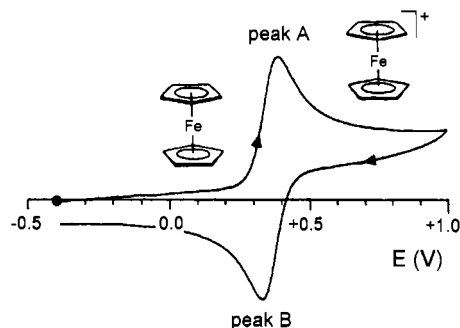


Figure 4 Cyclic voltammogram exhibited by $[Fe(C_5H_5)_2]$ in dichloromethane solution

Finally, it must be taken into account that electrochemistry not only points out the occurrence of redox changes at molecular levels and their possible structural consequences, but also determines the electrode potentials at which such electron exchanges take place. For instance, Figure 4 shows that the $[Fe(C_5H_5)_2]/[Fe(C_5H_5)_2]^+$ oxidation takes place at $E^\circ = +0.44$ V (as we will see later, with respect to the experimental

conditions used). For inorganic chemists such quantitative information can be of interest in that it allows them to calibrate properly the power of the eventual oxidizing agents to be used in a large-scale preparation of ferrocenium salts.

BASIC ASPECTS OF ELECTROCHEMISRY

CHAPTER 1

Fundamentals of Electrode Reactions

Electrochemistry is essentially based on the relationships between chemical changes and flows of electrons (*i.e.* the passage of electricity). In this connection it is well known that electron transfer processes play an essential role in many physical, chemical and biological mechanisms and a number of such examples will be illustrated in the text. Perhaps in no other field of chemical reactivity has one looked for and found so many relationships between theory and experimental measurements.

Two disciplines cover the majority of the theoretical and practical aspects of the mechanisms through which electron transfers proceed: *electrochemistry* and *photochemistry*. In this book only mechanisms relating to electrochemistry will be considered.

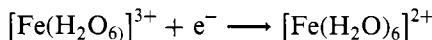
1 ELECTRON TRANSFER REACTIONS

In a purely formal manner the description of an electron transfer event, such as the reduction in solution of Fe(III) ion, can be written in two ways, depending on whether the reduction is operated by a chemical agent or by an electrode:

- *through a reducing agent* (redox reaction in a *homogeneous* phase):



- *through an electrode* (redox reaction in a *heterogeneous* phase):



In both cases, the adopted symbolism only gives a picture of the overall process. In fact, from a mechanistic viewpoint, the redox reactions (as with any other type of reaction) proceed by a series of intermediate steps involving phenomena such as:

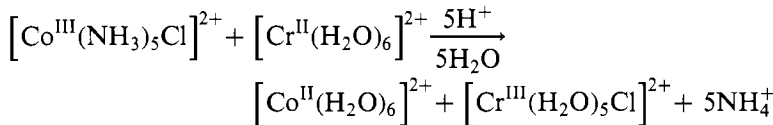
- *diffusion* of the species through the solution;
- *interaction between reagents*, in the case of reactions in a homogenous phase, or interactions between reagents and electrode, in the case of reactions in a heterogenous phase;
- *formation of short- or long-lived intermediates* due to variations in electronic configurations, to the eventual substitution of ligands, etc.

Commonly, oxidation–reduction reactions in a homogenous phase are classified as:

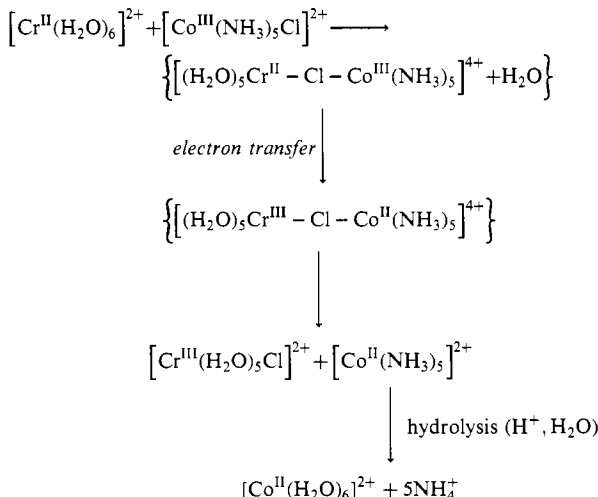
- *outer-sphere* reactions;
- *inner-sphere* reactions.

In the inner-sphere reactions, the process involves a ‘transition state’ in which a mutual strong penetration of the coordination spheres of the reagents occurs (and, therefore, strong interaction between reagents), whereas in the outer-sphere reactions there is no overlap of the coordination spheres of the reagents (and, therefore, there is weak interaction between reagents).

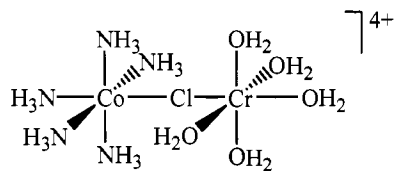
The classical example of inner-sphere mechanism is the reduction of the Co(III) salt $[\text{Co}(\text{NH}_3)_5\text{Cl}]^{2+}$ by Cr(II) ions ($[\text{Cr}(\text{H}_2\text{O})_6]^{2+}$):



The fact that from a chloro-cobalt complex a chloro-chromium complex is formed, suggests that the reaction must proceed through an intermediate state that enables the transfer of a chlorine atom from cobalt to chromium. The proposed mechanism for this reaction is:

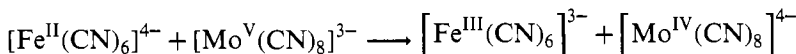


It is assumed that the intermediate product is $[(\text{NH}_3)_5\text{Co}^{\text{III}}-\text{Cl}-\text{Cr}^{\text{II}}(\text{H}_2\text{O})_5]^{4+}$:



in which there is a clear overlap of the coordination spheres of the two reagents. It follows that the electron-transfer can take place only after such an intermediate has formed.

As an example of a reaction which involves an outer-sphere mechanism the following reaction can be considered:



In this case one may assume that the charge transfer takes place as soon as the two reagents collide, without the occurrence of any exchange of ligands (which would imply breaking of old or formation of new bonds in the reaction intermediate).

As a consequence, the mechanism with which a homogeneous reaction proceeds is conditioned by the rate of either the *ligand exchange* or the *electron transfer*. An outer-sphere mechanism is certainly active when the exchange of ligands between reagents is slower than the exchange of electrons between reagents.

In this picture, the electron transfer processes mediated by metallic electrodes (redox reactions in a heterogeneous phase) can also be classified to proceed according to outer-sphere or inner-sphere mechanisms (obviously, considering the electrode surface as a reagent).

One can define as outer-sphere electrode processes those in which the electron transfer between the electrode and the active site occurs through the layer of solvent directly in contact with the electrode surface. The electrode and electroactive species are, therefore, separated such that the chemical interaction between them can be considered practically nil (obviously, apart from their electrostatic interaction), see Figure 1.

Inner-sphere electrode processes are defined as those in which the electron exchange occurs between the electrode and the electroactive species (the metal core or its ligand) that are in direct contact with the electrode surface, see Figure 2.

It should be emphasized that the majority of electrochemically induced redox processes in inorganic chemistry proceed (or are assumed to proceed) through outer-sphere mechanisms.

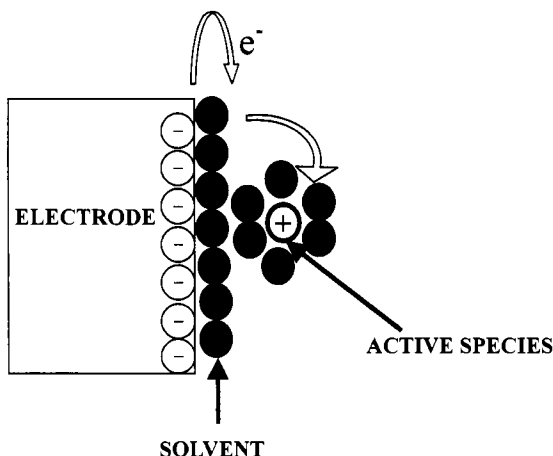


Figure 1 Schematic representation of an heterogeneous electron transfer taking place through an outer-sphere mechanism at a negatively charged electrode

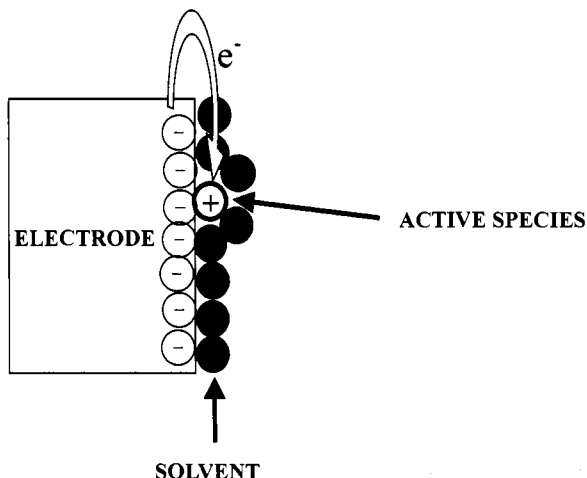


Figure 2 Schematic representation of an heterogeneous electron transfer taking place through an inner-sphere mechanism at a negatively charged electrode

2 FUNDAMENTALS OF ELECTRON TRANSFERS AT AN ELECTRODE

As we shall be considering the electrochemical characterization of chemical systems, it is useful at this point to make clear a few fundamental concepts inherent in electrochemical processes.¹⁻⁶

2.1 The Electrode/Solution System

An electrode reaction is always a heterogeneous chemical process, in that it involves the passage of an electron from an electrode (metal or semiconductor) to a chemical species in solution, or *vice versa*.

As illustrated in Figure 3, one can depict the *electrode/solution system* as being partitioned roughly into four regions:

- the electrode
- the double layer
- the diffusion layer
- the mass (or bulk) of the solution

The *electrode/solution interface* represents a discontinuous plane with respect to the distribution of the electrical charge. This is the result of electrode possessing an excess of charge of a given sign (for example, negative in the figure) in immediate contact with an excess of charge of opposite sign, due to the electrostatic attraction. This situation generates the so-called double layer, which, as we shall see, has important consequences on the electrochemical events.

The so-called diffusion layer is still a region dominated by an unequal charge distribution (*i.e.* in such a zone the principle of electro-neutrality is not valid) due to the electron transfer processes occurring at the electrode surface. In fact, the electrode acts as an electrostatic pump for species of

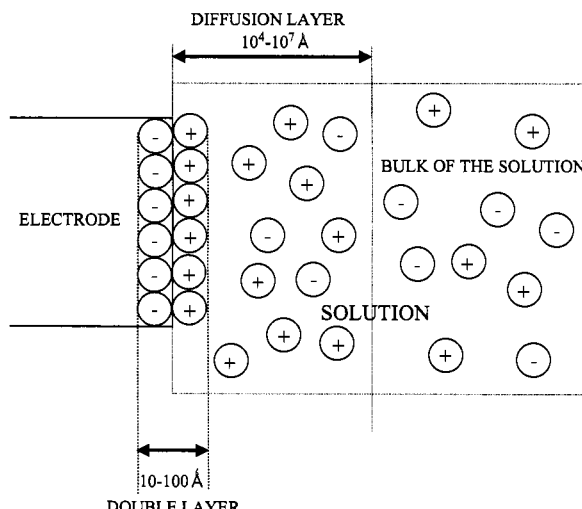


Figure 3 The zones which characterize the electrode/solution system. Negatively charged electrode

a certain charge, resulting in a flow of these charged systems from the mass of the solution (*i.e.* the bulk of the solution where the principle of electro-neutrality is fully valid) towards the electrode, or *vice versa*.

2.2 The Nature of Electrode Reactions

Let us consider a chemical species which possesses two different oxidation states, *oxidized* (Ox) and *reduced* (Red), both stable and soluble in the electrolytic medium (solvent + inert electrolyte). The simplest formulation of the electrode reaction which converts Ox to Red:



in reality hides a sequence of elementary processes. In fact, in order to maintain a continuous flow of electrons:

- first, the electrode surface must be continually supplied with reagent (Ox);
- then, the heterogeneous electron transfer process from the solid electrode to the species Ox must take place (through an inner- or outer-sphere mechanism);
- finally, the reaction product (Red) must be removed from the electrode surface, in order to allow the access of further amounts of Ox to the electrode surface.

Consequently, we can rationalize the process represented by Equation (1) as involving at least the following three elementary steps:



Clearly, the overall rate of the reduction process will be conditioned by the slowest elementary step, which can be associated either with the *mass transport* (from the bulk of the solution to the electrode surface, and *vice versa*) or with the *heterogeneous electron transfer* (from the electrode to the electroactive species, or *vice versa*).

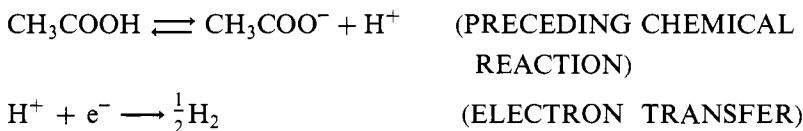
As pointed out, the electrode process (1) can be described by the mentioned sequence of ‘at least’ three elementary stages. In reality, quite

often other phenomena complicate the electrode reactions. These consist of fundamentally three types:

- **coupled chemical reactions**

It is possible that the species Red generated at the electrode surface may be unstable and tend to decompose. It may also be involved in chemical reactions with other species present in solution while it is moving towards the mass of the solution (homogeneous chemical reactions) or while it is still adsorbed on the electrode surface (heterogeneous chemical reactions). Furthermore, the new species formed during such reactions may be electroactive. These kind of reactions are called *following* chemical reactions (following, obviously, the electron transfer).

In addition, though less common, there are cases of *preceding* chemical reactions (preceding, naturally, the electron transfer). In this case, the reagent Ox is the product of a preliminary chemical reaction of a species that is not itself electroactive. For example, the reduction of acetic acid proceeds through the two microscopic stages:



- **adsorption**

In the sequence of reactions (2)–(3)–(4) it was assumed that electron exchange takes place without the interaction of the species Ox and Red with the electrode surface. However, it is possible that the exchange of electrons does not occur unless the reagent Ox, or the product Red, is weakly or strongly adsorbed on the electrode surface. It is also possible that the adsorption of the species Ox or Red might cause poisoning of the electrode surface, thus preventing any electron transfer process.

- **formation of phases**

The electrode reaction can involve the formation of a new phase (*e.g.* electro-deposition processes used in galvanizing metals). The formation of a new phase is a multi-stage process since it requires a first nucleation step followed by crystal growth (in which atoms must diffuse through the solid phase to then become located in the appropriate site of the crystal lattice).

2.3 The Current as a Measurement of the Rate of an Electrode Reaction

An electrode reaction always implies a transfer of electrons. If we consider again the reaction:



it is easily deduced that for each mole of species Ox which is reduced, n mol of electrons must be released from the electrode (the *working electrode*, WE) and supplied to the species. As illustrated in Figure 4, these electrons are supplied, through an external circuit, by an electrode reaction that occurs at a second electrode (the *counter electrode*, CE) at the expense of any other redox-active species Red' present in the same electrolytic solution (solvent itself included).

It is clear that if, as in this case, the process occurring at the working electrode is a reduction half-reaction then there will be an oxidation half-reaction at the counter-electrode.

Faraday's law states that if M mol of reagent Ox are reduced, the total charge spent is given by:

$$Q = n \cdot F \cdot M$$

where F is the Faraday constant ($96\ 485\ \text{C mol}^{-1}$).

The variation of charge with time, *i.e.* the current, i , will be equal to:

$$\frac{dQ}{dt} = i = n \cdot F \cdot \frac{dM}{dt}$$

The variation of the mol number with time, dM/dt , reflects the variation of concentration per unit time, or the reaction rate, v (in mol s^{-1}).

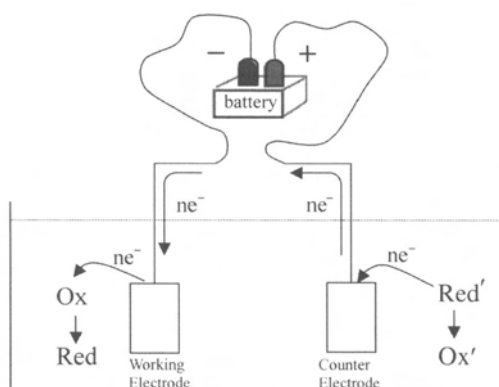


Figure 4 A schematic way to set up the reduction reaction: $\text{Ox} + n\text{e}^- \rightarrow \text{Red}$, at an electrode

Since we are considering heterogeneous processes, the rate of which is commonly proportional to the area of the electrode, one can normalize with respect to the electrode area, A , so that:

$$\frac{i}{n \cdot F \cdot A} = \frac{1}{A} \cdot \frac{dM}{dt} = v (\text{mol s}^{-1} \cdot \text{m}^{-2})$$

This expression shows that the current flowing in the external circuit of Figure 4 is proportional to the rate of the electrode reaction:

$$i = n \cdot F \cdot A \cdot v$$

the proportionality constant being the factor $n \cdot F \cdot A$.

This type of current, which originates from chemical processes which obey Faraday's law, is called a *faradaic current*, to distinguish it from *non-faradaic currents* which, as we shall see in Section 5, arise from processes of a strictly physical nature.

In the course of an electrochemical experiment the experimental conditions are carefully controlled to minimize the onset of non-faradaic currents as much as possible.

2.4 The Potential as a Measurement of the Energy of the Electrons Inside the Electrode

According to *band theory*, the electrons inside a metal populate the valence band up to the highest occupied molecular orbital, which is called the *Fermi level*. The potential applied to a metallic electrode governs the energy of its electrons according to Figure 5.

If the electrode potential is made more negative with respect to the zero-current value, the energy of the Fermi level is raised to a level at which the electrons of the metal (or, the electrode) flow into the empty orbitals (LUMO) of the electroactive species S present in solution, Figure 5a. Thus, a reduction process takes place, written as: $\text{S} + \text{e}^- \rightarrow \text{S}^-$

In an analogous way, the energy of the Fermi level can be decreased by imposing an electrode potential more positive than the zero-current value. A situation is now reached in which it is energetically more favourable that the electroactive species donates electrons from its occupied molecular orbital (HOMO) to the electrode, see Figure 5b. An oxidation process has been activated, which can be depicted as: $\text{S} \rightarrow \text{S}^+ + \text{e}^-$

The critical potential at which these electron-transfer processes occur identifies the *standard potential*, E° , of the couples S/S^- and S^+/S , respectively.

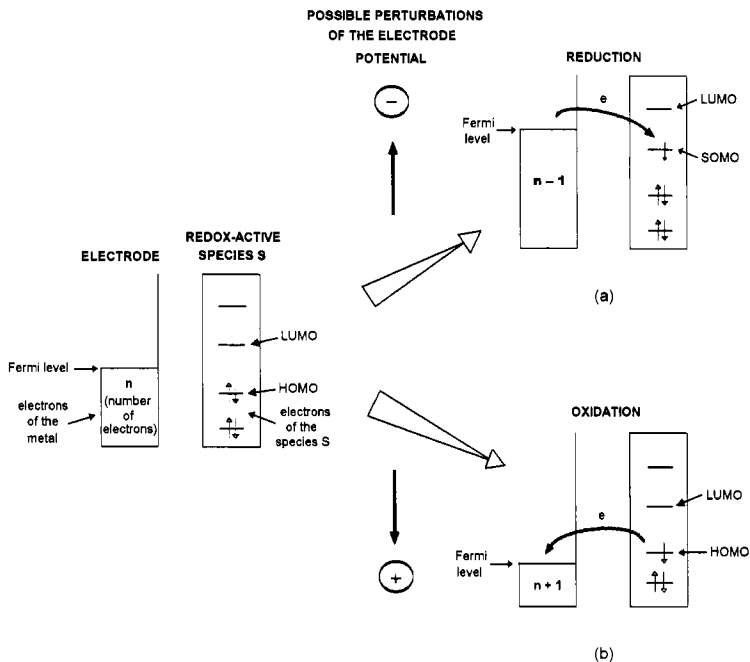
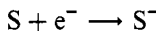


Figure 5 The potential of an electrode can be perturbed in order to trigger: (a) reduction processes; (b) oxidation processes

Let us consider the case of the reduction process:



By raising the electrode potential towards more and more negative values a threshold value will be reached: above this value the reduced form S^- is stabilized at the electrode surface, whereas below this value the oxidized form S is stabilized at the electrode surface. This threshold value is just defined as the standard potential of the S/S^- couple.

2.5 The Biunique Relationship Between Current and Potential

Since the potential regulates the energy of the electron exchanges, it also controls the rate of such exchanges and, hence, the current. This biunique correspondence between current and potential implies that if one of the two parameters is fixed the other, consequently, also becomes fixed.

3 POTENTIAL AND ELECTROCHEMICAL CELLS

As discussed in Section 2.3, for an electrode reaction to take place one needs two electrodes: a *working electrode*, at which the electron transfer

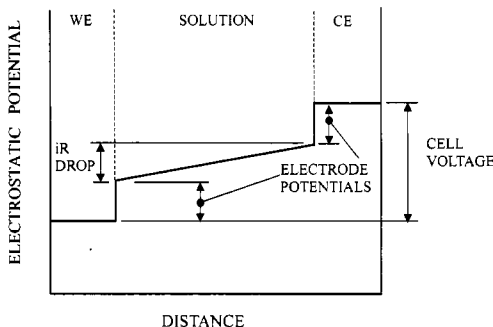


Figure 6 Potential profile along the path from the interior of the working electrode to the interior of the counterelectrode in the electrochemical experiment illustrated in Figure 4

process of interest occurs, and a *counter electrode*, that operates to maintain the electro-neutrality of the solution through a half-reaction of opposite sign, see Figure 4. Unfortunately, it is not possible to measure rigorously the absolute potential of each of the two electrodes (*i.e.* the energy of the electrons inside each electrode). The difference of potential set up between the two electrodes is, instead, easily experimentally measured and is defined as *cell voltage*, V . However, as illustrated in Figure 6, this cell voltage is the sum of a series of differences of potential.

At each of the two electrode/solution interfaces, where an electrical double layer is set up, there are sharp changes in potential. These changes of potential control the rate of the faradaic reactions that occur at the two electrodes. Each of the two jumps in potential is identified as the electrode potential of the respective electrodes. In addition, the cell voltage includes a further term because the solution has an intrinsic resistance, R_s . Therefore, when the current flows through the solution between the two electrodes it gives rise to the so-called *ohmic drop*, that, being equal to the product $i \cdot R_s$, is defined as the iR_s drop. Only when one is able to make $iR_s = 0$ (or at least render it negligible) does the measured cell voltage reflect the difference between the two electrode potentials (or, $V = \Delta E$).

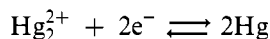
Since we are interested in controlling accurately the potential of the working electrode (in order to condition the rate of the electron transfer between this electrode and the electroactive species), we must work on the difference of potential between the two electrodes. It is clear, however, that changing the applied potential between the two electrodes causes unpredictable variations in the potential of either the working electrode, or the counter electrode, or in the iR drop. This implies that it

is impossible to control accurately the potential of the working electrode unless one resorts to a cell in which:

- the potential of the counter electrode is invariant;
- the iR drop is made negligible.

A counter electrode of constant potential is obtained making use of a half-cell system in which the components are present in concentrations so high as to be appreciably unaffected by a flow of current through it. The *saturated calomel electrode* (SCE) is the most common example of such an electrode. As shown in Figure 7, it is comprised of a mercury pool in contact with solid mercury(I) chloride and potassium chloride that lie at the bottom of the KCl saturated solution. The aqueous solution is thus saturated with Hg_2^{2+} , K^+ and Cl^- ions, the concentrations of which are governed by the solubility of the respective salts.

The eventual current flow through the electrode causes the following reaction to proceed in one of the two directions:



depending upon the direction of the current flow itself. Nevertheless, the activity of the solid species Hg and Hg_2Cl_2 is constant (by definition) and that of the Hg_2^{2+} ions, which are present in high concentration, also remains substantially constant. Consequently, the electrode potential also remains constantly fixed at the value determined by the well known *Nernst equation*, which we will examine in more detail in Section 4.1:

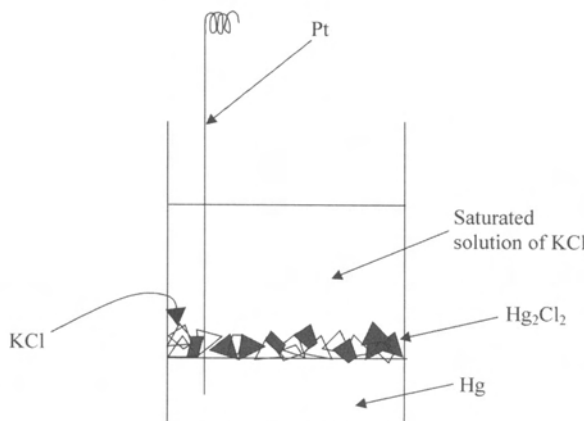


Figure 7 Schematic representation of the Saturated Calomel Electrode (SCE)

$$E = E_{\text{Hg}_{2+}/\text{Hg}}^{\circ} + \frac{2 \cdot 3 \cdot R \cdot T}{2 \cdot F} \log \frac{(a_{\text{Hg}_{2+}})}{(a_{\text{Hg}})^2}$$

This type of counter electrode is defined as a *reference electrode*. As we will see in Chapter 3, Section 1.2, at 25°C the saturated calomel electrode (SCE) has a potential of +0.2415 V with respect to the *standard hydrogen electrode* (NHE), which, although difficult to use, is the internationally accepted standard for the potential scale, having conventionally: $E^{\circ} = 0.000$ V.

Returning to the control of the potential of the working electrode in the electrochemical cell, the use of a reference electrode as a counter electrode makes every change in the applied potential difference between the two electrodes entirely assigned to the working electrode, provided that the iR drop is negligible. In this manner we would be able to control accurately the reaction rate at the working electrode.

Really, the use of a *two-electrode cell* (working and reference electrodes) must be considered only as a first attempt to control adequately the potential of the working electrode. In principle, that a reference electrode does function as a counter electrode has the disadvantage that the incoming current can cause instantaneous variations in the concentration of its components, therefore leading to a potential value different from the nominal one. In the majority of cases the relatively large surface area and the high concentration of active species typical of the reference electrodes make such variations in potential negligible. However, there are cases, such as large-scale electrolysis or fast voltammetric techniques in nonaqueous solvents, where the current flow is so high that the effects become non-negligible. Furthermore, there is still the problem of ohmic drop that, for example, in experiments performed in non-aqueous solvents, is by no means insignificant.

To overcome these difficulties one must use a *three-electrode cell*, which is shown schematically in Figure 8. Here, a third electrode, *auxiliary electrode* (AE) is inserted together with the working and the reference electrodes.

In principle, the auxiliary electrode can be of any material since its electrochemical reactivity does not affect the behaviour of the working electrode, which is our prime concern. To ensure that this is the case, the auxiliary electrode must be positioned in such a way that its activity does not generate electroactive substances that can reach the working electrode and interfere with the process under study. For this reason, in some techniques the auxiliary electrode is placed in a separate compartment, by means of sintered glass separators, from the working electrode.

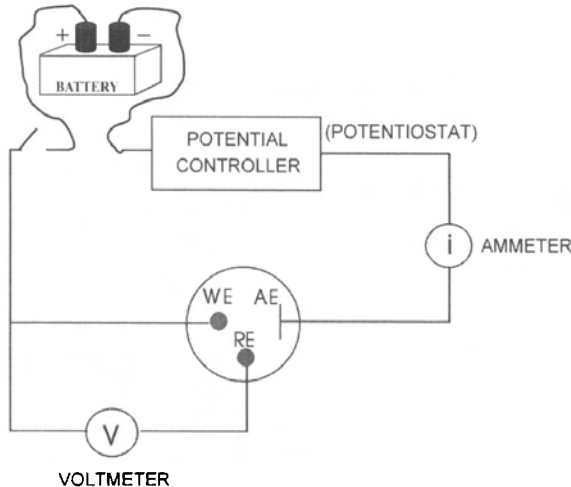


Figure 8 The electrode arrangement in a three-electrode cell: WE = working electrode; RE = reference electrode; AE = auxiliary electrode

In addition, the iR drop can be minimized by positioning the reference electrode close to the working electrode.

As deducible from Figure 8, to apply a precise ‘potential’ value to the working electrode means to apply a precise difference of potential between the working and the reference electrodes. Since the electronic circuit to monitor such potential difference, V , is properly assembled to possess a high input resistance, only a small fraction of the current generated in the electrochemical cell as a consequence of the applied potential enters the reference electrode (thus not modifying its intrinsic potential): most current is channelled between the working and the auxiliary electrodes.

Nevertheless, even with this experimental set-up, the iR drop is not completely eliminated. The situation can be improved if the reference electrode is placed very close to the working electrode through a *Luggin capillary*, see Figure 9.

The ideal positioning for the Luggin capillary is at a distance $2d$ from the surface of the working electrode, where d is the outlet diameter of the capillary.

If one bears in mind this new cell design, the iR drop can be reconsidered according to Figure 10 with respect to that represented in Figure 6.

As already mentioned, since the majority of the current has been conveyed towards the region between the working and the auxiliary electrodes, most of the ohmic drop iR_s has no influence on the cell voltage V between the working and the reference electrodes, thus allowing the condition:

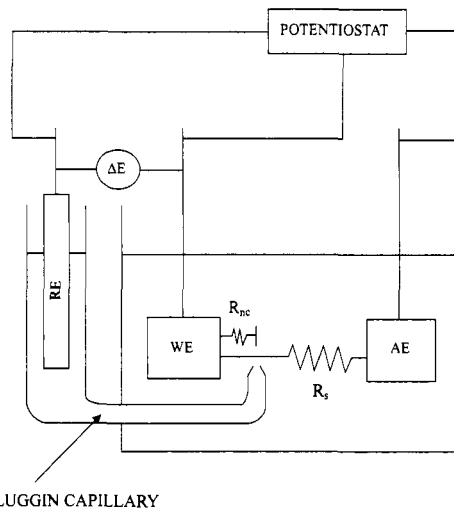


Figure 9 The ideal assembly of a three-electrode cell. R_s = (compensated) solution resistance; R_{nc} = uncompensated solution resistance

$$V = E_{WE} - E_{RE} = \Delta E$$

to be essentially reached.

It must, however, be kept in mind that one cannot eliminate the fraction of the non-compensated solution resistance R_{nc} , which generates the ohmic drop iR_{nc} . Unfortunately, the positioning of the reference electrode even closer to the working electrode ($< 2d$) would cause current oscillations.

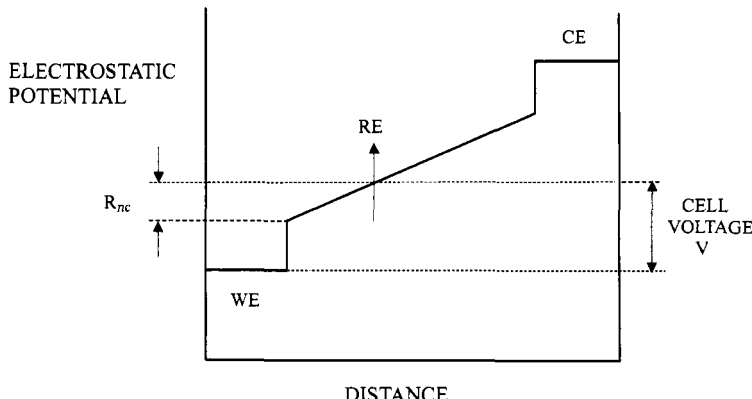


Figure 10 Potential profile in a three-electrode cell of the type illustrated in Figure 9 (see also Figure 6)

It should be emphasized that this design of the three-electrode cell gives good results in the majority of cases. However, as mentioned, in fast electrochemical techniques in non-aqueous solvents, iR_{nc} can assume values which compromise the accurate control of the potential of the working electrode and hence the achievement of reliable electrochemical data. In such cases one must employ *electronic circuits which compensate for the resistance of the solution*.

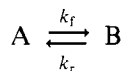
Nevertheless, it is important to appreciate that this type of three-electrode cell usually enables one to control easily the potential of the working electrode by forcing it to assume all the desired values and hence to control either the start of electrode processes or their rate.

4 KINETIC ASPECTS OF THE ELECTRODE REACTIONS

It was mentioned in Section 2.2 that even in the case of a simple electrode reaction one must take into account both heterogeneous electron transfer and mass transport processes. Let us therefore examine the mathematical relationships which govern the two processes.

4.1 Electron Transfer

Before examining the electrode reaction kinetics it is necessary to recall a few basic aspects of chemical kinetics. Consider the following elementary process:



where k_f ($f = \text{forward}$) and k_r ($r = \text{reverse}$) represent the rate constants of the reactions from left to right and from right to left, respectively.

Since, for an elementary step, *reaction order* and *molecularity* coincide, one can write:

$$\begin{aligned} v_f &= k_f \cdot C_A \\ v_r &= k_r \cdot C_B \end{aligned}$$

where C is the concentration of the species A and B respectively.

The overall rate of transformation of A into B can, therefore, be expressed by:

$$v = k_f \cdot C_A - k_r \cdot C_B$$

At equilibrium, the rate of conversion will be zero ($v_f = v_r$). Hence:

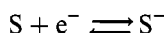
$$\frac{k_f}{k_r} = \frac{C_B}{C_A} = K$$

where K is the equilibrium constant of the reaction.

Thus, chemical kinetics predicts that under equilibrium conditions the ratio of the concentrations of the products and reagents is constant, as demanded by chemical thermodynamics. The agreement between kinetic and thermodynamic data is the ultimate test of any kinetic theory.

It is known that in chemical kinetics one can determine how the *free energy* of the system varies as a function of the *reaction coordinate*, i.e. the progress of the reaction.

Let us consider a simple faradaic process (*i.e.* accompanied neither by chemical complications nor by significant molecular rearrangements) of the type:



If a potential value corresponding to the equilibrium (zero-current) is applied to the working electrode so that both S and S⁻ are stable at the electrode surface, the process can be represented as in Figure 11.

The curves relative to the half-reactions intersect at the point corresponding to the formation of the so-called *activated complex*. The height of the energy barrier of the two redox processes (oxidation, h_{Ox} ; reduction, h_{Red}) is inversely proportional to the respective reaction rates. Since in this case $h_{\text{Ox}} = h_{\text{Red}}$, it is immediately apparent that these conditions identify the equilibrium conditions.

If one now sets the potential of the working electrode more positive than that of equilibrium, the oxidation process is facilitated (as seen in Figure 5). Thus, the profile of the free energy curves becomes that illustrated in Figure 12, in which the energy barrier for the oxidation is lower than that of reduction.

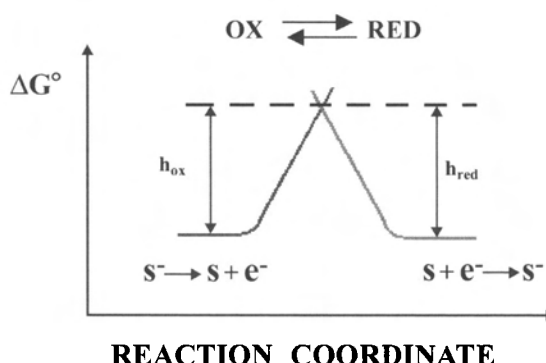


Figure 11 Free energy changes for the faradaic process $\text{S} + \text{e}^- \rightleftharpoons \text{S}^-$ as a function of the reaction coordinate at the equilibrium potential

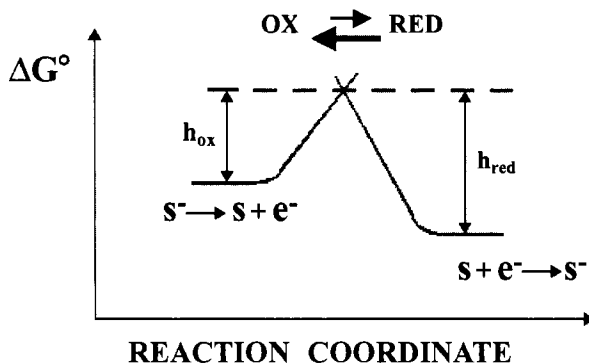
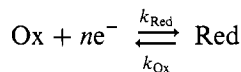


Figure 12 Free energy changes for the faradaic process $S + e^- \rightleftharpoons S^-$ at potential values more positive than the equilibrium value

On the other hand, if a potential more negative than that of equilibrium is applied to the working electrode, as indicated in Figure 13, the reduction process is favoured.

This being stated, it is now possible to examine the kinetic aspects of the electron-transfer processes.

Consider the general electron-transfer process:



where *Red* and *Ox* indicate *reduction* and *oxidation*, respectively.

Under equilibrium conditions the Nernst equation holds:

$$E_{\text{eq}} = E^\circ + \frac{R \cdot T}{n \cdot F} \ln \frac{a_{\text{Ox}}}{a_{\text{Red}}}$$

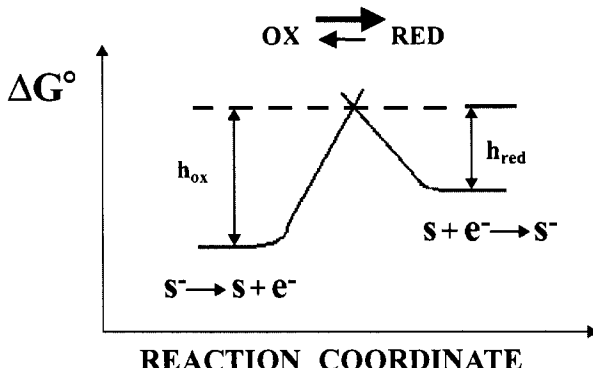


Figure 13 Free energy changes for the faradaic process $S + e^- \rightleftharpoons S^-$ at potential values more negative than the equilibrium value

where E° is the *standard potential* of the couple Ox/Red and a_{Ox} , a_{Red} express the activities of the two species. Substituting concentrations for activities one obtains:

$$E_{\text{eq}} = E^\circ + \frac{R \cdot T}{n \cdot F} \ln \frac{\gamma_{\text{Ox}}}{\gamma_{\text{Red}}} + \frac{R \cdot T}{n \cdot F} \ln \frac{C_{\text{Ox}}^*}{C_{\text{Red}}^*} = E^\circ' + \frac{R \cdot T}{n \cdot F} \ln \frac{C_{\text{Ox}}^*}{C_{\text{Red}}^*}$$

where:

γ = activity coefficient;

C^* = concentration of the active species in the bulk of the solution;

E°' = *formal electrode potential* of the couple Ox/Red. It differs from the thermodynamic *standard potential* E° by a factor related to the activity coefficients of the two partners Ox and Red:

$$E^\circ' = E^\circ + \frac{R \cdot T}{n \cdot F} \ln \frac{\gamma_{\text{Ox}}}{\gamma_{\text{Red}}}$$

As a consequence of the Nernst equation it follows that, when $C_{\text{Ox}}^* = C_{\text{Red}}^*$:

$$E^\circ' = E_{\text{eq}}$$

Since we have preliminarily stated that any kinetic theory must involve agreement between kinetic and thermodynamic data, it follows that, under equilibrium conditions, kinetic theory must afford relationships that coincide with the Nernst equation.

In the electrode process under consideration there is either the reduction path $[\text{Ox} \rightarrow \text{Red}]$ or the (inverted) oxidation path $[\text{Ox} \leftarrow \text{Red}]$. Expressing the concentration of a species, at a distance x from the electrode surface and at the time t , as $C(x,t)$, it follows from Section 2.3 that the reaction rate for the reduction reaction is given by:

$$v_{\text{Red}} = k_{\text{Red}} \cdot C_{\text{Ox}}(0,t) = \frac{i_c}{n \cdot F \cdot A}$$

where $C(0,t)$ is the concentration at the electrode surface ($x = 0$) and i_c is the produced *cathodic current*.

In a similar manner, for the oxidation reaction one obtains:

$$v_{\text{Ox}} = k_{\text{Ox}} \cdot C_{\text{Red}}(0,t) = \frac{i_a}{n \cdot F \cdot A}$$

where i_a is the produced *anodic current*.

The overall reaction rate can therefore be written as:

$$v = v_{\text{Red}} - v_{\text{Ox}} = k_{\text{Red}} \cdot C_{\text{Ox}}(0,t) = \frac{1}{n \cdot F \cdot A} (i_c - i_a)$$

This means that the current generated at the electrode is expressed by:

$$i = i_c - i_a = n \cdot F \cdot A \cdot [k_{\text{Red}} \cdot C_{\text{Ox}}(0,t) - k_{\text{Ox}} \cdot C_{\text{Red}}(0,t)]$$

The *rate constants* of the electron transfers vary with the electrode potential. In particular, in their Arrhenius form, they are expressed by:

$$k_{\text{Red}} = k^\circ \frac{\alpha \cdot n \cdot F}{k^\circ \cdot e^{R \cdot T}} (E - E^\circ) \quad k_{\text{Ox}} = \frac{(1 - \alpha) \cdot n \cdot F}{k^\circ \cdot e^{R \cdot T}} (E - E^\circ)$$

where:

k° = standard rate constant, which expresses the value of k_{Red} or k_{Ox} when the applied potential E is equal to E° ;

α = transfer coefficient ($0 < \alpha < 1$);

n = number of electrons (simultaneously) transferred per molecule of Ox.

Upon substituting in the preceding relationship:

$$i = i_c - i_a = n \cdot F \cdot A \cdot [k_{\text{Red}} \cdot C_{\text{Ox}}(0,t) - k_{\text{Ox}} \cdot C_{\text{Red}}(0,t)]$$

one obtains:

$$i = n \cdot F \cdot A \cdot k^\circ \cdot \left[C_{\text{Ox}}(0,t) \cdot e^{-\frac{\alpha \cdot n \cdot F}{R \cdot T} (E - E^\circ)} - C_{\text{Red}}(0,t) \cdot e^{\frac{(1 - \alpha) \cdot n \cdot F}{R \cdot T} (E - E^\circ)} \right]$$

This *current–potential* relationship, also known as the *Butler–Volmer equation*, governs all the (fast and single step) heterogeneous electron transfers.

4.1.1 A Deeper Insight into the Meaning of k° and α . At this point a better understanding of the two factors k° and α is called for.

The *heterogeneous* standard (or conditional) rate constant k° measures the *intrinsic ability* of a species (say, Ox) to exchange electrons with the electrode in order to convert to its redox partner (say, Red). A species with a large k° will convert to its redox partner on a short time scale; a species with a small k° will convert to its redox partner on a long time scale.

The largest values for the standard rate constant k° (expressed in metre/second) range from 0.01 m s^{-1} to 0.1 m s^{-1} , and commonly characterize redox processes which do not involve significant molecular reorganizations.

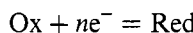
The smallest values for the standard rate constant k° are around $10^{-11} \text{ m s}^{-1}$.

We must however note that even if one partner of a redox couple does not possess a high propensity to exchange electrons with the electrode (*i.e.* low k°), we can force it to increase its electron transfer rate by applying to the working electrode a potential value higher than the formal electrode potential $E^{\circ'}$ of the couple itself (*i.e.* more negative for a reduction process; more positive for an oxidation process). In fact, as seen:

$$k_{\text{Red}} = k^\circ \cdot e^{-\frac{\alpha \cdot n \cdot F}{R \cdot T} (E - E^{\circ'})} \quad k_{\text{Ox}} = k^\circ \cdot e^{\frac{(1-\alpha) \cdot n \cdot F}{R \cdot T} (E - E^{\circ'})}$$

The transfer coefficient α is generally an index indicative of the symmetry of the energy barrier for a redox half-reaction. The significance of this definition is the following.

It has been shown previously that an electrode reaction can be depicted through ΔG° /reaction coordinate plots. Reconsidering the simple half-reaction:



let us apply to the working electrode a potential value E equal to the formal potential $E^{\circ'}$ of the couple Ox/Red. This means that the system is in equilibrium and the free energy curve will be of the type represented in Figure 14 (solid line).

If we apply to the working electrode a potential value different from $E^{\circ'}$, based on the well-known relationship: $\Delta G = -n \cdot F \cdot \Delta E$, the free energy of the electrode process will vary by $n \cdot F \cdot (E - E^{\circ'})$.

For instance, following the dashed line, if the potential of the electrode is made more positive than $E^{\circ'}$, we increase the activation barrier for the reduction process by $\alpha \cdot n \cdot F \cdot (E - E^{\circ'})$, while the activation barrier

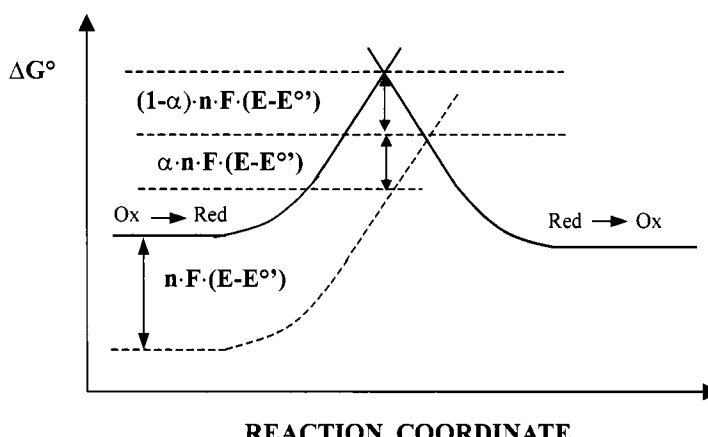


Figure 14 Free energy changes for a faradaic process. (—) $E = E^{\circ'}$; (---) $E > E^{\circ'}$

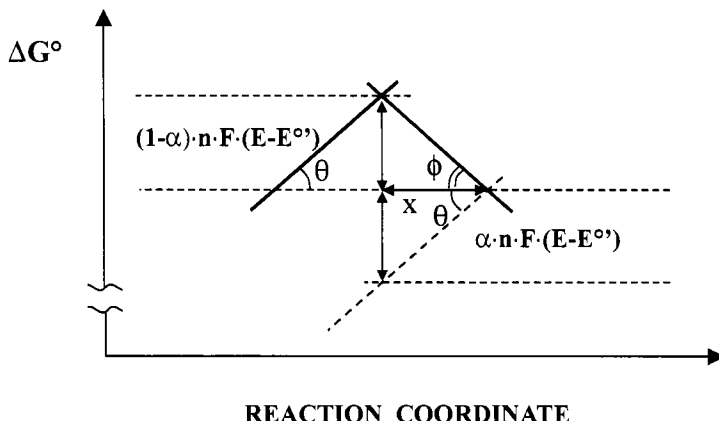


Figure 15 Relationship between the transfer coefficient α and the intersection angles of the free energy curves

for the oxidation process is lowered by an amount equal to the residual variation of the overall energy: $[n \cdot F \cdot (E - E^{\circ'}) - (\alpha \cdot n \cdot F \cdot (E - E^{\circ'})]$, or $(1 - \alpha) \cdot n \cdot F \cdot (E - E^{\circ'})$.

As far as the definition of α as a measure of the symmetry of the activation barrier is concerned, as shown in Figure 15, let us focus on the apical region of the intersection between the free energy curves illustrated in Figure 14.

If θ measures the slope of the curve of the reduction half-reaction and ϕ the slope of the oxidation half-reaction, simple trigonometric rules afford:

$$\tan \theta = \frac{\alpha \cdot n \cdot F \cdot (E - E^{\circ'})}{x} \quad \tan \phi = \frac{(1 - \alpha) \cdot n \cdot F \cdot (E - E^{\circ'})}{x}$$

so that:

$$\alpha = \frac{\tan \theta}{\tan \phi + \tan \theta}$$

As illustrated in Figure 16, it follows that if the slope of the reduction curve equals that of oxidation (*i.e.* if $\theta = \phi$) then $\alpha = 0.5$. Otherwise, α can assume values:

- between 0.0 and 0.5, if $\theta < \phi$
- between 0.5 and 1.0, if $\theta > \phi$.

4.1.2 Verification of the Theory Under Equilibrium Conditions. It has already been remarked that the ultimate test of any kinetic theory is that, under equilibrium conditions, the kinetic equations must coincide with the thermodynamic equations.

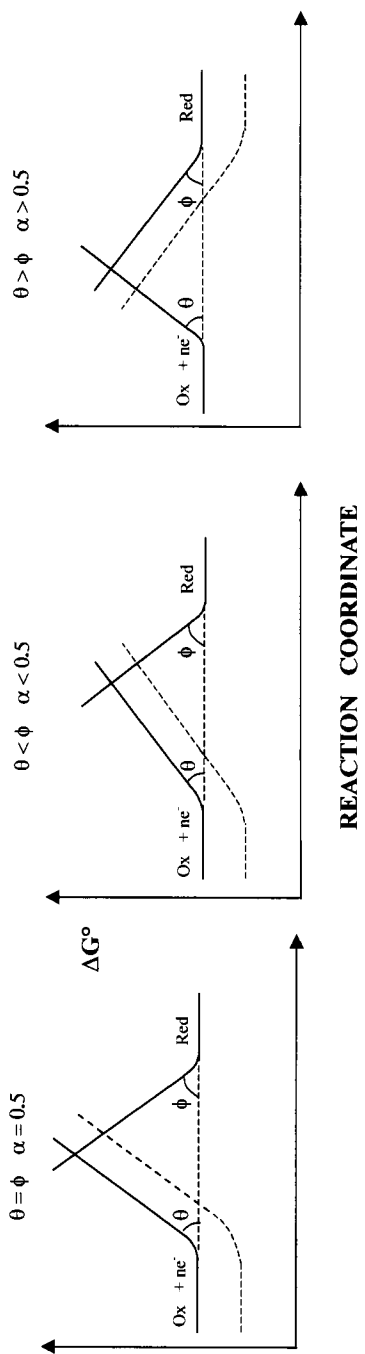


Figure 16 The transfer coefficient α as a measure of the symmetry of the activation barrier for a Faradaic process. The electrode conditions are those cited in Figure 14

The fundamental relationship for a heterogeneous charge transfer (Butler–Volmer equation) is:

$$i = n \cdot F \cdot A \cdot k^\circ \left[C_{\text{Ox}}(0,t) \cdot e^{-\frac{x \cdot n \cdot F}{R \cdot T} (E - E^{\circ'})} - C_{\text{Red}}(0,t) \cdot e^{\frac{(1-x) \cdot n \cdot F}{R \cdot T} (E - E^{\circ'})} \right]$$

Thus, when the electrode, depending upon the concentrations of Ox and Red, assumes an equilibrium potential, E_{eq} , (keep in mind that $E^{\circ'}$ is the ‘particular’ equilibrium potential set up when the concentrations of Ox and Red at the electrode surface are identical) it will reach the zero current condition ($i = 0$), so that:

$$\begin{aligned} n \cdot F \cdot A \cdot k^\circ \cdot C_{\text{Ox}}(0,t) \cdot e^{-\frac{x \cdot n \cdot F}{R \cdot T} (E_{\text{eq}} - E^{\circ'})} \\ = n \cdot F \cdot A \cdot k^\circ \cdot C_{\text{Red}}(0,t) \cdot e^{\frac{(1-x) \cdot n \cdot F}{R \cdot T} (E_{\text{eq}} - E^{\circ'})} \end{aligned}$$

from which:

$$\frac{C_{\text{Ox}}(0,t)}{C_{\text{Red}}(0,t)} = \frac{e^{\frac{(1-x) \cdot n \cdot F}{R \cdot T} (E_{\text{eq}} - E^{\circ'})}}{e^{-\frac{x \cdot n \cdot F}{R \cdot T} (E_{\text{eq}} - E^{\circ'})}} = e^{\frac{(1-x+x) \cdot n \cdot F}{R \cdot T} (E_{\text{eq}} - E^{\circ'})}$$

or:

$$\frac{C_{\text{Ox}}(0,t)}{C_{\text{Red}}(0,t)} = e^{\frac{n \cdot F}{R \cdot T} (E_{\text{eq}} - E^{\circ'})}$$

However, if there is an equilibrium between the two species at the electrode surface, such an equilibrium must also exist in the bulk of the solution. Hence:

$$\frac{C_{\text{Ox}}^*}{C_{\text{Red}}^*} = e^{\frac{n \cdot F}{R \cdot T} (E_{\text{eq}} - E^{\circ'})}$$

In reality such an expression is nothing more than the exponential form of the Nernst equation seen previously (Sections 3 and 4.1):

$$E_{\text{eq}} = E^{\circ'} + \frac{R \cdot T}{n \cdot F} \ln \frac{C_{\text{Ox}}^*}{C_{\text{Red}}^*}$$

thus confirming the validity of the Butler–Volmer equation.

4.1.3 Further Considerations on the Fundamental Equation of the Electron Transfer Process. The Exchange Current. It has been shown that, under equilibrium conditions (*i.e.* when both forms of a redox couple are present in solution), the faradaic current is zero. Such a result must be seen, however, in a dynamic context: the current is zero because the cathodic current (i_c) generated by the reduction process equals the

anodic current (i_a) generated by the oxidation process. This current, equal in both directions and exchanged under equilibrium conditions, is defined as the *exchange current*, i_0 .

As will now be discussed, the exchange current is proportional to the standard rate constant, thus resulting in the common practice of using i_0 instead of k° in kinetic equations.

Recall that under equilibrium conditions one has:

$$\begin{aligned} n \cdot F \cdot A \cdot k^\circ \cdot C_{\text{Ox}}(0,t) \cdot e^{-\frac{\alpha \cdot n \cdot F}{R \cdot T}(E_{\text{eq}} - E^\circ)} \\ = n \cdot F \cdot A \cdot k^\circ \cdot C_{\text{Red}}(0,t) e^{\frac{(1-\alpha) \cdot n \cdot F}{R \cdot T}(E_{\text{eq}} - E^\circ)} \end{aligned}$$

that can be rewritten substituting the concentrations at the electrode surface, $C(0,t)$, for the concentrations in the bulk of the solution, C^* .

The terms on either side of the equation are, in fact, now equal to i_c and i_a , respectively, under equilibrium conditions and each of the two terms represents i_0 . Considering one of the terms (for example, that on the left of the equation) one can write:

$$i_0 = n \cdot F \cdot A \cdot k^\circ \cdot C_{\text{Ox}}^* \cdot e^{-\frac{\alpha \cdot n \cdot F}{R \cdot T}(E_{\text{eq}} - E^\circ)}$$

Under equilibrium conditions it was also found that:

$$\frac{C_{\text{Ox}}^*}{C_{\text{Red}}^*} = e^{\frac{n \cdot F}{R \cdot T}(E_{\text{eq}} - E^\circ)}$$

Raising this expression to the power $-\alpha$ one obtains:

$$\left[\frac{C_{\text{Ox}}^*}{C_{\text{Red}}^*} \right]^{-\alpha} = e^{-\frac{\alpha \cdot n \cdot F}{R \cdot T}(E_{\text{eq}} - E^\circ)}$$

which, substituting in the expression for the exchange current i_0 , gives:

$$i_0 = n \cdot F \cdot A \cdot k^\circ \cdot C_{\text{Ox}}^{*(1-\alpha)} \cdot C_{\text{Red}}^{*\alpha}$$

Indeed, this is just the general expression that one uses to express the *exchange current*.

Sometimes, the exchange current is expressed as the *exchange current density*, J_0 :

$$J_0 = \frac{i_0}{A}$$

where A has its usual meaning of the electrode area.

Like the *standard rate constant*, k° , the *exchange current*, i_0 , characterizes the rate of the electron transfer process inside a redox couple.

As k° can range from about $0.1 \text{ m} \cdot \text{s}^{-1}$, for very fast processes, to about $10^{-11} \text{ m} \cdot \text{s}^{-1}$, for very slow processes, analogously the exchange current density varies from a few hundred $\text{kA} \cdot \text{m}^{-2}$ to a few tenths of $\text{nA} \cdot \text{m}^{-2}$ on passing from very fast to very slow electron exchanges.

As noted above, often the kinetic equations are written as a function of i_0 rather than k° . One of the advantages of using i_0 is that the faradaic current can be described as a function of the difference between the potential applied to the electrode, E , and the equilibrium potential, E_{eq} , rather than with respect to the formal electrode potential, E° , (which, as previously mentioned, is a particular case of equilibrium potential [$C_{\text{Ox}}(0,t) = C_{\text{Red}}(0,t)$]), and at times may be unknown). In fact, dividing the fundamental expression of i by that of i_0 one obtains:

$$\begin{aligned} \frac{i}{i_0} &= \frac{C_{\text{Ox}}(0,t) e^{-\frac{x \cdot n \cdot F}{R \cdot T}(E-E^\circ)}}{C_{\text{Ox}}^{*(1-x)} \cdot C_{\text{Red}}^{*x}} - \frac{C_{\text{Red}}(0,t) e^{-\frac{(1-x) \cdot n \cdot F}{R \cdot T}(E-E^\circ)}}{C_{\text{Ox}}^{*(1-x)} \cdot C_{\text{Red}}^{*x}} \\ &= \frac{C_{\text{Ox}}(0,t)}{C_{\text{Ox}}^*} e^{-\frac{x \cdot n \cdot F}{R \cdot T}(E-E^\circ)} \left(\frac{C_{\text{Ox}}^*}{C_{\text{Red}}^*} \right)^x - \frac{C_{\text{Red}}(0,t)}{C_{\text{Red}}^*} e^{\frac{(1-x) \cdot n \cdot F}{R \cdot T}(E-E^\circ)} \left(\frac{C_{\text{Ox}}^*}{C_{\text{Red}}^*} \right)^{-(1-x)} \end{aligned}$$

Since in the previous section it was shown that:

$$\frac{C_{\text{Ox}}^*}{C_{\text{Red}}^*} = e^{\frac{n \cdot F}{R \cdot T}(E_{\text{eq}}-E^\circ)}$$

substituting, one can write:

$$i = i_0 \cdot \left[\frac{C_{\text{Ox}}(0,t)}{C_{\text{Ox}}^*} e^{-\frac{x \cdot n \cdot F}{R \cdot T}(E-E_{\text{eq}})} - \frac{C_{\text{Red}}(0,t)}{C_{\text{Red}}^*} e^{\frac{(1-x) \cdot n \cdot F}{R \cdot T}(E-E_{\text{eq}})} \right]$$

Indicating with η , defined as *overvoltage*, the difference between the applied potential and the equilibrium potential ($\eta = E - E_{\text{eq}}$), one obtains:

$$i = i_0 \cdot \left[\frac{C_{\text{Ox}}(0,t)}{C_{\text{Ox}}^*} e^{-\frac{x \cdot n \cdot F}{R \cdot T}\eta} - \frac{C_{\text{Red}}(0,t)}{C_{\text{Red}}^*} e^{\frac{(1-x) \cdot n \cdot F}{R \cdot T}\eta} \right]$$

This important equation can be qualitatively interpreted in the following way. When the two components Ox and Red are present in solution at certain concentrations, the working electrode will spontaneously find its equilibrium potential (imposed by the Nernst equation) and there will be no overall current flow. In order for Ox to be reduced or Red oxidized, the system must be moved from equilibrium. This can be achieved by setting a potential different from that for equilibrium. The process of oxidation or reduction will be favoured depending on whether

the potential is moved towards more positive or more negative values, respectively, compared to the equilibrium potential. Moreover, the more the potential is removed from equilibrium the greater will be the current and, hence, the faster the faradaic process.

In fact, the above equation quantifies these considerations. The first term describes the *cathodic* component of the current, whereas the second term describes the *anodic* component.

As an example, Figure 17 shows how, for the generic process $\text{Ox} + ne^- = \text{Red}$, the current varies as a function of the electrode overvoltage.

The solid curve is the sum of the cathodic and anodic components, which are represented by the respective dashed lines.

It is evident that at very negative potential values (compared to E_{eq}) the anodic component is zero, so that the current is due only to the reduction process. The inverse effect occurs for very positive potentials (compared to E_{eq}). On the other hand, moving away from the equilibrium potential in either direction, even only slightly, the current rises rapidly as a consequence of the exponential terms in the equation. However, at high values of η the current reaches a *limiting value* (i_l), beyond which it can rise no more. This happens because the current is limited by the rate of the mass transport of the species Ox or Red from the bulk of the solution to the electrode surface, rather than from the rate of the heterogeneous electron transfer. Hence, one can say that the effect of the exponential factors in the equation is restrained by the ratios $C_{\text{Ox}}(0,t)/C^*_{\text{Ox}}$ and $C_{\text{Red}}(0,t)/C^*_{\text{Red}}$, which

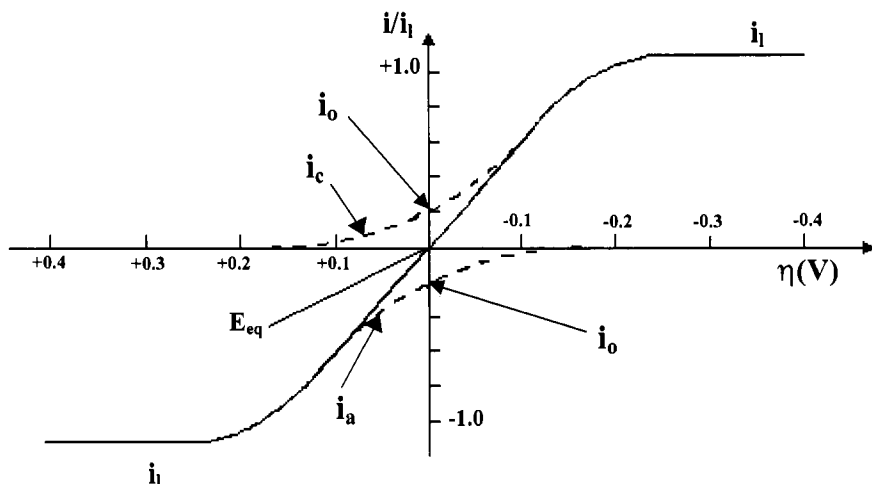


Figure 17 Current-overvoltage profiles for the process $\text{Ox} + ne^- = \text{Red}$. Experimental conditions: $\alpha = 0.5$; $n = 1$; $T = 25^\circ \text{C}$. The current is normalized with respect to the limiting value i_l

are directly related to the rate with which the electrode is supplied with electroactive material.

One can obtain a useful approximation of the preceding equation when the concentrations of Ox and Red at the electrode surface are not significantly different from their respective concentrations in the body of the solution (one can, for example, achieve such a condition by stirring the solution continuously). In fact, if $C(0,t) = C^*$, then:

$$i = i_0 \cdot \left[e^{-\frac{x \cdot n \cdot F \cdot \eta}{R \cdot T}} - e^{\frac{(1-x) \cdot n \cdot F \cdot \eta}{R \cdot T}} \right]$$

In some texts this relationship is also called the *Butler–Volmer* equation.

It is common practice to use this equation experimentally in one of the following three limiting forms:

- if one applies a potential that is much more negative than the equilibrium potential, the anodic component of the current will be negligible (as shown previously) and the equation becomes:

$$i = i_0 \cdot e^{-\frac{x \cdot n \cdot F \cdot \eta}{R \cdot T}}$$

- conversely, if one applies a potential much more positive than the equilibrium potential, the cathodic component will be negligible, hence:

$$-i = i_0 \cdot e^{-\frac{(1-x) \cdot n \cdot F \cdot \eta}{R \cdot T}}$$

The signs of the current refer to the American convention that reduction currents are positive, whereas oxidation currents are negative (remember that in electrochemistry the signs are conventional).

- when the difference between the applied and the equilibrium potential is very small, one can exploit the mathematical expression that, if x is small, $e^{-x} \approx 1 + x$, and the equation reduces to:

$$i = i_0 \cdot \left(\frac{n \cdot F}{R \cdot t} \cdot \eta \right)$$

This relationship indicates that the current which flows in a faradaic process is proportional to the applied overvoltage only in a small interval of potential values very close to E_{eq} (less than ± 100 mV).

4.2 Mass Transport

As seen previously (Section 2.2), the rate of an electron transfer is also conditioned by the rate with which the electrode is supplied with reagent and cleared of the electrogenerated product.

4.2.1 Possible Ways to Move a Species from the Bulk of the Solution to the Electrode Surface. There are three physical mechanisms by which a redox-active species can move from the mass of the solution to the electrode surface.

- *Convection* is the movement of a species under the action of a mechanical force (a gradient of pressure). The convective movements can be *fortuitous* (resulting from collisions or vibrations of the electrochemical cell) or *intentionally forced* (through controlled stirring).
- *Diffusion* is the movement caused by the presence in solution of regions with different concentrations of the active species (*a gradient of concentration*). It tends to randomize the distribution of molecules in a system transporting species from regions of high concentration to regions of low concentration. Electrode reactions are an ideal mode to generate diffusive movement. In fact, if a reaction $\text{Ox} \rightarrow \text{Red}$ is occurring at the electrode surface, it is obvious that in a layer of solution close to the electrode surface (thickness of about 0.0001 m) the concentration of Red will be higher and the concentration of Ox lower than that present in the mass of the solution, respectively. This concentration gradient of the two species makes more Ox move from the bulk of the solution to the electrode, while the species Red moves from the electrode surface (where it was generated) to the mass of the solution. The propulsive force clearly is to establish a uniform distribution of the two species in the whole of the solution.
- *Migration* is the movement of an ionic solute under the action of an electric field (*a gradient of electrical potential*). As a matter of fact, it is simply the movement of the ions in solution during an electrode process: the positive ions are attracted by the negatively charged electrode, while the negative ions are attracted by the positively charged electrode.

In order to derive mathematical equations able to describe the movement of a species towards or from an electrode surface it would be necessary to know the physical laws which govern the three modes of the mass transport.

Apart from a limited number of cases (laminar flows around a rotating disk or through a tubular electrode), it is very difficult to make a rigorous treatment of the convective movements.

It is even more difficult to handle mathematically migration (which depends on the dimensions of the ions, on the form and disposition of the electrodes, on the resistance of the solution, and so on).

Diffusion is the only mode of mass transport for which we possess well known mathematical treatments.

For this reason one always tries to minimize the effect of migration by adding a supporting electrolyte to the solution (*i.e.* a salt which produces non-electroactive ions in the potential region of interest) in a ratio of at least 100:1 compared to the electroactive species. In this way it is statistically more probable that, under the effect of an applied potential, the inert ions of the supporting electrolyte migrate to the electrodes rather than those of the electroactive species under study. Analogously, in order to avoid convection, the solution is maintained unstirred (or under accurately controlled stirring).

In conclusion, one always tries to study the electron transfer process under conditions where mass transport is governed only by diffusion (for which the laws are rigorously known).

4.2.2 Linear Diffusion at a Planar Electrode. Commonly, in order to deduce the mathematical relationships that govern the diffusion of an electroactive species towards the electrode, one considers an electron transfer process taking place at a *planar* electrode, in an unstirred solution, so to make active only the diffusive motion of the redox-active species in a direction perpendicular to the electrode surface, Figure 18.

The diffusive event involves two aspects:

- the variation of the concentration of the active species along the approaching distance to the electrode surface (*concentration gradient with space*)
- the variation of the concentration of the active species with time (*concentration gradient with time*).

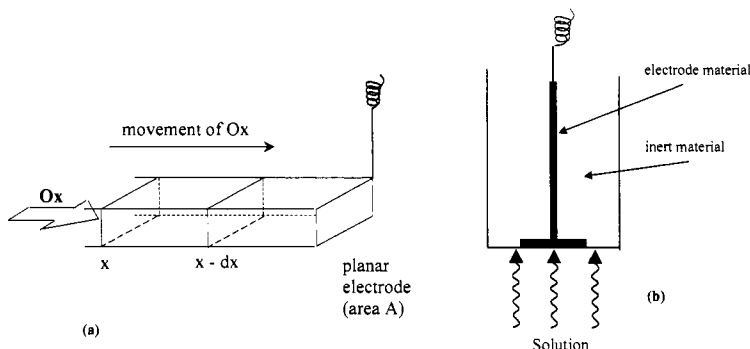
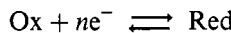


Figure 18 (a) Model of the linear diffusion to a planar electrode for the faradaic process $Ox + ne^- = Red$; (b) typical planar electrode for linear diffusion

To discuss these two aspects let us consider the usual electrode process:



Within the solution, let us consider the parallel-to-the-electrode plane at position x , see Figure 18a. The mole number of species Ox crossing the unit area of the plane per unit time is called *flux of Ox*, $J_{\text{Ox}}(x, t)$ (mol s⁻¹ m⁻²), and represents the rate of the mass transport.

According to *Fick's first law*, the flux of Ox is proportional to the concentration gradient of Ox along the direction of propagation:

$$-J_{\text{Ox}}(x, t) = D_{\text{Ox}} \cdot \frac{\delta C_{\text{Ox}}(x, t)}{\delta x}$$

The constant of proportionality, D_{Ox} , is defined as the *diffusion coefficient* of the species Ox. The units of the diffusion coefficients are m² s⁻¹. The negative sign is conventional.

As the reduction process $\text{Ox} \rightarrow \text{Red}$ proceeds, the species Ox, flowing through the plane x at the time t , reaches the electrode surface ($x = 0$) and instantaneously disappears to generate the species Red, which in turn will cross the plane x in the opposite direction. This means that:

$$-J_{\text{Ox}}(x, t) = J_{\text{Red}}(0, t)$$

Since the amount of species Ox reaching the electrode [or, $J_{\text{Ox}}(0, t)$] will generate a current, the intensity of which is proportional to the number of electrons exchanged with time (Section 2.3):

$$\frac{i}{n \cdot F \cdot A} = \frac{1}{A} \frac{dM}{dt}$$

we can write:

$$\begin{aligned} -J_{\text{Ox}}(0, t) &= \frac{i}{n \cdot F \cdot A} = D_{\text{Ox}} \cdot \left| \frac{\delta C_{\text{Ox}}(x, t)}{\delta x} \right|_{x=0} \\ &= J_{\text{Red}}(0, t) = -D_{\text{Red}} \cdot \left| \frac{\delta C_{\text{Red}}(x, t)}{\delta x} \right|_{x=0} \end{aligned}$$

In the first instance such an expression tells us that the current is a function of the concentration of the active species at any distance from the electrode. However the concentration of the active species depends either on distance or time. *Fick's second law* just determines how the concentration of species Ox changes with time.

Stated that $C_{\text{Ox}}(x, t)$ represents the concentration of Ox in the infinitesimal volume of solution between the planes x and $x - dx$ in Figure 18a,

the time dependence of the concentration will be given by the difference between the flux of Ox which enters the infinitesimal volume of solution and the flux of Ox which leaves the same element of volume, or:

$$\frac{\delta C_{\text{Ox}}(x, t)}{\delta t} = - \frac{\delta J_{\text{Ox}}(x, t)}{\delta x}$$

Upon substituting such a relationship in Fick's first law, we obtain:

$$\frac{\delta C_{\text{Ox}}(x, t)}{\delta t} = D_{\text{Ox}} \cdot \frac{\delta^2 C_{\text{Ox}}(x, t)}{\delta x^2}$$

The same holds for the species Red moving away from the electrode:

$$\frac{\delta C_{\text{Red}}(x, t)}{\delta t} = D_{\text{Red}} \cdot \frac{\delta^2 C_{\text{Red}}(x, t)}{\delta x^2}$$

4.2.3 Spherical Diffusion. If, as it might happen, the electrode is spherical rather than planar (*e.g.* using a hanging drop mercury electrode), See Figure 19, Fick's second law should be integrated by corrective terms accounting for the sphericity, or the radius r , of the electrode:

$$\frac{\delta C_{\text{Ox}}(x, t)}{\delta t} = D_{\text{Ox}} \frac{\delta^2 C_{\text{Ox}}(x, t)}{\delta x^2} + \frac{2}{r} \left(\frac{\delta C_{\text{Ox}}(x, t)}{\delta r} \right)$$

4.2.4 Concentration Profiles. Cottrell Equation. As previously mentioned, the region close to the electrode surface where the concentrations

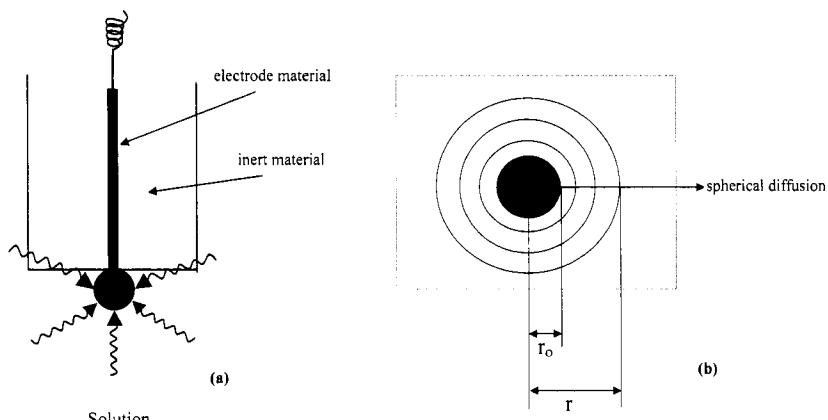


Figure 19 (a) Typical electrode for spherical diffusion; (b) parameters of the spherical diffusion: r_0 = radius of the electrode; r = radial distance at the time t

of Ox and Red are different from the corresponding ones in the bulk of the solution is defined as the *diffusion layer*.

During an electrode reaction in an unstirred solution, the thickness of the diffusion layer grows with time up to a limiting value of about 10^{-4} m, beyond which, because of the Brownian motion, the charges become uniformly distributed. At ambient temperature the diffusion layer reaches such a limiting value in about 10 s. This implies that in an electrochemical experiment, the variation of concentration of a species close to the electrode surface can be attributed to diffusion only for about 10 s, then convection takes place.

The graphs that show the dependence of the concentration of a species on distance from the electrode surface and how it evolves with time are called *concentration profiles*.

To obtain such diagrams, one must mathematically solve Fick's second law:

$$\frac{\delta C_{\text{Ox}}(x, t)}{\delta t} = D_{\text{Ox}} \cdot \frac{\delta^2 C_{\text{Ox}}(x, t)}{\delta x^2}$$

The resolution makes use of non-elementary mathematical treatments (Laplace transformation). Neglecting such treatments, one obtains:

$$C_{\text{Ox}}(x, t) = C_{\text{Ox}}^* \cdot \text{erf} \left[\frac{x}{2 \cdot (D_{\text{Ox}} \cdot t)^{1/2}} \right]$$

$$C_{\text{Red}}(x, t) = C_{\text{Ox}}^* \cdot \left(\frac{D_{\text{Ox}}}{D_{\text{Red}}} \right)^{1/2} \cdot \text{erfc} \left[\frac{x}{2 \cdot (D_{\text{Red}} \cdot t)^{1/2}} \right]$$

where, *erf* (*error function*) and *erfc* [*error function complement* ($\text{erfc} = 1 - \text{erf}$)] are trascendental functions of exponential type.

Figure 20 shows a series of concentration profiles at different times for the reaction: $\text{Ox} + ne^- \rightarrow \text{Red}$. In the experiment, at time $t = 0$ only the species Ox is present in solution, then the electrode potential is suddenly changed from a value more positive than the formal potential of the couple Ox/Red to a value much more negative, so that the reduction process $\text{Ox} \rightarrow \text{Red}$ immediately takes place.

The slope of each concentration profile expresses the concentration gradient of species Ox at various times, $\delta C_{\text{Ox}}(x, t)/\delta x$, where $\delta C_{\text{Ox}}(x, t) = C_{\text{Ox}}(x, t) - C_{\text{Ox}}^*$. The point at which the concentration gradient becomes zero (*i.e.* when $C_{\text{Ox}}(x, t) = C_{\text{Ox}}^*$, or $C_{\text{Ox}}(x, t)/C_{\text{Ox}}^* = 1$) identifies the thickness of the diffusion layer.

The thickness of the diffusion layer (in metres) is approximately: $6(D_{\text{Ox}} \cdot t)^{1/2}$.

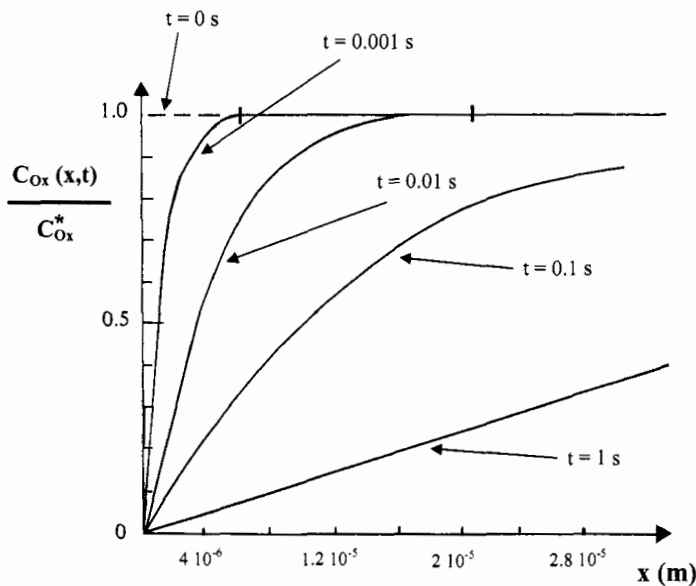


Figure 20 Concentration profiles of the species Ox at different times for the reaction $\text{Ox} + n\text{e}^- \rightarrow \text{Red}$. $D_{\text{Ox}} = 1 \cdot 10^{-9} \text{ m}^2 \text{ s}^{-1}$

For instance, for $D_{\text{Ox}} = 1 \cdot 10^{-9} \text{ m}^2 \text{ s}^{-1}$, we obtain:

time (s)	10^{-3}	10^{-2}	10^{-1}	1
thickness (m)	$6 \cdot 10^{-6}$	$2 \cdot 10^{-5}$	$6 \cdot 10^{-5}$	$2 \cdot 10^{-4}$

Figure 20 shows the accuracy of the calculation for the first two cases.

Clearly, as represented in Figure 21, concomitantly the concentration profiles of the species Red are opposite to those of Ox.

As the current is a function of the flux of species Ox that reaches the electrode surface:

$$\frac{i}{n \cdot F \cdot A} = D_{\text{Ox}} \cdot \left[\frac{\delta C_{\text{Ox}}(x,t)}{\delta x} \right]_{x=0}$$

it is well conceivable that the decrease of the gradient of Ox with time makes the current also decrease with time.

The dependence of the current upon time, once again, can be obtained by solving (in a non-elementary way) Fick's second law. The final result is:

$$i_{(t)} = \frac{n \cdot F \cdot A \cdot D_{\text{Ox}}^{1/2} \cdot C_{\text{Ox}}^*}{\pi^{1/2} \cdot t^{1/2}}$$

known as the *Cottrell equation*.

The linear dependence of the current on the square root of the time is just used as a diagnostic test for electrochemical reactions controlled by diffusion.

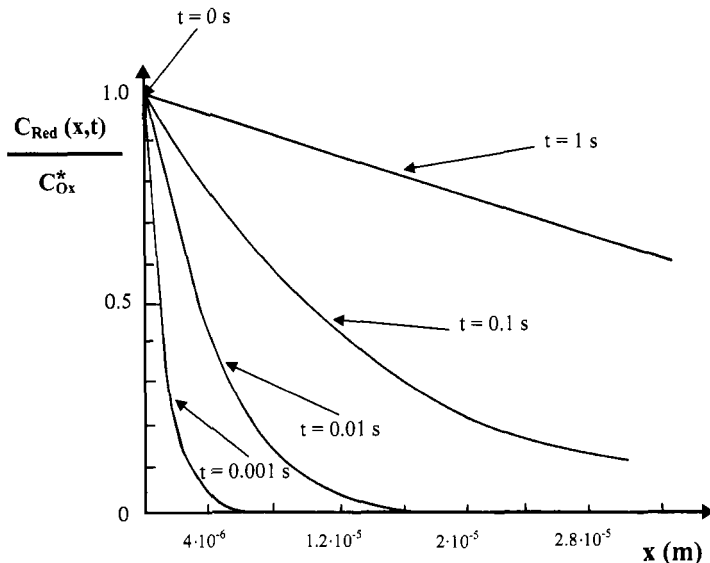


Figure 21 Concentration profiles of the species Red at different times for the reaction $\text{Ox} + n\text{e}^- \rightarrow \text{Red}$. $D_{\text{Red}} = D_{\text{Ox}} = 110^{-9} \text{ m}^2 \text{s}^{-1}$

It must be noted that the above relationship is derived from linear diffusion at a planar electrode. In the case of a spherical electrode of radius, r_0 , the above relationship becomes:

$$i_{(t)} = n \cdot F \cdot A \cdot D_{\text{Ox}} \cdot C_{\text{Ox}}^* \cdot \left[\frac{1}{(\pi \cdot D_{\text{Ox}} \cdot t)^{1/2}} + \frac{1}{r_0} \right]$$

which means that:

$$i_{(t) \text{spherical}} = i_{(t) \text{linear}} + \frac{n \cdot F \cdot A \cdot D_{\text{Ox}} \cdot C_{\text{Ox}}^*}{r_0}$$

It has been calculated, for example, that for an electrode of radius $r_0 = 0.001 \text{ m}$, the second term on the right of the equation becomes negligible (*i.e.* the simple laws of linear diffusion are valid also for spherical electrodes) if the response is recorded for a time lower than 3 s from the start of the faradaic process. Obviously, increasing r_0 also increases the time for which linear diffusion remains valid. It has been calculated that to an accuracy of 10%, and for $D_{\text{Ox}} = 1 \cdot 10^{-9} \text{ m}^2 \text{s}^{-1}$, the following relation holds:

$$\frac{\sqrt{t}}{r_0} \leq 1.8 \cdot 10^3$$

with t in s and r_0 in m.

Hence, the time t (in s) in which linear diffusion is valid for a spherical electrode of radius r_0 (in m) is:

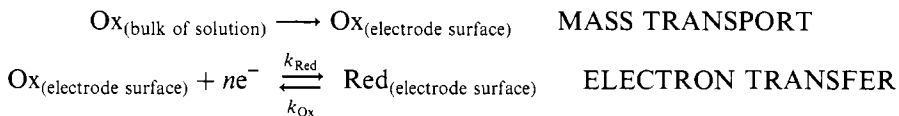
$$t \approx 3.2 \cdot 10^6 \cdot (r_0)^2$$

4.3 Influence of Mass Transport on Charge Transfer. Electrochemically ‘Reversible’ and ‘Irreversible’ Processes

In Sections 4.1 and 4.2, the *electron transfer* and the *mass transport* involved in a simple electrode reaction [simple = not complicated by preceding or following reactions, by absorption, or by formation of phases (see Section 2.2)] have been treated separately. However, it is to be expected that in reality both phenomena act in a concerted manner during a faradaic process. Thus, as seen previously, even the simple electrode process:



must be pictured, at its initial stage, in the following way:



In this connection, there are two fundamental types of behaviour:

- if the rate of the electron transfer is higher than the rate of the mass transport (or, if both k_{Red} and k_{Ox} are large, and greater than the rate constant of the mass transport), the process is defined as electrochemically *reversible*;
- if the rate of the electron transfer is lower than the rate of the mass transport (or, if k_{Red} and k_{Ox} are not both large, and lower than the rate constant of the mass transport), the process is defined as electrochemically *irreversible*.

It is commonly accepted that if:

$k^0 > 2 \cdot 10^{-4} \text{ m s}^{-1}$ the process is *reversible*

$k^0 < 5 \cdot 10^{-7} \text{ m s}^{-1}$ the process is *irreversible*

It must, however, be taken into account that the concept of electrochemical *reversibility* or *irreversibility* of an electron transfer is relative. In fact, to accelerate the redox processes one can act either on the mass transport (by stirring the solution) or on k_{Red} and k_{Ox} (by changing the electrode potential, as seen in Section 4.1.1).

As will become evident from an examination of the various voltammetric techniques, the electrochemical reversibility or irreversibility of a process influences the form of the relative current/potential curves.

5 NON-FARADAIIC PROCESSES. CAPACITIVE CURRENTS

Based on the way in which an electrode process has been illustrated, until now it would seem reasonable to assume that the only source of electron flow between the electrode and the species in solution might be attributed to faradaic processes of the type: $\text{Ox} + ne^- = \text{Red}$. It has already been mentioned in Section 2.3, however, that non-faradaic currents exist. Let us discuss their origin.

Recalling the arguments of Section 2.1, the electrode/solution interface can be considered to a first approximation as a double layer of the type reported in Figure 22.

A charge distribution of this type is completely analogous to that of a *capacitor*. Figure 23 illustrates what a capacitor is: two parallel metal plates separated by a dielectric material.

When a difference of potential ΔE is applied to the two plates, an excess q of electrons accumulates on one of them (which is equal to the

ELECTRODE	SOLUTION	ELECTRODE	SOLUTION
-	+	+	-
-	++	+	--
-	++	+	--
-	++	+	--
-	++	+	--
-	++	+	--
-	++	+	--

Figure 22 Approximate representation of the electrode/solution interface when the electrode potential is made: (a) negative, (b) positive

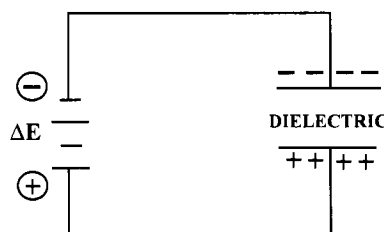


Figure 23 Scheme of the charging circuit of a capacitor

defect of electrons generated on the other plate) until the following relation is satisfied:

$$\frac{q}{\Delta E} = C$$

where:

- q = the charge on the capacitor (in coulombs),
- ΔE = the difference of potential applied between the two plates (in volts),
- C = the capacitance of the capacitor (in farads).

In other words, when one applies a difference of potential between the two plates of a capacitor, a current flows through the circuit until the capacitor is charged; this current is called the *capacitive current*.

This is just what happens in an electrochemical cell when a potential is applied between the working and the reference electrodes: the double layer setting up at the working electrode/solution interface generates capacitive currents.

To evaluate the magnitude of capacitive currents in an electrochemical experiment, one can consider the equivalent circuit of an electrochemical cell. As illustrated in Figure 24, in a simple description this is composed by a capacitor of capacitance C , representing the electrode/solution double layer, placed in series with a resistance R , representing the solution resistance.

As a result of the difference of potential ΔE applied between the working and reference electrodes, a capacitive current generates inside the cell which flows as a function of time, according to the relation:

$$i = \left(\frac{\Delta E}{R} \right)^{-t/R \cdot C}$$

This means that during an electrode reaction the capacitive currents decrease exponentially with time ($i \propto 1/\exp(t)$), whereas, as seen in

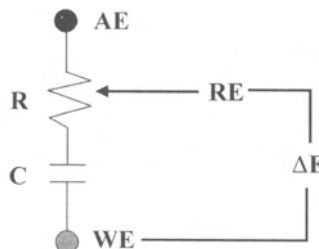


Figure 24 The simplest equivalent circuit of an electrochemical cell

Section 4.2.4, the faradaic currents fall off more slowly with time in that they decrease as a function of the square root of time ($i \propto 1/\sqrt{t}$). Consequently, the time dependence is a diagnostic test to discriminate between faradaic and capacitive (*i.e.* non-faradaic) currents.

In passing, it has to be underlined that the use of high concentrations of supporting electrolyte is also useful to minimize the capacitive currents (also called *charging* or *residual currents*).

6 THE ELECTRICAL DOUBLE LAYER. A DEEPER EXAMINATION

The description of the double layer reported in Figures 3 and 22 is only approximate; the composition of the electrode/solution region is somewhat more complex. The double layer has been studied in most detail for a mercury electrode immersed in an aqueous solution. According to Gouy–Chapman–Stern there are several layers of solution in contact with the electrode, see Figure 25.

The charge on the metallic electrode, q^M , (which, depending on the potential applied, can be negative or positive compared to the charge of the solution, q^S) is considered to be concentrated in a layer of about 0.1 Å close to the electrode surface.

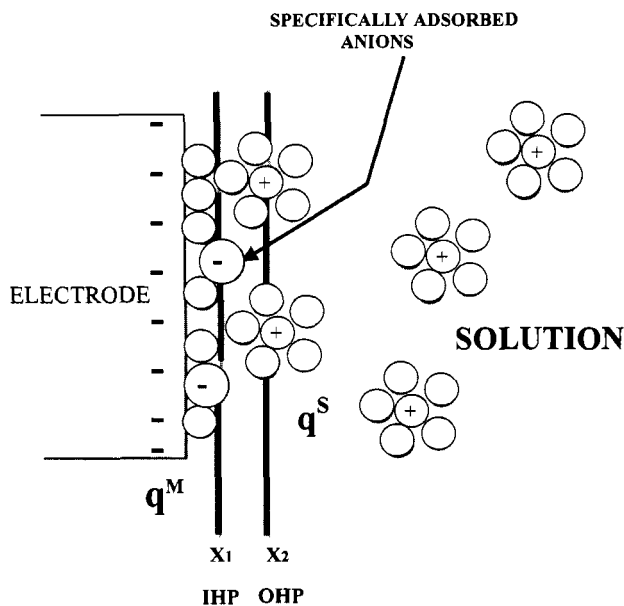


Figure 25 A detailed picture of the electrode/solution double layer

By contrast, the charge of the solution, q^S , is distributed in a number of layers. The layer in contact with the electrode, called the *internal layer*, is largely composed of solvent molecules and in a small part by molecules or anions of other species, that are said to be specifically adsorbed on the electrode. As a consequence of the particular bonds that these molecules or anions form with the metal surface, they are able to resist the repulsive forces that develop between charges of the same sign. This most internal layer is also defined as the *compact layer*. The distance, x_1 , between the nucleus of the specifically adsorbed species and the metallic electrode is called the *internal Helmholtz plane* (IHP). The ions of opposite charge to that of the electrode, that are obviously solvated, can approach the electrode up to a distance of x_2 , defined as the *outer Helmholtz plane* (OHP).

As the electrostatic interaction between the solvated ions and the metal is indirect, it is virtually independent of the chemical nature of the ions; these latter are said to be *non-specifically adsorbed*.

The region of solution between the OHP and the bulk of the solution is called the *diffusion layer*. The majority of the charge present in solution resulting from the applied electrode potential resides in this layer.

If one defines the *electrostatic potential of phase*, ϕ , as the work necessary to carry the unit charge from infinity to within this phase, all the layers of the double layer can be assigned a phase potential. In Figure 26 the variation in the potential profile within the double layer is shown.

The potential difference ($\phi^M - \phi^S$), known as the *interface potential*, cannot be measured, in that it would need the insertion of another electrode, *i.e.* another interface. What one can measure is the *electrochemical potential* of the electrode, E , with respect to a reference electrode; obviously every change of ($\phi^M - \phi^S$) is reflected in a variation of E , or *vice versa*.

6.1 The Kinetic Consequences of the Double Layer Composition on the Electron Transfer

In the treatment of the kinetics of the electron transfer illustrated in Section 4.1, it has been assumed that the propulsive force for the electron transfer was the electrochemical potential E (*i.e.* a quantity directly related to $\phi^M - \phi^S$). However, since the solvated ions cannot enter the inner layer of the double layer (IHP), the true propulsive force should be: $\phi^M - \phi^S - \phi_2$, or a quantity proportional to the term $(E - \phi_2)$. With this more precise statement (called *Frumkin's correction*) both the standard rate constant, k° , and the exchange current, i_0 , should become respectively:

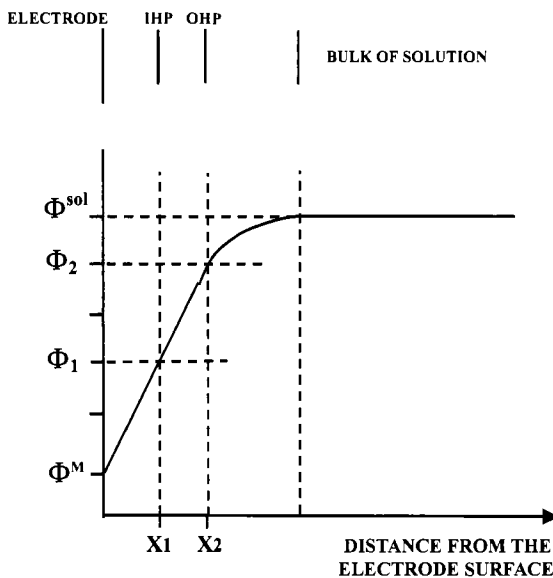
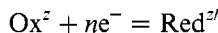


Figure 26 Profile of the phase electrostatic potential inside the double layer. See also Figure 25

$$k^\circ = k_{(t)}^\circ \cdot e^{\frac{(\alpha \cdot n - z) \cdot F \cdot \phi_2}{R \cdot T}} \quad i_0 = i_{0(t)} \cdot e^{\frac{(\alpha \cdot n - z) \cdot F \cdot \phi_2}{R \cdot T}}$$

where the subscript *t* (true) indicates the corrected factor, *z* is the charge of the species undergoing the general electrode process:



Such relationships allow one to calculate $k_{(t)}^\circ$ and $i_{0(t)}$ from the experimental determination of k° and i_0 (through the use of the Butler–Volmer equation).

It is noted that although it is possible to calculate ϕ_2 for mercury electrodes (*e.g.* through the so-called *electrocapillary curves*), for electrodes of other materials there is not this possibility, in that for such electrodes the composition of the double layer is unknown (one normally assumes it to be similar to that of mercury).

Finally, it must be taken into account that the use of large concentrations of supporting electrolyte minimizes the Frumkin effects. This is important in that we can now realize that high concentrations of supporting electrolyte not only minimize either migration or the capacitive currents, but also allow us to adopt the simple electrode kinetics discussed in Section 4.

REFERENCES

1. A.J. Bard and L.R. Faulkner, *Electrochemical Methods. Fundamentals and Applications*, 2nd Edn, J. Wiley, 2001.
2. L.R. Faulkner, *Electrochemical Characterization of Chemical Systems*. Physical Methods in Modern Chemical Analysis, Vol. 3, Academic Press, 1983.
3. Southampton Electrochemistry Group, *Instrumental Methods in Electrochemistry*, 2nd Edn, Horwood Publishing Limited, 2001.
4. P.H. Rieger, *Electrochemistry*, Chapman & Hall, London, 1994.
5. K.B. Oldham and J.C. Myland, *Fundamentals of Electrochemical Science*, Academic Press, 1994.
6. F. Scholz, Ed., *Electroanalytical Methods. Guide to Experiments and Applications*, Springer, 2002.

CHAPTER 2

Voltammetric Techniques

In inorganic electrochemistry the main target of an electrochemical experiment is to study in detail the electron transfer process of a species (whereas in analytical electrochemistry is that to analyse the composition of a sample).

An understanding of the redox behaviour of a species requires:

- the study of the *kinetic aspects* of the electron transfer processes exhibited by that species;
- the study of the *thermodynamic aspects* of such electron transfer processes.

We will examine here the simplest voltammetric techniques that allows one to gain such kinetic and thermodynamic parameters.^{1–5}

1 CYCLIC VOLTAMMETRY

A preliminary electrochemical overview of the redox aptitude of a species can easily be obtained by varying with time the potential applied to an electrode immersed in a solution of the species under study and recording the relevant current–potential curves. These curves first reveal the potential at which redox processes occur. In addition, the size of the currents generated by the relative faradaic processes is normally proportional to the concentration of the active species. Finally, the shape of the response as a function of the potential scan rate allows one to determine whether there are chemical complications (adsorption or homogeneous reactions) which accompany the electron transfer processes.

Voltammetric techniques involve perturbing the initial *zero-current* condition of an electrochemical cell by imposing a change in potential to the working electrode and observing the fate of the generated current as

a function of time (or, in some cases, by imposing a current and observing the potential).

Without any doubt, *cyclic voltammetry* is the most popular voltammetric technique used in the field of inorganic chemistry. Unfortunately, the power of the technique is frequently overestimated in that simple cyclic voltammetric measurements rarely allow one to gain complete electrochemical information. As we will discuss, it must be always coupled with complementary techniques.

Cyclic voltammetry belongs to the category of voltammetric techniques based on a *linear potential sweep chronoamperometric technique*. It certainly constitutes the most useful technique for a preliminary determination of the redox properties of a given species.

The experiment is carried out under stationary conditions (*i.e.* the solution is kept unstirred) in order to ensure that the mass transport is purely diffusive.

In linear sweep voltammetric techniques the applied electrode potential is varied from an initial value E_i to a final value E_f at a constant scan rate v (*single sweep voltammetry*). Once the value E_f is reached the direction of the scan can be reversed, maintaining the same scan rate v , and the potential brought back to the initial value (*cyclic voltammetry*). In the two cases the form of the potential-time impulse can be represented as shown in Figure 1.

The scan rate of the potential is usually in the range from 0.020 V s^{-1} to 100 V s^{-1} . Until a few years ago the resulting current–potential curves were recorded with a normal X–Y recorder up to a scan rate of about 0.5 V s^{-1} ; for higher scan rates it was necessary to use an oscilloscope. Recently, however, the use of personal computers interfaced with the electrochemical apparatus has overcome most recording problems.

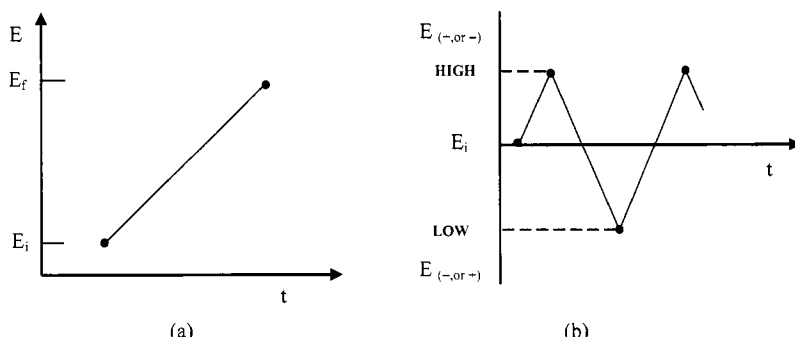
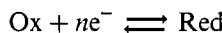


Figure 1 Potential–time pulses in: (a) linear sweep voltammetry; (b) cyclic voltammetry. The slope of each line measures the potential scan rate

1.1 Reversible (Nernstian) Processes

In order to look at the multiple shapes that the cyclic voltammograms can assume as a function of the nature of the different electrode processes, let us begin by examining the case of a reversible reduction process, not complicated by homogeneous reactions:



As previously stated, an electrode process is defined as *electrochemically reversible* when the rate of the electron transfer is higher than the rate of the mass transport.

Let us assume that only species Ox is initially present in solution, and that its movement to/from the electrode is governed by linear diffusion. If one starts from a potential value more positive than the formal potential $E^{\circ'}$ of the redox couple Ox/Red and proceeds at a certain scan rate towards values more negative than $E^{\circ'}$ (according to the potential-time pulse of the type illustrated in Figure 1a), a current–potential curve of the type shown in Figure 2 for the trace ABC is obtained.

The reason for the shape of the curve is not immediately obvious and can be explained by recalling the concentration profiles reported in Figure 3 (already seen in Chapter 1, Section 4.2.4).

When the scan of the potential reaches a value appropriate for the reduction of Ox, the concentration of Ox at the electrode surface begins to decrease with respect to that present in the bulk of the solution, C_{Ox}^* . This implies that a concentration gradient ($\delta C_{\text{Ox}}(x,t)/\delta x$) becomes established (recalling that: $\delta C_{\text{Ox}}(x,t) = C_{\text{Ox}}(x,t) - C_{\text{Ox}}^*$), and thus, from

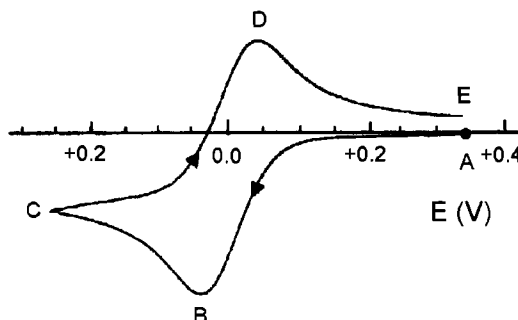


Figure 2 Typical cyclic voltammetric profile exhibited by a species which undergoes a reversible reduction at $E^{\circ'} = 0.00\text{ V}$

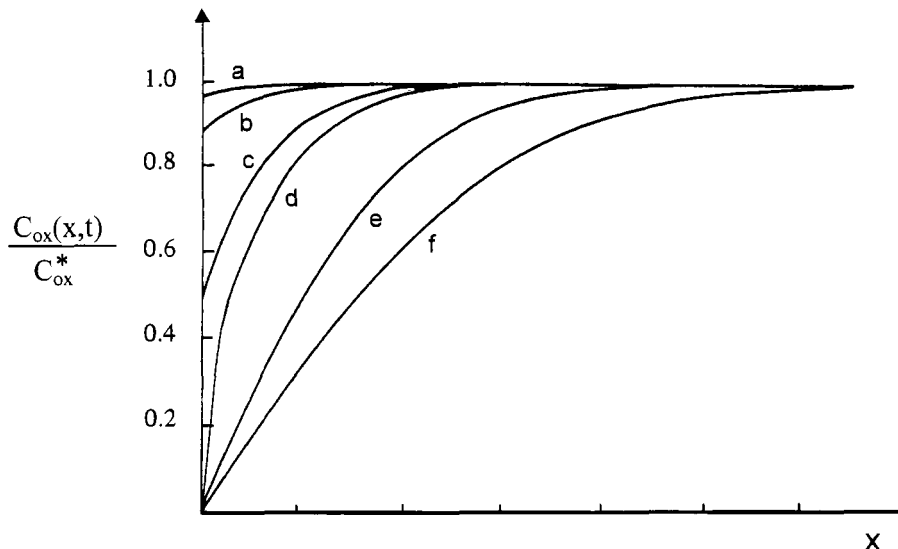


Figure 3 Concentration profiles of the species *Ox* during the proceeding of the half-reaction: $\text{Ox} + n\text{e}^- \rightarrow \text{Red}$

Fick's first law, a current begins to flow. Such an initial concentration gradient (assumed to be represented, for instance, by the curve 'a' in Figure 3) does not remain constant since, as shown previously, the diffusion layer tends to increase with time. However, more important than this effect is the linear scan of the potential towards negative values. This implies that to maintain the concentrations imposed by the Nernst equation an ever greater quantity of *Ox* is reduced such that the concentration gradient rises (say, curves 'b' and 'c' in Figure 3). The maximum value of this increase is reached when the concentration at the electrode surface becomes zero (*i.e.* $C_{\text{Ox}}(0,t) = 0$, which corresponds to curve 'd' in Figure 3). Consequently, the current increases to a maximum value. After this point, however, even increasing the potential towards more and more negative values, the gradient cannot increase further. Rather, it decreases due to the relaxation resulting from the enlargement of the diffusion layer with time; in fact: $\delta C_{\text{Ox}} = \text{constant}$, δx increases (curves 'e' and 'f' in Figure 3). Therefore, the current decreases.

When the direction of scan is reversed (according to the potential-time impulse of the type illustrated in Figure 1b), the voltammetric curve resembles the trace CDE of Figure 2 because exactly the same phenomenon becomes established for the newly electro generated species

$C_{\text{Red}}(x,t)$, still present close to the electrode surface. Obviously, as a consequence of the variation of the potential towards more positive values, this new species will be reoxidized.

The above qualitative discussion is quantitatively described by solving Fick's second law for both Ox and Red.

$$\frac{\delta C_{\text{Ox}}(x, t)}{\delta t} = D_{\text{Ox}} \cdot \frac{\delta^2 C_{\text{Ox}}(x, t)}{\delta x^2}$$

$$\frac{\delta C_{\text{Red}}(x, t)}{\delta t} = D_{\text{Red}} \cdot \frac{\delta^2 C_{\text{Red}}(x, t)}{\delta x^2}$$

The solution of these equations needs a few boundary conditions.

- **Initial boundary conditions**

If initially only the species Ox is present in solution and one assumes that $D_{\text{Ox}} = D_{\text{Red}} = D$, the initial conditions are:

$$\left. \begin{array}{l} \text{at time } t = 0 \quad C_{\text{Ox}}(x, 0) = C_{\text{Ox}}^* \\ \quad C_{\text{Red}}(x, 0) = 0 \end{array} \right\} \quad \text{for any distance } x \text{ from the electrode}$$

- **Semi-infinite boundary conditions**

$$\left. \begin{array}{l} \text{for } x \rightarrow \infty \quad C_{\text{Ox}}(x, t) = C_{\text{Ox}}^* \\ \quad C_{\text{Red}}(x, t) = 0 \end{array} \right\} \quad \text{at all times } t$$

- **Electrode surface boundary conditions**

The conditions at the electrode surface, once the reduction process has been triggered, are (see Chapter 1, Section 4.2.2):

$$-J_{\text{Ox}}(0, t) = \frac{i}{n \cdot F \cdot A} = D_{\text{Ox}} \cdot \left| \frac{\delta C_{\text{Ox}}(x, t)}{\delta x} \right|_{x=0}$$

If the process is reversible, $J_{\text{Ox}}(0, t) = -J_{\text{Red}}(0, t)$, and therefore:

$$D_{\text{Ox}} \cdot \left| \frac{\delta C_{\text{Ox}}(x, t)}{\delta x} \right|_{x=0} + D_{\text{Red}} \cdot \left| \frac{\delta C_{\text{Red}}(x, t)}{\delta x} \right|_{x=0} = 0$$

Such boundary conditions are common to all electrochemical processes. In the case of a linear scan of the potential with time, we

must also take into consideration that the following potential-time relationships hold at any time:

$$\begin{aligned} 0 < t < t_f \quad E &= E_i - v \cdot t \\ t > t_f \quad E &= E_i - 2 \cdot v \cdot t_f + v \cdot t \end{aligned}$$

where:

t_f = time at which the direction of the potential scan is reversed;

E_i = initial potential;

v = scan rate.

This being stated, applying *Laplace's transform* one obtains from Fick's second law that the maximum current (*i.e.* the current at the potential corresponding to the maximum of the peak) for a planar electrode is expressed by:

$$i_p = 0.4463 \cdot A \cdot C_{\text{Ox}}^* \cdot \frac{n^3 \cdot F^3 \cdot D_{\text{Ox}} \cdot v}{\sqrt{R \cdot T}}$$

which, at 25°C, gives:

$$i_p = 2.69 \cdot 10^5 \cdot n^{3/2} \cdot A \cdot D_{\text{Ox}}^{1/2} \cdot C_{\text{Ox}}^* \cdot v^{1/2}$$

where:

i_p = forward peak-current (A);

n = number of electrons exchanged per molecule of O_x ;

A = area of the electrode (m^2);

D_{Ox} = diffusion coefficient of Ox ($\text{m}^2 \text{s}^{-1}$);

C_{Ox}^* = concentration of Ox (mol l^{-1})

v = potential scan rate (V s^{-1}).

Such an expression is called the *Randles–Sevcik equation*.

It is evident that (once the electrochemical reversibility of the process under examination has been checked, see the next section) the experimental measurement of the peak current, i_p , allows one to calculate one of the parameters appearing in the equation. For instance, if the peak current i_p at a certain scan rate v is measured, knowing the area of the electrode A , the diffusion coefficient D and the concentration C of the species under study, one can compute the number of electrons n involved in the redox change. On the other

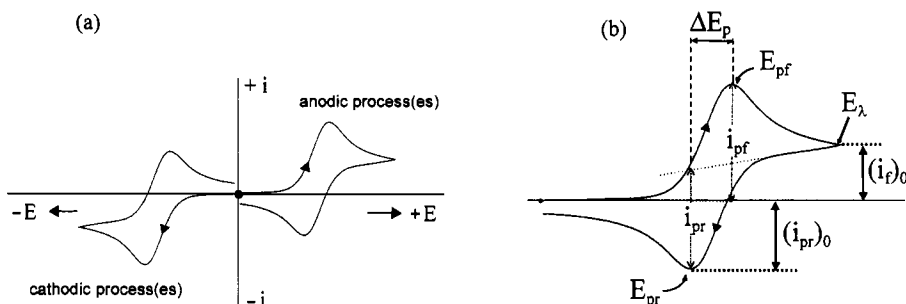


Figure 4 (a) The conventional signs of currents and potentials in cyclic voltammetry. (b) Basic parameters for a cyclic voltammogram: E_{pf} = potential of the forward peak; E_{pr} = potential of the return peak; E_λ = potential value at the inversion of the scan direction; i_{pf} = current of the forward peak with respect to its baseline; i_{pr} = current of the return peak with respect to its baseline; ΔE_p = peak-to-peak separation; $(i_{pr})_0$ = current of the return peak with respect to the zero current baseline; $(i_f)_0$ = current at the inversion potential with respect to the zero current baseline

hand, if one knows the number of electrons n that the species can exchange, one can calculate the diffusion coefficient D of the species; and so on.

1.1.1 Diagnostic Criteria to Identify a Reversible Process. The foregoing mathematical treatment offers the opportunity to determine the characteristics of a cyclic voltammetric response originating from a reversible process, when the voltammogram is recorded at several scan rates [possibly progressively going from low (about 0.02 V s^{-1}) to high (about 50 V s^{-1}) scan rates].

Firstly, however, one should consider, on the basis of Figure 4, which are the IUPAC recommendations on the signs of the currents[†] and the main parameters of a cyclic voltammogram.

For any process the ratio between the current of the *reverse* peak and that of the *forward* peak, i_{pr}/i_{pf} , is particularly important. This current ratio is the parameter which allows one to judge the *chemical reversibility* of an electrode reaction. In fact, when such a ratio is equal to 1, the electrogenerated species Red is stable (at least on the cyclic voltammetric timescale). The i_{pr}/i_{pf} ratio is easily calculated in computerized instrumentation or must be determined graphically in

[†]The potential/current signs in the IUPAC convention follows the criterium: 'positive currents for processes occurring at positive potentials', and *vice versa*. The American convention still adopts the opposite criterium: 'positive currents for processes occurring at negative potentials', and *vice versa*. Even if the present theoretical treatment follows the American convention (positive sign to reduction processes), in presenting cyclic voltammetric profiles the IUPAC recommendation will be adopted.

the older instrumentation. In the latter case it can be estimated in the way indicated in Figure 4b, either by drawing the baselines of the curves for both the forward and the reverse peaks, or through the empirical relation:

$$\frac{i_{\text{pr}}}{i_{\text{pf}}} = \frac{(i_{\text{pr}})_0}{i_{\text{pf}}} + \frac{0.485 \cdot (i_f)_0}{i_{\text{pf}}} + 0.086$$

where, as illustrated in Figure 4b:

$(i_{\text{pr}})_0$ = reverse peak current not corrected for the baseline;

$(i_f)_0$ = forward peak current at the inversion potential E_f [$(i_f)_0 \neq i_{\text{pf}}$].

This relationship is particularly useful when the forward peak is accompanied by successive peaks at a distance which inhibits a good baseline from being drawn for the reverse peak. In this case, the automatic data given by computerized apparatus may not be completely reliable.

Returning now to the diagnostic criteria for a reversible process, they can be subdivided as follows.

Properties of the Potential

- the potential of the forward peak, E_{pf} , is independent of the scan rate;
- the separation between the potentials of the forward and reverse peaks (called *peak-to-peak separation*), ΔE_p , at 25°C, is equal to $59/n$ mV (n being the number of electron exchanged per molecule of O_x), and such value maintains constant with scan rate.

This value arises from the relationship:

$$\Delta E_p = \frac{2.3 \cdot R \cdot T}{n \cdot F}$$

It means that, for reversible one-electron processes, the peak-to-peak separation assumes different values as a function of the temperature; namely:

$T(^{\circ}\text{C})$	50	25	20	10	0	-10	-20	-50
$\Delta E_p(\text{mV})$	64	59	58	56	54	52	50	44

Similar to the current ratio, the peak-to-peak separation ΔE_p is another important parameter in that it relates to the *electrochemical*

reversibility of an electrode reaction, *i.e.* the rate of the electron transfer (see also below).

It must be however underlined that, in measuring the peak-to-peak separation, a departure of 10–20 mV from the theoretical value (especially at relatively high scan rates) does not compromise the criterion of *reversibility*, in that the eventual presence of solution resistances not adequately compensated by the electrochemical instrumentation (see Chapter 3, Section 2) tends to lay down the forward/reverse peaks system, thus increasing the relative ΔE_p value.

Properties of the Current

- the ratio between the current of the forward peak and the square root of the scan rate, $i_{\text{pf}}/\nu^{1/2}$, is constant with the scan rate;
- the current ratio between the reverse and the forward peaks, $i_{\text{pr}}/i_{\text{pf}}$, is constant and equal to 1.0.

Let us finally point out that the characterization of an electrochemically reversible step lies on the only thermodynamic parameter: the *formal electrode potential* of the redox couple Ox/Red, $E_{\text{Ox}/\text{Red}}^{\circ'}$, which is commonly measured as the average value:

$$E_{\text{Ox}/\text{Red}}^{\circ'} = \frac{1}{2}(E_{\text{pf}} + E_{\text{pr}})$$

under the assumption that $D_{\text{Ox}} = D_{\text{Red}}$.

1.1.2 The Chemical Meaning of an Electrochemically Reversible Process. Before passing to subsequent electrochemical mechanisms, it is important to discuss briefly the chemical meaning of an electrochemically reversible process. In this connection, we must take into account that one of the most important factors which contribute to the enhancement of the activation barrier of a redox step is the extent of *geometrical reorganization* which accompanies the electron transfer (see Chapter 11). In this light, the occurrence of an electrochemically reversible process (or an electrode process in which the rate of the electron transfer is higher than the rate of the mass transport) suggests that no important structural reorganization is likely to accompanies the redox step.

For instance, Figure 5 shows the electrochemical response given by $[\text{Fe}(\eta^5\text{-C}_5\text{Me}_5)_2]$, in dichloromethane solution.

The well known ferrocene/ferrocenium oxidation possesses the features typical of electrochemical reversibility. This foreshadows the substantial maintenance of the original molecular geometry on passing from decamethylferrocene to decamethylferrocenium. As a matter

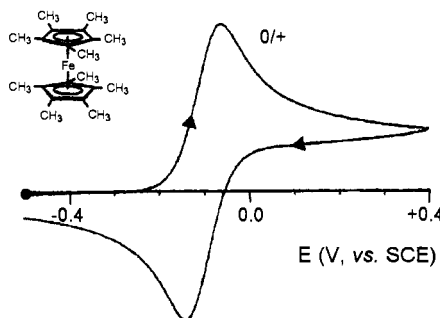


Figure 5 Cyclic voltammogram recorded at a platinum electrode in a dichloromethane solution of $[Fe(\eta^5\text{-}C_5\text{Me}_5)_2]$. Scan rate 0.2 V s^{-1}

of fact, as we will see in Chapter 4, Section 1.1 in more detail and as deducible from Table 1, the X-ray structure of the two redox congeners support such an assumption.

The sandwich geometry is maintained upon one-electron removal, and only a slight elongation of the Fe–C bonding distances occurs.

1.1.1.1 Cyclic voltammetry at spherical electrodes. As discussed in Chapter 1, Section 4.2.3, diffusion laws at a spherical electrode must take into account the curvature r_0 of the electrode. The mathematical treatment of diffusion at a spherical electrode becomes somewhat more complicated⁶ with respect to the preceding one for planar diffusion and we will not dwell on it. On the basis of what we will see in Chapter 11, Section 2, it is important to consider that, under *radial* diffusion, the cyclic voltammogram loses its peak-shaped profile to assume a sigmoidal profile, see Figure 6.

From a qualitative viewpoint this happens because the mass transport is specifically oriented towards the electrode surface, so that more amounts of species Ox reach the electrode surface in the unit time for unit area with respect to a planar electrode. This allows a steady-state condition to be reached (or the total depletion of Ox at the electrode

Table 1 Comparison of the bonding distances (\AA) of $[Fe(\eta^5\text{-}C_5\text{Me}_5)_2]$ and $[Fe(\eta^5\text{-}C_5\text{Me}_5)_2]^+$ (bond lengths rounded off to the second decimal figure)

	$Fe\text{-}C$	$Fe\text{-}Cp_{(centroid)}$	$C_{(ring)}\text{-}C_{(ring)}$	$C_{(ring)}\text{-}C_{(methyl)}$
$[Fe(\eta^5\text{-}C_5\text{Me}_5)_2]$	2.05	1.66	1.42	1.50
$[Fe(\eta^5\text{-}C_5\text{Me}_5)_2]^+$	2.10	1.71	1.42	1.50

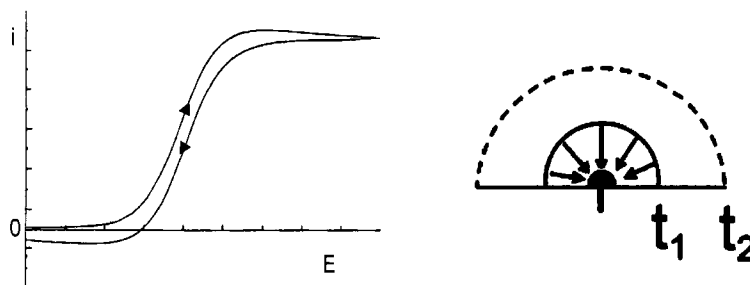


Figure 6 Typical cyclic voltammogram obtained at a spherical (or hemispherical) (micro)electrode under experimental conditions such that only radial diffusion is operative

surface is prevented) because the mass transport predominates over the rate of the electron transfer.

Obviously, in order to obtain experimental conditions under which the *radial diffusion* might dominate over the *linear diffusion* (recall that in Chapter 1, Section 4.2.4, we have stated that at short times even at spherical, normal-sized electrodes linear diffusion holds), two requirements are needed:

- the radius of the electrode must be micron-sized ($r_0 \approx 1\text{--}10 \mu\text{m}$; these electrodes are defined as *microelectrodes*^{3,7})
- the experiment must involve relatively long times (i.e. slow scan rates).

1.2 Irreversible Processes

If the rate of the electron transfer is lower than that of the mass transport, or in the case of irreversible processes (see Chapter 1, Section 4.3), the potential at which the reduction reaction $\text{Ox} + ne^- \rightarrow \text{Red}$ takes place can be much more cathodic than the formal electrode potential of the couple Ox/Red . In addition, commonly the separation between the forward peak and the reverse peak is so large that the reverse peak is undetected.

A typical shape of an electrochemically irreversible process is shown in Figure 7.

Also in this case the shape of the voltammogram can be mathematically accounted for by solving Fick's second law for the two species Ox and Red .

The initial conditions and those at semi-infinite distance are the same as for the reversible case. The conditions at the electrode surface differ. In this case they are:

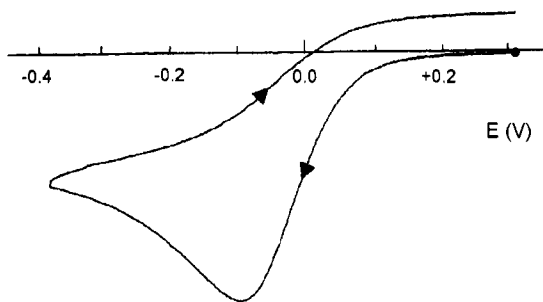


Figure 7 Typical cyclic voltammetric profile of an irreversible reduction process

$$\frac{i}{n \cdot F \cdot A} = D_{\text{Ox}} \cdot \left| \frac{\delta C_{\text{Ox}}(x, t)}{\delta x} \right|_{x=0} = k_{\text{Red}} \cdot C_{\text{Ox}}(0, t) = C_{\text{Ox}}(0, t) \cdot k^\circ \cdot e^{-\frac{x n_\alpha \cdot F}{R \cdot T} (E - E^\circ)}$$

where n_α is the number of electrons exchanged in the slowest step. Clearly, n_α can be smaller or equal to the overall number of electrons n exchanged per molecule of Ox. Obviously, for a one-electron process, $n_\alpha = 1$.

The numeric solution of the relative differential equations gives that, at 25°C:

$$i_p = 2.99 \cdot 10^5 \cdot n \cdot (\alpha \cdot n_\alpha)^{1/2} \cdot A \cdot D_{\text{Ox}}^{1/2} \cdot C_{\text{Ox}}^* \cdot v^{1/2}$$

where the various parameters are expressed in the same units as in the case of the reversible process.

As anticipated, for an irreversible process the forward peak is located at potentials more negative than if it were reversible (*i.e.* compared to its standard thermodynamic potential). Moreover, since the above relationship shows that the peak current depends on the square root of the transfer coefficient α , under equivalent conditions the height of the irreversible peak equals 78.6% of the reversible peak given that, as often happens, $\alpha = 0.5$.

1.2.1 Diagnostic Criteria to Identify an Irreversible Process. In order to characterize an irreversible process it would be necessary to be able to calculate either the thermodynamic parameter E°' or the kinetic parameters α and k° . Unfortunately, we will see below that k° can only be calculated if E°' is known, and E°' cannot be calculated by voltammetric techniques. Thus, either one knows E°' (for example, by using potentiometric techniques in solutions containing both Ox and Red), or one is limited to give simply the peak potential of the electrode process at a certain rate (usually at 0.1 V s^{-1} or at 0.2 V s^{-1}).

The criteria for an irreversible process are the following.

Properties of the potential

- At variance with the reversible case, in the irreversible case the forward peak potential, E_{pf} , shifts with the scan rate (towards more cathodic values for reduction processes).

At 25°C, the shift is of about $30/\alpha n_\alpha$ mV for a tenfold increase of the scan rate.

- If $E_{\text{p}/2}$ is the potential value at $i_{\text{p}/2}$, it holds that, at 25°C:

$$|E_p - E_{\text{p}/2}| = \frac{1.857 \cdot R \cdot T}{\alpha \cdot n_\alpha \cdot F} = \frac{47.7}{\alpha \cdot n_\alpha} \text{ (in mV)}$$

Such a relationship is commonly employed to calculate the term $\alpha \cdot n_\alpha$.

As a consequence, if, as it commonly happens, $n = 1$ (or, $n_\alpha = 1$), the value of α can be determined.

- The precise dependence of E_p with scan rate v is expressed by:

$$E_p = E^{\circ'} - \frac{R \cdot T}{\alpha \cdot n_\alpha \cdot F} \cdot \left[0.780 + \ln\left(\frac{D_{\text{Ox}}^{1/2}}{k^\circ}\right) + \ln\left(\frac{\alpha \cdot n_\alpha \cdot F \cdot v}{R \cdot T}\right)^{1/2} \right]$$

It shows that if one knows $E^{\circ'}$ and D_{Ox} , the value of k° can be determined.

Properties of the current

- The current function $i_{\text{pf}}/v^{1/2}$ is constant
- No current ratio $i_{\text{pr}}/i_{\text{pf}}$ exists. In this connection, it must be taken into account that the lack of any reverse response is not sufficient to diagnose an electrochemically irreversible step. As we will see below, the presence of chemical reactions involving the electrogenerated species can make the reverse response disappear.
- The following relation has been derived:

$$i_p = 0.227 \cdot n \cdot F \cdot A \cdot C_{\text{Ox}}^* \cdot k^\circ \cdot e^{-\frac{\alpha \cdot n_\alpha \cdot F}{R \cdot T} \cdot (E_p - E^{\circ'})}$$

which (at least in principle) would allow one to calculate α and k° , if $E^{\circ'}$ is known. In fact, a plot of $\ln i_p$ as a function of $(E_p - E^{\circ'})$ would give a straight line with a slope of $(\alpha \cdot n_\alpha \cdot F / R \cdot T)$ and intercept of $\ln(0.227 \cdot n \cdot F \cdot A \cdot C_{\text{Ox}}^* \cdot k^\circ)$.

1.2.2 The Chemical Meaning of an Electrochemically Irreversible Process. As a chemical consideration, the occurrence of an electrochemically irreversible process implies so large an activation barrier to the electron transfer that it is likely that (as discussed in the introductory section, Figure I.2) it causes breakage of the original molecular frame with formation of new species (see Chapter 7, Section 5).

1.3 Quasireversible Processes

It is not uncommon that in electron transfer processes one observes that at low scan rates the process behaves reversibly, whereas at high scan rates the process behaves irreversibly (such behaviour is more easily seen for processes that are not complicated by coupled reactions). Processes occurring in the transition zone between reversible and irreversible behaviour are called *quasireversible*.

A quasireversible process occurs when the rate of the electron transfer $\text{Ox} + ne^- \rightarrow \text{Red}$ is of the same order of magnitude as the mass transport (concomitantly, the inverse reaction $\text{Ox} + ne^- \rightarrow \text{Red}$ has a non-negligible rate).

It is commonly assumed that an electron transfer behaves quasi-reversibly when the standard rate constant lies within the values expressed as a function of the highest and lowest scan rates v :

$$3 \cdot 10^{-3} \cdot v^{1/2} \geq k^\circ \geq 2 \cdot 10^{-7} \cdot v^{1/2}$$

where k° is expressed in m s^{-1} and v in V s^{-1} .

Since in cyclic voltammetry the potential scan rate commonly ranges from $\approx 0.02 \text{ V s}^{-1}$ to $\approx 50 \text{ V s}^{-1}$, it follows that for a quasireversible process:

$$(\text{from } 2 \cdot 10^{-2} \text{ to } 4 \cdot 10^{-4} \text{ ms}^{-1}) \geq k^\circ \geq (\text{from } 2 \cdot 10^{-6} \text{ to } 3 \cdot 10^{-8} \text{ ms}^{-1})$$

This criterion is slightly different from that assessed in Section 1.4.3 on the reversibility or irreversibility of an electron transfer:

$$k^\circ \geq 2 \times 10^{-4} \text{ m s}^{-1} \quad \text{the process is } \textit{reversible}$$

$$k^\circ \leq 5 \times 10^{-7} \text{ m s}^{-1} \quad \text{the process is } \textit{irreversible}$$

So we can make the new statement:

$k^\circ \geq 3 \cdot 10^{-3} \cdot v^{1/2}$ (*i.e.* $> 2 \cdot 10^{-2} \div 4 \cdot 10^{-4} \text{ m s}^{-1}$) the process is *reversible*

$k^\circ \leq 2 \cdot 10^{-7} \cdot v^{1/2}$ (*i.e.* $< 2 \cdot 10^{-6} \div 5 \cdot 10^{-8} \text{ m s}^{-1}$) the process is *irreversible*

$$3 \cdot 10^{-3} \cdot v^{1/2} \geq k^\circ \geq 2 \cdot 10^{-7} \cdot v^{1/2}$$

(*i.e.* $2 \cdot 10^{-2} \div 4 \cdot 10^{-4} \text{ ms}^{-1} \geq k^\circ \geq 2 \cdot 10^{-6} \div 5 \cdot 10^{-8} \text{ ms}^{-1}$)

the process is *quasireversible*

Coming to the mathematical treatment of the quasireversible case, the solution of the differential equations for Ox and Red needs, as boundary condition at the electrode surface, the relation:

$$\begin{aligned} \frac{i}{n.F.A} &= D_{\text{Ox}} \cdot \left| \frac{\delta C_{\text{Ox}}(x, t)}{\delta x} \right|_{x=0} \\ &= C_{\text{Ox}}(0, t) \cdot k^\circ \cdot e^{\frac{x \cdot n \cdot F}{R \cdot T} (E - E^\circ)} - C_{\text{Red}}(0, t) \cdot k^\circ \cdot e^{\frac{(1-x) \cdot n \cdot F}{R \cdot T} (E - E^\circ)} \end{aligned}$$

In this case the solution is mathematically more complex than in the previous cases. From such a solution one obtains:

- the forward peak height is not directly proportional to $v^{1/2}$
- the shape of the peaks and the peak-to-peak separation depend, through a complex mathematical function Ψ , from α , k° , and v :

$$\Psi = \frac{k^\circ \cdot \left[\frac{D_{\text{Ox}}}{D_{\text{Red}}} \right]^{\alpha/2}}{\left[D_{\text{Ox}} \cdot \pi \cdot v \cdot \frac{n \cdot F}{R \cdot T} \right]^{1/2}}$$

which, under the usual assumptions: $\alpha \approx 0.5$; $D_{\text{Ox}} = D_{\text{Red}} = D$, becomes:

$$\Psi = \frac{k^\circ}{\left[\frac{\alpha \cdot n \cdot F \cdot v \cdot D}{R \cdot T} \right]^{1/2}}$$

The first effect that one notices in the voltammetric response is that quasireversibility induces a separation between the forward and the reverse peaks (*i.e.* the peak-to-peak separation ΔE_p) much greater than that of a reversible process (to determine this parameter correctly one must use instrumentation able to compensate for the solution resistance).

In order to understand better the distinction between reversibility, quasireversibility and irreversibility in cyclic voltammetry, the typical cyclic voltammetric profiles for the three cases are represented in Figure 8.

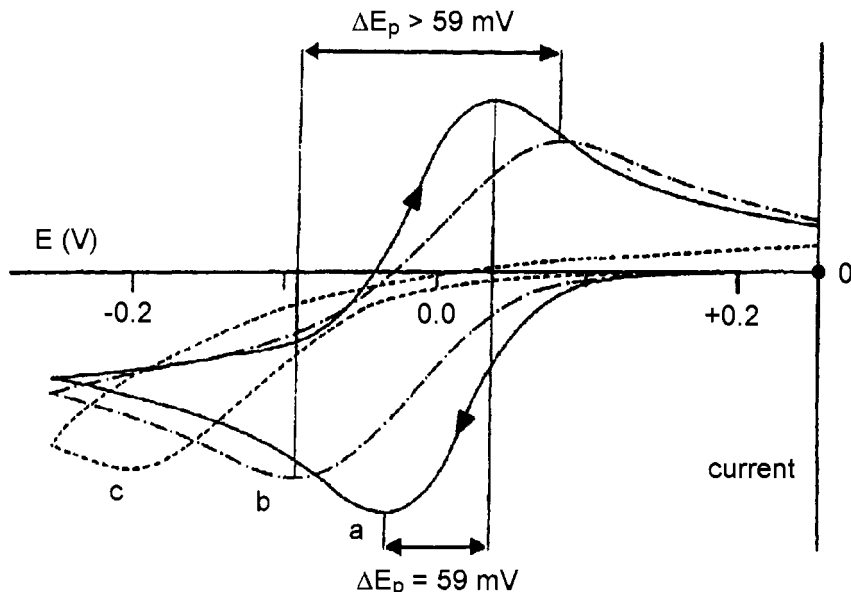


Figure 8 Qualitative behaviour of the cyclic voltammetric profiles for a reduction process having features of: (a) reversibility; (b) quasireversibility; (c) irreversibility. $\alpha = 0.5$; $E^{\circ'} = 0.00$ V. $T = 25^{\circ}\text{C}$

1.3.1 Diagnostic Criteria to Identify a Quasireversible Process. A quasireversible process is characterized by determining either the thermodynamic parameter $E^{\circ'}$ or the kinetic parameters α and k° .

The parameter $E^{\circ'}$ can be calculated to a good approximation as the average value between the forward and the reverse peaks, given that $0.3 < \alpha < 0.7$. In fact, in this case, the shift of the cathodic peak towards more negative potential values and the shift of the reoxidation peak towards more positive values, both caused by the kinetic effects, essentially compensate each other.

The parameter k° is generally calculated from the working curve shown in Figure 9.⁸

In it the peak-to-peak separation, ΔE_p , is plotted as a function of the above discussed parameter Ψ . Thus, if one knows the number of electrons, n , exchanged per molecule of Ox, measuring the peak-to-peak separation (preferably at different scan rates) the corresponding value of Ψ is obtained. Then, from the previous relationship:

$$\Psi = \frac{k^\circ}{\left[\frac{\alpha \cdot n \cdot F \cdot v \cdot D}{R \cdot T} \right]^{1/2}}$$

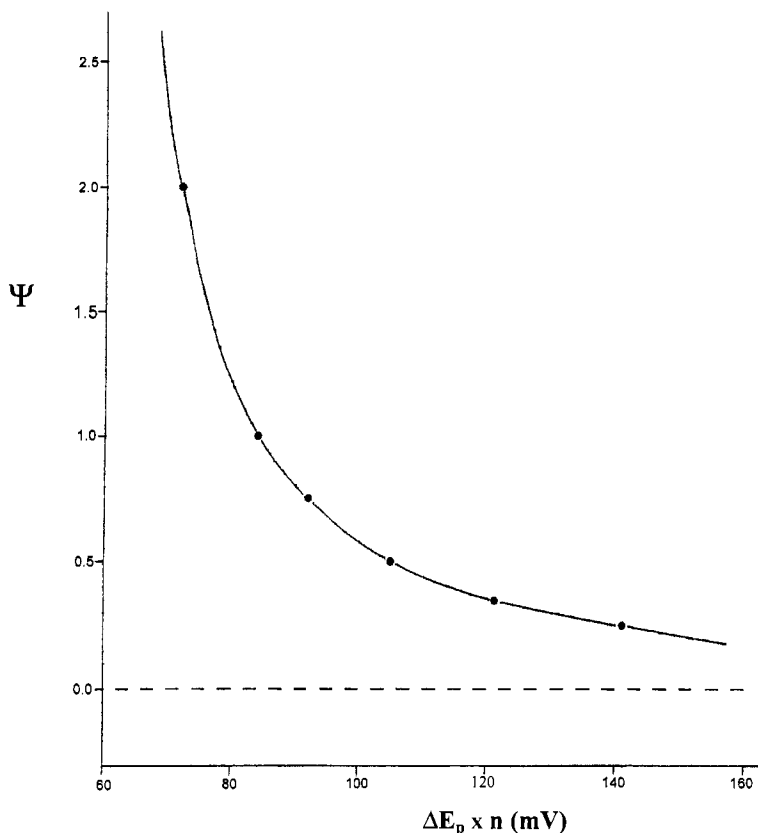


Figure 9 Working curve to calculate k° from the parameter ΔE_p

one can calculate k° if both D and α are known.

Generally, the value of α is assumed to be about 0.5; otherwise one must calculate it by comparing theoretical curves for several values of α with the experimental curve (the latter method being very rarely used). On the other hand one can roughly evaluate the value of α taking into account the effect of α on the shape of the voltammogram:

- for $\alpha > 0.5$, the forward peak is sharper than the reverse peak, thus $i_{pf} > i_{pr}$;
- for $\alpha < 0.5$, the opposite effect is apparent.

On the basis of the previous discussion, the criteria for defining a process as *quasireversible* are the following.

Properties of the Potential

- The forward peak potential E_{pf} shifts (towards more negative potential values for reduction steps) with scan rate;

- as mentioned, the ΔE_p value, at 25°C, is higher than $59/n$ (mV), even if at low scan rates it might approach such value. Nevertheless, on increasing the scan rate the departure from $59/n$ mV becomes significant

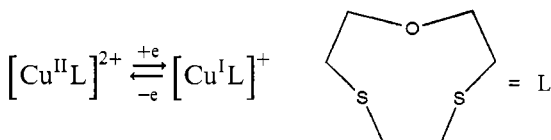
Properties of the Current

- The current of the forward peak i_{pf} increases with $v^{1/2}$, but the dependence may be non-linear; i.e. the current function $i_p/v^{1/2}$ might not be constant;
- the current ratio i_{pr}/i_{pf} is equal to 1 only if $\alpha = 0.5$. Otherwise, if $\alpha > 0.5$: $i_{pr}/i_{pf} < 1$; if $\alpha < 0.5$: $i_{pr}/i_{pf} > 1$.

1.3.2 The Chemical Meaning of an Electrochemically Quasireversible Process. It is conceivable that since quasireversibility lies in between reversibility and irreversibility, the structural consequences of a quasireversible process would also be intermediate between the occurrence of no significant reorganizations (typical of a reversible process) and framework destroying reorganizations (typical of an irreversible process). Therefore we can conclude that electrochemical quasireversibility suggests that some important structural reorganization accompanies the redox step, but the molecular framework does not undergo fragmentation.

However, how significant can such geometrical reorganizations be? From a qualitative viewpoint we can roughly relate the extent of structural reorganization to the departure of the peak-to-peak separation from the theoretical value of $59/n$ mV, expected for a reversible process.

In this connection, let us consider the following example (which will be discussed further in Chapter 5, Section 7), which illustrates the case of a significant, but not too important, structural reorganization:



In acetonitrile solution, the $\text{Cu}^{\text{II}}/\text{Cu}^{\text{I}}$ reduction of $[\text{Cu}^{\text{II}}\text{L}]^{2+}$ appears as a quasireversible process, giving rise to a forward-backward peak-system with $\Delta E_p = 114$ mV, at a scan rate of 0.1 V s^{-1} .

Figure 10 shows the molecular structures of both the copper(II) and copper(I) congeners. As seen, the copper(II) complex possesses an octahedral S_4O_2 coordination, whereas the copper(I) complex assumes a tetrahedral S_4 coordination releasing the bonding with the two oxygen atoms.

In contrast, let us examine a case of very important structural consequences. As we will discuss in Chapter 7, Section 2.4, the carbonyl cluster $[Os_6(CO)_{18}]$ undergoes a two-electron reduction with marked features of electrochemical quasireversibility: $\Delta E_p = 255$ mV at 0.01 Vs^{-1} .

Figure 11 shows the molecular structures of $[Os_6(CO)_{18}]$ and $[Os_6(CO)_{18}]^{2-}$.

We must conclude that the marked electrochemical quasireversibility is due to the remarkable geometrical reorganization from the bicapped tetrahedron of $[Os_6(CO)_{18}]$ to the octahedron of $[Os_6(CO)_{18}]^{2-}$ occurring upon the two electron addition.

It is important to underline finally that quasireversibility is an electrochemical criterion and it does not mean ‘partial chemical reversibility’.

1.4 The Effect of Chemical Reactions Coupled to Electron Transfers

As mentioned in Chapter 1, Section 2.2, it is quite common that a heterogeneous electron transfer process is complicated by homogeneous chemical reactions that involve the species Ox and/or Red. In this light, the chemical complications are classified as:

- preceding (the electron transfer) *chemical reactions*
- following (the electron transfer) *chemical reactions*

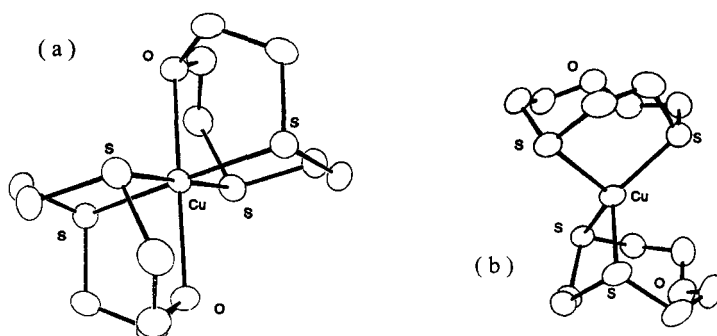


Figure 10 The molecular structures of: (a) $[Cu^{II}L_2]^{2+}$; (b) $[Cu^I L_2]^+$

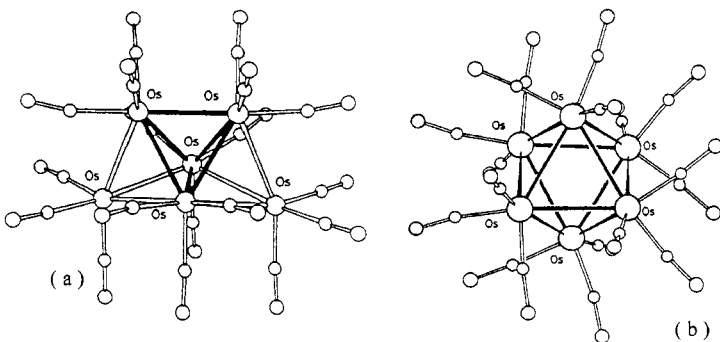


Figure 11 The molecular structures of: (a) $[Os_6(CO)_{18}]$; (b) $[Os_6(CO)_{18}]^{2-}$

It is conceivable that the presence of such complications must affect the shape of the cyclic voltammograms, and hence perturb to some extent the diagnostic criteria for the above-mentioned fundamental electron transfer processes. As these reactions proceed at their own rates, cyclic voltammetry will be able to detect them only if their rates fall within the time scale of the voltammetric technique (which ranges from a few tens of seconds to a few milliseconds).

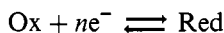
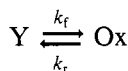
Commonly, in the description of chemical reactions coupled to electron transfer, the homogeneous chemical reaction is indicated by *C* and the heterogeneous electron transfer by *E*. The order of *C* with respect to *E* then follows the chronological order in which the two events occur. Furthermore, while Ox and Red indicate the electro active species, other non-electro active species which result from the coupled chemical complications are indicated by Y, Z, W, etc.

Also in these cases, mathematical treatments of Fick's second law, under proper boundary conditions, afford diagnostic criteria to identify the possible electrode mechanisms.

1.4.1 Preceding Chemical Reactions. It is conceivable that if the species Ox is the product resulting from a chemical reaction preceding the electron transfer, such a reaction will influence the amount of Ox able to be reduced, so essentially perturbing the forward peak.

For a preceding chemical reaction two mechanisms are possible, depending on whether the electron transfer is reversible or irreversible.

1.4.1.1 First-order chemical reaction preceding a reversible electron transfer. The process in which a homogeneous chemical reaction precedes a reversible electron transfer is schematized as follows:



where Y represents the non-electro active species, whereas Ox and Red are the electro active congeners.

A similar process is indicated as a CE mechanism, or more specifically as a C_rE_r mechanism (where the subscript r indicates the reversibility of the respective process).

As the supply of the electroactive species Ox results from the chemical reaction, it will be important to know, at least qualitatively, how much of Ox is formed during the time scale of the cyclic voltammogram. In this connection it must be taken into account that the time scale of cyclic voltammetry is measured by the parameters:

$$\frac{n \cdot F \cdot v}{R \cdot T} \quad \text{for a reversible process}$$

$$\frac{\alpha \cdot n_a \cdot F \cdot v}{R \cdot T} \quad \text{for a quasireversible or an irreversible process}$$

It follows that the time scale of cyclic voltammetry is a function of the potential scan rate v, in the sense that the higher the scan rate the higher is the competition of the voltammetric intervention with respect to the rate of the chemical complication.

Coming back to the electrode process under examination, the limit at which the chemical complication can proceed is governed either by the equilibrium constant K or by the kinetics of the homogeneous reaction (*i.e.* k_f + k_r). In this regard it is convenient to distinguish three limiting cases depending upon the rate of the chemical complication.

- ‘Slow’ preceding chemical reaction ($k_f + k_r \ll n \cdot F \cdot v / R \cdot T$)

When K is large (for example, ≥ 20), most of Ox will already be present in solution, hence, given the low kinetics of the chemical reaction the response is apparently not disturbed by the latter, *i.e.* it appears as a simple reversible electron transfer.

When K is small, the electron transfer reaction again appears as a simple reversible process, except that the peak current will be smaller than what one would expect on the basis of the quantity of the (erroneously assumed to be active) Y species placed in solution. This results because the concentration of the really active species C_{Ox}, being determined by the equilibrium of the preceding reaction, is equal to only a fraction of the species Y placed in solution:

$$C_{\text{Ox}}(x, 0) = \frac{K}{K+1} \cdot C^*$$

where:

$$C^* = C_{\text{Ox}}(x, 0) + C_{\text{Y}}(x, 0)$$

- ‘Fast’ preceding chemical reaction ($k_f + k_r \gg n \cdot F \cdot v / R \cdot T$)

When K is large, once again the response appears as a simple reversible electron transfer, but the measured standard potential, $E^{\circ/\ast}$, is shifted towards more negative values compared to the standard potential, E° , of the couple Ox/Red by a factor of:

$$\frac{R \cdot T}{n \cdot F} \ln \frac{K}{K+1}$$

or, at 25°C, by:

$$\frac{59}{n} \log \frac{K}{K+1} (\text{mV})$$

Obviously, for $K \rightarrow \infty$, $E^{\circ/\ast} = E^\circ$.

When K is small, because of the fast continuous maintaining of the small equilibrium amount of Ox, the complete depletion of Ox at the electrode surface will never be reached, so that the forward profile no longer maintains the peak-shaped form, rather it assumes a sigmoidal S-shaped curve (similar to a polarogram), the height of which remains constant at all the scan rates, Figure 12.

For this kind of limiting current, i_L , the following equation holds:

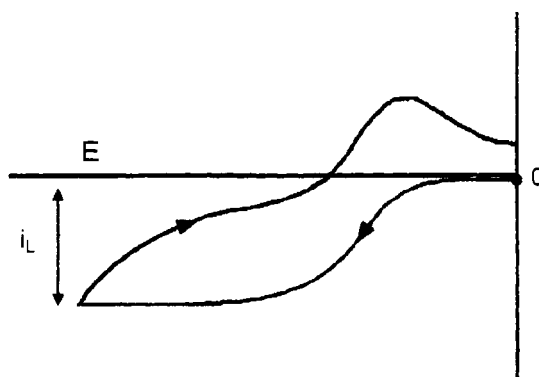


Figure 12 Cyclic voltammogram for a CrEr mechanism in which the preceding chemical reaction is fast, but the equilibrium is shifted towards the reagents

$$i_L = n \cdot F \cdot A \cdot D_{\text{Ox}}^{1/2} \cdot C_Y \cdot K \cdot (k_f + k_r)^{1/2}$$

Hence, if the value of K is known from the literature, one can calculate k_f and k_r .

- ‘Intermediate’ preceding chemical reaction ($k_f + k_r \cong n \cdot F \cdot v / R \cdot T$)

In the case when the preceding chemical reaction occurs at a rate of the same order as the intervention time scale of cyclic voltammetry, the repercussions of the chemical complication on the potential of the electrode process are virtually negligible, whereas there is a significant effect on the current. In particular, it is characteristic of this mechanism that the forward current decreases with the scan rate much more than the reverse current. This implies that the current ratio $i_{\text{pr}}/i_{\text{pf}}$ is always greater than 1, increasing as scan rates are increased.

The forward peak current measured under the effect of the kinetic reaction, i_k (kinetic current), is a fraction of the peak current i_d (diffusive current) that one would record at the same scan rate in the absence of the preceding chemical reaction, according to the relationship:

$$\frac{i_k}{i_d} = \frac{1}{1.02 + \frac{0.471}{K} \sqrt{\frac{n \cdot F \cdot v}{R \cdot T \cdot (k_f + k_r)}}}$$

One can exploit such a relationship to determine the values of k_f and k_r (provided that K is known). To do this, one needs to obtain the value of the diffusion current i_d ; this value can be obtained in two ways:

- recording the voltammogram at a very slow scan rate such that the chemical reaction goes to completion. Then extrapolating from the peak current value obtained the i_d value at the rate used to measure i_k (in fact, under diffusion conditions, the peak current is directly proportional to $v^{1/2}$)
- if the species Ox is available, one records the peak current at the desired scan rate (at the concentration experimentally used for Y).

Should it be impossible to measure i_d , the problem can be overcome by using the working curve reported in Figure 13.⁹

Based on the experimental value $i_{\text{pr}}/i_{\text{pf}}$ obtained at a given scan rate, the curve enables one to calculate the parameter:

$$\frac{1}{K} \sqrt{\frac{n \cdot F \cdot v}{R \cdot T \cdot (k_f + k_r)}}$$

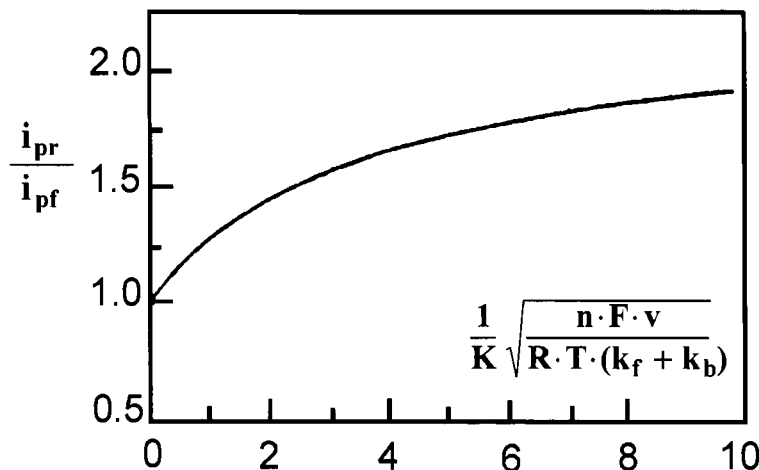


Figure 13 Working curve to obtain the kinetic parameters for a C_rE_r mechanism from the current ratio i_{pr}/i_{pf}

Therefore, if K is known, one can determine the values of k_f and k_r .

1.4.1.1.1 Diagnostic criteria to identify a chemical reaction preceding a reversible electron transfer. Granted that when the chemical reaction has a large K value, or its rate is slow, the response looks like an unperturbed reversible process, the simplest and most wished-for opportunity to detect the presence of a preceding equilibrium reaction lies on the possible appearance of an S-shaped curve in the forward scan. Otherwise, other criteria are the following.

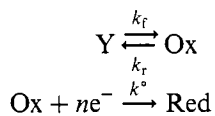
Properties of the Potential

- For a reduction process the forward peak potential E_{pf} shifts towards less negative potential values with scan rate

Properties of the Current

- The current function $i_{pf}/v^{1/2}$ decreases with the scan rate
- The current ratio i_{pr}/i_{pf} is always greater than 1, and further increases with scan rate

1.4.1.2 First-order chemical reaction preceding an irreversible electron transfer. The case in which a chemical reaction precedes an irreversible electron transfer can be depicted by the scheme:



In this case, that one defines as a C_rE_i mechanism, not only the thermodynamic ($K = k_f/k_r$) and kinetic ($k_f + k_r$) parameters of the preceding reaction will play a role, but also the kinetic parameters of the electron transfer (α, k°).

Obviously, the lack of a reverse peak is immediately apparent, due to the irreversibility of the charge transfer.

Also in this case, if the kinetics of the preceding chemical reaction are very slow ($k_f + k_r \ll \alpha \cdot n_\alpha \cdot F \cdot v / R \cdot T$), the process appears as a simple irreversible electron transfer. The peak height of the process depends on the equilibrium constant because, as mentioned previously, the concentration of the active species C_{Ox} is a fraction of the amount C^* ($= C_{\text{Ox}} + C_{\text{Y}}$) put in solution:

$$C_{\text{Ox}}(x, 0) = \frac{K}{K+1} \cdot C^*$$

If instead the reaction kinetics are fast ($k_f + k_r \gg \alpha \cdot n_\alpha \cdot F \cdot v / R \cdot T$) there are two possibilities:

- If K is large, again the response appears as if the preceding chemical reaction would be absent. However, the peak potential is shifted towards more negative values than those that would be recorded in the absence of the chemical complication by a factor equal to:

$$\frac{R \cdot T}{\alpha \cdot n_\alpha \cdot T} \ln \frac{K}{K+1}$$

or, at 25°C, by:

$$\frac{59}{\alpha \cdot n_\alpha} \log \frac{K}{K+1} \text{ (mV)}$$

- If K is small, as in the preceding case, an easily recognizable S-like curve voltammogram is obtained having a limiting current independent from the scan rate:

$$i_L = n \cdot (\alpha \cdot n_\alpha)^{1/2} \cdot F \cdot A \cdot D_{\text{Ox}}^{1/2} \cdot C_{\text{Y}} \cdot K \cdot (k_f + k_r)^{1/2}$$

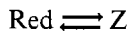
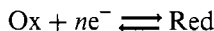
Finally, when the reaction kinetics are neither too fast nor too slow and K is 'neither too large nor too small' one can study the kinetics using

the ratio between the kinetic and the diffusive currents, (analogous to the preceding case) according to the relationship:

$$\frac{i_k}{i_d} = \frac{1}{1.02 + \frac{0.531}{K} \sqrt{\frac{\alpha \cdot n_2 \cdot F \cdot v}{R \cdot T \cdot (k_f + k_r)}}}$$

1.4.1.2.1 Diagnostic criteria to identify a chemical reaction preceding an irreversible electron transfer. Other than the particular case of an S-like shaped voltammogram (not accompanied by a return peak), there are no criteria which define this case except for the decrease of the current function $i_{pf}/v^{1/2}$ with increasing v .

1.4.2 Following chemical reactions. The process in which the primary product of an electron transfer becomes involved in a chemical reaction is indicated as an *EC* mechanism. It can be represented by:

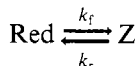
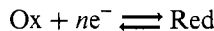


where Ox and Red are the electro active congeners, whereas Z represents the non-electro active species.

At least from a theoretical viewpoint, several situations are possible depending on the extent of electrochemical reversibility of the electron transfer and on the reversibility or irreversibility of the chemical reaction following the electron transfer.

As a general criterion one must bear in mind that, in cyclic voltammetry, the presence of a following chemical reaction has little influence on the forward peak, whereas it has a considerable effect on the reverse peak.

1.4.2.1 First-order reversible chemical reaction following a reversible electron transfer. The E_rC_r mechanism can be written as:



Once again the voltammetric response will differ to a greater or lesser extent with respect to a simple electron transfer depending on the values of either the equilibrium constant, K , or the kinetics of the chemical complication (k_f and k_r).

Analogously to that discussed for preceding equilibrium reactions (Section 1.4.1.1), three limiting cases can be distinguished.

- ‘Slow’ following chemical reaction ($k_f + k_r \ll n \cdot F \cdot v / R \cdot T$)

If the rate of the chemical reaction is low, it has little effect on the process, thus reducing it to a simple reversible electron transfer.

- ‘Fast’ following chemical reaction ($k_f + k_r \gg n \cdot F \cdot v / R \cdot T$)

If the rate of the chemical complication is high, the system will always be in equilibrium and the voltammogram will apparently look like a non-complicated reversible electron transfer. However, as a consequence of the continual partial removal of the species Red from the electrode surface, the response (if, as in the present case, one is considering a reduction process) is found at potential values less negative than that of a simple electron transfer by an amount of:

$$\frac{R \cdot T}{n \cdot F} \ln(1 + K)$$

or, at 25°C, by:

$$\frac{59}{n} \log(1 + K) \text{ (mV)}$$

Due to the fast kinetics of the chemical complication, the potential will remain at this value regardless of the scan rate.

- ‘Intermediate’ following chemical reaction ($k_f + k_r \cong n \cdot F \cdot v / R \cdot T$)

If the kinetics of the chemical complication are intermediate, with increasing the scan rate the response gradually shifts from the previous value for a fast chemical reaction [which was more anodic by $(R \cdot T / n \cdot F) \cdot \ln(1 + K)$ (volts) with respect to the $E^{\circ'}$ value of the couple Ox/Red] towards the $E^{\circ'}$ value, assuming more and more the values predicted by the relationship:

$$E_p = E^{\circ'} - \frac{R \cdot T}{n \cdot F} \left[0.780 + \frac{1}{2} \ln \frac{n \cdot F \cdot v}{R \cdot T \cdot (k_f + k_r)} + \ln \frac{K}{1 + K} \right]$$

In other words, the response (which for fast kinetics is more anodic compared to $E^{\circ'}$), due to the competitive effects of the potential scan rate, moves towards more cathodic values by $30/n$ (mV) for every ten-fold increase in the scan rate. However, as shown in Figure 14, it is noted that at the same time the reverse peak tends to disappear, in that on increasing the scan rate, the species Z does not have time to restore Red. This is demonstrated by the current ratio i_{pr}/i_{pf} which is about 1 at low scan rates, but it tends to zero at high scan rates.

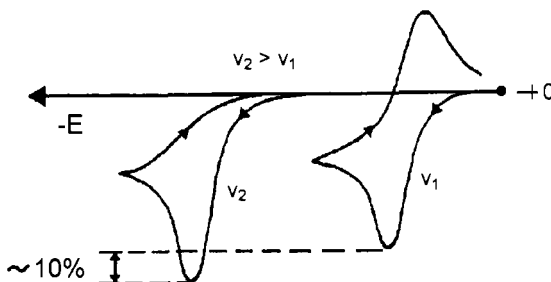


Figure 14 Changes in the cyclic voltammetric response with scan rate for an E,C_r mechanism in which the chemical reaction C_r is neither too fast nor too slow.

1.4.2.1.1 Diagnostic criteria to identify a first-order reversible chemical reaction following a reversible electron transfer. To be able to ascertain the presence of a following reversible chemical reaction, the reaction must be neither too slow nor too fast. Under these conditions the following criteria hold.

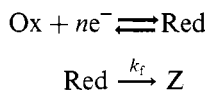
Properties of the Potential

- The potential of the forward peak, E_{pf} , moves towards negative values (for a reduction reaction) with the scan rate, shifting by $30/n$ (mV) for every 10-fold increase in the scan rate

Properties of the Current

- The current ratio, i_{pr}/i_{pf} , becomes smaller than 1 with increasing ν (this is the most significant criterion for defining the process in question)
- the current function, $i_{pf}/\nu^{1/2}$, remains essentially invariant (it should slightly increase) with the scan rate

1.4.2.2 First-order irreversible chemical reaction following a reversible electron transfer. The general scheme of the E_rC_i mechanism is:



This is a particular case of the preceding treatment in that one can consider the equilibrium of the *following* chemical reaction to be completely shifted to the right. As already noted, this is quite a common process in inorganic electrochemistry.

Also for this case, the localization of the voltammetric response depends on the kinetics of the chemical reaction. However, it differs from the preceding one in that the parameters k_r and K of the chemical reaction are not present.

If $k_f \ll n \cdot F \cdot v / R \cdot T$ (*i.e.* if the chemical reaction is very slow compared to the intervention times of cyclic voltammetry) the response is very similar to that of a simple reversible electron transfer and occurs at the formal potential, $E^{\circ'}$, of the couple Ox/Red.

Conversely, if $k_f \gg n \cdot F \cdot v / R \cdot T$ (*i.e.* if the chemical reaction is very fast) the forward peak (for a reduction process) is found at potentials more positive than the formal potential, $E^{\circ'}$, of the Ox/Red couple. Furthermore, the reverse peak is virtually absent because as soon as Red is generated, it is removed from the electrode surface by the chemical reaction.

If $k_f \cong n \cdot F \cdot v / R \cdot T$ (*i.e.* if the chemical complication is neither too slow nor too fast and, consequently, the kinetics of the chemical complication are of the same order as the time scale of cyclic voltammetry) the potential of the forward peak, which has been localized at more anodic potentials than $E^{\circ'}$ by the chemical complication, shifts towards less anodic values with the scan rate according to the relationship:

$$E_p = E^{\circ'} - \frac{R \cdot T}{n \cdot F} \left[0.780 + \frac{1}{2} \ln \frac{n \cdot F \cdot v}{k_f \cdot R \cdot T} \right]$$

This implies that the peak potential moves towards negative values by a factor of $30/n$ (mV) for every 10-fold increase in the potential scan rate. At the same time, as shown in Figure 15, increasing the scan rate will allow a condition to be reached at which the reverse peak begins to appear as there is no longer sufficient time for Red to be completely converted to Z.

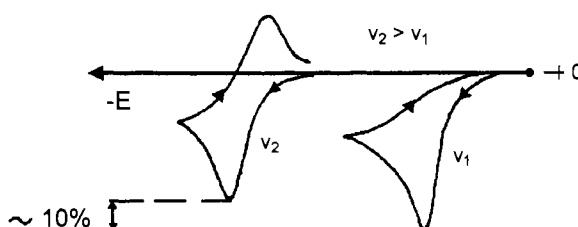


Figure 15 Changes in the cyclic voltammetric response with scan rate for an E_rC_i mechanism in which the chemical reaction C_i is neither too fast nor too slow.

Above this threshold scan rate the current ratio, $i_{\text{pr}}/i_{\text{pf}}$, progressively increases. If the value of $i_{\text{pr}}/i_{\text{pf}} = 1$ is achieved, it signifies that the chemical reaction has been completely prevented (under these conditions $E^{\circ'}$ can be calculated as the average of the forward and reverse peaks).

The conditions in which $i_{\text{pr}}/i_{\text{pf}}$ assumes values between 0.45 and 0.95 are the best for calculating the rate constant of the following reaction. In fact, from the working curve reported in Figure 16, based on the current ratio $i_{\text{pr}}/i_{\text{pf}}$, one can determine the value of $k_f \cdot \tau$.⁹ Since τ is easily calculated, being the time necessary to move from $E^{\circ'}$ (calculated under the conditions where $i_{\text{pr}}/i_{\text{pf}} = 1$) to the inversion potential E_f , k_f is determined.

Recalling that for a first-order reaction it holds that $t_{1/2} = 0.693/k$, one can determine the half-life of the electrogenerated species Red from the value of k_f . In order to obtain a reliable value of k_f it is always wise to have a series of measurements at different scan rates and possibly at different E_f values.

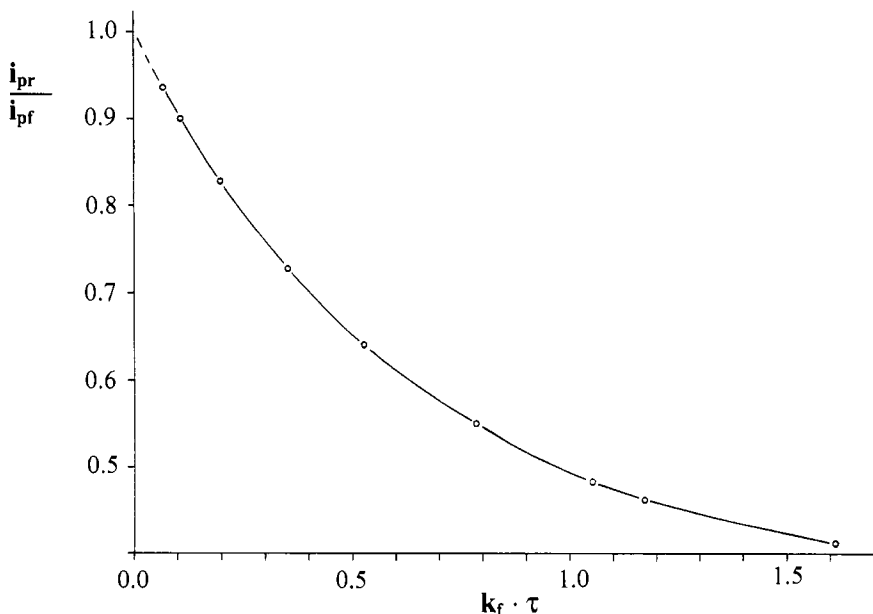


Figure 16 Working curve to calculate the rate constant k_f for an E, C_i mechanism from the current ratio $i_{\text{pr}}/i_{\text{pf}}$

1.4.2.2.1 Diagnostic criteria to identify a first-order irreversible chemical reaction following a reversible electron transfer.

Properties of the Potential

- For a reduction process, the potential of the forward peak, E_{pf} , moves towards negative values with the scan rate by a factor of $30/n$ (mV) for a ten-fold increase in the scan rate

Properties of the Current

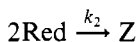
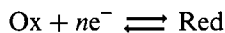
- The current ratio, $i_{\text{pr}}/i_{\text{pf}}$, progressively increases with the scan rate from values smaller than 1 up to a maximum of 1 (this is the most significant criterion for defining the process in question)

It is noted that this is the opposite behaviour to that seen when the following chemical reaction is in equilibrium.

- The current function, $i_{\text{pf}}/v^{1/2}$, remains essentially invariant (it should slightly decrease) with the scan rate

1.4.2.3 Second-order irreversible chemical reaction following a reversible electron transfer: dimerization.

It is quite common in chemical reactions that newly formed radicals couple to each other. This also often happens in the electrochemical generation of radicals according to a dimerization process that can be written as:



As for first-order following chemical reactions, if the dimerization reaction (that is a second-order reaction) is slow (*i.e.* k_2 is small), or if the scan rate is very high, only the reversible electron transfer is effectively active.

It is important to bear in mind that when dimerization occurs the potential of the forward peak shifts towards more negative values (for a cathodic process) by about $20/n$ (mV) for a ten-fold increase in the scan rate, whereas for a ten-fold increase in the concentration of Ox it shifts by the same amount, but towards more positive values.

There are two ways in which one can calculate the kinetic parameter k_2 . The first is based on the measurement of the variation of the forward peak E_p with the scan rate. As can be seen in Figure 17, the shift of the peak potential is particularly marked at low scan rates, whereas at high scan rates it tends to disappear.

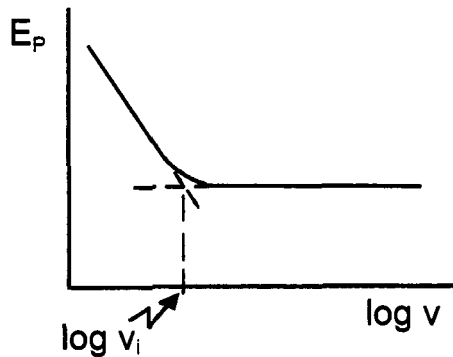


Figure 17 Variation of the forward peak potential with the scan rate for a dimerization reaction following an electron transfer

The intersection value, v_i (Vs^{-1}), enables one to calculate k_2 according to the relationship:

$$k_{2(\text{mol}^{-1}\text{s}^{-1})} = \frac{0.8 \cdot n \cdot F \cdot v_i}{R \cdot T \cdot C_{\text{Ox}}^*}$$

which, at 25°C, gives:

$$k_{2(\text{mol}^{-1}\text{s}^{-1})} = \frac{31.14 \cdot n \cdot v_i}{C_{\text{Ox}}^*}$$

The second method is based on the measurement of the current ratio $i_{\text{pr}}/i_{\text{pf}}$ at a given scan rate. Through the use of the working curve reported in Figure 18, one is able to determine k_2 .¹⁰

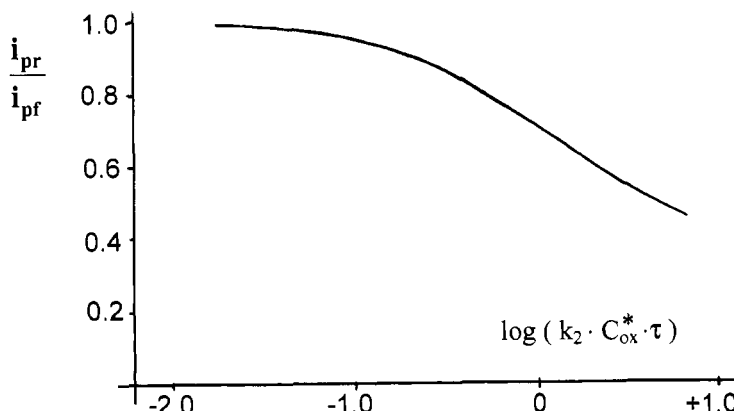


Figure 18 Working curve to obtain the dimerization constant from the current ratio $i_{\text{pr}}/i_{\text{pf}}$

The parameter τ has the same meaning as before (i.e. the time, in seconds, necessary to run from $E^{\circ'}$ to E_f).

It is noted that the curve shown in Figure 18 was obtained for an E_f value more cathodic by 100 mV (exactly 103 mV) with respect to the $E^{\circ'}$ of the couple Ox/Red. One must therefore record first a cyclic voltammogram at high scan rate (in order to reach the condition: $i_{pr}/i_{pf} = 1$) to be able to calculate $E^{\circ'}$. A cyclic voltammogram is then recorded at slow scan rate (to ensure $0.5 \leq i_{pr}/i_{pf} \leq 0.9$) setting $E_f = E^{\circ'} - 100$ mV. Finally, i_{pr}/i_{pf} can be evaluated.

In case that the measurement of the current ratio, i_{pr}/i_{pf} , would need a graphical evaluation, one can exploit the following relationship:

$$\frac{i_{pr}}{i_{pf}} = \frac{(i_{pr})_0}{(i_{pf})_0} + \left[\frac{(i_f)_0}{(i_{pf})_0} \right]^2 \cdot 0.9678 - \frac{(i_f)_0}{(i_{pf})_0} \cdot 0.537 + 0.3337$$

where the symbols represent the parameters shown in Figure 19.

1.4.2.3.1 Diagnostic criteria to identify an irreversible dimerization reaction following a reversible electron transfer. In the presence of a chemical reaction following an electron transfer, the dependence of the cyclic voltammetric parameters from the concentration of the redox active species are sufficient by themselves to reveal preliminarily a second-order complication (a ten-fold change in concentration from $\approx 2 \cdot 10^{-4}$ mol dm $^{-3}$ to $\approx 2 \cdot 10^{-3}$ mol dm $^{-3}$ represents a typical path).

Properties of the Potential

- When a dimerization reaction occurs, the potential of the forward peak, E_{pf} , shifts (for a reduction process) towards more cathodic

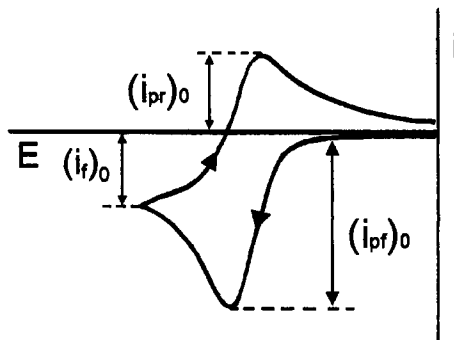


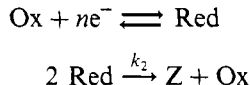
Figure 19 Meaning of the parameters useful to obtain graphically the current ratio i_{pr}/i_{pf} to insert in the relationship valid for a dimerization reaction

values by $20/n$ (mV) for every ten-fold increase in the scan rate, whereas it shifts to more anodic values by $20/n$ (mV) for every ten-fold increase in the concentration of the Ox species

Properties of the Current

- The current ratio, $i_{\text{pr}}/i_{\text{pf}}$, increases with the scan rate and decreases with the increase of the concentration of Ox
- the current function, $i_{\text{pf}}/\nu^{1/2}$, decreases slightly (at most by 20%) with the scan rate

1.4.2.4 Second-order irreversible chemical reaction following a reversible electron transfer: disproportionation. The disproportionation reaction can be represented as:



It is a particular case of the mechanism in which ‘the initial product is regenerated’, that will be treated in the next section.

This mechanism has some analogy with the dimerization complication. The parameter which distinguishes them is the variation of the peak current with the scan rate. In fact, decreasing the scan rate will allow the chemical reaction to regenerate the initial species Ox, thus causing a significant increase in the forward peak current.

To obtain the kinetic parameter k_2 one measures (as in the dimerization case) the current ratio $i_{\text{pr}}/i_{\text{pf}}$ at a given scan rate. Then, by use of the working curve reported in Figure 20 one can determine k_2 .¹¹

As for the dimerization case, the curve was obtained for a value of E_f more cathodic by 103 mV with respect to the $E^{\circ'}$ of the couple Ox/Red. Therefore, once again one must first record a cyclic voltammogram at high scan rate (in order to reach the condition: $i_{\text{pr}}/i_{\text{pf}} = 1$) to be able to calculate $E^{\circ'}$. A cyclic voltammogram is then recorded at slow scan rate (to ensure $0.7 \leq i_{\text{pr}}/i_{\text{pf}} \leq 0.9$) setting $E_f = E^{\circ'} - 100$ mV. Finally, $i_{\text{pr}}/i_{\text{pf}}$ can be evaluated through the usual equation:

$$\frac{i_{\text{pr}}}{i_{\text{pf}}} = \frac{(i_{\text{pr}})_0}{(i_{\text{pf}})_0} + \left[\frac{(i_f)_0}{(i_{\text{pf}})_0} \right]^2 \cdot 0.9678 - \frac{(i_f)_0}{(i_{\text{pf}})_0} \cdot 0.537 + 0.3337$$

where the symbols represent the parameters shown in Figure 19.

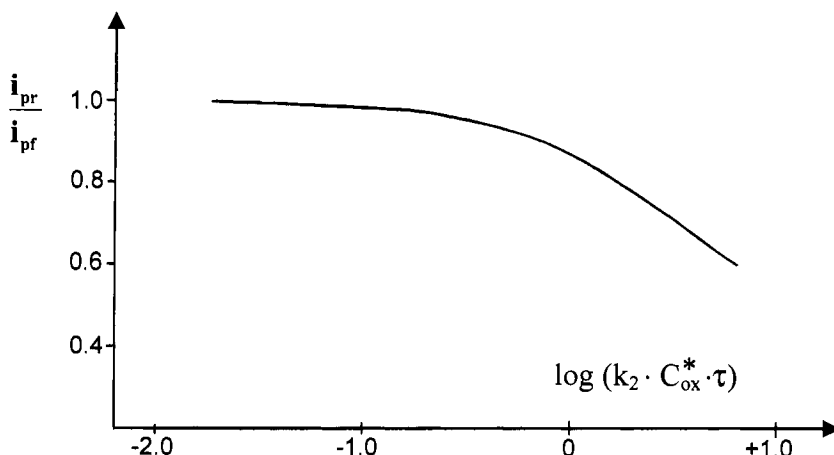


Figure 20 Working curve to obtain the disproportionation constant from the current ratio i_{pr}/i_{pf}

1.4.2.4.1 Diagnostic criteria to identify an irreversible disproportionation reaction following a reversible electron transfer. Once again the dependence of the parameters of the cyclic voltammetric response from the concentration of the species Ox preliminarily reveals the second-order complication.

Properties of the Potential

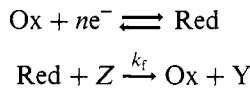
- When a disproportionation reaction occurs, the potential of the forward peak E_{pf} shifts (for a reduction process) towards more cathodic values by $20/n$ (mV) for every ten-fold increase in the scan rate, whereas it shifts to more anodic values by $20/n$ (mV) for every ten-fold increase in the concentration of the Ox species

Properties of the current

- The current ratio, i_{pr}/i_{pf} , increases with the scan rate and decreases with the increase of the concentration of Ox
- the current function, $i_{pf}/v^{1/2}$, decreases by more than a factor of two with the scan rate

1.4.2.5 Catalytic regeneration of the reagent following a reversible electron transfer. A particular case of following chemical reaction is constituted by that in which the product of the electrode reaction undergoes a homogeneous, irreversible, first-order (or pseudo-first-order)

chemical reaction which regenerates the initial electro active reagent, according to the scheme:



In order to ensure that the process takes place, a powerful oxidant Z (to ensure the irreversibility of the complication), but electro inactive (at least in the potential region of interest), must be present in solution at concentrations normally much higher than that of Ox, in order to guarantee pseudo-first-order reaction conditions.

In considering the cyclic voltammetric response, one must recall that if k_f is small, or at very high potential scan rates, the following chemical reaction does not take place and one has a simple reversible electron transfer.

As k_f becomes larger, or the scan rate is reduced, the regeneration of the reagent causes the forward response to have a higher current than that of a simple reversible electron transfer. The increase in the peak current on decreasing the scan rate continues up to a limiting value, beyond which further lowering of the scan rate has no effect on the current. This is a consequence of having attained conditions such that the rate with which the species Ox disappears, due to reduction at the electrode, equals the speed with which Ox is regenerated by the oxidant Z. At such a limiting value the response loses its peak-shaped form, assuming an S-like shape reminiscent of a polarographic wave, Figure 21.

It differs from the sigmoidal curve illustrated in Section 1.4.1.1, Figure 12, in that the reverse response strictly adheres to the forward response.

Under these limiting conditions, the limiting current is given by:

$$i_L = n \cdot F \cdot A \cdot C_{\text{Ox}}^* \cdot D_{\text{Ox}}^{1/2} \cdot k_f^{1/2}$$

and the half-wave potential, $E_{1/2}$, for this wave coincides with the E°' of the couple Ox/Red.

If the value of k_f allows the limiting conditions to be achieved, the determination of k_f can be made in two ways:

- if one knows D_{Ox} , k_f can be found using the above expression for the limiting current;
- one can compare the value of the limiting current obtained at a given scan rate, i_L , with the value (i_d) that the current would have

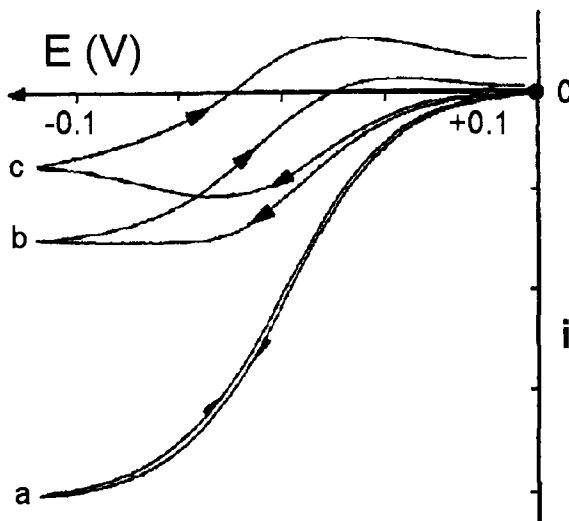


Figure 21 Typical cyclic voltammograms recorded at increasing scan rates ($a < b < c$) for a reversible electron transfer (having $E^{\circ'} = 0.0\text{ V}$) coupled to catalytic regeneration of the reagent

at the same scan rate if the species Z were not present (as usual, i_k indicates a kinetic current, whereas i_d indicates a diffusion current). To calculate i_d , one can record a cyclic voltammogram at high scan rate such that the following chemical reaction does not occur, then one can extrapolate from this value the current at the previous scan rate (in fact, i_p is proportional to $v^{1/2}$).

Alternatively, one could record the voltammogram of the species Ox at the preceding concentration and at the required scan rate, but in the absence of Z.

Once i_k and i_d are known, the following relationship is used:

$$\frac{i_k}{i_d} = 2.242 \left(\frac{k_f \cdot R \cdot T}{n \cdot F \cdot v} \right)^{1/2}$$

which, at 25°C, becomes:

$$\frac{i_k}{i_d} = 0.359 \left(\frac{k_f}{n \cdot v} \right)^{1/2}$$

It is noted that this relationship is valid, provided that the kinetic current is at least 2- or 3-fold greater than the diffusive current.

When the value of k_f is such that one does not obtain an S-like curve, k_f can be determined from the working curve reported in Figure 22a,⁹

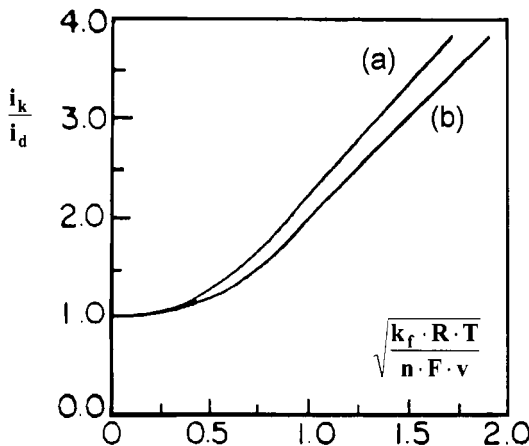


Figure 22 Working curve for the catalytic regeneration of the reagent following a reversible (a) or irreversible (b) electron transfer

which plots the ratio i_k/i_d , calculated as described previously, as a function of the parameter $(k_f \cdot R \cdot T/n \cdot F \cdot v)^{1/2}$.

1.4.2.5.1 Diagnostic criteria to identify a catalytic regeneration of the reagent following a reversible electron transfer. In addition to the eventual obtainment of a sigmoidal curve for either the forward and the reverse profile, other criteria which define the case in question are the following.

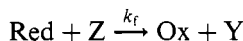
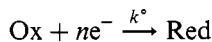
Properties of the Potential

- In the case of an S-like wave, the half-wave potential is independent from the scan rate. Otherwise, the potential of the forward peak shifts towards less negative values (for a reduction process) for a maximum of $60/n$ (mV) for every ten-fold increase in the scan rate

Properties of the Current

- Apart from the case of the sigmoidal wave, the current ratio i_{pr}/i_{pf} is always equal to 1
- the current function, $i_{pf}/v^{1/2}$, significantly increases with the decrease of the scan rate up to a maximum value which is independent of v (formation of an S-like curve)

1.4.2.6 Catalytic regeneration of the reagent following an irreversible electron transfer. When the *catalytic* reaction follows an irreversible electron transfer, the process can be represented as follows:



In this case, the cyclic voltammetric response is essentially similar to the preceding case, with the difference that, given the irreversibility of the electron transfer, the return peak is missing. Thus, if k_f is low, the response is that of a simple irreversible electron transfer. As k_f increases, the greater the potential scan rate the higher the peak current (compared to simple irreversible electron transfer). This continues up to a maximum value at which the response assumes a S-like shape.

Under these limiting conditions one can calculate the value of k_f from the relation:

$$\frac{i_k}{i_d} = 2.016 \cdot \left(\frac{k_f \cdot R \cdot T}{\alpha \cdot n_a \cdot F \cdot v} \right)^{1/2}$$

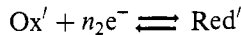
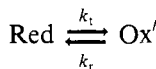
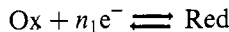
which, at 25°C, becomes:

$$\frac{i_k}{i_d} = 0.323 \cdot \left(\frac{k_f}{\alpha \cdot n_a \cdot v} \right)^{1/2}$$

Alternatively, one can obtain k_f by using the working curve reported in Figure 22b.⁹

1.4.2.6.1 Diagnostic criteria to identify a catalytic regeneration of the reagent following an irreversible electron transfer. The criteria which define the catalytic regeneration of the reagent following an irreversible electron transfer are the same as those given for the catalytic regeneration of the reagent following a reversible electron transfer, if one excludes that the parameter i_{pr}/i_{pf} cannot be measured due to the absence of the return peak.

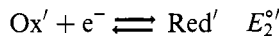
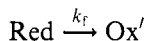
1.4.3 A Chemical Reaction Interposed Between Two Electron Transfers. An electrochemical process in which the product of the electron transfer undergoes a chemical reaction that generates a species which in turn is electrochemically active is defined as an *ECE mechanism*. It is commonly schematized as:



Such a series of events can have associated aspects of more or less complicated nature depending upon:¹²

- the degree of reversibility of the two electron transfers;
- the number of electrons exchanged in the two electron transfers; *i.e.* the ratio n_2/n_1 ;
- the difference between the redox potential of the first couple Ox/Red and that of the second couple Ox'/Red';
- the value of the equilibrium constant of the interposed chemical reaction ($K = k_f/k_r$).

1.4.3.1 An ‘irreversible’ chemical reaction interposed between two reversible one-electron transfers (case R-R). The so-called E_rC_iE_r process, if $n_1 = n_2 = 1$, can be written as:



Amongst the ECE mechanisms, this one is perhaps the most commonly encountered in inorganic electrochemistry.

The cyclic voltammetric response depends on the separation between E_2° and E_1° , or ΔE° . Hence, several cases are possible depending on whether:

- the species Ox' is more difficult to reduce than the original species Ox (ΔE° negative)
- the species Ox' is reduced at the same potential as the species Ox ($\Delta E^\circ = 0$)
- the species Ox' is easier to reduce than the species Ox (ΔE° positive)

1.4.3.1.1 Standard potential of the second electron transfer more cathodic than that of the first electron transfer ($\Delta E^{\circ'}$ negative). One can consider the case where the formal electrode potential of the second couple is more cathodic, by at least 180 mV, with respect to the first couple (which has, for example, $E_1^{\circ'} = 0.00$ V). If k_f is low (compared to the intervention times of cyclic voltammetry; i.e. if $k_f \ll n \cdot F \cdot v / R \cdot T$), the response will be due to the first electron transfer process, without complications caused by the following chemical reaction. As k_f increases, the second process will have increasing effect up to the limiting case in which $k_f \gg n \cdot F \cdot v / R \cdot T$. In this limiting case the voltammogram will display two forward peaks, but only the second electron transfer will exhibit a return peak.

Figure 23 shows schematically these two extremes.

It can be seen that when the cyclic voltammetric time scale (i.e. the scan rate v) is much faster than the chemical reaction (or, when the rate of the interposed chemical reaction is low), the curve I is the response of a simple reversible process (solid line). As k_f grows (dashed line), peak I shifts towards more anodic values and increases slightly in height (maximum of 10%), concomitantly with the appearance of an easily observable second peak, peak II.

It is noted that under these latter conditions the ratio of the currents of the two forward peaks is directly related to the rate of the interposed

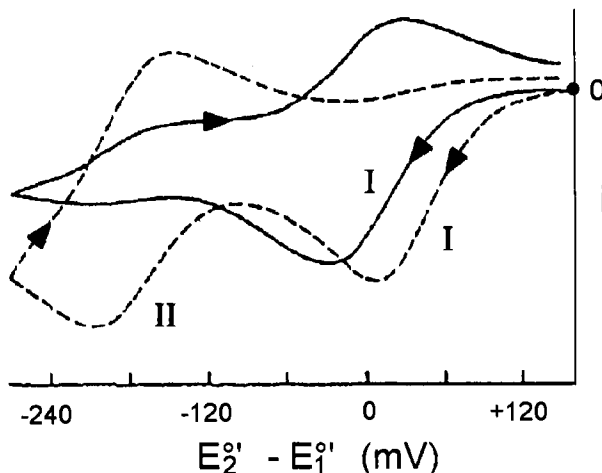


Figure 23 Cyclic voltammetric responses for an $E_1C_1E_2$ mechanism: $\Delta E^{\circ'} = -180$ mV.
 $(—)$ $k_f/(nFv/RT) = 0.05$; $(--)$ $k_f/(nFv/RT) = 10$. $E_1^{\circ'} = 0.00$ V;
 $E_2^{\circ'} = -0.18$ V

chemical reaction. Therefore, this enables k_f to be determined using the working curve illustrated in Figure 24, obtained from data reported in Ref. 12 ($T = 25^\circ\text{C}$).

However, if the redox couples Ox/Red and Ox'/Red' have sufficiently different standard potentials, k_f can be also calculated using the working curve reported in Figure 16. In fact, considering the process simply as ‘a reversible electron transfer followed by an irreversible first-order chemical reaction’ (see Section 1.4.2.2), one measures only the current ratio $i_{\text{pr}}/i_{\text{pf}}$ of the first couple Ox/Red. Obviously, the return peak must be recorded before the second process begins to appear; this means that the direction of the potential scan must be reversed immediately after having traversed the first forward peak.

1.4.3.1.2 Standard potential of the second electron transfer equal to that of the first electron transfer ($\Delta E^{\circ'} = 0$). When the potential of the couple Ox/Red is equal to that of the couple Ox'/Red' it is quite probable that the entire system displays a single forward peak associated with a single reverse peak.

If the kinetics of the chemical reaction are very fast it is possible that the height of the forward peak is two times greater than that of the reverse peak, in that the return peak corresponds to the reoxidation of the only Red', whereas the forward peak corresponds to the reduction of both Ox and Ox'.

In the case of $\Delta E^{\circ'} = 0$, it is not possible to obtain information on the interposed chemical reaction.

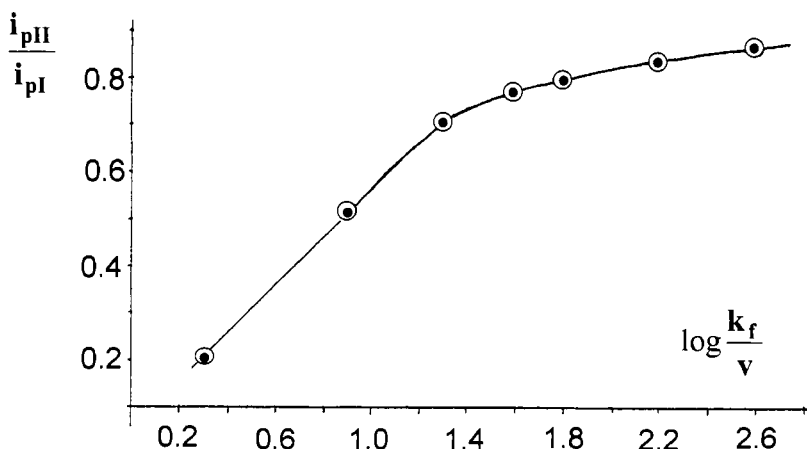


Figure 24 Working curve for the determination of k_f in an E_rC_iE , mechanism in which the second electron transfer is more cathodic than the first one. v in V s^{-1}

1.4.3.1.3 Standard potential of the second electron transfer more anodic than that of the first electron transfer ($\Delta E^{\circ'}$ positive). The case in which the product Ox' , generated by the chemical reaction following the first electron transfer, is more easily reduced than the original species Ox constitutes another common ECE mechanism in inorganic electrochemistry.

As usual, if the rate constant k_f of the interposed chemical reaction is low, only the first electron transfer will occur; conversely, if k_f is very high both the electron transfers will take place.

The typical cyclic voltammogram for the case in which the second electron transfer proceeds ($k_f \cong n \cdot F \cdot v / R \cdot T$) and the potential of the couple Ox'/Red' is more anodic than that of the couple Ox/Red by at least 180 mV, is shown in Figure 25.

The system of peaks I/II results from the couple Ox/Red , whereas the system of peaks III/IV results from the couple Red'/Ox' .

One can easily infer that if k_f is very high, the return peak II can be absent.

To obtain k_f one can adopt two approaches, both based on the response of the Ox/Red system.

- The first is to compare the current of peak I, which under ECE conditions is due to Ox and in part to Ox' , at a given scan rate, i_k , with the peak current i_d that one would record in the absence of chemical complications, hence due to only Ox . The diffusion current i_d can be obtained by recording the voltammogram at a very high scan rate (to prevent the occurrence of the chemical reaction following the first electron transfer) and then extrapolating from

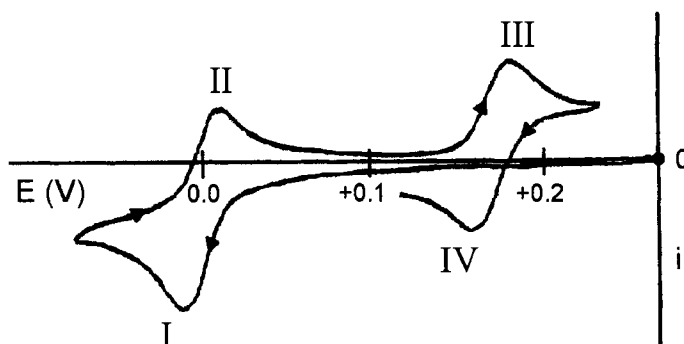


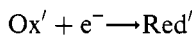
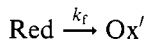
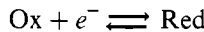
Figure 25 Cyclic voltammetric responses for an $E_rC_iE_r$ mechanism: $\Delta E^{\circ'} = +180$ mV. $k_f \cong nFv/RT$. $E_1^{\circ'} = 0.00$ V; $E_2^{\circ'} = +0.18$ V

that value the value of i_d at the desired scan rate (recalling as usual that i_p is proportional to $v^{1/2}$). The value of k_f is derived from the following relationship, under the assumption that $n_1 = n_2 = 1$:

$$\frac{i_k}{i_d} = \frac{0.400 + \frac{k_f \cdot R \cdot T}{F \cdot v}}{0.396 + 0.469 \frac{k_f \cdot R \cdot T}{F \cdot v}}$$

- The second way is to evaluate the ratio $i_{p(II)}/i_{p(I)}$ at a given scan rate and subsequently determine k_f from the working curve reported in Figure 16 (valid for ‘an irreversible chemical reaction following a reversible electron transfer’; Section 1.4.2.2).

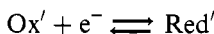
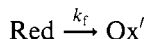
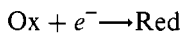
1.4.3.2 An ‘irreversible’ chemical reaction interposed between a reversible and an irreversible electron transfer (case R-I). The $E_rC_iE_i$ mechanism, involving one-electron transfers, can be written as:



The cyclic voltammetric response is essentially analogous to the case of $E_rC_iE_r$ (either for $\Delta E^{\circ'} = -180$ mV, or $\Delta E^{\circ'} = 0$ mV, or $\Delta E^{\circ'} = +180$ mV), except that the return peak (due to the reoxidation of Red to Ox') is always absent.

The kinetic parameter k_f can be found by determining the current ratio i_{pr}/i_{pf} of the first reversible couple Ox/Red and approximating the process to “a reversible electron transfer followed by a first-order irreversible chemical reaction”, as illustrated in the previous R-R case.

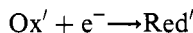
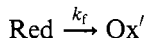
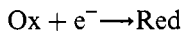
1.4.3.3 An ‘irreversible’ chemical reaction interposed between an irreversible and a reversible electron transfers (case I-R). The $E_iC_iE_r$ mechanism, involving one-electron transfers, is represented as:



Also in this case, the cyclic voltammetric response is substantially similar to the case of $E_rC_iE_r$, except that the return peak of the first electron transfer (due to reoxidation of Red to Ox) is always absent.

There are no simple ways to calculate the kinetic parameter k_f .

1.4.3.4 An 'irreversible' chemical reaction interposed between two irreversible electron transfers (case I-I). The $E_iC_iE_i$ mechanism, involving one-electron transfers, is represented as:



As for the preceding cases, the cyclic voltammetric response is rather similar to the case of $E_rC_iE_r$, except that both the return peaks are absent.

Once again there are no simple ways to calculate the kinetic parameter k_f .

1.4.3.5 Diagnostic criteria for ECE type processes. It is difficult to assign criteria to identify every type of ECE mechanism (R-R, R-I, I-R, I-I) and for every value of $\Delta E^\circ'$ ($\Delta E^\circ' \pm 180$ mV; $\Delta E^\circ' = 0$ mV).

The best approach is to calculate the current function $i_p/v^{1/2}$ as a function of the scan rate for every peak (both forward and reverse) and compare the resulting trends with those reported in Figures 26–28.¹²

These diagrams should be considered from a qualitative point of view. Furthermore, it is often not necessary to determine the trends of all the forward and reverse peaks, but only those that one judges to be the most significant. The scale of the potential scan rate in these plots is only illustrative and chosen to highlight the variations of the parameters that become evident on passing from slow to high scan rate.

1.4.4 Electrocatalysis. There is a particular type of ECE electrode reaction mechanism which is designated as $\overline{\text{E}}\overleftarrow{\text{C}}\overleftarrow{\text{E}}$ (the arrows indicate that the second electron transfer consists of a inverse reaction with respect to the first). This process is called *electrocatalysis* and is of importance in inorganic chemistry.¹³

Before proceeding it is necessary to clarify the terminology of two fairly similar processes, at least as far as their nomenclature is concerned: 'redox' catalysis and 'electron-transfer chain' catalysis.

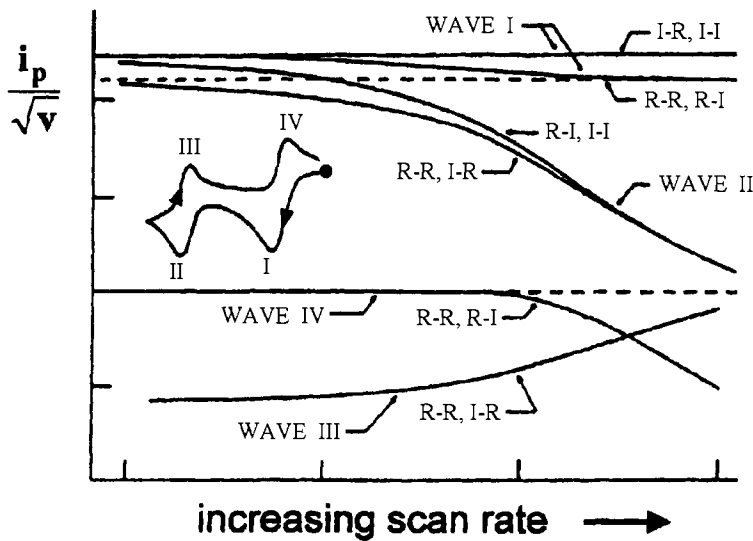


Figure 26 Diagnostic criteria showing the variation of the parameter $i_p \cdot v^{-1/2}$ as a function of the scan rate. $\Delta E^{\circ'} = -180 \text{ mV}$; $n_2/n_1 = 1.0$

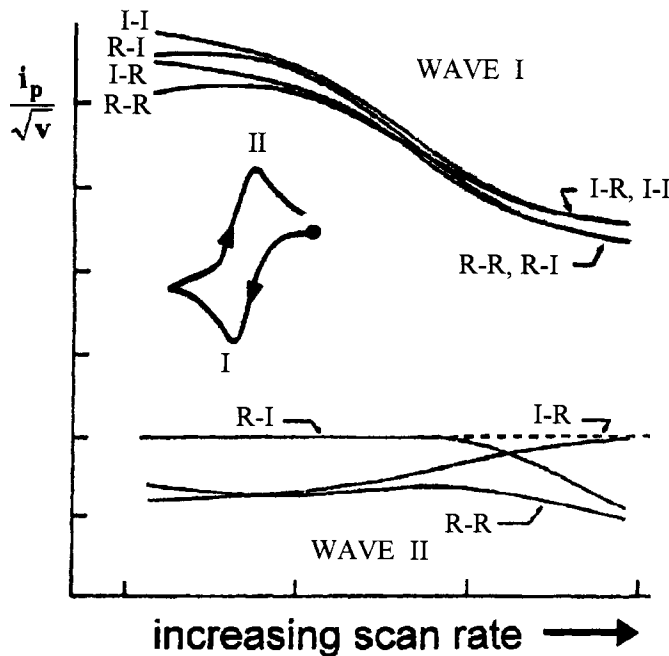


Figure 27 Diagnostic criteria showing the variation of the parameter $i_p \cdot v^{-1/2}$ as a function of the scan rate. $\Delta E^{\circ'} = 0 \text{ mV}$; $n_2/n_1 = 1.0$. (The wave II is absent in the case I-I)

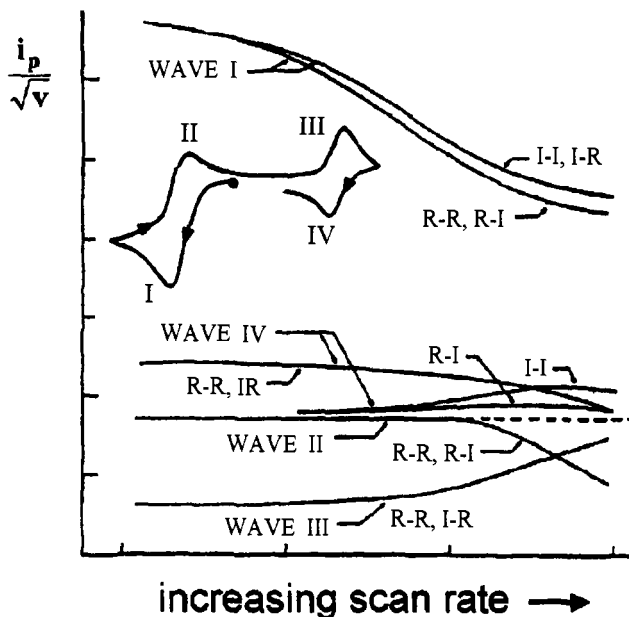
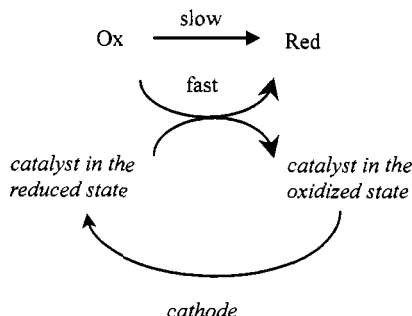


Figure 28 Diagnostic criteria showing the variation of the parameter $i_p \cdot v^{-1/2}$ as a function of the scan rate. $\Delta E^\circ' = +180 \text{ mV}$; $n_2/n_1 = 1.0$. (The wave II is absent in the cases I-R and I-I; the wave III is absent in the cases R-I and I-I)

Redox catalysis, which will not be discussed in detail herein, consists of lowering the kinetic barrier of the reduction (or the oxidation) process of a species, which thermodynamically is little inclined to be reduced (or oxidized), by use of a *redox mediator*. The latter has the role of carrying electrons towards (or away from) the low redox-active original species.

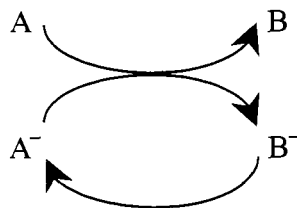
If we consider a particular species Ox, which is difficult to reduce, the above process can be described by the following scheme:



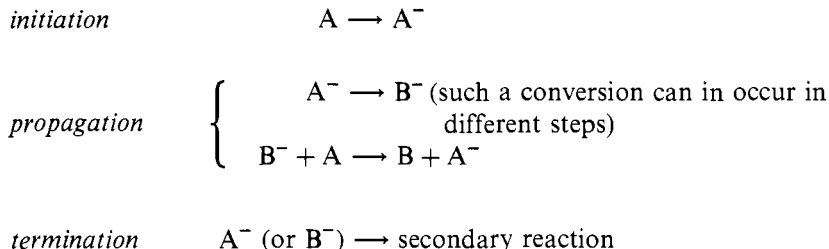
By applying a potential to the electrode equal to the reduction potential of the catalyst (the redox mediator) the catalyst is reduced, but, upon contact with the oxidized form Ox, a redox reaction takes place in which Ox is reduced to Red and the mediator reoxidized. At this point the continuous cathodic reduction of the catalyst reactivates the whole process and the catalytic cycle is repeated.

The *electron-transfer chain* (ETC) catalytic process (or, electrocatalysis) is the catalysis of a reaction triggered by electrons (through a minimal quantity of an oxidizing or reducing agent) without the occurrence of an overall change in the oxidation state of the reagent.

For example, let's suppose that the conversion reaction $A \rightarrow B$ is slow. If the substrate A becomes activated in its anionic radical form A^- (or, if proper, in its cationic radical form A^+) and it rapidly converts to the radical anion B^- , this latter can in turn react rapidly with the initial species A to form B, so closing the reaction cycle.



Written in a more detailed scheme:



To ensure that the redox cross-reaction $B^- + A \longrightarrow B + A^-$ can take place, it is essential that the radical species B^- be oxidized more easily than A^- . Hence:

$$E_{A/A^-}^{\circ'} > E_{B/B^-}^{\circ'}$$

where $>$ implies less negative or more positive.

It must be noted that the activation process $A \longrightarrow A^-$ (*initiation*) can be triggered either by chemical routes (through a proper reducing agent) or

electrochemically (by a cathodic reaction). We are therefore interested in the *electrochemically induced catalytic* processes.

One obtains the first indication of the possible existence of an electrocatalytic process from cyclic voltammetry.

A typical electrocatalytic reaction is the ligand exchange in metal complexes (see Chapter 8, Sections 3.1 and 3.2).

One may suppose, for example, that, as illustrated in Figure 29a, an original complex $M(L^1)_n$ gives a cathodic response consistent with a reversible one-electron process (say at $E^{\circ'} = -0.50$ V).

When the cyclic voltammogram is recorded in the presence of the new ligand, L^2 , the curve illustrated in Figure 29b is obtained. This profile shows that the first cathodic response reduces in intensity, opening the way for a new process at lower potential (*i.e.* $E^{\circ'} = -0.80$ V).

To demonstrate the existence of an electrocatalytic ligand exchange it is sufficient to carry out a controlled potential electrolysis in correspondence of the first reduction process. In the absence of ligand L^2 , the electrolysis at about -0.7 V involves (over a period of about 10 min; really depending on the dimensions of the working electrode and the concentration of the solution) the consumption of one-electron per molecule [*i.e.* 96500 C

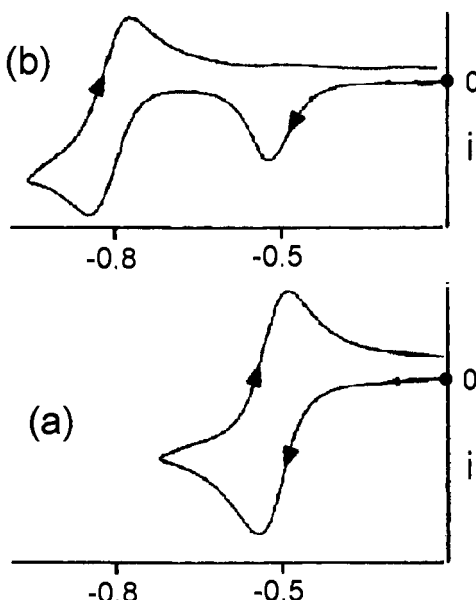
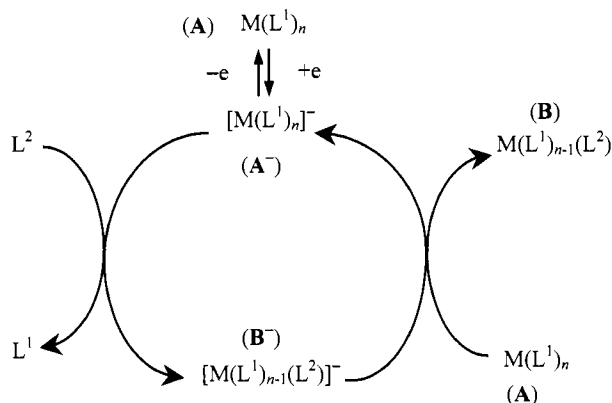


Figure 29 (a) Cyclic voltammetric response relative to the reduction of the complex $M(L^1)_n$. (b) Cyclic voltammetric response after the addition in solution of the free ligand L^2 . Scan rate identical in the two cases

per mole of $M(L^1)_n$. In the presence of ligand L^2 , if the electrocatalytic process takes place, the electrolysis current decays rapidly (in a few seconds) consuming a fraction of one-electron per molecule (typically about 0.02 electrons per molecule). When a cyclic voltammogram is recorded on the resulting solution, one notes the presence of only the cathodic peak-system at $E^\circ' = -0.80$ V.

The electrocatalytic process can, thus, be written:



where the symbols A , A^- , B , B^- are as referred to in the previous scheme.

One must bear in mind that if the initial complex would be able to exchange more than one ligand molecule to give rise to $M(L^1)_{n-2}(L^2)_2$, $M(L^1)_{n-3}(L^2)_3$, and so on, the cyclic voltammogram would display a number of reduction peaks in addition to the more cathodic one shown in Figure 29b, equal to the further number of ligand molecules exchanged.

A few terms of the electrocatalytic process still need to be defined.

The first is the catalytic efficiency of the electrocatalytic process, which in the case of the electrochemically induced reaction is called *coulombic efficiency*. It is determined by the number of product molecules formed per electron consumed. In our example, the consumption of 0.02 electrons per molecule indicates a coulombic efficiency of 50 molecules produced per electron consumed.

The *driving force* of the electrocatalytic process is expressed by the variation of the free energy of the overall process (which must clearly be negative), according to the relationship:

$$\Delta G_{ET} = 96.485 \left(E_B^\circ - E_A^\circ + \frac{e^2}{\epsilon_0 \cdot r} \right) \text{ (kJ mol}^{-1}\text{)}$$

where E°_B and E°_A are the standard potentials (in volts) of the final B/B^- and the initial A/A^- redox couples, respectively. The coulombic energy term, $e^2/\epsilon_0 \cdot r$ can be usually neglected.

For the case illustrated in Figure 29, where the difference between the redox potential of the initial couple $M(L^1)_n/[M(L^1)_n]^-$ and of the final couple $M(L^1)_{n-1}(L^2)/[M(L^1)_{n-1}(L^2)]^-$ is 0.3 V, the driving force is $\Delta G_{ET} \approx -29 \text{ kJ mol}^{-1}$.

1.5 Consecutive Electron Transfer Processes

In an aqueous medium the reduction of inorganic ions (for example, Cu^{2+} , Zn^{2+} , Cd^{2+}) to their respective metallic states takes place by a single two-electron process. In effect, however, the process only apparently involves a two-electron step, in that it is assumed that multi-electron processes proceed by a sequence of elementary one-electron steps. Every elementary step is characterized by its own rate constant and its own standard potential.

In confirmation of such an assumption, as illustrated in Figure 30, the Cu^{2+} ion in non-aqueous solvents (*e.g.* acetonitrile) is reduced in two separate steps, which correspond to:

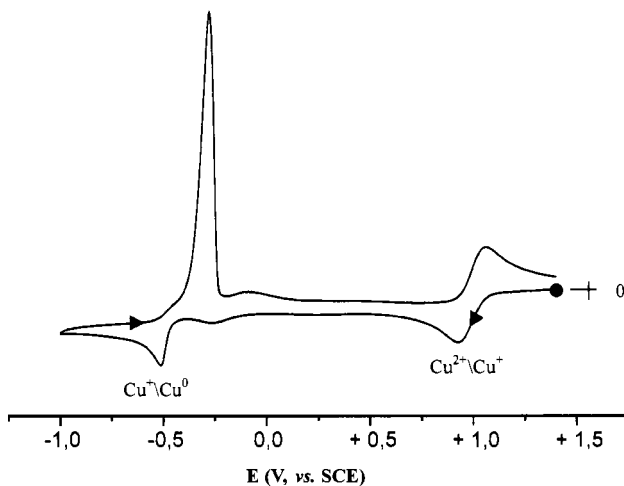
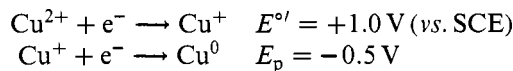


Figure 30 Cyclic voltammogram recorded at a platinum electrode in an acetonitrile solution of $\text{Cu}(\text{ClO}_4)_2$, $\{\text{NEt}_4\}/[\text{ClO}_4]$ (0.1 mol dm^{-3}) supporting electrolyte}. Scan rate 0.2 V s^{-1}

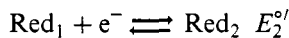
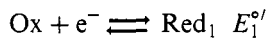
The high current intensity associated with the return peak relative to the second reduction process is characteristic of the so-called *anodic stripping*, which originates from the fast reoxidation of the metallic copper deposited on the electrode surface during the Cu^+/Cu^0 reduction.

Therefore, given that a multi-electron process can be described as a series of one-electron transfers, more or less separated from each other, the shape of the cyclic voltammogram depends on the following factors:¹⁴

- the degree of reversibility of the successive electron transfers;
- the separation between the respective standard potentials.

1.5.1 Two reversible one-electron transfers. The simplest case to treat consists of two successive one-electron transfers (*EE mechanism*).

If both processes are reversible the mechanism can be represented as:



When Ox is more easily reduced than Red₁ (by at least 120 mV), hence $E_1^\circ' \gg E_2^\circ'$ (intending that E_1°' can be either less negative or more positive than E_2°'), the cyclic voltammogram will show two discrete reversible peaks systems, Figure 31a.

As the difference between the standard potential of the two processes ($\Delta E^\circ' = E_2^\circ' - E_1^\circ'$) decreases, the two peaks tend to overlap and become less distinguishable. This is the case in Figure 31b, where E_2°' is more cathodic than E_1°' by only 90 mV.

As shown in Figure 31c, when $E_2^\circ' = E_1^\circ'$, one obtains a single catho-anodic peak-system, the peak height of which is twice that of a one-electron process and the peak-to-peak separation (ΔE_p) is equal to 42 mV.

Finally, if Red₁ is more easily reduced than Ox (*i.e.* $E_2^\circ' > E_1^\circ'$), once again one has a single catho-anodic peak-system, Figure 31d. However, in this case the peaks are sharper. In fact, ΔE_p is equal to 28.5 mV and the forward peak current is 2.83-fold larger than that of a one-electron process (*i.e.* $2^{3/2}$, according to the Randles–Sevcik equation, Section 1.1). The average potential measured between E_{pr} and E_{pr} is, in this case, intermediate between E_1°' and E_2°' .

It is conceivable that from the molecular viewpoint there are some important differences between the occurrence of separate and simultaneous two-electron transfers. In fact, in principle, the addition of the first electron must make the second electron addition electrostatically

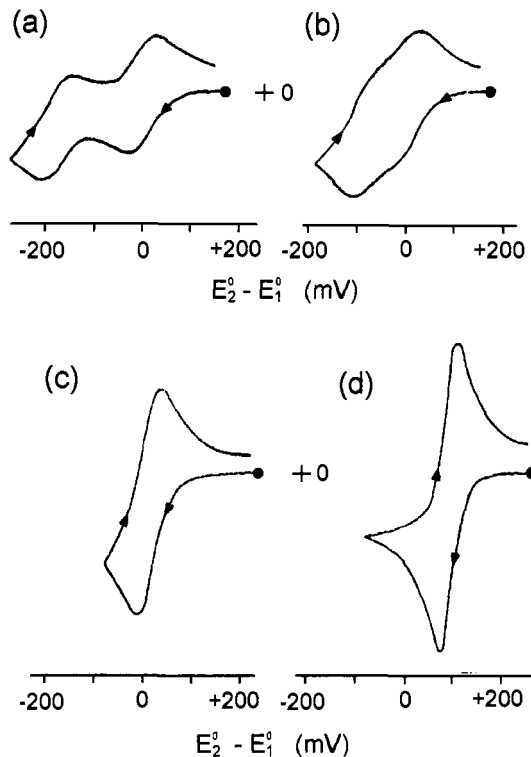
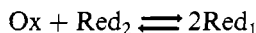


Figure 31 Cyclic voltammograms for the E_rE_r mechanism. (a) $\Delta E^{\circ'} = -180 \text{ mV}$; (b) $\Delta E^{\circ'} = -90 \text{ mV}$; (c) $\Delta E^{\circ'} = 0 \text{ mV}$; (d) $\Delta E^{\circ'} = +180 \text{ mV}$. $E_i^{\circ} = 0.00 \text{ V}$

unfavourable (and this is what commonly happens in separate electron transfer processes), unless some molecular reorganization at the microscopic level occurs within the original molecule, which, rendering available a non-bonding molecular orbital, can allow the second electron to enter simultaneously or even more favourably than the first one.

It should be recalled that in the case of the EE mechanism, in solution one can have the *comproportionation* reaction:



the equilibrium constant of which, K_{com} , in its most general form, is expressed by:¹⁵

$$K_{\text{com}} = e \frac{n_1 \cdot n_2 \cdot \Delta E^{\circ'} \cdot F}{R \cdot T}$$

In order to have a positive exponent, $\Delta E^{\circ'}$ is given by $(E_1^{\circ'} - E_2^{\circ'})$ for cathodic processes, or by $(E_2^{\circ'} - E_1^{\circ'})$ for anodic processes. In the present case, since $n_1 = n_2 = 1$:

$$K_{\text{com}} = e^{\frac{(E_1^{\circ'} - E_2^{\circ'})F}{R \cdot T}}$$

As discussed above, when $E_1^{\circ'}$ and $E_2^{\circ'}$ are closely spaced, the curve is distorted in that the two peak-systems are ill-resolved. This makes it difficult to determine separately the values of $E_1^{\circ'}$ and $E_2^{\circ'}$. As a matter of fact, the separation ($\Delta E^{\circ'}$) between $E_1^{\circ'}$ and $E_2^{\circ'}$ as a function of the difference ($\Delta E_p'$) between the potential of the most cathodic and the most anodic peaks (see Figure 32) has been calculated theoretically.

Such values are reported in Table 2, together with those of a 'current function'. The latter parameter is correlated to the variation of the relative height of the peak current as a function of $\Delta E^{\circ'}$, where one considers the first value of 0.619 as indicative of a one-electron process.

The data partly give a quantitative presentation of the preceding discussion and can also be converted into the working curve shown in Figure 33.¹⁵ The use of this curve enables an immediate evaluation of $\Delta E^{\circ'}$ through the measurement of $\Delta E_p'$.

This type of treatment is particularly interesting as it allows one to understand, in a molecule containing two redox sites, whether or not there is an electronic interaction (independently from its *through-bond* or *through-space* nature) between the sites, or, with a more attracting term, an electronic 'communication' between the sites.

In fact, when there is no interaction a statistical treatment shows that the comproportionation constant, K_{com} , takes a value of 4 and, therefore, $\Delta E^{\circ'} = 35.6$ mV. In this case the cyclic voltammogram is of

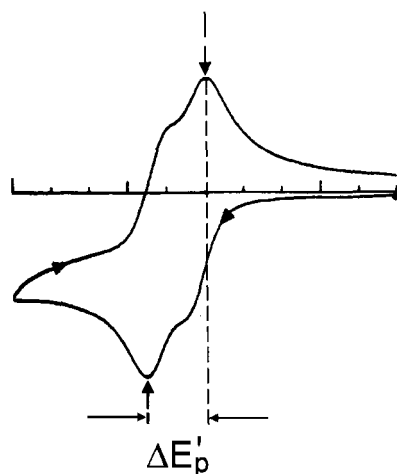
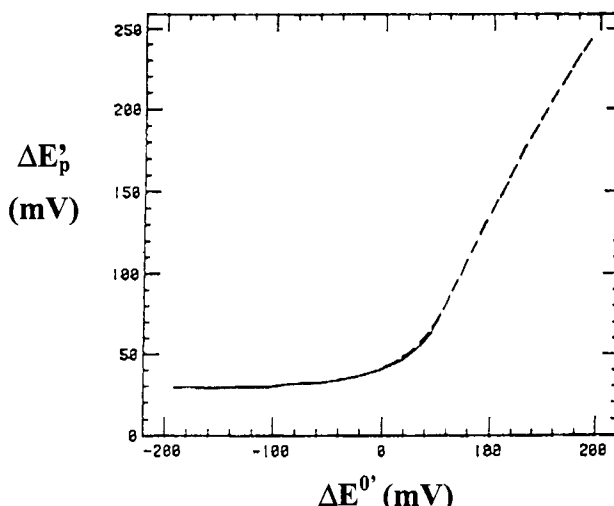


Figure 32 The meaning of the parameter $\Delta E_p'$

Table 2 Cyclic voltammetric parameters for an EE process (obtained at scan rates of 20–50 mVs⁻¹)

$\Delta E_p'$ (mV)	$\Delta E^{\circ'}$ (mV)	Current function	$\Delta E_p'$ (mV)	$\Delta E^{\circ'}$ (mV)	Current function
252	-200	0.619	62.7	-40	0.872
210	-160	0.639	58.5	-35.6	0.892
188	-140	0.674	54.9	-30	0.909
164	-120	0.694	49.3	-20	0.945
152	-110	0.706	45.2	-10	0.980
140	-100	0.720	42.2	0	1.019
126	-90	0.739	37.0	+20	1.078
113	-80	0.755	35.9	+40	1.124
98.9	-70	0.779	34.0	+60	1.162
85.2	-60	0.807	30.8	+100	1.212
72.4	-50	0.838	29.8	+200	1.254

the type reported in Figure 31c, but as is deduced from Table 2, with a peak-to-peak separation $\Delta E_p' = 60$ mV. The voltammogram is, therefore, apparently similar to that of a reversible one-electron process. In reality, the peak current is higher than that of a one-electron process, but this cannot be preliminarily detected. Conversely, if there is an electronic interaction between the sites, $\Delta E^{\circ'}$ increases and K_{com} increases.

**Figure 33** Working curve $\Delta E_p'/\Delta E^{\circ'}$ for an EE process, in which both the electron transfers are reversible

A more detailed discussion on this topic will be considered in Chapter 4, Section 1.3. Structurally, to a first approximation, a criterium to determine the electronic interaction between redox active sites is to evaluate the distance between the sites: *the greater the distance between redox centres, the smaller their interaction.*

Finally, given a certain distance between two redox centres, the *delocalization* of the first added electron between the two centres makes the addition of the successive electron electrostatically more difficult; therefore, $\Delta E^{\circ'}$, and hence K_{com} , increase.¹⁶

1.5.2 Two one-electron transfers with different extents of reversibility. In the case where not all the processes of a consecutive electron transfer sequence are reversible, the irreversibility of a particular step becomes evident by the absence of the reverse peak in its pertinent response. For all other aspects the preceding considerations remain valid.

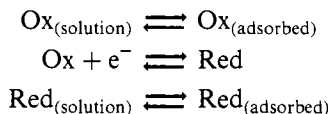
Figure 34 shows some typical cyclic voltammetric responses for two-electron processes in which one of the steps is irreversible.

1.5.2.1 Diagnostic criteria for two-electron transfers with different extents of reversibility. The voltammetric responses of *EE* processes can be qualitatively confused with processes complicated by coupled chemical reactions. The only distinctive criterium to define these processes is the constancy of the parameter $i_p/v^{1/2}$ relative to each step with the scan rate.

1.6 Adsorption Processes.

The transport of electro active species from the bulk of the solution to the electrode may be governed not only by diffusion but also by adsorption of the species on the electrode surface. When both the mechanisms are operative, the overall electrochemical process may give considerably complicated results. The theoretical treatment is complex and of limited interest to inorganic chemists, therefore, a qualitative approach will be adopted to identify the presence of adsorption phenomena.

The typical scheme describing the electrode mechanism complicated by adsorption processes is the following:



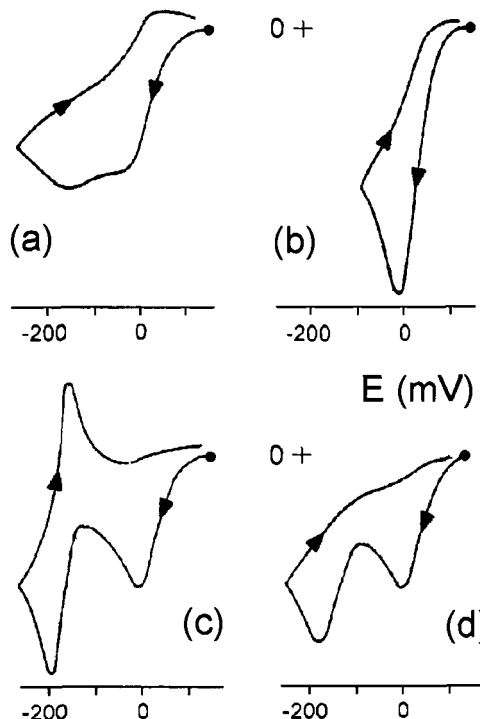


Figure 34 Typical cyclic voltammograms for a two-electron transfer process in which one of the steps is irreversible. Case R-I: (a) $\Delta E^{\circ\prime} = -180 \text{ mV}$; (b) $\Delta E^{\circ\prime} = 0 \text{ mV}$. Case I-R: (c) $\Delta E^{\circ\prime} = -180 \text{ mV}$. Case I-I: (d) $\Delta E^{\circ\prime} = -180 \text{ mV}$

It represents a reversible electron transfer complicated by adsorption (in equilibrium with diffusive motions) of either Ox or Red.

Figure 35 shows the typical cyclic voltammetric responses of the four most common cases of electron transfer processes complicated by adsorption compared with a simple reversible electron transfer.¹⁷

As Figures 35a,b show, with respect to an uncomplicated electron transfer process, for a weak adsorption one expects:

- a significant increase in the height of the forward peak, when the reagent Ox is the adsorbed species
- a significant increase in the height of the reverse peak, when the product Red is the adsorbed species.

This anomaly becomes more evident with the scan rate. In fact, while in the case of a simple reversible electron transfer the current function, $i_p/v^{1/2}$, remains constant with the scan rate, in the case

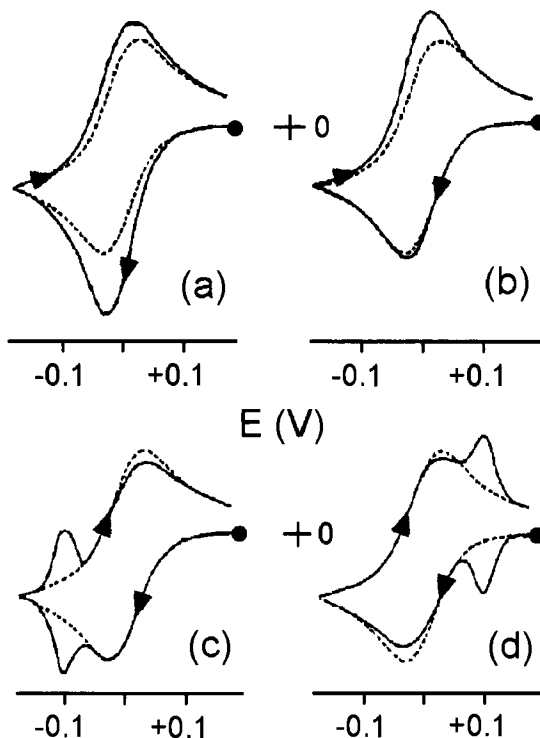


Figure 35 Comparison between the cyclic voltammetric responses of a reversible one-electron process ($E^{\circ'} = 0.00\text{ V}$) complicated by different adsorption phenomena (—) and that of a reversible one-electron process (---). (a) Weak adsorption of the reagent Ox; (b) weak adsorption of the product Red; (c) strong adsorption of the reagent Ox; (d) strong adsorption of the product Red

of weak adsorption of the reagent such a current function increases markedly (this is the only case in which such an effect is observed). In fact, under the effects of adsorption what remains constant with the scan rate is the ratio i_p/v . On the other hand, for weak adsorption of the product, the anomalous increase in the height of the reverse peak with the scan rate makes the current ratio, i_{pr}/i_{pf} , become greater than 1.

Finally, as shown in Figures 35c,d, for strong adsorption pre- and post-peaks appear in the cyclic voltammetric response. Namely:

- a *pre-peak* appears when the adsorbed species is the *product Red*
- a *post-peak* appears when the adsorbed species is the *reagent Ox*.

The separation between the adsorption peak (pre- or post-peak) and the peak due to the diffusive electron transfer can be taken as a qualitative

measure of the adsorption energy. The larger the separation, the stronger the adsorption.

It is noted that on increasing the scan rate the intensity of the adsorption peak (which linearly increases with v) tends to become larger than that of the diffusive peak (which linearly increases with $v^{1/2}$), such that at high scan rates the diffusive peak may completely disappear.

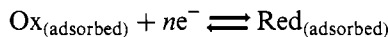
A simpler case occurs when only the adsorbed species on the electrode surface are electro active.

Such a situation may be found when:

- the species in solution Ox/Red are not electro active in the potential range considered
- the concentration of Ox in solution is so low (with respect to the amount of Ox adsorbed) that a negligible diffusive current is produced.

In such cases it is clear that the diffusive transport plays no role, as only the species already adsorbed on the electrode surface are electro active.

Let us consider the case in which the electron transfer of the adsorbed species is reversible:



As Figure 36 illustrates, in such cases the cyclic voltammetric response is quite sharp and the forward and reverse peaks are completely symmetric (*i.e.* the peak-to-peak separation $\Delta E_p \approx 0$; both the forward and reverse currents start at zero, reach a maximum value then return to zero).

When this happens the adsorption phenomenon follows the so-called *Langmuir isotherm** and the current intensity at the maximum of the forward peak is correlated with the parameter $\Gamma_0^\#$ (that represents the quantity of Ox, in mol m^{-2} , initially adsorbed on the electrode surface) and with the scan rate according to the relationship:

$$i_p = \frac{n^2 \cdot F^2 \cdot \Gamma_0^\# \cdot A}{4 \cdot R \cdot T} v$$

This expression shows that, as previously mentioned, the peak current increases linearly with the scan rate (as it happens for

* An *adsorption isotherm* describes the way in which the concentration of the species adsorbed on the electrode, Γ_t , depends on the activity, a_i , of the species in solution. Langmuir's isotherm is the simplest equation for adsorption phenomena, but it must be kept in mind that it is generally valid only for non-ionic species.

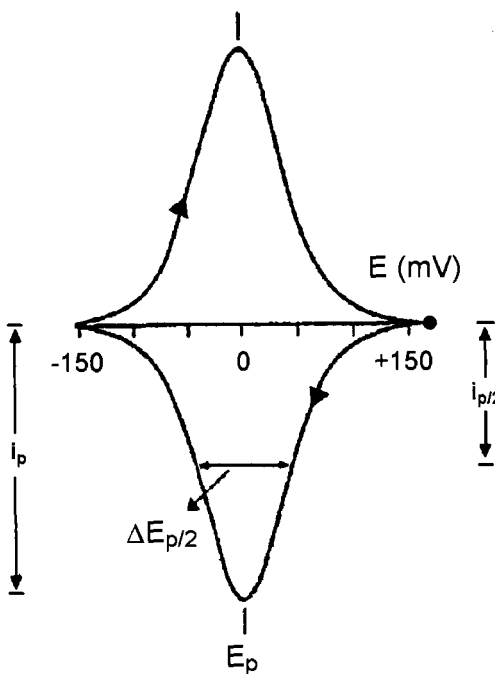


Figure 36 Cyclic voltammetric response theoretically expected for the reversible reduction of $Ox_{(adsorbed)}$

the *capacitive currents*, see Chapter 1, Section 5), in contrast with diffusive processes where the peak currents increase with the square root of the scan rate.

The area subtended by the forward peak represents the charge flown in the course of the reduction process of $Ox_{(adsorbed)}$, thus:

$$\text{peak area} = n \cdot F \cdot A \cdot \Gamma_0^{\#}$$

The peak potential E_p is correlated with the formal electrode potential $E^{\circ'}$ of the couple Ox/Red by the expression:

$$E_p = E^{\circ'} - \frac{R \cdot T}{n \cdot F} \ln \frac{b_{\text{Ox}}}{b_{\text{Red}}}$$

where b_{Ox} and b_{Red} represent the degree of absorption of Ox and Red, respectively. This implies that if $b_{\text{Ox}} = b_{\text{Red}}$: $E_p = E^{\circ'}$.

In this ideal case it is useful to bear in mind that the width of the peak at half height, $\Delta E_{p/2}$, shown in Figure 36, can be exploited to

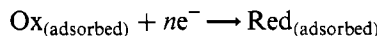
calculate the number of electrons spent in the process $\text{Ox}_{(\text{adsorbed})}/\text{Red}_{(\text{adsorbed})}$, since:

$$\Delta E_{p/2} = 3.53 \frac{R \cdot T}{n \cdot F}$$

or, at 25°C:

$$\Delta E_{p/2} = \frac{90.6}{n} \text{ (mV)}$$

In the case that the reduction process of the adsorbed species is irreversible:



the peak shape is still quite sharp, however, not only the reverse peak results are now absent, but the forward peak also loses its symmetry, Figure 37.

In this case, the width of the half-peak is given by the relationship:

$$\Delta E_{p/2} = 2.44 \frac{R \cdot T}{\alpha \cdot n_\alpha \cdot F}$$

or, at 25°C:

$$\Delta E_{p/2} = \frac{62.5}{\alpha \cdot n_\alpha} \text{ (mV)}$$

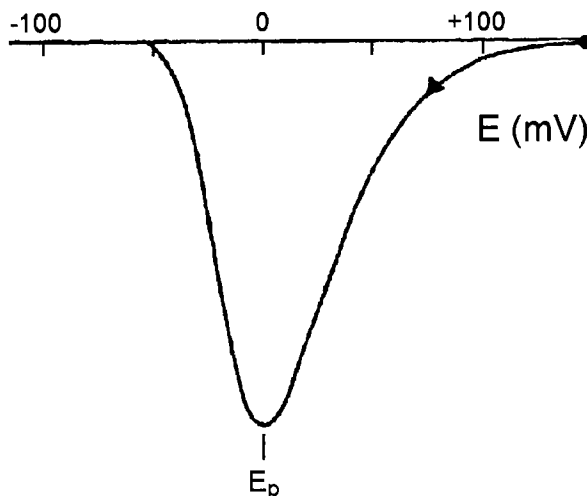


Figure 37 Cyclic voltammetric response theoretically expected for the irreversible reduction of $\text{Ox}_{(\text{adsorbed})}$

Finally, if the reduction process of the adsorbed species is *quasireversible* the curve will exhibit the reverse peak, but the peak-system will not be completely symmetric.

2 ELECTROCHEMICAL TECHNIQUES COMPLEMENTARY TO CYCLIC VOLTAMMETRY

2.1 Pulsed Voltammetric Techniques

As outlined in Section 1.5, consecutive electron transfers possessing electrode potentials separated by less than 0.1 V afford in cyclic voltammetry more or less overlapping peak-systems which cannot be adequately resolved to obtain the precise standard electrode potential for each step. In these cases it is convenient to make use of pulsed techniques.

All the pulsed techniques have as a target to exalt the faradaic currents while minimizing the interfering *capacitive currents*. These techniques exploit the different decay rate of the faradaic currents (which, decaying with the square root of the time, *decay rather slowly*) with respect to the decay rate of the capacitive currents (which, decaying exponentially with time, *decay quickly*). This means that, after a short time (from μs to ms) from the application of a potential value to the working electrode proper to trigger the electron transfer, the current is purely faradaic.

In this connection, two techniques are particularly useful in the analysis of partially overlapping processes:

- differential pulse voltammetry
- square wave voltammetry

These techniques usually make use of the same equipment used for cyclic voltammetry.

2.1.1 Differential Pulse Voltammetry. As illustrated in Figure 38, in the Differential Pulse Voltammetry (DPV) the perturbation of the potential with time consists in superimposing small constant-amplitude potential pulses ($10 < \Delta E_{\text{pulse}} < 100 \text{ mV}$) upon a staircase waveform of steps of constant height but smaller than the previous pulses ($1 < \Delta E_{\text{base}} < 5 \text{ mV}$).

The important parameters are:

- the *pulse amplitude* (ΔE_{pulse}), which is the height (in mV) of the applied potential pulse;
- the *pulse width*, which is the length of the time (in ms) in which the pulse is maintained;

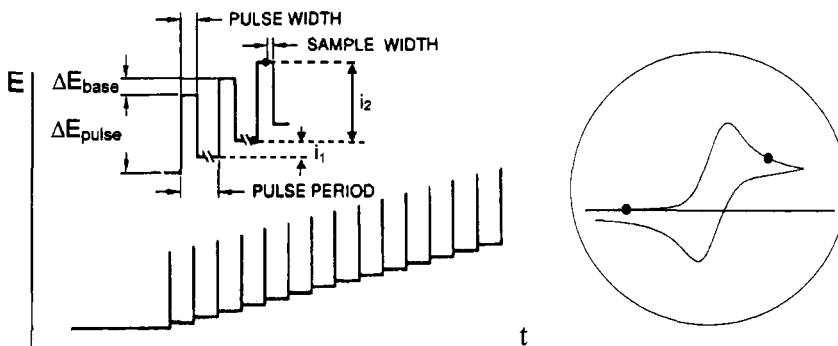


Figure 38 Potential-time pulses in Differential Pulse Voltammetry

- the *sample width*, which is the time (in ms) at which the current is measured after the application of the potential pulse;
- the *pulse period*, which is the time (in ms) needed to make one cycle of variation of potential.

As illustrated by the dots in Figure 38, during a pulse period the current is periodically sampled twice: before the pulse, i_1 , and at the end of the pulse, i_2 , respectively. For the sake of simplicity, as illustrated in the inset, if we could extrapolate to a cyclic voltammogram, it would correspond to sampling the currents at the foot of the forward peak and just after having traversed the forward peak. It is evident that after subtracting the two currents (*i.e.* $i_2 - i_1$) most of the capacitive currents are eliminated. Thus a differential-pulse voltammogram is a plot of the difference ($i_2 - i_1$) *vs.* the potential progression.

In contrast to linear single sweep or cyclic voltammetry, which give non-symmetric peaks, DPV affords symmetric peaks which start from zero-current values and finish at zero-current values, see Figure 39.

It is noted that for reversible electron transfers, the peak potential in DPV is almost coincident with the $E^{\circ'}$ value of the couple under study, in that:

$$E_p = E^{\circ'} - \frac{\Delta E_{\text{pulse}}}{2}$$

but as said, ΔE_{pulse} is usually low (~50 mV).

For a reversible process the width of the peak at half height, $\Delta E_{p/2}$, is given by:

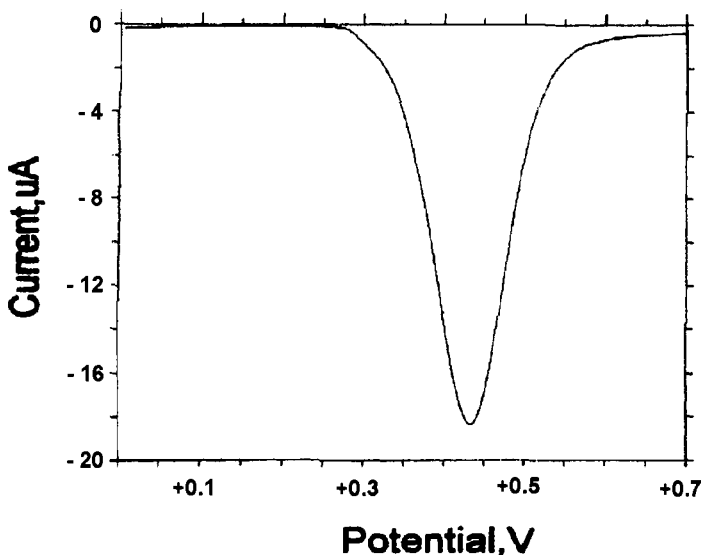


Figure 39 Typical voltammogram in DPV

$$\Delta E_{p/2} = 3.52 \frac{R \cdot T}{n \cdot F}$$

or, at 25°C:

$$\Delta E_{p/2} = \frac{90.4}{n} \text{ (mV)}$$

As it happens for adsorption (Section 1.6), such relationships would allow in principle the number of electrons involved in the electrode process to be determined.

As mentioned, DPV is particularly useful to determine accurately the formal electrode potentials of partially overlapping consecutive electron transfers. For instance, Figure 40 compares the cyclic voltammogram of a species which undergoes two closely spaced one-electron oxidations with the relative differential-pulse voltammogram. As seen in DPV the two processes are well separated.

Nevertheless, it must be taken into account that DPV presents two limitations:

- in principle, it would need the use of the dropping mercury electrode (even if it also works very well with solid electrodes under stationary conditions);
- it employs rather low scan rates (lower than 0.02 V s^{-1}), which can lead to difficulty in interpreting responses in those cases in which

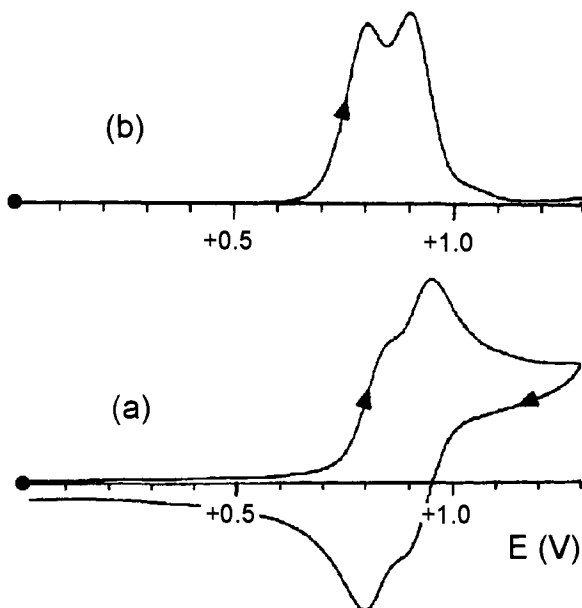


Figure 40 Comparison between the cyclic (0.2 V s^{-1}) and the differential-pulse (0.02 V s^{-1}) voltammetric responses of a species which undergoes two sequential one-electron oxidations

the electrogenerated species are not stable (*i.e.* in cases of following chemical complications).

2.1.2 Square Wave Voltammetry. As illustrated in Figure 41, in the Square Wave Voltammetry (SWV), in particular in the Osteryoung Square Wave Voltammetry (OSWV), the perturbation of the potential with time consists of an in-phase combination of a staircase waveform of small and constant step height ($1 < \Delta E_{\text{base}} < 40 \text{ mV}$) with periodic square wave pulses ($1 \leq \Delta E_{\text{SW}}$ ($= 1/2$ square wave amplitude) $\leq 250 \text{ mV}$). This last perturbation consists of pulses alternating in direction, *i.e.* a succession of forward (reduction, or oxidation) and reverse (oxidation, or reduction) cycles ($1 \leq \text{frequency SW} \leq 2000 \text{ Hz}$). The overall result is a sequence of equally spaced steps: the forward step of height: $2\Delta E_{\text{SW}} + \Delta E_{\text{base}}$; the reverse step of height: $-2\Delta E_{\text{SW}}$.

As indicated by the dots, the current is sampled at the end of either the forward pulse, i_f , or the reverse pulse, i_r . Schematically, as illustrated in the inset, making reference to a cyclic voltammogram, we can imagine that the currents are sampled after traversing the forward peak and after traversing the reverse peak, respectively. It is evident that the waiting times before each sampling make the capacitive currents disappear.

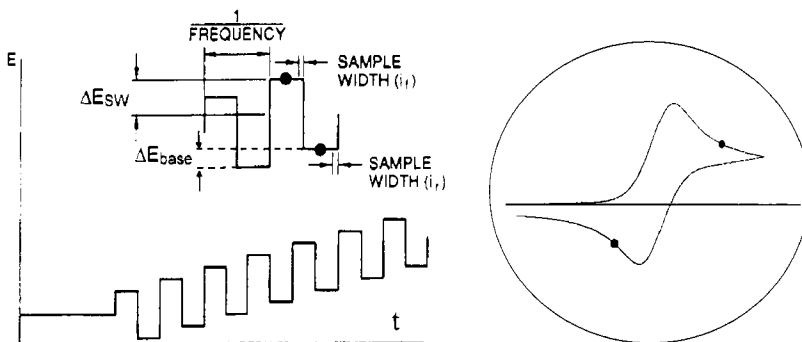


Figure 41 Potential–time perturbation in Osteryoung Square Wave Voltammetry

As shown in Figure 42, the square wave voltammogram, as in DPV, is peak-shaped, but it consists of a differential curve between the current recorded in the forward half-cycle and the current recorded in the reverse half-cycle (pay attention to the fact that, since the forward and the reverse currents have opposite signs, their difference corresponds in absolute to their sum).

As it happens in DPV, if ΔE_{SW} is small (about $50/n$ mV), the peak-potential for a reversible process virtually coincides with the formal electrode potential.

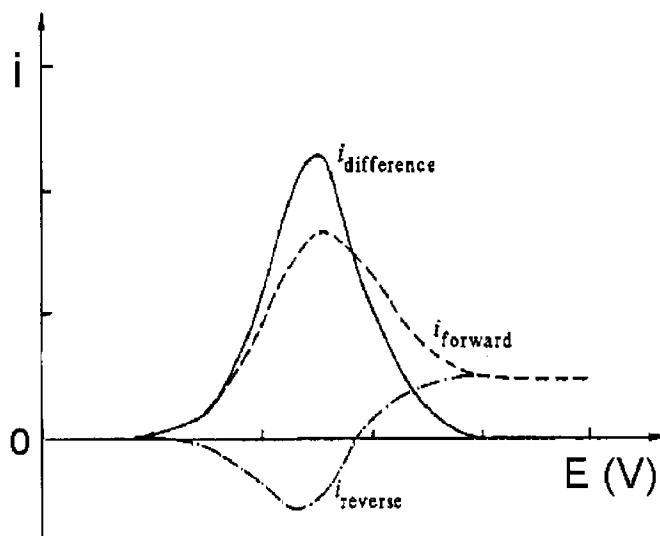


Figure 42 Typical voltammogram in OSWV

In addition, for a reversible process the width of the peak at half height, $\Delta E_{p/2}$, is given by:

$$\Delta E_{p/2} = 4.90 \frac{R \cdot T}{n \cdot F}$$

or, at 25°C:

$$\Delta E_{p/2} = \frac{126}{n} \text{ (mV)}$$

Like DPV, OSWV is very effective in solving almost overlapping processes. With respect to DPV, OSWV can use higher scan rates (from a few hundreds of mV s^{-1} to a few V s^{-1}). The typical scan rate (which is given by the product: $SW\ frequency \times \Delta E_{base}$) is around 0.2 V s^{-1} (which is the typical scan rate of cyclic voltammetry). This allows one to compete with the eventual presence of chemical complications coupled to the electron transfers.

2.2 Hydrodynamic Techniques

There are a few electrochemical techniques in which the working electrode is moved with respect to the solution (*i.e.* either the solution is agitated or the electrode is vibrated or rotated). Under these conditions, the thickness of the diffusion layer decreases so that the concentration gradient increases. Since the rate of the mass transport to an electrode is proportional to the concentration gradient (Chapter 1, Section 4.2.2), the thinning of the diffusion layer leads to an increase of the mass transport, and hence to an increase of the faradaic currents.

The ability of varying the rate of the mass transport by agitating the solution (or the working electrode) constitutes the basis of *hydrodynamic* methods (hydrodynamics = liquids in motion), which are a further support to the study of electrode kinetics. Nevertheless we wish to cite them here simply to cover a drawback of cyclic voltammetry. In fact, cyclic voltammetry is unable to discriminate between oxidation and reduction processes, and *vice-versa*.

In order to understand the meaning of such a sentence one must consider that the *starting potential* for a cyclic voltammetric scan must be selected on the basis of the *zero-current* condition, or to start from a potential value at which no electron transfer occurs at the working electrode. Even if one was wrong in the choice of the starting potential, *i.e.* one could have selected a potential at which an electrode process is taking place, it is very unlikely that one can realize it, in that the

stationary conditions of the solution and the common use of electrodes of a small area both lead to very small currents (even if some modern instruments are able to detect zero-current potential values).

As an example, Figure 43 shows the cyclic voltammetric profiles of a species which undergoes sequential electron transfers.

It is quite evident that it is very difficult to decide if the first process is a reduction step, Figure 43a, or an oxidation step, Figure 43b.

To obviate possible erroneous interpretation of the cyclic voltammetric profiles (particularly in those cases in which an oxidation process occurs at negative potential values as well as a reduction process occurring at positive potential values), it is always wise to perform preliminarily hydrodynamic tests.

The most well-known hydrodynamic technique is the Rotating Disk Electrode (RDE) voltammetry, which, however, needs proper equipment. For information on this technique the reader is referred to specialized treatments.²⁻⁴ We prefer here to mention a simpler technique which can be carried out on the same equipment used for cyclic voltammetry. This technique is referred to as voltammetry at an

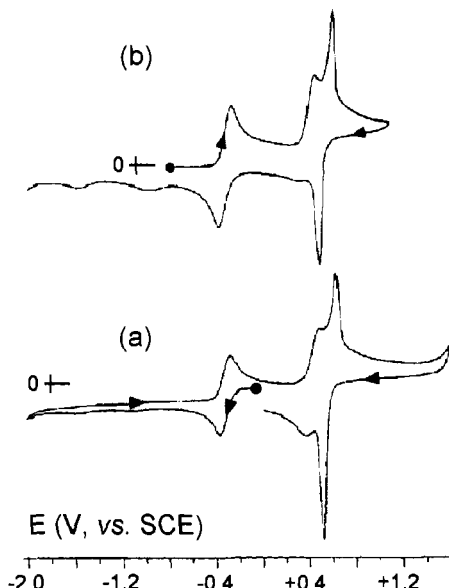


Figure 43 Cyclic voltammograms recorded at a platinum electrode in a solution of a species able to undergo consecutive electron transfers. Starting potentials: (a) 0.0 V; (b) -0.8 V

electrode with periodical renewal of the diffusion layer.¹⁸ It consists of setting the working electrode in periodical motion either along its axis or perpendicular to its axis. In its simplest version, the periodical renewal of the diffusion layer can be achieved by percussing the top of the electrode through a timed knocker (from 3 s to 5 s) (in a rough application the percussion can also be performed with a finger) during a linear potential sweep (scan rates from 0.005 V s^{-1} to 0.02 V s^{-1}). This periodical electrode motion causes a periodical agitation of the solution at the electrode surface (something similar to the dropping mercury electrode). The resulting voltammogram is similar to a classical polarogram, which, independently from the starting potential, is able to distinguish the anodic or cathodic nature of the process. The technique could be defined as ‘polarography’ at solid electrodes.

In confirmation, Figure 44 compares the cyclic voltammogram illustrated in Figure 43b with the voltammogram obtained through the use of a platinum electrode with periodical renewal of the diffusion layer. As seen, it confirms that the species undergoes consecutive oxidation processes.

2.3 Controlled Potential Electrolysis

Measurement of the current intensity in cyclic voltammetry provides an indirect method to determine the number n of electrons involved in

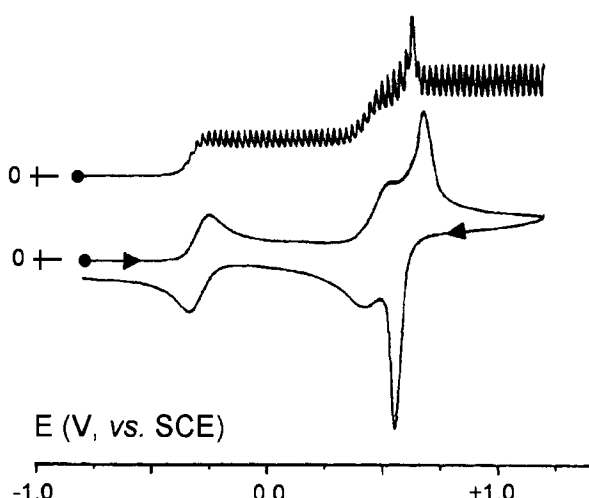


Figure 44 Comparison between the cyclic (0.2 V s^{-1}) and the hydrodynamic (0.01 V s^{-1}) voltammetric responses of the species cited in Figure 43

a redox process. In principle, any relation we have discussed in giving diagnostic criteria in which n appears could be suitable for such a use. For instance, the Randles-Sevcik equation states that:

$$i_p = 2.69 \cdot 10^5 \cdot n^{3/2} \cdot A \cdot D_{\text{Ox}}^{1/2} \cdot C_{\text{Ox}}^* \cdot v^{1/2}$$

but its utilization for the determination of n needs:

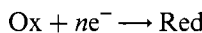
- the absence of chemical complications;
- an electrochemically reversible process;
- the measurement of the diffusion coefficient D ;
- the measurement of the area of the electrode A .

Substantially the same difficulties hold for any other relation (evaluations based on the shift of potentials need the knowledge of α ; and so on).

Often, to simplify the measurement of n , the current recorded on the process under examination is compared with that given, under the same experimental conditions, by an equimolar amount of a species whose n is known. This is really a good and simple method, but it requires that the compared species possess a comparable diffusion coefficient D (*i.e.* in first instance, the species used for comparison must possess a molecular weight roughly similar to that of the species under examination).

The best method to determine the number n of electrons involved in a redox process is through controlled potential coulometry.

The principle of controlled potential coulometry is very simple. If, for instance, we wish to study the usual process:



and only the oxidized species Ox is initially present in solution, setting the potential of a macroelectrode at a value sufficiently negative to trigger the reduction will mean that after some time only the *reduced species Red* will be present in solution.

According to Faraday's law, the charge passed in the experiment is given by:

$$Q = n_{\text{app}} \cdot F \cdot m$$

where:

Q = total amount of electricity passed, in C;

n_{app} = number of electrons involved in the process;

F = Faraday's constant, 96500 C mol^{-1} ;

m = number of mol of oxidized species initially present.

As Figure 45a shows, as the bulk electrolysis proceeds, the current decreases exponentially according to the relationship:

$$i = i_0 \cdot e^{-\beta t}$$

where:

t = electrolysis time (second);

i_0 = initial current (ampere);

$\beta = D \cdot A / (\text{vol} \cdot \delta)$;

the initial current being expressed by:

$$i_0 = \frac{n \cdot F \cdot D \cdot A \cdot C}{\delta}$$

where in turn:

D = diffusion coefficient of species Ox ($\text{m}^2 \text{ s}^{-1}$);

A = area of the electrode (m^2);

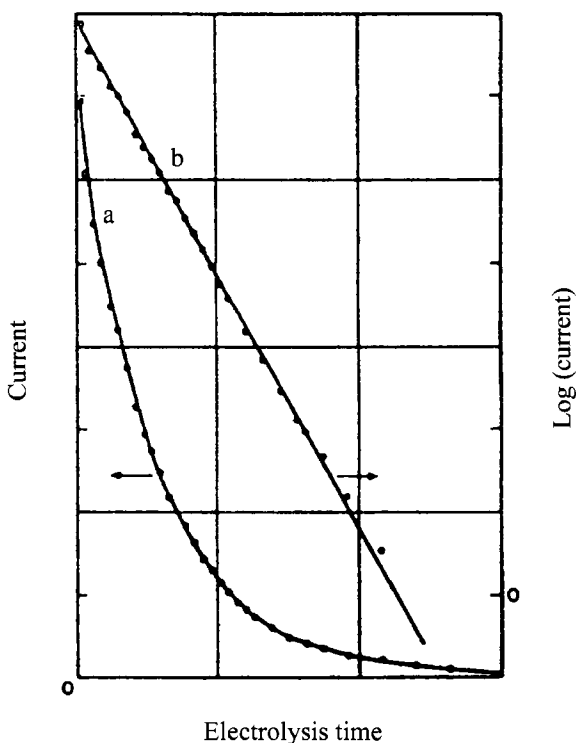


Figure 45 The variation of the electrolysis current with time: (a) i vs. t ; (b) $\log i$ vs. t

δ = thickness of the diffusion layer (m);

vol = volume of the solution (l);

C = initial concentration of Ox (mol l⁻¹).

On the other hand, a plot of $\log i$ vs. t affords a straight line of slope $-\beta/2.303$ and intercept $\log i_0$, Figure 45b.

In order to carry out the coulometric measurement at a controlled potential one must first record a cyclic voltammogram of the redox active substance. Let's suppose that it generates the cathodic response illustrated in Figure 46.

To measure the number of electrons involved in such a cathodic process one prepares, directly in the electrolysis cell (see Chapter 3, Section 2.2), a solution of known concentration of the substance of interest and applies under stirring (in order to accelerate the mass transport to the electrode) a potential slightly more negative (by about 0.2 V) with respect to the peak potential of the reduction process. In this case, for example, $E_w \approx -0.9$ V (E_w representing the working potential). In this way one is working under diffusion conditions. Obviously, in the case of oxidation processes, one must apply potentials which are slightly more positive than the peak potential of the oxidation process.

Since as illustrated in Figure 45a, the electrolysis current decreases asymptotically, the process is considered to be concluded when the current drops to about 1/10–1/100 of the initial current. On applying

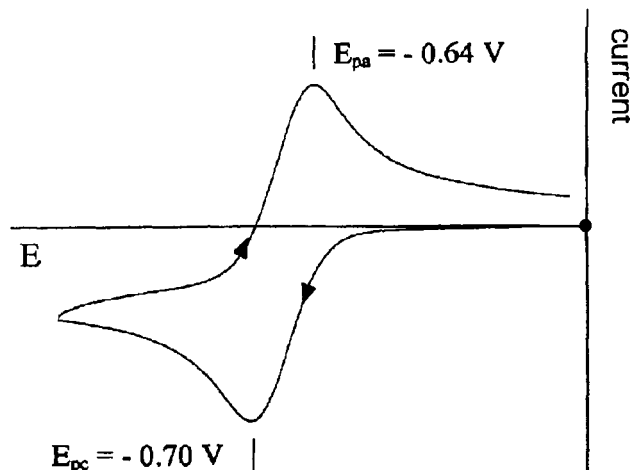


Figure 46 Cyclic voltammogram exhibited by a species, which undergoes reduction at $E^{\circ\prime} = -0.67$ V, before exhaustive electrolysis

Faraday's law, based on the amount of electricity spent, one determines the number of electrons involved per mole of substance.

It should be kept in mind that controlled potential electrolysis is indispensable in ascertaining the stability of every electrogenerated species (*i.e.* to determine the chemical reversibility of a redox process). Such a determination simply requires the recording of a cyclic voltammogram on the exhaustively electrolysed solution. The chemical reversibility implies that such a response must be quite complementary to that initially recorded. For instance, if the voltammetric profile of Figure 46 had been obtained before electrolysis, one must obtain a complementary response of the type illustrated in Figure 47 after electrolysis.

There are cases, fortunately quite rare, in which the number n of electrons effectively involved in an electrode process cannot be measured by means of controlled potential electrolysis, *i.e.* $n_{\text{app}} \neq n$. They generally involve:

- *electrode poisoning processes*, which don't allow the measurement to be completed (at times this can be avoided by changing the electrode material; *e.g.* passing from platinum to gold or mercury or carbon, and *vice versa*);
- *fragmentation processes of the primary electrogenerated species giving fragments which are in turn electro active*; this leads to the consumption of a number of electrons higher than the effective

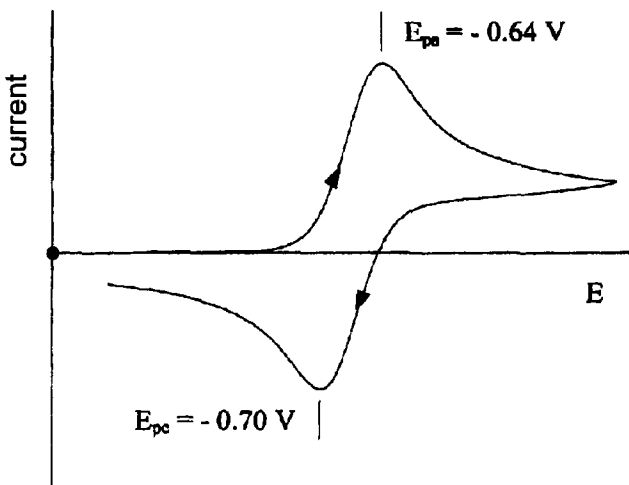


Figure 47 Cyclic voltammogram obtained under the experimental conditions of Figure 46 after exhaustive electrolysis at $E_w = -0.9 \text{ V}$

- one (except for ECE processes, where the coulometric determination is essential for their definition);
- *catalytic regeneration of the initial species*, which means that the electrolysis continues indefinitely.

Table 3 provides more detailed information on those cases in which the number of experimentally measured electrons (n_{app}) equals, or is different from, the theoretical number (n) involved in a particular electrode mechanism.

At times it can be useful to carry out a sort of reversal electrolysis, *i.e.* reoxidize the reduced species (or reduce that oxidized) immediately after generating it to re-obtain the initial species. As shown in Table 3, the comparison between the amount of electricity (in C) consumed in the forward process, Q_f , and that consumed in the return process, Q_r , can be useful in the identification of the electrode mechanism involved in the process under study (even if in general it is less simple than appears).

Finally, an aspect of controlled potential electrolysis that is growing in importance in inorganic chemistry is the generation of appreciable

Table 3 Diagnostic criteria in controlled potential coulometry ^a

Electrode mechanism	n_{app} ^b	Reversal coulometry	$(\log i)/t$
<i>simple processes</i>			
$\text{Ox} + ne^- \rightarrow \text{Red}$	$n_{app} = n^c$	$Q_r^d = Q_f^e$	linear
<i>preceding reactions</i>			
$\text{Y} = \text{Ox}$			
$\text{Ox} + ne^- \rightarrow \text{Red}$	$n_{app} = n$	$Q_r = Q_f$	concave upward
<i>following reactions</i>			
$\text{Ox} + ne^- \rightarrow \text{Red}$	$n_{app} = n$	$Q_r < Q_f$	linear
$\text{Red} \rightarrow \text{Z}$	$n_{app} = n$	$Q_r < Q_f$	linear
$\text{Ox} + ne^- \rightarrow \text{Red}$	$n_{app} = n$	$Q_r < Q_f$	linear
$2 \text{ Red} \rightarrow \text{Z}$	$n_{app} = n$	$0 \leq Q_r < Q_f$	concave upward
$\text{Ox} + ne^- \rightarrow \text{Red}$			
$\text{Red} + \text{Z} \rightarrow \text{Ox} + \text{Y}$	$n_{app} > n$	$0 \leq Q_r < Q_f$	concave upward
$\text{Ox} + n_1 e^- \rightarrow \text{Red}$			
$\text{Red} \xrightarrow{k_f} \text{Ox}'$	$n_{app} = n_1 + n_2$	$Q_r = Q_f \cdot \left[\frac{n_2}{n_1 + n_2} \right]$	linear, or concave
$\text{Ox}' + n_2 e^- \rightarrow \text{Red}'$			
<i>consecutive reactions</i>			
$\text{Ox} + n_1 e^- \rightarrow \text{Red}_1$			
$\text{Red}_1 + n_2 e^- \rightarrow \text{Red}_2$	$n_{app} = n_1 + n_2$	$Q_r = Q_f$	linear, or concave upward

^aIf the reversibility or irreversibility of the chemical reactions as well as of electron transfer is not specified, this implies that the indicated criteria are valid independently of the degree of reversibility;

^b n_{app} = number of electrons experimentally measured; ^c n = number of electrons theoretically involved in the electrode process; ^d Q_r = quantity of electricity passed in the reversal electrolysis; ^e Q_f = quantity of electricity passed in the forward electrolysis.

quantities of certain species not easily obtained by means of common redox agents. The availability of discrete quantities of electrogenerated material opens opportunities for the spectroscopic characterization (*e.g.* UV-visible, IR, EPR, mass spectroscopy) of the various species. In principle, preparation of crystals for use in X-ray structural determinations is also possible; unfortunately, often the electrogenerated product is difficult to separate from the supporting electrolyte, especially if the electrogenerated species is ionic. It must however be taken into account that *electrocrySTALLIZATION* techniques are becoming popular.¹⁹

2.4 Chronoamperometry

The term ‘chronoamperometry’ means the measurement of currents as a function of time, and can be thought of as a kind of ‘controlled-potential voltammetry’ or ‘controlled-potential microelectrolysis (in unstirred solution)’.

Chronoamperometry is a useful technique in those cases where cyclic voltammetry does not succeed in identifying the electrode mechanisms underlying certain redox changes. It is important to state that chronoamperometric measurements can be performed using the same equipment of cyclic voltammetry.

The simplest chronoamperometric technique is that defined as *single potential step chronoamperometry*. It consists of applying an appropriate potential to an electrode (under stationary conditions similar to those of cyclic voltammetry), which allows the electron transfer process under study (for instance: $\text{Ox} + n\text{e}^- \rightarrow \text{Red}$) to run instantaneously to completion (*i.e.* $C_{\text{Ox}}(0,t) \rightarrow 0$). At the same time the decay of the generated current is monitored.²⁰

The choice of the potential to be applied is based on the same criteria discussed for controlled potential electrolysis, *i.e.* for a species able to undergo a reduction process a potential more negative by about 0.2 V with respect to the peak potential of the cathodic process is selected.

The fundamental law of chronoamperometry is the *Cottrell equation* (see Chapter 1, Section 4.2.4):

$$i = \frac{n \cdot F \cdot A \cdot D_{\text{Ox}}^{1/2} \cdot C_{\text{Ox}}^*}{\pi^{1/2}} \cdot \frac{1}{t^{1/2}}$$

As already discussed, it indicates that for a diffusion controlled process (*i.e.* one which does not involve adsorption processes) taking place at a planar electrode, the current (which is proportional to

the concentration of the electroactive species present in the bulk of the solution) decays following a function which is inversely proportional to the square root of time.

A more useful chronoamperometric method involves a double potential step (somewhat reminiscent of the previously discussed reversal electrolysis). In this case, for instance for a reduction process, a first cathodic potential step is applied according to the preceding criteria (such that instantaneously $C_{\text{Ox}}(0,t) \rightarrow 0$), followed at a time τ by the application of a second anodic potential step which causes the species Red previously generated at times $t < \tau$ to be instantaneously reoxidised (such that $C_{\text{Red}}(0,t) \rightarrow 0$).

Figure 48 illustrates a typical chronoamperometric response.

Clearly, for times $t < \tau$, the diagram represents the chronoamperometric single potential step response. In this time interval ($t < \tau$) the current-time curve follows the Cottrell equation; therefore, the cathodic current is expressed by the relationship:

$$i_c = n \cdot F \cdot A \cdot C_{\text{Ox}}^* \cdot \left| \frac{D_{\text{Ox}}}{\pi \cdot t} \right|^{1/2}$$

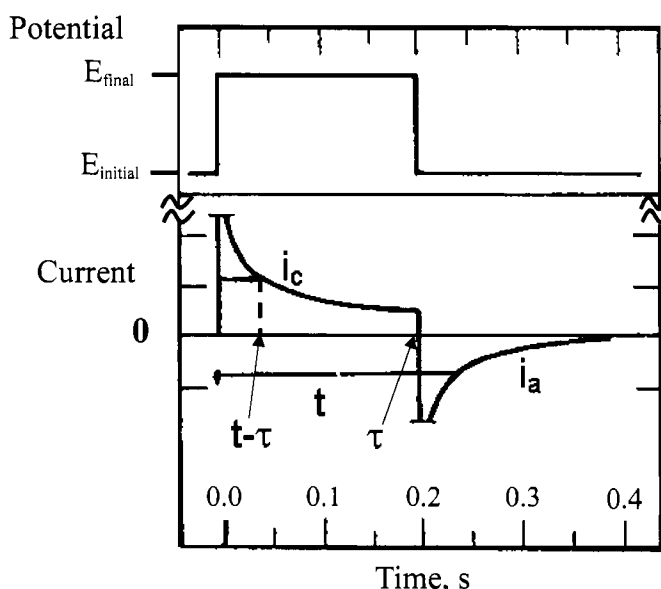


Figure 48 Chronoamperometric double potential step experiment for the process: $\text{Ox} + ne^- \rightleftharpoons \text{Red}$; inversion time $\tau = 0.2$ s. The top part shows the perturbation of the potential applied to the working electrode with time

For times $t > \tau$, where the reoxidation of the previously generated species Red takes place, the diagram represents the double potential step response. Under these conditions, the anodic current follows the equation:

$$i_a = \frac{n \cdot F \cdot A \cdot D_{\text{Ox}}^{1/2} \cdot C_{\text{Ox}}^*}{\pi^{1/2}} \left[\frac{1}{(t - \tau)^{1/2}} - \frac{1}{t^{1/2}} \right]$$

Thus, the ratio between the return (at the time t) and forward (at the time $t - \tau$) currents (expressed as the absolute value, since i_a and i_c have, conventionally, opposite signs) is equal to:

$$\left| \frac{i_a}{i_c} \right| = 1 - \left| \frac{\theta}{1 + \theta} \right|^{1/2}$$

where:

$$\theta = \frac{t - \tau}{\tau}$$

At this point, depending on whether or not the experimental data (*i.e.* the ratio between the anodic currents at the times t and the cathodic currents at the times $t - \tau$) follow the diagram reported in Figure 49, valid for Ox/Red couples that undergo diffusion-controlled processes, one can

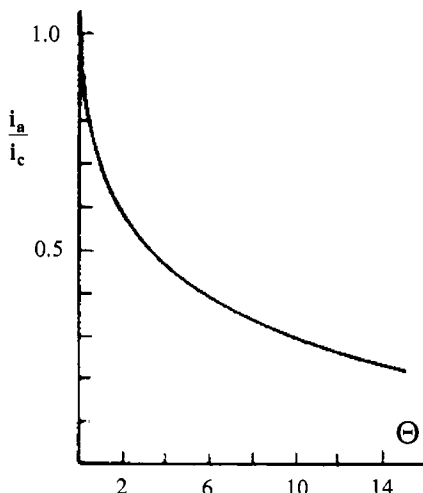


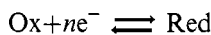
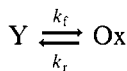
Figure 49 The variation of the current ratio in a double potential step experiment for a simple reduction process ($t > \tau$)

gain information concerning the possible presence of coupled chemical reactions.²⁰

One must take into account that the maximum time for a chronoamperometric experiment is of about 10 s; as mentioned in Chapter 1, Section 4.2.4, for longer times *convection* becomes dominant over *diffusion*.

2.4.1 Coupled Chemical Reactions

2.4.1.1 'Preceding' chemical reactions. The typical case of a preceding chemical reaction is that of the species Ox in equilibrium with an electro inactive substance Y, which follows the sequence of events already seen in Section 1.4.1.1, relative to cyclic voltammetry:



Since the effects of the preceding chemical reaction substantially affect the forward response, the single potential step experiment can be adequately used.

If the kinetics of the preceding reaction are slow, the current–time response is governed by the virtually unchanged initial concentration of Ox; hence, the Cottrell equation is valid.

If, instead, the reaction kinetics are neither too slow nor too fast, the conversion Y/Ox is significant and assuming $D_{\text{Ox}} = D$ one has:

$$i_k = n \cdot F \cdot A \cdot \left(C_{\text{Ox}}^* + C_Y^* \right) \cdot [D \cdot k_f \cdot K]^{1/2} \cdot e^{k_f \cdot K \cdot t} \cdot \text{erfc}[k_f \cdot K \cdot t]^{1/2}$$

For very high reaction kinetics the reciprocal conversion Y/Ox is very rapid, the concentration of Ox can be assumed constant, and the current is expressed by:

$$i_c = i_d = n \cdot F \cdot A \cdot \left(C_{\text{Ox}}^* + C_Y^* \right) \cdot \left| \frac{D}{\pi \cdot t} \right|^{1/2}$$

Hence, the ratio i_k/i_d is theoretically given by:

$$\frac{i_k}{i_d} = (\pi \cdot k_f \cdot K \cdot t)^{1/2} \cdot e^{k_f \cdot K \cdot t} \cdot \text{erfc}(k_f \cdot K \cdot t)$$

erfc being the already mentioned error function complement.

A plot of such ratio as a function of the parameter $(k_f \cdot K \cdot t)^{1/2}$ is illustrated in Figure 50.¹⁹

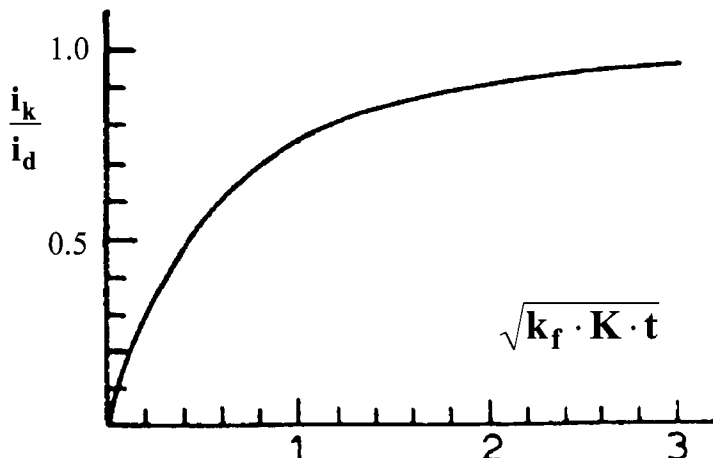


Figure 50 Working curve for the chronoamperometric evaluation of the kinetics of a chemical reaction preceding a reversible electron transfer

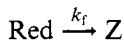
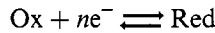
If one possesses the values of the ratio i_k/i_d at different times one can obtain the term $k_f \cdot K$ (that in order to be valid must be constant for the various times). If the value of K is known through other techniques, one can determine both k_f and k_r .

The value of i_k/i_d at a given time represents the ratio of the kinetic current, i_k , recorded experimentally and the value of diffusion current, i_d , that one would have if the process was not complicated by the preceding chemical reaction.

The value of i_d at various times is determined by measuring the current value at the longest times (at which the conversion Y/Ox is more likely to be complete) and applying the Cottrell equation (in practice, considering its linear decay with $t^{1/2}$) at the shorter times of interest.

2.4.1.2 'Following' chemical reactions.

2.4.1.2.1 First-order chemical reaction. Among first-order chemical complications following electron transfers, the most convenient case to study by chronoamperometry is that of a first-order irreversible chemical reaction ($E_r C_i$), which constitutes a frequently encountered case:



As far as the electron transfer process Ox/Red is concerned, it is noted that chronoamperometry cannot distinguish between reversible

and irreversible processes. Therefore, even if the electron transfer is represented as reversible, the treatment that follows is also valid if it is irreversible.

The kinetics of following chemical reactions cannot be studied by the *single potential step* technique in that the response would simply obey the Cottrell equation. In contrast, the *double potential step* technique, that measures the response exhibited by either the reagent Ox or the product Red, is sensitive to the chemical fate of Red. The cathodic response before the inversion of the applied potential ($t < \tau$) is expressed by the Cottrell equation:

$$i_c = n \cdot F \cdot A \cdot C_{\text{Ox}}^* \cdot \left| \frac{D_{\text{Ox}}}{\pi \cdot t} \right|^{1/2}$$

The anodic response after the inversion of the potential ($t > \tau$) is given by:

$$i_a = n \cdot F \cdot A \cdot C_{\text{Ox}}^* \cdot \left| \frac{D_{\text{Ox}}}{\pi} \right|^{1/2} \cdot \left[\frac{\Phi}{(t - \tau)^{1/2}} - \frac{1}{t^{1/2}} \right]$$

where Φ is a complex function of k_f , τ and t , and is equal to 1 in the absence of chemical complications.

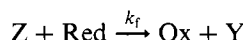
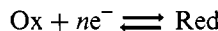
Hence, the ratio between the anodic and cathodic currents is theoretically expressed by:

$$\left| \frac{i_a}{i_c} \right| = \Phi - \left| \frac{\theta}{1 + \theta} \right|^{1/2}$$

where θ is again the term $(t - \tau)/\tau$.

Obviously, the complicated nature of Φ makes the numerical solution impossible. To overcome the problem, Figure 51 shows a few working curves calculated for certain values of θ , which enable one to determine, from the experimental values of i_a/i_c , the value of $k_f \cdot \tau$ and thus k_f , knowing τ .^{20,21}

2.4.1.2.2 Catalytic regeneration of the reagent. The particular case in which the following chemical reaction is a first-order redox reaction which regenerates the initial species is described by the mechanism:



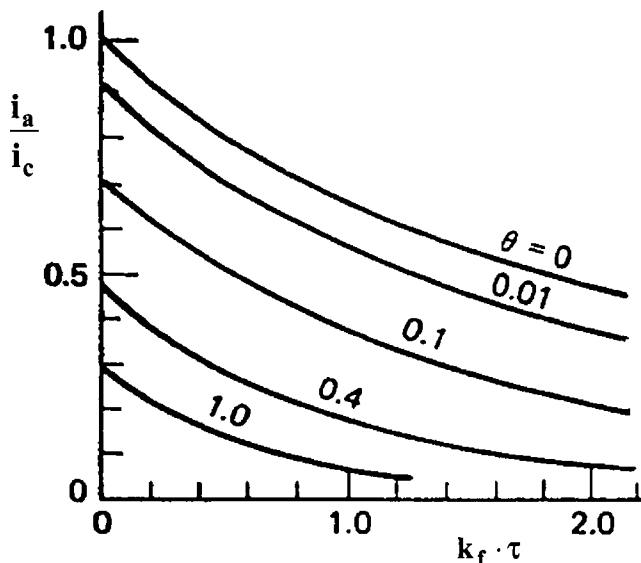


Figure 51 Working curves for selected values of the parameter θ for the chronoamperometric determination of the rate constant of an irreversible chemical reaction following an electron transfer

The responses of the forward and reverse steps are both affected by the chemical complication; in fact, the reduction current will be greater than that predicted by the Cottrell equation, whereas the reoxidation current will be lower than that predicted by the Cottrell equation. This implies that to gain information on the regeneration of the reagent it is sufficient to use the single potential step technique.

In this regard, one compares the current under catalytic conditions (i_k):

$$i_k = n \cdot F \cdot A \cdot C_{\text{Ox}}^* \cdot D_{\text{Ox}}^{1/2} \cdot \left[k_f^{1/2} \cdot \text{erf}(k_f \cdot t)^{1/2} + \frac{e^{-k_f t}}{(\pi \cdot t)^{1/2}} \right]$$

with the diffusive current observed in the absence of Z:

$$i_{k_f=0} = n \cdot F \cdot A \cdot C_{\text{Ox}}^* \cdot \left[\frac{D_{\text{Ox}}}{\pi \cdot t} \right]^{1/2}$$

to obtain the current ratio:

$$\frac{i_k}{i_{k_f=0}} = (k_f \cdot t)^{1/2} \cdot \left[\pi^{1/2} \cdot \text{erf}(k_f \cdot t)^{1/2} + \frac{e^{-k_f t}}{(k_f \cdot t)^{1/2}} \right]$$

As illustrated in Figure 52, if one plots the ratio $i_k/i_{k_f=0}$ as a function of the kinetic parameter $(k_f \cdot t)^{1/2}$, a working curve is obtained that permits (knowing $i_k/i_{k_f=0}$ at different times) to calculate k_f .²⁰

As seen, the plot becomes linear only for high values (namely, > 1) of the parameter $(k_f \cdot t)^{1/2}$, where it assumes a slope equal to $\pi^{1/2}$.

One can use this treatment when the kinetics are first-order (*i.e.* under conditions in which the concentration of Z is not significantly modified by the redox process) such that:

$$\frac{C_z^*}{C_{\text{Ox}}^*} \gg (\pi \cdot k_f \cdot t)^{1/2}$$

Hence, it is necessary to have an excess of Z in solution.

2.4.1.2.3 The ECE mechanism. The ECE mechanisms can be generalized by the following sequence of reactions:

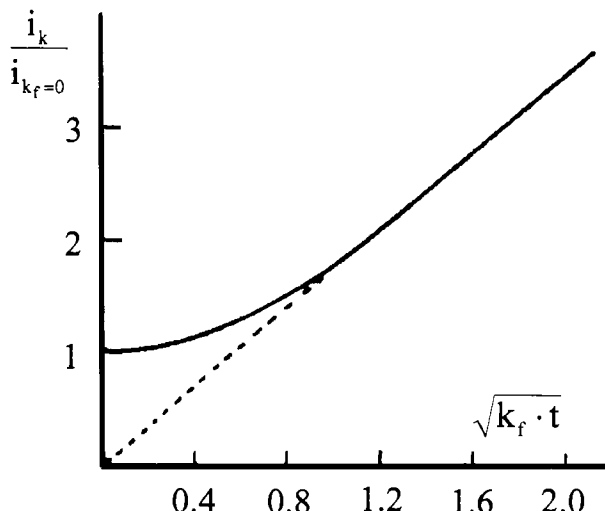
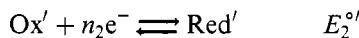
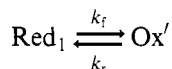
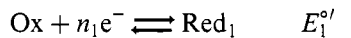


Figure 52 Working curve for the chronoamperometric determination of the rate constant of a catalytic regeneration of the reagent following an electron transfer

The simplest and most useful case that one can study by single potential step chronoamperometry is that in which $E^{\circ'}_2 \gg E^{\circ'}_1$ (*i.e.* $\Delta E^{\circ'} = E^{\circ'}_2 - E^{\circ'}_1 \geq 180$ mV). This means that the primarily electro-generated species Red converts to a new species Ox', which is more easily reducible than the initial species Ox. As seen in Section 1.4.3, in cyclic voltammetry such a system exhibits a single reversible process in the forward scan.

In this case one has the following limiting situations depending upon the rate of the interposed chemical reaction:

- for $k_f t \rightarrow 0$ (or slow chemical kinetics), the first electron transfer is not complicated by following kinetics, hence:

$$i_{k_f \rightarrow 0} = n_1 \cdot F \cdot A \cdot C_{\text{Ox}}^* \cdot \left[\frac{D_{\text{Ox}}}{\pi \cdot t} \right]^{1/2}$$

- for $k_f t \rightarrow \infty$ (or fast chemical kinetics), both the electron transfers take proceed, hence:

$$i_{k_f \rightarrow \infty} = (n_1 + n_2) \cdot F \cdot A \cdot C_{\text{Ox}}^* \cdot \left[\frac{D_{\text{Ox}}}{\pi \cdot t} \right]^{1/2}$$

- for intermediate values of $k_f t$, it has been found that:

$$i_k = [n_1 + n_2 \cdot (1 - e^{-k_f t})] \cdot F \cdot A \cdot C_{\text{Ox}}^* \cdot \left[\frac{D_{\text{Ox}}}{\pi \cdot t} \right]^{1/2}$$

This being stated, the occurrence of a chemical reaction interposed between two electron transfers can be easily detected by plotting a graph of i vs. $t^{-1/2}$.^{20,22} Figure 53 shows that at short times after the potential step (corresponding to $k_f = 0$) the current depends only on the process Ox → Red, thus the slope of the function depends on the number n_1 of electrons.

At longer times (corresponding to $k_f = \infty$) the current is a function of the complete reduction of Ox to Red', thus the slope is determined by the overall number of electrons $n_1 + n_2$. At intermediate times the current varies from one limit to the other. The time at which this passage from one limit to the other takes place is a function of the rate constant of the interposed chemical reaction.

The simplest case to treat (which is also the commonest one) is that in which the interposed chemical reaction is irreversible and $n_1 = n_2 = 1$. The way in which the rate constant of the interposed chemical reaction is calculated is now considered.

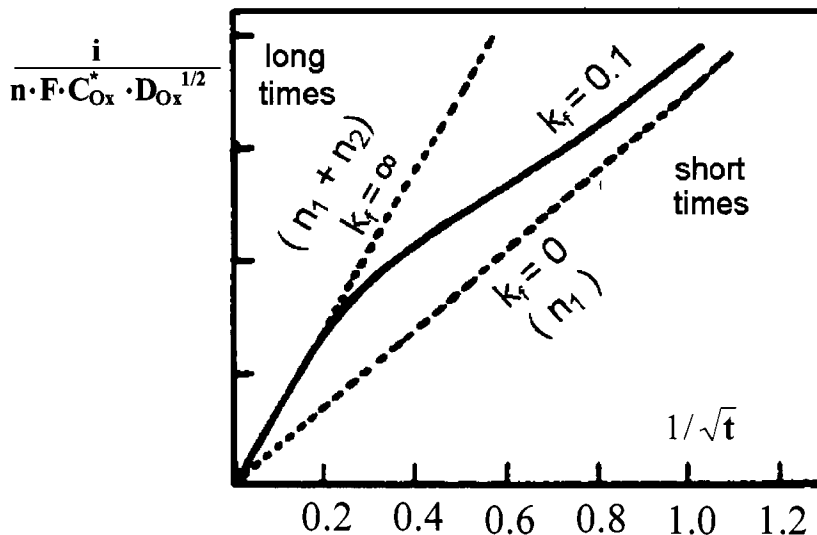


Figure 53 Potentiostatic behaviour for an ECE mechanism as a function of the rate constant k_f of the interposed chemical reaction

Since, based on previous relationships, the ratio of the actual kinetic current i_k and a purely diffusion current i_d due to $n_1 + n_2$ electrons is given by:

$$\frac{i_k}{i_d} = \frac{\left[n_1 + n_2 \cdot (1 - e^{-k_f t}) \cdot F \cdot A \cdot C_{Ox}^* \cdot \left[\frac{D_{Ox}}{\pi \cdot t} \right] \right]^{1/2}}{(n_1 + n_2) \cdot F \cdot A \cdot C_{Ox}^* \cdot \left[\frac{D_{Ox}}{\pi \cdot t} \right]^{1/2}} = 1 - \frac{n_2}{n_1 + n_2} \cdot e^{-k_f t}$$

If $n_1 = n_2 = 1$, one has:

$$e^{-k_f t} = 2 \cdot \left[1 - \frac{i_k}{i_d} \right]$$

This implies that a graph of $\ln[2(1 - i_k/i_d)]$ against time gives a straight line of slope k_f .

It now remains to calculate the diffusion currents, i_d , at the required times. An apparently simple way would be to use a substance fairly similar to Ox (or having a similar diffusion coefficient) capable of being reduced simply by a diffusion process (or, without coupled chemical reactions) through a process involving $n_1 + n_2$ electrons. A solution of this substance could therefore be prepared with the same molarity as that containing Ox, such that one can measure the potentiostatic current at the required times. In practice, however, this method is quite laborious.

A second, easier method to follow is based on the fact that in the potentiostatic experiment on Ox at long times $n_1 + n_2$ electrons have passed so that the current is purely diffusive. Therefore, by the use of such current values, recalling that i is proportional to $t^{-1/2}$ for diffusive processes, one can determine the values of i_d at the various times of interest.

Clearly, the limit of this second method is having the certainty that, at the long times at which one makes the measurements, the interposed chemical reaction has completely finished (bear in mind that, as already pointed out, the maximum time is about 10 s). A simple way to ascertain this is to verify that the product $i \cdot t^{1/2}$ (that is proportional to the number of electrons involved in the process), that initially (at short times) tends to increase, reaches a constant value at longer times.

2.5 Determination of the Number of Electrons Involved in an Electron Transfer Process from the Correlation Between Cyclic Voltammetry and Chronoamperometry

As mentioned in the introduction to controlled potential electrolysis (Section 2.3), there are various indirect methods to calculate the number of electrons transferred in a redox process. One method which can be rapidly carried out, but can only be used for electrochemically reversible processes (or for processes not complicated by chemical reactions), compares the cyclic voltammetric response exhibited by a species with its chronoamperometric response obtained under the same experimental conditions.²³ This is based on the fact that in cyclic voltammetry the peak current is given by the Randles-Sevcik equation:

$$i_p(\text{in ampere}) = 2.69 \cdot 10^5 \cdot n^{3/2} \cdot A \cdot C_{\text{Ox}}^* \cdot D_{\text{Ox}}^{1/2} \cdot v^{1/2}$$

For the same process, in chronoamperometry, the Cottrell equation holds:

$$i_{(\text{in ampere})} = \frac{n \cdot F \cdot A \cdot C_{\text{Ox}}^* \cdot D_{\text{Ox}}^{1/2} \cdot \pi^{-1/2}}{t^{1/2}}$$

The ratio between the two relationships affords:

$$R = \frac{i_p \cdot v^{-1/2}}{i \cdot t^{1/2}} = 4.93 \cdot n^{1/2}$$

Experimentally, this means that for a given (reversible) redox process one records a series of cyclic voltammograms at different scan rates

and then the (constant) ratio $i_p \cdot v^{-1/2}$ is calculated. For the same solution, with the same electrode, one plots a curve of potentiostatic current against time and the (constant) product $i \cdot t^{1/2}$ is calculated:

- if the process involves one electron, a value $R \approx 4.93$ is obtained;
- if the process involves two electrons, one obtains a value of $R \approx 6.97$.

REFERENCES

1. L.R. Faulkner, *Electrochemical Characterization of Chemical Systems*. Physical Methods in Modern Chemical Analysis, Vol. 3, Academic Press, 1983.
2. Southampton Electrochemistry Group, *Instrumental Methods in Electrochemistry*, 2nd Edn, Horwood Publishing Limited, 2001.
3. A.J. Bard and L.R. Faulkner, *Electrochemical Methods. Fundamentals and Applications*, 2nd Edn, J. Wiley, 2001.
4. (a) S. Pierkaski and R.N. Adams, *Voltammetry with Stationary and Rotated Electrodes*. Physical Methods of Chemistry. Part II A. Electrochemical Methods. A. Weissberger and B.W. Rossiter eds, Wiley Interscience, New York, 1971. (b) Z. Galus, *Voltammetry with Stationary and Rotated Electrodes*. Physical Methods of Chemistry. Part II A. Electrochemical Methods. A. Weissberger and B.W. Rossiter eds, Wiley Interscience, New York, 1986.
5. (a) E.R. Brown and R.F. Large, *Cyclic Voltammetry, A.C. Polarography and Related Techniques*. Physical Methods of Chemistry. Part II A. Electrochemical Methods. A. Weissberger and B.W. Rossiter eds., Wiley Interscience, New York, 1971. (b) E.R. Brown and J.R. Sandifer, *Cyclic Voltammetry, A.C. Polarography and Related Techniques*. Physical Methods of Chemistry. Electrochemical Methods. A. Weissberger and B.W. Rossiter eds, Vol. 2. Wiley Interscience, New York, 1986. (c) F. Scholz, *Electroanalytical Methods. Guide to Experiments and Applications*, Springer, 2002.
6. C.G. Zoski, K.B. Oldham, P.J. Mahon, T.L.E. Henderson and A.M. Bond, *J. Electroanal. Chem.*, 1991, **297**, 1 and references therein.
7. K. Štulík, C. Amatore, K. Holub, V. Mareček and W. Kutner, *Pure Appl. Chem.*, 2000, **72**, 1483.
8. (a) R.S. Nicholson and I. Shain, *Anal. Chem.*, 1965, **37**, 1351. (b) A.S.N. Murthy and K.S. Reddy, *Electrochim. Acta*, 1983, **28**, 1677.
9. R.S. Nicholson and I. Shain, *Anal. Chem.*, 1964, **36**, 706.
10. M.L. Olmstead, R.G. Hamilton and R.S. Nicholson, *Anal. Chem.*, 1969, **41**, 260.
11. M.L. Olmstead and R.S. Nicholson, *Anal. Chem.*, 1969, **41**, 862.

12. R.S. Nicholson and I. Shain, *Anal. Chem.*, 1965, **37**, 178.
13. D. Astruc, *Electron Transfer and Radical Processes in Transition Metal Chemistry*. Wiley-VCH, New York, 1995.
14. D.S. Polcyn and I. Shain, *Anal. Chem.*, 1966, **38**, 370.
15. D.E. Richardson and H. Taube, *Inorg. Chem.*, 1981, **20**, 1278.
16. R.R. Gagné, C.L. Spiro, T.J. Smith, C.A. Hamann, W.R. Thies and A.K. Shiemke, *J. Am. Chem. Soc.*, 1981, **103**, 4073.
17. R.H. Wopschall and I. Shain, *Anal. Chem.*, 1967, **39**, 1514.
18. (a) D. Cozzi, G. Raspi and L. Nucci, *J. Electroanal. Chem.*, 1966, **12**, 36.
(b) G. Schiavon, G.A. Mazzocchin and G.G. Bombi, *J. Electroanal. Chem.*, 1971, **29**, 401 and references therein.
19. E. Budevski, G. Staikov and W.J. Lorenz, *Electrochemical Phase Formation and Growth: an Introduction to the Initial Stages of Metal Deposition*, VCN, Veinheim, 1996.
20. R.W. Murray, *Chronoamperometry, Chronocoulometry and Chronopotentiometry*, Physical Methods of Chemistry. Electrochemical Methods. A. Weissberger and B.W. Rossiter eds, Vol. 2. Wiley Interscience, New York, 1986.
21. W.M. Schwarz and I. Shain, *J. Phys. Chem.*, 1965, **69**, 30.
22. G.S. Alberts and I. Shain, *Anal. Chem.*, 1963, **35**, 1859.
23. P.A. Malachesky, *Anal. Chem.*, 1969, **41**, 1493.

PRACTICAL ASPECTS

CHAPTER 3

Basic Equipment for Electrochemical Measurements

There are many publications which discuss not only the principles of electrochemistry, but also its practical aspects (electrodes, cells, solvents, supporting electrolytes, and so on).^{1–8} In addition, all the electrochemical instrumentation manufacturers have catalogues of commercial products which allow proper experiments to be carried out. Therefore, the present discussion will be limited to point out the minimal basic knowledge required to set up an electrochemical experiment.

1 ELECTRODES

As already mentioned in Chapter 1, Section 3, a reliable electrochemical cell must involve the use of three types of electrodes:

- the *working* (or *indicator*) electrode;
- the *reference* electrode;
- the *auxiliary* (or *counter*) electrode.

1.1 Indicator Electrodes

The guiding criterion for the choice of a working electrode is that it must be made of a *redox-inert material*, at least in the potential range of interest.

In addition, one must choose the most appropriate geometrical form for such an electrode. The most common forms for fast voltammetric techniques are the planar geometry and the spherical (or hemispherical) geometry. In this regard, we have seen (Chapter 1, Section 4.2.2) that the simplest theoretical relationships describing the kinetics of electrode processes are valid under conditions of linear diffusion (even if we have briefly discussed also radial diffusion).

The materials normally used in the construction of working electrodes are: platinum, gold, mercury and carbon. However, there have been recent attempts to use more sophisticated materials such as superconductors (as will be discussed in Chapter 10, Section 1), but at moment, due to their poor chemical and mechanical properties, they are not very promising electrode materials.

The accessible potential ranges for platinum and mercury electrodes, in the commonest organic solvents are reported in Table 1. It is noted that gold exhibits characteristics very similar to platinum.

One can see immediately that the easy oxidation of mercury renders it of little use for anodic scans. Note that to construct a ‘solid’ mercury electrode one can simply immerse a gold electrode in mercury for a few seconds. The amalgam that forms produces a mercury electrode much more manageable than the dropping electrode used in polarography.

Carbon electrodes can be made from a number of various crystalline forms of carbon. The two most common versions are the carbon paste electrode and the glassy carbon electrode. In Chapter 11, devoted to the electrochemistry of biological functions, it will be seen that pyrolytic graphite electrodes have also found wide application. Recently, attempts to use carbon-nanotube electrodes have been also proposed.⁹

The carbon paste electrode is suitable for aqueous solutions and is prepared by mixing finely ground carbon with mineral oil (in a typical preparation, 15 g of ground carbon is mixed with 9 ml of Nujol). A paste of butter-like consistency is obtained that can be shaped into small disks.

Table 1 Potential windows (*V*, vs. SCE) for a few common non-aqueous solvents on platinum and mercury electrodes

Solvent	Supporting electrolyte	Potential region	Electrode
CH_2Cl_2	$[\text{NBu}_4]\text{[PF}_6]$	from + 1.7 to -2.0	Pt
		from + 0.9 to -2.0	Hg
thf	$[\text{NBu}_4]\text{[PF}_6]$	from + 1.3 to -2.4	Pt
		from + 0.8 to -2.9	Hg
MeCN	$[\text{NBu}_4]\text{[PF}_6]$	from + 2.0 to -2.0	Pt
		from + 0.6 to -2.8	Hg
Me ₂ CO	$[\text{NBu}_4]\text{[PF}_6]$	from + 1.4 to -2.1	Pt
		from + 0.6 to -2.5	Hg
dmf	$[\text{NBu}_4]\text{[PF}_6]$	from + 1.5 to -2.8	Pt
		from + 0.5 to -2.8	Hg
dmso	$[\text{NBu}_4]\text{[PF}_6]$	from + 1.0 to -2.3	Pt
		from + 0.3 to -2.8	Hg

The disk is then placed on the tip of a small glass tube and the electrical contact made through a conducting metallic thread (*e.g.* copper, or preferably, platinum).

The glassy carbon electrode (a patented material) is particularly suitable for non-aqueous solvents. Its main properties are that it is isotropic, impermeable to gases, resistant to chemical attack and has high conductivity.

It may happen that the use of different electrode materials leads to different degrees of reversibility in redox processes. This means that when one obtains voltammograms which depart significantly from electrochemical reversibility it is advisable to use different electrode materials in order to ascertain that the effect is really due to the slow rate of the electron transfer of the species under examination rather than from surface phenomena connected with the electrode material.

1.2 Reference Electrodes

Even though the *normal hydrogen electrode* (NHE) is the best known and internationally accepted reference electrode, it is difficult to construct and handle, rendering it of little practical use.

For non-aqueous solvents, the two most common reference electrodes are:

- the *saturated calomel electrode* (SCE), in an appropriate form to avoid the KCl solution inside percolating into the non-aqueous solution under examination. In fact, it is better to employ a solution of NaCl, as KCl is poorly soluble in non-aqueous solvents and on contact with the non-aqueous solvent it may block the separator from the working electrode region;
- the *Ag/Ag⁺ electrode* (if possible in the easier to handle form of Ag/AgCl), that can use as a solvent the same solution to which the electroactive substance under examination will be added.

Figure 1 shows the most common version of the two electrodes.

A scale showing the potential values of the most commonly used reference electrodes is given in Figure 2. The potentials are quoted both with respect to the normal hydrogen electrode and the saturated calomel electrode.

1.3 Auxiliary Electrodes

In voltammetric techniques the *auxiliary electrode*, which is placed directly in the solution under study (see the next section), is usually made of platinum wire that is coiled around the working electrode. In contrast,

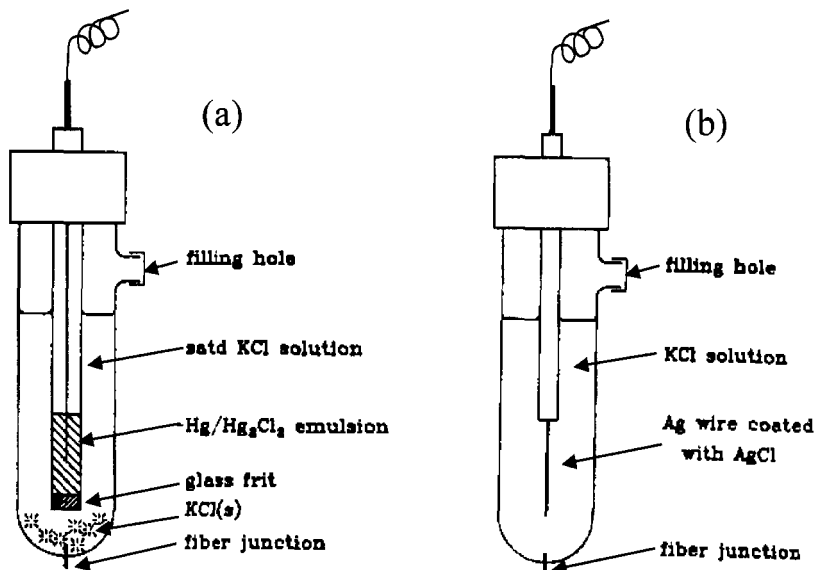


Figure 1 The composition of commercial: (a) calomel electrode; (b) silver/silver chloride electrode

in controlled potential electrolysis the auxiliary electrode is placed in a compartment separated from the solution under study, and is usually made of a mercury pool with a platinum wire forming the electrical contact.

2 ELECTROCHEMICAL CELLS

Generally, irrespective of the technique for which they are used, electrochemical cells are constructed in a way which minimizes the resistance of the solution. The problem is particularly accentuated for those techniques which require high current flows (large-scale electrolysis and fast voltammetric techniques). When current flows in an electrochemical cell there is always an error in the potential due to the non-compensated solution resistance. The error is equal to $i \cdot R_{nc}$ (see Chapter 1, Section 3). This implies that if, for example, a given potential is applied in order to initiate a cathodic process, the effective potential of the working electrode will be less negative compared to the nominally set value by a amount equal to $i \cdot R_{nc}$. Consequently, for high current values, even when R_{nc} is very small, the control of the potential can be critical.

Let us consider, for example, a single potential step experiment that takes place in the equivalent circuit illustrated in Figure 3 (see Chapter 1, Section 5).

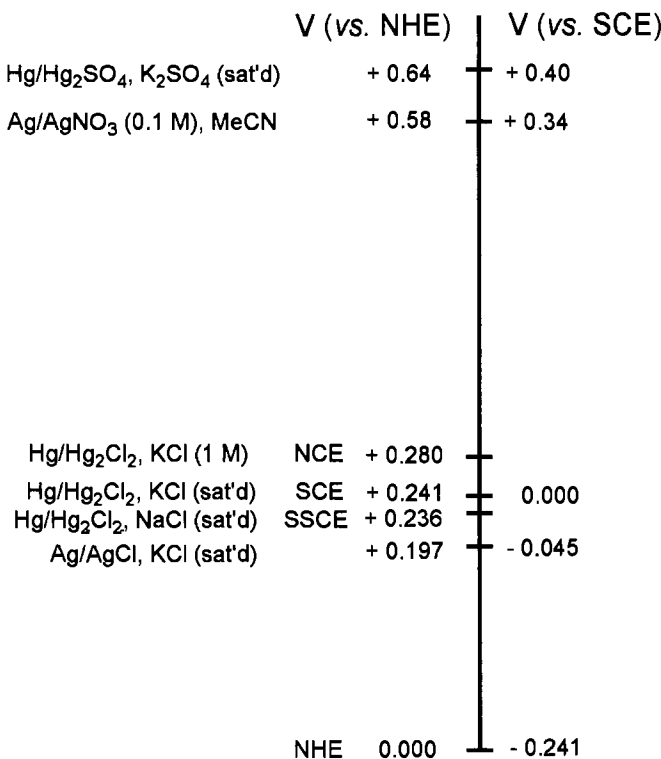


Figure 2 Potential values (in V) of a few reference electrodes

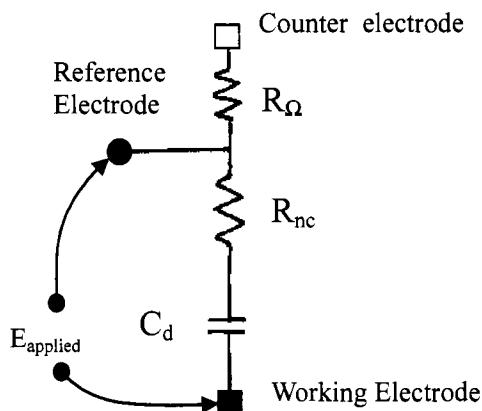


Figure 3 The simplest equivalent circuit of an electrochemical cell. C_d = capacitor emulating the double layer; $R_\Omega + R_{nc}$ = solution resistance

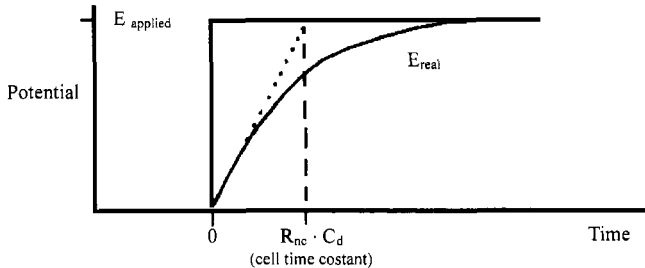


Figure 4 The effect of the cell time constant on the potential value assumed by the working electrode when a potential step is applied

If a given potential difference, E_{app} , is applied between the working and the reference electrodes, the true potential value will not be instantaneously equal to that nominally set, but:

$$E_{\text{true}} = E_{\text{app}} \cdot [1 - e^{-t/(R_{\text{nc}} \cdot C_d)}]$$

or, as illustrated in Figure 4, the true potential will equal the nominal potential when the capacitor is completely charged ($C_d = 0$) and/or R_{nc} is zeroed.

The tendency for the potential to assume the applied value is exponential with time and is governed by the time constant of the cell, $R_{\text{nc}} \cdot C_d$, that represents the minimum time within which the cell reacts to the perturbation of the potential.

The situation is not improved if an equivalent circuit more closely resembling the nature of the electrochemical cell is considered, see Figure 5.

In this case, a faradaic impedance Z_f is placed in parallel with the capacitor C_d , based on the consideration that the current generated at the working electrode is the sum of the faradaic current (due to the redox process) and the capacitive current (due to the electrode/solution double layer).

These considerations demonstrate that an electrochemical experiment may be lacking in reliability if the time constant of the cell is not sufficiently low compared to the time scale of the experiment.

There are three ways in which the time constant $R_{\text{nc}} \cdot C_d$ can be reduced:

- reduce the total resistance of the solution $R_\Omega + R_{\text{nc}}$ increasing its conductivity either by adding further amounts of supporting electrolyte or employing solvents of high polarity and/or lower viscosity;

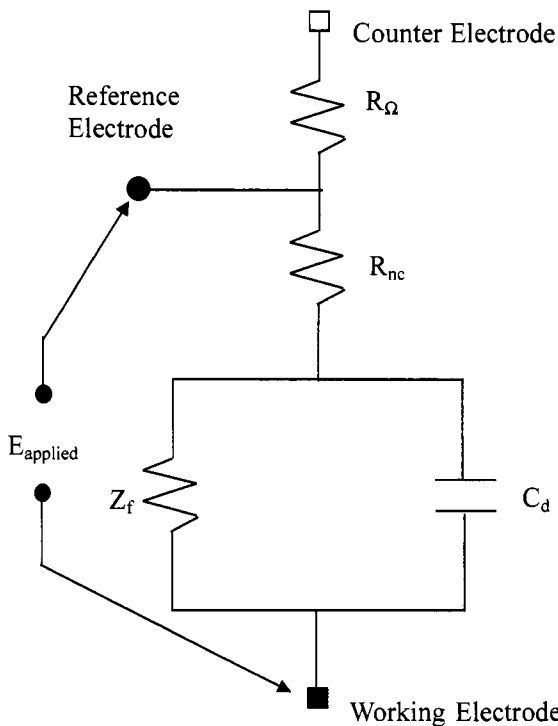


Figure 5 An equivalent circuit representing the phenomena occurring in an electrochemical cell better than that illustrated in Figure 3

- reduce the size of the working electrode so as to reduce, in a proportional manner, the capacitance of the capacitor C_d ;
- place the tip of the reference electrode as close as possible to the working electrode, such that R_{nc} is a still smaller fraction of the total resistance $R_{\Omega} + R_{\text{nc}}$, that remains constant.

On occasions it is not possible to satisfy all three of these criteria (because either the choice of the solvent or the supporting electrolyte has been determined by the substance under study or there are practical limits imposed on the construction of the electrode).

One must also bear in mind that when high currents flow through the electrolytic solution they give rise to non-uniform current density phenomena at the working electrode/solution interface. This results in the effective area of the working electrode being reduced with respect to the geometric area, which introduces errors when one wants to obtain correlations between theory and experiment. The problem can be overcome by building cells with a symmetric disposition of the electrodes.

2.1 Cells for Cyclic Voltammetry and Chronoamperometry

As noted above, a symmetric disposition of the electrodes in the electrochemical cell considerably reduces the problems connected with the control of the potential of the working electrode.

While bearing in mind that, within the criterion of the symmetric disposition of electrodes, each researcher commonly uses either commercial cells or cells built ‘in-house’ based on personal experience, Figure 6 shows a typical cyclic voltammetry (and chronoamperometry) cell, particularly suitable for non-aqueous solvents.

- The volume of the solution within the cell is about 20–25 ml. Should a significantly lower volume required (up to about 5 ml), one can insert glass pellets in the working electrode compartment.
- The active part of the working electrode normally consists of a small disk or sphere of platinum (depending on whether one wishes to work under conditions of planar or radial diffusion). Alternatively, one can use gold, mercury (as a gold–mercury amalgam), or carbon.
- The counter electrode consists of a platinum spiral placed symmetrically around the working electrode.

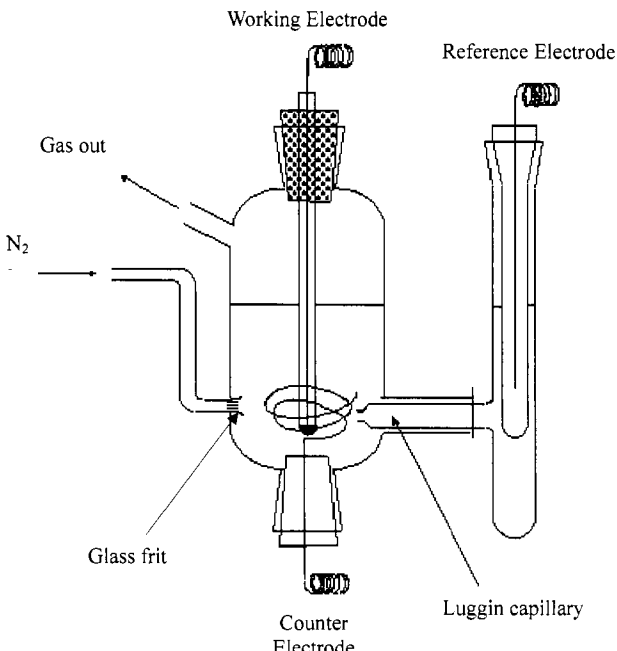


Figure 6 Typical cell for cyclic voltammetry

- The reference electrode (commonly a saturated calomel electrode or a silver/silver chloride electrode) is, ideally, placed in close proximity to the working electrode *via* a Luggin capillary.

One must keep in mind that modern electrochemical instrumentation compensates for the potential drop $i \cdot (R_\Omega + R_{nc})$ through the use of appropriate circuitry (positive feedback compensation). This adds a supplementary potential to the input potential of the potentiostat (equal to the ohmic drop of the potential), which is generated by taking a fraction of the faradaic current that passes through the electrochemical cell, such that in favourable cases there will be no error in the control of the potential. However, such circuitry can give rise to problems of reliability in the electrochemical response on occasions when an overcompensation is produced.

It is often useful to carry out voltammetric measurements at low temperatures in order to evaluate both the stability of an electro-generated species (the decrease in temperature will slow down the kinetics of any decomposition processes of the species formed in the electrode process) and the variation in formal electrode potential of a redox couple as a function of temperature. The latter point regards thermodynamic considerations of the redox processes, which will be discussed in Chapter 13, Section 3.

Normally, voltammetric studies in the temperature range from -25°C to $+25^\circ\text{C}$ do not require particularly sophisticated apparatus for regulating the temperature. The simplest design of a low temperature cell is the so-called *non-isothermal cell*. It is similar to that shown in Figure 6, but the central part (*i.e.* excluding the mobile compartment consisting of the Luggin capillary and the reference electrode) is enclosed by a thermostatic jacket through which a cooled liquid (such as ethanol) is forced to flow. In this way one can systematically vary the temperature of the half-cell in which the redox process takes place, while the temperature of the reference half-cell is maintained constant (normally at room temperature).

2.2 Cells for Controlled Potential Electrolysis

Cells used in exhaustive electrolysis present more problems of electrodes symmetry than those for cyclic voltammetry, due to the long experimental times and high currents involved.

The *working electrode* generally consists of a cylindrical platinum gauze or a mercury pool; thereby offering the largest surface area possible to the redox process.

The *auxiliary electrode*, which is normally a mercury pool, must be positioned in a compartment separate from the working electrode. Such a separation compromises the desired symmetric disposition of the electrodes. Normally, the compartments of a macroelectrolysis cell are separated by sintered glass frits, such that the catholyte and the anolyte are not mixed. In fact, if the working electrode is involved, for example, in a cathodic process, the auxiliary electrode will act as an anode. This implies that the auxiliary electrode will produce oxidized material (by anodic decomposition of the solvent itself, of the supporting electrolyte, of mercury-contaminated products or of electroactive residues diffused at the auxiliary electrode) that may subsequently be reduced at the working electrode, contaminating and falsifying the primary process.

As for the case of cells for cyclic voltammetry, electrolysis cells are either of commercial type or 'in-house' constructed according to the experience of each researcher.

Figure 7 shows a typical electrolysis cell with a platinum gauze working electrode. Eventually the platinum gauze can be replaced by a mercury pool working electrode. The volume of solution contained in such a cell is about 30–50 ml.

It is recommended to insert into the cell an electrode for cyclic voltammetry. This allows one to record a cyclic voltammogram of the species under study directly before and after exhaustive electrolysis,

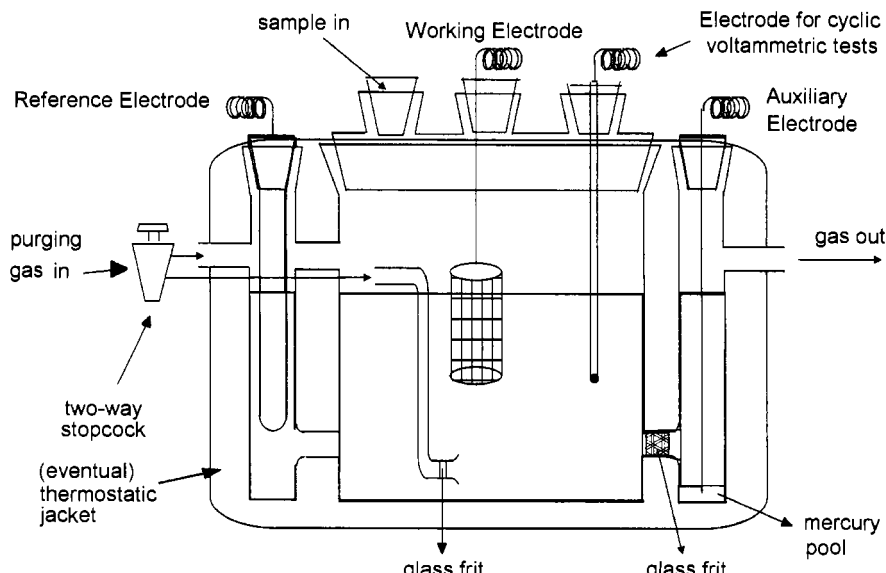


Figure 7 Typical cell for electrolysis with a working platinum gauze electrode

thereby permitting a rapid evaluation of the effects produced by the electrolysis.

As in the case of cyclic voltammetry, the electrolysis cell can be built with a thermostatic jacket to carry out measurements at low temperatures. In this case, the apparatus is of an isothermal type (*i.e.* the compartment containing the reference electrode is also cooled). In this case the most suitable reference electrode is the silver/silver chloride electrode filled by the same solution that will be used to dissolve the electroactive substance. One cannot use the saturated calomel electrode or the aqueous Ag/AgCl electrode because the KCl (or NaCl) solution would freeze.

3 SOLUTIONS FOR ELECTROCHEMICAL STUDIES. SOLVENTS AND SUPPORTING ELECTROLYTES

Analogous to common chemical reactions, the electrolytic medium, which is constituted by the solvent and the supporting electrolyte, has a great importance on the manner in which an electrochemical process proceeds.

Solutions for electrochemical studies, however, have physical limitations imposed by the necessity to facilitate the heterogeneous electron transfer from the electrode to the solute, or *vice versa*.

The most common requirements of a solvent are:

- to dissolve the compound under study, but to be chemically inert with respect to it;
- to dissolve relatively high quantities of supporting electrolyte, to improve the electrical conductivity of the solution and reduce its resistance;
- it must be easily purified – impurities which can react with the compound under study, or be electroactive (water included), must be easy to remove;
- to have an adequate temperature range in which it remains liquid;
- not to produce toxic vapours.

Table 2 summarizes some chemical and physical properties of the most frequently used organic solvents in inorganic electrochemistry. As aqueous solutions have only a limited use in inorganic electrochemistry they will not be considered herein.

An important aspect related to the choice of the solvent lies in its coordinating ability towards the redox species under study. This property is related to the polarity of the solvent (we will discuss this in

Table 2 Physico-chemical properties of a few organic solvents commonly used in inorganic electrochemistry

Solvent	Liquid range (°C)	Dielectric constant	Viscosity (cP)	Supporting electrolytes
acetone	from -95 to +56	21	0.32	[NEt ₄][ClO ₄], [NBu ₄][PF ₆], NaClO ₄
acetonitrile	from -45 to +82	36	0.33	[NEt ₄][ClO ₄], [NBu ₄][PF ₆], LiClO ₄
dichloromethane	from -97 to +40	8.9	0.39	[NBu ₄][PF ₆], [NBu ₄][ClO ₄], [NBu ₄][halides]
(trifluoromethyl)- benzene ^a	from -29 to +102	9.2	0.57	[NBu ₄][ClO ₄], [NBu ₄][BF ₄],
dimethylformamide	from -61 to +153	37	0.80	[NEt ₄][ClO ₄], [NBu ₄][PF ₆], LiCl, NaClO ₄
dimethylsulfoxide	from +18 to +189	47	1.99	[NEt ₄][ClO ₄], NBu ₄ PF ₆
tetrahydrofuran	from -108 to +66	7.6	0.55	LiClO ₄ , [NBu ₄][PF ₆], NaClO ₄

^a See Ref. 8.

more detail in Chapter 13, Section 2). At the moment, we can relate it to the dielectric constant, in the sense that the higher the dielectric constant, the higher the coordinating ability of the solvent.

In this connection, Figure 8 illustrates the anodic voltammetric behaviour of complex $[(\mu-C_5H_5)Fe(CO)_2]_2$ either in a solution of

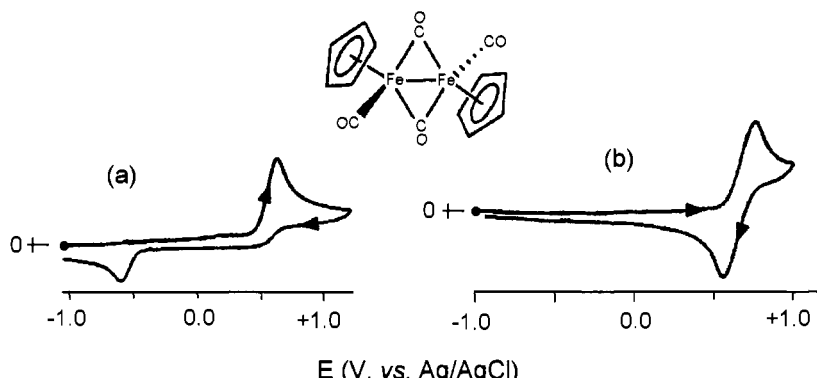
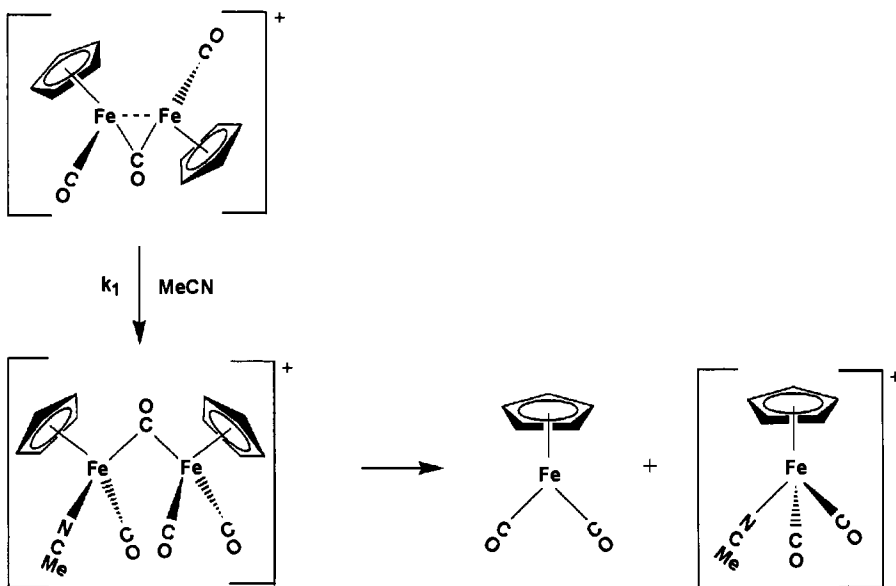


Figure 8 Cyclic voltammograms recorded at a glassy carbon electrode in solution of $[(\mu-C_5H_5)Fe(CO)_2]_2$ in: (a) MeCN; (b) CH_2Cl_2 . Supporting electrolyte: $[NBu_4][PF_6]$. Scan rate 0.25 V s^{-1}

acetonitrile (a coordinating solvent) or in solution of dichloromethane (a noncoordinating solvent).¹¹

As can be seen, in acetonitrile solution the dimer undergoes an irreversible (one-electron) oxidation, whereas in dichloromethane solution it undergoes a reversible oxidation.

In short, the explanation lies in the coordinating ability of acetonitrile, which, being able to coordinate the electrogenerated monocation, makes its decomposition easier, Scheme 1.



Scheme 1

Coming back to Table 2, it also reports the most suitable supporting electrolytes for each solvent (generally they are quaternary alkylammonium salts).

An important parameter for electrochemical solutions is the range of the electrical potential within which they are electroinactive. In other words, the anodic or cathodic windows they have available in which investigations on the redox properties of various compounds can be performed. We have already reported in Table 1; Figure 9 shows graphically the potential ranges of the most common solutions at a platinum electrode.

It is common practice to choose the supporting electrolyte solely on the basis of its solubility in the solvents used, without paying much attention to the anion of the ammonium salt. For example, when using the solvent dichloromethane, the most convenient supporting electrolyte

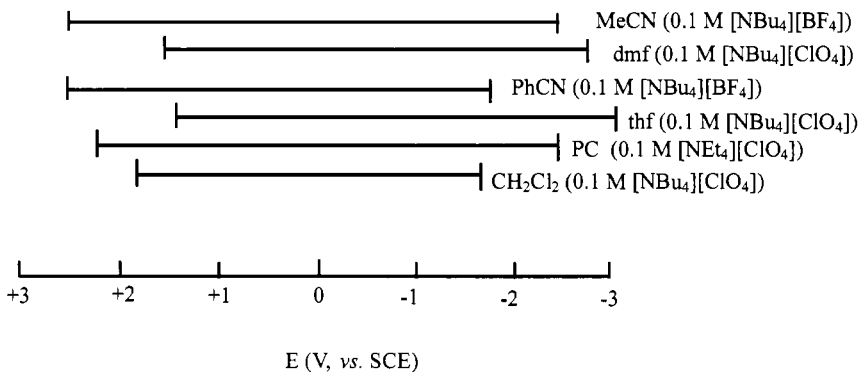


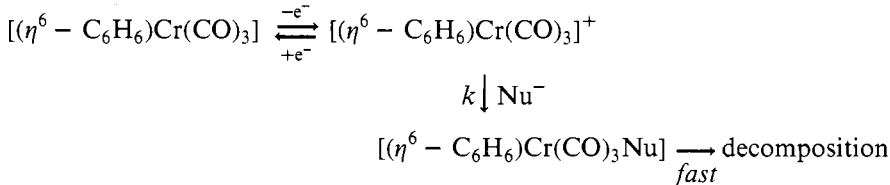
Figure 9 Potential windows for platinum electrodes in non-aqueous solvents

is a *tetrabutylammonium* salt (and not *tetraethylammonium*, that would not be sufficiently soluble). Otherwise, if one needs to use benzene as the solvent (which is the case for poorly soluble organic or organometallic compounds) one can make use of a *tetrahexylammonium* salts as the supporting electrolyte. One does not then give much attention to whether the salt anion is, for example, $\text{[ClO}_4^-\text{]}$ or $\text{[PF}_6^-\text{]}$. Since the coordinating ability, or *nucleophilicity*, of the $\text{[ClO}_4^-\text{]}$ anion[#] is greater than that of the $\text{[PF}_6^-\text{]}$ anion, it becomes evident how this difference can have significant consequences on the stability of the electrogenerated products.

In this case, it is highly educational to look at the voltammetric behaviour of the three-legged piano stool $[(\eta^6\text{-C}_6\text{H}_6)\text{Cr}(\text{CO})_3]$ in dichloromethane solution,¹⁰ see Figure 10.

As illustrated in Figure 10a, the compound displays the $[(\eta^6\text{-C}_6\text{H}_6)\text{Cr}(\text{CO})_3]/[(\eta^6\text{-C}_6\text{H}_6)\text{Cr}(\text{CO})_3]^+$ oxidation possessing characteristics of reversibility if one uses $[\text{NBu}_4]\text{[PF}_6^-]$ as the supporting electrolyte. By contrast, the same oxidation becomes irreversible if one uses $[\text{NBu}_4]\text{[ClO}_4^-]$ as the supporting electrolyte, Figure 10b.

This results as a consequence of the following mechanism:



where Nu^- represents the nucleophilic agent (in this case the counter-anions of the supporting electrolyte).

[#]Solutions containing perchlorate ion must be handled with care. Their drying may cause explosion.

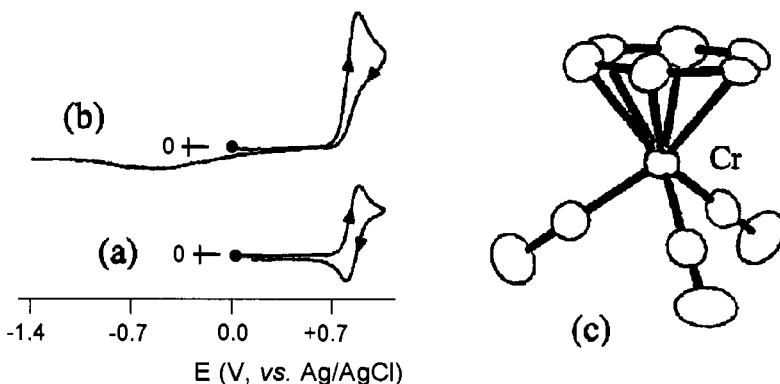


Figure 10 Cyclic voltammograms recorded at a platinum electrode in a CH_2Cl_2 solution of $[(\eta^6\text{-C}_6\text{H}_6)\text{Cr}(\text{CO})_3]$. Supporting electrolytes: (a) $[\text{NBu}_4]\text{[PF}_6]$; (b) $[\text{NBu}_4]\text{[ClO}_4]$. Scan rate 0.2 V s^{-1} . (c) Molecular structure of $[(\eta^6\text{-C}_6\text{H}_6)\text{Cr}(\text{CO})_3]$

Therefore, the greater the nucleophilic power of the supporting electrolyte counteranion ($\text{ClO}_4^- >> \text{PF}_6^-$), the more extensive the decomposition of the $[(\eta^6\text{-C}_6\text{H}_6)\text{Cr}(\text{CO})_3]^+$ cation which forms instantaneously at the electrode. This explains the different degree of chemical reversibility in the presence of $[\text{NBu}_4]\text{[ClO}_4]$ or $[\text{NBu}_4]\text{[PF}_6]$.

Recently, a very poorly coordinating supporting electrolyte has been proposed, namely $[\text{NBu}_4]\text{[B(C}_6\text{F}_5)_4]$.¹² The poor coordinating ability of the large anion $[\text{B(C}_6\text{F}_5)_4]^-$ makes soluble in non-aqueous solvents highly charged cations which can be generated in the course of anodic

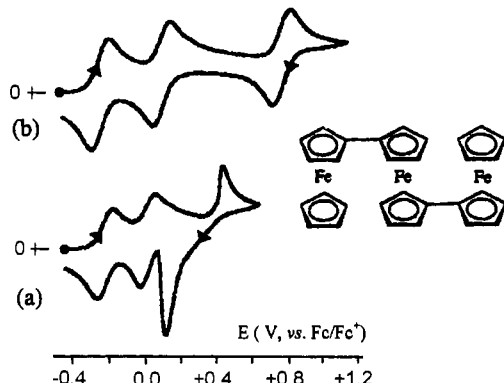


Figure 11 Cyclic voltammograms recorded at a glassy carbon electrode in a CH_2Cl_2 solution of terferrocene. Supporting electrolytes: (a) $[\text{NBu}_4]\text{[PF}_6]$ (0.1 mol dm^{-3}); (b) $[\text{NBu}_4]\text{[B(C}_6\text{F}_5)_4]$ (0.1 mol dm^{-3}). Scan rate 0.2 V s^{-1}

paths performed on molecules of high redox propensity. In addition $[\text{B}(\text{C}_6\text{F}_5)_4]^-$ possesses a very low ion-pairing capacity. This means that in sequential oxidation processes the electrostatic repulsion between the progressively electrogenerated charged cations notably increases, thus leading to high separations of the relative anodic processes. This is the case for instance of terferrocene, a molecule which will be examined in more details in Chapter 4, Section 3. As illustrated in Figure 11a, in dichloromethane solution containing $[\text{NBu}_4][\text{PF}_6]$ (0.1 mol dm^{-3}) as the supporting electrolyte, terferrocene gives rise to two first reversible one-electron oxidations followed by a third oxidation complicated by electrode adsorption of the electrogenerated trication.

In contrast, in dichloromethane solution containing $[\text{NBu}_4][\text{B}(\text{C}_6\text{F}_5)_4]$ (0.1 mol dm^{-3}) as supporting electrolyte, terferrocene affords three subsequent, remarkably separated, reversible oxidation processes.¹³

It is therefore useful to recall that for the most common counter-anions, the coordinating ability decreases in the order:



REFERENCES

1. J.B. Headridge, *Electrochemical Techniques for Inorganic Chemists*, Academic Press, London, 1969.
2. A.J. Bard and L.R. Faulkner, *Electrochemical Methods. Fundamentals and Applications*, 2nd Edn, J. Wiley, 2001.
3. A.M. Bond, *Modern Polarographic Methods in Analytical Chemistry*, Marcel Dekker, 1980.
4. P.T. Kissinger and W.R. Heineman, *Laboratory Techniques in Electroanalytical Chemistry*. Marcel Dekker, Inc., New York, 1984.
5. W.E. Geiger and M.D. Hawley, *Cyclic voltammetry, A.C. Polarography and Related Techniques*. Physical Methods of Chemistry. Electrochemical Methods. A. Weissberger and B.W. Rossiter eds, Vol. 2., Chapter 1. Wiley Interscience, New York, 1986.
6. D.T. Sawyer, A. Sobkowiak, J.L. Roberts, Jr, *Electrochemistry for Chemists*, J. Wiley and Sons., New York, 1995.
7. F. Scholz, ed., *Electroanalytical Methods. Guide to Experiments and Applications*, Springer, 2002.
8. K. Izutsu, *Electrochemistry in Nonaqueous Solutions*, Wiley-VCH, 2002.
9. J.K. Campbell, L. Sun, and R.M. Crooks, *J. Am. Chem. Soc.*, 1999, **121**, 3779.
10. C. Ohrenberg and W.E. Geiger, *Inorg. Chem.*, 2000, **39**, 2948.

11. J.P. Bullock, M.C. Palazzotto and K.R. Mann, *Inorg. Chem.*, 1991, **30**, 1284.
12. C.G. Zoski, D.A. Sweigart, N.J. Stone, P.H. Rieger, E. Mocellin, T.F. Mann, D.R. Mann, D.K. Gosser, M.M. Doeffer and A.M. Bond, *J. Am. Chem. Soc.*, 1988, **110**, 2109.
13. N. Camire, U.T. Mueller-Westerhoff and W.E. Geiger, *J. Organomet. Chem.*, 2001, **637–639**, 823.

APPLICATIVE ASPECTS

CHAPTER 4

The Electrochemical Behaviour of First Row Transition Metal Metallocenes

We now wish to illustrate the role of electrochemistry in various fields of inorganic chemistry ranging from organometallics to coordination chemistry, from material science to biomimetics. The present chapter is devoted to *metallocenes*.

We will begin our electrochemical survey with metallocenes as, from a conceptual viewpoint, they are involved in relatively simple redox processes. Undoubtedly the most representative metallocene is *ferrocene*, $[\text{Fe}(\eta^5\text{-C}_5\text{H}_5)_2]$, which constitutes a milestone in the development of organometallic chemistry. One of the main characteristics of ferrocene is its capacity to lose an electron without the molecule being broken-up, thereby generating the corresponding ferrocenium ion $[\text{Fe}(\eta^5\text{-C}_5\text{H}_5)_2]^+$ (see Introduction). In fact, it is this property that has resulted in ferrocene and its derivatives being amongst the molecules most studied by electrochemistry.

In order to understand the origin of the high redox capability of metallocenes one must examine their molecular orbital diagram, Figure 1 (already reported in Figure 3 of the Introduction). The arrangement of the orbital energies was derived for ferrocene, but it is accepted as valid for all the metallocenes of the first row transition metals ranging from vanadocene (15 valence electrons) to nickelocene (20 valence electrons).

The e_1'' (antibonding), a'_1 (nonbonding) and e_2' (bonding) are assumed to be the frontier orbitals for metallocenes. The non-bonding nature of the a'_1 orbitals, the HOMO, is in agreement with the observation that for ferrocene (18 valence electrons; terminal electronic configuration $e_2'^4a'_1^2$) the removal of one electron to form the ferrocenium ion (17 valence electrons) does not substantially destabilize the molecular frame.

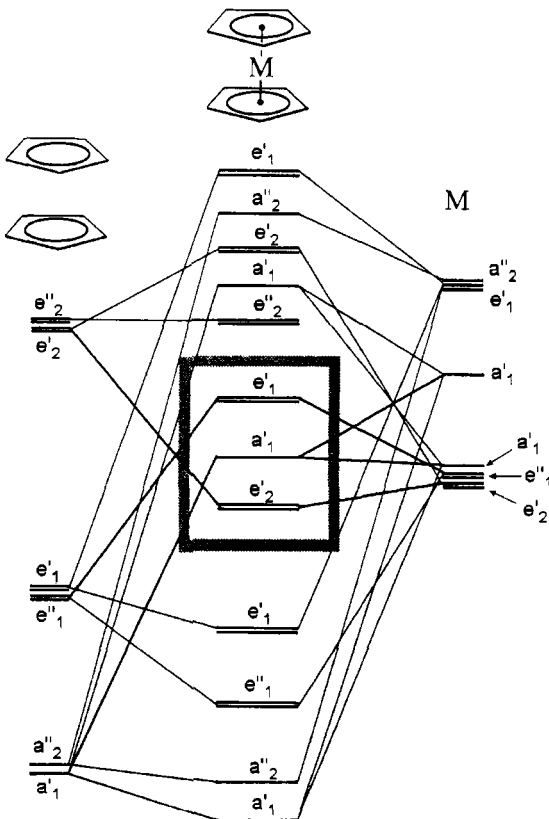


Figure 1 Molecular orbital diagram for metallocenes (in the eclipsed configuration)

We therefore open our electrochemical examination of metallocenes by starting with ferrocene derivatives and then the other metallocenes. It has to be anticipated that the chemistry of these latter compounds is, however, considerably less developed.

1 FERROCENES

There is an enormous number of ferrocene derivatives ranging from monoferrocenes to ferrocene-based polymers.

1.1 Monoferrocenes

As one of our main objectives is to correlate the electrochemical characteristics of inorganic molecules with the structural consequences of their electron transfer processes, ferrocene is an ideal molecule with which to begin.

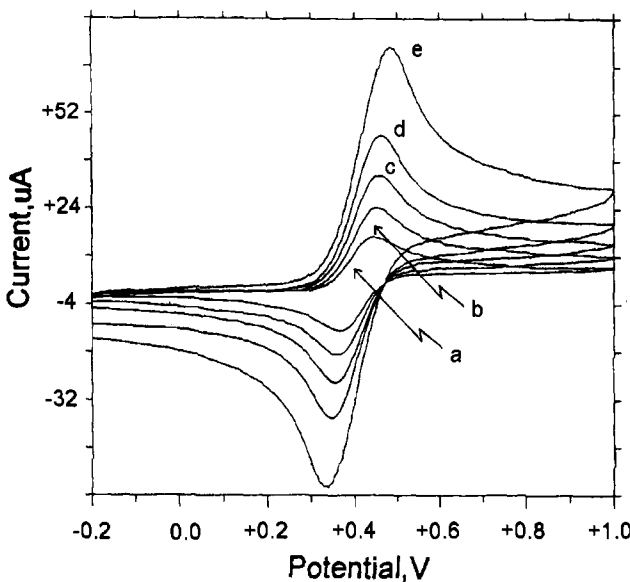


Figure 2 Cyclic voltammograms recorded at a platinum electrode on a CH_2Cl_2 solution of $[\text{Fe}(\eta^5\text{-C}_5\text{H}_5)_2]$ (1.0×10^{-3} mol dm^{-3}). Supporting electrolyte $[\text{NBu}_4]\text{[PF}_6]$ (0.2 mol dm^{-3}). Scan rates: (a) 0.02 Vs^{-1} ; (b) 0.05 Vs^{-1} ; (c) 0.10 Vs^{-1} ; (d) 0.20 Vs^{-1} ; (e) 0.50 Vs^{-1}

Figure 2 shows a sequence of cyclic voltammograms recorded at a platinum electrode on a dichloromethane solution of ferrocene at increasing scan rates, at 25°C .

Ferrocene gives rise to an anodic process, which in controlled potential coulometry involves one electron per molecule. As a consequence of the exhaustive oxidation the original yellow solution turns blue-green, a colour typical of the iron-centred ferrocenium ion ($\lambda_{\text{max}} = 620$ nm). The voltammogram of the final solution is complementary to that shown in Figure 2.

Given the one electron nature and chemical reversibility of the oxidation, let us pass to the cyclic voltammetric analysis of the process, Table 1.

Looking at the data, one can deduce that:

- the current ratio between the return and the forward peaks (in the present case: $i_{\text{pc}}/i_{\text{pa}}$) is equal (under the limits of the experimental conditions) to 1.0 at all scan rates, suggesting chemical reversibility of the electron transfer on the cyclic voltammetric time scale (the result was obviously expected on the basis of the macroelectrolysis experiment);

Table 1 Typical tabulation of cyclic voltammetric data. $[Fe(\eta^5-C_5H_5)_2]$ solution (1.0×10^{-3} mol dm $^{-3}$) in CH_2Cl_2 . Supporting electrolyte: $[NBu_4][PF_6]$ (0.2 mol dm $^{-3}$). Platinum disc electrode: radius = 1 mm. Potential values are referred to SCE

v	E_p	i_p	E_p	i_p	ΔE_p	$i_{p(forward)}$	$i_{p(forward)}/v^{1/2}$	E°
	(forward)		(return)		(mV)			
	(mV s $^{-1}$)	(mV)	(μ A)	(mV)	(μ A)		$i_{p(return)}$	(mV)
20	+ 450	15.6	+ 368	16.0	82	1.02	3.49	+ 409
50	+ 449	25.2	+ 356	25.7	93	1.01	3.56	+ 403
100	+ 459	33.8	+ 360	33.7	98	1.00	3.38	+ 409
200	+ 464	45.6	+ 350	44.8	112	0.98	3.22	+ 407
500	+ 485	68.3	+ 338	66.1	145	0.97	3.05	+ 411
1003	+ 493	96.1	+ 331	93.8	160	0.97	3.03	+ 412
							(average: + 408)	

- the peak-to-peak separation, ΔE_p , which is 82 mV at 0.02 V s $^{-1}$, tends to increase with the scan rate;
- the current function relative to the forward peak (in the present case: $i_{pa}/v^{1/2}$) remains substantially constant, indicating that the process is diffusion controlled;
- the average value between the (forward) anodic peak E_{pa} and the (return) cathodic peak E_{pc} affords a value of + 0.41 V (vs. SCE; at 25°C).

The fact that either the peak-to-peak separation, ΔE_p , somewhat departs from the value of 59 mV or the current function $i_{pa}/v^{1/2}$ is not rigorously constant seems to contrast with the diagnostic criteria (illustrated in Chapter 2, Section 1.1.1) for an electrochemically reversible one-electron process. This can be largely attributed to the non-compensated resistance given by the dichloromethane solution, which is a low conducting solvent.

It is interesting to note that the redox potential of the $[Fe(\eta^5-C_5H_5)_2]/[Fe(\eta^5-C_5H_5)_2]^+$ couple varies appreciably from one solvent to another, Table 2.

This contrasts with the assumption made until a few years ago that the redox potential of the ferrocene/ferrocenium couple was independent of solvent and fixed at a constant value of + 0.400 V vs. NHE. It is, in fact, this controversial assumption that is at the origin^{1a} of the IUPAC recommendation^{1b} (not yet always followed) of expressing the potential of any redox couple in non-aqueous solvents with respect to the potential of the $[Fe(\eta^5-C_5H_5)_2]/[Fe(\eta^5-C_5H_5)_2]^+$ couple.

Table 2 Formal electrode potentials (V vs. SCE, at $25^\circ C$) and peak-to-peak separation (mV) for the couple $[Fe(\eta^5-C_5H_5)_2]/[Fe(\eta^5-C_5H_5)_2]^+$ in different solutions. Platinum working electrode (measured in our laboratory)

Solvent	Supporting electrolyte (0.2 M)	E°'	$\Delta E_p (0.1\text{ V s}^{-1})$
MeNO ₂	$[\text{NBu}_4][\text{ClO}_4]$	+0.31	66
MeCN	$[\text{NEt}_4][\text{ClO}_4]$	+0.38	90
dmso	$[\text{NEt}_4][\text{ClO}_4]$	+0.40	88
CH ₂ Cl ₂	$[\text{NBu}_4][\text{ClO}_4]$	+0.45	95
	$[\text{NBu}_4][\text{PF}_6]$	+0.41	98
Me ₂ CO	$[\text{NBu}_4][\text{ClO}_4]$	+0.46	88
dmf	$[\text{NEt}_4][\text{ClO}_4]$	+0.49	72
Py	$[\text{NBu}_4][\text{ClO}_4]$	+0.50	76
thf	$[\text{NBu}_4][\text{ClO}_4]$	+0.54	137

It can be also deduced that the potential of the ferrocene/ferrocenium couple, for the same solvent, also varies with the supporting electrolyte.

As far as the ΔE_p values are concerned, it cannot be ruled out that the molecular rearrangements that occur on passing from ferrocene to ferrocenium ion might also play a role, even if minimal, in their departure from the value of 59 mV, or in lowering the degree of electrochemical reversibility of the process.

In this connection, in order to judge the level of these molecular rearrangements, the solid state X-ray structures of ferrocene and ferrocenium ion could be compared. Unfortunately, the molecular disorder caused by the rotation of the cyclopentadienyl rings in ferrocene means that the comparison procedure is far from simple and, in fact, the first results were interpreted in terms of a staggered conformation of the two cyclopentadienyl rings. It is now believed that the eclipsed conformation is the more stable (with a rotation angle of about 10°).² However, as the rotational barrier is notably low (about 4 kJ mol^{-1}), the conformation that one observes is probably that imposed by crystal packing forces.

A similar situation occurred for the ferrocenium ion. Until 1983, on the basis of the available structural data, it was thought that the cyclopentadienyl rings assumed an eclipsed conformation. However, more recent data demonstrate that it assumes a staggered conformation, even if once again the crystal packing forces are considered to be the determining factor.³

In order to have a reliable means of defining the extent of the molecular rearrangement that follows the removal of an electron one can consider the variation in bonding distances, since the bond length is

Table 3 Comparison between the bond lengths (rounded off to the second decimal figure) of ferrocene and ferrocenium ion

	<i>Fe-C</i> (\AA)	<i>C-C</i> (\AA)	<i>Fe-Cp</i> _(centroid) (\AA)
$[\text{Fe}(\eta^5\text{-C}_5\text{H}_5)_2]$	2.04	1.40	1.66
$[\text{Fe}(\eta^5\text{-C}_5\text{H}_5)_2]^+$	2.07	1.42	1.69

independent of the mutual disposition of the cyclopentadienyl rings. Table 3 shows that the transition from ferrocene to the ferrocenium ion results in a slight lengthening of the Fe–C distance. In other words, upon one-electron removal, the cyclopentadienyl rings move away from the iron atom by about 0.03 Å, while the C–C distance within the cyclopentadienyl rings remains virtually unchanged.

The structural reorganization that accompanies the oxidation of the permethylated analogue, decamethylferrocene, $[\text{Fe}(\eta^5\text{-C}_5\text{Me}_5)_2]$, is apparently easier to determine.

Firstly, let us discuss its electrochemical behaviour. As previously illustrated in Chapter 2, Figure 5, the anodic response in dichloromethane solution also shows features of chemical reversibility ($i_{pc}/i_{pa} = 1$). The peak-to-peak separation ($\Delta E_p = 76$ mV) again indicates a slight deviation from the theoretical value of 59 mV expected for an electrochemically reversible one-electron process.

The variation of the redox potential of the decamethylferrocene/decamethylferrocenium couple with the nature of the solvent is reported in Table 4.

It is evident that the deviations of ΔE_p from the theoretical value of 59 mV are of the same order of magnitude as that seen, under the same

Table 4 Formal electrode potentials (V vs. SCE, at 25°C) and peak-to-peak separation (mV) for the couple $[\text{Fe}(\eta^5\text{-C}_5\text{Me}_5)_2]/[\text{Fe}(\eta^5\text{-C}_5\text{Me}_5)_2]^+$ in different non-aqueous solutions. Platinum working electrode (measured in our laboratory)

Solvent	Supporting electrolyte (0.2 M)	E°'	ΔE_p (0.1 V s ⁻¹)
MeNO ₂	$[\text{NBu}_4][\text{ClO}_4]$	-0.19	70
MeCN	$[\text{NEt}_4][\text{ClO}_4]$	-0.12	70
CH ₂ Cl ₂	$[\text{NBu}_4][\text{ClO}_4]$	-0.10	80
	$[\text{NBu}_4][\text{PF}_6]$	-0.12	88
dmso	$[\text{NEt}_4][\text{ClO}_4]$	-0.01	65
dmf	$[\text{NEt}_4][\text{ClO}_4]$	+ 0.02	66
Me ₂ CO	$[\text{NBu}_4][\text{ClO}_4]$	+ 0.08	103
thf	$[\text{NBu}_4][\text{ClO}_4]$	+ 0.13	102

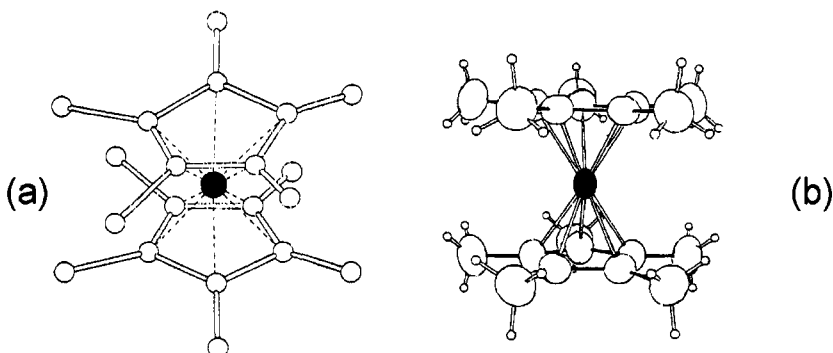


Figure 3 X-Ray structures of: (a) $[\text{Fe}(\eta^5\text{-C}_5\text{Me}_5)_2]$; (b) $[\text{Fe}(\eta^5\text{-C}_5\text{Me}_5)_2]^+$, in $[\text{Fe}(\eta^5\text{-C}_5\text{Me}_5)_2](\text{Br})_3$

conditions, for unsubstituted ferrocene. Hence, one might roughly infer that the structural variations which follow the removal of the electron are substantially similar in the two cases.

The X-ray structures of decamethylferrocene and the decamethylferrocenium ion are illustrated in Figure 3.^{4,5}

One can see that in the neutral derivative the pentamethylcyclopentadienyl rings assume a staggered conformation. Conversely, in the monocation they are disposed in an eclipsed conformation.⁵ A comparison between the bonding distances of decamethylferrocene and the decamethylferrocenium ion (already reported in Chapter 2, Table 1) reveals that the rotation of the rings following the electron removal is accompanied by a lengthening of the Fe–C distance by about 0.05 Å. This is approximately equal to that measured in the case of ferrocene.

In conclusion, also in the case of the $[\text{Fe}(\eta^5\text{-C}_5\text{H}_5)_2]/[\text{Fe}(\eta^5\text{-C}_5\text{H}_5)_2]^+$ couple, the slight deviation from the electrochemical reversibility could be due not only to the lengthening of the Fe–C distances, but also to a different disposition of the cyclopentadienyl rings.

Such behaviour, in particular the slight elongation of the Fe–C distance following the one-electron removal, is a common feature which has been found in different, structurally resolved, ferrocene/ferrocenium couples. Table 5 shows a few examples.

Returning to the simple electrochemical aspects of $[\text{Fe}(\eta^5\text{-C}_5\text{H}_5)_2]$ and $[\text{Fe}(\eta^5\text{-C}_5\text{Me}_5)_2]$, one should note how the substitution of the 10 hydrogen atoms of the cyclopentadienyl rings of ferrocene with 10 methyl groups lowers the redox potential of the oxidation process by about 500 mV (about 50 mV for each methyl group). This can be ascribed to the electron-donating effect of the alkyl groups which, by

Table 5 Structural and redox data for a few ferrocene/ferrocenium couples (bond lengths rounded off to the second decimal figure)

	$E^{\circ/}_{Fe(II)/Fe(III)}$	$Fe(II)-Cp_{(centroid)}$	$Fe(III)-Cp_{(centroid)}$	Reference
	V (vs. SCE)	(Å)	Å	
$[Fe(\eta^5-C_5H_4Me)_2]^{0/+}$	+ 0.38 ^a	1.65	1.71	6
$[Fe\{\eta^5-C_5H_4(SiMe_3)\}_2]^{0/+}$	+ 0.48 ^b	1.66	1.71	7, 6b
$[Fe\{\eta^5-C_5H_2(SiMe_3)_3\}_2]^{0/+}$	+ 0.28 ^a	1.69	1.75	8
$[Fe(\eta^5-C_5HMe_4)_2]^{0/+}$	- 0.01 ^a	1.65	1.69	9

pushing electron density towards the metal, facilitates the electron removal by the electrode.

The important role which the inductive effects of the substituent groups plays in the thermodynamic aspects of redox processes (*i.e.* on the value of the standard potential) is shown by the data reported in Table 6. Ferrocene derivatives are listed which have either electron-donating (which render the oxidation easier) or electron-withdrawing (which render the oxidation more difficult) substituent groups.

It can be seen that the oxidation potential of the ferrocene/ferrocenium process shifts by about 1 V with the inductive effects.

Most of the countless ferrocene derivatives which have been synthesized display a one-electron ferrocene/ferrocenium oxidation process at potentials roughly predictable on the basis of the inductive effects of the substituents. It should be noted, however, that at times the introduction of substituents renders the corresponding ferrocenium species unstable.

Table 6 Formal electrode potential (V vs. SCE, at 25°C) for the one-electron oxidation of a few substituted ferrocenes. Dichloromethane solution; $[NBu_4][ClO_4]$ supporting electrolyte

Derivative	$E^{\circ/}_{0/+}$
$[Fe(\eta^5-C_5Me_5)_2]$	- 0.12
$[Fe(\eta^5-C_5Me_5)(\eta^5-C_5H_5)]$	+ 0.18
$[Fe(\eta^5-C_5Bz_5)_2]^a$	+ 0.38
$[Fe(\eta^5-C_5H_5)_2]$	+ 0.45
$[Fe(\eta^5-C_5H_4SH)_2]$	+ 0.65
$[Fe(\eta^5-C_5H_4(CF_3))_2]$	+ 1.09

^aBz = CH_2Ph .

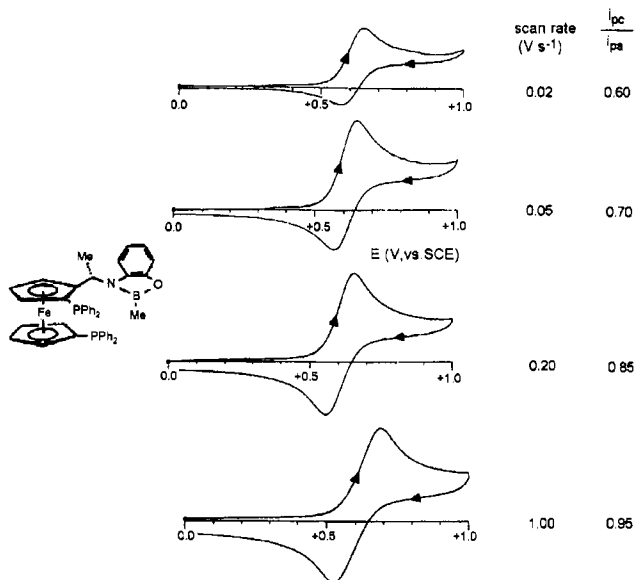


Figure 4 Cyclic voltammograms recorded at different scan rates of a CH_2Cl_2 solution of 1,1'-bis(diphenylphosphino)-2-[1-((1-hydroxy-2-phenyl)amino)methylboronate]ethylferrocene. Platinum working electrode. Supporting electrolyte $[\text{NBu}_4][\text{ClO}_4]$ (0.2 mol dm^{-3})

The electrochemical response of the boronato-functionalized 1,1'-bis(diphenylphosphino)-2-[1-((1-hydroxy-2-phenyl)amino)ethyl]ferrocene shown in Figure 4 gives a typical example of such an effect.¹⁰

In fact, at low scan rates the current ratio i_{pc}/i_{pa} is lower than 1.0. Nevertheless, increasing the scan rate allows the decomposition of the monocation to be more and more prevented until at the scan rate of 1 Vs^{-1} , the current ratio reaches unity. Assuming the occurrence of a first-order chemical complication, this permits the life-time of the monocation to be determined as about 6 s (see Chapter 2, Section 1.4.2.2).

1.2 Ferrocenophanes

To conclude the matter of monoferrocene molecules we consider those cases in which the cyclopentadienyl substituents form bridges between the two rings. Such derivatives are named *ferrocenophanes*. The best known ferrocenophanes are those which contain saturated (tri- or tetramethylene) carbon chains. Like ferrocenes, these molecules also exhibit reversible one-electron oxidation to the corresponding ferrocenium ions.

For example, for the trimethylene-bridged derivative $[\text{Fe}(\eta^5,\eta^5-\text{C}_5\text{H}_4(\text{CH}_2)_3\text{C}_5\text{H}_4)]$ (also known as [3]ferrocenophane) the oxidation

process occurs at $E^{\circ'} = +0.31$ V in acetonitrile solution.¹¹ As it has been observed that the oxidation of unsubstituted ferrocene in the same medium occurs at $E^{\circ'} = +0.38$ V, one can infer that the trimethylene bridge donates electron density to the ferrocene fragment facilitating the electron removal.

Figure 5 shows the molecular structures of the $[\text{Fe}(\eta^5,\eta^5\text{-C}_5\text{H}_4(\text{CH}_2)_3\text{C}_5\text{H}_4)]/[\text{Fe}(\eta^5,\eta^5\text{-C}_5\text{H}_4(\text{CH}_2)_3\text{C}_5\text{H}_4)]^+$ redox couple.^{11,12}

In both cases the presence of the carbon bridge constrains the cyclopentadienyl rings to assume an eclipsed conformation, but, above all, they are constrained to take a non-parallel mutual disposition. In particular, since the oxidation process results in the usual lengthening of the $\text{Fe}-\text{C}_{(\text{ring})}$ distance (by about 0.03 Å), the restraint imposed by the carbon bridge means that the tilting angle between the cyclopentadienyl rings in the monocation increases (by about 6°) with respect to that of the neutral species.

The bis-trimethylene bridged $[\text{Fe}(\eta^5\text{-C}_5\text{H}_3)_2(1,1',3,3'-(\text{CH}_2)_3)_2]$ (also known as [3](1,1')[3](3,3')ferrocenophane) is oxidized in acetonitrile at $E^{\circ'} = +0.30$ V.¹¹ The molecular structure of the neutral derivative and the corresponding monocation is shown in Figure 6.^{11,13}

The molecular structures are qualitatively similar, but for the fact that, also in this case, the oxidation causes an increase (by about 5°) of the tilting angle.

Finally, the tris-trimethylene-bridged $[\text{Fe}(\eta^5\text{-C}_5\text{H}_2)_2(1,1',2,2',4,4'-(\text{CH}_2)_3)_3]$ (or, [3](1,1')[3](2,2')[3](4,4')ferrocenophane) is also oxidized at +0.30 V.¹¹ The X-ray structures of the neutral and the monocation derivatives are shown in Figure 7.^{13,14}

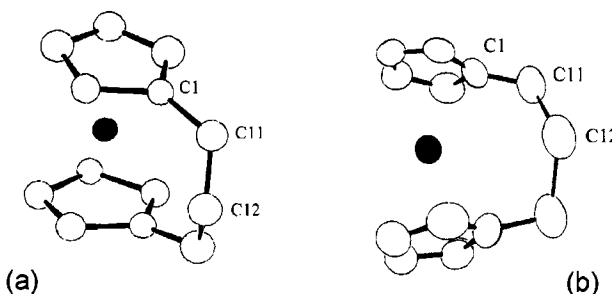


Figure 5 X-Ray structures of: (a) $[\text{Fe}(\eta^5\text{-C}_5\text{H}_4)_2(\text{CH}_2)_3]$. $\text{Fe}-\text{C}_{(\text{ring})} = 2.01$ Å; $\text{Fe}-\text{Cp}_{(\text{centroid})} = 1.63$ Å; $\text{C}-\text{C}_{(\text{ring})} = 1.38$ Å; $\text{C1-C11} = 1.49$ Å; $\text{C11-C12} = 1.45$ Å; tilting angle = 7.4°; (b) $[\text{Fe}(\eta^5\text{-C}_5\text{H}_4)_2(\text{CH}_2)_3]^+$ in $[\text{Fe}(\eta^5\text{-C}_5\text{H}_4)_2(\text{CH}_2)_3]/(\text{TCNQ})_2$ ($\text{TCNQ} = 7,7,8,8\text{-tetracyano-p-quinodimethane}$). $\text{Fe}-\text{C}_{(\text{ring})} = 2.12$ Å; $\text{Fe}-\text{Cp}_{(\text{centroid})} = 1.66$ Å; $\text{C}-\text{C}_{(\text{ring})} = 1.40$ Å; $\text{C1-C11} = 1.56$ Å; $\text{C11-C12} = 1.56$ Å; tilting angle = 13.7°

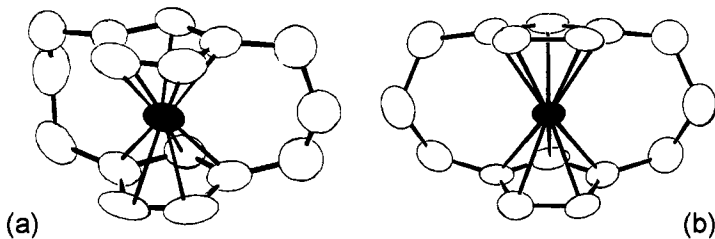


Figure 6 X-Ray structures of: (a) $[Fe(\eta^5\text{-}C_5H_3)_2(1,1',3,3'-(CH_2)_3)_2]$. $Fe\text{-}Cp_{(centroid)} = 1.60 \text{ \AA}$; $C\text{-}C_{(ring)} = 1.42 \text{ \AA}$; tilting angle = 9.6° ; (b) $[Fe(\eta^5\text{-}C_5H_4)_2(1,1',3,3'-(CH_2)_3)_2]^{+}$ ($[I_3]^-$ counteranion). $Fe\text{-}Cp_{(centroid)} = 1.66 \text{ \AA}$; $C\text{-}C_{(ring)} = 1.42 \text{ \AA}$; tilting angle = 14.3°

As is evident, the most significant structural variations observed on passing from tris(trimethylene)ferrocene to tris(trimethylene)ferroceum ion reflect those discussed above: the Fe–C bond lengths increase and the tilting angle of the rings also becomes slightly greater (it is obvious that the presence of more than one bridge attenuates the cyclopentadienyl derangement).

The relative insensitivity of the redox potential to the introduction of a second or third trimethylene bridge is rather unexpected.

There also exist a number (very few due to the relative difficulty of synthesis) of derivatives containing four or five carbon bridges.¹⁵ Unfortunately, the electrochemistry of these compounds has not been studied.

It is noted that there are also ferrocenophanes in which the bridge is formed by heteroatoms. For example, Figure 8 shows the molecular structure of ferrocenophanes containing one¹⁶ or two¹⁷ trisulfur bridges.

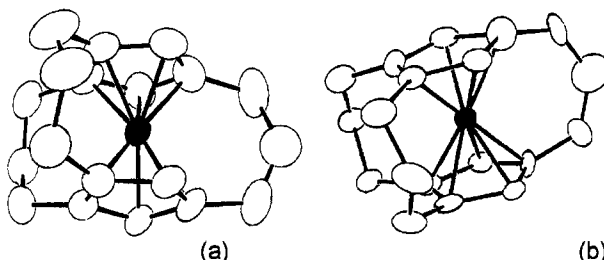


Figure 7 X-Ray structures of: (a) $[Fe(\eta^5\text{-}C_5H_3)_2(1,1',3,3'-(CH_2)_3)_3]$. $Fe\text{-}Cp_{(centroid)} = 1.57 \text{ \AA}$; $C\text{-}C_{(ring)} = 1.44 \text{ \AA}$; tilting angle = 2.5° . (b) $[Fe(\eta^5\text{-}C_5H_3)_2(1,1',3,3'-(CH_2)_3)_3]^{+}$ ($[I_3]^-$ counteranion). $Fe\text{-}Cp_{(centroid)} = 1.62 \text{ \AA}$; $C\text{-}C_{(ring)} = 1.43 \text{ \AA}$; tilting angle = 4.3°

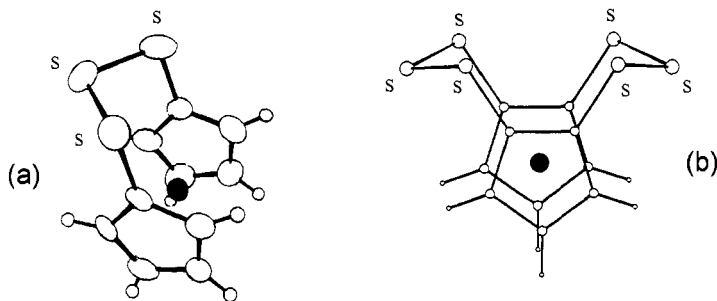


Figure 8 X-Ray structures of: (a) 1,2,3-trithia[3]ferrocenophane. Fe-C average bond length: 2.044 Å. (b) [3](1,1')[3](2,2')(1,2,3)trithia-ferrocenophane. Fe-C average bond length: 2.043 Å

It is clear from Figure 9 and Table 7 that there is a considerable difference in the redox potential of the two species.¹⁸

The comparison with the redox potential of ferrocene highlights the electron-withdrawing effect of each trisulfur chain (which renders more difficult the removal of electrons).

To close the discussion on ferrocenophanes, we would like to point out that there also exist molecules containing more complex bridging systems, which, however, display the usual chemically reversible ferrocene/ferrocenium oxidation. Figure 10 for instance, shows the molecular structure and the redox behaviour of an (*ansa*)-ferrocenophane containing a pyrazabole bridge.¹⁹

As suggested by the chemical (i_{pc}/i_{pa} constantly equal to 1.0) and electrochemical ($\Delta E_p = 76$ mV, at 0.1 Vs^{-1}) reversibility of the oxidation

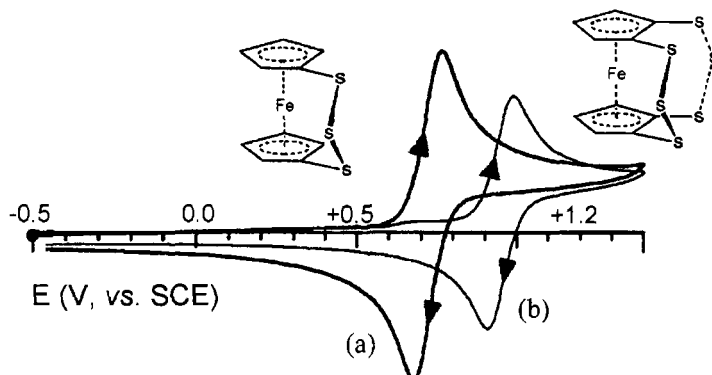


Figure 9 Cyclic voltammograms recorded at a platinum electrode on CH_2Cl_2 solutions containing: (a) $[\text{Fe}(\eta^5\text{-C}_5\text{H}_4)_2(\text{S}_3)]$; (b) $[\text{Fe}(\eta^5\text{-C}_5\text{H}_4)_2(\text{S}_3)_2]$. Supporting electrolyte: $[\text{NBu}_4][\text{ClO}_4]$ (0.2 mol dm^{-3}). Scan rate 0.2 Vs^{-1}

Table 7 Redox potential (V vs. SCE, at $25^\circ C$) for the oxidation of a few trithiaferrocenophanes in CH_2Cl_2 solution

Complex	$E^{\circ'}_{0/+}$
$[\text{Fe}(\eta^5\text{-C}_5\text{H}_4)_2(\text{S}_3)]$	+0.72
$[\text{Fe}(\eta^5\text{-C}_5\text{H}_3)_2(\text{S}_3)_2]$	+0.95
$[\text{Fe}(\eta^5\text{-C}_5\text{H}_5)_2]$	+0.44

process, the corresponding monocation is stable and essentially maintains the original geometry. As a consequence of the elongation of the Fe–C bond lengths following the electron removal, the tilting angle of the rings increases from 3.4° to 7.4° .²⁰

1.3 Oligoferroocene Derivatives

Let us now pass to *multiferrocene* compounds. Many compounds containing two, three, four or more ferrocene groups have been prepared and characterized. For these derivatives one can confidently expect that the number of one-electron oxidations equal the number of ferrocene groups. However, one must still determine whether these processes occur at separate or at identical potential values (according to that discussed in Chapter 2, Section 1.5, for consecutive electron transfers).

With this objective in mind we begin by considering bis(ferrocene) molecules.

The first derivative is bisferrocene, $[(\eta^5\text{-C}_5\text{H}_5)\text{Fe}(\eta^5\text{-C}_5\text{H}_4)(\eta^5\text{-C}_5\text{H}_4)\text{Fe}(\eta^5\text{-C}_5\text{H}_5)]$, whose molecular structure is shown in Figure 11.²¹

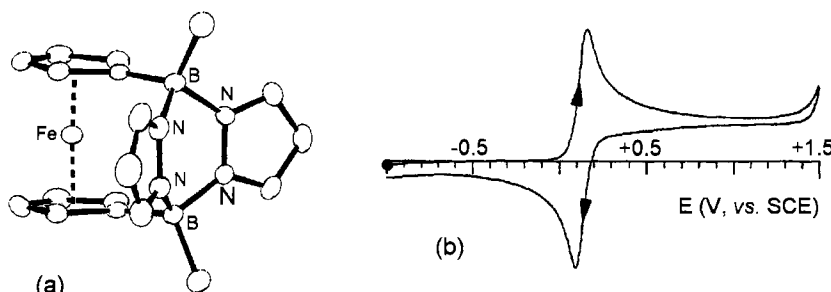


Figure 10 X-Ray structure (a) and cyclic voltammetric behaviour (Pt working electrode; CH_2Cl_2 solution; scan rate 0.2 Vs^{-1}) (b) of *ansa*-1,*I'*-[$\text{Fe}(\eta^5\text{-C}_5\text{H}_4)_2(\text{BMe}(\mu\text{-pz}))_2$] (*pz* = pyrazole)

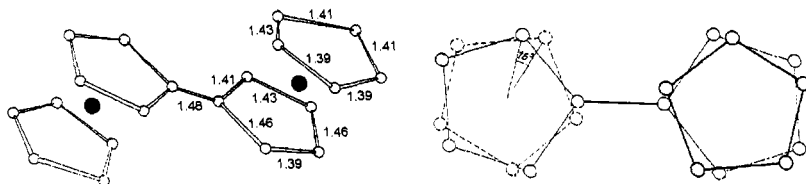


Figure 11 *X-Ray structure of biferrrocene, together with the relevant bond lengths*

The relative disposition of the cyclopentadienyl rings is partially staggered (with a rotation angle of about 16° , compared to an angle of 36° expected for an exactly staggered conformation).

As illustrated in Figure 12, biferrrocene undergoes two reversible (on the cyclic voltammetric time scale) one-electron oxidations at separated potential values ($E_{0/+}^{\circ'} = +0.31$ V; $E_{+/2+}^{\circ'} = +0.65$ V).²²

On the longer time scale of controlled potential electrolysis, only the monocation $[(\eta^5\text{-C}_5\text{H}_5)\text{Fe}(\eta^5\text{-C}_5\text{H}_4)(\eta^5\text{-C}_5\text{H}_4)\text{Fe}(\eta^5\text{-C}_5\text{H}_5)]^+$ is stable. It has been crystallized with various counteranions and the respective molecular structures solved. As an example, Figure 13 shows the molecular structure of the monocation in $[(\eta^5\text{-C}_5\text{H}_5)\text{Fe}(\eta^5\text{-C}_5\text{H}_4)(\eta^5\text{-C}_5\text{H}_4)\text{Fe}(\eta^5\text{-C}_5\text{H}_5)][\text{FeBr}_4]$.²³

The cyclopentadienyl rings around the Fe1 atom are almost eclipsed (rotation angle 6.5°), whereas those around atom Fe2 are almost

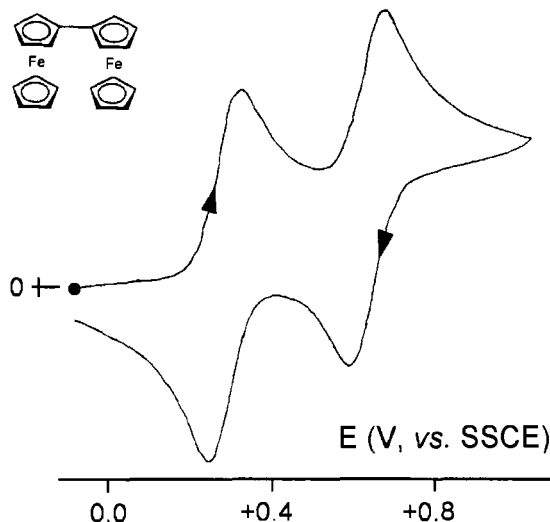


Figure 12 *Cyclic voltammogram recorded at a platinum electrode in a $\text{CH}_2\text{Cl}_2\text{-MeCN}$ (1:1) solution of biferrrocene. Supporting electrolyte: $[\text{NBu}_4][\text{PF}_6]$ (0.1 mol dm^{-3}). Scan rate: 0.2 Vs^{-1}*

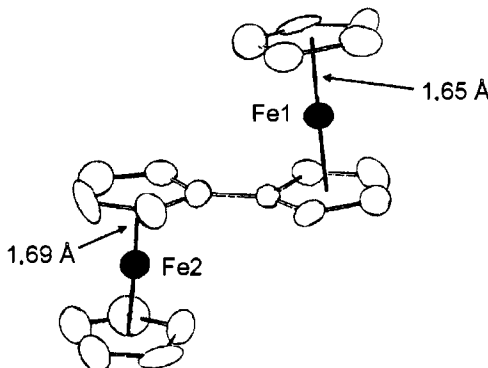


Figure 13 X-Ray structure of biferrocenium ion $[(\eta^5\text{-C}_5\text{H}_5)\text{Fe}(\eta^5\text{-C}_5\text{H}_4)(\eta^5\text{-C}_5\text{H}_4)\text{Fe}(\eta^5\text{-C}_5\text{H}_5)]^+$ ($[\text{FeBr}_4]^-$ counteranion)

staggered (rotation angle 23.5°). Although it has been shown that the mutual disposition of the cyclopentadienyl rings cannot be taken as an index of the oxidation state of the central iron atom, the $\text{Fe}-\text{Cp}_{(\text{centroid})}$ mean bond lengths show that in the case of Fe1 it is 1.65 \AA , whereas for Fe2 it is significantly longer at 1.69 \AA . This would apparently suggest that Fe1 is in the Fe(II) state, while Fe2 is in the Fe(III) state, thus implying that the first oxidation removes an electron from Fe2.

On this basis it would seem that the biferrocenium ion can be classified as a *mixed-valent* ($\text{Fe}^{\text{II}}\text{-Fe}^{\text{III}}$) compound displaying localized charge. At this point it is useful to digress briefly and consider more deeply the concept of mixed-valent compounds.

In order to understand the nature of mixed-valent compounds one must consider both electrostatic and magnetic interactions between centres which have different oxidation states. Nevertheless, as schematically shown in Figure 14, simple electrostatic effects can help to clarify the so-called *Robin-Day classification*.²⁴ This is based on the degree of electronic delocalization in (usually binuclear) mixed-valent compounds.

In fact, such a classification defines:

- compounds of *Class I*: those in which the charge is *localized* on one of the two redox centres
- compounds of *Class II*: those in which the charge is *slightly delocalized* between the two redox centres
- compounds of *Class III*: those in which the charge is *completely delocalized* between the two redox centres.

The degree of delocalization of the charge is directly related to what is called the extent of *electronic communication* between the redox centres.

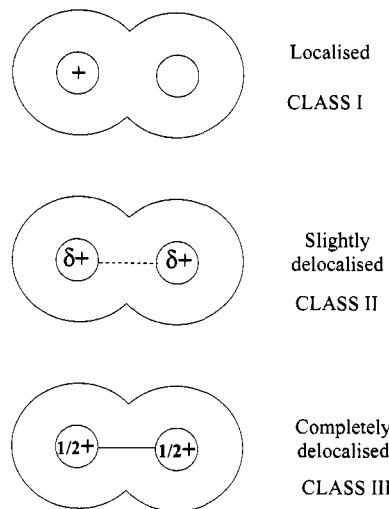


Figure 14 Schematic representation of the electronic effects in mixed-valent species according to the Robin-Day classification. Here the charge has been assumed to be positive as in ferrocenium ions

This electronic interaction constitutes an important parameter as far as the properties of polynuclear molecules are concerned.

Figure 15 qualitatively depicts the cyclic voltammetric responses that one would expect for diferrocenyl molecules according to their charge delocalization.

In summary, depending upon the degree of delocalization one would pass from a single two-electron process to two, more or less separated, one-electron processes.

Hence, according to the analysis of the structure reported in Figure 13, the biferrocenium ion would appear to belong to the charge-localized Class I. This result is, however, in sharp contrast with the electrochemical response of biferroocene, which, as suggested by comparison of Figures 12 and 15, would belong to the delocalized Classes II or III. In fact, the degree of charge delocalization in mixed-valent compounds can be easily determined by electrochemical measurements²⁵ through a calculation of the *comproportionation constant*, K_{com} .* In fact, according to Chapter 2, Section 1.5.1, for one-electron transfers it holds that:

$$K_{\text{com}} = 10^{(F \cdot \Delta E^\circ / 2.303 R T)}$$

*Indeed, it has been shown²⁶ that in addition to the delocalization factor, there are several other contributions to the magnitude of K_{com} such as structural, electrostatic, inductive and magnetic factors; so one must be cautious in attributing electrochemically calculated K_{com} values only to charge delocalization.

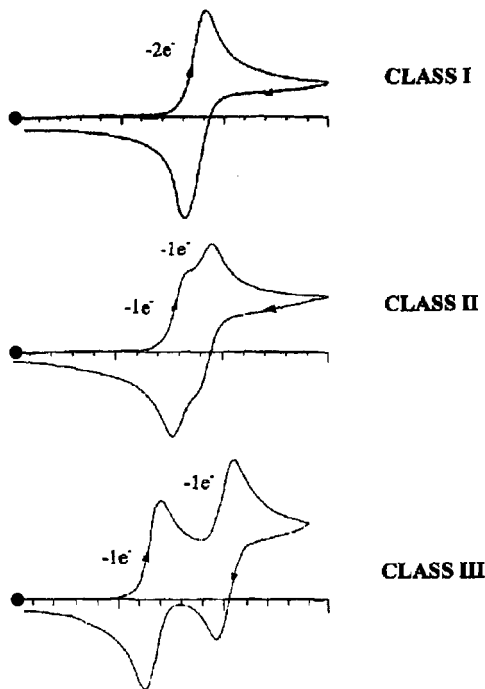


Figure 15 Schematic representation of the cyclic voltammetric responses expected from biferrocenes, depending upon the extent of electronic delocalization

So that, at 25 °C:

$$K_{\text{com}} = 10^{(38.92 \cdot \Delta E^\circ / 2.303)} = 10^{(16.90 \cdot \Delta E^\circ)}$$

where ΔE° must be expressed in volts.

In this connection, it is commonly agreed that when:

- $K_{\text{com}} < 4$, the compound belongs to Class I
- $K_{\text{com}} > 10^6$, the compound belongs to Class III

Nevertheless, since such limits are not exactly defined, it is routinely accepted²⁵ that:

- $K_{\text{com}} < 10^2$, the compound belongs to Class I
- $10^2 < K_{\text{com}} < 10^6$, the compound belongs to Class II
- $K_{\text{com}} > 10^6$, the compound belongs to Class III

For the response illustrated in Figure 12, in which the difference between the two redox potentials is $\Delta E^\circ = 0.34$ V, one can calculate that $K_{\text{com}} \approx 10^5 - 10^6$. This value is typical of a mixed-valent compound which, on the electrochemical time scale, is at the border between

partially and completely delocalized. It is important, however, to keep in mind that other physico-chemical techniques with very different time scales can lead to quite different conclusions.

In support of the electrochemical evidence, the molecular structure of the bisferrocenium ion in $[(\eta^5\text{-C}_5\text{H}_5)\text{Fe}(\eta^5\text{-C}_5\text{H}_4)(\eta^5\text{-C}_5\text{H}_4)\text{Fe}(\eta^5\text{-C}_5\text{H}_5)]^{+}$ $[\text{I}_3]^{-}$ shows that both pairs of cyclopentadienyl rings have an eclipsed conformation, Figure 16. Furthermore, the mean $\text{Fe}-\text{Cp}_{(\text{centroid})}$ distance is equivalent in both the ferrocenyl units and equal to 1.68 Å. Speculatively, this value is intermediate between the values previously observed for ferrocene and ferrocenium ions, thus supporting charge delocalization between the two centres.²⁷

If allowance is made to neglect the occurrence of crystal packing effects, this would mean that the direct C–C bond between the two ferrocenyl subunits allows a high electronic interaction between the two iron centres.

We consider now the bis(ferrocenyl) molecule in which the two ferrocenyl subunits are separated by a methylene group, namely diferrocenylmethane. The molecular structure of this molecule is known. The two ferrocenyl subunits occupy two positions of the tetrahedral coordination of the bridging methylene carbon atom. In each ferrocenyl group, the cyclopentadienyl rings assume an eclipsed disposition.²⁸

Figure 17 shows the cyclic voltammetric response exhibited by diferrocenylmethane in dichloromethane solution.²⁸

Two successive, closely spaced oxidation processes are observed. By exhaustive electrolysis, the overall process proves to be a chemically reversible two-electron process. The separation of the two processes

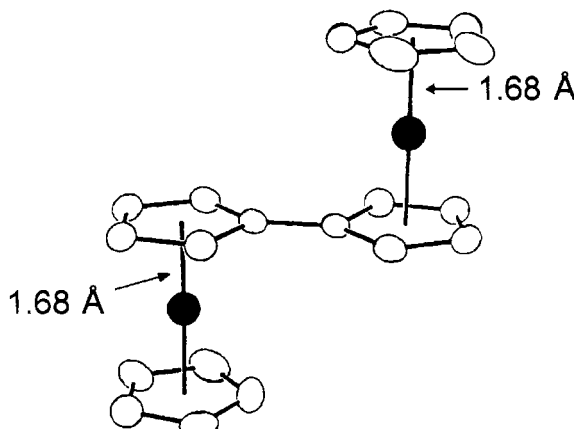


Figure 16 X-Ray structure of the bisferrocenium ion $[(\eta^5\text{-C}_5\text{H}_5)\text{Fe}(\eta^5\text{-C}_5\text{H}_4)(\eta^5\text{-C}_5\text{H}_4)\text{Fe}(\eta^5\text{-C}_5\text{H}_5)]^{+}$ ($[\text{I}_3]^{-}$ counteranion)

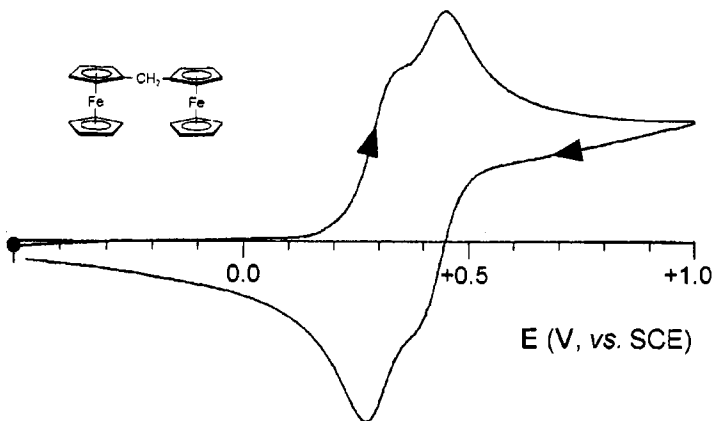


Figure 17 Cyclic voltammogram recorded at a platinum electrode in a CH_2Cl_2 solution of diferrocenylmethane. Supporting electrolyte: $[\text{NBu}_4][\text{PF}_6]$ (0.2 mol dm^{-3}). Scan rate 0.1 V s^{-1}

($\Delta E^{\circ'} = 120 \text{ mV}$) allows a K_{com} of about 10^2 to be calculated. Therefore, the corresponding monocation should be classified as a Class I/II mixed-valent derivative, in which the two ferrocene groups are substantially non-communicating.

It is, however, useful to note that changing the nature of the single atom interposed between the two ferrocenyls can vary the nature of the corresponding mixed-valent congener. As an example, Figure 18 shows the molecular structure²⁹ and the electrochemical behaviour of diferrocenyolphosphine.³⁰

As seen, apart from a minor adsorption process (at about 0.4 V), with respect to diferrocenylmethane, the two successive one-electron oxidations are notably more separate ($\Delta E^{\circ'} = 250 \text{ mV}$). In fact, a K_{com} of 1.7×10^4 can be calculated, thus classifying the corresponding monocation as a partially delocalized Class II derivative.

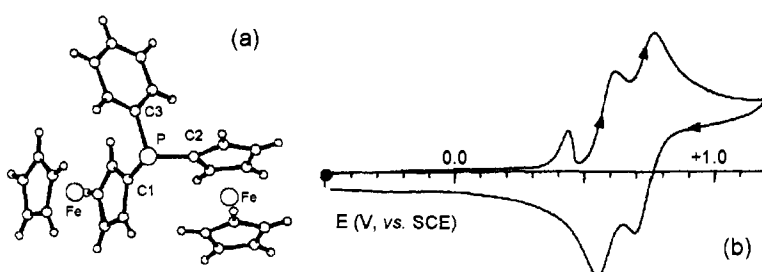


Figure 18 (a) X-Ray structure of $[\text{P}(\text{C}_6\text{H}_5)\{(\eta^5\text{-C}_5\text{H}_4)\text{Fe}(\eta^5\text{-C}_5\text{H}_5)\}_2]$ ($\text{P-C1} = 1.82 \text{ \AA}$; $\text{P-C2} = 1.81 \text{ \AA}$; $\text{P-C3} = 1.84 \text{ \AA}$) and (b) relative cyclic voltammetric profile (CH_2Cl_2 solution; scan rate 0.2 V s^{-1})

Finally, a molecule in which the two ferrocenyl subunits are separated by a C_2H_4 bridge is considered, namely 1,2-bis(ferrocenyl)ethane. Its X-ray structure shows that the mean $Fe-Cp_{(centroid)}$ distance in both the ferrocenyl subunits is 1.67 Å and the cyclopentadienyl rings are slightly rotated (8.5°) with respect to the eclipsed conformation.³¹

As illustrated in Figure 19, the compound displays in CH_2Cl_2 solution a single oxidation process (the small return peak marked by an asterisk is due to a slight adsorption of the oxidation product at the electrode surface). Controlled potential electrolysis shows that such an oxidation is chemically reversible and involves a two-electron step.²⁸

The appearance of a single two-electron oxidation indicates that the C_2H_4 spacer does not permit any electronic communication between the two ferrocenyl sites.

However, also in this case one must keep in mind that changing the nature of the two-atom bridging system can change the extent of the electronic communication. For example, the substitution of the saturated dicarbon chain for unsaturated ethene or ethyne units restores a certain degree of electronic interaction between the two outer ferrocenyls. In fact both diferrocenylethene and diferrocenylethyne exhibit, in dichloromethane solution, two slightly separated one-electron oxidations.^{28,32}

In conclusion, as summarized in Table 8, limiting our attention to ferrocenyl-interposed saturated carbon chains, as the carbon chain

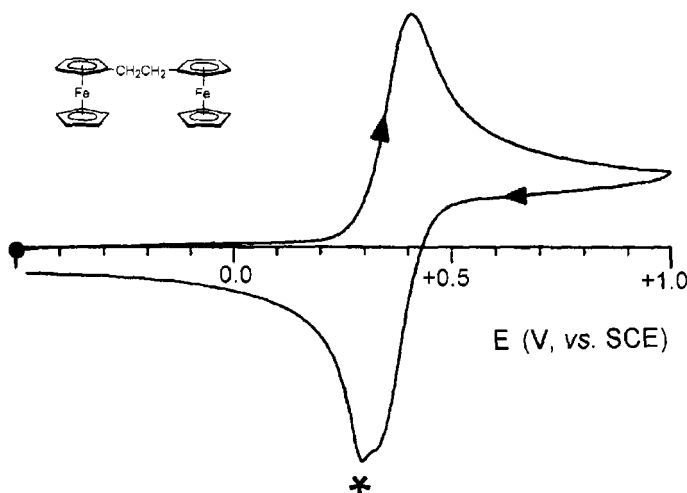


Figure 19 Cyclic voltammogram recorded at a platinum electrode in a CH_2Cl_2 solution of $[(\eta^5-C_5H_5)Fe(\eta^5-C_5H_4)CH_2CH_2(\eta^5-C_5H_4)Fe(\eta^5-C_5H_5)]$. Supporting electrolyte: $[NBu_4][PF_6]$ 0.2 mol dm^{-3} . Scan rate 0.2 V s^{-1}

Table 8 Formal electrode potentials (*V*, vs. SCE), and relative separation (*V*), for the two one-electron oxidations of a few diferrocenyl molecules

Complex	$E_{0/+}^{\circ'}$	$E_{+/2+}^{\circ'}$	$\Delta E^{\circ'}$	Solvent
biferrocene	+0.31	+0.65	0.34	MeCN-CH ₂ Cl ₂
diferrocenylmethane	+0.30	+0.42	0.12	CH ₂ Cl ₂
diferrocenylethane	+0.35	+0.35	0.00	CH ₂ Cl ₂
diferrocenylethene	+0.31	+0.47	0.16	CH ₂ Cl ₂
diferrocenylethyne	+0.61	+0.75	0.14	CH ₂ Cl ₂

become longer, the difference of potential between the two oxidation processes tends to zero. This reflects the growing difficulty of electronic communication between the ferrocenyl subunits as the bridge becomes longer. Nevertheless, conjugated unsaturated carbon/carbon bonds tend to attenuate such barrier effects.

Derivatives which have more than two ferrocenyl subunits exhibit a qualitatively similar behaviour, but their responses can appear more varied.

For example, in triferrrocene compounds one can obtain three distinct one-electron oxidation processes provided that all the three subunits are communicating with each other. This is the case for 1,1'-triferrrocene, which, as previously illustrated in Chapter 3, Figure 11, displays three consecutive oxidation processes (CH₂Cl₂-MeCN (1:1), {[NBu₄][PF₆] 0.1 mol dm⁻³}): $E_{0/+}^{\circ'} = -0.27$ V, $E_{+/2+}^{\circ'} = -0.05$ V, $E_{2+/3+}^{\circ'} = +0.36$ V, vs. Fc/Fc⁺^{22a}; CH₂Cl₂, {[NBu₄][B(C₆F₅)₄] 0.1 mol dm⁻³}: $E_{0/+}^{\circ''} = -0.23$ V, $E_{+/2+}^{\circ''} = +0.11$ V, $E_{2+/3+}^{\circ''} = +0.79$ V^{22b}.

On occasions one may observe only two oxidation processes, a one-electron and a two-electron event, respectively, if there is an electronic interaction between only two of the three sites. This is, for example, the case of the triferrrocene molecule in which selenium atoms bridge the three ferrocene units, Figure 20.³³

It is reasonable to assume that the first two-electron process result in the simultaneous oxidation of the two outer ferrocenyl units of the molecule (which are quite distant from each other, and hence not electrostatically interacting), whereas the second one-electron oxidation should be centred on the central ferrocenyl group (that can interact electrostatically with the now positively charged lateral subunits).

As Figure 21 shows, even closer are the two oxidations in triferrrocenylphosphate, [O=P{O(C₅H₄)Fe(C₅H₅)₃}₃]. The small spurious peak present at about +0.2 V in the reverse scan of the cyclic voltammogram is likely due to electrode adsorption phenomena, given the ascertained stability of the corresponding trication.³⁴

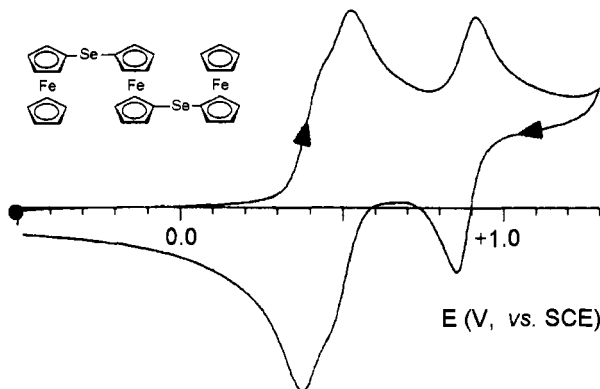


Figure 20 Cyclic voltammogram recorded at a platinum electrode in a CH_2Cl_2 solution of $(\text{C}_5\text{H}_5)\text{Fe}(\text{C}_5\text{H}_4)\text{Se}(\text{C}_5\text{H}_4)\text{Fe}(\text{C}_5\text{H}_4)\text{Se}(\text{C}_5\text{H}_4)\text{Fe}(\text{C}_5\text{H}_5)$. Supporting electrolyte: $[\text{NBu}_4][\text{ClO}_4]$ 0.2 mol dm^{-3} . Scan rate 0.2 V s^{-1}

Finally, one can also observe a single three-electron oxidation when there is no communication between the sites. For example, as illustrated in Figure 22, 1,3,5-tris(ethynylferrocenyl)benzene exhibits such behaviour.³⁵

In fact, this molecule displays a single three-electron process characterized by chemical reversibility (even if slight adsorption phenomena make the reverse peak slightly higher than the forward peak).

Therefore, one can infer that the central 1,3,5-triethynylbenzene fragment does not allow any electronic communication among the ferrocenyl groups. In fact, such a consideration is too simplistic and one must take into account that the ability of the fragment interposed between redox active centres to block the charge flow cannot be

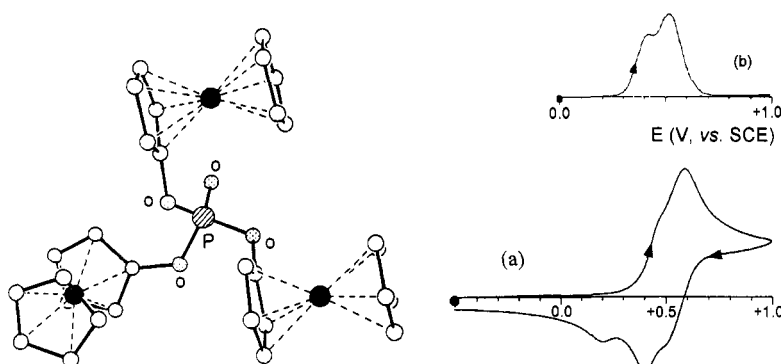


Figure 21 X-ray structure and voltammetric behaviour (in cyclic (a) and differential pulse (b) voltammetry) of $[O=P\{O(\text{C}_5\text{H}_4)\text{Fe}(\text{C}_5\text{H}_5)\}_3]$ in CH_2Cl_2 solution

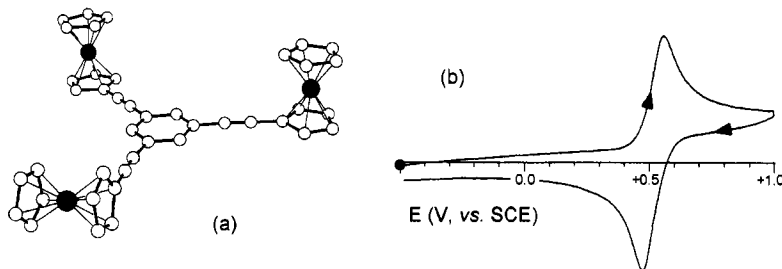


Figure 22 (a) X-Ray structure and (b) cyclic voltammogram in CH_2Cl_2 solution [platinum working electrode; $[\text{NBu}_4][\text{PF}_6]$ supporting electrolyte (0.2 mol dm^{-3}); scan rate 0.1 V s^{-1}] of $[1,3,5-\{\text{C}\equiv\text{CFe}(\eta^5-\text{C}_5\text{H}_4)(\eta^5-\text{C}_5\text{H}_5)\}_3\text{C}_6\text{H}_3]$

rigorously determined, as it also depends on the nature of the terminal metal fragments. This is further demonstrated in Figure 23, which reports the electrochemical responses of the related Ru(II) complex $[1,3,5-\{\text{C}\equiv\text{CRu}(\eta\text{-C}_5\text{H}_5)(\text{PPh}_3)_2\}_3\text{C}_6\text{H}_3]$.

As seen, in spite of the presence of the central triethynyl fragment, in this case the three successive Ru(II)/Ru(III) oxidations show some degree of separation, indicating the presence of an electronic communication (even if minimal) among the three metal centres.³⁶

Finally, to prove how in some cases the mutual interactions among ferrocene units in multiferrocenes can be difficult to predict, consider

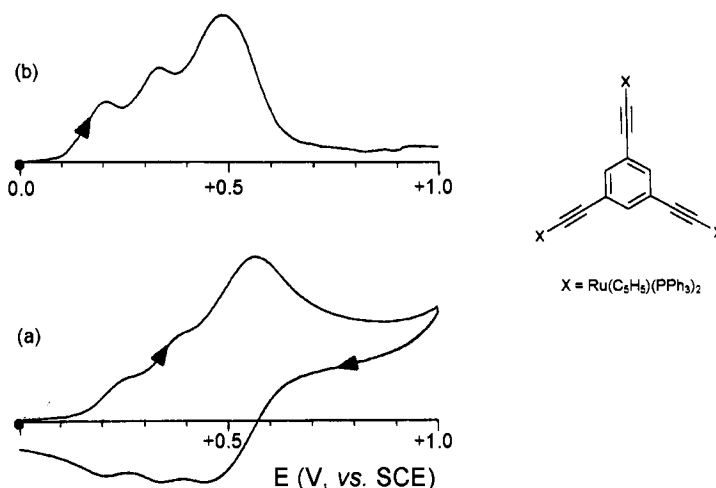


Figure 23 Cyclic and differential pulse voltammograms recorded at a platinum electrode in a CH_2Cl_2 solution of $[1,3,5-\{\text{C}\equiv\text{CRu}(\eta\text{-C}_5\text{H}_5)(\text{PPh}_3)_2\}_3\text{C}_6\text{H}_3]$. Supporting electrolyte $[\text{NBu}_4][\text{PF}_6]$ (0.2 mol dm^{-3}). Scan rates: (a) 0.2 V s^{-1} ; (b) 0.004 V s^{-1}

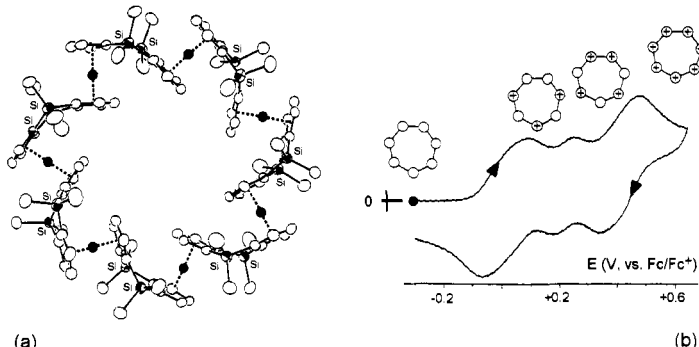


Figure 24 (a) X-Ray structure ($Fe-Cp_{(centroid)} = 1.66 \text{ \AA}$; $Fe - - - Fe \approx 5.72 \text{ \AA}$) and (b) cyclic voltammetric behaviour ($CH_2Cl_2/MeCN$ (1:1) solution; platinum electrode) of Fe_7L

the Fe_7L complex (L = tetrahydro-4,4,8,8-tetramethyl-4,8-disila-*s*-indacenediyl), which contains seven ferrocene units linked by seven pairs of Me_2Si groups according to a regular cyclic shape. As Figure 24 illustrates, the complex exhibits three subsequent oxidations each involving (according to simulation procedure) the concomitant removal of three, one, three electrons, respectively.³⁷ The appearance of the intermediate one-electron oxidation is due to the odd number of ferrocene units, which prevents the regular removal of electrons from alternate sites which may occur, as we will see in the following section, in multiferenes containing an even number of ferrocene subunits.

1.4 Ferrocene Polymers

Recently, the preparation and characterization of polymers containing transition metal fragments as monomeric building blocks has aroused interest in the possibility that such materials might exhibit unusual electrical, optical, magnetic and redox properties.³⁸ Amongst these derivatives, polymers containing ferrocene units are acquiring importance.

1.4.1 Ferrocene-based Linear Polymers. The first derivative that was studied from the electrochemical point of view was polyvinylferrocene (PVF). As illustrated in Figure 25, it displays a single oxidation process, which in some solvents is affected by problems of adsorption of the oxidation product (though not of the ideal *Langmuir isotherm* type discussed in Chapter 2, Section 1.6).

The process is shown to involve the removal of one electron for each ferrocenyl subunits in that the number of electrons consumed in controlled potential electrolysis (n_{app}) is essentially equal to the degree

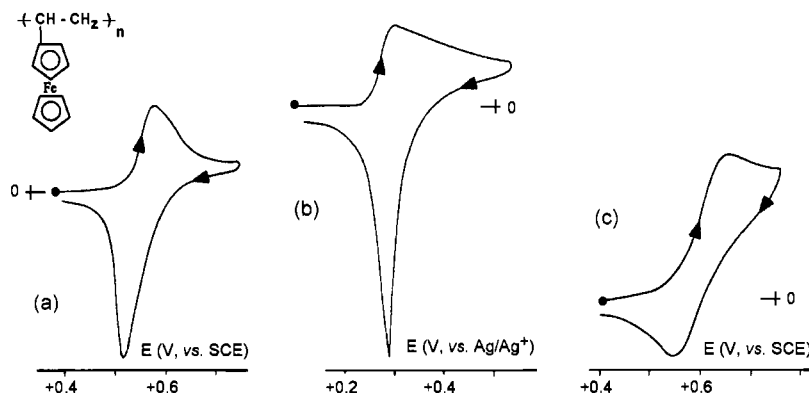


Figure 25 Cyclic voltammograms recorded in solutions of PVF in: (a) CH_2Cl_2 ; (b) thf; (c) hmpa (hexamethylphosphoramide)

of polymerisation (DP). These results and the relative oxidation potentials are reported in Table 9.

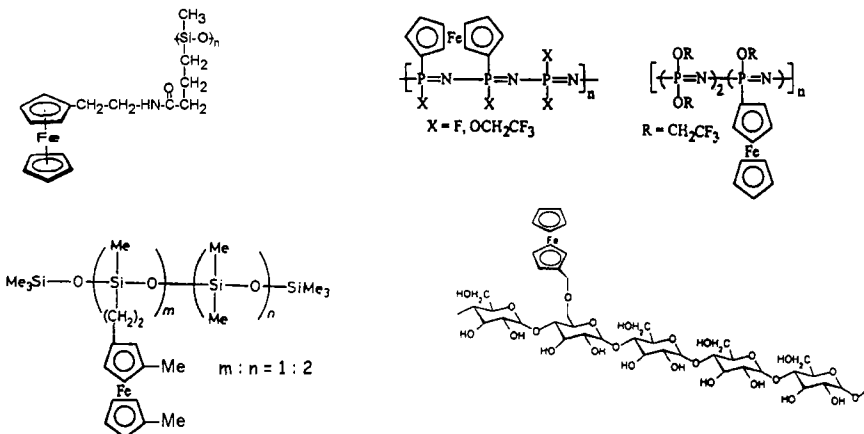
The oxidation potential of the polymer is not very different from that of the vinylferrocene monomer, which in turn is not very different from that of ferrocene.

It is important to note that the appearance of a single oxidation process for PVF indicates that there is no interaction between the ferrocene subunits in the polymer chain, which means that the carbon chain creates a barrier blocking the electronic communication between the ferrocenyl groups.

This kind of electronic situation is rather common in ferrocene polymers. In fact, it has been found also in the polymers represented in Scheme 1.

Table 9 Oxidation potential (V , vs. SCE) for the system $\text{PVF}/[\text{PVF}]^+$ in various solvents

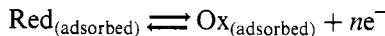
Complex		$E_{0/+}^\circ$	Solvent	n_{app}	DP	Reference
PVF	molecular weight 4930	+ 0.55	CH_2Cl_2			39
		+ 0.62	hmpa			39
		+ 0.46	thf	21	23.2	40
	15750	+ 0.54	hmpa			39
		+ 0.48	thf	75	74.3	40
		+ 0.56	thf			40
vinylferrocene		+ 0.43	CH_2Cl_2			
		+ 0.55	thf			
ferrocene		+ 0.45	CH_2Cl_2			
		+ 0.58	hmpa			39



Scheme 1

As far as the electrode adsorption phenomena caused by polyferrocenes are concerned, Figure 26 shows the cyclic voltammetric response of the illustrated fluorenyl-ferrocene polymer ($F_w \approx 7000$).⁴¹

As seen, it affords a single oxidation process the cyclic voltammetric profile of which is very close to that expected for the mechanism:



In fact, the parameter i_p/v remains constant with the scan rate (see Chapter 2, Section 1.6).

Recently, however, polyferrocenes have been found which display a different electrochemical behaviour. For example, Figure 27 shows the cyclic voltammetric response of poly(*tert*-butylferrocenyl)persulfide.

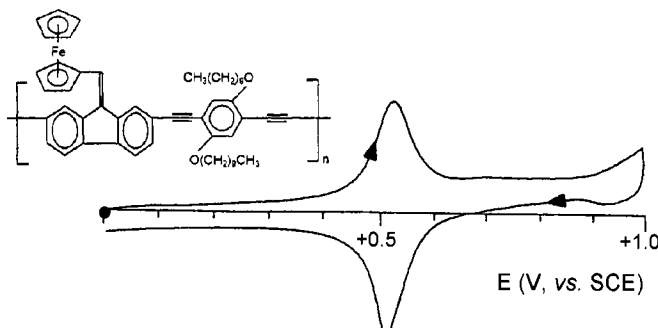


Figure 26 Cyclic voltammogram of the (schematized) polyfluorenylferrocene in CH_2Cl_2 solution. Scan rate 0.2 V s^{-1}

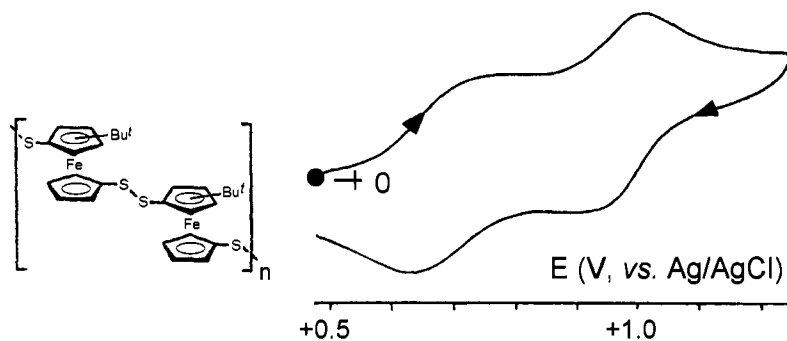
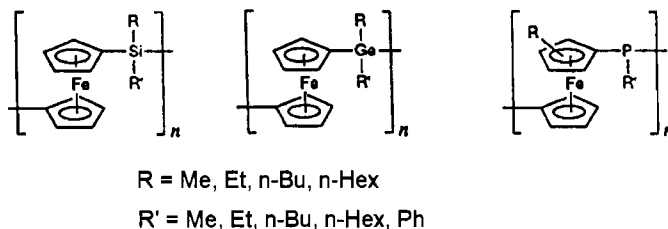


Figure 27 Cyclic voltammogram recorded in a CH_2Cl_2 solution of poly(tert-butylferrocenyl)persulfide

Two oxidation processes appear ($E_{0/+}^{\circ} = +0.66$ V; $E_{+/2+}^{\circ} = +0.96$ V).⁴²

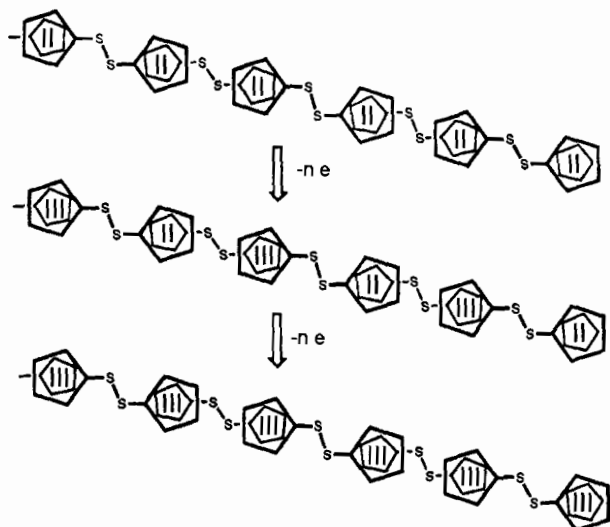
A similar behaviour has been found for the polymers illustrated in Scheme 2.⁴³



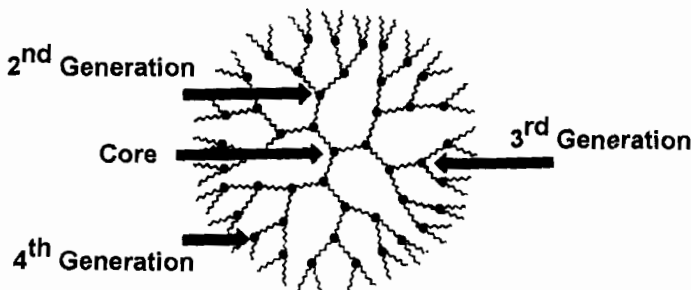
Scheme 2

The appearance of two separate oxidation processes in these polymers is attributed to the existence of electronic communication between the ferrocene units, so that the first oxidation is centred on alternating ferrocene sites, whereas the second oxidation is centred on the remaining sites. For example, for polyferrocenyl-persulfide, the electron removal path reported in Scheme 3 has been proposed (the oxidation state of the iron atoms is represented).⁴²

1.4.2 Ferrocene-based Branched Polymers (Dendrimers). One of the topics in macromolecular chemistry is constituted by *dendrimers*, or hyperbranched macromolecules of tridimensional globular structure, the surface of which is characterized by a large number of functional groups, Scheme 4. Such functionalities impart to the molecules solubility, viscosity and thermal properties different from those of the common linear polymers.^{38c,d,44}



Scheme 3



Scheme 4

As shown, starting from the central nucleus, each subsequent bifurcation leads to the dendrimer being classified as *1st generation*, *2nd generation*, *3rd generation*, and so on.

Organometallic chemistry, in particular the chemistry of ferrocenes, is affording significant contributions to the field. As illustrated in Figure 28, ferrocene-based dendrimers can assume compositions ranging from a single ferrocene unit properly functionalized⁴⁵ to multiferrocene units placed in the outer zone of the surface.⁴⁶

Let us discuss the electrochemical behaviour of these types of ferrocene complexes, starting with the monoferrocenyl derivative illustrated in Scheme 5.

As expected, it shows in dichloromethane solution a quasireversible one-electron oxidation ($E^{\circ'} = +0.54$ V, vs. Ag/AgCl).⁴⁷

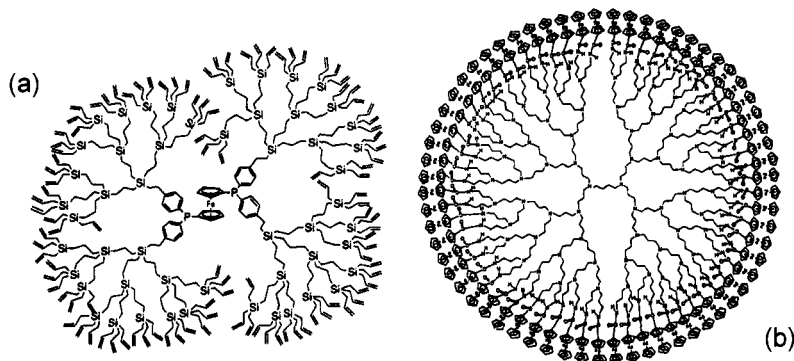
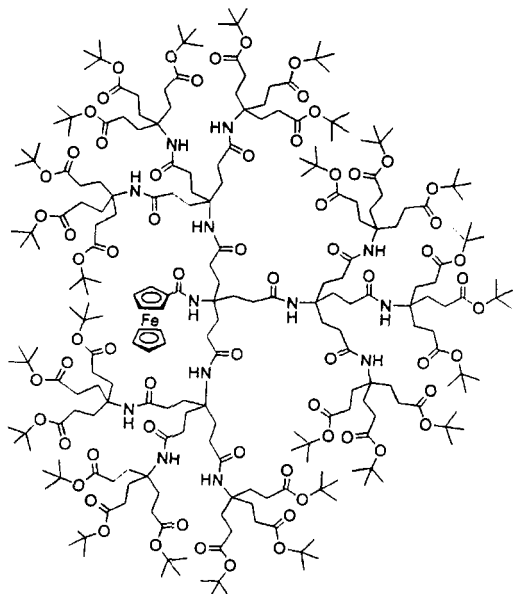


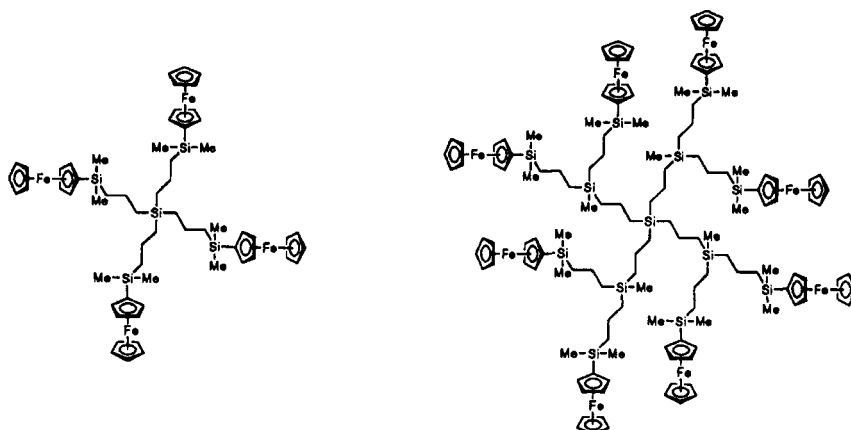
Figure 28 A schematic representation of the possible composition of ferrocene-based dendrimers. (a) Dendrimers containing a single ferrocene unit; (b) dendrimers containing multiple ferrocene units

The dendrimers containing more ferrocene units are more interesting from the electrochemical viewpoint. Scheme 6 shows the 1st and 2nd generation members of a silicon-centred series containing four and eight ferrocenyl units, respectively.⁴⁸

Both the complexes display, in dichloromethane solution, a single oxidation process which involves four ($E^{\circ'} = +0.40$ V, *vs.* SCE) and eight ($E^{\circ'} = +0.44$ V, *vs.* SCE) electrons, respectively. This means that no electronic communication exists among the ferrocenyl units.



Scheme 5



Scheme 6

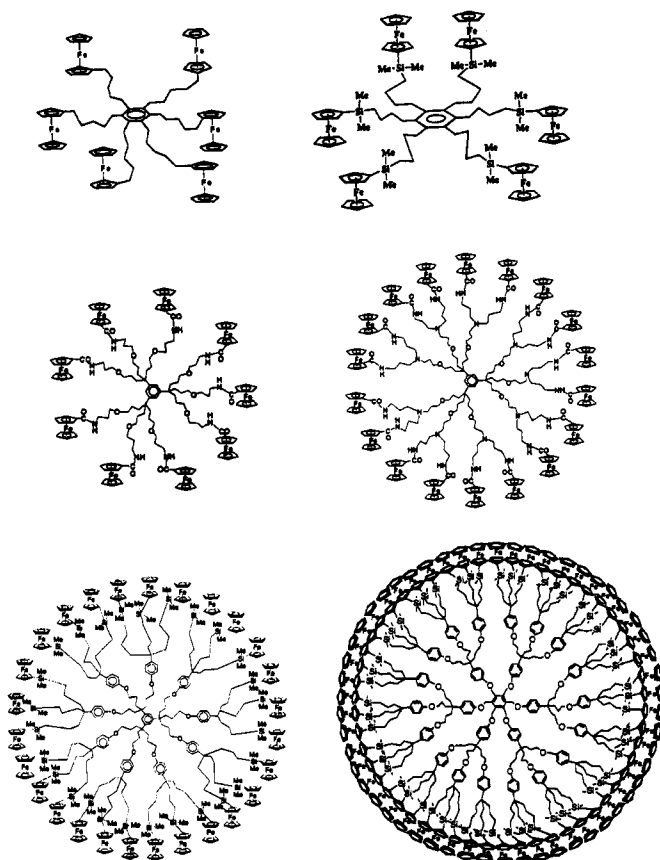
The appearance of a single multielectron oxidation is a quite common response for most ferrocene dendrimers. For instance, all the derivatives shown in Scheme 7, which contain 5, 6, 9, 18, 27, 54, as well as similar derivatives containing 81 and 243 ferrocene subunits, respectively,^{45, 49–53} display such behaviour.

In this connection, Figure 29 shows the cyclic voltammetric response of the 4th generation 64-Fc dendrimer.⁴⁵

It exhibits a single oxidation process ($E^{\circ'} = +0.59$ V, *vs.* SCE) affected by some adsorption problems. These adsorption phenomena, which typically affect the electrochemical response of these derivatives, sometimes make it difficult to ascertain by controlled potential coulometry the effective number of electrons involved in the oxidation step. In this case, the (approximate) number of electrons involved per molecule of dendrimer, n_d , can be roughly calculated by comparing the cyclic voltammetric responses of the dendrimer with that of the ferrocene monomer using the following empirical equation.^{27,40}

$$n_d = \frac{\frac{i_{p(d)}}{C_{(d)}}}{\frac{i_{p(m)}}{C_{(m)}}} \cdot \left(\frac{MW_{(d)}}{MW_{(m)}} \right)^{0.275}$$

where $i_{p(d)}$, $i_{p(m)}$ are the peak currents for the oxidation of the dendrimer and monomer, respectively (obviously recorded at the same scan rate), $C_{(d)}$, $C_{(m)}$ are the concentrations of the dendrimer and monomer, respectively, $MW_{(d)}$, $MW_{(m)}$ are the molecular weights of the dendrimer and monomer, respectively.



Scheme 7

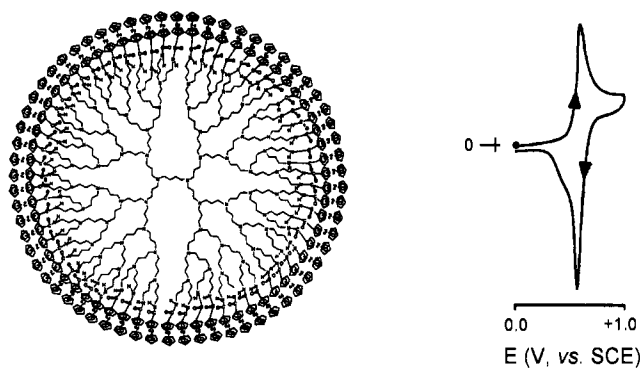
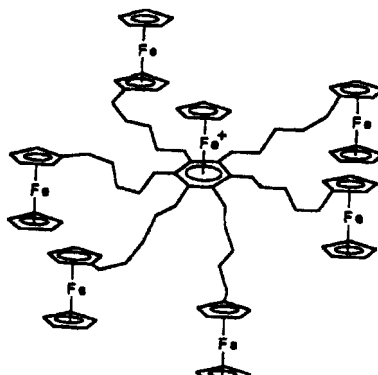


Figure 29 Cyclic voltammogram recorded at a platinum electrode in a CH_2Cl_2 solution of the illustrated 64Fc dendrimer. Scan rate 0.1 V s^{-1}

Obviously the determination of n_d can be of help in the synthetic path. It is interesting to note that the substitution of the central benzene ring in dendrimers of the type illustrated in Scheme 7 for a $[\text{Fe}(\eta^5\text{-C}_5\text{H}_5)(\eta^6\text{-C}_6\text{R}_6)]^+$ group affords dendrimers of the type illustrated in Scheme 8.⁴⁹



Scheme 8

This complex exhibits in DMF solution a one-electron reduction ($E^{\circ'} = -1.60 \text{ V vs. SCE}$) which is centred on the central $[\text{Fe}(\eta^5\text{-C}_5\text{H}_5)(\eta^6\text{-C}_6\text{R}_6)]^+$ core, as well as a single six-electron oxidation ($E^{\circ'} = +0.44 \text{ V}$), which is centred on the outer, not-interacting ferrocenyl groups.

In this connection it is useful to look at the voltammetric response of the dendrimer illustrated in Figure 30, which is constituted by a central ferrocene core branched to ten outer ferrocenyl units.⁵⁴

It exhibits a first, inner-ferrocene-centred one-electron oxidation (peak-system A/D; $E^{\circ'} = -0.10 \text{ V vs. Ag/AgCl}$) followed by the

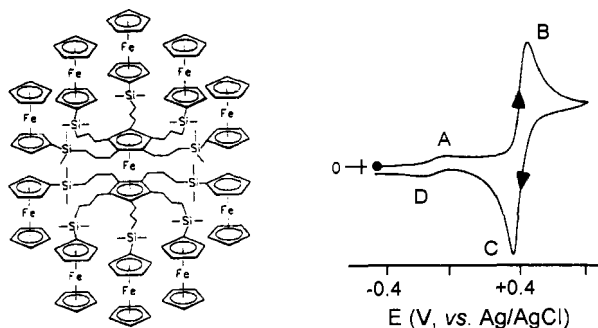


Figure 30 Cyclic voltammogram recorded at a gold electrode in a CH_2Cl_2 solution of the dendrimer shown. Scan rate 0.05 V s^{-1}

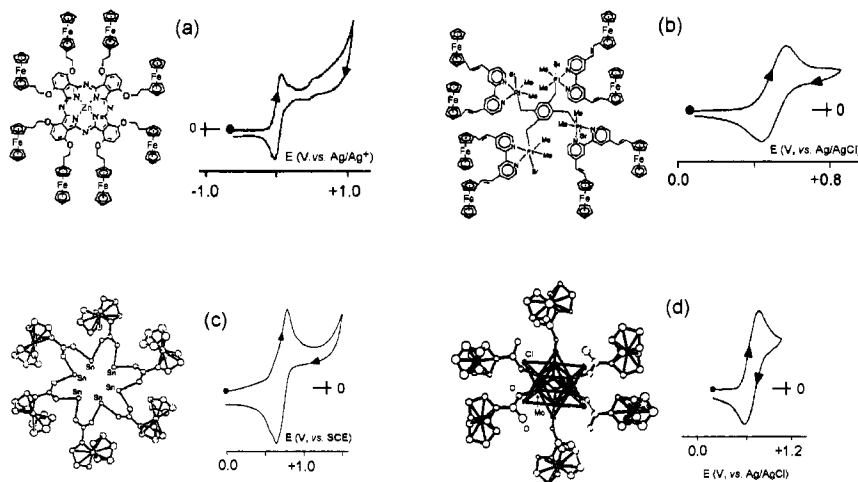


Figure 31 Cyclic voltammograms recorded at a platinum electrode in: (a) $[1,4,8,11,15,18,22,25\text{-}\{2\text{-}(\eta^5\text{-}C_5H_4CH_2CH_2O)\text{Fe}(\eta^5\text{-}C_5H_5)\}_8ZnPc]$ (Pc = phthalocyaninato) (dmf solution); (b) $\{\text{PtMe}_2\text{Br}(4,4\text{-}(\eta^5\text{-}C_5H_4CH=CH)\text{Fe}(\eta^5\text{-}C_5H_5)\}_2\text{CH}_2\}_4(1,2,4,5\text{-}C_6H_2)$ (MeCN solution); (c) $\{\text{BuSn}(O)\text{OC}(O)(\eta^5\text{-}C_5H_4)\text{Fe}(\eta^5\text{-}C_5H_5)\}_6$ (CH_2Cl_2 solution); (d) $[\text{Mo}_6\text{Cl}_8\{\text{(}\eta^5\text{-}C_5H_4\text{CO(O)}\text{Fe}(\eta^5\text{-}C_5H_5)\text{)}\}_6]^{2-}$ (DMF solution)

external-ferrocene-centred ten-electron oxidation (peak-system B/C; $E^\circ' = +0.40$ V), thus supporting the electronic non-equivalence of the central and the outer ferrocene units.

It must be taken into account that there are dendrimers in which the central core is constituted by metallic assemblies.^{38d} This is the case for example of the multiferrocene assemblies illustrated in Figure 31, which bear a phthalocyaninato-zinc, a tetraplatinum, a hexatin, or a hexamolybdenum central core, respectively.⁵⁵⁻⁵⁸

As seen, these complexes also exhibit a single oxidation process involving a number of electrons equal to the number of ferrocene units.

Interesting from the electrochemical viewpoint is the heterobimetallic ferrocene-cobaltocenium dendrimer whose electrochemical response is shown in Figure 32.⁵⁹

As seen the complex displays either a single ferrocenyl-centred oxidation (which however looks like it is partially chemically reversible) or a single cobaltocenium-centred reduction (which is affected by electrode adsorption), thus testifying that no interaction exists among the different metallocene units.

Finally, as discussed for linear polyferrocenes, dendrimers displaying more than a single multielectron oxidation have been found. This is the case of the complexes illustrated in Scheme 9.⁶⁰

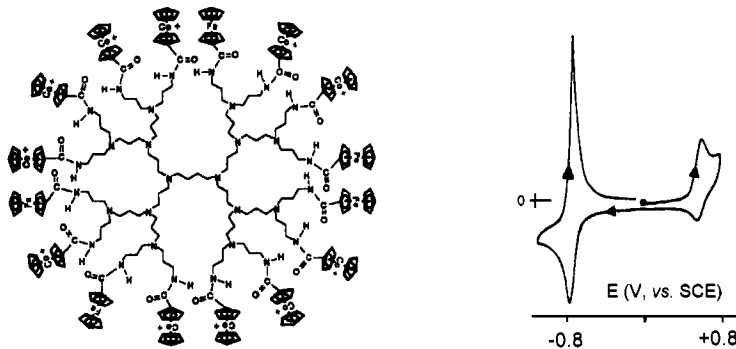
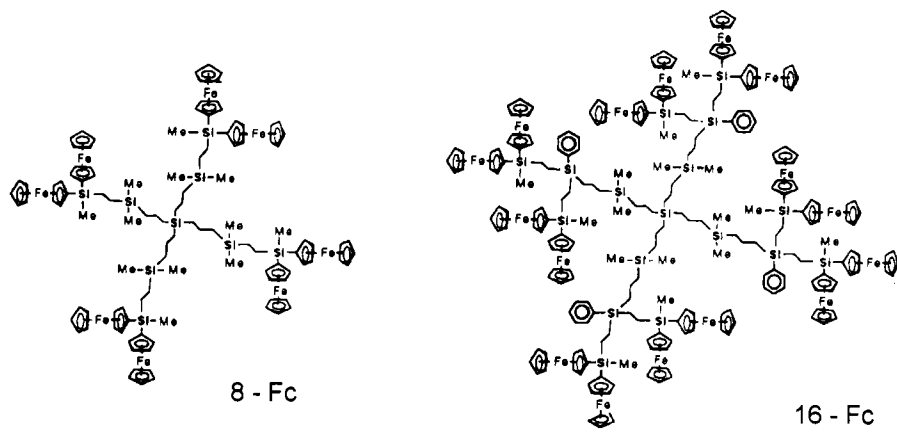


Figure 32 Cyclic voltammogram recorded at a glassy carbon electrode in a MeCN solution of the 16-metallocene complex illustrated in the scheme. Scan rate 0.1 V s^{-1}



Scheme 9

Figure 33 shows the cyclic voltammetric response of the 8-Fc derivative. It gives rise to two separate reversible oxidations (each one involving four electrons) separated by 0.19 V. This means that the overall oxidation proceeds through two separated steps each one involving four alternate ferrocene units.

The 16-Fc derivative displays a similar behaviour ($\Delta E^{\circ\prime} = 0.16 \text{ V}$). Such an electronic situation arises from the presence in each tentacle of the diferrocyne unit illustrated in Scheme 10, which displays two separated one-electron oxidations ($E_{0/+}^{\circ\prime} = +0.45 \text{ V}$; $E_{+/2+}^{\circ\prime} = +0.63 \text{ V}$), typical of communicating diferrocenies.

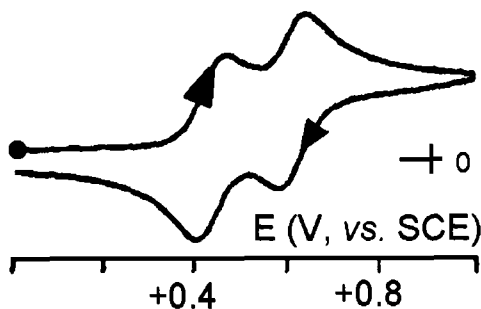
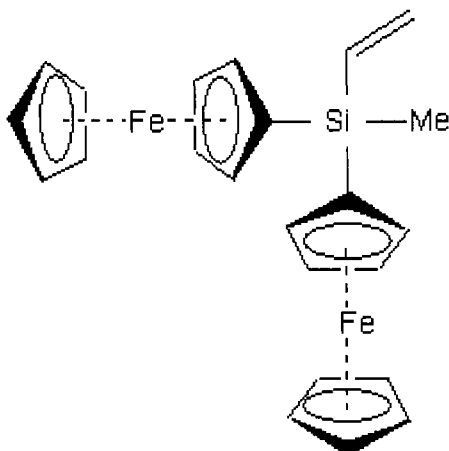


Figure 33 Cyclic voltammogram recorded at a platinum electrode in a $\text{CH}_2\text{Cl}_2/\text{MeCN}$ (5:1) solution of the 8-Fc complex illustrated in Scheme 9. Scan rate 0.05 V s^{-1}



Scheme 10

1.5 Recent Applications of Ferrocenes

There have been two major recent uses of ferrocene molecules:

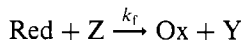
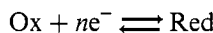
- electrochemical sensors
- materials for non-linear optics

1.5.1 Ferrocenes as Electrochemical sensors. The field of *sensing* molecules of interest in environmental pollution or biomedicine is rapidly growing. As far as *electrochemical sensors* are concerned their use is based on two different ways to gain information:

- amperometric sensors
- potentiometric sensors

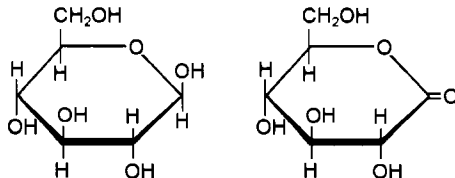
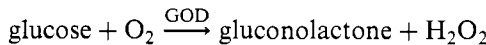
As easily conceivable, from a qualitative viewpoint the former exploit the generation of abnormally great currents, whereas the latter are based on the inducement of potential shifts caused by variation of the environment around the redox-active species.

As far as the use of ferrocene molecules as amperometric sensors is concerned, they have found wide use as redox mediators in the so-called enzymatic electrodes, or biosensors. These are systems able to determine, in a simple and rapid way, the concentration of substances of clinical and physiological interest. The methodology exploits the fact that, in the presence of enzyme-catalysed reactions, the electrode currents are considerably amplified.⁶¹ Essentially it is an application of the mechanism of ‘catalytic regeneration of the reagent following a reversible charge transfer’, examined in detail in Chapter 2, Section 1.4.2.5:



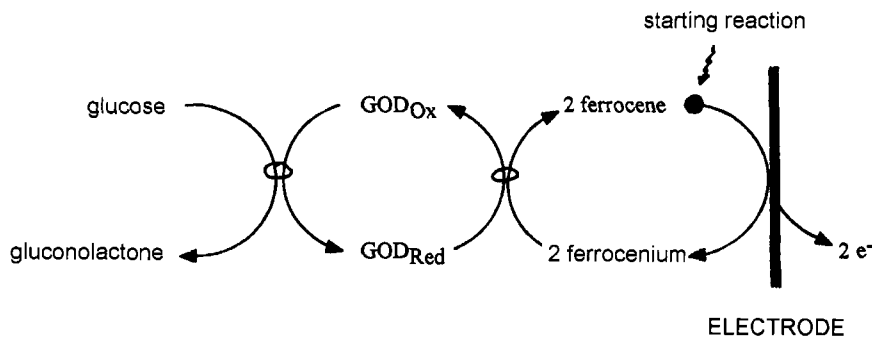
We will illustrate herein the basis underlying one of the prime applications of this technique: the dosage of small concentrations of glucose in the blood. This is of considerable use to people affected by diabetes,⁶¹ who have levels of glucose in the blood of the order 1–30 mM.

One of the best known enzymatic reactions involving glucose is the following oxidation reaction catalysed by glucose oxidase (GOD):



Historically, the first dosage of glucose in the blood was just based on this reaction (by titration of the generated hydrogen peroxide).

When one substitutes molecular oxygen for an electrogenerated ferrocenium [Fe(III)] ion, the catalytic reaction produces the corresponding ferrocene [Fe(II)] (rather than hydrogen peroxide), which in turn is re-oxidized at the electrode, thus triggering the glucose → gluconolactone conversion according to the catalytic mechanism illustrated in Scheme 11.



Scheme 11

In this connection, Figure 34 shows the cyclic voltammogram of an aqueous solution of ferrocencarboxylic acid and glucose before (a) and after (b) the addition of glucose oxidase.⁶²

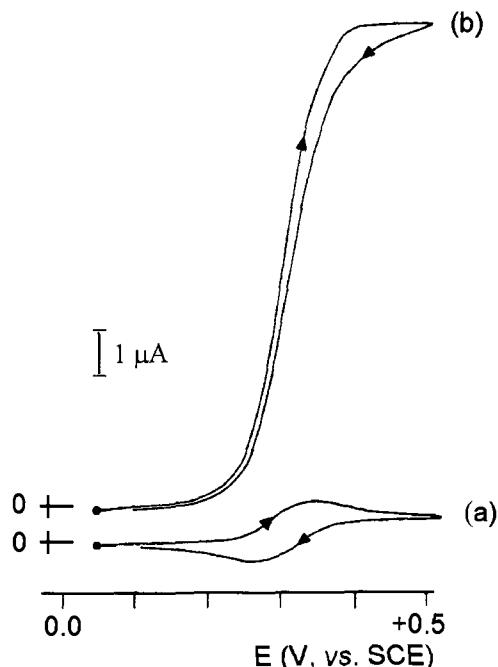


Figure 34 Cyclic voltammograms recorded at a pyrolytic graphite electrode in an aqueous solution ($pH\ 7$) containing: (a) $[(\eta^5-C_5H_5)Fe(\eta^5-C_5H_4COOH)]$ ($0.5\ \mu M$) and D-glucose ($50\ \mu M$); (b) after the addition of glucose oxidase ($10.9\ \mu M$). Scan rate $0.001\ Vs^{-1}$

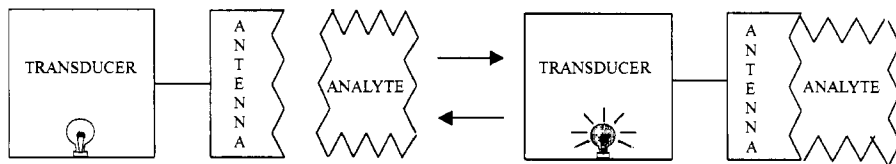
The presence of the enzyme produces a catalytic oxidation of the ferrocenyl molecule giving rise to an S-like curve with fairly high currents, which is typical of 'catalytic regeneration of the reagent'. It is noted that an extremely slow scan rate is employed (1 mV s^{-1}) in order to allow the catalytic reaction following the electron transfer to run to completion.

Attempts have been performed to analyse (in terms of rate constants) the steric-to-electrochemical factors which can influence the interaction of ferrocenium derivatives with reduced GOD, or the ability of ferrocenes to act as mediators in the enzymatic oxidation of glucose as a function of cyclopentadienyl substituents.⁶³

For diagnostic purposes, both the ferrocene derivative and the enzyme are immobilized on the electrode surface, by appropriate chemical pretreatment. To determine the concentration of the glucose present in the physiological liquid of interest it is not necessary to carry out the cyclic voltammogram; knowing and applying the potential at which the limiting current takes place, one simply reads the corresponding current. From it, through a preliminary calibration curve (*limiting current/glucose concentration*), the glucose concentration is immediately found.

Enormous progress is being made in the development of amperometric sensors, based on enzyme catalysed reactions, in widely varying clinical and immunological diagnostic methods.

As far as the use of ferrocene molecules as potentiometric sensors is concerned, they are part of the more general reactivity pattern illustrated in Scheme 12.



Scheme 12

A sensing molecule must contain a transducer unit linked to an antenna group. The transducer is any chemical fragment possessing easily detectable physical properties (UV, NMR, EPR, mass spectroscopy, electrochemical or magnetic activity, *etc.*). The antenna part is a chemical fragment able to recognize selectively and link (in any way) to the species to be detected, thus causing a variation in the physical properties of the transducer.

The principle is illustrated in Figure 35 for a ferrocene molecule able to detect cationic species.

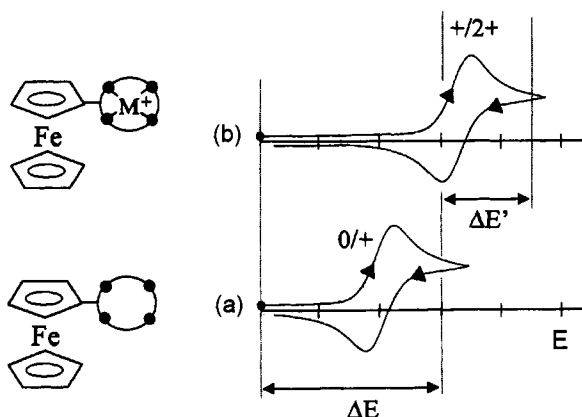


Figure 35 Cyclic voltammetric response of a ferrocene molecule: (a) initial; (b) after cation complexation

Let us suppose we have a ferrocene molecule bearing a peripheral functional group able to complex a cationic species. The one-electron oxidation of the ferrocene complex, Figure 35b, undergoes an anodic shift with respect to the ferrocene precursor, Figure 35a, simply because of the electrostatic effect to remove electrons from a cationic complex with respect to the neutral original molecule.

It is hence evident that if we would have applied a difference of potential ΔE between the reference and the working electrodes before the complexation, we would have generated a current due to the oxidation process, Figure 35a. In contrast, upon applying the same potential difference ΔE after the cation complexation, we do not produce current; if we wish to generate current we have to apply an extra potential $\Delta E'$, Figure 35b. The extent of $\Delta E'$ is intuitively correlated to the nature of the complexed cation. From here we get the term *cationic sensor*.

An example is illustrated in Figure 36a, which shows the cyclic voltammogram of octamethyl-5,5'-di(2-pyridyl)ferrocene in the absence (a) and in the presence (b) of Cu(I) ions.⁶⁴

As seen, the original ferrocene molecule oxidizes at $E^{\circ'} = -0.05$ V (vs. SCE). In the presence of Cu(I) ions the redox potential shifts to $E^{\circ'} = +0.40$ V. This means that before the complexation, the application of a potential of about 0.1 V generates a current flow, whereas in the presence of Cu(I) ions, in order to generate the same current, we must apply a potential value of about +0.6 V. It is likely that in the presence of different cations, the potential shift would be different, thus allowing the specific recognition of cations.

Anionic sensors are based on the same principles, but work in the opposite direction. In this case we must have available ferrocene

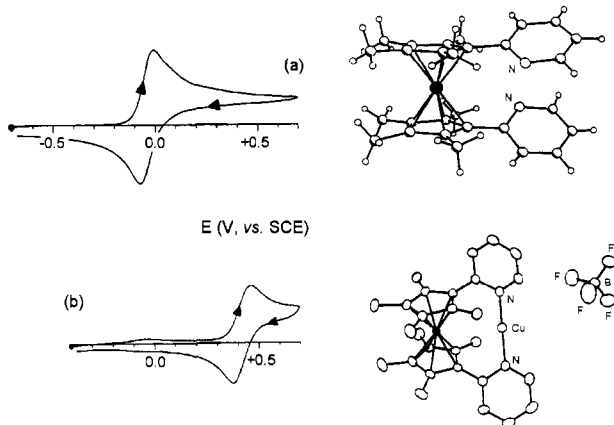


Figure 36 Cyclic voltammograms recorded at a platinum electrode in a CH_2Cl_2 solution of octamethyl-5,5'-di(2-pyridyl)ferrocene. (a) Initial; (b) in the presence of $\text{Cu}(\text{I})$ ions. Scan rate 0.2 V s^{-1}

molecules bearing substituents able to complex anions. The simple electrostatic effects to remove electrons from a negatively charged ferrocene complex makes the process easier, hence the oxidation potential shifts towards less positive values with respect to the original ferrocene derivative.⁶⁵

Even if less common and less investigated, ferrocene molecules able to recognize neutral molecules have been found.⁶⁶

1.5.2 Ferrocenes as Materials Displaying Non-linear Optical Properties. One of the most recent applications of ferrocene molecules exploits their *non-linear optical properties*. Firstly, however, we must describe the concept of non-linear optical properties.^{67,68}

The best known interactions between light and matter are those that occur in phenomena such as refraction, reflection and diffraction, which produce linear effects. In other words, the magnitude of the effect resulting from the interaction is a linear function of the intensity of the light. The advent of the laser, able to generate high intensity monochromatic electromagnetic radiation has afforded important changes with respect the usual linear responses stimulating impressive studies on such new phenomena.

In general, the oscillating electric field of an electromagnetic wave incident on a given material interacts with the electrical charges within the molecules inducing charge polarizations. As a consequence, these molecules behave as oscillating dipoles and emit electromagnetic radiation that can be detected at some point external to the material.

The study of the changes of phase, frequency and intensity that the incident radiation undergoes on passing through the material constitutes the field of *non-linear optics* (NLO). It, in fact, focuses on the description of deviations from the linear behaviour predicted by the laws of classical optics.

An electric field induces a polarization of the charge within a single molecule by the instantaneous displacement of the electrons with respect to the nucleus. In this manner an induced dipole and, hence, a dipolar moment, μ , are generated. When the applied field is weak, the induced charge displacement is proportional to the strength of the field:

$$\text{polarization} = \mu = \alpha \cdot E$$

where α is the linear polarizability of the irradiated molecule. Under these conditions, the induced polarization oscillates with the same frequency and phase as the applied field, E .

When the material is composed of an aggregation of molecules, one speaks of 'macroscopic polarization' P , and for weak applied fields this is linearly dependent on the susceptibility χ of the material in question, according to the relationship: $P = \chi \cdot E$.

Figure 37 exemplifies such a behaviour.

When very strong electric fields are applied (by irradiating with laser light) the induced macroscopic polarization deviates from linearity and can display either centrosymmetric non-linearity or non-centrosymmetric non-linearity, Figure 38.

It is evident that in centrosymmetric non-linear media the induced polarization in the $+E$ direction is equal (in absolute value) to the induced polarization in the opposite direction $-E$. However, in

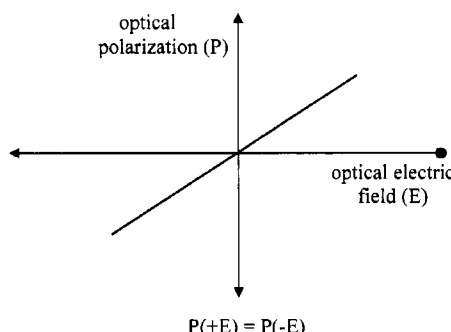


Figure 37 Schematic representation of the optically induced polarization in optically linear materials

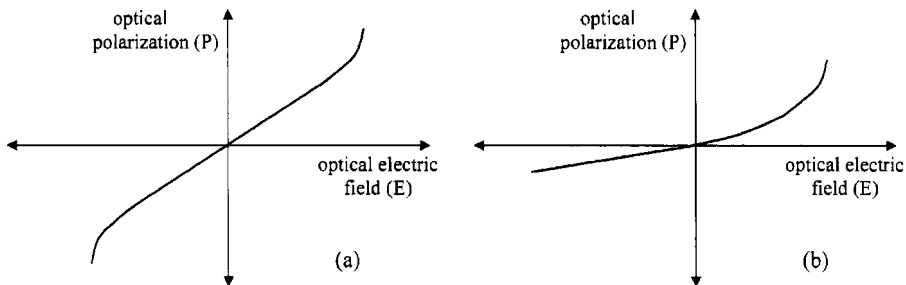


Figure 38 Schematic representation of the optically induced polarization in: (a) centrosymmetric non-linear materials; (b) non-centrosymmetric non-linear materials

non-centrosymmetric non-linear media the induced polarization in the direction $+E$ is different from that in the opposite direction $-E$.

To account for the *non-linear optical* (NLO) behaviour, the foregoing expressions, relating the induced polarization with the applied electric field, are expressed as a power series of the electric field.

For a single molecule one obtains:

$$\text{polarization} = \alpha E + \beta E^2 + \gamma E^3 + \dots$$

where the coefficients β and γ are called first and second molecular hyperpolarizability, respectively.

For aggregates of molecules (or, materials) one obtains:

$$P = \chi^{(1)} \cdot E + \chi^{(2)} \cdot E^2 + \chi^{(3)} \cdot E^3 + \dots$$

where the coefficients $\chi^{(n)}$ represent the susceptibility of the material to the power n .

It is important to note that the exponents of χ for centrosymmetric molecules cannot be even numbers (*i.e.* materials composed by centrosymmetric molecules cannot generate effects of second order, fourth order, *etc.*). In fact, if one applies a field $+E$, the first non-linear term would induce a polarization of $+\beta \cdot E^2$ (*or* $+\chi^{(2)} \cdot E^2$). If one were to apply instead a field of $-E$, the mathematical expression would lead to an induced polarization again of $+\beta \cdot E^2$, whereas, as shown in Figure 38a, the induced polarization is $-\beta \cdot E^2$. This contradiction can only be resolved if β (*or* $\chi^{(2)} = 0$).

Conversely, for non-centrosymmetric materials the second order non-linear effect may exist (*i.e.* β or $\chi^{(2)} \neq 0$).

Furthermore, for centrosymmetric or non-centrosymmetric materials alike, third order non-linear effects can exist (γ or $\chi^{(3)} \neq 0$).

The connection between the non-linear polarization response and the generation of optical harmonics by NLO materials can be understood by considering Figure 39, which shows a typical non-linear optical response produced by a non-centrosymmetric molecule.

The molecule under subject is a 'push-pull' system which contains a benzene ring with either a donor group D (*i.e.* an electron-rich fragment) and an acceptor group A (*i.e.* an electron-poor fragment) which are positioned at the opposite sides of the π -unsaturated ring.⁶⁹

As illustrated in Figure 39a, the application of a symmetrically oscillating electric field $E(\omega)$ of frequency ω makes the molecule respond with an asymmetric polarization (or the wave amplitude of the polarization response in the positive ordinate is different from that in the negative ordinate) in that the electron density can only flow in the direction donor \rightarrow acceptor, and not *vice versa*.

If one bears in mind that the Fourier theorem states that a periodic non-sinusoidal response can be described by a series of sinusoidal

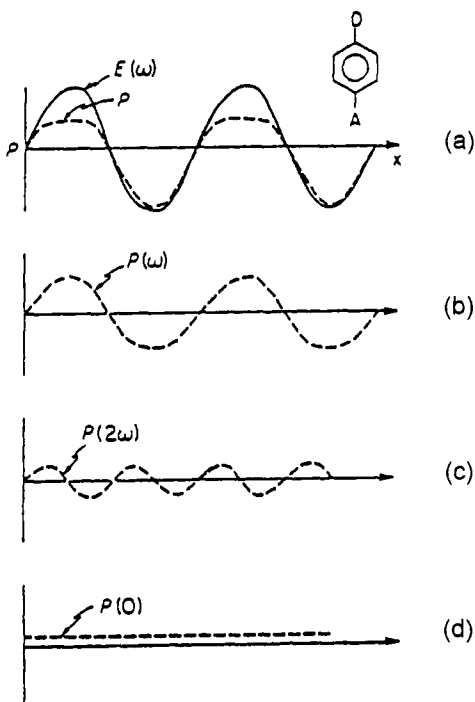


Figure 39 (a) Non-linear polarization response (P) along the direction x , as a function of the time, exhibited by a non-centrosymmetric molecule under the effect of an electric field oscillating at a frequency ω . (b, c, d) Fourier components of the polarization at the frequencies ω , 2ω , 0 , respectively

functions, with suitable coefficients for the harmonics of the fundamental frequency ω , it follows that, as shown in Figures 39b,c the asymmetric polarization can be described as a sum of the Fourier components of frequency ω , 2ω , $(3\omega, \text{etc.})$, the intensity of which decreases progressively with the increase in the frequency coefficient.

In the case of a centrosymmetric molecule the Fourier decomposition would be described by polarizations of frequency ω , 3ω , 5ω , etc.

As the intensity of the electromagnetic field, $E(\omega)$, increases the non-linear terms become increasingly significant and, consequently, more easily measurable.

One of the more interesting applications of non-linear optical effects is the generation of the second harmonic. This phenomenon results when a laser beam passes through a material having second-order NLO properties (hence, composed by non-centrosymmetric molecules); the light emitted has a frequency double that of the incident radiation (or the wavelength has been halved).

This effect can be mathematically deduced from the relationship:

$$P = \chi^{(1)} \cdot E + \chi^{(2)} \cdot E^2 + \chi^{(3)} \cdot E^3 + \dots$$

In fact, expressing the electric field of a plane light wave as:

$$E = E_0 \cdot \cos(\omega \cdot t)$$

and substituting, one obtains:

$$\begin{aligned} P &= \chi^{(1)} \cdot E_0 \cdot \cos(\omega \cdot t) + \frac{1}{2} \chi^{(2)} \cdot E_0^2 \cdot [1 + \cos(2\omega \cdot t)] + \frac{1}{4} \chi^{(3)} \cdot E_0^3 \cdot [\cos(3\omega \cdot t) + 3\cos(\omega \cdot t)] + \dots \\ &= \frac{1}{2} \chi^{(2)} \cdot E_0^2 + \left[\chi^{(1)} \cdot E_0 + \frac{3}{4} \chi^{(3)} \right] \cos(\omega \cdot t) + \frac{1}{2} \chi^{(2)} \cdot \cos(2\omega \cdot t) + \frac{1}{4} \chi^{(3)} \cdot E_0^3 \cdot \cos(3\omega \cdot t) + \dots \end{aligned}$$

It is evident that the polarization contains a frequency doubled component (2ω), a frequency tripled component (3ω), and so on.

These effects can be explained by the coupling of two photons of frequency ω to generate a single photon of frequency 2ω , or of three photons of frequency ω to generate a single photon of frequency 3ω , etc.

These effects of second and third order optical non-linearity are just exploited in the generation of the second and third harmonics, respectively. In this connection, Figure 40 schematizes an experiment in which the incidence of a laser light working in the near infrared at λ 1060 nm on a crystal of $\text{KUO}_2(\text{PO}_4)$ emits a light of $\lambda = 532 \text{ nm}$.⁷⁰

The non-linear optical properties of a material are evaluated by measuring (using techniques from the field of physics) its molecular hyperpolarizability coefficient β .

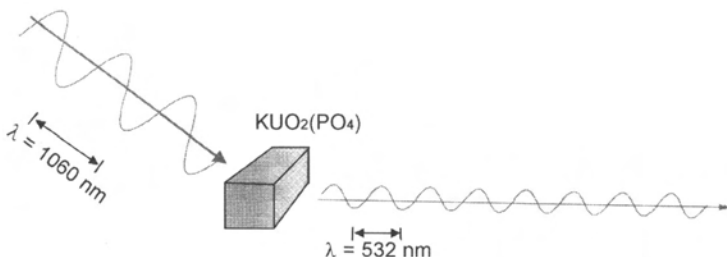
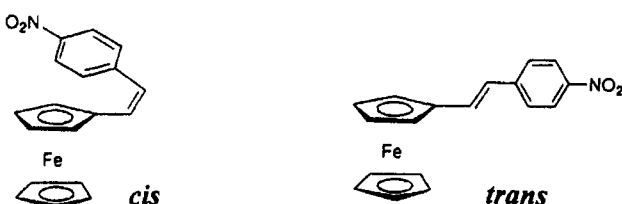


Figure 40 Second harmonic generation

There are many organic and inorganic materials available which exhibit significant non-linear optical properties. In the present context, however, we underline that ferrocene derivatives were the first organometallic materials observed possessing non-linear optical properties. In fact, in 1987 it was reported that *cis*-ferrocenyl-2-(4-nitrophenyl)ethylene has a 62-fold greater efficiency than urea in generating the second harmonic, Scheme 13.⁷¹

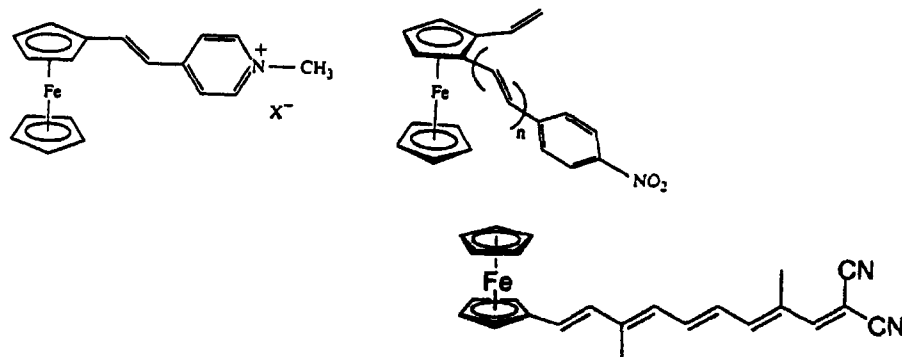


Scheme 13

Urea is the compound commonly used as the reference standard; it has a second harmonic generation efficiency approximately 400-fold greater than quartz. The ferrocene derivative molecule, which crystallizes in a non-centrosymmetric space group, obeys the requirements illustrated in Figure 39, in that it contains a donor group (ferrocene) and an acceptor group (nitro group) conjugated through a π -unsaturated system. Conversely, the *trans* isomer does not show second harmonic generation activity, due to the presence of a centre of symmetry.

One of the preliminary indications which reveals the potential capacity of a material to generate second harmonics is its solvatochromatic behaviour, *i.e.* the ability of a material to give rise to considerable differences in its UV-visible spectrum on changing solvent. For example, the electronic absorption spectrum of *cis*-ferrocenyl-2-(4-nitrophenyl) ethylene in dimethylformamide shows two bands at 340 and 492 nm, respectively, whereas in heptane it displays three bands at 320, 406 and 462 nm, respectively.

Since 1987 numerous metallocenes, in particular ferrocenes, have been found to possess NLO properties, many of which have substituents containing polyene conjugate groups,⁷² Scheme 14.



Scheme 14

The high hyperpolarizability β of these ferrocene molecules is thought to be linked to the ease with which they are oxidized, which causes easy electron movement across the polyene bridge. For instance, ferrocenyl-2-(4-nitrophenyl)ethylene is oxidized at the ferrocene centre at +0.03 V and reduced at the NO₂ centre at -1.67 V (*vs.* Fc/Fc⁺) in tetrahydrofuran solution.⁷²

2 VANADOCENES

The low temperature molecular structure of vanadocene, [V(η^5 -C₅H₅)₂], is shown in Figure 41.⁷³

It is evident that the cyclopentadienyl rings assume a mutual staggered conformation.

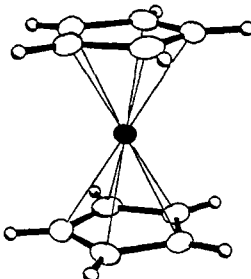


Figure 41 *X-Ray structure of* [V(η^5 -C₅H₅)₂]*, at 108 K. Average V-C bond length = 2.27 Å. V-Cp_(centroid) = 1.92 Å*

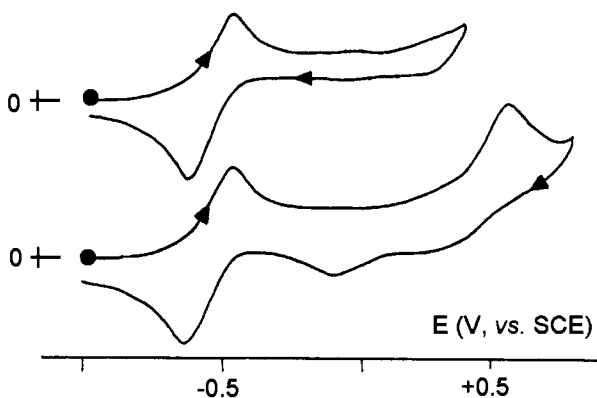


Figure 42 Cyclic voltammogram recorded at a platinum electrode in a THF solution of $[V(\eta^5-C_5H_5)_2]$. Scan rate 0.1 V s^{-1}

In agreement with only half of the bonding and non-bonding orbitals being populated (15 valence electrons; terminal electron configuration: $e_2^{1/2} a_1^{1/1}$), the bond distance V–C (2.27 Å) is significantly longer than the Fe–C distance (2.04 Å) of ferrocene. In fact, the 18-electron ferrocene has a terminal electron configuration $e_2^{1/4} a_1^{1/2}$; as such, it has the strongest metal–carbon bond of the 3d-metallocene family and, hence, the shortest M–C distance.

Despite not being electronically saturated, vanadocene is able to lose two further electrons through two distinct oxidation processes corresponding to V^{II}/V^{III} ($E^{\circ'} = -0.55\text{ V}$, vs. SCE) and V^{III}/V^{IV} ($E_p = +0.59\text{ V}$), the first of which is chemically reversible, Figure 42.⁷⁴

This shows that vanadocene maintains its molecular structure essentially unaltered on passing to 14 valence electrons. One might expect vanadocene to have a high predisposition to accept electrons in order to achieve the stability of 18 valence electrons. Nevertheless, it displays only a single, chemically reversible, reduction process at very negative potential values ($E^{\circ'} = -2.74\text{ V}$).

Analogous to ferrocene, vanadocene can be permethylated to decamethylvanadocene (the X-ray structure of which is known⁷⁵). In contrast with decamethylferrocene, which is reversibly oxidized more easily than ferrocene, decamethylvanadocene does not seem able to undergo reversible oxidation.⁷⁶

3 CHROMOCENES

Figure 43 shows the (low-temperature) molecular structure of chromocene, $[Cr(\eta^5-C_5H_5)_2]$.⁷⁷

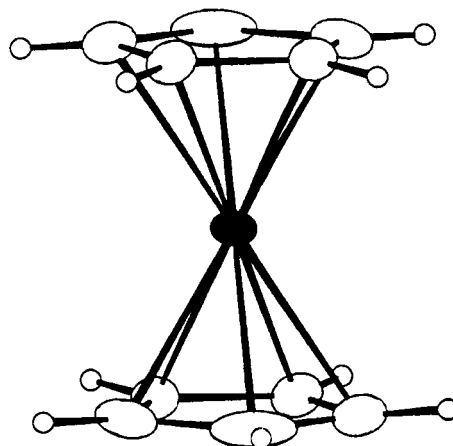


Figure 43 X-Ray structure of $[Cr(\eta^5\text{-C}_5\text{H}_5)_2]$, at 173 K. Average Cr-C bond length = 2.15 Å. Cr-Cp_(centroid) = 1.79 Å

The cyclopentadienyl rings of chromocene, as for vanadocene, assume a staggered conformation.

In agreement with the presence of an additional electron in the bonding orbital, compared to vanadocene (chromocene: 16 valence electrons, terminal electronic configuration: $e_2^{1/3} a_1^{1/1}$), the metal–carbon distance is shorter (2.15 Å compared to 2.27 Å of vanadocene).

As illustrated in Figure 44, chromocene exhibits both a Cr^{II}/Cr^{III} oxidation and a Cr^{II}/Cr^I reduction.⁷⁸

Like ferrocene and vanadocene, chromocene can be permethylated to decamethylchromocene ($\text{Cr-Cp}^*_{(\text{centroid})}$ = 1.78 Å⁷⁹).

As compiled in Table 10 and as may be expected on the basis of the inductive effects, decamethylchromocene is more easily oxidized (i.e. at

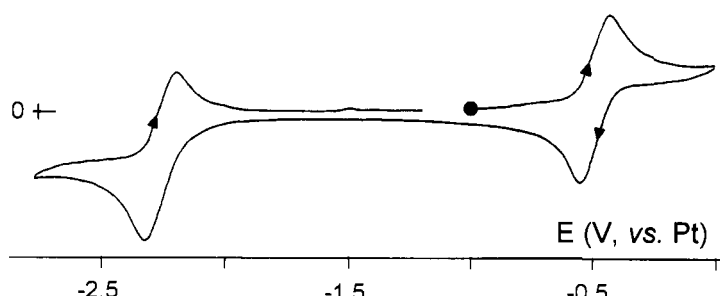


Figure 44 Cyclic voltammogram recorded at a platinum electrode in a THF solution of $[Cr(\eta^5\text{-C}_5\text{H}_5)_2]$. Scan rate 0.1 V s⁻¹

Table 10 Redox potentials (*V* vs. SCE) of chromium in sandwich molecules in different solvents

Complex	$E_{+/0}^{\circ'}$	$E_{0/-}^{\circ'}$	Solvent	Reference
$[\text{Cr}(\eta^5\text{-C}_5\text{H}_5)_2]$	-0.67	-2.30	MeCN	74
	-0.64	-2.36	thf	80
$[\text{Cr}(\eta^5\text{-C}_5\text{Me}_5)_2]$	-1.04	-	MeCN	76
$[\text{Cr}(\eta^5\text{-C}_5\text{Ph}_4\text{H})_2]$	-0.33	-1.69	thf	81

considerably more negative potentials) to the corresponding decamethylchromoceneum ion than chromocene, which in turn oxidizes more easily than (octaphenyl)chromocene.

The cyclopentadienyl rings of decamethylchromoceneum ion in $[\text{Cr}(\text{C}_5\text{Me}_5)_2][(\text{C}_5\text{Me}_5)\text{CrCl}_3]$ are staggered (and the Cr–Cp*_(centroid) distance elongates by about 0.05 Å with respect to decamethylchromocene),⁸² whereas in $[\text{Cr}(\text{C}_5\text{Me}_5)_2][(\text{NC})_2\text{C}=\text{C}(\text{CN})_2]$ they are eclipsed.⁸³

4 MANGANOCENES

Manganocene has a high spin electronic configuration (17 valence electrons; terminal electronic configuration: $e_2'^2 a_1'^1$) and is a material difficult to handle due to its extreme reactivity (it is pyrophoric and hydrolyses instantly on contact with water). Its molecular structure in the gaseous phase, determined by electronic diffraction, indicates a mean Mn–C distance of 2.38 Å.⁸⁴ Such a long bond distance may possibly be ascribed to occupation of the e_1'' antibonding orbital. Consequently, in order to make a comparative analysis of the metallocene structures of the first row transition metals as a function of their electronic configuration it is better to consider decamethylmanganocene, $[\text{Mn}(\eta^5\text{-C}_5\text{Me}_5)_2]$, which has a low spin electronic configuration (terminal electronic configuration: $e_2'^3 a_1'^2$). Its molecular structure is illustrated in Figure 45.⁸⁵

It is evident from the structure that the disposition of the cyclopentadienyl rings is staggered. The mean metal–carbon bond length is 2.11 Å, which is shorter than that of vanadocene (2.27 Å) and chromocene (2.15 Å). This reflects the progressive occupation of the bonding or non-bonding orbitals. However, one must note that there are distortions present in the molecule. These are reflected, for example, in the Mn–C distance, which ranges from 2.10 Å to 2.12 Å. This distribution of distances has been attributed to the *Jahn–Teller effect* following the occupation of the degenerate e_2' orbitals.⁸⁵

Decamethylmanganocene is easily oxidized to the corresponding decamethylmanganocenium ion, $[\text{Mn}(\eta^5\text{-C}_5\text{H}_5)_2]^+$. In fact, Figure 46

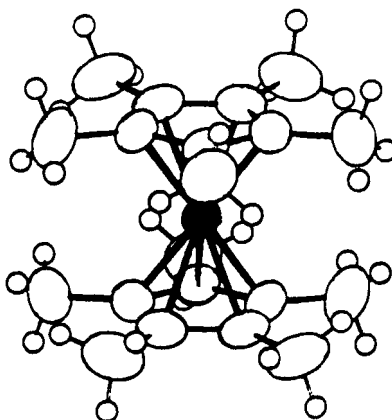


Figure 45 X-Ray structure of $[Mn(\eta^5\text{-C}_5\text{Me}_5)_2]$

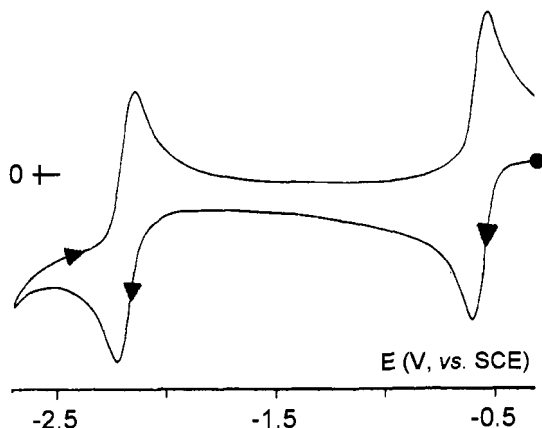


Figure 46 Cyclic voltammogram recorded at a platinum electrode in a MeCN solution of $[Mn(\eta^5\text{-C}_5\text{Me}_5)_2](PF_6)$. Scan rate 0.1 V s^{-1}

shows that in acetonitrile solution the decamethylmanganocene ion undergoes two separate, chemically reversible, reductions $[Mn(\text{C}_5\text{Me}_5)_2]^{+/-}$, corresponding to the $\text{Mn}^{\text{III}}/\text{Mn}^{\text{II}}$ ($E^\circ' = -0.56\text{ V}$) and $\text{Mn}^{\text{II}}/\text{Mn}^{\text{I}}$ ($E^\circ' = -2.17\text{ V}$) sequences,⁸⁶

5 COBALTOCENES

The molecular structure of cobaltocene is illustrated in Figure 47.⁸⁷

Once again the disposition of the cyclopentadienyl rings is staggered. The metal–carbon bond length in cobaltocene (19 valence electrons, terminal electronic configuration: $e_2'^4 a_1'^2 e_1''^1$) is greater than in ferrocene

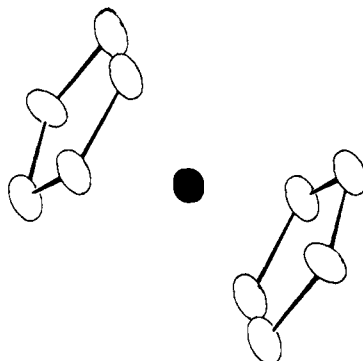


Figure 47 X-Ray structure of $[\text{Co}(\eta^5\text{-C}_5\text{H}_5)_2]$. Average Co-C bond length 2.10 \AA

(2.10 \AA vs. 2.04 \AA). This is in agreement with the progressive population of the antibonding e_1'' orbital for the 3d transition metal metallocenes beyond ferrocene.

In a similar manner to manganocene, cobaltocene is easily oxidized to the corresponding cobaltocenium ion $[\text{Co}(\eta^5\text{-C}_5\text{H}_5)_2]^+$, which, as illustrated in Figure 48, exhibits two distinct chemically reversible reductions corresponding to $\text{Co}^{\text{III}}/\text{Co}^{\text{II}}$ and $\text{Co}^{\text{II}}/\text{Co}^{\text{I}}$.⁸⁸

The redox potentials for these reduction processes in different solvents are reported in Table 11, together with the $\text{Co}^{\text{III}}/\text{Co}^{\text{II}}$ redox potential for some related derivatives.

The electronic effects of the methyl and phenyl substituents have been already discussed for the corresponding chromocenes.

It is useful to note that in contrast to the elongation of the M–C bonds observed on passing from ferrocene to ferrocenium ion, in the case of the cobaltocene/cobaltocenium transition, because of the removal of

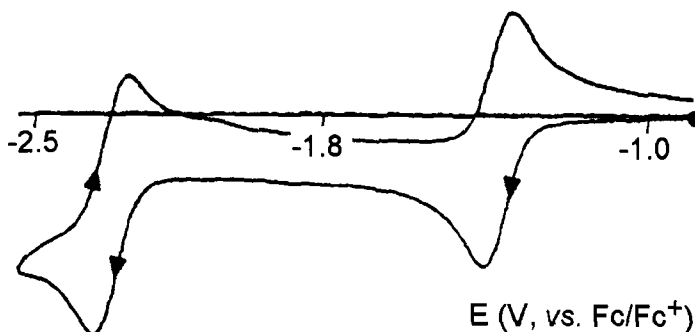


Figure 48 Cyclic voltammogram recorded at a glassy carbon electrode in a MeCN solution of $[\text{Co}(\eta^5\text{-C}_5\text{H}_5)_2](\text{PF}_6)$. Scan rate 0.1 V s^{-1}

Table 11 Formal electrode potentials (V vs. SCE) for the redox processes exhibited by a few cobaltocenes in different solvents

Complex	$E_{+/0}^{\circ'}$	$E_{0/-}^{\circ'}$	Solvent	Reference
$[\text{Co}(\eta^5\text{-C}_5\text{H}_5)_2]$	-0.98	-1.96	MeCN	88
	-0.95	-1.92	CH_2Cl_2	88
	-0.90	-2.04	thf	89
$[\text{Cr}(\eta^5\text{-C}_5\text{Me}_5)_2]$	-1.47	-	MeCN	76
	-1.48	-	CH_2Cl_2	90
$[\text{Co}(\eta^5\text{-C}_5\text{Ph}_4\text{H})_2]$	-0.46	-1.36	thf	81

the electron populating the e''_1 antibonding orbital, the Co–C bond lengths decrease. In fact, they have an averaged length of 2.01 Å in $[\text{Co}(\eta^5\text{-C}_5\text{H}_5)_2]^{+}$ ⁹¹ and 2.10 Å in $\text{Co}(\eta^5\text{-C}_5\text{H}_5)_2$.⁸⁷

6 NICKELOCENES

The molecular structure of nickelocene $[\text{Ni}(\eta^5\text{-C}_5\text{H}_5)_2]$ is illustrated in Figure 49, together with its cyclic voltammetric behaviour.^{92,93}

Concerned with the electron diffraction structure, the rotation of the cyclopentadienyl rings appears even faster than in ferrocene, hence their mutual disposition is difficult to establish. An X-ray diffraction study at 101 K has however shown that at this temperature the conformation is staggered.⁹⁴ The increment in the Ni–C distance (2.18 Å) compared to the Co–C distance (2.10 Å) in cobaltocene reflects once again the increased population of the antibonding e''_1 orbital (nickelocene has 20 valence electrons and a terminal electronic configuration: $e''_2^4 a''_1^2 e''_1^2$).

As far as the redox aptitude is concerned, two separate chemically reversible oxidations are evident corresponding to the $\text{Ni}^{\text{II}}/\text{Ni}^{\text{III}}$ and $\text{Ni}^{\text{III}}/\text{Ni}^{\text{IV}}$ electron transfers. The relative potentials are summarized in Table 12, together with those for the permethylated derivative.

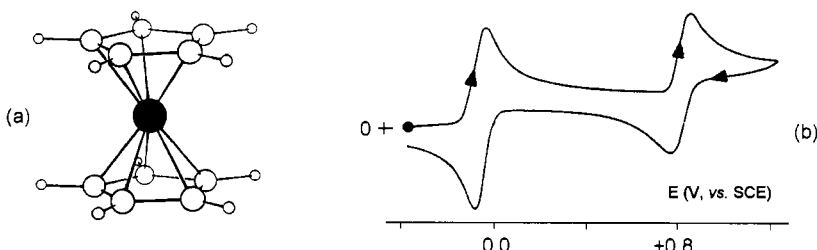


Figure 49 (a) Electron diffraction structure of $[\text{Ni}(\eta^5\text{-C}_5\text{H}_5)_2]$. Average Ni–C bond length: 2.18 Å. (b) Cyclic voltammogram recorded at a platinum electrode on a MeCN solution of $[\text{Ni}(\eta^5\text{-C}_5\text{H}_5)_2]$. Scan rate 0.05 V s^{-1} . $T = -40^\circ\text{C}$

Table 12 Formal electrode potentials (V vs. SCE) for the redox processes exhibited by nickelocene and decamethylnickelocene in different solvents

Complex	$E_{0/+}^{\circ'}$	$E_{+/2+}^{\circ'}$	Solvent	Reference
$[\text{Ni}(\eta^5\text{-C}_5\text{H}_5)_2]$	-0.09	+0.77	MeCN	93
	+0.09	+0.77	CH_2Cl_2	95
	+0.01	+0.81	thf	96
$[\text{Ni}(\eta^5\text{-C}_5\text{Me}_5)_2]$	-0.65	+0.31	MeCN	88
	-0.73	+0.37	CH_2Cl_2	95

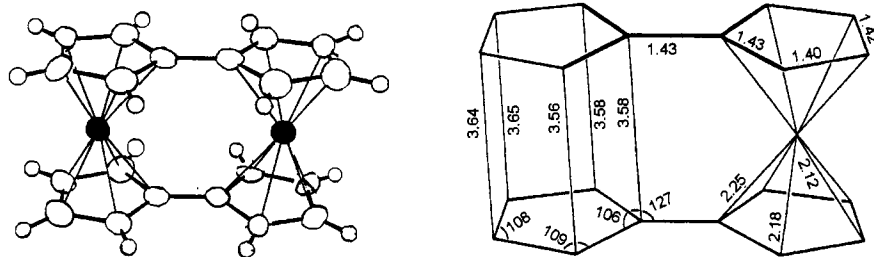


Figure 50 X-Ray structure of $[\text{Ni}_2(\eta^5\text{:}\eta^5\text{-C}_{10}\text{H}_8)_2]$, with the relevant bond distances

As happens for ferrocenes, almost all metallocenes can be incorporated in multimetallocenic assemblies. We thus conclude the discussion by considering the redox behaviour of bis(fulvalene)dinickel(II,II), $[\text{Ni}_2(\eta^5\text{:}\eta^5\text{-C}_{10}\text{H}_8)_2]$. Its X-ray structure is shown in Figure 50.⁹⁷ The inequivalence of the Ni–C and C–C distances is attributed to the structural constraints imposed by the two bridges which join the two nickelocene units.

In acetone solution $[\text{Ni}_2(\eta^5\text{:}\eta^5\text{-C}_{10}\text{H}_8)_2]$ undergoes two distinct oxidations with characteristics of chemical reversibility, which correspond to $\text{Ni}_2^{\text{II,II}}/\text{Ni}_2^{\text{II,III}}$ ($E^{\circ'} = -0.29 \text{ V}$) and $\text{Ni}_2^{\text{II,III}}/\text{Ni}_2^{\text{III,III}}$ ($E^{\circ'} = +0.12 \text{ V}$), respectively.⁹⁷ This observation indicates that there is electronic communication between the two nickelocene units.

REFERENCES

- (a) R.R. Gagné, C.A. Kowal and G.D. Lisensky, *Inorg. Chem.*, 1980, **19**, 2854; (b) G. Gritzner and J. Kuta, *Pure Appl. Chem.*, 1984, **56**, 461.
- A. Haaland, *Acc. Chem. Res.*, 1979, **12**, 415.

3. R. Martinez and A. Tiripicchio, *Acta Cryst.*, 1990, **C46**, 202.
4. Yu.T. Struchkov, V.G. Andrianov, T.N. Sal'nikova, I.R. Lyatifov and R.B. Materikova, *J. Organomet. Chem.*, 1978, **145**, 213.
5. J. Pickardt, H. Schumann and R. Mohtachemi, *Acta Cryst.*, 1990, **C46**, 39.
6. (a) P.M. Treichel, J.W. Johnson and K.P. Wagner, *J. Organomet. Chem.*, 1975, **88**, 227; (b) D.A. Foucher, C.H. Honeyman, A.J. Lough, I. Manners and J.M. Nelson, *Acta Cryst.*, 1995, **C51**, 1795; (c) J.W. Bats, J.J. de Boer and D. Bright, *Inorg. Chim. Acta*, 1971, **5**, 605.
7. G. Cerveau, C. Chuit, E. Colomer, R.J.P. Corriu and C. Reyé, *Organometallics*, 1990, **9**, 2415.
8. (a) J. Okuda and E. Herdtweck, *Chem. Ber.*, 1988, **121**, 1899; (b) J. Okuda, R.W. Albach, E. Herdtweck and F.E. Wagner, *Polyhedron*, 1991, **10**, 1741.
9. (a) P. Zanello, unpublished data; (b) Yu.T. Struchkov, V.G. Andrianov, T.N. Sal'nikova, I.R. Lyatifov and R.B. Materikova, *J. Organomet. Chem.*, 1978, **145**, 213; (c) J.S. Miller, D.T. Glatzhofer, D.M. O'Hare, W.M. Reiff, A. Chakraborty and A.J. Epstein, *Inorg. Chem.*, 1989, **28**, 2930.
10. P. Zanello, A. Cinquantini, M. Fontani, M. Giardiello, G. Giorgi, C.R. Landis and B.F.M. Kimmich, *J. Organomet. Chem.*, 2001, **637–639**, 800.
11. M. Hillman and J.D. Austin, *Organometallics*, 1987, **6**, 1737.
12. C. Willi, A.H. Reis, Jr., E. Gebert and J.S. Miller, *Inorg. Chem.*, 1981, **20**, 313.
13. T.-Y. Dong and S.-H. Lee, *J. Organomet. Chem.*, 1995, **487**, 77.
14. M. Hillman and E. Fujita, *J. Organomet. Chem.*, 1978, **155**, 87.
15. See for example: (a) M. Hisatome, Y. Kawaziri, K. Yamakawa and Y. Iitaka, *Tetrahedron Lett.*, 1979, **20**, 1777; (b) M. Hisatome, J. Watanabe, Y. Kawajiri, K. Yamakawa and Y. Iitaka, *Organometallics*, 1990, **9**, 497.
16. B.R. Davis and I. Bernal, *J. Cryst. Mol. Struct.*, 1972, **2**, 107.
17. N.J. Long, S.J. Sharkey, M.B. Hursthouse and M.A. Mazid, *J. Chem. Soc., Dalton Trans.*, 1993, 23.
18. N.J. Long, P.R. Raithby and P. Zanello, *J. Chem. Soc., Dalton Trans.*, 1995, 1245.
19. F. Jäkle, T. Priermeier and M. Wagner, *Organometallics*, 1996, **15**, 2033.
20. E. Herdtweck, F. Jäkle, G. Opronolla, M. Spiegler, M. Wagner and P. Zanello, *Organometallics*, 1996, **15**, 5524.
21. Z. Kaluski, *Bull. Acad. Pol. Sci.*, 1964, **12**, 873.
22. (a) G.M. Brown, T.J. Meyer, D.O. Cowan, C. LeVanda, F. Kaufman, P.V. Roling and M.D. Rausch, *Inorg. Chem.*, 1975, **14**, 506; (b) N. Camire, U.T. Mueller-Westerhoff and W.E. Geiger, *J. Organomet. Chem.*, 2001, **637–639**, 823.
23. S.J. Geib, A.L. Rheingold, T.-Y. Dong and D.N. Hendrickson, *J. Organomet. Chem.*, 1986, **312**, 241.
24. M.B. Robin and P. Day, *Adv. Inorg. Chem. Radiochem.*, 1967, **10**, 247.
25. A.W. Bott, *Current Separations* (Bioanalytical Systems), 1997, **16**, 61.

26. (a) D. Astruc, *Electron Transfer and Radical Processes in Transition-Metal Chemistry*. Wiley-VCH, New York, 1995; (b) B.S. Brunschwig and N. Sutin, *Coord. Chem. Rev.*, 1999, **187**, 233; (c) V. Palaniappan, R.M. Singru and U.C. Agarwala, *Inorg. Chem.*, 1988, **27**, 181.
27. M.J. Cohn, T.-Y. Dong, D.N. Hendrickson and A.L. Rheingold, *J. Chem. Soc., Chem. Commun.*, 1985, 1095.
28. G. Ferguson, C. Glidewell, G. Opronolla, C.M. Zakaria and P. Zanello, *J. Organomet. Chem.*, 1996, **517**, 183.
29. A. Houlton, R.M.G. Roberts and J. Silver, *J. Chem. Soc., Dalton Trans.*, 1990, 1543.
30. I.R. Butler, U. Griesbach, P. Zanello, M. Fontani, D. Hibbs, M.B. Hursthouse and K.L.M.A. Malik, *J. Organomet. Chem.*, 1998, **565**, 243.
31. J.R. Doyle, N.C. Baenziger and R.L. Davis, *Inorg. Chem.*, 1974, **13**, 101.
32. C. LeVanda, D.O. Cowan, C. Leitch and K. Bechgaard, *J. Am. Chem. Soc.*, 1974, **96**, 6788.
33. P. Zanello, G. Opronolla, M. Herberhold and H.-D. Brendel, *J. Organomet. Chem.*, 1994, **484**, 67.
34. M. Herberhold, A. Hofmann, W. Milius, F. Fabrizia de Biani and P. Zanello, *Inorg. Chim. Acta*, 1998, **273**, 24.
35. H. Fink, N.J. Long, A.J. Martin, G. Opronolla, A.J.P. White, D.J. Williams and P. Zanello, *Organometallics*, 1997, **16**, 2646.
36. N.J. Long, A.J. Martin, F. Fabrizi de Biani and P. Zanello, *J. Chem. Soc., Dalton Trans.*, 1998, 2017.
37. B. Grossmann, J. Heinze, E. Herdtweck, F.H. Köhler, H. Nöth, H. Schwenk, M. Spiegler, W. Wachter and B. Weber, *Angew. Chem. Int. Ed. Engl.*, 1997, **36**, 387.
38. (a) I. Manners, *Angew. Chem. Int. Ed. Engl.*, 1996, **35**, 1602; (b) P. Nguyen, P. Gómez-Elipe and I. Manners, *Chem. Rev.*, 1999, **99**, 1515; (c) A.W. Bosman, H.M. Janssen and E.W. Meijer, *Chem. Rev.*, 1999, **99**, 1665; (d) G.R. Newkome, E. He and C.N. Moorefield, *Chem. Rev.*, 1999, **99**, 1689.
39. T.W. Smith, J.E. Kuder and D. Wychick, *J. Polymer Sci.*, 1976, **14**, 2433.
40. J.B. Flanagan, S. Margel, A.J. Bard and F.C. Anson, *J. Am. Chem. Soc.*, 1978, **100**, 4248.
41. P. Zanello, G. Opronolla, F. Fabrizi de Biani, A. Ceccanti and G. Giorgi, *Inorg. Chim. Acta*, 1997, **255**, 47.
42. D.L. Compton and T. Rauchfuss, *Organometallics*, 1994, **13**, 4367.
43. D.A. Foucher, C.H. Honeyman, J.M. Nelson, B.Z. Tang and I. Manners, *Angew. Chem. Int. Ed. Engl.*, 1993, **32**, 1709.
44. J.-P. Majoral and A.-M. Caminade, *Chem. Rev.*, 1999, **99**, 845.
45. G.E. Oosterom, R.J. van Haaren, J.N.H. Reek, P.C.J. Kamer and P.W.N. M. van Leeuwen, *Chem. Commun.*, 1999, 1119.

46. I. Cuadrado, M. Morán, C.M. Casado, B. Alonso, F. Lobete, B. García, M. Ibisate and J. Losada, *Organometallics*, 1996, **15**, 5278.
47. C.M. Cardona and A.E. Kaifer, *J. Am. Chem. Soc.*, 1998, **120**, 4023.
48. B. Alonso, I. Cuadrado, M. Morán and J. Losada, *J. Chem. Soc., Chem. Commun.*, 1994, 2575.
49. J.-L. Fillaut, J. Linares and D. Astruc, *Angew. Chem. Int. Ed. Engl.*, 1994, **33**, 2460.
50. J. Ruiz, E. Alonso, J.-C. Blais and D. Astruc, *J. Organomet. Chem.*, 1999, **582**, 139.
51. C. Valério, J.-L. Fillaut, J. Ruiz, J. Guittard, J.-C. Blais and D. Astruc, *J. Am. Chem. Soc.*, 1997, **119**, 2588.
52. S. Nlate, J. Ruiz, J.-C. Blais and D. Astruc, *Chem. Commun.*, 2000, 417.
53. S. Nlate, J. Ruiz, V. Sartor, R. Navarro, J.-C. Blais and D. Astruc, *Chem. Eur. J.*, 2000, **6**, 2544.
54. P. Jutzi, C. Batz, B. Neumann and H.-G. Stammler, *Angew. Chem. Int. Ed. Engl.*, 1996, **35**, 2118.
55. K.-W. Poon, Y. Yan, X. Li and D.K.P. Ng, *Organometallics*, 1999, **18**, 3528.
56. S. Achar, C.E. Immoos, M.G. Hill and V.J. Catalano, *Inorg. Chem.*, 1997, **36**, 2314.
57. V. Chandrasekhar, S. Nagendran, S. Bansal, M.A. Kozee and D.R. Powell, *Angew. Chem. Int. Ed. Engl.*, 2000, **39**, 1833.
58. N. Prokopuk and D.F. Schriver, *Inorg. Chem.*, 1997, **36**, 5609.
59. (a) B. González, I. Cuadrado, C.M. Casado, B. Alonso and C.J. Pastor, *Organometallics*, 2000, **19**, 5518; (b) C.M. Casado, B. González, I. Cuadrado, B. Alonso, M. Morán and J. Losada, *Angew. Chem. Int. Ed. Engl.*, 2000, **39**, 2135.
60. I. Cuadrado, C.M. Casado, B. Alonso, M. Morán, J. Losada and V. Belsky, *J. Am. Chem. Soc.*, 1997, **119**, 7613.
61. M.J. Green and H.A.G. Hill, *J. Chem. Soc., Faraday Trans. 1*, 1986, **82**, 1237.
62. A.E.G. Cass, G. Davis, G.D. Francis, H.A.O. Hill, W.J. Aston, I.J. Higgins, E.V. Plotkin, L.D.L. Scott and A.P.F. Turner, *Anal. Chem.*, 1984, **56**, 667.
63. N.J. Forrow, G.S. Sanghera and S.J. Walters, *J. Chem. Soc., Dalton Trans.*, 2002, 3187.
64. B. Neuman, U. Siemeling, H.-G. Stammler, U. Vorfeld, J.G.P. Delis, P.W.N.M. van Leeuwen, K. Vrieze, J. Fraanje, K. Goubitz, F. Fabrizi de Biani and P. Zanello, *J. Chem. Soc., Dalton Trans.*, 1997, 4705.
65. P.D. Beer, *Acc. Chem. Res.*, 1998, **31**, 71 and references cited therein.
66. J.D. Carr, L. Lambert, D.E. Hibbs, M.B. Hursthouse, K.M. Abdul Malik and J.H.R. Tucker, *Chem. Commun.*, 1997, 1649.
67. D.R. Kanis, M.A. Ratner and T.J. Marks, *Chem. Rev.*, 1994, **94**, 195.

68. N.J. Long, *Angew. Chem. Int. Ed. Engl.*, 1995, **34**, 21.
69. D.J. Williams, *Angew. Chem. Int. Ed. Engl.*, 1984, **23**, 690.
70. D.F. Eaton, *Science*, 1991, **253**, 281.
71. M.L.H. Green, S.R. Marder, M.H. Garcia, M.E. Thompson, J.A. Bandy, D. Bloor, P.V. Kolinsky and R.J. Jones, *Nature*, 1987, **330**, 360.
72. (a) S. Barlow and S.R. Marder, *Chem. Commun.*, 2000, 1555; (b) M. Malaun, Z.R. Reeves, R.L. Paul, J.C. Jeffery, J.A. McCleverty, M.D. Ward, I. Asselberghs, K. Clays and A. Persoons, *Chem. Commun.*, 2001, 49.
73. M.Yu. Antipin, K.A. Lyssenko and R. Boese, *J. Organomet. Chem.*, 1996, **508**, 259.
74. J.D.L. Holloway and W.E. Geiger Jr., *J. Am. Chem. Soc.*, 1979, **101**, 2038.
75. S. Gambarotta, C. Floriani, A. Chiesi-Villa and C. Guastini, *Inorg. Chem.*, 1984, **23**, 1739.
76. J.L. Robbins, N. Edelstein, B. Spencer and J.C. Smart, *J. Am. Chem. Soc.*, 1982, **104**, 1882.
77. K.R. Flower and P.B. Hitchcock, *J. Organomet. Chem.*, 1996, **507**, 275.
78. J.D.L. Holloway, W.L. Bowden and W.E. Geiger, Jr., *J. Am. Chem. Soc.*, 1977, **99**, 7089.
79. J. Blümel, M. Herker, W. Hiller and F.H. Köhler, *Organometallics*, 1996, **15**, 3474.
80. E.U. van Raaij, S. Mönkeberg, H. Kiese and H.-H. Brintzinger, *J. Organomet. Chem.*, 1988, **356**, 307.
81. M.P. Castellani, S.J. Geib, A.L. Rheingold and W.C. Trogler, *Organometallics*, 1987, **6**, 1703.
82. S. Aldridge, M. Shang and T.P. Fehlner, *Acta Cryst.*, 1998, **C54**, 47.
83. J.S. Miller, R.S. Mclean, C. Vasquez, J.C. Calabrese, F. Zuo and A.J. Epstein, *J. Mater. Chem.*, 1993, **3**, 215.
84. A. Haaland, *Inorg. Nucl. Chem. Lett.*, 1979, **15**, 267.
85. D.P. Freyberg, J.L. Robbins, K.N. Raymond and J.C. Smart, *J. Am. Chem. Soc.*, 1979, **101**, 892.
86. J.L. Robbins, N. Edelstein, S.R. Cooper and J.C. Smart, *J. Am. Chem. Soc.*, 1979, **101**, 3853.
87. W. Bünder and E. Weiss, *J. Organomet. Chem.*, 1975, **92**, 65.
88. R.S. Stojanovic and A.M. Bond, *Anal. Chem.*, 1993, **65**, 56.
89. A.J. Bard, E. Garcia, S. Kukharenko and V.V. Strelets, *Inorg. Chem.*, 1993, **32**, 3528.
90. W. Kläui and L. Ramacher, *Angew. Chem. Int. Ed. Engl.*, 1986, **25**, 97.
91. P. Legzdins, B. Wassink, F.W.B. Einstein and R.H. Jones, *Organometallics*, 1988, **7**, 477.
92. L. Hedberg and K. Hedberg, *J. Chem. Phys.*, 1970, **53**, 1228.
93. R.J. Wilson, L.F. Warren, Jr. and M.F. Hawthorne, *J. Am. Chem. Soc.*, 1969, **91**, 758.

94. P. Seler and J.D. Dunitz, *Acta Cryst.*, 1980, **B36**, 2255.
95. U. Koelle and F. Khouzami, *Angew. Chem. Int. Ed. Engl.*, 1980, **19**, 640.
96. P.R. Sharp, K.N. Raymond, J.C. Smart and R.J. McKinney, *J. Am. Chem. Soc.*, 1981, **103**, 753.
97. J.C. Smart and B.L. Pinsky, *J. Am. Chem. Soc.*, 1980, **102**, 1009.

CHAPTER 5

The Electrochemical Behaviour of Transition Metal Complexes

An exhaustive treatment of the electrochemical behaviour of transition metal complexes is beyond the scope of this book, because the enormous number of ligands available, combined with the possibility to prepare mono- and/or polynuclear complexes using identical or mixed ligands, would render such a task almost impossible. Therefore, the discussion is limited to some aspects associated with the redox properties of (essentially) *mononuclear* metal complexes. In particular, we will concentrate representatively on the redox changes of *first row transition metal* complexes (excluding the metallocene complexes, as they have been already discussed in Chapter 4) that give stable, or relatively stable products. A systematic and useful examination of the redox activity of organometallic complexes of transition metals dated to 1984 has appeared.¹

It should be recalled that one of the principal properties of transition metals is their aptitude to accede to multiple oxidation states. Thus, the main scope of an electrochemical study is to ascertain whether a metal complex, prepared in a certain oxidation state, is stable also in different oxidation states, or whether the lifetimes of these oxidation states are too short to observe stable products. Whenever stable oxidation states are identified, the chemist might be able to prepare and fully characterize these new complexes.

The choice of the most appropriate reducing or oxidizing agent is an important question in the access to particular oxidation states. In this connection, it must be considered that a certain species, in order to be able to act as an ‘oxidizing’ agent towards another species (or to remove electrons from another species), must have a tendency to add electrons (or to be reduced) higher than that of the second species to lose electrons

Table 1 Common one-electron oxidizing agents and their (approximate) reduction potentials (V vs. SCE)

Oxidizing agent	Redox potential	Solvent
duroquinone	-0.8	MeCN
O ₂	-0.8	MeCN, DMF
1,4-benzoquinone	-0.5	MeCN
2,6-dichloro-1,4-benzoquinone	-0.2	MeCN
[C ₇ H ₇][BF ₄]	0.0	CH ₂ Cl ₂
tetrachloro-1,4-benzoquinone	+0.1	MeCN
tcne	+0.2	MeCN
tcnq	+0.2	MeCN
I ₂	+0.7	MeCN
[CPh ₃][PF ₆]	+0.3	CH ₂ Cl ₂ , MeCN
[Fe(η^5 -C ₅ H ₅) ₂][PF ₆]	+0.4	CH ₂ Cl ₂ , MeCN
[Ag][PF ₆]	+1.0	CH ₂ Cl ₂
NOBF ₄	+1.3	MeCN

(or to be oxidized). Analogously, in order that a species might act as a ‘reducing’ agent towards another species (or to add electrons to another species), it must possess a propensity to lose electrons (or to be oxidized) higher than that of the second species to add electrons (or to be reduced). Since the tendency to add (or lose) electrons is measured by the standard reduction (or oxidation) potentials, the choice of the most appropriate redox agent must be based on the standard potentials of the redox processes under study.

Tables 1 and 2 show a series of commercially available redox agents covering a wide range of redox potentials. A more complete picture is available in literature.²

From a practical viewpoint, the choice of the most appropriate redox agent follows the same criteria applied to the choice of the working potential in controlled potential electrolysis. The redox agent must possess a standard electrode potential 100–200 mV more positive

Table 2 Common one-electron reducing agents and their (approximate) reduction potentials (V vs. SCE)

Reducing agent	Redox potential	Solvent
[Fe(η^5 -C ₅ H ₅) ₂]	+0.4	CH ₂ Cl ₂ , MeCN
[Fe(η^5 -C ₅ Me ₅) ₂]	-0.1	CH ₂ Cl ₂ , MeCN
[Co(η^5 -C ₅ H ₅) ₂]	-0.9	CH ₂ Cl ₂ , MeCN, thf
[NBu ₄][BH ₄]	-1.2	CH ₂ Cl ₂

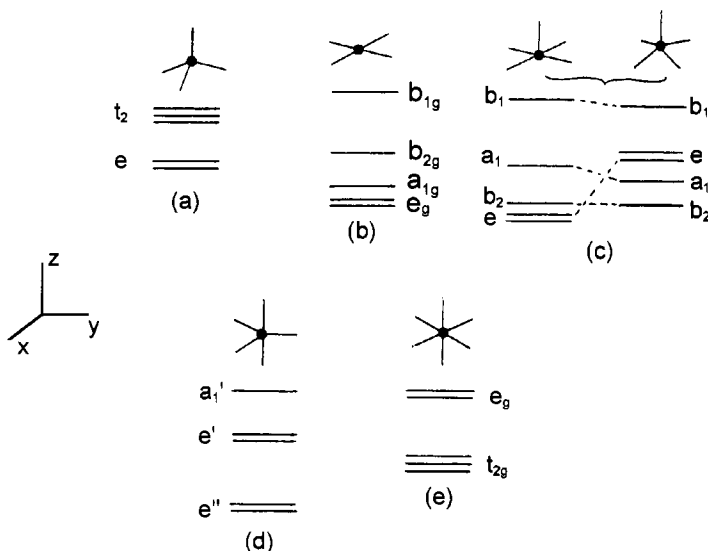


Figure 1 Diagrams of the frontier orbitals of: (a) tetrahedral, (b) square planar, (c) square pyramidal, (d) trigonal bipyramidal, and (e) octahedral complexes

(for oxidation) or more negative (for reduction) than the potential of the redox process given by the complex under study.

Ligands that are able to stabilize metal complexes in high oxidation states and other ligands that stabilize the same metal in low oxidation states will also be discussed.

The redox ability of a metal complex will be considered in the context of its *molecular orbital composition* and *spin state*. In this regard, Figure 1 shows the molecular orbital diagrams for the most common geometries encountered in transition metal complexes.

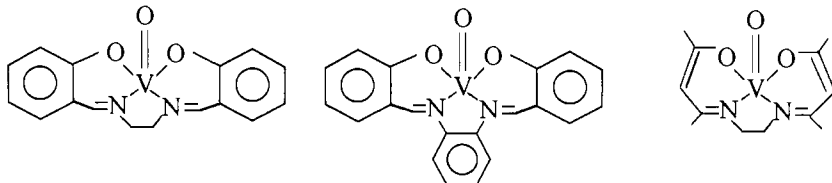
Finally, it is important to underline that in order to compare correctly the redox potentials of different complexes, reference must be made to the same solvent.

1 VANADIUM COMPLEXES

Inorganic complexes of vanadium are normally found in the following forms:

- *oxo-complexes* of VO^{2+} and VO^{3+} (or VO_2^+), which correspond thus to V^{IV} and V^{V} oxidation states, respectively;
- *non-oxo-complexes* in the oxidation states V^{IV} , V^{III} and V^{II} (electronic configuration d^1 , d^2 , d^3 , respectively).

Oxo-vanadium derivatives include numerous examples of Schiff base complexes, the importance of which is increasing in that they can act as *insulin*-enhancing agents.³ For instance, the vanadyl(IV) derivatives of *N,N'*-ethylenebis(salicylideneimine), [VO(salen)], *N,N'*-disalicylidene-*o*-phenylenediamine, [VO(saloph)], and *N,N'*-ethylenebis(acetylacetatoimine), [VO(acen)], are shown in Scheme 1.



Scheme 1

As illustrated in Figure 2, which refers to [VO(salen)], these complexes possess square-pyramidal geometries, with the oxygen atom of

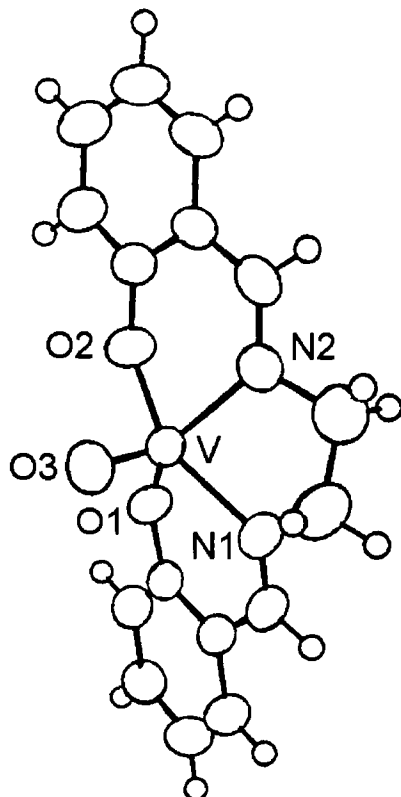


Figure 2 *X-Ray structure of [VO(salen)]. Bond lengths: V–O1 = V–O2 = 1.92 Å; V–O3 = 1.59 Å; V–N1 = V–N2 = 2.05 Å*

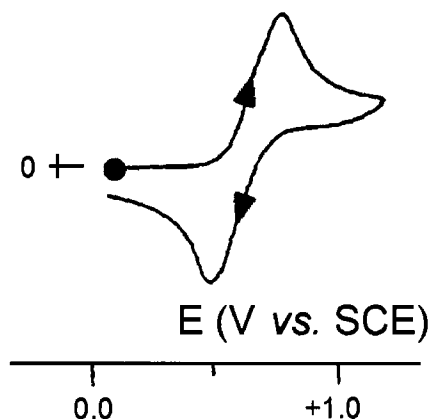


Figure 3 Cyclic voltammogram recorded at a platinum electrode in a MeCN solution of $[VO(\text{acen})]$. Scan rate 0.2 V s^{-1}

the vanadyl ion positioned at the apex of the pyramid and the vanadium(IV) atom raised slightly above the plane formed by the N_2O_2 atoms.⁴⁻⁶

These 3d¹ complexes display a quasireversible one-electron oxidation corresponding to the chemically reversible step $[\text{VO}^{\text{IV}}\text{L}] / [\text{VO}^{\text{V}}\text{L}]^+$ (L = Schiff base ligand). As an example, Figure 3 shows the cyclic voltammetric response of $[\text{VO}(\text{acen})]$.⁷ The relative potential values are reported in Table 3.

The role played by the electron-donating or electron-withdrawing effects of the various ligands in rendering the oxidation process easier for $[\text{VO}(\text{salen})]$ compared to $[\text{VO}(\text{saloph})]$ or $[\text{VO}(\text{acen})]$ is evident. The influence of the solvent on the redox potentials is also clear.

It should be emphasized that $[\text{VO}(\text{salen})]$ in its oxidized form $[\text{VO}(\text{salen})]^+$ ($[\text{ClO}_4]^-$ counteranion) maintains the original square-pyramidal geometry, but, in accord with the electrochemical quasireversibility of the couple $\text{V}^{\text{IV}}/\text{V}^{\text{V}}$, there are some variations in bond

Table 3 Redox potentials (V vs. SCE) for the one-electron oxidation of Schiff base complexes of vanadyl ion

Complex	$E^\ddagger_{[\text{VO}^{2+}/\text{VO}^{3+}]}$	Solvent	Reference
$[\text{VO}(\text{salen})]$	+0.47	MeCN	7
	+0.34	dmsol	8
	+0.50	CH_2Cl_2	9
$[\text{VO}(\text{saloph})]$	+0.47	dmsol	8
	+0.55	CH_2Cl_2	9
$[\text{VO}(\text{acen})]$	+0.45	dmsol	10
	+0.66	CH_2Cl_2	10

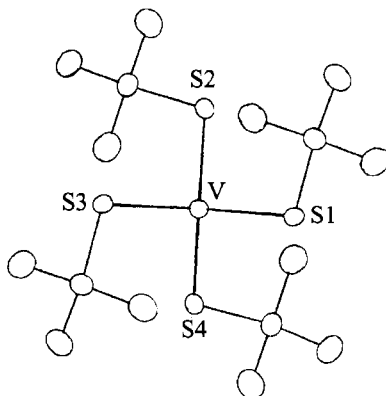


Figure 4 X-Ray structure of $[V(SBu^t)_4]$. Average V–S bond length: 2.22 Å. Bond angles: $S3-V-S2 = S2-V-S1 = S3-V-S4 = S4-V-S1 = 107^\circ$; $S3-V-S1 = S2-V-S4 = 114.5^\circ$

lengths (in particular, the distances $V-O_{(\text{phenolate})}$ are considerably shortened (≈ 0.1 Å), the distances V–N are slightly lengthened (≈ 0.02 Å) and the distance $V=O$ remains essentially unaltered).⁸

As far as the non-oxo complexes are concerned, one can start, in order of increasing coordination, with the tetrahedral vanadium(IV)-tetrabutylthiolate complex $[V(SBu^t)_4]$, Figure 4.¹¹

In agreement with the oxidation state $V(\text{IV})-\text{d}^1$, it has a magnetic moment $\mu_{\text{eff}} = 1.75 \mu_B$. The V–S bond lengths are substantially identical, but the bonding angles are grouped as four smaller and two larger.

The redox behaviour of this vanadium(IV) complex is shown in Figure 5.¹¹

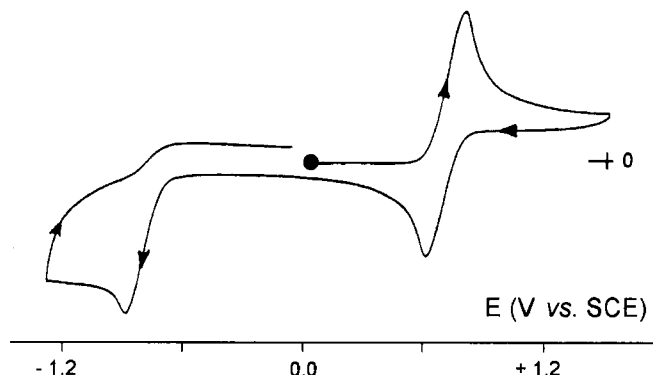


Figure 5 Cyclic voltammogram recorded at a glassy carbon electrode in a CH_2Cl_2 solution of $[V(SBu^t)_4]$. Scan rate $0.1 V s^{-1}$

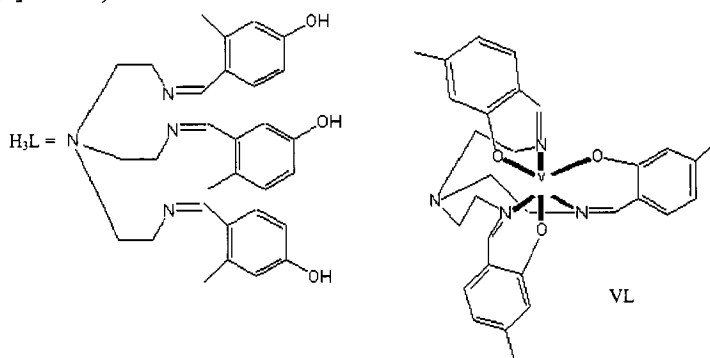
It displays an irreversible oxidation ($E_p = +0.81$ V) and a one-electron reduction ($V^{IV} \rightarrow V^{III}$; $E^{\circ'} = -0.69$ V vs. SCE) with features of chemical reversibility and electrochemical quasireversibility ($\Delta E_p = 130$ mV, at 0.1 V s $^{-1}$).

The corresponding vanadium(III) monoanion $[V(SBu^t)_4]^-$ has been isolated and X-ray characterized. It maintains the tetrahedral geometry of the neutral precursor, but with a larger distortion. In fact, even though the V–S distances are virtually identical (but a little longer than those of the neutral complex) and the angles can again be subdivided into two larger and four smaller, there is not the same distribution as found in the neutral precursor ($S_2\text{--V--}S_4 = 120.9^\circ$; $S_3\text{--V--}S_2 = 117.9^\circ$; $S_3\text{--V--}S_1 = 104.4^\circ$; $S_1\text{--V--}S_2 = 102.3^\circ$; $S_1\text{--V--}S_4 = 101.5^\circ$; $S_4\text{--V--}S_3 = 106.9^\circ$).¹¹

From a speculative viewpoint, the quasireversibility of the electrochemical reduction V^{IV}/V^{III} could account for such structural rearrangements.

Let us pass to six-coordinate derivatives, starting with a few Schiff base complexes.

For example, the octahedral complex $V^{III}L$ illustrated in Scheme 2 has a N_3O_3 coordination sphere { $L = \text{tris}[2\text{-(4'-methyl-2'-hydroxobenzylidene)ethyl}]amine$ }.



Scheme 2

In agreement with the $V(\text{III})\text{-}d^2$ oxidation state, it has a magnetic moment $\mu_{\text{eff}} = 2.89 \mu_B$.

As shown in Figure 6, this $V(\text{III})$ complex undergoes both a one-electron oxidation ($V^{III} \rightarrow V^{IV}$; $E^{\circ'} = +0.26$ V) and a one-electron reduction ($V^{III} \rightarrow V^{II}$; $E^{\circ'} = -1.52$ V) with characteristics of chemical and substantial electrochemical reversibility ($\Delta E_{p(\text{III/II})} = 100$ mV; $\Delta E_{p(\text{III/IV})} = 80$ mV; both measured at the scan rate of 0.05 V s $^{-1}$).¹²

The same N_3O_3 coordination sphere is exhibited by tris(picolinato)-vanadium(III) complex, $[\text{V(pic)}_3]$, the significantly distorted octahedral geometry of which is shown in Figure 7.¹³

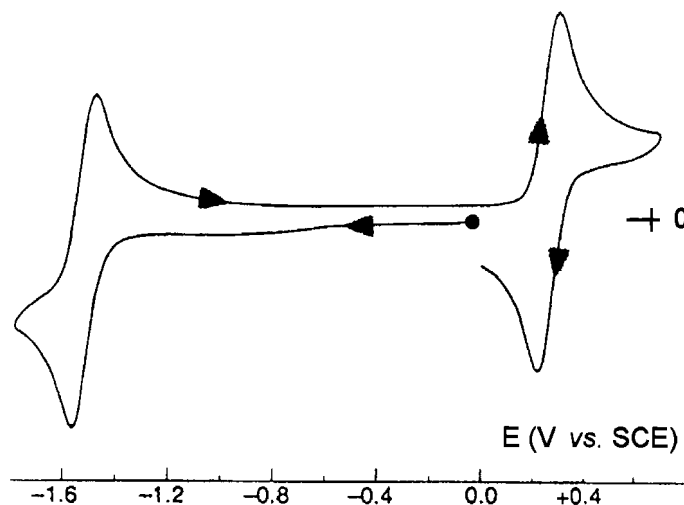
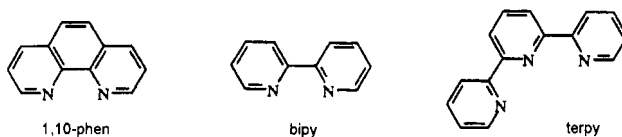


Figure 6 Cyclic voltammogram recorded at a platinum electrode in a dmso solution of VL. Scan rate 0.05 V s^{-1}

In agreement with the oxidation state V(III)-d^2 it has a magnetic moment $\mu_{\text{eff}} = 2.77 \mu_B$.

In dmso solution it displays a reversible $\text{V}^{\text{III}/\text{IV}}$ oxidation ($E^{\circ'} = +0.63 \text{ V}$ vs. Ag/AgCl), and a quasireversible $\text{V}^{\text{III}/\text{II}}$ reduction ($E^{\circ'} = -1.01 \text{ V}$).¹³

Let us now consider the N_6 -coordinated octahedral vanadium complexes with the polypyridine ligands 1,10-phenanthroline (phen), 2,2'-bipyridine (bipy) and 2,2':6,2''-terpyridine (terpy), Scheme 3.



Scheme 3

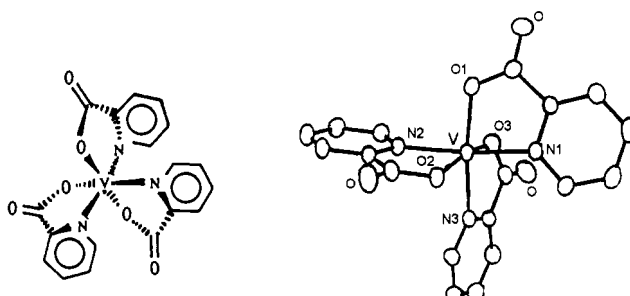


Figure 7 X-Ray structure of $[\text{V(pic)}_3] \cdot \text{H}_2\text{O}$. Bond lengths: $\text{V}-\text{N}3 = 2.15 \text{ \AA}$; $\text{V}-\text{N}1 = 2.12 \text{ \AA}$; $\text{V}-\text{N}2 = 2.12 \text{ \AA}$; $\text{V}-\text{O}3 = 1.97 \text{ \AA}$; $\text{V}-\text{O}1 = 1.94 \text{ \AA}$; $\text{V}-\text{O}2 = 1.94 \text{ \AA}$

The same type of coordinating ligands will be discussed for other metal complexes.

The only X-ray structure available is that for $[V(\text{bipy})_3]$, Figure 8.¹⁴

There is some uncertainty whether this complex should be described as $[\text{V}^{\text{III}}(\text{bipy}^-)^3]$ or as $[\text{V}^0(\text{bipy})_3]$. In fact, given that 2,2'-bipyridine can act either as a σ -donor or a π -acceptor, the metal–ligand bond in these complexes is constituted by a σ -bond between the lone pair of electrons of the nitrogen atom and an unoccupied s-orbital of the metal. Such electron donation, increasing the electron density on the metal, can in turn favour a back-bonding from the d-orbitals of the metal and the unoccupied π^* -orbitals of the aromatic pyridine ring. In short, if the metal ion is in a high oxidation state pyridine will act as a σ donor, whereas if the metal is in a low oxidation state pyridine will act as a π acceptor.

It is the mutual redox ability of the metal and the ligand which hinders a clear definition of the redox character of these complexes and often gives rise to a considerable number of redox processes. For instance, Figure 9 shows the cyclic voltammetric behaviour of the dication $[\text{V}^{\text{II}}(\text{phen})_3]^{2+}$ in dichloromethane solution.¹⁵

It undergoes either two separated reductions or one oxidation, all having features of chemical reversibility in the cyclic voltammetric time scale. Since no detailed studies have been carried out on the underlying electrode mechanism, it is noted that these redox transformations could formally correspond to the sequence V(III)/V(II)/V(I), but, as far as the reduction processes are concerned, it is also likely that they are centred on the polypyridine ligand.

Table 4 reports some electrochemical data for the $[\text{V}(\text{bipy})_3]^{2+}$ and $[\text{V}(\text{phen})_3]^{2+}$ complexes.

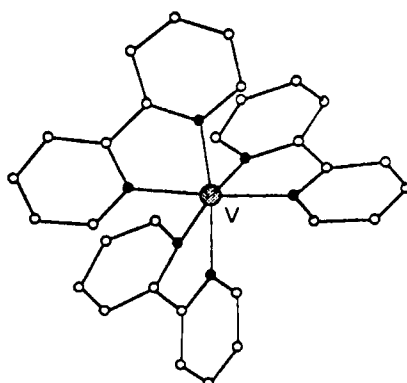


Figure 8 X-Ray structure of $[\text{V}(\text{bipy})_3]$. Average V–N distance = 2.10 \AA ; average N–V–N angle = 73.6°

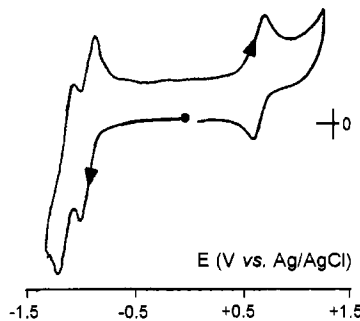


Figure 9 Cyclic voltammogram of $[V(\text{phen})_3]^{2+}$ in $(O_3\text{SCF}_3)_2$ in CH_2Cl_2 solution. Platinum working electrode. Scan rate 0.5 V s^{-1}

Table 4 Formal electrode potentials (V , vs. Ag/AgCl) for the redox changes exhibited by $[V(\text{bipy})_3]^{2+}$ and $[V(\text{phen})_3]^{2+}$

Complex	$E_{3+/2+}^{\circ}$	$E_{2+/+}^{\circ}$	$E_{+/0}^{\circ}$	Solvent	Reference
$[V(\text{bipy})_3]^{2+}$	+0.52	-0.52 ^a	-	MeCN	16
$[V(\text{phen})_3]^{2+}$	+0.56	-0.37	-	MeCN	16
	+0.63	-0.97	-1.16	CH_2Cl_2	15

^a Irreversible.

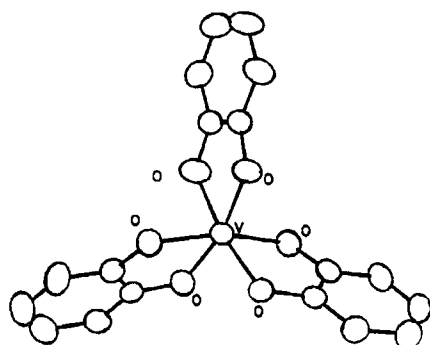
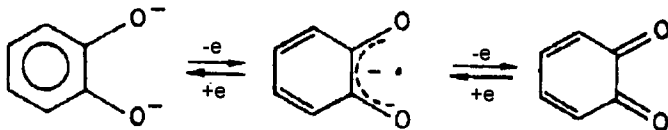


Figure 10 X-Ray structure of $[V(\text{cat})_3]^{2-}$. Average $V\text{-}O$ distance = 1.94 \AA ; average $C\text{-}O$ distance = 1.34 \AA ; average cis $O\text{-}V\text{-}O$ angle = 80.7° ; average trans $O\text{-}V\text{-}O$ angle = 162.8°

An interesting behaviour is shown by the V(IV)-catecholate complex $[V(\text{cat})_3]^{2-}$, the distorted octahedral O_6 coordination of which is shown in the Figure 10.¹⁷

Such a complex is constituted not only by the redox-active V(IV) centre, but also by the redox-active catecholate ligand. In fact, as we will see in more detail in Chapter 6, Section 3, *o*-dioxolene ligands can undergo the redox processes illustrated in Scheme 4.



Scheme 4

As shown in Figure 11, $[V(\text{cat})_3]^{2-}$ undergoes in MeCN solution a chemically reversible one-electron reduction to the corresponding trianion $[V(\text{cat})_3]^{3-}$, provided that an excess of catechol is present in solution.¹⁷

This means that, given the catecholate nature of the original dianion, the reduction process can be only assigned to the $\text{V}^{\text{IV}}/\text{V}^{\text{III}}$ step. The need of free catecholate ligand suggests that, in the absence of free ligand, such reduction process is accompanied by chemical complications (equilibria between coordinated and uncoordinated ligand). In spite of such (slow) chemical complications, chemical reduction and rapid precipitation allowed the $[V^{\text{III}}(\text{cat})_3]^{3-}$ trianion to be obtained and structurally characterized.¹⁷ In agreement with the electrochemical reversibility of the $\text{V}^{\text{IV}}/\text{V}^{\text{III}}$ reduction, $[V^{\text{III}}(\text{cat})_3]^{3-}$ has essentially the same structural features as the dianion precursor, but for a significantly longer V–O distance (which would testify to the metal-centred reduction. Average V–O distance = 2.01 Å; average C–O distance = 1.34 Å; average *cis* O–V–O angle = 81.3°; average *trans* O–V–O angle = 168.1°).

On passing we note that the complex also undergoes a ligand-centred (catecholate/semiquinone), reversible one-electron oxidation. Such types of redox processes will be discussed in Chapter 6, Section 3.

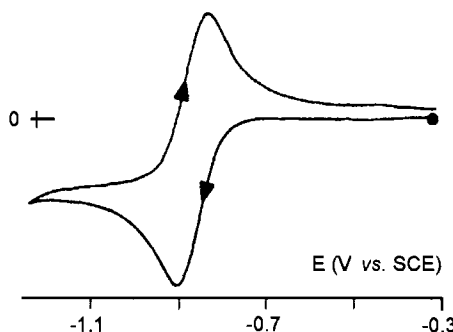
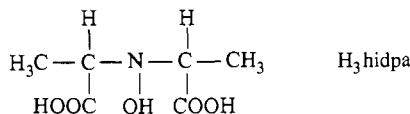


Figure 11 Cyclic voltammogram recorded at a mercury electrode in a MeCN solution of $[V(\text{cat})_3]^{2-}$ in the presence of an excess of catechol

The last vanadium derivative that we will consider is the N_2O_6 octacoordinated complex called *Amavadin*. It consists of a vanadium(IV) ion and two trideprotonated molecules of *N*-hydroxyl-2,2'-iminodipropionic acid (H_3hidpa), $[\text{V}(\text{hidpa})_2]^{2-}$.



The interest in this complex derives not only from its unusually high coordination, but also because it introduces us to the field of ‘vanadium in biology’,¹⁸ namely, those vanadium complexes present in living systems (such as *vanadium nitrogenases*, which we will discuss in Chapter 9, Section 2). As early as 1931 it was observed that mushrooms of the *Amanita* family, in particular *Amanita muscaria* (the well-known ‘fly agaric’), were able to concentrate vanadium at high levels. Attempts were made over many years to determine the oxidation state and coordination mode of vanadium in these mushrooms. It is now known that vanadium is present just as the $[\text{V}(\text{hidpa})_2]^{2-}$ complex. Even if the crystal structure of such a dianion has not been long available, it has been observed that the complex can be reversibly oxidized (with ceric nitrate) to the corresponding vanadium(V) complex $[\text{V}(\text{hidpa})_2]^-$, the X-ray structure of which has been solved, Figure 12.¹⁹

An electrochemical investigation of the Amavadin dianion has established not only the chemical reversibility of the V(IV)/V(V) oxidation,

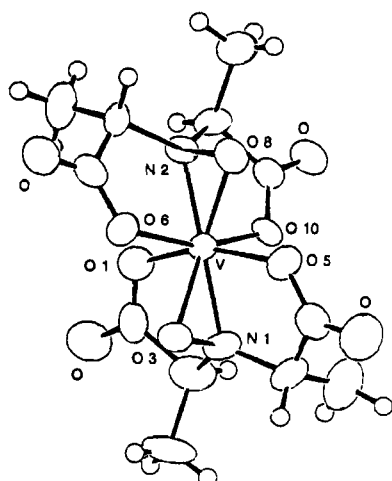


Figure 12 X-Ray structure of the monoanion $[\text{V}(\text{hidpa})_2]^-$

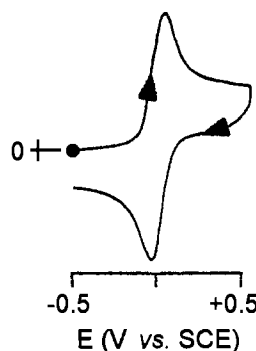


Figure 13 Cyclic voltammogram recorded at a platinum electrode in a dmso solution of $[V(hidpa)_2]^{2-}$ (after addition of tetraethylammonium hydroxide). Scan rate 0.2 V s^{-1}

but also its electrochemical reversibility, Figure 13, ($E_{\text{V(IV)/V(V)}}^{\circ} = 0.00 \text{ V}$ in dmso; $\Delta E_p = 60 \text{ mV}$, at 0.2 V s^{-1}).²⁰

This suggested that the molecular structure of the reduced Amavadin complex, $[V(hidpa)_2]^{2-}$, should be essentially similar to that of the monoanion. Based on the structural data of the related redox couple $[V(hida)_2]^{2-/1-}$ ($H_3hida = N$ -hydroxyl-2,2'-imino diacetic acid),²¹ it was hypothesised that in the V(IV)/V(V) transformation only the V–O_(carboxylate) (VO1, VO5, VO6, VO10) distances would have been altered, while the V–N and V–O distances (VO3 and VO8) of the hydroxylimine group would have to remain substantially invariant.

As a matter of fact, the recent solution of the crystal structure of reduced Amavadin (as the calcium salt $[\text{Ca}(\text{H}_2\text{O})_5][V(hidpa)_2]$) fully confirmed the prevision in that the V(IV) dianion possesses the same geometry of the V(V) monoanion and the bond lengths follow the expected trend, Table 5.²²

Table 5 Comparison between the bond distances (in Å) of the redox couple $[V(hidpa)_2]^{2-/1-}$ ^{19,22}

Bond	$[V(hidpa)_2]^-$	$[V(hidpa)_2]^{2-}$
V–O1	1.99	2.03
V–O5	1.96	2.03
V–O6	1.98	2.04
V–O10	1.94	2.07
V–O3	1.93	1.94
V–O8	1.97	1.96
V–N1	2.02	2.00
V–N2	2.00	1.98

2 CHROMIUM COMPLEXES

The commonest oxidation states of chromium in its complexes are III and II (electronic configuration d^3 and d^4 , respectively), even if Cr(I)-d⁵ complexes are known.

Cr(III) complexes, in particular those of the above discussed polypyridine ligands phen, bipy, terpy usually possess a considerably distorted octahedral geometry.^{23,24} As illustrated in Figure 14, $[Cr(terpy)_2]^{3+}$ ²⁵ displays four successive reversible one-electron reduction processes.²⁵

The first three steps have been tentatively assigned to the sequence Cr(III)/Cr(II)/Cr(I)/Cr(0), while the fourth has been assigned as ligand centred. However, in judging the remarkable redox ability of these complexes one must bear in mind the comments made previously concerning the reciprocal redox ability of the metal ion and the polypyridine ligands.

Table 6 compiles the electrode potentials of the chromium complexes with phenantroline, bipyridine and terpyridine ligands, respectively^{25–27}.

It is clear that the Cr(III)/Cr(II) reduction becomes progressively more difficult on passing from terpyridine to bipyridine to phenantroline.

In the absence of crystallographic data one cannot discuss in detail the structural variations triggered by these reduction processes, but their electrochemical reversibility, or quasireversibility, suggests that there are not significant structural rearrangements.

As a further confirmation of the extended redox aptitude of polypyridine ligands, Figure 15 shows the cyclic voltammetric behaviour of the heteroleptic chromium(III) complex with 2,2'-6',2'',6'',2'''-quaterpyridine (qpy), together with its molecular structure.²⁸

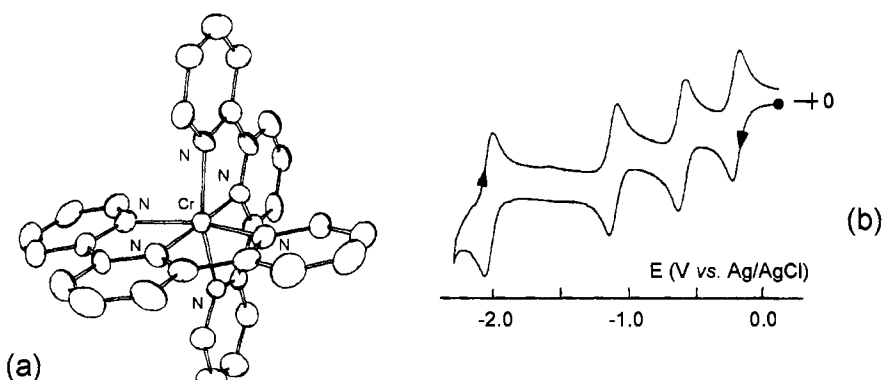


Figure 14 (a) X-Ray structure of $[Cr(terpy)_2]^{3+}$ ($[ClO_4]^-$ counteranion). Average $Cr-N$ distance = 2.03 Å; average $N-Cr-N$ angle = 78.7°. (b) Cyclic voltammogram recorded at a dropping mercury electrode in a MeCN solution of $[Cr(terpy)_2][ClO_4]_3$. Scan rate 0.1 V s⁻¹

Table 6 Formal electrode potentials (V vs. SCE) for the redox processes exhibited by polypyridine complexes of chromium

Complex	$E_{3+/2+}^{\circ'}$	$E_{2+/+}^{\circ'}$	$E_{+/0}^{\circ'}$	Solvent
$[\text{Cr}(\text{terpy})_2]^{3+}$	-0.15	-0.56	-1.33	MeCN
	-0.41			H_2O
$[\text{Cr}(\text{bipy})_3]^{3+}$	-0.25	-0.75	-1.32	MeCN
	-0.50			H_2O
$[\text{Cr}(\text{phen})_3]^{3+}$	-0.28	-0.77	-1.33	MeCN
	-0.50			H_2O

It undergoes three successive one-electron reductions ($E_{+/0}^{\circ'} = -0.69 \text{ V}$ vs. SCE; $E_{0/-}^{\circ'} = -1.14 \text{ V}$; $E_{-/-2}^{\circ'} = -1.48 \text{ V}$), all possessing features of chemical reversibility.

The first reduction, which is likely centred on the Cr(III) \rightarrow Cr(II) process, has substantial electrochemical reversibility ($\Delta E_p = 70 \text{ mV}$, at 0.2 V s^{-1}), thus suggesting that no significant structural rearrangements accompany such redox step. Unfortunately, no further investigations have been carried out to clarify whether the successive reductions are centred on the metal or on the ligand.

We turn our attention now to a few Cr(III) complexes with mixed ligands.

Figure 16 shows the octahedral geometry of two chromium complexes with N_2O_4 coordination. The first with the Schiff base [N,N -ethylene-bis(salicylideneimine)] + two water molecules, $[\text{Cr}(\text{salen}) (\text{H}_2\text{O}_2)_2]^+$,²⁹ the second with two molecules of [2,2'-bipyridine-6-phenolate], $[\text{Cr}\{6-(2-\text{C}_6\text{H}_4\text{O})\text{bipy}\}_2]^+$.³⁰

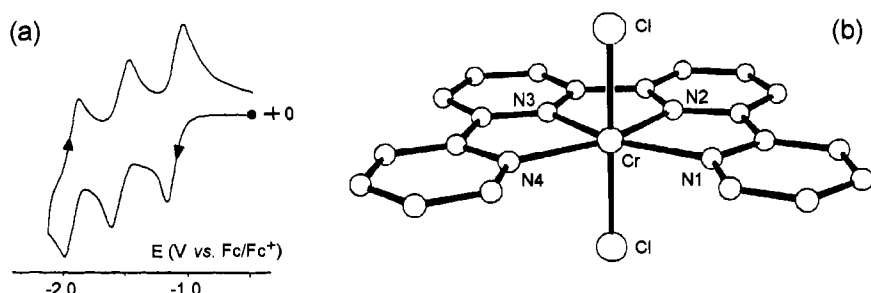


Figure 15 (a) Cyclic voltammogram recorded at a platinum electrode in a MeCN solution of $[\text{Cr}(\text{qpy})\text{Cl}_2]\text{Cl}$. Scan rate 0.2 V s^{-1} . (b) X-Ray structure of the monocation $[\text{Cr}(\text{qpy})\text{Cl}_2]^+$. Average bond lengths: $\text{Cr}-\text{Cl} = 2.28 \text{ \AA}$; $\text{Cr}-\text{N}1 = \text{Cr}-\text{N}4 \approx 2.10 \text{ \AA}$; $\text{Cr}-\text{N}2 = \text{Cr}-\text{N}3 \approx 2.00 \text{ \AA}$

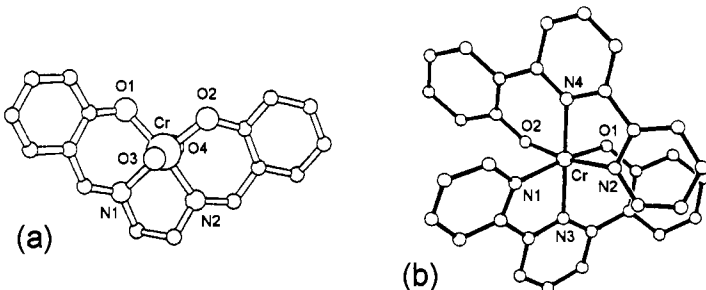


Figure 16 X-Ray structure of: (a) $[\text{Cr}(\text{salen})(\text{H}_2\text{O})_2]^+$. Bond lengths: $\text{Cr}-\text{N} = 2.00 \text{ \AA}$; $\text{Cr}-\text{O}1 = 1.92 \text{ \AA}$; $\text{Cr}-\text{O}2 = 1.95 \text{ \AA}$; $\text{Cr}-\text{O}3 = 2.08 \text{ \AA}$; $\text{Cr}-\text{O}4 = 1.92 \text{ \AA}$; $\text{Cl}-\text{C}2 = 1.52 \text{ \AA}$. (b) $[\text{Cr}(\text{hydroxyphenylbpy})_2]^+$. Bond lengths: $\text{Cr}-\text{N}1 = \text{Cr}-\text{N}2 \approx 2.04 \text{ \AA}$, $\text{Cr}-\text{N}3 = \text{Cr}-\text{N}4 \approx 2.06 \text{ \AA}$, $\text{Cr}-\text{O}1 = \text{Cr}-\text{O}2 \approx 1.89 \text{ \AA}$

As illustrated in Figure 17, both complexes display chemically reversible $\text{Cr}^{\text{III}}/\text{Cr}^{\text{II}}$ reduction processes ($[\text{Cr}(\text{salen})(\text{H}_2\text{O})_2]^{+/\text{0}}$: $E^{\text{o}/\text{i}} = -1.30 \text{ V vs. SCE}$; $[\text{Cr}(\text{hydroxyphenylbpy})_2]^{+/\text{0}}$: $E^{\text{o}/\text{i}} = -1.00 \text{ V vs. SCE}$).^{29,30}

The discussion up to this point might lead one to believe that the $\text{Cr}(\text{III})/\text{Cr}(\text{II})$ redox change is always reversible; this is not really the case. The monoanion $[\text{Cr}^{\text{III}}(\text{salen})(\text{ox})]^-$ ($\text{ox} = \text{oxalate dianion}$) illustrated in Figure 18 constitutes an example of such a situation. At variance with $[\text{Cr}(\text{salen})(\text{H}_2\text{O})_2]^+$, in which the $\text{Cr}(\text{III})$ ion achieves hexacoordination through two water oxygen atoms in axial position, here the hexacoordination is reached through the two oxalate oxygen atoms in equatorial positions.³¹

As shown in Figure 19, the $\text{Cr}^{\text{III}}/\text{Cr}^{\text{II}}$ reduction of this complex is clearly irreversible.³¹

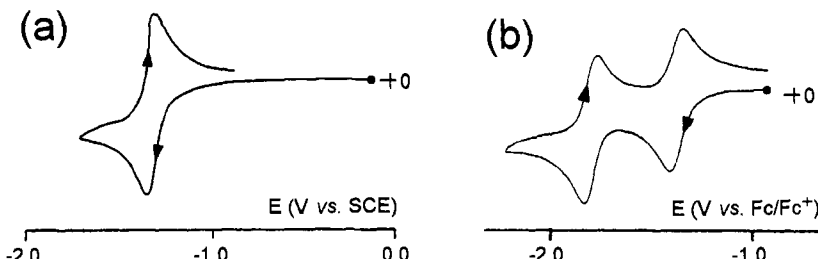


Figure 17 Cyclic voltammograms recorded at a platinum electrode in: (a) dmsol solution of $[\text{Cr}(\text{salen})(\text{H}_2\text{O})_2]\text{Cl}$; scan rate 0.1 V s^{-1} ; (b) MeCN solution of $[\text{Cr}\{6-(2-\text{C}_6\text{H}_4\text{O})\text{bipy}\}_2]\text{[PF}_6\text{]}$; scan rate 0.2 V s^{-1}

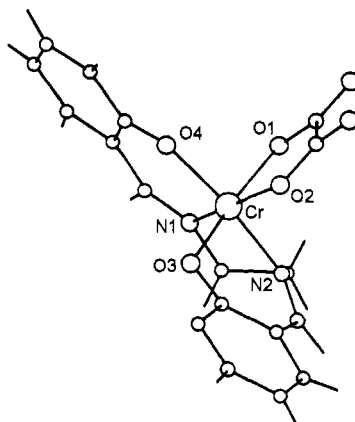


Figure 18 X-Ray structure of $[Cr(salen)(ox)]^-$. Bond lengths: $Cr-O1 = 2.02 \text{ \AA}$; $Cr-O2 = 1.99 \text{ \AA}$; $Cr-O3 = 1.92 \text{ \AA}$; $Cr-O4 = 1.94 \text{ \AA}$; $Cr-N1 = 2.03 \text{ \AA}$; $Cr-N2 = 2.01 \text{ \AA}$

A plausible explanation of the observed irreversibility may lie in the following. Given that the addition of one electron generates the Cr(II) ion which has a greater ionic radius than the original Cr(III) (0.89 \AA vs. 0.63 \AA), in those cases (like the original) in which the molecular assembly is such that there are severe constraints at the metal site environment, any increase in the metal size would result in a rupturing of the molecule. It is evident that such a situation will lead to irreversible electron transfers.

This kind of argument may also be invoked for some Cr(III)-azamacrocyclic complexes. In this regard, it is noted that the *macrocyclic effect* (which is essentially an enhanced *chelate effect*) stabilizes metal ions entrapped in the cavity formed by macrocyclic organic ligands

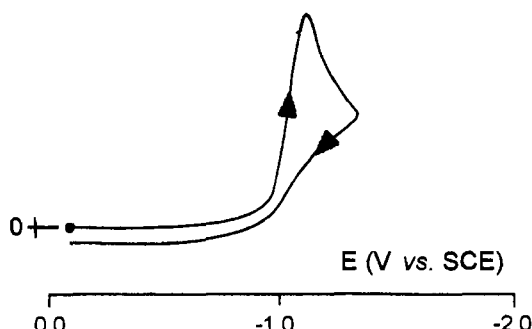
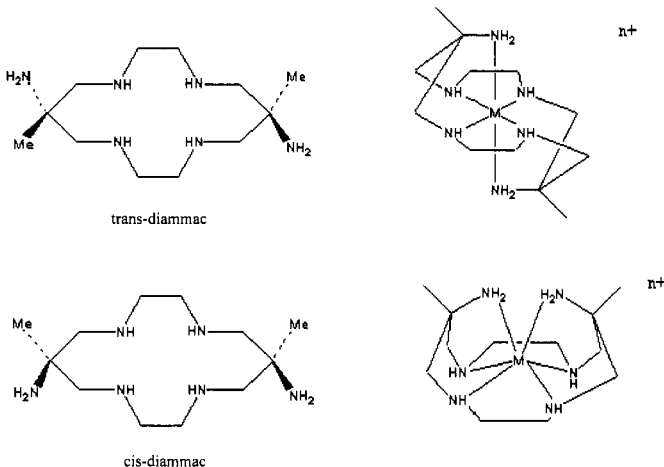


Figure 19 Cyclic voltammogram recorded at a platinum electrode in a dmso solution of $[Cr(salen)(ox)]^-$. Scan rate 0.1 V s^{-1}

having N, S or O donor atoms. Moreover, one must bear in mind that the size of the macrocycle is an important factor in determining the coordination selectivity of the metal ions, since the metal ions too have well-defined sizes. Hence, the metal ion and the ligand cavity must possess complementary sizes.

The macrocyclic ligand 6,13-diamino-6,13-dimethyl-1,4,8,11-tetraazacyclotetradecane (diammac), illustrated in Scheme 5 for the two *cis* and *trans* conformations, is properly suited to fulfil the requirement of six donor atoms to satisfy the Cr(III) hexacoordination. In fact, in addition to the four central N atoms it has two amine groups (a sort of head and tail, from which the name *scorpiands* is given to these ligands).



Scheme 5

As seen, the two isomers result in structurally different metal complexes. In fact, in the octahedral *trans* complex, the two NH_2 groups are positioned axially, whereas in the *cis* complex the two NH_2 groups are positioned in close proximity imposing a trigonal prismatic geometry.

In fact, Figure 20 shows the crystal structure of the two Cr(III) complexes.^{32,33}

In aqueous solution (pH 10) the *trans* complex displays a $\text{Cr(III)} \rightarrow \text{Cr(II)}$ reduction process ($E^{\circ'} = -1.50 \text{ V}$ vs. SCE) quasireversible in character and complicated by a relatively slow degradation of the electrogenerated Cr(II) complex ($\Delta E_p = 150 \text{ mV}$ and $i_{pa}/i_{pc} = 0.7$, at 0.1 V s^{-1}).³³

Conversely, under the same experimental conditions, the *cis* complex undergoes a completely irreversible reduction ($E_p = -1.35 \text{ V}$), indicating an extreme instability of the corresponding Cr(II) complex.³³

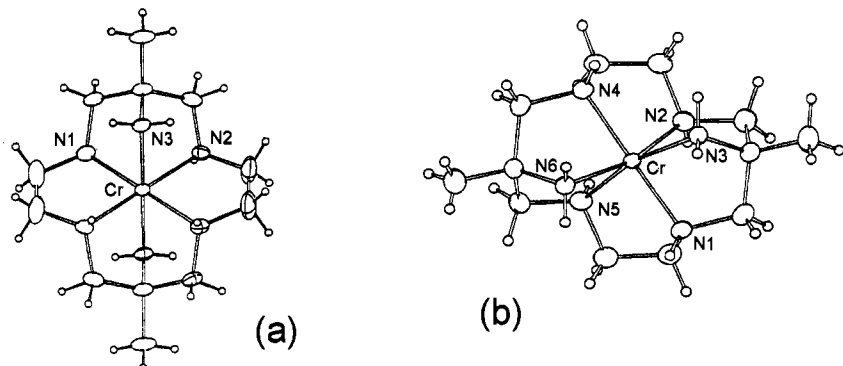


Figure 20 *X-Ray structures of: (a) $[Cr(\text{trans-diammac})]^{3+}$. Bond lengths: $Cr-N1 = Cr-N2 \approx 2.04 \text{ \AA}$; $Cr-N3 = 2.07 \text{ \AA}$; (b) $[Cr(\text{cis-diammac})]^{3+}$. Bond lengths: $Cr-N1 = Cr-N4 \approx 2.05 \text{ \AA}$; $Cr-N3 = Cr-N5 = Cr-N6 \approx 2.06 \text{ \AA}$; $Cr-N2 \approx 2.07 \text{ \AA}$*

A possible explanation for the different behaviour could derive from the Cr(III)-hosting cavity being different in the two cases. Recalling that the ionic radius of the Cr(II) ion is much greater than that of the Cr(III), one might argue that in the trigonal prismatic *cis*-diammac complex the structural constraints are such that an enlargement of the cavity to host the electrogenerated Cr(II) ion, even for a very short time, is impossible. In contrast, this may be allowed, at least in a transient manner, in the octahedral *trans*-diammac complex.

A further Cr(III) complex to be considered is that formed by the macrobicyclic ligand 1,8-diamino-3,6,10,13,16,19-hexaazabicyclo[6.6.6.]eicosane, which is the founder member of a series of ‘cage’ ligands having assigned to them a rather funereal terminology. In fact, in abbreviated form it is called *diamsar*, from diamino-sarcophagine. The octahedral geometry of the molecule is illustrated in Figure 21.³⁴

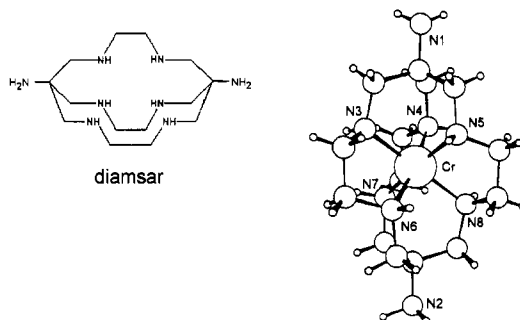


Figure 21 *X-Ray structure of $[Cr(\text{diamsar})]^{3+}$. Average $Cr-N$ bond length: 2.07 \AA*

In aqueous solution it exhibits a chemically reversible $\text{Cr(III)} \rightarrow \text{Cr(II)}$ reduction ($E^{\circ'} = -1.35 \text{ V}$; $\Delta E_p = 70 \text{ mV}$, at 0.05 V s^{-1}).³⁴ This indicates that, contrary to the previous scorpions, the sarcophagine cavity is sufficiently large (or the molecular structure sufficiently flexible) to host the electrogenerated Cr(II) ion without significant structural strains.

3 MANGANESE COMPLEXES

The commonest oxidation states of manganese in its complexes are III and II (electronic configuration d^4 and d^5 , respectively) but, as will be seen later, Mn(IV) (d^3) complexes can also be stable. The IV oxidation state of manganese complexes though is rather puzzling. In fact, until a few years ago it was relatively uncommon in coordination chemistry, despite the fact that Mn(IV) complexes are involved in the photosynthetic oxidation of water and that manganese is present as Mn(IV) in the widely diffuse manganese mineral pyrolusite (MnO_2).

We will examine here exclusively octahedral manganese complexes in that they have been more extensively characterized. It is noted though that there exists a large number of *pentacoordinate* complexes with trigonal bipyramidal or square pyramidal geometry.

The first manganese complex to be considered is the tris(pyrazolyl)-borate-Mn(IV) (d^3) dication $[\text{Mn}(\text{Tp}^*)_2]^{2+}$, ($\text{Tp}^* = [\text{HB}(3,5\text{-Me}_2\text{pz})_3]^-$), which possesses a N_6 coordination, Figure 22.³⁵

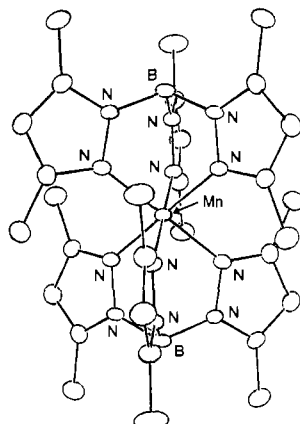


Figure 22 X-Ray structure of $[\text{Mn}(\text{Tp}^*)_2]^{2+}$. Average Mn-N bond length: 1.97 \AA

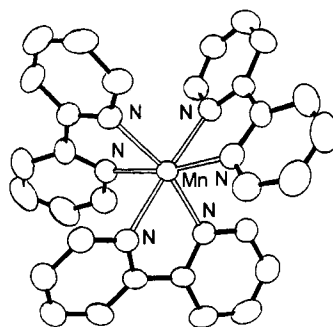


Figure 23 X-Ray structure of $[Mn(\text{bipy})_3]^{2+}$ ($[\text{ClO}_4]^-$ counteranion). Average Mn–N bond length: 2.24 \AA

The oxidation state of the complex is confirmed as Mn(IV) by the value of its magnetic susceptibility ($\mu_{\text{eff}} = 3.81 \mu_B$), resulting from the d^3 electronic configuration. The complex results easily reducible in that it displays in MeCN solution a chemically reversible Mn(IV)/Mn(III) reduction at a very high potential ($E^\circ' = +1.35 \text{ V}$).³⁵

The Mn(II) polypyridine complexes $[\text{Mn}(\text{phen})_3]^{2+}$, $[\text{Mn}(\text{bipy})_3]^{2+}$ and $[\text{Mn}(\text{terpy})_2]^{2+}$ are further examples of N₆ coordination. As an example, Figure 23 shows the considerably distorted octahedral structure of the $[\text{Mn}(\text{bipy})_3]^{2+}$.³⁶

$[\text{Mn}(\text{phen})_3]^{2+}$ possesses a similar distorted molecular structure.³⁷

The $[\text{Mn}(\text{bipy})_3]^{2+}$ complex has $\mu_{\text{eff}} = 5.98 \mu_B$, whereas the $[\text{Mn}(\text{terpy})_2]^{2+}$ complex has $\mu_{\text{eff}} = 6.02 \mu_B$. Both the values indicate an octahedral geometry with a high spin Mn(II)-d⁵ electronic configuration.

All the three polypyridyl complexes display the reversible reduction sequence 2+/+/0. The relative potential values are reported in Table 7. As far as the nature of such redox changes is concerned, it is important to recall the ambiguity that exists in attributing metal-centred or ligand-centred redox processes for metal-polypyridine complexes.

Table 7 Formal electrode potentials (V vs. SCE) for the redox processes exhibited by polypyridyl complexes in acetonitrile solution

Complex	$E^\circ'_{3+/2+}$	$E^\circ'_{2+/+}$	$E^\circ'_{+/0}$	Reference
$[\text{Mn}(\text{bipy})_3]^{3+}$	+ 1.36 ^a	-1.36	-1.54	38
$[\text{Mn}(\text{phen})_3]^{3+}$	+ 1.32 ^a			38
$[\text{Mn}(\text{terpy})_2]^{3+}$	+ 1.28	-1.11	-1.45	39

^a Accompanied by chemical complications (see text).

It is worthwhile emphasizing that there are important differences between the $2+/3+$ oxidation of the $[\text{Mn}(\text{terpy})_2]^{2+}$ complex, which is reversible on the time scale of cyclic voltammetry, and that of the $[\text{Mn}(\text{phen})_3]^{2+}$ and $[\text{Mn}(\text{bipy})_3]^{2+}$ complexes, which is complicated by following chemical reactions. A study of these chemical complications has shown that oxidation of the $[\text{Mn}(\text{phen})_3]^{2+}$ and $[\text{Mn}(\text{bipy})_3]^{2+}$ complexes leads to the formation of the oxo-dimers $[\text{Mn}_2\text{O}_2(\text{phen})_4]^{n+}$ and $[\text{Mn}_2\text{O}_2(\text{bipy})_4]^{n+}$ ($n = 3, 4$), respectively. Figure 24 shows the molecular structures of the dimers with $n = 3$.^{40,41}

It is interesting to note that these complexes are ‘mixed-valent’ $\text{Mn}^{\text{III}}\text{Mn}^{\text{IV}}$ complexes. Based on the relative structural data [the bond distances of the MnA atom are shorter than those of MnB], it has been concluded that in $[\text{Mn}_2\text{O}_2(\text{bipy})_4]^{3+}$ one of the manganese ions is in the oxidation state IV [Mn(B)] and the other in the oxidation state III [Mn(A)]. Hence, the complex would have to be classified as a mixed-valent derivative with localized charge (Robin–Day Class I). Conversely, the two manganese sites are identical in $[\text{Mn}_2\text{O}_2(\text{phen})_4]^{n+}$, from which one can infer that the charge is delocalized over the two centres (Robin–Day Class III).

The two oxo-dimers have been indicated as $[\text{Mn}_2\text{O}_2(\text{phen})_4]^{n+}$ and $[\text{Mn}_2\text{O}_2(\text{bipy})_4]^{n+}$ ($n = 3, 4$), respectively, because they display reversibility in the $3+/4+$ redox change (in MeCN: $E^{\circ'} = +1.34$ V, vs. SCE, for $[\text{Mn}_2\text{O}_2(\text{phen})_4]^{4+/3+}$; $E^{\circ'} = +1.33$ V, for $[\text{Mn}_2\text{O}_2(\text{bipy})_4]^{4+/3+}$).⁴² As an example, Figure 25 shows the cyclic voltammetric response of $[\text{Mn}_2\text{O}_2(\text{phen})_4]^{3+}$ in acetonitrile solution.

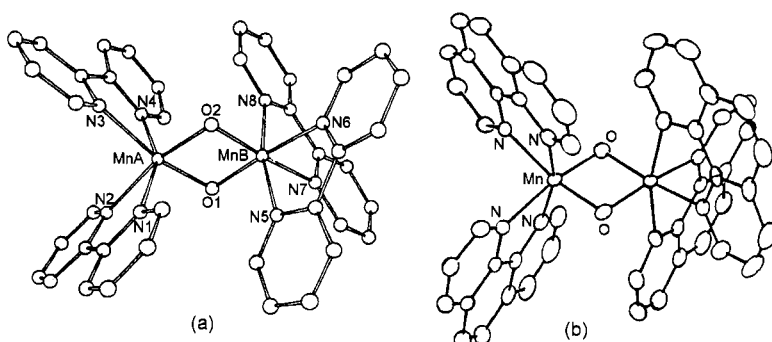


Figure 24 X-Ray structures of: (a) $[\text{Mn}_2\text{O}_2(\text{bipy})_4]^{3+}$. Average bond lengths: $\text{MnA}-\text{O} = 1.89 \text{ \AA}$; $\text{MnA}-\text{N}1 \approx \text{MnA}-\text{N}4 = 2.21 \text{ \AA}$; $\text{MnA}-\text{N}2 \approx \text{MnA}-\text{N}3 = 2.13 \text{ \AA}$; $\text{MnB}-\text{O} = 1.81 \text{ \AA}$; $\text{MnB}-\text{N}5 \approx \text{MnB}-\text{N}8 = 2.01 \text{ \AA}$; $\text{MnB}-\text{N}6 \approx \text{MnB}-\text{N}7 = 2.08 \text{ \AA}$; (b) $[\text{Mn}_2\text{O}_2(\text{phen})_4]^{3+}$. Average bond lengths: $\text{Mn}-\text{N}_{(\text{equatorial})} = 2.11 \text{ \AA}$; $\text{Mn}-\text{N}_{(\text{axial})} = 2.13 \text{ \AA}$; $\text{Mn}-\text{O} = 1.85 \text{ \AA}$

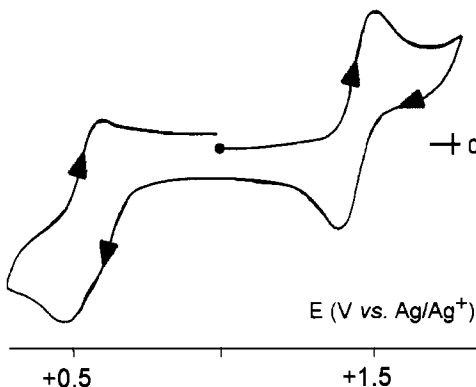


Figure 25 Cyclic voltammogram recorded in a MeCN solution of $[\text{Mn}_2\text{O}_2(\text{phen})_4]^{3+}$. Scan rate 0.1 V s^{-1}

It is evident that the $3+/4+$ oxidation is reversible. The molecular structure of the tetracation $[\text{Mn}_2\text{O}_2(\text{phen})_4]^{4+}$ has been solved.⁴¹ The coordination geometry around each Mn(IV) site is still virtually identical, even if there are significant differences in the bond lengths compared to those of the trication $[\text{Mn}_2\text{O}_2(\text{phen})_4]^{3+}$ ($\text{Mn}-\text{N}_{(\text{equatorial})} = 2.08 \text{ \AA}$; $\text{Mn}-\text{N}_{(\text{axial})} = 2.01 \text{ \AA}$; $\text{Mn}-\text{O} = 1.80 \text{ \AA}$).

It is noted that the redox and EPR spectroscopic characteristics of these dimeric manganese complexes have led them to acquire some importance in the formulation of inorganic models able to mimic the manganese centre involved in the photosynthetic oxidation of water (discussed in the following section).

Another octahedral Mn(IV) complex (d^3 , $\mu_{\text{eff}} = 4.05 \mu_B$) is the derivative with the Schiff base 1,8-bis(2-hydroxylbenzamide)-3,6-diazaoctane, MnL, with N_4O_2 coordination. Its solid state structure is shown in Figure 26.⁴³

This complex in methanol exhibits a chemically reversible, but electrochemically quasireversible, reduction ($E^{\circ'} = +0.01 \text{ V}$; $\Delta E_p = 100 \text{ mV}$ at 0.1 V s^{-1}).⁴³

Interesting redox activity is displayed by the N_4Cl_2 coordinated Mn(II) complex of the macrocycle 4,10-dimethyl-1,4,7,10-tetraazabicyclo[5.5.2]tetradecane, $[\text{MnL}'\text{Cl}_2]$, the distorted molecular structure of which is illustrated in Figure 27.⁴⁴

In agreement with a high-spin Mn(II)- $d^5(t_{2g}^3e_g^2)$ electronic configuration, it has $\mu_{\text{eff}} = 5.93 \mu_B$. As illustrated in Figure 28, this complex displays two reversible one-electron oxidations corresponding to the Mn(II)/Mn(III)/Mn(IV) sequence ($E^{\circ'} = +0.23 \text{ V}$ and $+0.99 \text{ V}$ vs. SCE, respectively).

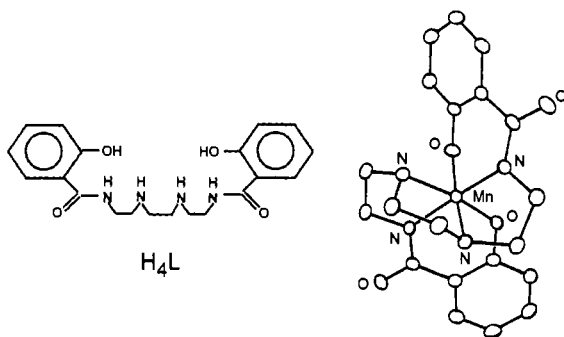


Figure 26 *X-Ray structure of complex $[\text{MnL}]$. Average bond lengths: $\text{Mn}-\text{N}_{(\text{amide})} = 1.95 \text{ \AA}$; $\text{Mn}-\text{N}_{(\text{amine})} = 2.04 \text{ \AA}$; $\text{Mn}-\text{O} = 1.84 \text{ \AA}$*

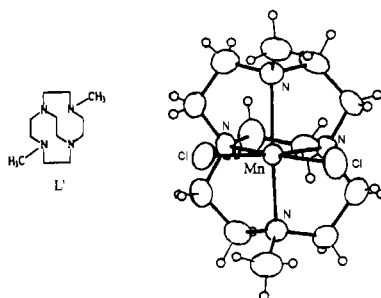


Figure 27 *X-Ray structure of complex $[\text{MnL}'\text{Cl}_2]$. Average bond lengths: $\text{Mn}-\text{N} = 2.32 \text{ \AA}$; $\text{Mn}-\text{Cl} = 2.43 \text{ \AA}$*

Reducing further the number of nitrogen atoms in favour of the oxygen atoms in the ligand, let us consider the N_3O_3 -coordinate octahedral manganese complex with the tris[2-(salicylideneamino)ethyl]-amine ligand $\text{N}[\text{CH}_2\text{CH}_2\text{N}=\text{CH-C}_6\text{H}_3(\text{Cl})(\text{OH})]_3$, Figure 29.⁴⁵

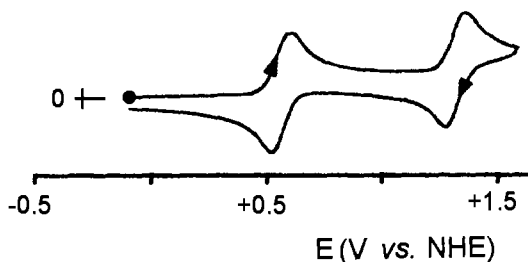


Figure 28 *Cyclic voltammogram recorded in a MeCN solution of $[\text{MnL}'\text{Cl}_2]$*

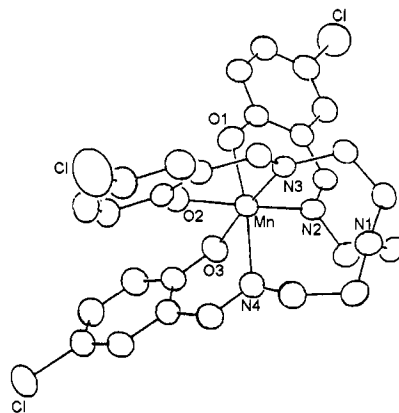


Figure 29 X-Ray structure of $[Mn\{N(CH_2CH_2N=CH-C_6H_3-5-Cl-2-O)_3\}]\cdot MeOH$. Average bond lengths: $Mn-O_2 = Mn-O_3 = 1.90 \text{ \AA}$; $Mn-N_2 \approx Mn-N_3 = 2.04 \text{ \AA}$; $Mn-O_1 = 2.01 \text{ \AA}$; $Mn-N_4 = 2.37 \text{ \AA}$

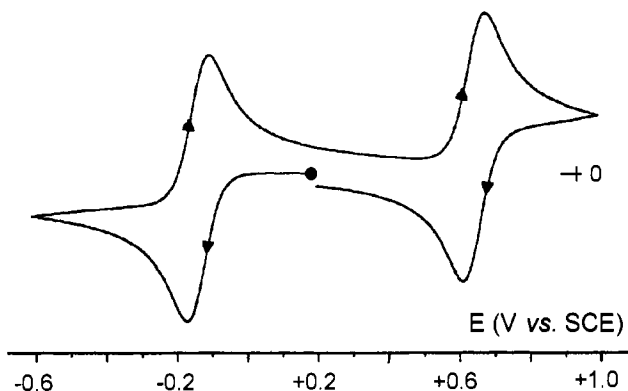
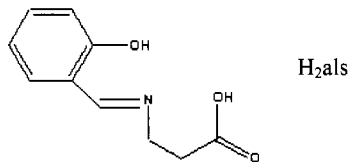


Figure 30 Cyclic voltammogram recorded at a platinum electrode in a MeCN solution of $[Mn\{N(CH_2CH_2N=CH-C_6H_3-5-Cl-2-O)_3\}]$

The magnetic moment of the complex ($\mu_{\text{eff}} = 4.82 \mu_B$) confirms that it is a Mn(III)-d⁴ high spin ($t_{2g}^3 e_g^1$) ion.

As shown in Figure 30, this complex undergoes both a reversible oxidation to the corresponding Mn(IV) complex ($E^{\circ'} = +0.65 \text{ V}$) and a reversible reduction to the corresponding Mn(II) complex ($E^{\circ'} = -0.13 \text{ V}$).⁴⁵

The next manganese complex to be considered is that with the Schiff base ligand shown in Scheme 6.



Scheme 6

The magnetic moment of $[\text{Mn}(\text{als})_2]$ ($\mu_{\text{eff}} = 3.96 \mu_B$) indicates its Mn(IV) ($d^3-t_{2g}^3$) oxidation state. The essentially regular octahedral geometry of this N_2O_4 coordinated complex is illustrated in Figure 31.⁴⁶

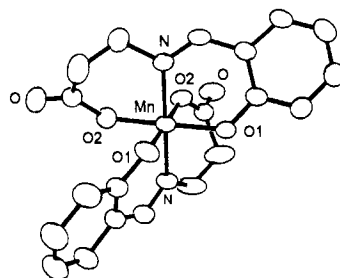


Figure 31 X-Ray structure of $[\text{Mn}^{IV}(\text{als})_2]$. Bond lengths: $\text{Mn}-\text{N} = 2.00 \text{ \AA}$; $\text{Mn}-\text{O1}_{(\text{phenolate})} = 1.86 \text{ \AA}$; $\text{Mn}-\text{O2}_{(\text{carboxylate})} = 1.91 \text{ \AA}$

Such a Mn(IV) complex in methanol undergoes a chemically reversible and electrochemically quasireversible one-electron reduction to the corresponding Mn(III) monoanion ($E^{\circ'} = +0.50 \text{ V}$; $\Delta E_p = 80 \text{ mV}$, at 0.05 Vs^{-1}), followed by a second irreversible reduction to Mn(II) ($E_p = -0.22 \text{ V}$), Figure 32a.

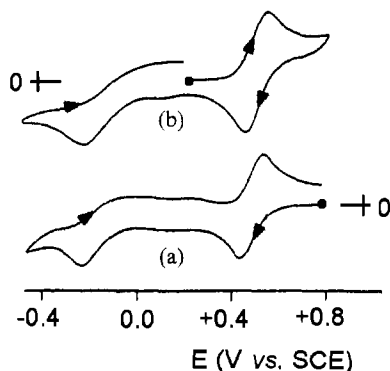


Figure 32 Cyclic voltammograms recorded at a platinum electrode in a CH_3OH solution of: (a) $[\text{Mn}^{IV}(\text{als})_2]$; (b) $[\text{Mn}^{III}(\text{als})_2]^+$. Scan rate 0.05 V s^{-1}

Figure 32b shows that the corresponding Mn(III) complex, $[\text{Mn}(\text{als})_2]^-$, gives rise to an electrochemical response quite complementary to that of $[\text{Mn}(\text{als})_2]$, thus confirming the chemical reversibility of the $[\text{Mn}(\text{als})_2]/[\text{Mn}(\text{als})_2]^-$ redox change. As a matter of fact the monoanion $[\text{Mn}(\text{als})_2]^-$ has been isolated and characterized. It has a magnetic moment of $4.95 \mu_B$, which indicates its high spin configuration ($d^4-t_{2g}^3e_g^1$). The X-ray structure reveals that the interatomic distances of this complex are on average longer, by about 0.1 \AA , compared to those of the corresponding Mn(IV) complex. In addition the distances between the manganese atom and identical bound atoms are not equivalent; so one finds: $\text{Mn}-\text{N} = 2.06 \text{ \AA}$ and 1.98 \AA ; $\text{Mn}-\text{O}_{(\text{phenolate})} = 2.05 \text{ \AA}$ and 1.86 \AA ; $\text{Mn}-\text{O}_{(\text{carboxylate})} = 2.24 \text{ \AA}$ and 1.93 \AA .⁴⁷

Figure 33 shows the octahedral geometry of the Mn(II) complex with the ligand dithio-methyl-triazene-1-oxide, $[\text{MeN}(\text{O})\text{N}-\text{NHC}_6\text{H}_4\text{S}]_2(\text{CH}_2)_2$. Because of the presence of different $\text{N}_2\text{O}_2\text{S}_2$ chelating atoms the complex is considerably distorted.⁴⁸

In agreement with the high spin configuration ($d^5-t_{2g}^3e_g^2$), this Mn(II) complex has $\mu_{\text{eff}} = 5.86 \mu_B$. In acetonitrile, it exhibits a chemically reversible oxidation ($E^\circ' = +0.37 \text{ V vs. SCE}$). The corresponding monocation $[\text{Mn}(\{\text{MeN}(\text{O})\text{N}-\text{NC}_6\text{H}_4\text{S}\}_2(\text{CH}_2)_2)]^+$ has been isolated. Its magnetic moment ($\mu_{\text{eff}} = 4.86 \mu_B$) indicates a high spin Mn(III) derivative ($d^4-t_{2g}^3e_g^1$). A comparison of the bond lengths of the monocation with those of the neutral precursor indicates that the electron removal causes a shortening of about 0.1 \AA of the $\text{Mn}-\text{N}$ and $\text{Mn}-\text{O}$ distances and of about 0.2 \AA of the $\text{Mn}-\text{S}$ distances.

Finally, it is noted that, unexpectedly, the Mn(IV) complex with 2-hydroxyisobutyric acid, $[\text{Mn}\{\text{O}-\text{C}(\text{CH}_3)_2\text{C}(\text{O})\text{O}\}_3]^{2-}$, having a MnO_6 coordination, Figure 34, is unable of being reduced to Mn(III).⁴⁹

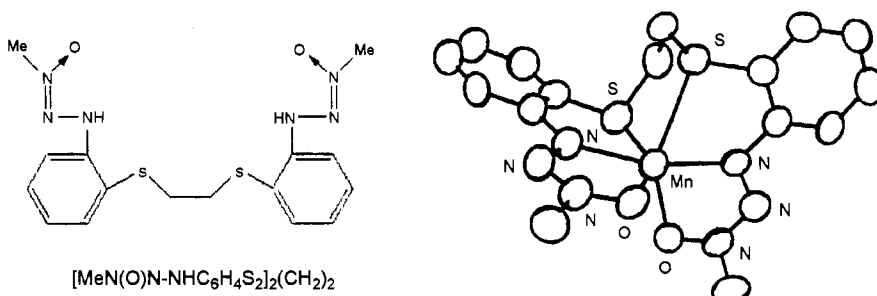


Figure 33 X-Ray structure of $[\text{Mn}(\{\text{MeN}(\text{O})\text{N}-\text{NC}_6\text{H}_4\text{S}\}_2(\text{CH}_2)_2)]$. Average bond lengths: $\text{Mn}-\text{O} = 2.12 \text{ \AA}$; $\text{Mn}-\text{N} = 2.14 \text{ \AA}$; $\text{Mn}-\text{S} = 2.70 \text{ \AA}$

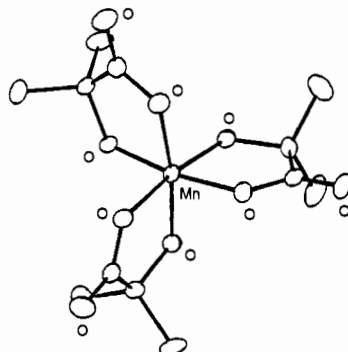


Figure 34 X-Ray structure of the dianion $[Mn\{O-C(CH_3)_2C(O)O\}_3]^{2-}$. Average bond lengths: $Mn-O_{(hydroxo)} = 1.84 \text{ \AA}$; $Mn-O_{(carboxylate)} = 1.93 \text{ \AA}$

3.1 The Role of Manganese Complexes in Photosynthesis

A discussion of the redox capacity of manganese complexes cannot neglect a short mention of one of the most active areas of research in bioinorganic chemistry: the determination of the structure and function of the *Water Oxidizing Centre* (WOC) in *photosystem II* (*PSII*). This is the active site responsible for the thermodynamically unfavoured oxidation of water to oxygen in *photosynthesis*. Figure 35 shows a schematic representation of the photosynthetic process, a crucial element in the exploitation of solar energy enabling the development of life on Earth in the form of green plants, algae and some bacteria.⁵⁰

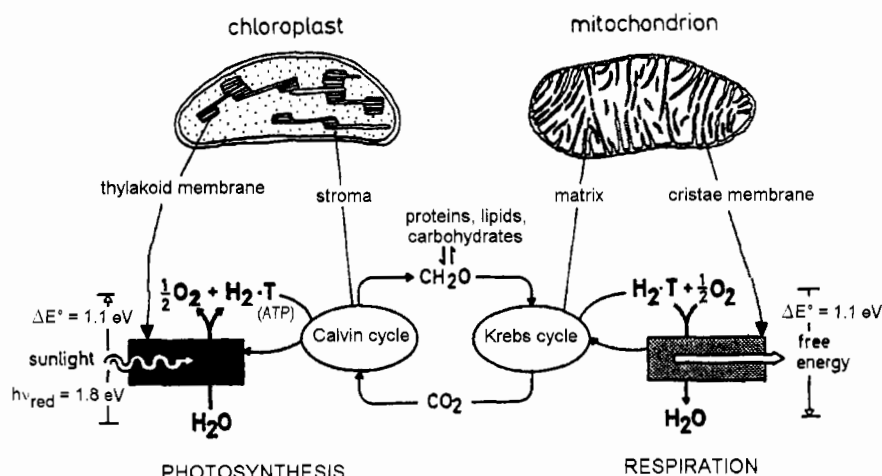
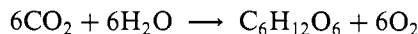


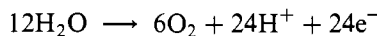
Figure 35 Schematic representation of the bioenergetic mechanisms which govern the life cycles in green plants

The overall process occurring in photosynthesis is:

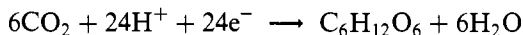


In reality, it results from the following two thermodynamically disfavoured half-reactions:

- oxidation of water to dioxygen:



- reduction of carbon dioxide to carbohydrates:



As represented in Figure 36, the trigger of these half-reactions is light, or photochemical reactions brought on by radiant energy through two biological assemblies called *photosystem I* (PS I) and *photosystem II* (PS II), respectively.

In particular, as illustrated in Figure 37, the absorption of light by chlorophylls (the green pigment of the vegetable kingdom; Scheme 7) triggers a sequence of oxidation–reduction reactions inside the cell organelles called *chloroplasts* making use of a series of electron carriers (*e.g.* cytochromes, iron–sulfur proteins, blue copper proteins, *etc.*; see Chapter 12) that lead to the reduction of CO₂ in photosystem I (which selectively absorbs electromagnetic radiation of wavelength of 700 nm, from which it is also defined as *P-700*) and

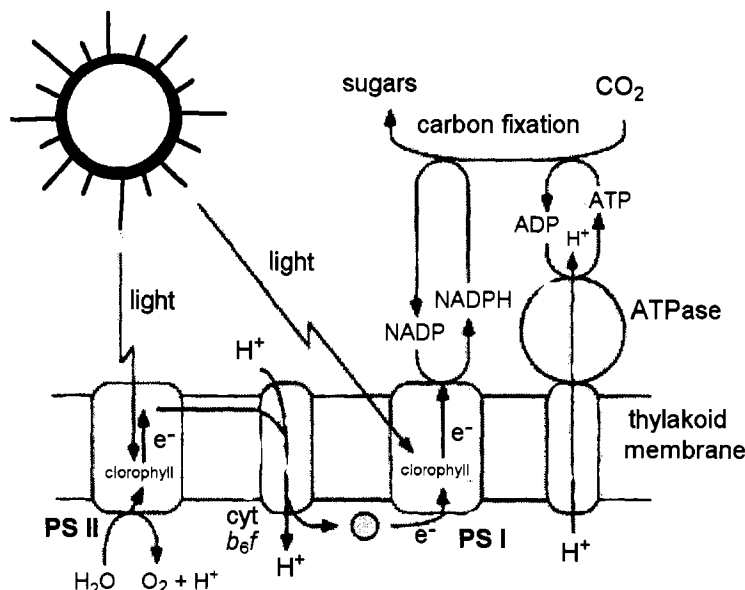


Figure 36 A panoramic view of the photosynthetic pathway in green plants

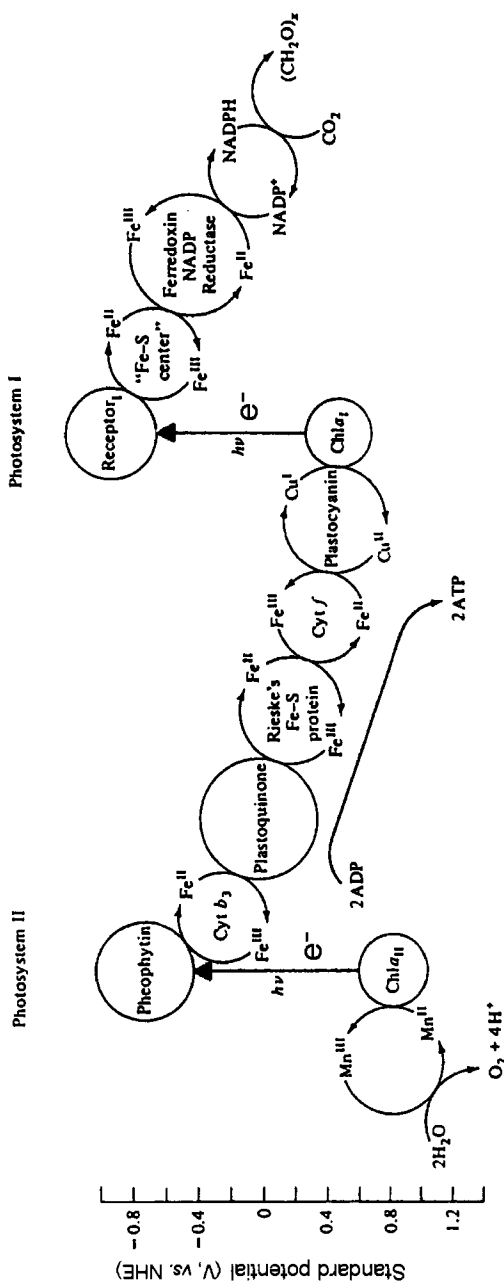
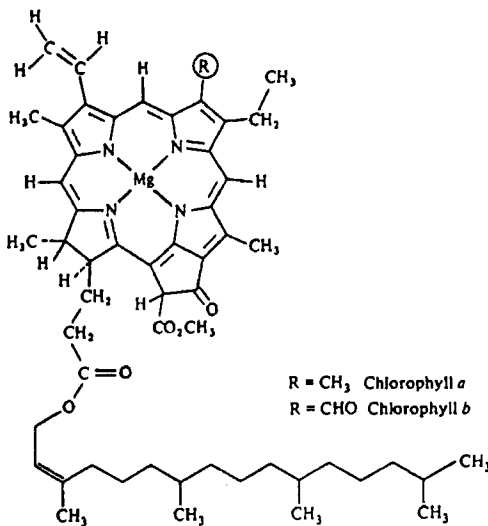


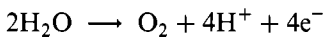
Figure 37 Schematic representation of the redox sequences occurring in photosynthesis

the oxidation of water in photosystem II, (which selectively absorbs electromagnetic radiation of wavelength of 680 nm, from which it is also defined as *P-680*).



Scheme 7

The present discussion is only concerned with the structure/redox capacity of the site responsible for the oxidation of water. The starting point is the evidence that the photosynthetic pathway is triggered by photooxidation of the chlorophylls in photosystem II. The need for chlorophylls to recover the electrons lost in photooxidation (in order to regenerate their ability to absorb light) induces water to undergo oxidation, according to:



The mechanism of simultaneously releasing two electrons per water molecule helps Nature to avoid one-electron processes such as:

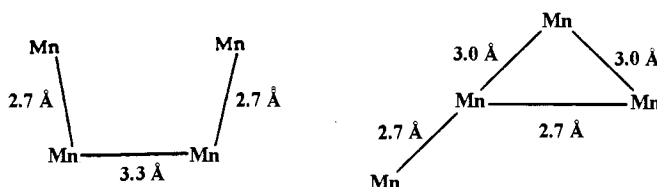


which generate highly reactive OH^\bullet radicals seriously detrimental to biological systems.

There is evidence that it is a manganese complex that acts as a mediator in supplying the electrons [through the Mn(II)/Mn(III)/Mn(IV) redox cycle] necessary to return the photo-oxidized chlorophylls back to their reduced state. The manganese centre is able to provide the four electrons produced in the oxidation of water in four successive steps.

The previously discussed mixed-valent Mn(III)/Mn(IV) complexes $[\text{Mn}_2\text{O}_2(\text{phen})_4]^{3+}$ and $[\text{Mn}_2\text{O}_2(\text{bipy})_4]^{3+}$, because of their EPR

properties and redox capacity, created considerable initial interest in their use as models of the manganese complex in WOC. Experimental evidence now indicates that the WOC is composed by a tetranuclear manganese complex (although it cannot be completely excluded that it might consist of two fairly close binuclear complexes or a trinuclear complex in the proximity of a mononuclear complex). In this regard, the most significant structural information on the photosynthetic enzyme (which resides in the thylakoid membrane of chloroplasts) has been obtained by EXAFS measurements^{51a} and by X-ray crystallography.^{51b} These studies indicate that the active site would be formed by a cluster of four manganese atoms with Mn–Mn interatomic distances varying from 2.7 Å to 3.0 Å, respectively, Scheme 8.



Scheme 8

This means that each manganese atom would have to be surrounded by carboxylate or phenolate oxygen atoms, in that, among the known Mn–Mn interatomic distances, a distance of 2.7 Å is found in μ_2 -oxo-dimers. On this basis, possible structural models are illustrated in Figure 38.⁵²

Based on photochemical experiments, it is believed that dioxygen is produced in photosystem II by a stepwise process which passes through five intermediate states, so-called ‘S-states’ of the Kok cycle, which are accessed through successive absorptions of photons. The picture of the

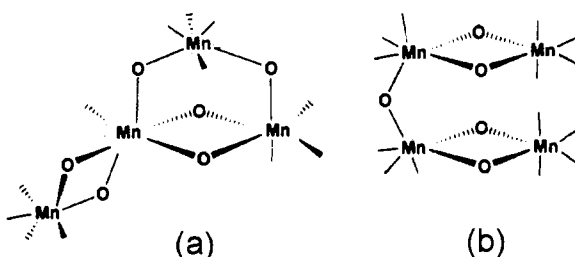


Figure 38 Structural models of the manganese complex which constitutes the active site responsible for the water oxidation in WOC

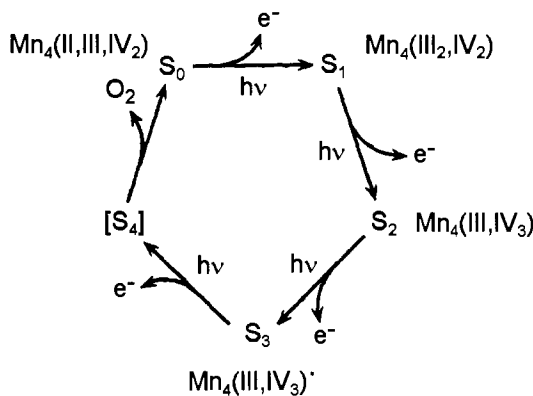


Figure 39 Schematic representation of the S-state cycle operating in the water oxidation process of photosynthesis together with the oxidation states of the manganese atoms of the Mn_4 cluster in the different S-states

experimental data is completed by the XANES and EPR results on the oxidation states of the various S-states, Figure 39.^{52a,53}

The S_0 and S_1 states are completely stable, S_2 and S_3 have half-lives of about a minute and S_4 is extremely unstable with a life-time of about one microsecond.

The presence of Ca^{2+} and Cl^- ions also plays a fundamental role in the oxidation of water.

Despite these extensive experimental studies, the precise mechanism by which water is oxidized to molecular oxygen has not yet been clarified. It is evident, however, that during the catalytic cycle two water molecules must be brought close enough together to form an O–O bond. A number of synthetic models have been proposed to mimic such a catalytic cycle;⁵⁴ one of the most useful is perhaps represented by the Ru(III) oxo-dimer $[(bipy)_2(H_2O)Ru-O-Ru(H_2O)(bipy)_2]^{4+}$ ($bipy = 2,2'$ -bipyridine), the molecular structure of which is shown in Figure 40.⁵⁵

The two water molecules appear to be fairly close ($Ow \cdots Ow = 4.7 \text{ \AA}$).

In fact, by oxidizing aqueous solutions of this compound with Ce(IV) salts, molecular oxygen is developed.

Figure 41 shows that in acid solution this tetracation undergoes a first reversible oxidation $Ru^{III}Ru^{III}/Ru^{III}Ru^{IV}$ ($E^{\circ'} = +0.79 \text{ V}$), followed by a second three-electron process ($E^{\circ'} = +1.22 \text{ V}$).

This behaviour does not allow the catalytic processes of water oxidation to be detected on the time scale of cyclic voltammetry. However, during exhaustive electrolysis at the potential of the second process ($E_w = +1.38 \text{ V}$), catalytic generation of gaseous oxygen is observed with restoration of the original complex.⁵⁵

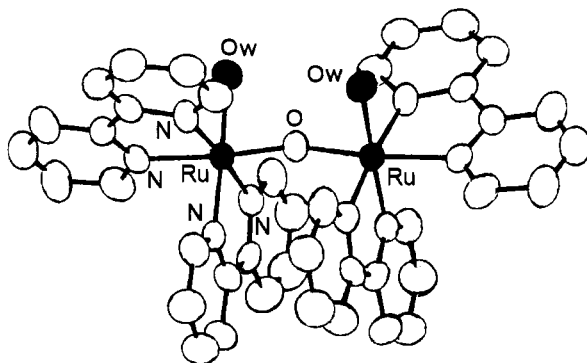


Figure 40 X-Ray structure of the tetracation $[\{ \text{Ru}(\text{bipy})_2(\text{H}_2\text{O}) \}_2\text{O}]^{4+}$. Average bond lengths: $\text{Ru}-\text{N} = 2.06 \text{ \AA}$; $\text{Ru}-\text{O}_{(\text{water})} = 2.14 \text{ \AA}$; $\text{Ru}-\text{O}_{(\text{oxo})} = 1.87 \text{ \AA}$

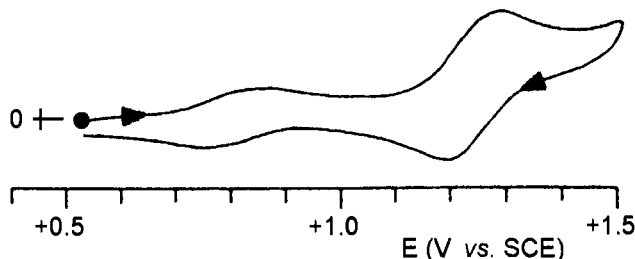
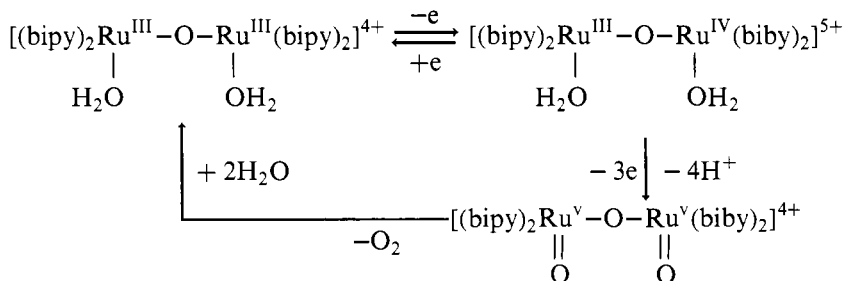


Figure 41 Cyclic voltammogram recorded at a glassy carbon electrode in a aqueous solution ($\text{CF}_3\text{SO}_3\text{H}$ 0.1 M) of $[\{ \text{Ru}(\text{bipy})_2(\text{H}_2\text{O}) \}_2\text{O}]^{4+}$. Scan rate 0.05 V s^{-1}

A plausible mechanism suggests that the second oxidation process converts the two closely positioned water molecules, intuitively an important structural observation, into *oxo* ligands (by deprotonation). This is followed by formation of the O–O bond and the development of molecular oxygen, with the concomitant coordination of new water molecules regenerating the original complex.⁵⁵



3.2 Tetrานuclear Manganese Complexes Modelling the Photosynthetic Water Oxidation Site

The search for inorganic compounds that can act as model systems of the tetrานuclear manganese centre of photosystem II, responsible for the oxidation of water, has led to the characterization of a number of complexes of diverse nature and geometry.

The observed geometric arrangements of the four manganese atoms can be classified as follows:

- a) diamantoidal
- b) cuboidal
- c) planar
- d) butterfly
- e) linear chain
- f) layered

Discussion of these derivatives is limited to those that have also been electrochemically characterized.

3.2.1 Derivatives of Diamantoidal Geometry. Figure 42 shows the tetrahedral (diamantoidal) geometry assumed by the four manganese atoms in complex $[\text{Mn}_4\text{O}_6(\text{tacn})_4]^{4+}$ ($\text{tacn} = 1,4,7\text{-triazacyclononane}$), which was the first tetrานuclear manganese complex to be structurally characterized.^{56,57}

The oxidation state of the tetramanganese cluster, having octahedral geometry and N_3O_3 coordination, is Mn_4^{IV} . Electrochemical investigation shows that the complex undergoes a reversible oxidation ($\text{Mn}_4^{\text{IV}} \rightarrow \text{Mn}_3^{\text{IV}}\text{Mn}^{\text{V}}$; $E^{\circ'} = +1.32$ V vs. SCE) and a reversible reduction ($\text{Mn}_4^{\text{IV}} \rightarrow \text{Mn}_3^{\text{IV}}\text{Mn}^{\text{III}}$; $E^{\circ'} = -0.68$ V).⁵⁸

In confirmation of the redox aptitude of the diamantoidal derivatives, the complex $[\text{Mn}_4\text{O}_6(\text{bpea})_4]^{4+}$ ($\text{bpea} = N,N\text{-bis}(2\text{-pyridylmethyl})ethy-lamine$), Figure 43a,⁵⁸ displays in acetonitrile solution a reversible one-electron reduction $\text{Mn}_4^{\text{IV}} \rightarrow \text{Mn}_3^{\text{IV}}\text{Mn}^{\text{III}}$ ($E^{\circ'} = +0.10$ V), followed by

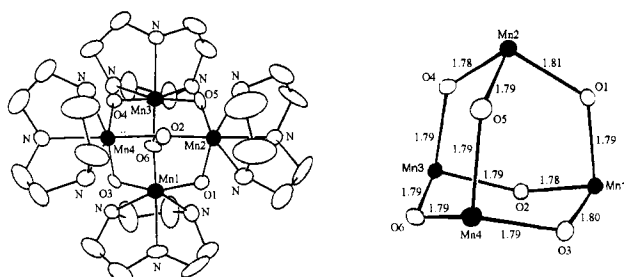


Figure 42 X-Ray structure of the tetracation $[\text{Mn}_4\text{O}_6(\text{tacn})_4]^{4+}$ with the relevant interatomic distances. Average $\text{Mn}\cdots\text{Mn}$ distance = 3.22 \AA

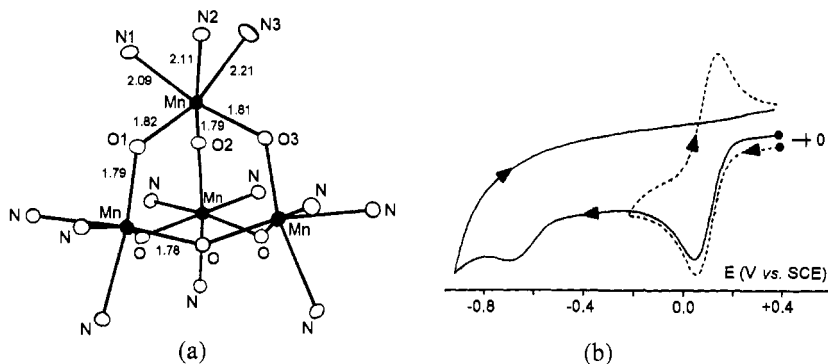


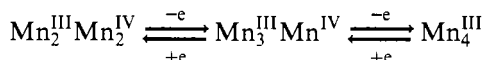
Figure 43 X-Ray structure (a) and cyclic voltammogram in MeCN solution (b) of the tetracation $[Mn_4O_6(bpea)_4]^{4+}$

an ill-defined further reduction ($E_p = -0.65$ V), which causes framework destruction, Figure 43b.

The corresponding trication $[Mn_4O_6(bpea)_4]^{4+}$ has been isolated and crystallographically characterized.⁵⁸ It maintains the original diamantoidal geometry, but some significant variation in bond lengths is observed for the apical manganese atom (Mn–N1 = 2.13 Å; Mn–N2 = 2.13 Å; Mn–N3 = 2.30 Å; Mn–O1 = 1.87 Å; Mn–O2 = 1.81 Å; Mn–O3 = 1.81 Å), to which the redox change $Mn^{IV} \rightarrow Mn^{III}$ is assigned.

3.2.2 Derivatives of Cuboidal Geometry. Since a few cuboidal Mn_4 complexes did not display any redox activity^{59–61}, it was thought that the cuboidal clustering of Mn atoms might lead to redox inactivity. However, the $Mn_3^{III}Mn^{IV}$ complex $[Mn_4O_3Cl(O_2CMe)_3(dbm)_3]$ (dbm = dibenzoylmethane), the molecular structure of which is reported in Figure 44,⁶² proved to be redox active.

Figure 45 shows that in dichloromethane solution, this complex displays both a reversible oxidation process ($E_{0/+}^{\circ} = 1.14$ V vs. Fc/Fc⁺) and a reversible reduction ($E_{0/-}^{\circ} = -0.25$ V) (in turn followed by a further irreversible step), according to the sequence:⁶²



Similar cuboidal geometries and redox behaviour are displayed by the members of the series $Mn_4O_3X(O_2CR)_3(dbm)_3$ [X = O₂CR (R = Me, Ph), OMe, OH].^{63,64}

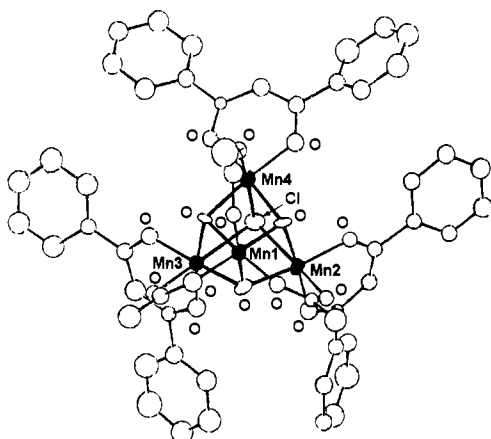


Figure 44 X-Ray structure of $[Mn_4O_3Cl(O_2CMe)_3(dbm)_3]$. Interatomic distances: $Mn_1 \cdots Mn_2 = Mn_1 \cdots Mn_3 \approx 2.80 \text{ \AA}$; $Mn_1 \cdots Mn_4 \approx 2.79 \text{ \AA}$; $Mn_2 \cdots Mn_4 = 3.24 \text{ \AA}$; $Mn_2 \cdots Mn_3 \approx 3.35 \text{ \AA}$; $Mn_3 \cdots Mn_4 = 3.26 \text{ \AA}$

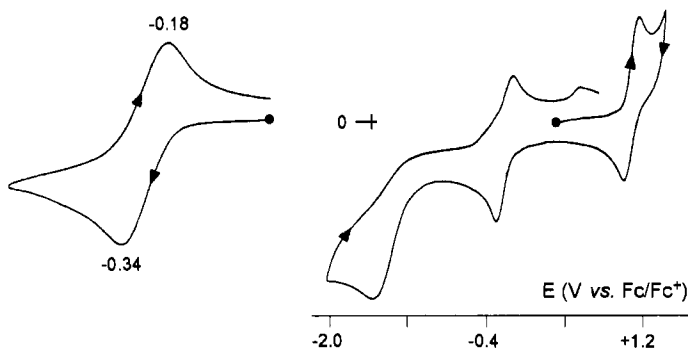


Figure 45 Cyclic voltammogram recorded at a glassy carbon electrode in a CH_2Cl_2 solution of $[Mn_4O_3Cl(O_2CMe)_3(dbm)_3]$. Scan rate 0.1 V s^{-1}

As a further confirmation that cuboidal tetramanganese complexes can be redox active, the phosphinate derivative $[Mn_4O_4(O_2PPh_2)_6]$ illustrated in Figure 46 displays in dichloromethane solution a quasireversible $Mn_2^{III}Mn_2^{IV} \rightarrow Mn^{III}Mn_3^{IV}$ oxidation ($E^{\circ'} = +1.08 \text{ V}$ vs. SCE).⁶⁵

3.2.3 Derivatives of Planar Geometry. The first planar tetramanganese derivative that we will consider is $[Mn_4O_2(O_2CMe)_6(bipy)_2]$.

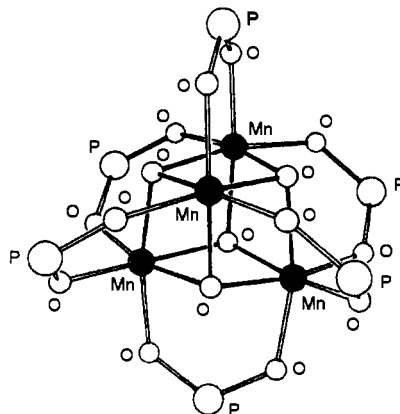


Figure 46 X-Ray structure of $[Mn_4O_4(O_2PPh_2)_6]$. $Mn \cdots Mn = 2.91 \text{ \AA}$; $Mn-O = 1.92 \text{ \AA}$

The molecular structure of the $Mn_2^{II}Mn_2^{III}$ complex is illustrated in Figure 47.⁶¹

Within the central Mn_4O_2 unit the Mn_4 group is rigorously planar, whereas the two triply bridging oxygen atoms O1 lie one above and one below the Mn_4 plane. A $Mn_2^{II}Mn_2^{III}$ oxidation state has been assigned to the Mn_4 cluster.

In dichloromethane solution this complex displays a reversible one-electron oxidation to the corresponding $Mn^{II}Mn_3^{III}$ monocation ($E^{\circ'} = +0.42 \text{ V vs. SCE}$).^{61,66}

A quite similar structural Mn_4O_2 assembly is present in the salicylaldimine dication $[Mn_4O_2\{N(CH_2CH_2=NCHC_6H_4O)_3\}_2]^{2+}$, Figure 48.⁶⁷

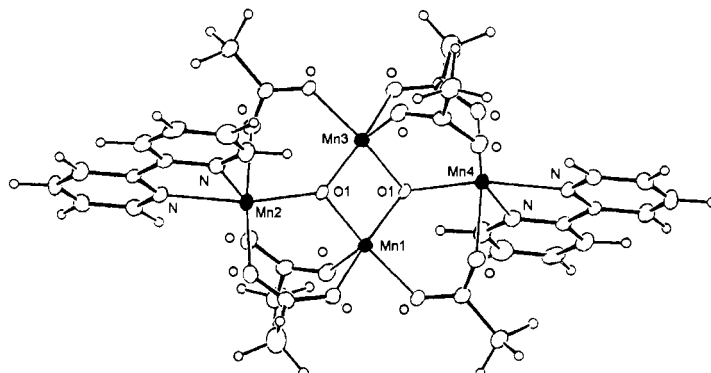


Figure 47 X-ray structure of $[Mn_4O_2(O_2CMe)_6(bipy)_2]$. Interatomic distances: $Mn1 \cdots Mn3 = 2.78 \text{ \AA}$; $Mn1 \cdots Mn2 = 3.29 \text{ \AA}$; $Mn1 \cdots Mn4 = 3.48 \text{ \AA}$

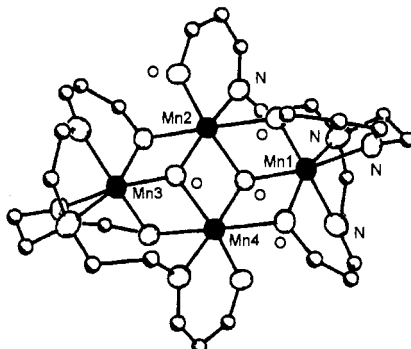


Figure 48 X-ray structure of $[Mn_4O_2\{N(CH_2CH_2N=CHC_6H_4O)_3\}_2]^{2+}$. Interatomic distances: $Mn1 \cdots Mn2 = 3.00 \text{ \AA}$; $Mn2 \cdots Mn4 = 2.91 \text{ \AA}$

The present Mn_4^{III} complex displays in acetonitrile solution two quasireversible one-electron oxidations ($Mn_4^{III} \rightarrow Mn_3^{III}Mn^{IV} \rightarrow Mn_2^{III}Mn_2^{IV}$; $E^{\circ'} = +0.82 \text{ V vs. SCE}$, and $+0.98 \text{ V}$, respectively) and two quasireversible one-electron reduction ($Mn_4^{III} \rightarrow Mn_3^{III}Mn^{II} \rightarrow Mn_2^{III}Mn_2^{II}$; $E^{\circ'} = +0.03 \text{ V}$ and -0.20 V , respectively).⁶⁷

A last electrochemically active planar derivative is the Mn_4^{III} complex $[Mn_4O_2(O_2CMe)_6(dbm)_2(py)_2]$ (dbm = dibenzoylmethane monoanion) shown in Figure 49.^{64,68}

In acetonitrile solution this complex displays a one-electron oxidation ($E^{\circ'} = +0.99 \text{ V vs. SCE}$), that is chemically reversible on the cyclic voltammogram time scale. However, exhaustive oxidation produces the $Mn_3^{III}Mn^{IV}$ derivative $[Mn_4O_3(O_2CMe)_4(dbm)_3]$, which, as previously mentioned, possesses a cuboidal geometry. The conversion mechanism is

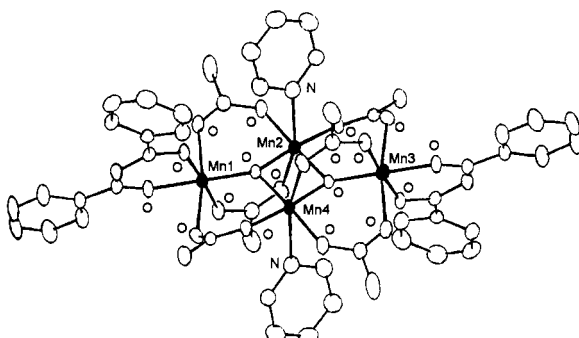


Figure 49 X-Ray structure of $[Mn_4O_2(O_2CMe)_6(dbm)_2(py)_2]$. Interatomic distances: $Mn2 \cdots Mn4 = 2.87 \text{ \AA}$; $Mn2 \cdots Mn1 = 3.31 \text{ \AA}$; $Mn2 \cdots Mn3 = 3.40 \text{ \AA}$

probably due to the presence of a small amount of water that triggers the decomposition of the monocation $[\text{Mn}_4\text{O}_2(\text{O}_2\text{CMe})_6(\text{dbm})_2(\text{bipy})_2]^+$.^{64,69} This example thus shows how a change in the oxidation state of these tetranuclear complexes make them extremely reactive, such to induce changes in their molecular geometry.

3.2.4 Derivatives of Butterfly Geometry. The molecular structure of the monocation $[\text{Mn}_4\text{O}_2(\text{O}_2\text{CMe})_7(\text{bipy})_2]^+$ is illustrated in Figure 50.⁶⁶ The Mn_4 group has been assigned a Mn_4^{III} oxidation state and assumes a butterfly geometry, in which the atoms Mn1 and Mn3 form the ‘body’, while Mn2 and Mn4 are positioned at the tips of the ‘wings’.

The electrochemical behaviour of this acetato complex has not been reported, but the analogous benzoato derivative $[\text{Mn}_4\text{O}_2(\text{O}_2\text{CPh})_7(\text{bipy})_2]^+$ in dichloromethane solution displays a quasireversible one-electron reduction to the corresponding neutral derivative $\text{Mn}^{\text{II}}\text{Mn}_3^{\text{III}}$ ($E^{\circ'} = +0.28$ V vs. SCE) and a quasireversible one-electron oxidation to the corresponding dication $\text{Mn}_3^{\text{III}}\text{Mn}^{\text{IV}}$ ($E^{\circ'} = +1.34$ V).⁶⁶

A butterfly geometry quite similar to that of the preceding monocations $[\text{Mn}_4\text{O}_2(\text{O}_2\text{CR})_7(\text{bipy})_2]^+$ is possessed by a series of Mn_4^{III} monoanions with different chelating ligand $[\text{Mn}_4\text{O}_2(\text{O}_2\text{CR})_7(\text{chel})_2]^-$ [$\text{chel} = \text{dbm}$,⁶⁴ pic (picolinic acid monoanion),⁷⁰ dpm (dipivaloylmethane monoanion)].⁷¹ In these cases too the oxidation state of the tetramanganese cluster is assigned as Mn_4^{III} . Figure 51 shows the molecular structure of $[\text{Mn}_4\text{O}_2(\text{O}_2\text{CMe})_7(\text{pic})_2]^-$.

Figure 52 shows that the benzoato derivative $[\text{Mn}_4\text{O}_2(\text{O}_2\text{CPh})_7(\text{pic})_2]^-$ undergoes a $\text{Mn}_4^{\text{III}}/\text{Mn}_3^{\text{III}}\text{Mn}^{\text{IV}}$ oxidation ($E^{\circ'} = +0.54$ V vs. Fc/Fc^+)⁷⁰ having features of chemical reversibility (the same behaviour is

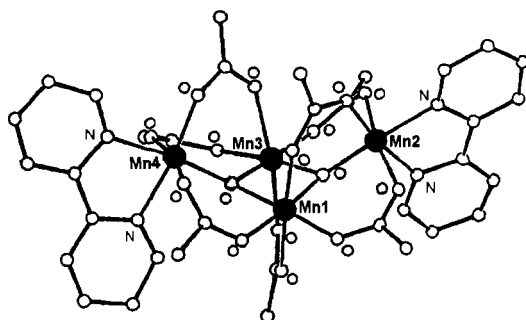


Figure 50 X-Ray structure of the monocation $[\text{Mn}_4\text{O}_2(\text{O}_2\text{CMe})_7(\text{bipy})_2]^+$. Interatomic distances: $\text{Mn}1 \cdots \text{Mn}3 = 2.85 \text{ \AA}$; $\text{Mn}1 \cdots \text{Mn}2 = 3.31 \text{ \AA}$; $\text{Mn}1 \cdots \text{Mn}4 = 3.38 \text{ \AA}$; $\text{Mn}3 \cdots \text{Mn}4 = 3.30 \text{ \AA}$

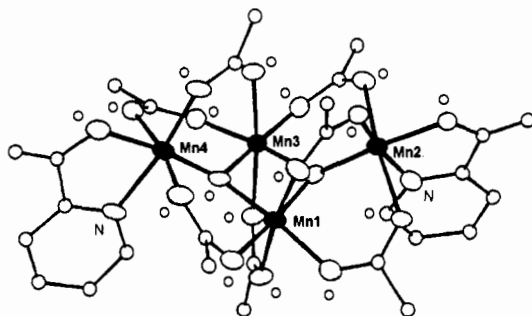


Figure 51 X-Ray structure of the monoanion $[Mn_4O_2(O_2CMe)_7(pic)_2]^-$. Interatomic distances: $Mn_1 \cdots Mn_3 = 2.84 \text{ \AA}$; $Mn_1 \cdots Mn_2 = 3.31 \text{ \AA}$; $Mn_1 \cdots Mn_4 = 3.39 \text{ \AA}$; $Mn_3 \cdots Mn_4 = 3.31 \text{ \AA}$; $Mn_2 \cdots Mn_3 = 3.41 \text{ \AA}$

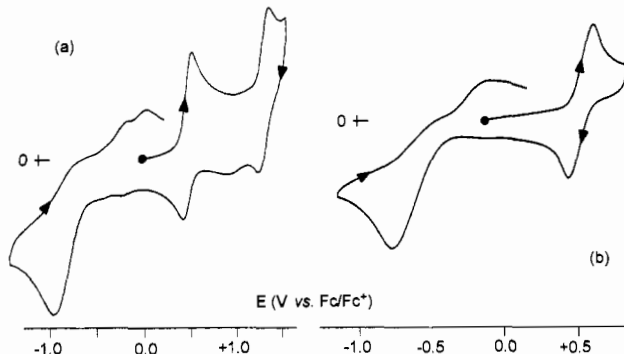


Figure 52 Cyclic voltammograms recorded at a glassy carbon electrode in: (a) a CH_2Cl_2 solution of $[Mn_4O_2(O_2CPh)_7(pic)_2]^-$; (b) a $MeCN$ solution of $[Mn_4O_2(O_2CPh)_7(dbm)_2]^-$. Scan rate 0.1 V s^{-1}

exhibited by $[Mn_4O_2(O_2CPh)_7(dpm)_2]^-$ ($E^{\circ/0} = +0.66 \text{ V}$)⁷¹, whereas the related derivative $[Mn_4O_2(O_2CPh)_7(dbm)_2]^-$ undergoes the two oxidations $Mn_4^{III}/Mn_3^{III}Mn^{IV}$ ($E^{\circ/0} = +0.47 \text{ V}$) and $Mn_3^{III}Mn^{IV}/Mn_2^{III}Mn_2^{IV}$ ($E^{\circ/0} = +1.17 \text{ V}$), which, however, look partially chemically reversible.

It is interesting to note that also in the latter case exhaustive electrolysis at the potential of the first oxidation generates the previously discussed $Mn_3^{III}Mn^{IV}$ cuboidal $[Mn_4O_3(O_2CPh)_4(dbm)_3]$ derivative.^{64,71}

As discussed previously for the case of the *planar-to-cuboidal* structural reorganization $[Mn_4O_2(O_2CMe)_6(dbm)_2(py)_2]/[Mn_4O_3(O_2CMe)_4(dbm)_3]$, it is thought that also in the present *butterfly-to-cuboidal* reorganization $[Mn_4O_2(O_2CPh)_7(dbm)_2]^-/[Mn_4O_3(O_2CPh)_4(dbm)_3]$ the

presence of traces of water might trigger the conversion of the electrogenerated $[\text{Mn}_4\text{O}_2(\text{O}_2\text{CPh})_7(\text{dbm})_2]$ to $[\text{Mn}_4\text{O}_3(\text{O}_2\text{CPh})_4(\text{dbm})_3]$, thus leading to an enrichment of the oxygen content of the central unit from Mn_4O_2 to Mn_4O_3 .

In the attempt to approach the chemical components of the biological functions better than bpyridine-based $[\text{Mn}_4\text{O}_2(\text{O}_2\text{CR})_7(\text{bipy})_2]^+$ or picolinate-based $[\text{Mn}_4\text{O}_2(\text{O}_2\text{CR})_7(\text{pic})_2]^-$ complexes, imidazole-carboxylate complexes have been prepared. $[\text{Mn}_4\text{O}_2(\text{O}_2\text{CPh})_7(\text{imidac})_2]^-$ (imidac = 4-imidazoleacetate) possesses a butterfly geometry, but its redox ability is very poor (in MeCN it gives rise to a partially chemically reversible $\text{Mn}_4^{\text{III}}/\text{Mn}_3^{\text{III}}\text{Mn}^{\text{IV}}$ oxidation at $E^\circ' = +0.60 \text{ V vs. SCE}$).⁷²

3.2.5 Derivatives of Linear Chain Geometry. The molecular structure of complex $[\text{Mn}_4\text{O}(\text{tpdp})_2(\text{O}_2\text{CMe})_2(\text{H}_2\text{O})_2]^{4+}$ ($\text{Htpdp} = N,N,N',N'$ -tetrakis(2-pyridyl-methyl)-2-hydroxylpropane-1,3-diamine) is shown in Figure 53.^{73,74}

The complex can be viewed as a dimer of $\text{Mn}^{\text{II}}\text{Mn}^{\text{III}}$ dimers joined by a single oxygen bridge, with the four manganese atoms assuming a chain disposition. It is interesting to note the presence of two coordinated water molecules ($\text{O}1$), even if their positions at opposite ends prevent any possible mutual interaction to form an O–O bond able to lead to the development of dioxygen.

Figure 54 shows that the complex undergoes three separate, relatively poorly defined, one-electron oxidations ($E^\circ' = +0.83 \text{ V}$, $+1.05 \text{ V}$ and $+1.35 \text{ V}$, respectively).⁷³

Closely related to this complex is the trication $[\text{Mn}_4\text{O}_2(\text{tpdp})_2(\text{CF}_3\text{SO}_3)_2(\text{H}_2\text{O})_2]^{3+}$, whose crystal structure is illustrated in Figure 55.⁷⁵

In this case too the chain is formed by a *dimer of dimers* with a double oxygen bridge. The overall oxidation state is $\text{Mn}_2^{\text{II}}\text{Mn}^{\text{III}}\text{Mn}^{\text{IV}}$. There are

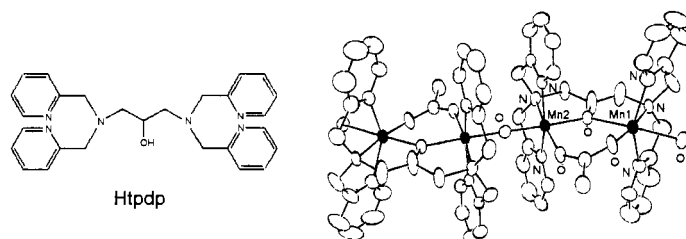


Figure 53 X-Ray structure of the tetracation $[\text{Mn}_4\text{O}(\text{tpdp})_2(\text{O}_2\text{CMe})_2(\text{H}_2\text{O})_2]^{4+}$. Interatomic distances: $\text{Mn}1 \cdots \text{Mn}2 = 3.69 \text{ \AA}$; $\text{Mn}2 \cdots \text{Mn}2' = 3.53 \text{ \AA}$

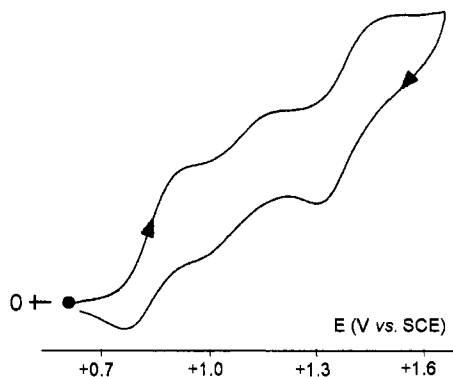


Figure 54 Cyclic voltammogram recorded at a platinum electrode in a MeCN solution of $[\text{Mn}_4\text{O}(\text{tpdp})_2(\text{O}_2\text{CMe})_2(\text{H}_2\text{O})_2]^{4+}$. Scan rate 0.05 V s^{-1}

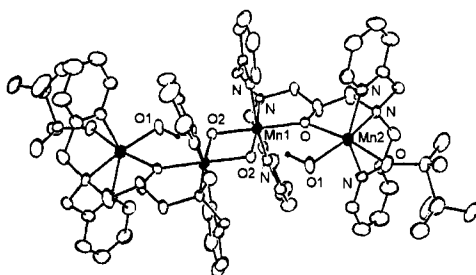


Figure 55 X-Ray structure of the trication $[\text{Mn}_4\text{O}_2(\text{tpdp})_2(\text{CF}_3\text{SO}_3)_2(\text{H}_2\text{O})_2]^{3+}$. Interatomic distances: $\text{Mn}1 \cdots \text{Mn}2 = 3.87 \text{ \AA}$; $\text{Mn}1 \cdots \text{Mn}1' = 2.72 \text{ \AA}$

two coordinated water molecules (O1) in this complex which, although they are positioned distant from each other, might interact (*via* hydrogen bonds) with the bridging oxygen atoms (O2) to form an O–O bond.

In MeCN solution the complex displays both a quasireversible one-electron oxidation ($E^{\circ'} = +0.87 \text{ V vs. SCE}$) and a quasireversible one-electron reduction ($E^{\circ'} = +0.36 \text{ V}$).⁷⁵

The complex in which two molecules of trifluoromethanesulfonate of the preceding compound have been substituted by two molecules of water, namely $[\text{Mn}_4\text{O}_2(\text{tpdp})_2(\text{H}_2\text{O})_4]^{5+}$, has an analogous crystal structure,⁷⁶ and analogously exhibits a quasireversible one-electron oxidation ($E^{\circ'} = +0.93 \text{ V vs. SCE}$) and a quasireversible one-electron reduction ($E^{\circ'} = +0.39 \text{ V}$).⁷⁶

Other linear tetramanganese complexes have been crystallographically characterized^{77–80}, but they do not display a significant redox activity.

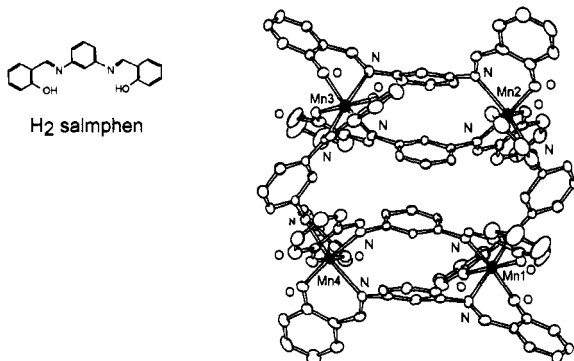


Figure 56 *X-Ray structure of the tetracation $[Mn_4(salphen)_6]^{4+}$. Interatomic distances: $Mn1 \cdots Mn2 = 7.27 \text{ \AA}$; $Mn1 \cdots Mn4 = 7.52 \text{ \AA}$*

To conclude the present section, it is noted that closed-chain Mn_4 complexes have been also prepared. This is, for example, the case of $[Mn_4O_4(tpdp)_2]^{4+}$ (the electrochemical behaviour of which has not been examined)⁸¹ or that of $[Mn_4^{III}(\text{salphen})_6]$, (salphen = N,N' -disalicylidene-1,3-diaminobenzene), Figure 56.⁸²

In CH_2Cl_2 solution the last complex displays a partially chemically reversible one-electron oxidation ($E^{\circ'} = +0.81 \text{ V}$ vs. SCE) and a quasireversible one-electron reduction.⁸²

3.2.6 Derivatives of Layered Geometry. The definition of ‘layered’ geometry can be made clearer by considering the molecular structure of the tetracation $[Mn_4O_4(tmfpd)_2(H_2O)_2]^{4+}$, Figure 57.⁸³ The Htmfpd

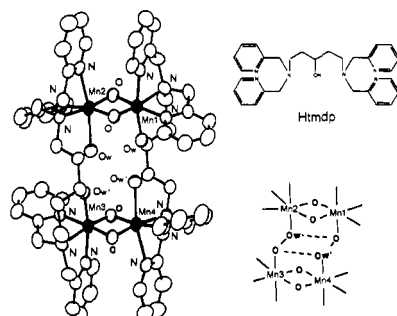


Figure 57 *X-Ray structure of the tetracation $[Mn_4O_4(tmfpd)_2(H_2O)_2]^{4+}$. Interatomic distances: $Mn1 \cdots Mn2 = 2.64 \text{ \AA}$; $Mn1 \cdots Mn4 = 5.86 \text{ \AA}$*

ligand (1,5-bis[bis(2-pyridylmethyl)amine]-3-pentanol) is strictly related to the Htpdp ligand discussed in the previous section.

It is evident that the four manganese atoms assume a two-by-two disposition in the two layers formed by the atoms of manganese and oxygen. The most important structural aspect of this $Mn_2^{III}Mn_2^{IV}$ cluster is, as already discussed, the relative proximity of the two coordinated water molecules (O_w , $O_{w'}$).

It has been briefly reported that in acetonitrile this complex exhibits a first reversible one-electron oxidation process ($E^{\circ'} = +1.0$ V vs. SCE), corresponding to the transformation $Mn_2^{III}Mn_2^{IV}/Mn_2^{III}Mn_3^{IV}$, and a second irreversible process ($E_p \approx +1.2$ V).⁸³

A higher redox aptitude characterizes the Mn_4^{III} complex with 1,5-bis(salicylideneammino)-3-pentanol (H_3L), Figure 58.⁸⁴

Also in this case each couple of Mn_2O_2 sheets lies on separated layers.

As illustrated in Figure 59, it undergoes in methanol solution two subsequent two-electron reductions ($Mn_4^{III} \rightarrow Mn_2^{III}Mn_2^{II}$, $E^{\circ'} = +0.00$ V and $Mn_2^{III}Mn_2^{II} \rightarrow Mn_2^{II}Mn_2^{II}$, $E^{\circ'} = -0.39$ V (vs. SCE), respectively) and a one-electron oxidation ($Mn_4^{III} \rightarrow Mn_3^{III}Mn^{IV}$, $E^{\circ'} = +0.31$ V),

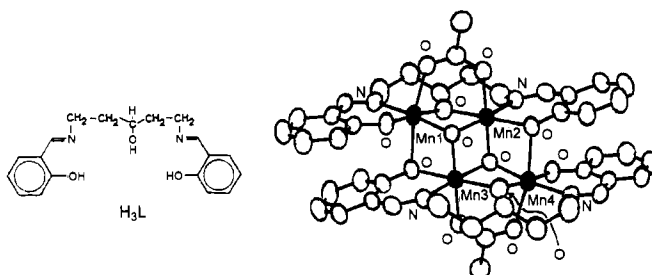


Figure 58 X-Ray structure of $[Mn_4O_2(L)_2(CH_3CO_2)_2]$. Interatomic distances: $Mn1 \cdots Mn2 = 2.93 \text{ \AA}$; $Mn1 \cdots Mn4 = 3.12 \text{ \AA}$; $Mn2 \cdots Mn4 = 2.87 \text{ \AA}$

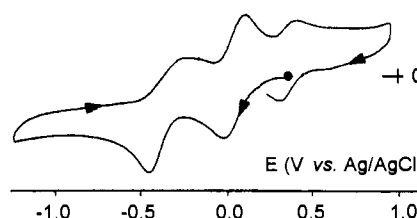


Figure 59 Cyclic voltammogram recorded at a glassy carbon electrode in a CH_3OH solution of $[Mn_4O_2(L)_2(CH_3CO_2)_2]$. Scan rate 0.1 V s^{-1}

only the first reduction and the oxidation processes showing features of chemical reversibility.⁸⁴

3.3 The Role of Manganese Complexes in Material Science

Having dealt with cuboidal Mn_4O_3 carboxylate complexes, we briefly mention here a few related $Mn_{12}O_{12}(O_2CR)_{16}$ complexes which behave as *nanoscale magnets*, or *single-molecule magnets*. The term derives from the fact that the magnetic properties of this kind of derivative are due to individual molecules which possess enough spin and magnetoanisotropy to function as a magnet, rather than, as commonly happens, from mutual interactions between molecules in the bulk material. In fact, below a critical temperature each molecule behaves as a magnet, and under an applied external field its spin becomes ‘up’ or ‘down’ oriented along its axial magnetoanisotropy axis.⁸⁵

Figure 60 shows the molecular structure of $[Mn_{12}O_{12}(O_2CR)_{16}(H_2O)_4]$ ($R = Ph$).⁸⁶ It consists of a central cuboidal core $[Mn^{IV}_4O_4]^{8+}$ rounded by a non-planar ring of eight Mn^{III} atoms connected to the cubane core by eight triply-bridging O^{2-} ions.

As illustrated in Figure 61, this complex gives rise to a series of one-electron transfers: namely one oxidation ($E_{0/+}^{\circ\circ} = +0.79$ V vs. Fc/Fc^+ ; $\Delta E_p = 160$ mV at 0.1 V s $^{-1}$) and two successive reductions having features of chemical reversibility, but electrochemical quasireversibility ($E_{0/-}^{\circ\circ} = +0.10$ V, $\Delta E_p = 170$ mV at 0.1 V s $^{-1}$; $E_{-/2-}^{\circ\circ} = -0.24$ V, $\Delta E_p = 320$ mV at 0.1 V s $^{-1}$) followed by a third irreversible reduction ($E_p = -0.85$ V).⁸⁷

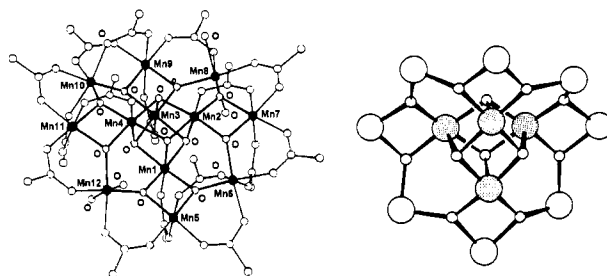


Figure 60 X -Ray structure of $[Mn_{12}O_{12}(O_2CPh)_{16}(H_2O)_4]$. Interatomic distances in the central cubane: $Mn^{IV}1 \cdots Mn^{IV}3 \cong Mn^{IV}2 \cdots Mn^{IV}4 = 2.99 \text{ \AA}$; $Mn^{IV}1 \cdots Mn^{IV}2 \cong Mn^{IV}1 \cdots Mn^{IV}4 \cong Mn^{IV}2 \cdots Mn^{IV}3 \cong Mn^{IV}3 \cdots Mn^{IV}4 = 2.83 \text{ \AA}$; $Mn^{IV}-O =$ from 1.89 \AA to 1.99 \AA . Other average distances: $Mn^{IV} \cdots Mn^{III} = 2.80 \text{ \AA}$; $Mn^{III} \cdots Mn^{III} = 3.35 \text{ \AA}$.

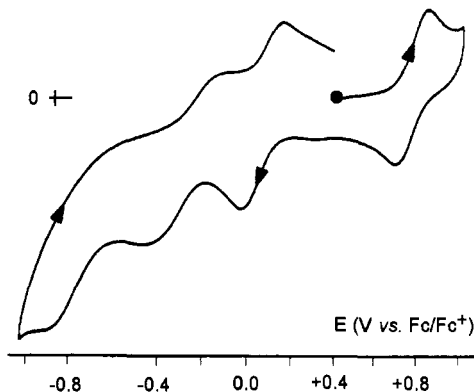


Figure 61 Cyclic voltammogram recorded at a glassy carbon electrode in a CH_2Cl_2 solution of $[\text{Mn}_{12}\text{O}_{12}(\text{O}_2\text{CPh})_{16}(\text{H}_2\text{O})_4]$

The related anions $[\text{Mn}_{12}\text{O}_{12}(\text{O}_2\text{CR})_{16}(\text{H}_2\text{O})_4]^-$ ($\text{R} = \text{Et}$ ^{87a}, C_6F_5 ^{87b}) and $[\text{Mn}_{12}\text{O}_{12}(\text{O}_2\text{CR})_{16}(\text{H}_2\text{O})_4]^{2-}$ ($\text{R} = \text{CHCl}_2$)⁸⁸) have been isolated. Such redox derivatives maintain the overall geometrical assembly of the neutral precursor, but, based on the Mn–O distances, it is thought that the added electrons enter the outer manganese sites affording the $\text{Mn}^{\text{II}}\text{Mn}^{\text{III}}_7\text{Mn}^{\text{IV}}_4$ and $\text{Mn}^{\text{II}}_2\text{Mn}^{\text{III}}_6\text{Mn}^{\text{IV}}_4$ assemblies, respectively.

Studies devoted to create high-density molecular memory devices (ideally, it is hoped to find materials in which each bit of digital information might be stored on a single molecule) are very active⁸⁹ and larger manganese–carboxylate assemblies have been obtained (up to Mn_{30}).⁹⁰

4 IRON COMPLEXES

The commonest oxidation states of iron in its complexes are II and III (electronic configuration d^6 and d^5 , respectively), but, as we shall see, the I and IV oxidation states are also accessible.

Stated that in the vast majority of cases, the $\text{Fe}(\text{III})/\text{Fe}(\text{II})$ process is chemically reversible, we begin the survey of these two oxidation states of iron with tetracoordinated complexes.

Figure 62 shows the molecular structure of the tetrahedral $\text{Fe}(\text{II})$ complex $[\text{FeCl}_4]^{2-}$.⁹¹

Tetrachloroferrates(II) are high spin ($d^6-e^3t_2^3$, four unpaired electrons). For example, the derivative $[\text{H-TMPP}]_2[\text{Fe}^{\text{II}}\text{Cl}_4]$ (H-TMPP = protonated tris(2,4,6-trimethoxyphenyl)phosphine) has magnetic

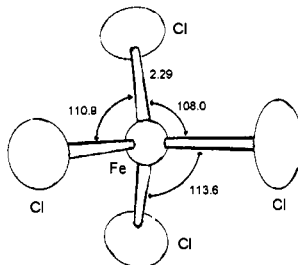


Figure 62 X-Ray structure of the dianion $[FeCl_4]^{2-}$

susceptibility $\mu_{\text{eff}} = 5.29 \mu_B$.⁹² These derivatives undergo an easy oxidation to the corresponding Fe(III) derivatives. For example, $[\text{H-TMPP}]_2[\text{Fe}^{\text{II}}\text{Cl}_4]$ in dichloromethane solution is reversibly oxidized to the corresponding tetrachloroferrate(III) at a potential value of $E^\circ' = -0.03 \text{ V}$ (vs. SCE).⁹² Tetrachloroferrates(III) maintain the tetrahedral geometry of tetrachloroferrates(II), the electron removal $[\text{Fe}^{\text{II}}\text{Cl}_4]^{2-}/[\text{Fe}^{\text{III}}\text{Cl}_4]^-$ causing a significant shortening of the Fe–Cl distances, in that the averaged Fe–Cl bond length shortens by about 0.1 Å.^{92,93}

Tetrachloroferrates(III) are high spin complexes too ($d^5-e^2t_2^3$, five unpaired electrons). For example, $[\text{H-TMPP}][\text{Fe}^{\text{III}}\text{Cl}_4]$ has $\mu_{\text{eff}} = 6.11 \mu_B$.

The tetracoordinated complexes of iron can also assume planar (or pseudoplanar) geometry. Typical examples are the Fe(II) complexes of the already discussed Schiff bases *N,N'*-ethylenebis(salicylideneimine), salen, and *N,N'*-disalicylidene-*o*-phenylenediamine, saloph.

Figure 63 shows the cyclic voltammetric profiles exhibited in dmso solution by $[\text{Fe}^{\text{III}}(\text{salen})]^+$ and $[\text{Fe}^{\text{II}}(\text{saloph})]$, respectively.^{94,95}

$[\text{Fe}^{\text{II}}\text{saloph}]$ undergoes a one-electron oxidation ($E^\circ' = -0.28 \text{ V}$), whereas $[\text{Fe}^{\text{III}}(\text{salen})]^+$ undergoes a one-electron reduction ($E^\circ' = -0.33 \text{ V}$). In both cases the Fe(III)/Fe(II) process is chemically and electrochemically reversible ($i_{\text{p(reverse)}}/i_{\text{p(forward)}} = 1$; $\Delta E_p \approx 60 \text{ mV}$, at 0.2 V s^{-1}). Therefore, one may reasonably expect that the corresponding $[\text{Fe}^{\text{III}}(\text{saloph})]^+$ and $[\text{Fe}^{\text{II}}(\text{salen})]$ congeners maintain the initial planar geometry.

There are numerous iron(II) pentacoordinate complexes. An example is constituted by $[\text{Fe}(\text{saldppt})]$, the N_3O_2 coordinated iron(II) complex of the Schiff base bis(salicylideneamine-3-propyl)amine, Scheme 9.

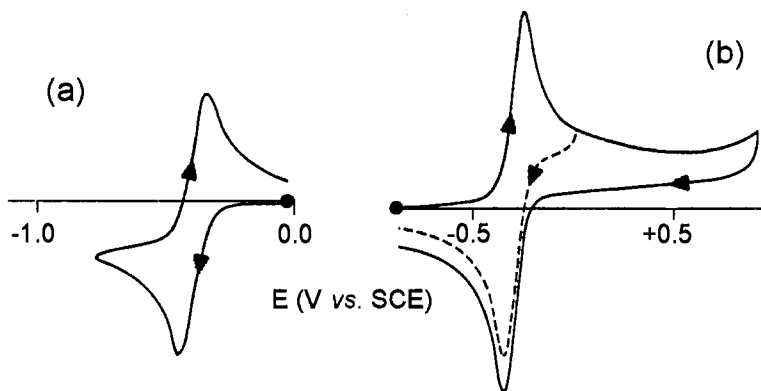
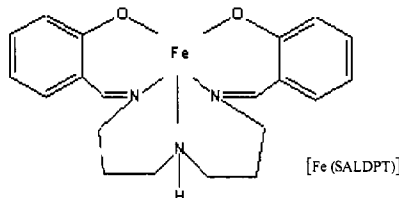


Figure 63 Cyclic voltammograms recorded at a platinum electrode in dmso solution of: (a) $[\text{Fe}^{\text{III}}(\text{salen})]^+$; (b) $[\text{Fe}^{\text{II}}(\text{saloph})]$. Scan rate 0.2 V s^{-1}



Scheme 9

It has a magnetic moment of $5.22 \mu_{\text{B}}$, which testifies a high spin ($d^6-e'^3e'^2a_1'$, four unpaired electrons) complex. $[\text{Fe}(\text{SALDPT})]$ in dmso solution also displays a reversible $\text{Fe}(\text{II})/\text{Fe}(\text{III})$ oxidation ($E^{\circ'} = -0.29 \text{ V}$).⁹⁶

A further example of pentacoordinate iron complexes is constituted by $[\text{FeLCl}_2]$ ($\text{L} = 2,6\text{-diacetylpyridinebis}(2,6\text{-diisopropylanil})$), the (distorted) square pyramidal structure of which is illustrated in Figure 64.⁹⁷

Also in this case, its high spin nature is revealed by the magnetic moment: $5.34 \mu_{\text{B}}$ ($\text{Fe}(\text{II}) d^6-e'^3e'^2a_1'$, four unpaired electrons).

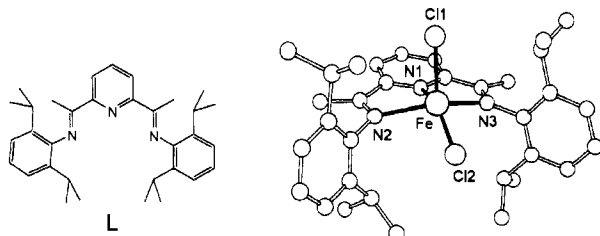


Figure 64 X-Ray structure of $[\text{FeLCl}_2]$. Bond lengths: $\text{Fe}-\text{N}1 = 2.09 \text{ \AA}$; $\text{Fe}-\text{N}2 = 2.24 \text{ \AA}$; $\text{Fe}-\text{N}3 = 2.25 \text{ \AA}$; $\text{Fe}-\text{Cl}2 = 2.27 \text{ \AA}$; $\text{Fe}-\text{Cl}1 = 2.31 \text{ \AA}$

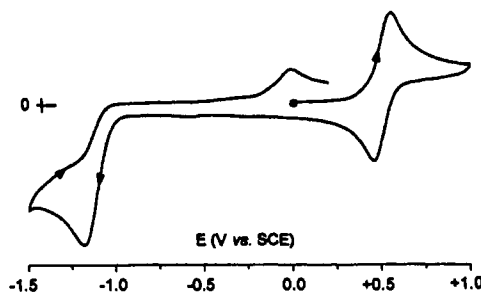
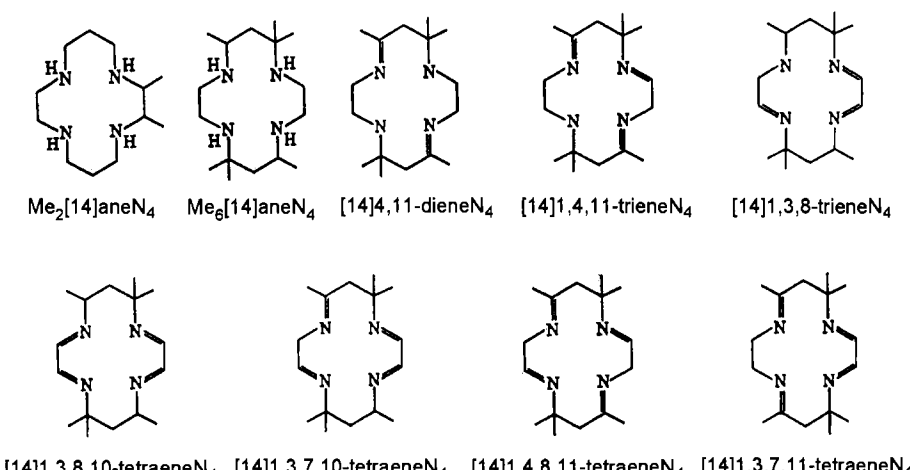


Figure 65 Cyclic voltammogram recorded at a platinum electrode in a CH_2Cl_2 solution of $[\text{Fe}^{\text{II}}\text{LCl}_2]$. Scan rate 0.2 V s^{-1}

As illustrated in Figure 65, such a complex undergoes a chemically reversible $\text{Fe}^{\text{II}}/\text{Fe}^{\text{III}}$ oxidation (in the long times of macro electrolysis the original blue solution turns red) and an irreversible reduction. As we will discuss in Chapter 6, Section 5, this latter process is probably ligand-centred.

Another important class of iron compounds is that of the tetraazamacrocyclic ligands. As a typical example we can cite the Fe(II) complexes of the 14-membered macrocycles illustrated in Scheme 10, which have different degrees of unsaturation.



Scheme 10

These Fe(II) complexes are low spin ($d^6-t_{2g}^6$), as deducible from their negligible magnetic moment ($\mu_{\text{eff}} = 0.5 \mu_{\text{B}}$). In acetonitrile solution they display a chemically reversible $\text{Fe}(\text{II})/\text{Fe}(\text{III})$ oxidation. It must be taken into account that in acetonitrile solution they possess an octahedral

Table 8 Formal electrode potentials (*V* vs. SCE) for the redox processes exhibited by the tetraazamacrocycles–Fe(II) complexes in MeCN solution

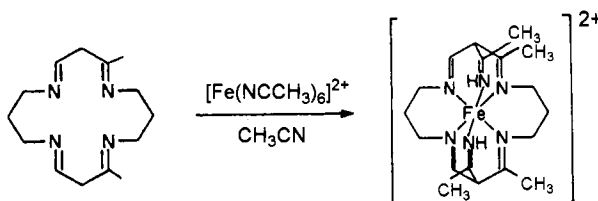
Complex	$E^{\circ'}$ ($Fe^{III/II}$)	$E^{\circ'}$ ($Fe^{II/I}$)
[Fe(Me ₂ [14]aneN ₄)] ²⁺	+ 0.61	—
[Fe(Me ₆ [14]aneN ₄)] ²⁺	+ 0.72	—
[Fe([14]4,11-dieneN ₄)] ²⁺	+ 0.78	—
[Fe([14]1,4,11-trieneN ₄)] ²⁺	+ 0.85	—
[Fe([14]1,3,8-trieneN ₄)] ²⁺	+ 1.10	—
[Fe([14]1,4,8,11-tetraeneN ₄)] ²⁺	+ 0.93	—
[Fe([14]1,3,7,11-tetraeneN ₄)] ²⁺	+ 1.06	—
[Fe([14]1,3,7,10-tetraeneN ₄)] ²⁺	+ 1.16	—
[Fe([14]1,3,8,10-tetraeneN ₄)] ²⁺	+ 1.23	-0.46

geometry, in that the central Fe(II) ion, in addition to the four planar nitrogen atoms of the macrocycle, coordinates two acetonitrile molecules in axial positions as the synthesis reagent is $[Fe(NCMe)_6]^{2+}$. Their redox potentials are compiled in Table 8.⁹⁸

It is evident that the oxidation process becomes more and more difficult with the increase of the macrocycle unsaturation.

It is however important to note that those complexes which have conjugated diimine groups in the macrocycle also display a reversible Fe(II)/Fe(I) reduction. This is for example the case of $[Fe([14]1,3,8,10\text{-tetraeneN}_4)]^{2+}$. The formation of an unusually stable low spin Fe(I) complex ($d^7\text{-}t_{2g}^6e_g^1$, one unpaired electron) is revealed both by EPR spectroscopy and by its magnetic moment ($\mu_{eff} = 2.3 \mu_B$).⁹⁹

Surprisingly, on reacting $[Fe(NCMe)_6]^{2+}$ with unsaturated tetraazamacrocycles similar to those described above, but containing 15 or 16 atoms in the ring, the two axially positioned acetonitrile molecules from the reagent become electrophilically bound to the apical carbon atom of the macrocycle giving rise to new, low spin, bis(macrocycle)hexadentate Fe(II) complexes, Scheme 11.

**Scheme 11**

The octahedral geometry of one of these complexes, the *cis*-[(3,11-bis(1-iminoethyl-2,12-dimethyl-1,5,9,13-tetracyclohexadecane-1,3,9,11-

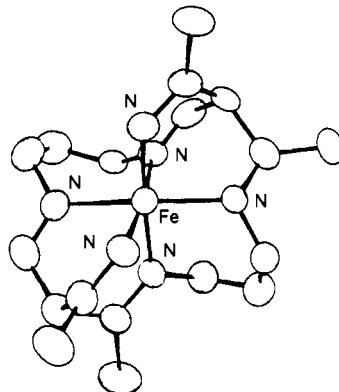


Figure 66 *X-Ray structure of $cis\text{-}[Fe(\text{Me}_4\text{I}\text{E}_2\text{[16]tetraeneN}_4)]^{2+}$ ($[\text{PF}_6]^-$ counter-anion). Average Fe-N bond length = 1.95 \AA*

tetraene]Fe(II) dication ($cis\text{-}[\text{Fe}(\text{Me}_4\text{I}\text{E}_2\text{[16]tetraeneN}_4)]^{2+}$) is illustrated in Figure 66.^{100,101}

In acetonitrile solution these complexes also display a reversible Fe(II)/Fe(III) oxidation. For example, in the case of $cis\text{-}[\text{Fe}(\text{Me}_4\text{I}\text{E}_2\text{[16]tetraeneN}_4)](\text{PF}_6)_2$, the oxidation occurs at $E^{\circ'} = +0.65 \text{ V}$ (vs. SCE).¹⁰²

A related hexacoordinate macrocycle complex is the Fe(III) derivative with the ‘scorpiand’ 6,13-diamino-6,13-dimethyl-1,4,8,11-tetraazacyclotetradecane (the *trans*-diammac ligand already discussed in Section 2), $[\text{Fe}(\text{trans-diammac})]^{3+}$. Its octahedral geometry is shown in Figure 67.¹⁰³

This low spin Fe(III) complex ($d^5 - t_{2g}^5$) exhibits, in aqueous solution, a chemically reversible reduction ($E^{\circ'} = -0.40 \text{ V}$ vs. SCE) to the corresponding Fe(II) derivative (low spin, $d^6 - t_{2g}^6$). As illustrated in Figure 68,

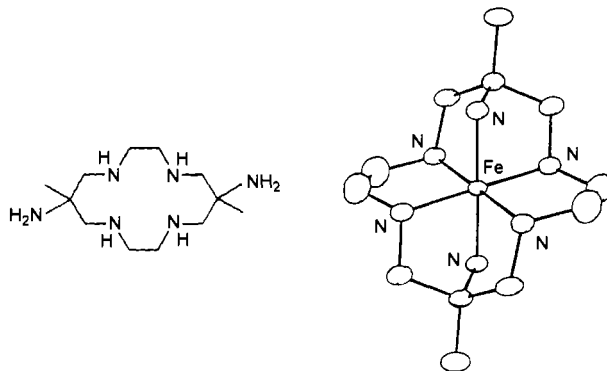


Figure 67 *X-Ray structure of $[\text{Fe}(\text{trans-diammac})]^{3+}$. Average bond lengths: $\text{Fe-N}_{(\text{equatorial})} = 1.96 \text{ \AA}$; $\text{Fe-N}_{(\text{axial})} = 1.98 \text{ \AA}$*

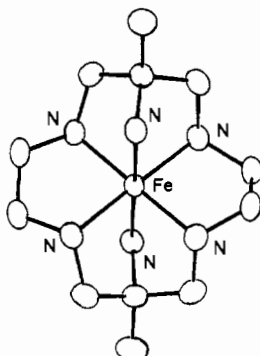


Figure 68 X-Ray structure of $[Fe(\text{trans-diammac})]^{2+}$. Average bond lengths: $Fe-N_{(\text{equatorial})} = 2.01 \text{ \AA}$; $Fe-N_{(\text{axial})} = 2.03 \text{ \AA}$

in agreement with the electrochemical reversibility of the reduction process, $[Fe(\text{trans-diammac})]^{2+}$ maintains the same geometry as the Fe(III) precursor, but for a slight elongation of the Fe–N bonding distances.¹⁰⁴

As usual, in a discussion of N₆ coordination, one cannot ignore polypyridine ligands. There are numerous X-ray structures available for iron complexes. We begin with the phenantroline $[Fe^{\text{II}}(\text{phen})_3]^{2+}$ complex, whose molecular structure is shown in Figure 69.¹⁰⁵

In agreement with the redox activity of the ligand, the complex shows a rich sequence of one-electron redox processes. The most significant is the $[Fe^{\text{II}}(\text{phen})_3]^{2+}/[Fe^{\text{III}}(\text{phen})_3]^{3+}$ oxidation, which is chemically and

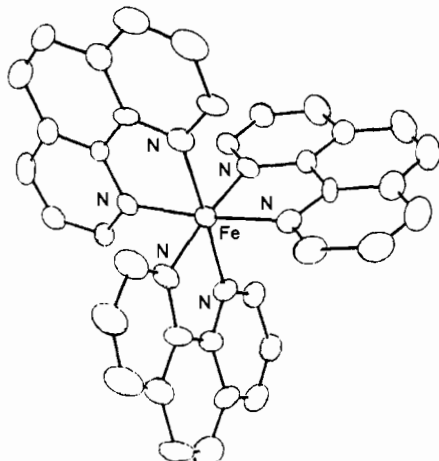


Figure 69 X-Ray structure of $[Fe(\text{phen})_3]^{2+}$ ($[ClO_4]^-$ counteranion). $Fe-N \approx 1.98 \text{ \AA}$

electrochemically reversible. The parameters of the redox processes are summarized in Table 9, together with those of the other polypyridine derivatives.

The electrochemical reversibility of the $2+/3+$ transformation, believed to be the only metal-centred redox process, allows one to predict that the $[\text{Fe}^{\text{III}}(\text{phen})_3]^{3+}$ complex maintains the octahedral structure of the $[\text{Fe}^{\text{II}}(\text{phen})_3]^{2+}$ complex virtually unaltered. As a matter of fact, this has been confirmed by the X-ray structure of $[\text{Fe}^{\text{III}}(\text{phen})_3][\text{ClO}_4]_3$ ($\text{Fe}-\text{N} \approx 1.97 \text{ \AA}$).¹⁰⁷

In a similar way, the X-ray structure of the couple $[\text{Fe}^{\text{II}}(\text{bipy})_3]^{2+}/[\text{Fe}^{\text{III}}(\text{bipy})_3]^{3+}$ has been determined.^{108,109} As deduced from Table 9, the interconversion has characteristics of electrochemical reversibility. In both cases there is an essentially regular octahedral geometry with mean $\text{Fe}-\text{N}$ distances of about 1.96 \AA .

Finally, as far as the $[\text{Fe}^{\text{II}}(\text{terpy})_2]^{2+}$ complex is concerned, its molecular structure is known. Its octahedral geometry is tetragonally distorted, in that the bond distance between the iron(II) ion and the central nitrogen atom of terpyridine is considerably shorter ($\text{Fe}-\text{N} = 1.89 \text{ \AA}$) than the distance between the iron(II) ion and the two more external nitrogen atoms ($\text{Fe}-\text{N} = 1.99 \text{ \AA}$).¹¹⁰

As reported in Table 9, $[\text{Fe}^{\text{II}}(\text{terpy})_2]^{2+}$ also displays an electrochemically reversible one-electron oxidation, which suggests the maintaining of the original geometry; the X-ray structure of $[\text{Fe}^{\text{II}}(\text{terpy})_2]^{3+}$ is however not available.

It is interesting to note that in a further confirmation of the redox-active character of the polypyridine ligands, reductive electrocrystallization of $[\text{M}^{\text{II}}(\text{bipy})_3]^{2+}$ and $[\text{M}^{\text{II}}(\text{terpy})_2]^{2+}$ complexes ($\text{M} = \text{Fe}, \text{Ru}, \text{Os}$) afforded the corresponding neutral species $[\text{M}(\text{bipy})_3]^0$ and $[\text{M}(\text{terpy})_2]^0$. Based on the relevant bond lengths, it seems likely that the two added electrons enter the polypyridine ligands according to the formulation $[\text{M}^{\text{II}}(\text{bipy}^-)_2(\text{bipy})]^0$ and $[\text{M}^{\text{II}}(\text{terpy}^-)_2]^0$.^{111,112}

Table 9 Formal electrode potentials (V vs. SCE) for the redox processes exhibited by $[\text{Fe}(\text{bipy})_3]^{2+}$, $[\text{Fe}(\text{phen})_3]^{2+}$ and $[\text{Fe}(\text{terpy})_2]^{2+}$ in dmso solution¹⁰⁶

Complex	$E_{(3+/2+)}^\circ$	ΔE_p^{a}	$E_{(2+/+)}^\circ$	$E_{(+/-)}^\circ$	$E_{(0/-)}^\circ$
$[\text{Fe}(\text{bipy})_3]^{2+}$	+ 1.29	65	-1.05	-1.23	-1.41
$[\text{Fe}(\text{phen})_3]^{2+}$	+ 1.27	67	-1.08	-1.27	-1.36
$[\text{Fe}(\text{terpy})_2]^{2+}$	+ 1.38	69	-0.99	-1.17	-

^a Peak-to-peak separation (mV) measured at 0.2 V s^{-1} .

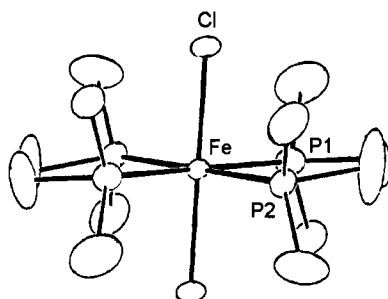


Figure 70 X-Ray structure of $[Fe(dmpe)_2Cl_2]$. Bond lengths: $Fe-Cl = 2.35 \text{ \AA}$; $Fe-P1 = 2.24 \text{ \AA}$; $Fe-P2 = 2.23 \text{ \AA}$

Another compound that exhibits redox properties of some interest is $[Fe(dmpe)_2Cl_2]$ [$dmpe = 1,2\text{-}(dimethylphosphino)ethane$]. It is a low spin Fe(II) derivative ($d^6 - t_{2g}^6$) having octahedral geometry, Figure 70.¹¹³

As shown in Figure 71, it displays in dichloromethane solution two successive oxidations ($E^{o'} = -0.09 \text{ V}$ and $+1.33 \text{ V}$, respectively).¹¹⁴

The first oxidation, which involves the Fe(II)/Fe(III) redox change, is chemically reversible ($i_{pc}/i_{pa} = 1$) and essentially electrochemically reversible ($\Delta E_p = 78 \text{ mV}$, at 0.2 V s^{-1}). The corresponding Fe(III) complex has been crystallographically characterized. The structural data ($Fe-Cl = 2.24 \text{ \AA}$; $Fe-P = 2.30 \text{ \AA}$) point out that the electron removal causes a considerable compression along the axial $Fe-Cl$ bonds, and a significant lengthening of the equatorial $Fe-P$ bonds.¹¹⁵

The second oxidation, which involves the Fe(III)/Fe(IV) change, is accompanied by a relatively slow degradation of the electrogenerated Fe(IV) complex. The electrochemical access to the high-valent Fe(IV) oxidation state is rather uncommon, even if a few bis(μ -oxo)diiron complexes have displayed the (III,III)/(III/IV) redox changes.^{116,117}

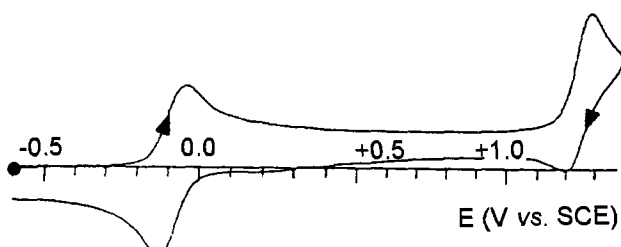


Figure 71 Cyclic voltammogram recorded at a platinum electrode in a CH_2Cl_2 solution of $[Fe(dmpe)_2Cl_2]$. Scan rate 0.2 V s^{-1}

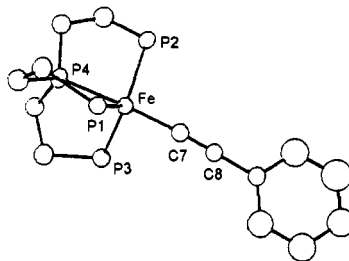


Figure 72 X-Ray structure of the monocation $[Fe(PP_3)(C\equiv C-Ph)]^+$. Bond lengths: $Fe-P_{(equatorial)} = 2.30 \text{ \AA}$; $Fe-P4 = 2.22 \text{ \AA}$; $Fe-C7 = 1.88 \text{ \AA}$

To conclude, we must consider that the Fe(I) oxidation state is also relatively unusual. Indeed, we have already mentioned that the reduction of a few 14-membered tetraaza-Fe(II) macrocycles leads to the corresponding Fe(I) complexes. Another example is given by the trigonal bipyramidal Fe(II)-alkynyl complex $[Fe(PP_3)(C\equiv C-Ph)]^+$ [$PP_3 = P(CH_2CH_2PPh_2)_3$], Figure 72.¹¹⁸

This low spin Fe(II) complex ($d^6-e^{1/4}e^{1/2}$; two unpaired electrons: $\mu_{eff} = 3.42 \mu_B$) in THF solution displays a chemically reversible, but electrochemically quasireversible, one-electron reduction, Figure 73 ($E^{o'} = -0.59 \text{ V}$; $\Delta E_p = 126 \text{ mV}$, at 0.2 V s^{-1}).

The corresponding $[Fe^I(PP_3)(C\equiv C-Ph)]$ complex has been isolated and characterized. As shown in Figure 74, it maintains the trigonal bipyramidal geometry of the Fe(II) precursor and its magnetic moment indicates a low spin d^7 configuration ($e^{1/4}e^{1/3}$; one unpaired electron: $\mu_{eff} = 2.10 \mu_B$).

From a comparison of the bond lengths one can deduce that the electron addition causes a structural distortion consistent with a significant shortening of the Fe–P distances and a lengthening of the Fe–C distance. This distortion might be responsible for the electrochemical quasireversibility of the corresponding redox process.

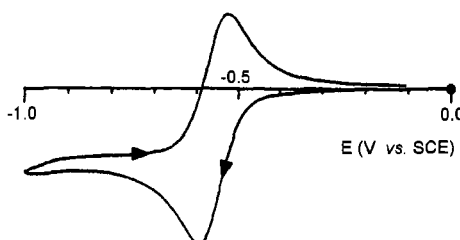


Figure 73 Cyclic voltammogram recorded at a platinum electrode in a THF solution of $[Fe(PP_3)(C\equiv C-Ph)](PF_6)$. Scan rate 0.02 V s^{-1}

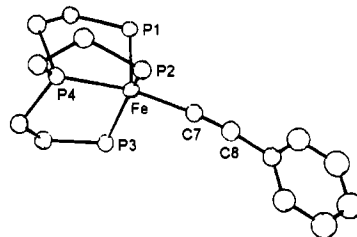


Figure 74 X-Ray structure of $[Fe(PP_3)(C\equiv C-Ph)]$. Bond lengths: $Fe-P1 = Fe-P2 = 2.21 \text{ \AA}$; $Fe-P3 = 2.19 \text{ \AA}$; $Fe-P4 = 2.15 \text{ \AA}$; $Fe-C7 = 1.92 \text{ \AA}$

It is worth noting that the Fe(II) complex $[Fe(dmpe)_2Cl(C\equiv C-Ph)]$, bearing the same alkyne but a different phosphine [the already mentioned 1,2-(dimethylphosphino)ethane)], Figure 75,¹¹⁹ can undergo reversibly the Fe(II)/Fe(III) oxidation ($E^{\circ'} = -0.14 \text{ V}$, in CH_2Cl_2), but, given the high stability of the Fe(II) oxidation state, it does not display any reduction process within the cathodic window of the solvent.¹¹⁴

On the other hand, the tetrahedral Fe(II) complex $[Fe(C_5Me_5)(dppe)(C\equiv C-Ph)]$ [$dppe = 1,2\text{-}(diphenylphosphino)ethane$] illustrated in Figure 76 also displays the only reversible Fe(II)/Fe(III) oxidation (in CH_2Cl_2 solution: $E^{\circ'} = -0.15 \text{ V}$ vs. SCE; $\Delta E_p = 80 \text{ mV}$, at 0.1 Vs^{-1}).¹²⁰

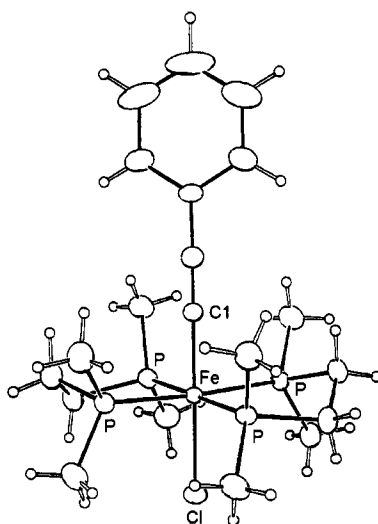


Figure 75 X-Ray structure of $[FeCl(dmpe)_2(C\equiv C-Ph)]$. Bond lengths: $Fe-Cl = 2.39 \text{ \AA}$; $Fe-P = 2.22 \text{ \AA}$; $Fe-Cl = 1.88 \text{ \AA}$

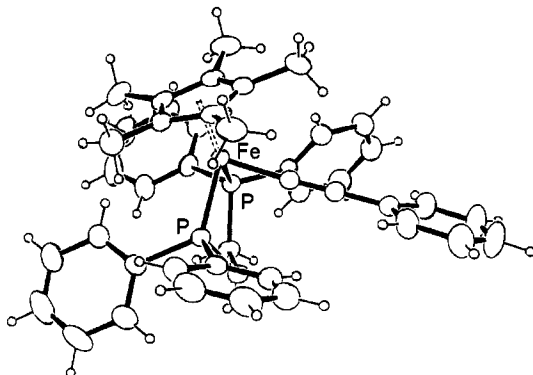


Figure 76 X-Ray structure of $[Fe(C_5Me_5)(dppe)(C\equiv C-Ph)]$. Bond lengths: $Fe-P = 2.18 \text{ \AA}$; $Fe-Cp_{(centroid)} = 1.74 \text{ \AA}$; $Fe-C_{(alkynyl)} = 1.89 \text{ \AA}$

Even without entering into a discussion at a molecular orbitals level, we naively note that while in the one-electron addition $[Fe^{II}(PP_3)(C\equiv C-Ph)]^+/[Fe^I(PP_3)(C\equiv C-Ph)]$ the Fe–P distances shorten meanly by about 0.08 \AA and the $Fe-C_{(alkynyl)}$ distance elongates by about 0.04 \AA , in the one-electron removal $[Fe^{II}(C_5Me_5)(dppe)(C\equiv C-C_6H_4-1,4-NO_2)]/[Fe^{III}(C_5Me_5)(dppe)(C\equiv C-C_6H_4-1,4-NO_2)]^+$, the Fe–P distances elongate by about 0.08 \AA (the $Fe-Cp_{(centroid)}$ elongate by about 0.04 \AA) and the $Fe-C_{(alkynyl)}$ distance remains substantially unaltered (it increases by about 0.01 \AA).¹²⁰

4.1 Intramolecular Electronic Communication in Polynuclear Iron Complexes

Even if the present chapter is essentially devoted to mononuclear complexes, we have already seen in Sections 3.2 and 3.3, that polynuclear complexes may hold great interest in applicative fields, in particular as far as their ability to undergo reversible multiple electron transfers; such a property is typical of semiconducting materials.

We cite here two examples of triiron complexes which can depict well the possible intramolecular electronic interactions in polymetallic complexes. First of all we take into account that, as discussed in Chapter 2, Section 1.5.1 and Chapter 4, Section 1.3, from the electrochemical viewpoint, the existence of a mutual electronic (through-space or through-bond) interaction in molecules containing two or more redox-active centres leads to the appearance of separate electron transfer processes. There are, however, two main classes of polynuclear molecules:

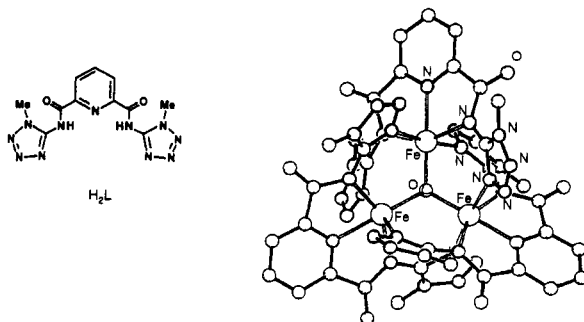


Figure 77 *X-Ray structure of $[Fe_3OL_3]$. Average bond lengths: $Fe-(\mu_3-O) = 1.89 \text{ \AA}$; $Fe-N_{(py)} = 2.07 \text{ \AA}$; $Fe-N_{(amide)} = 2.10 \text{ \AA}$; $Fe-N_{(tetrazole)} = 2.18 \text{ \AA}$. $Fe \cdots Fe = 3.27 \text{ \AA}$*

- those in which the various redox centres are coordinatively equivalent each other;
- those in which the various redox centres are not coordinatively equivalent.

Let us consider the mixed valent $Fe^{III}_2Fe^{II}$ oxo-centred complex $[Fe_3OL_3]$, the molecular structure of which is illustrated in Figure 77.¹²¹ It is evident that all the iron centres have the same coordination sphere.

Figure 78 shows that the complex undergoes three separate, reversible (one-electron) processes; namely, one Fe^{II}/Fe^{III} centred oxidation ($E_{0/+}^{\circ} = +0.08 \text{ V vs. } Fc/Fc^+$) and two Fe^{III}_2/Fe^{II}_2 centred reductions ($E_{0/-}^{\circ} = -0.64 \text{ V}$; $E_{-2/-}^{\circ} = -1.23 \text{ V}$).¹²¹

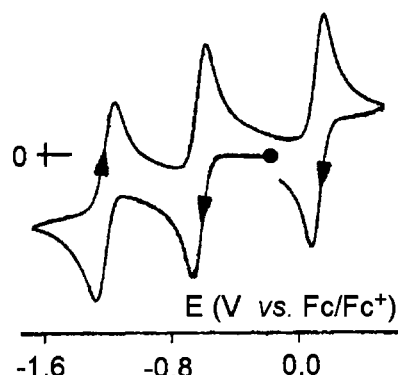


Figure 78 *Cyclic voltammogram recorded at a platinum electrode in a CH_2Cl_2 solution of $[Fe_3OL_3]$. Scan rate 0.05 V s^{-1}*

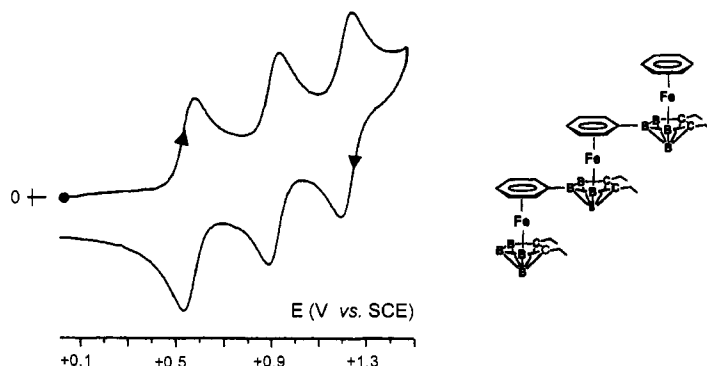


Figure 79 Cyclic voltammogram recorded at a platinum electrode in a CH_2Cl_2 solution of the schematised triferracarborane. Scan rate 0.1 Vs^{-1}

It is evident that the three iron centres are internally communicating. Based on the separation between the redox potential of the oxidation and that of the first reduction ($\Delta E^{\circ'} = 0.72 \text{ V}$), a K_{com} of 1×10^{12} can be calculated, which allows one to classify the neutral species $[\text{Fe}^{\text{III}}_2\text{Fe}^{\text{II}}\text{O}(\text{L})_3]$ as a fully delocalized mixed-valent species.¹²¹

Let us now consider the linear tris(ferracarborane) $[(\eta^6\text{-C}_6\text{H}_6)\text{Fe}(\text{Et}_2\text{C}_2\text{B}_4\text{H}_3\text{-5-})(\eta^6\text{-C}_6\text{H}_6)\text{Fe}(\text{Et}_2\text{C}_2\text{B}_4\text{H}_3\text{-5-})(\eta^6\text{-C}_6\text{H}_6)\text{Fe}(\text{Et}_2\text{C}_2\text{B}_4\text{H}_4)]$ vaguely reminiscent of triferroocene (see Chapter 3, Section 3, and Chapter 4, Section 1.3).

As illustrated in Figure 79, just like triferroocene, it displays three well separated (one-electron) oxidation processes, all possessing features of chemical reversibility on the cyclic voltammetric time scale. They are clearly attributed to the step-by-step electron removals Fe^{II}_3 / Fe^{III}_3 ($E_{0/+}^{\circ'} = +0.56 \text{ V}$ vs. SCE; $E_{+/2+}^{\circ'} = +0.93 \text{ V}$; $E_{2+/3+}^{\circ'} = +1.25 \text{ V}$).¹²²

As far as the appearance of separated electron transfer processes is concerned, we must now take into consideration that they can arise either from internal electronic communication, or from the different coordination environment of each Fe(II) subunit. As a matter of fact, theoretical calculations favour the last hypothesis,¹²² thus pointing out some difference with triferroocene, in which only two different Fe(II) coordinations are present.

5 COBALT COMPLEXES

The redox behaviour of cobalt complexes is fairly similar to that of iron complexes. The commonest oxidation states of cobalt are II (d^7) and III (d^6), though the IV and I oxidation states are not as rare as for iron.

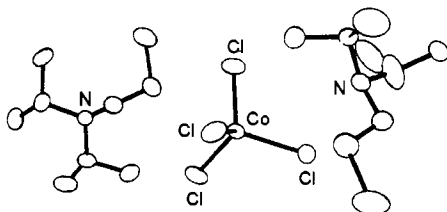


Figure 80 X-Ray structure of the dianion $[CoCl_4]^{2-}$ ($[C_8H_{19}ClN]^+$ counterion). Average Co–Cl bond length = 2.28 \AA

As usual, we begin our examination with tetracoordinate complexes.

By analogy with iron complexes, let us discuss the tetrachlorocobaltate(II) dianion $[CoCl_4]^{2-}$, the tetrahedral geometry of which is illustrated in Figure 80.¹²³

In spite of the structural analogies with $[Fe^{II}Cl_4]^{2-}$, which undergoes reversible oxidation to $[Fe^{III}Cl_4]^-$, the Co(II) complex is oxidized at notably higher potential values and the corresponding monoanion $[Co^{III}Cl_4]^-$ is not stable ($E_{2/-}^{\circ\prime} = +0.98 \text{ V vs. SCE}$; $\Delta E_p = 260 \text{ mV}$ and $i_{pc}/i_{pa} = 0.7$, at 0.2 V s^{-1}).¹²⁴

More interesting is the Co(IV) complex $[Co(1-nor)_4]$ (nor = norbornyl), which also possesses a (distorted) tetrahedral geometry, Figure 81.¹²⁵

As illustrated in Figure 82, the complex displays a rich redox activity in that it is able to be either reversibly oxidized to the really unusual Co(V) cation $[Co(1-nor)_4]^+$ ($E^{\circ\prime} = -0.65 \text{ V vs. Fc/Fc}^+$), or reversibly reduced to the corresponding Co(III) anion $[Co(1-nor)_4]^-$ ($E^{\circ\prime} = -2.02 \text{ V vs. Fc/Fc}^+$).¹²⁵

We now pass to the planar tetracoordinate Co(II) complexes with the many times cited Schiff bases salen and saloph.

The strictly planar geometry of these complexes¹²⁶ is illustrated in Figure 83 for $[Co^{II}(\text{saloph})]$.

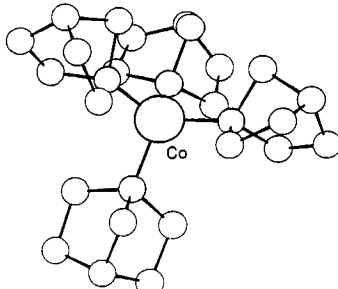


Figure 81 X-Ray structure of $[Co(1-nor)_4]$. Average Co–C bond length = 1.92 \AA

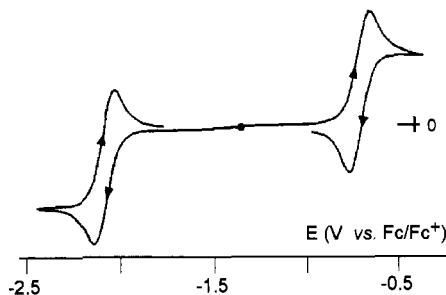


Figure 82 Cyclic voltammogram recorded at a platinum electrode in a *thf* solution of $[\text{Co}(\text{1-nor})_4]$. Scan rate 0.02 V s^{-1}

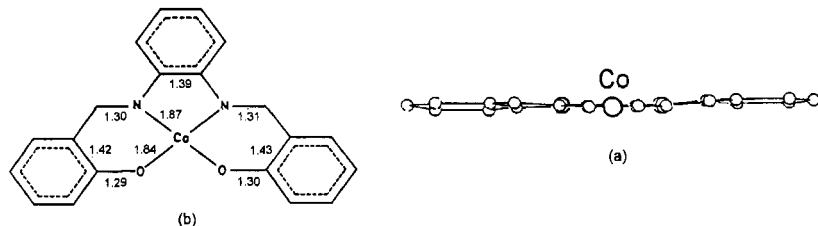


Figure 83 X-ray structure and relative parameters of $[\text{Co}^{\text{II}}(\text{saloph})]$

As deduced from their magnetic moments $\{[\text{Co}^{\text{II}}(\text{salen})]: \mu_{\text{eff}} = 2.38 \mu_{\text{B}}; [\text{Co}^{\text{II}}(\text{saloph})]: \mu_{\text{eff}} 2.74 \mu_{\text{B}}\}$,¹²⁷ they are low spin complexes. Even if the spin-orbit contribution makes such value slightly greater than expected, it indicates an electronic configuration with a single unpaired electron ($d^7-d_{yz}^2d_{xz}^2d_z^2d_{xy}^1$).

Figure 84 shows that $[\text{Co}^{\text{II}}(\text{saloph})]$ undergoes in *dmsol* solution a $\text{Co}(\text{II})/\text{Co}(\text{III})$ oxidation ($E^{\circ'} = -0.02 \text{ V}$) and two consecutive reductions

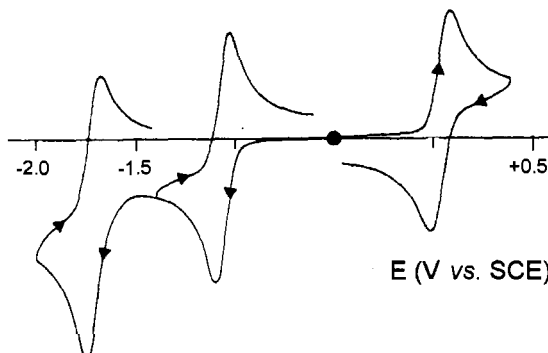
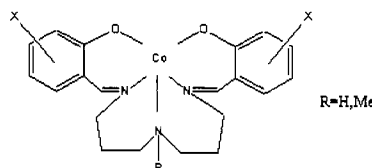


Figure 84 Cyclic voltammogram recorded at a platinum electrode in a *dmsol* solution of $[\text{Co}^{\text{II}}(\text{saloph})]$. Scan rate 0.2 V s^{-1}

Co(II)/Co(I) ($E^{\circ'} = -1.14$ V) and Co(I)/Co(0) ($E^{\circ'} = -1.87$ V).¹²⁸ However, only the monocation $[\text{Co}^{\text{III}}(\text{saloph})]^+$ and the monoanion $[\text{Co}^{\text{I}}(\text{saloph})]^-$ proved to be stable in the macroelectrolysis time scale.

$[\text{Co}^{\text{II}}(\text{salen})]$ also displays the two chemically reversible processes Co(II)/Co(III) ($E^{\circ'} = -0.09$ V) and Co(II)/Co(I) ($E^{\circ'} = -1.24$ V).¹²⁸

As for iron, cobalt forms pentacoordinate complexes of N_3O_2 coordination with the already mentioned bis(salicyldeneamine-3-propyl) amine affording the series $[\text{Co}(\text{R-X-saldpt})]$, Scheme 12.



Scheme 12

These Co(II) complexes are high spin derivatives ($d^7-e^{14}e^2a_1'^1$). The trigonal bipyramidal geometry of $[\text{Co}^{\text{II}}(\text{MeHsaldpt})]$ is illustrated in Figure 85.¹²⁹

In dmso solution these complexes also exhibit both the Co(II)/Co(III) oxidation and the Co(II)/Co(I) reduction, Figure 86, but only the Co(III) compound is completely stable.¹²⁹

The Co(II)/Co(III) oxidation potentials for a series of complexes having different substituents are reported in Table 10.

The influence of the inductive effects of the substituents present on both the amine nitrogen and benzene ring on the Co(II)/Co(III) redox potential is quite evident.

As for d^6 -iron(II), d^6 -cobalt(III) also forms complexes with the 14-membered tetraazamacrocycles shown in Scheme 13.

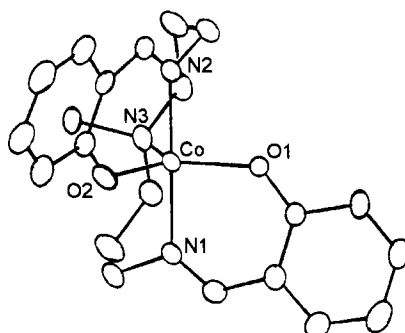


Figure 85 X-Ray structure of $[\text{Co}^{\text{II}}(\text{MeHsaldpt})]$. Bond lengths: $\text{Co}-\text{O} = 1.97 \text{ \AA}$; $\text{Co}-\text{N}3 = 2.15 \text{ \AA}$; $\text{Co}-\text{N}1 \approx \text{Co}-\text{N}2 = 2.04 \text{ \AA}$

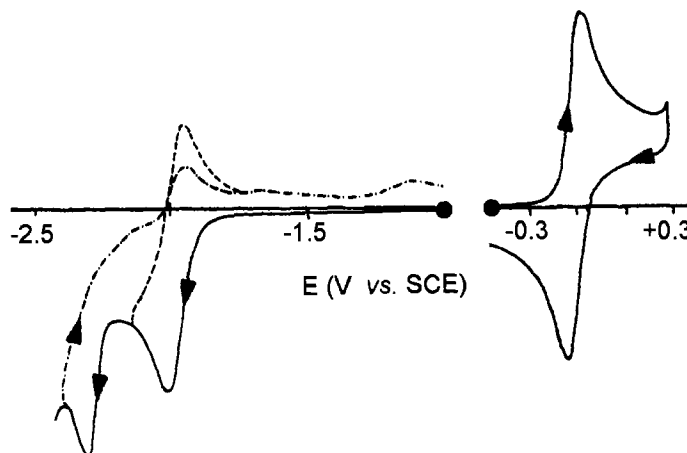
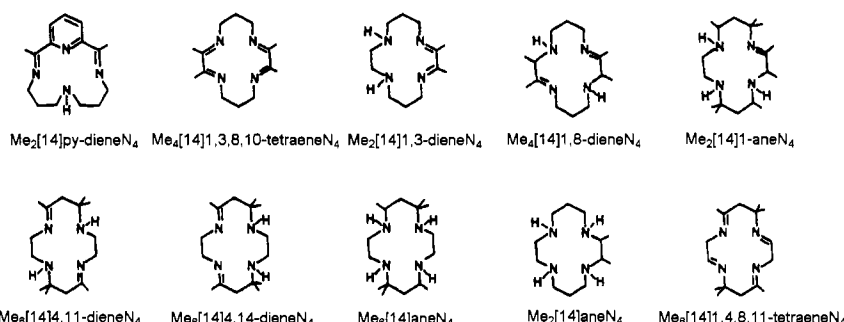


Figure 86 Cyclic voltammograms recorded at a mercury electrode in a dmso solution of $[Co^{II}(MeHsaldpt)]$. Scan rate 0.2 V s^{-1}

Table 10 Oxidation potentials (V vs. SCE) for the $[Co^{II}(R-X-saldpt)]$ complexes in dmso solution

R	X	$E^{\circ I}(Co^{II/III})$	R	X	$E^{\circ I}(Co^{II/III})$
H	H	-0.27	Me	H	-0.14
3-OMe		-0.32		3-OMe	-0.17
4-OMe		-0.26		4-OMe	-0.14
5-OMe		-0.29		5-OMe	-0.15
5-Cl		-0.21		5-Cl	-0.07
5-NO ₂		-0.11		5-NO ₂	+0.02



Scheme 13

As happens for the Fe(II) analogues, these low spin complexes have an octahedral geometry in that the four nitrogen atoms of the macrocycle form a square planar coordination in the equatorial plane while two molecules of acetonitrile are axially coordinated.

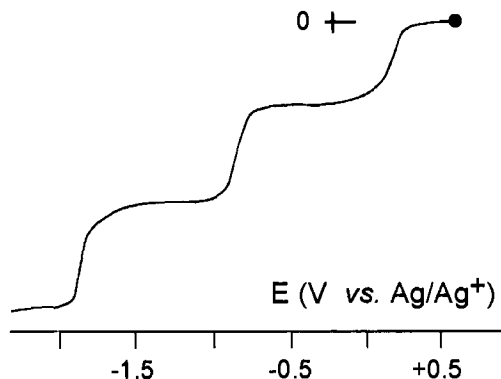


Figure 87 Voltammogram recorded at a rotating platinum electrode in a MeCN solution of $[Co^{III}(Me_2[14]py\text{-}dieneN_4)(MeCN)_2][ClO_4]_3$. Rotation frequency = 600 rpm (rpm = revolutions per minute)

Figure 87, which refers to $[Co^{III}(Me_2[14]py\text{-}dieneN_4)(MeCN)_2]^{3+}$, shows that, as expected, these complexes display the gradual reduction sequence $Co^{III/II/I/0}$, with features of electrochemical quasireversibility ($E_{3/4} - E_{1/4}$ slightly higher than 56.4).

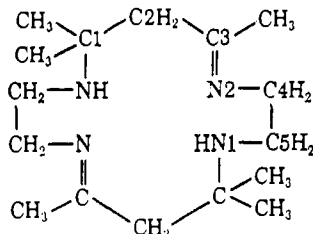
The respective potential values are compiled in Table 11.

By way of speculation, the structural variations which follow the Co(III)/Co(II) transformation can be tentatively evaluated by inspection of the X-ray data for the redox couple $[Co(Me_6[14]4,11\text{-dieneN}_4)(H_2O)_2](BF_4)_2/[Co(Me_6[14]4,11\text{-dieneN}_4)(NH_3)_2](ClO_4)_3$, even if the axial ligands are different in the two oxidation states.¹³⁰ Looking at

Table 11 Formal electrode potentials (V vs. SCE) for the reduction processes of a few Co(III)-tetraaza macrocycles in MeCN solution

macrocycle	$E^{\circ'}(Co^{III/II})$	$E^{\circ'}(Co^{II/I})$
$Me_2[14]py\text{-}dieneN_4$	+0.54	-1.20
$Me_4[14]1,3,8,10\text{-tetraeneN}_4$	+0.46	-1.06
$Me_2[14]1,3\text{-dieneN}_4$	+0.39	-1.51
$Me_6[14]1,4,8,11\text{-tetraeneN}_4$	+0.47	-1.64
$Me_6[14]4,11\text{-dieneN}_4$	+0.47	-2.03
$Me_6[14]4,14\text{-dieneN}_4$	+0.47	-2.03
$Me_6[14]1,8\text{-dieneN}_4$	+0.34	-2.08
$Me_2[14]1\text{-eneN}_4$	+0.42	-2.20
$Me_2[14]aneN_4$	+0.25	-2.37
$Me_6[14]aneN_4$	+0.42	-2.55

Scheme 14, in the Co(III) complex the bond distances are: Co–N1 = 1.99 Å; Co–N2 = 1.92 Å; Co–N(NH₃) = 1.95 Å, whereas in the Co(II) complex ($\mu_{\text{eff}} = 1.85 \mu_{\text{B}}$; $t_{2g}^6 e_g^1$, low spin complex) the bond distances are: Co–N1 = 1.97 Å; Co–N2 = 1.94 Å; Co–O(H₂O) = 2.48 Å.



Scheme 14

If allowance is made to neglect the different nature of the axial ligands, it appears that the addition of an electron causes a significant increase of only the axial distances (tetragonal distortion).

A ligand which links the cobalt complexes with those of chromium and iron is the ‘scorpiand’ diammac in its isomeric *trans* and *cis* conformations (see Scheme 5).

The geometry of the two Co^{III}-isomers is shown in Figure 88.^{131,132} As already discussed for the chromium complexes, the *trans*-isomer affords an octahedral geometry, whereas the *cis*-isomer gives rise to a trigonal prismatic geometry.

In aqueous solution (pH 7) the *trans*-complex exhibits a reversible one-electron reduction at significantly negative potentials ($E^{\circ'} = -0.81$ V), whereas the *cis*-complex is reduced at less negative potential values ($E^{\circ'} = -0.70$ V).^{131,132}

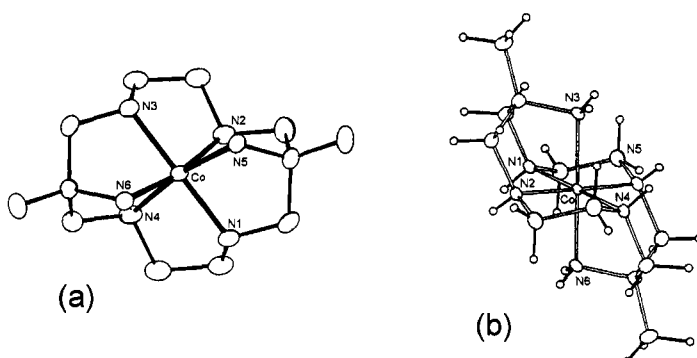


Figure 88 X-Ray structures of: (a) $[\text{Co}(\text{cis-diammac})]^{3+}$; average Co–N bond length = 1.96 Å. (b) $[\text{Co}(\text{trans-diammac})]^{3+}$; average Co–N bond length = 1.94 Å

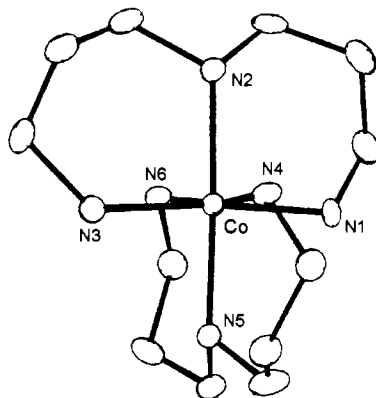


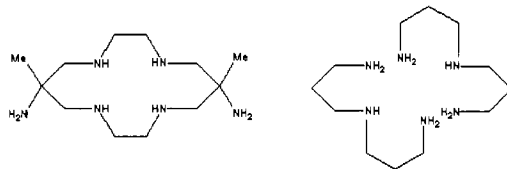
Figure 89 X-Ray structure of $[Co(dpt)_2]^{3+}$. Bond lengths: $Co-N1 \approx Co-N6 = 1.97 \text{ \AA}$; $Co-N4 = 2.00 \text{ \AA}$; $Co-N2 \approx Co-N3 \approx Co-N5 = 2.04 \text{ \AA}$

It is interesting to account for such negative Co^{III}/Co^{II} potential values with respect to that observed for the somewhat related bis(3-aminopropyl)amine complex $[Co^{III}(dpt)_2]^{3+}$, whose distorted octahedral CoN_6 structure is reported in Figure 89.¹³³

In fact, the reversible Co^{III}/Co^{II} reduction for this complex in aqueous solution occurs at $E^{\circ'} = +0.04 \text{ V}$ (vs. SCE).¹³³ This indicates that the $Co(III)/Co(II)$ reduction of $[Co(dpt)_2]^{3+}$ is about 0.8–0.9 V easier compared to the $[Co(\text{diammac})]^{3+}$ complexes.

Among the factors which govern the thermodynamic localization of the redox potential, in addition to the previously mentioned electronic effects, there are also the steric influences.¹³⁴

As illustrated in Scheme 15, the diammac and dpt ligands are fairly similar in nature (two primary amine groups, four secondary amine groups, twelve carbon atoms in diammac; four primary amine groups, two secondary amine groups, twelve carbon atoms in two molecules of dpt).



Scheme 15

Hence, it appears reasonable to assign the considerable difference in their redox potentials mainly to the different steric factors that accompany the Co^{III}/Co^{II} reduction. In this regard it should be recalled that the difference in free (reorganization) energy that accompanies the two redox processes can be quantitatively related to their electrode potentials:

$\Delta G^\circ = -n \cdot F \cdot \Delta E^\circ$. Therefore, a difference in potential of about 0.9 V between the $[\text{Co}(\text{diammac})]^{3+}$ and $[\text{Co}(\text{dpt})]^{3+}$ complexes corresponds to the notably high reorganization energy of about 90 kJ mol⁻¹.

The reasons for these structural constraints have been analysed in the following manner.¹³⁴ Firstly, one must consider that the $\text{Co}^{\text{III}}/\text{Co}^{\text{II}}$ reduction leads to an average increase in the Co–N bond distance of about 0.2 Å. It is known that in the $[\text{Co}(\text{diammac})]^{3+}$ complex the Co–N bond distances are about 1.95 Å, whereas in the $[\text{Co}(\text{dpt})_2]^{3+}$ complex they are about 2.01 Å. This suggests that the lengthening of the Co–N bond accompanying the $\text{Co}(\text{III})/\text{Co}(\text{II})$ reduction can be accommodated better by the ‘relaxed’ molecular organization of $[\text{Co}(\text{dpt})_2]^{n+}$ than by the more ‘compressed’ structure of $[\text{Co}(\text{diammac})]^{n+}$. This observation can account for the easier thermodynamic accessibility to $[\text{Co}^{\text{II}}(\text{dpt})_2]^{2+}$ compared to $[\text{Co}^{\text{II}}(\text{diammac})]^{2+}$.

One should not, however, underestimate the role played by the two peripheral methyl groups present in $[\text{Co}^{\text{III}}(\text{diammac})]^{3+}$ in determining the significant difference in redox potential between the two complexes. Their electron-donating ability certainly contributes in part to render the reduction process more difficult.

Another cobalt derivative with CoN_6 coordination is $[\text{Co}(\text{sep})]^{3+}$. This is the complex formed by $\text{Co}(\text{III})$ with the ligand 1,3,6,8,10,13,1,6,19-octaaazabicyclo[6.6.6]eicosane, which is related to the diamino-sarcophagine seen for the chromium complexes, and is called ‘sepulcrand’. Figure 90 shows the octahedral structure of this complex.¹³⁵

The reversible $\text{Co}(\text{III})/\text{Co}(\text{II})$ reduction of the $[\text{Co}(\text{sep})]^{3+}$ complex takes place at $E^\circ' = -0.49$ V in aqueous solution,¹³⁶ and at $E^\circ' = -0.67$ V in dmso.¹³⁷

The molecular structure of the $[\text{Co}^{\text{II}}(\text{sep})]^{2+}$ congener is illustrated in Figure 91.¹³⁸

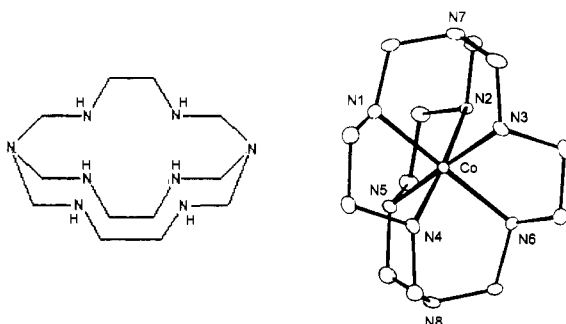


Figure 90 *X*-Ray structure of the trication $[\text{Co}(\text{sep})]^{3+}$. Average Co–N distance = 1.99 Å

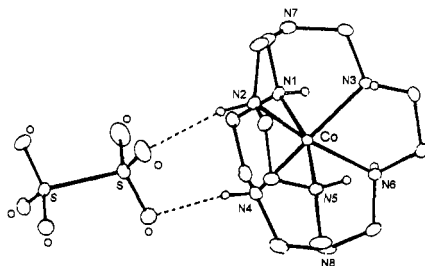


Figure 91 X-Ray structure of the dication $[Co(sep)]^{2+}$ in $[Co^{II}(sep)][S_2O_6]$. Bond lengths: $Co-N1 \approx Co-N5 = 2.15 \text{ \AA}$; $Co-N3 = 2.16 \text{ \AA}$; $Co-N2 \approx Co-N6 = 2.17 \text{ \AA}$; $Co-N4 = 2.18 \text{ \AA}$

A glance at the bond lengths shows that the reduction process induces a distortion and a significant increase in the Co–N bond distances.

To conclude our discussion of CoN_6 coordination we consider the complexes with polypyridine ligands. There is a good number of structures available for such complexes. As an example, Figure 92 shows the distorted octahedral geometry of $[Co^{II}(bipy)_3]^{2+}$.¹³⁹ The magnetic moment of the complex ($4.5 \mu_B$) indicates a high spin configuration ($d^7-t_{2g}^5e_g^2$).

$[Co(phen)_3]^{2+}$ possesses a geometry and a magnetic moment quite similar to that of $[Co(bipy)_3]^{2+}$.¹⁴⁰

The electrochemical activity of $[Co^{II}(bipy)_3](ClO_4)_2$ is shown in Figure 5.93.¹⁴¹

It undergoes an oxidation and a first reduction process, both of which involve a one-electron step and are chemically reversible. The more cathodic two-electron reduction is probably centred on the bipy ligand.

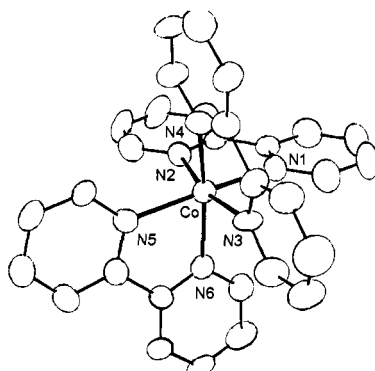


Figure 92 X-Ray structure of $[Co(bipy)_3]^{2+}$ in $[Co(bipy)_3][Cl]_2$

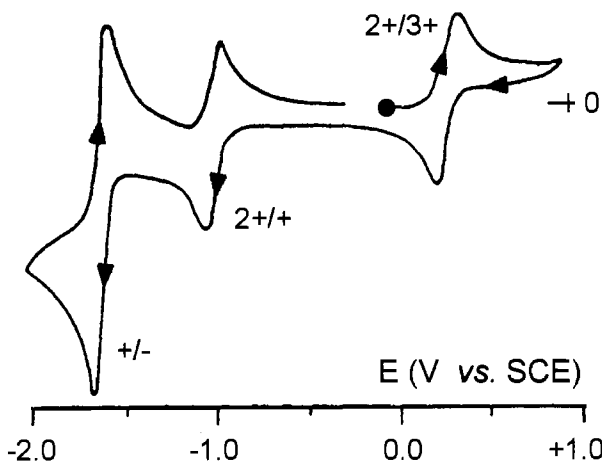


Figure 93 Cyclic voltammogram recorded at a glassy carbon electrode in a MeCN solution of $[\text{Co}^{\text{II}}(\text{bipy})_3]^{2+}$. Scan rate 0.1 V s^{-1}

Table 12 summarizes some structural parameters that characterize the $[\text{Co}(\text{bipy})_3]^{3+/2+/+/-}$ transformations.

It is interesting to note the increase of the Co–N distance on passing from Co(III) to Co(II). It is also noteworthy that there is a significant shortening of the carbon–carbon distance of the pyridine ring on passing to the (formally) Co(I) complex, compared with the free ligand. This would seem to confirm the metal–ligand backbonding ($\pi\text{d} \rightarrow \text{bipy } \pi^*$), that we have indicated to exist in the redox processes of the metal complexes of the present redox-active ligands.

Finally, Figure 94 shows the electrochemical behaviour of $[\text{Co}(\text{terpy})_2]^{2+}$ in acetonitrile solution.¹⁴³

Like $[\text{Co}(\text{bipy})_3]^{2+}$, it exhibits the $\text{Co}^{\text{II}}/\text{Co}^{\text{III}}$ oxidation and the $\text{Co}^{\text{II}}/\text{Co}^{\text{I}}$ reduction, but, at variance with $[\text{Co}(\text{bipy})_3]^{2+}$, the ligand-centred most cathodic step is a one-electron process. A further one-electron ligand-centred reduction has been detected at very negative

Table 12 Structural variations accompanying the redox sequence $[\text{Co}(\text{bipy})_3]^{3+/2+/+/-}$ ^{139,142}

Complex	$\text{Co}-\text{N} (\text{\AA})$	$\text{N}-\text{Co}-\text{N} (\text{\\textdegree})$	$\text{C}-\text{C}_{(\text{pyridine ring})} (\text{\AA})$
$[\text{Co}(\text{bipy})_3]^{3+}$	1.93	83.3	1.45
$[\text{Co}(\text{bipy})_3]^{2+}$	2.13	76.5	1.49
$[\text{Co}(\text{bipy})_3]^+$	2.11	76.6	1.42
bipy			1.49

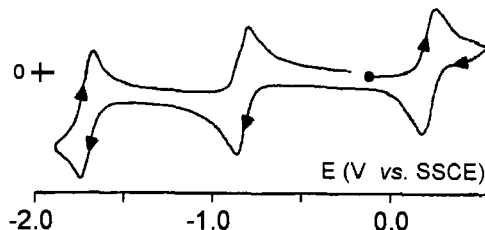


Figure 94 Cyclic voltammogram recorded at a platinum electrode in a MeCN solution of $[\text{Co}(\text{terpy})_2]^{2+}$. Scan rate 0.2 V s^{-1}

potential values.¹⁴⁴ Thus the fact that the ligand-centred two-electron wave present in $[\text{Co}(\text{bipy})_3]^{2+}$ is here split into two one-electron waves suggests that the electron mobility in the terpy complex is higher than that in the bipy complex.

The molecular structures of the couple $[\text{Co}(\text{terpy})_2]^{2+/3+}$ are available. Figure 95 shows the structure of $[\text{Co}(\text{terpy})_2]^{2+}$ in $[\text{Co}(\text{terpy})_2]\text{[Br]}_2$.¹⁴⁵

As for the analogous case of the iron(II) complex, the Co–N distances of the central pyridine (1.89 \AA) are shorter than those of the peripheral pyridines (2.10 \AA).

At room temperature $[\text{Co}(\text{terpy})_2]\text{[Br]}_2$ has a magnetic moment of $2.94 \mu_B$. It is important to specify the type of complex (namely, the counteranion) and the temperature¹⁴⁵ because it is thought that in $[\text{Co}(\text{terpy})_2]^{2+}$ an equilibrium exists between molecules having low spin and high spin configuration. As a matter of fact, the magnetic moment of $[\text{Co}(\text{terpy})_2]\text{[Br]}_2$ results in between $4.5 \mu_B$ (expected for the high spin $d^7-t_{2g}^5e_g^2$ configuration, or three unpaired electrons) and $2.0 \mu_B$ (expected

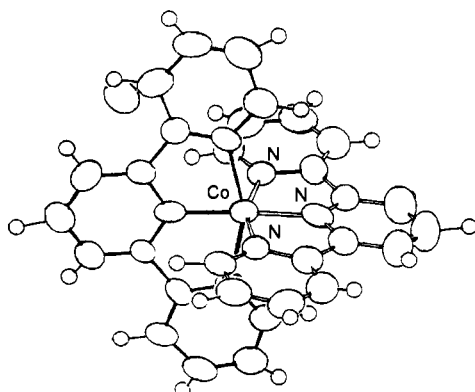


Figure 95 X-Ray structure of $[\text{Co}(\text{terpy})_2]^{2+}$ in $[\text{Co}(\text{terpy})_2]\text{[Br]}_2$

Table 13 Formal electrode potentials (V vs. SCE) for the redox processes exhibited by Co(II) -polypyridine complexes in MeCN solution^{141,143,144}

Complex	$E_{(3+/2+)}^{\circ'}$	$E_{(2+/+)}^{\circ'}$	$E_{(+/-)}^{\circ'}$	$E_{(0/-)}^{\circ'}$
$[\text{Co}(\text{bipy})_3]^{2+}$	+0.34	-0.95	-1.57 ^a	-
$[\text{Co}(\text{phen})_3]^{2+}$	+0.38	-	-	-
$[\text{Co}(\text{terpy})_2]^{2+}$	+0.35	-0.80	-1.67	-2.02

^a Two-electron process.

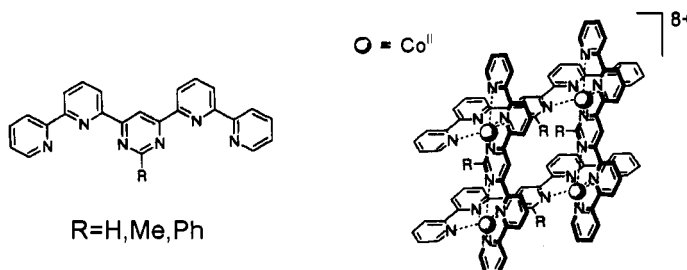
for the low spin $d^7-t_{2g}^6e_g^1$ configuration, or one unpaired electron). This should indicate that at room temperature 20% of the molecules are in the high spin configuration. By contrast, $[\text{Co}(\text{terpy})_2][\text{ClO}_4]_2$, independently from temperature, has a magnetic moment of $4.0 \mu_B$, which should suggest that in this case 70% of the molecules are constantly in the high spin configuration.¹⁴⁵

The structure of the corresponding $[\text{Co}(\text{terpy})_2]^{3+}$ ion in the complex $[\text{Co}(\text{terpy})_2][\text{Cl}]_3$ is also available.¹⁴⁶ In this case too, the C–N bond lengths of the central pyridine (1.86 Å) are shorter than those of the peripheral pyridines (1.93 Å).

Table 13 summarizes the electrode potentials of the redox processes for the complete set of polypyridine complexes.

5.1 Intramolecular Electronic Communication in Polynuclear Cobalt Complexes

Recently, tetracobalt(II) supramolecular arrays with the ligand 4,6-bis-(2',2'-bipyrid-6'-yl)-2-R-pyrimidine have been presented, Scheme 16.



Scheme 16

Figure 96 shows the square-planar $[2 \times 2]$ grid-like molecular assembly formed by the octacation $[\text{Co}^{\text{II}}_4\text{L}_4]^{8+}$ ($\text{R} = \text{Me}$).¹⁴⁷

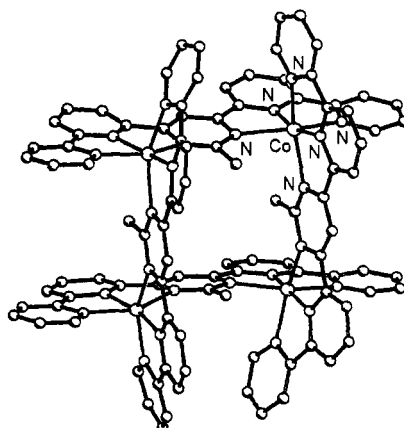


Figure 96 X-Ray structure of $[Co^{II}L_4]^{8+}$ in $[Co_4L_4][SbF_6]_8$ ($R = Me$). Average bond lengths: $Co-N(\text{pyridine}) = 2.10 \text{ \AA}$; $Co-N(\text{pyrimidine}) = 2.23 \text{ \AA}$. $Co \cdots Co = 6.35 \text{ \AA}$

As illustrated in Figure 97, complex $[Co^{II}4L_4]^{8+}$ ($R = Ph$) is able to give rise in dmf solution to a very high sequence of reduction steps, which display features of chemical reversibility.¹⁴⁸

Based on the redox capacity of the ligand, it is easily deducible that most electrons enter the pyrimidine as well as the pyridine fragments (as a matter of fact, theoretical calculations assign the first four electrons as entering the pyrimidine rings as well as the further four electrons as entering the ligand itself).¹⁴⁸ In MeCN solution a single Co^{II}/Co^{III} four-electron oxidation is also observed.¹⁴⁸ Such an example well testifies the potential interest covered by metal complexes containing redox-active ligands (see Chapter 6).

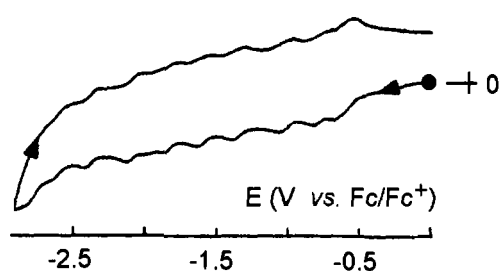


Figure 97 Cyclic voltammogram recorded at a glassy carbon electrode in a DMF solution of $[Co_4L_4][BF_4]_8$ ($R = Ph$). Scan rate 1.0 V s^{-1} . $T = -20^\circ C$

6 NICKEL COMPLEXES

In addition to the usual Ni(II) (d^8) oxidation state, the other common oxidation states for nickel in its complexes are III and I (d^7 and d^9 , respectively). Also the oxidation state IV (d^6) is not completely uncommon.

In order to give the usual overview of nickel complexes at increasing coordination numbers we begin with the usual square planar complexes of the Schiff bases salen and saloph.^{149,150} As an example, Figure 98 shows the molecular structure of $[Ni^{II}(\text{salen})]$.

In both cases the N_2O_2 coordination of the Ni(II) ion is essentially planar, though there is a slight tetrahedral distortion. However, the diamagnetism displayed by these complexes confirms that they are planar.

Electrochemical studies show that $[Ni(\text{salen})]$ in dmso undergoes a Ni(II)/Ni(III) oxidation ($E_p = +0.71$ V vs. SCE), complicated by fast chemical reactions, and a chemically reversible Ni(II)/Ni(I) reduction ($E^{\circ'} = -1.61$ V).^{151,152}

Conversely, $[Ni(\text{saloph})]$ and its phenyl-substituted analogues $[Ni(X\text{-saloph})]$ exhibit an irreversible Ni(II)/Ni(I) reduction and a chemically reversible Ni(II)/Ni(III) oxidation. For example, Figure 99 shows the anodic process for $[Ni(3,5\text{-Cl}_2\text{saloph})]$ ($E^{\circ'} = +0.84$ V vs. SCE). It shows characteristics of chemical reversibility (i_{pc}/i_{pa} constantly equal to 1) and electrochemical quasireversibility ($\Delta E_p = 110$ mV, at 0.05 V s $^{-1}$).¹⁵³

The oxidation product obtained by controlled potential electrolysis, $[Ni(3,5\text{-Cl}_2\text{saloph})]^+$, shows an EPR spectrum typical of a Ni(III) ion (d^7 – low spin) having an octahedral coordination, which is attributed to the axial coordination of two solvent molecules.¹⁵³ Therefore, from a speculative viewpoint, it could be assumed that the electrochemical quasireversibility is due to the change in coordination from square planar to octahedral.

The fact that the unsubstituted complex $[Ni(\text{saloph})]$ is oxidized at $E^{\circ'} = +0.77$ V ($\Delta E_p = 212$ mV, at 0.05 V s $^{-1}$) demonstrates once again

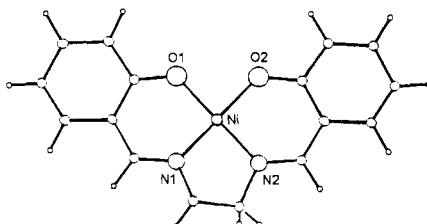


Figure 98 X-Ray structures of $[Ni(\text{salen})]$. Average bond lengths: $Ni-O \approx Ni-N = 1.85$ Å

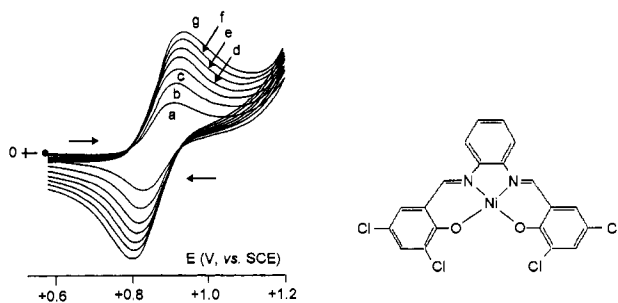


Figure 99 Cyclic voltammograms recorded at a platinum electrode in a dmso solution of $[Ni(3,5-Cl_2saloph)J]$. Scan rates: (a) 0.01 V s^{-1} ; (b) 0.02 V s^{-1} ; (c) 0.03 V s^{-1} ; (d) 0.04 V s^{-1} ; (e) 0.05 V s^{-1} ; (f) 0.06 V s^{-1} ; (g) 0.07 V s^{-1}

that the inductive effect of peripheral substituents, as expected, affect the Ni(II)/Ni(III) redox potential.

An interesting Ni(II) complex is the bis(dimethylphosphino)propane complex $[Ni(dmpp)_2]^{2+}$. As illustrated in Figure 100, it possesses a geometry intermediate between planar and tetrahedral in that the dihedral angle between the two coordinated dmpp ligands is about 44° .¹⁵⁴

As shown in Figure 101, this complex exhibits in benzonitrile solution two sequential, one-electron reductions reversible in character, that correspond to the stepwise Ni(II)/Ni(I) ($E^\circ' = -0.70\text{ V}$ vs. Fc/Fc^+) and Ni(I)/Ni(0) ($E^\circ' = -0.90\text{ V}$) processes, respectively.¹⁵⁴

The corresponding Ni(0) derivative $[Ni(dmpp)_2]$ has been structurally characterized, Figure 102.¹⁵⁴

The geometry becomes essentially tetrahedral (dihedral angle between the two planes formed by the Ni atom and the two P atoms of each dmpp ligands = 87°) and a significant shortening of the Ni–P distances (by about 0.06 \AA) occurs. Since within a given geometry reduction processes

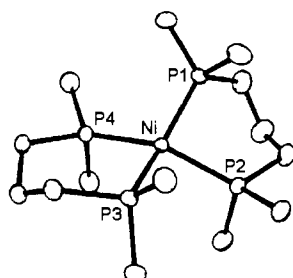


Figure 100 X-Ray structure of $[Ni(dmpp)_2]^{2+}$. Average bond lengths: $Ni-P = 2.21\text{ \AA}$. Dihedral angle bewtween the two NiPP fragments = 43.7°

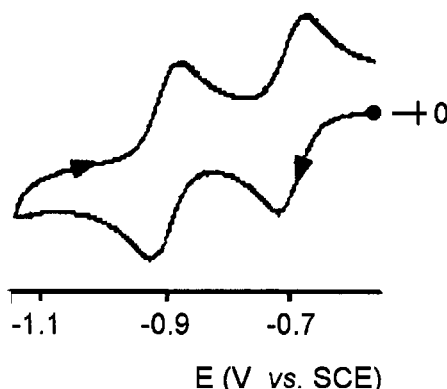


Figure 101 Cyclic voltammogram of $[Ni(dmpp)_2]^{2+}$ in PhCN solution

commonly cause lengthening of the metal–ligand bonds (because of the increase of the ionic radius of the metal atom), the actual shortening of the bond distances has been attributed to the fact that the original Ni(II) complex must be considered as a (distorted) planar complex which upon reduction passes to a Ni(0) tetrahedral complex.¹⁵⁴ As a matter of fact, the $[Ni(\text{diphosphine})_2]^{2+}$ analogues [diphosphine = bis(diphenyl phosphino) ethane, bis(diethylphosphino) ethane, bis(dimethylphosphino) ethane] are really planar.¹⁵⁴

Let us now consider a series of tetracoordinated Ni(II) complexes of general formula $[NiX(\text{triphos})]^+$ (triphos = $\text{MeC}(\text{CH}_2\text{PPh}_2)_3$; X = Cl, Br, I), which have a real tetrahedral geometry. In agreement with an electronic configuration $e^4t_2^4$ (two unpaired electrons), these complexes have magnetic moments in the range 2.91–3.04 μ_{B} . An example of

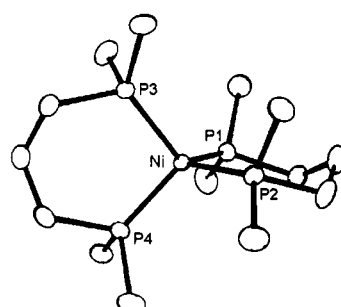


Figure 102 X-Ray structure of $[Ni(dmpp)_2]$. Average bond lengths: $\text{Ni}-\text{P} = 2.15 \text{ \AA}$. Dihedral angle between the two NiPP fragments = 87.4°

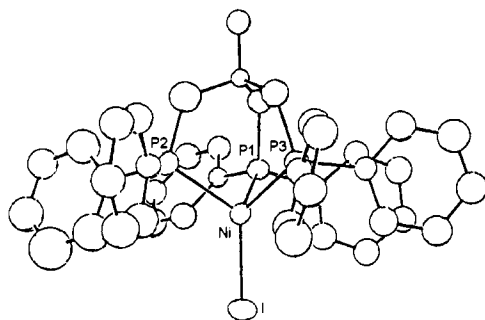


Figure 103 X-Ray structure of $[NiI(\text{triphos})]^+$. Bond lengths: $Ni-P \approx 2.24 \text{ \AA}$; $Ni-I = 2.41 \text{ \AA}$

their molecular structure is shown in Figure 103, which refers to $[NiI(\text{triphos})]^+$.¹⁵⁵

As illustrated in Figure 104 for $[NiBr(\text{triphos})]^+$, these complexes display the stepwise reductions $\text{Ni(II)}/\text{Ni(I)}/\text{Ni(0)}$. The former is chemically and electrochemically reversible, whereas the latter is essentially irreversible.¹⁵⁵

The respective potential values are reported in Table 14. It is evident that the nature of the coordinated halide (though in a way opposite to their electronegativity) has a significant influence on the redox potential of the $\text{Ni(II)}/\text{Ni(I)}$ couple (or, the terminal halide significantly contributes the LUMO of the molecule). This is in agreement with the structural data which show, for example, that in the neutral complex $[(\text{triphos})\text{Ni}^{\text{I}}\text{I}]$, which maintains the tetrahedral geometry of the Ni(II) precursor, the Ni-P distances remain essentially unchanged (2.22 \AA), whereas the Ni-I distance elongates by 0.14 \AA .

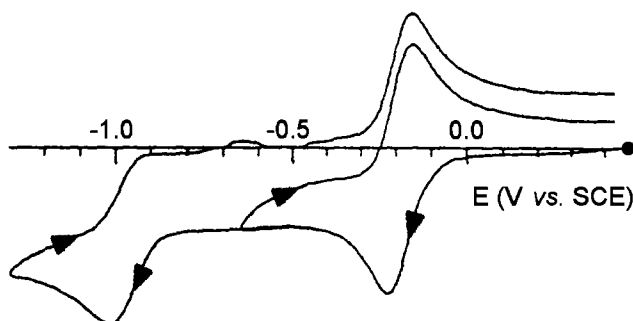


Figure 104 Cyclic voltammogram recorded at a platinum electrode in a MeCN solution of $[NiBr(\text{triphos})]^+$. Scan rate 0.5 V s^{-1}

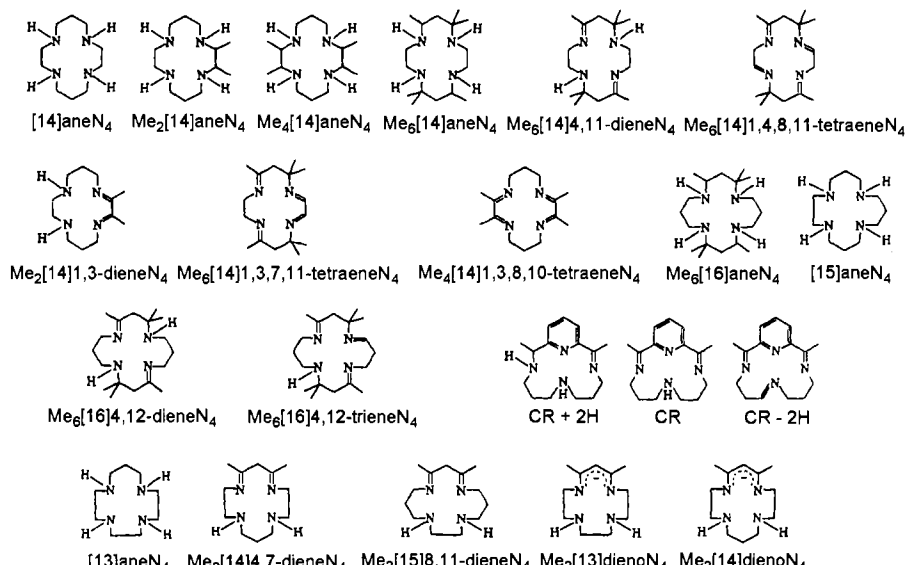
Table 14 Formal electrode potentials (V , vs. SCE) for the reduction processes exhibited by complexes $[NiX(\text{triphos})]^+$ in MeCN solution

X	$E^{\circ'}$ ($Ni^{II/I}$)	E_p ($Ni^{I/0}$)
Cl	-0.25	-1.03
Br	-0.19	-1.02
I	-0.09	-0.97

Let us now examine the pentacoordinate Ni(II) complexes with the already cited Schiff base bis(salicylideneimmine-3-propyl)amine, $[Ni(R-X-\text{saldpt})]$. As for the cases of iron(II) and cobalt(II) complexes, this ligand constrains the central nickel(II) ion to assume a trigonal bipyramidal geometry, Figure 105.¹⁵⁶

As exemplified in Figure 106 for $[Ni(5-\text{Cl}-\text{Hsaldpt})]$, these derivatives exhibit either a chemically and electrochemically reversible Ni(II)/Ni(III) oxidation ($E^{\circ'} = +0.50$ V for $[Ni(5-\text{Cl}-\text{Hsaldpt})]$), or a Ni(II)/Ni(I) reduction, which, in spite of the apparent chemical reversibility, is complicated by slow following chemical reactions ($E^{\circ'} = -1.70$ V for $[Ni(5-\text{Cl}-\text{Hsaldpt})]$).

The most extensive electrochemical study of nickel complexes is probably that carried out on tetraazamacrocyclic-Ni(II) derivatives, a few examples of which are reported in Scheme 17.



Scheme 17

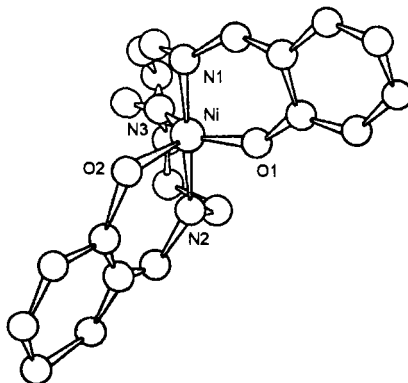


Figure 105 X-Ray structure of $[Ni(MeHsaldpt)]$. Average bond lengths: $Ni-O = 1.95 \text{ \AA}$; $Ni-N3 = 2.09 \text{ \AA}$; $Ni-N_{(axial)} = 2.01 \text{ \AA}$

As an example, Figure 107 shows the molecular structure of the $[Ni(Me_6[14]\text{aneN}_4)]^{2+}$ ¹⁵⁷. In confirmation of the planar geometry, the complex is diamagnetic ($d^8-d_z^2d_{xz}^2d_{yz}^2d_{xy}^2$).

Despite the planarity of the dication in the solid state, these complexes in solution easily assume an octahedral geometry, in that, as previously seen, two solvent molecules or two counteranions can coordinate the central metal ion. This is just the case for the derivative

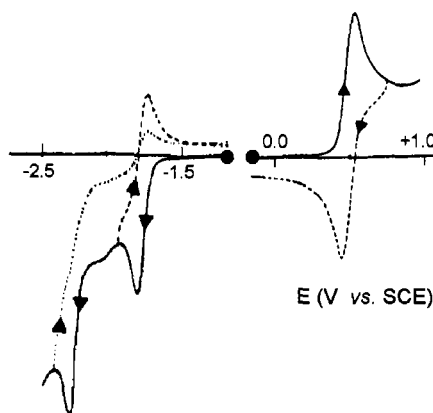


Figure 106 Cyclic voltammogram recorded at a platinum electrode in a dmso solution of $[Ni(5-\text{Cl}-Hsaldpt)]$. Scan rate 0.2 V s^{-1}

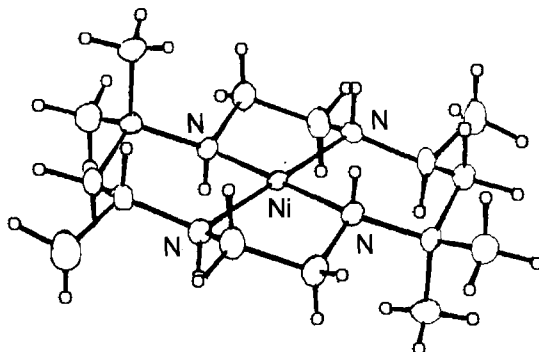


Figure 107 X-Ray structure of $[Ni(Me_6[14]aneN_4)]^{2+}$ ($[Cl]^-$ counteranion). Average Ni–N bond lengths $\approx 1.96 \text{ \AA}$

$[Ni^{II}(Me_6[14]aneN_4)Cl_2]$, whose molecular structure is illustrated in Figure 108. The macrocycle assumes a chair conformation.¹⁵⁷

As deducible from Figures 107 and 108, the Ni–N distances significantly increase on passing from the planar to the octahedral coordination.

As the cyclic voltammograms reported in Figure 109 show, these complexes commonly exhibit either a Ni(II)/Ni(III) oxidation or a Ni(II)/Ni(I) reduction.

The respective redox potentials are given in Table 15.^{158,159}

To evaluate the structural consequences that accompany the Ni(II)/Ni(III) oxidation in solution we can compare the molecular structures of the redox couple $[Ni^{II}Cl_2(Me_6[14]aneN_4)]/[Ni^{III}Cl_2(Me_6[14]aneN_4)]^+$.

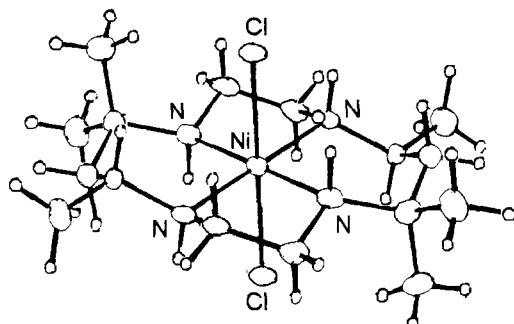


Figure 108 X-Ray structure of $[Ni(Me_6[14]aneN_4)Cl_2] \cdot 2H_2O$. Average bond lengths: $Ni-N = 2.08 \text{ \AA}$; $Ni-Cl = 2.56 \text{ \AA}$

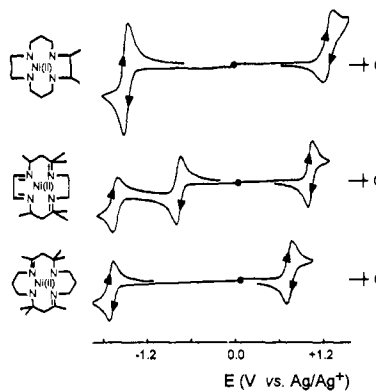


Figure 109 Typical cyclic voltammetric behaviour of a few Ni(II)-tetrazamacrocycles in MeCN solution. Platinum working electrode

Table 15 Formal electrode potentials (V , vs. Ag/Ag^+) for the redox processes exhibited by a few Ni(II)-tetraazamacrocycles in MeCN solution

Ligand	$E^{\circ'}$ ($\text{Ni}^{II/III}$)	$E^{\circ'}$ ($\text{Ni}^{II/I}$)	$E^{\circ'}$ ($\text{Ni}^{I/0}$)
[13]aneN ₄	+0.7	-1.70	
[14]aneN ₄	+0.67	-1.70	
Me ₂ [14]aneN ₄	+0.68	-1.73	
Me ₂ [14]4,7-dieneN ₄	+0.72	-1.5 ^a	
Me ₄ [14]aneN ₄	+0.71	-1.66	
Me ₄ [14]1,3,8,10-tetraeneN ₄	+1.00	-0.82	-1.15
Me ₆ [14]aneN ₄	+0.87	-1.57	
Me ₆ [14]4,11-dieneN ₄	+0.98	-1.57	
Me ₆ [14]1,4,8,11-tetraeneN ₄	+1.05	-1.35	-2.0 ^a
Me ₆ [14]1,3,7,11-tetraeneN ₄	+1.05	-0.76	-1.62
[15]aneN ₄	+0.90	-1.5 ^a	
Me ₂ [15]8,11-dieneN ₄	+0.94	-1.5 ^a	
Me ₆ [16]aneN ₄	+1.3 ^b	-1.40	
Me ₆ [16]4,12-dieneN ₄	+1.3 ^b	-1.37	
Me ₆ [16]1,4,12-trieneN ₄	+1.3 ^b	-1.30	
Me ₂ [14]1,3-dieneN ₄	+0.86	-1.16	
CR + 2H	+0.93	-1.25	-1.88 ^a
CR	+1.03	-0.96	-1.55
CR-2H	+1.05	-0.84	-1.45

^a irreversible process.

^b ill-shaped process.

The structure of the Ni(II) macrocycle complex has been reported in Figure 108, whereas that of the Ni(III) monocation is shown in Figure 110.¹⁶⁰

The overall octahedral geometry is maintained, but the electron removal causes a significant shortening of either the equatorial or the axial metal–ligand distances.

It is noted that the (tetragonally distorted) octahedral Ni(II)-tetraazamacrocyclic complexes of general formula *trans*[NiN₄X₂] are high spin ($d^8 - d_{yz}^2 d_{xz}^2 d_{xy}^2 d_{z^2}^1 d_{x^2-y^2}^1$).

To conclude this overview of nickel complexes we consider the NiN₆ coordination.

Let us start with the Ni(II) complexes of the already mentioned scorpiand diammac (6,13-diammino-6,13-dimethyl-1,4,8,11-tetraazacyclotetradecane) in its two *cis* and *trans* conformations. In contrast to the previously mentioned chromium-, iron-, and cobalt-diammac complexes, in which the geometry of $[M(\text{trans-diammac})]^{n+}$ was substantially octahedral and that of the $[M(\text{cis-diammac})]^{n+}$ was substantially trigonal prismatic, in the case of both $[\text{Ni}(\text{trans-diammac})]^{2+}$ and $[\text{Ni}(\text{cis-diammac})]^{2+}$ the structural differences are attenuated and both can be viewed as more or less distorted octahedral geometries, with two sets of averaged Ni–N bond lengths of 2.07 Å and 2.13 Å, respectively.^{161,162} This is reflected by the fact that both the two complexes exhibit in aqueous solution a chemically reversible Ni(II)/Ni(III) oxidation ($[\text{Ni}(\text{trans-diammac})]^{2+}$: $E^\circ' = +0.67$ V vs. SHE; $[\text{Ni}(\text{cis-diammac})]^{2+}$: $E^\circ' = +0.74$ V).¹⁶²

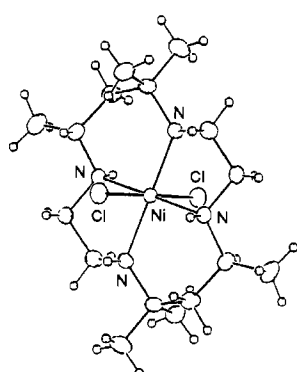


Figure 110 *X-Ray structure of $[\text{Ni}^{\text{III}}\text{Cl}_2(\text{Me}_6[14]\text{aneN}_4)]^+$ ($[\text{ClO}_4]^-$ counteranion). Average bond lengths: Ni–N = 1.99 Å; Ni–Cl = 2.47 Å*

Passing to the polypyridine complexes, Figure 111 shows the octahedral geometry of the $[\text{Ni}(\text{bipy})_3]^{2+}$ ion.¹⁶³

Substantially the same geometry has been found for $[\text{Ni}(\text{phen})_3]^{2+}$ ($\text{Ni}-\text{N} = 2.09 \text{ \AA}$)¹⁶⁴ and for $[\text{Ni}(\text{terpy})_2]^{2+}$.¹⁶⁵ As usual, in $[\text{Ni}(\text{terpy})_2]^{2+}$ the $\text{Ni}-\text{N}_{(\text{central pyridine})}$ distance (2.02 \AA) is shorter than the $\text{Ni}-\text{N}_{(\text{peripheral pyridine})}$ distance (2.14 \AA).

In agreement with an octahedral coordination that has two unpaired electrons ($d^8-t_{2g}^6e_g^2$), the complexes $[\text{Ni}^{II}(\text{bipy})_3](\text{ClO}_4)_2$ and $[\text{Ni}^{II}(\text{terpy})_2](\text{ClO}_4)_2$ possess magnetic moments of $3.20 \mu_B$ and $3.10 \mu_B$, respectively.

The electrochemical behaviour of these complexes is essentially described by a $2+/3+$ oxidation and a $2+/+$ reduction. However, whereas the oxidation process is chemically reversible, the reduction is accompanied by chemical complications (consistent with the probable loss of a ligand molecule and the formation of $[\text{Ni}^I(\text{ligand})_2]^+$).

As far as the trication $[\text{Ni}(\text{bipy})_3]^{3+}$ is concerned, both EPR spectroscopy¹⁶⁶ and the magnetic moment ($2.10 \mu_B$)¹⁶⁷ confirm its Ni(III) nature ($d^7-t_{2g}^6e_g^1$). Contrary to what has been observed for the corresponding Ni(II) complex, for which all the Ni–N distances are identical, in this case the equatorial Ni–N distances (2.02 \AA) are about 0.1 \AA longer than the axial Ni–N distances.¹⁶⁶ This has been attributed to the Jahn–Teller effect.

The redox potentials of the nickel(II) polypyridine complexes are reported in Table 16.^{167,168}

As mentioned, the Ni(IV) oxidation state is not unknown, and the NiN_6 coordination offers the opportunity to illustrate and further

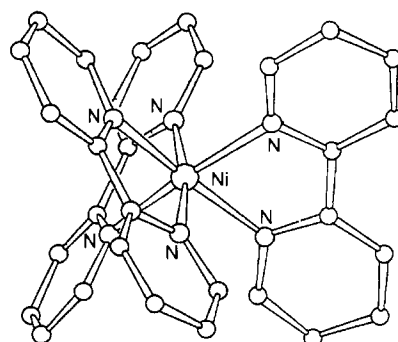


Figure 111 X-Ray structure of the dication $[\text{Ni}(\text{bipy})_3]^{2+}$ ($[\text{Cl}]^-$ counteranion). Average bond lengths: $\text{Ni}-\text{N} = 2.11 \text{ \AA}$; $\text{C}-\text{C} = 1.36 \text{ \AA}$

Table 16 Formal electrode potentials (V vs. SCE) for the redox processes displayed by the polypyridine Ni(II) complexes in MeCN solution

Complex	$E_{(3+/2+)}^{\circ'}$	$E_{(2+/1+)}^{\circ'}$
$[\text{Ni}(\text{bipy})_3]^{2+}$	+1.70	-1.31
$[\text{Ni}(\text{phen})_3]^{2+}$	+1.64	-
$[\text{Ni}(\text{terpy})_2]^{2+}$	+1.61	-1.29

confirm¹⁶⁹ its existence. As we will see also for copper complexes, deprotonated amides are ligands able to stabilize metal complexes in high oxidation states. In this connection Figure 112 shows the compressed octahedral geometry of the Ni(II) complex $[\text{NiL}_2]^{2-}$ (H_2L = 2,6-bis(*N*-phenylcarbamoyl)pyridine).¹⁷⁰

The Ni(II) nature is supported by its magnetic moment ($\mu_{\text{eff}} = 3.12 \mu_B$ in the solid state, at 300 K), which testifies the presence of two unpaired electrons.

As illustrated in Figure 113, cyclic voltammetry in MeCN solution of $[\text{Ni}^{II}\text{L}_2]^{2-}$ reveals the presence of two reversible one-electron oxidations corresponding to the Ni(II)/Ni(III) ($E^{\circ'} = +0.05$ V vs. SCE) and Ni(III)/Ni(IV) ($E^{\circ'} = +0.51$ V) sequence.¹⁷⁰

The effective magnetic moment of the monoanion $[\text{NiL}_2]^-$ ($\mu_{\text{eff}} = 2.14 \mu_B$ in the solid state, at 300 K) supports the Ni(III) attribution. In addition

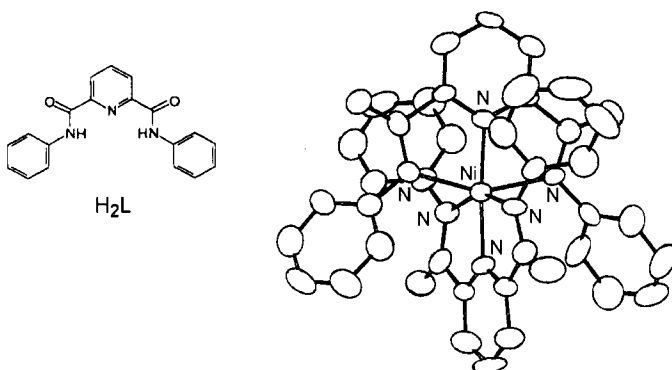


Figure 112 X-Ray structure of the dianion $[\text{Ni}^{II}\text{L}_2]^{2-}$. Average bond lengths: $\text{Ni}-\text{N}_{(\text{equatorial})} = 2.13 \text{ \AA}$; $\text{Ni}-\text{N}_{(\text{axial})} = 1.99 \text{ \AA}$

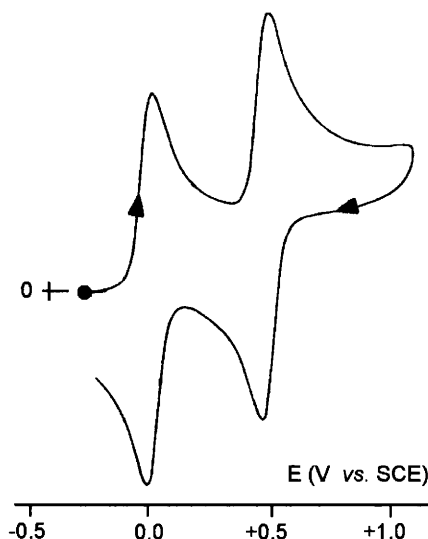


Figure 113 Cyclic voltammogram recorded at a glassy carbon electrode in a MeCN solution of $[Ni^{IV}L_2][Et_4N]_2$. Scan rate 0.05 V s^{-1}

the diamagnetic neutral Ni(IV) congener NiL_2 has been structurally characterized, Figure 114.¹⁷⁰

Upon passing from the Ni(II) to the Ni(IV) oxidation states, the complex maintains the octahedral geometry, but important Ni–N bond shortenings occur (by about 0.1 \AA in the equatorial plane and by about 0.15 \AA in the axial positions).

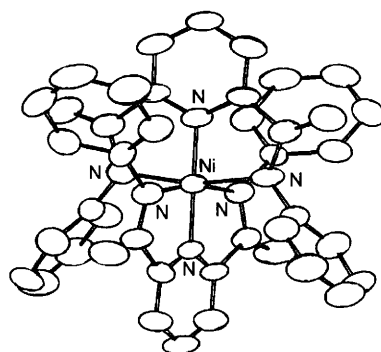


Figure 114 X-Ray structure of $[Ni^{IV}L_2]$. Average bond lengths: $Ni-N_{(equatorial)} = 1.95\text{ \AA}$; $Ni-N_{(axial)} = 1.85\text{ \AA}$

7 COPPER COMPLEXES

It is easy to imagine that the commonest oxidation states of copper are Cu(II) (d^9) and Cu(I) (d^{10}), but, as we shall see, the oxidation state III is not so rare.

It is largely accepted that in the prediction of the electrochemical behaviour of Cu(II) complexes, an important criterion to bear in mind resides in their geometrical structure. In fact, Cu(I) generally prefers a *tetrahedral* geometry, whereas Cu(III) prefers a rigidly *planar* geometry. One may infer from such a statement that if a Cu(II) complex, whatever its geometry, is sufficiently flexible to allow a structural reorganization to the tetrahedral geometry it will probably manifest a reversible access to the corresponding Cu(I) complex. On the other hand, if it is rigidly planar, it is likely that it will exhibit a reversible access to the corresponding Cu(III) complex. Clearly, if such reorganizations are not structurally allowed, the respective electrode processes will be irreversible.

Furthermore, one must bear in mind that if the geometry of the initial Cu(II) complex shows some predisposition towards that of the associated redox state, the relative process will occur at low potential values (*i.e.* weakly negative, or even positive, for reduction; weakly positive, or even negative, for oxidation (in both cases, depending obviously also from the used reference electrode)). As discussed in Section 5, this is due to the relatively low energy required for the pertinent structural reorganization. The so-called *blue copper proteins* constitute a classical example of such behaviour. As it will be discussed in Chapter 12, Section 4, the Cu(II) ion in the original active site is constrained by the protein matrix to assume a pseudotetrahedral geometry. Therefore, the protein is easily reduced to the tetrahedral geometry of the Cu(I) oxidation state at potentials which are in fact positive with respect to the NHE.^{171,172} It should be emphasized, however, that the ultimate position of the redox potential also depends on the overall inductive electronic effects (attractive or repulsive) of the ligand.

In spite of these preliminary considerations, a few unusual trigonal planar Cu(II) complexes have been characterized, which are able to afford the corresponding trigonal planar Cu(I) derivatives. These complexes have general formula CuL(R) and arise from the ligand L = 2,4-bis(2,6-diisopropylphenylimido)pentane anion, with R = chloride, thiolates, phenolates. As an example, Figure 115 illustrates the molecular structure of [CuLCl] and [CuL(SCPh₃)], respectively. In

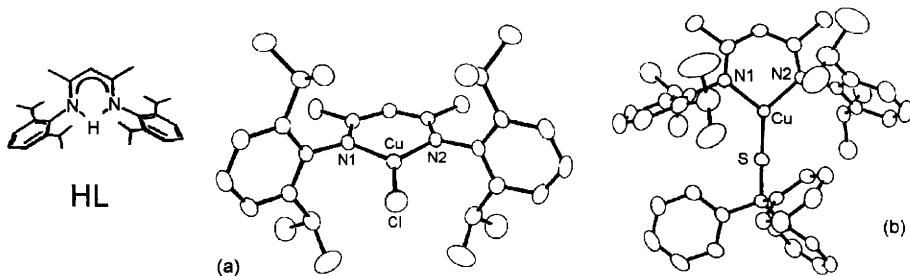


Figure 115 X-Ray structures of three-coordinate Cu(II) complexes: (a) $[\text{CuLCl}]$: $\text{Cu}-\text{N} = 1.87 \text{ \AA}$; $\text{Cu}-\text{Cl} = 2.13 \text{ \AA}$; $\text{N}1\text{CuN}2 = 97.3^\circ$; NCuCl (average) = 131° . (b) $[\text{CuL}(\text{SCPh}_3)]$: $\text{Cu}-\text{N} = 1.92 \text{ \AA}$; $\text{Cu}-\text{S} = 2.12 \text{ \AA}$; $\text{N}1\text{CuN}2 = 96.8^\circ$; NCuS (average) = 129.5° ; $\text{CuSC} = 119.4^\circ$

all cases, the copper atom is slightly displaced from the N_2X plane ($\text{X} = \text{Cl}, \text{S}, \text{O}$) by about 0.2 \AA .¹⁷³

As illustrated in Figure 116, in thf solution these complexes exhibit a chemically reversible (in the cyclic voltammetric time scale) Cu(II)/Cu(I) reduction ($[\text{CuLCl}]$: $E^{\circ'} = -0.88 \text{ V}$ vs. Fc/Fc^+ ; $\Delta E_p = 70 \text{ mV}$, at 0.02 V s^{-1} . $[\text{CuL}(\text{SCPh}_3)]$: $E^{\circ'} = -0.98 \text{ V}$; $\Delta E_p = 80 \text{ mV}$, at 0.01 V s^{-1} . $[\text{CuL}(\text{OC}_6\text{H}_4\text{Bu}^t)]$: -1.06 V).¹⁷³

Let us now pass to the commonest tetracoordinated copper complexes. Figure 117 shows the molecular structure of the Cu(II)-2-dipyridylamine

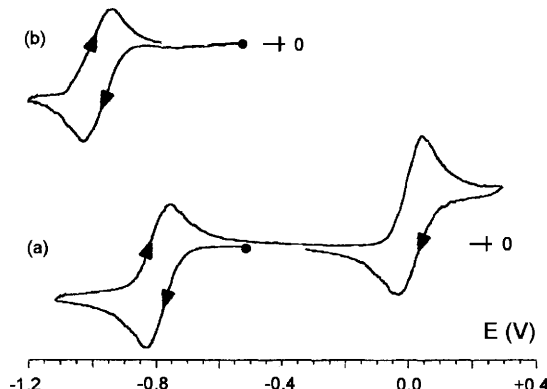


Figure 116 Cyclic voltammograms recorded at a platinum electrode in thf solutions of: (a) $[\text{CuLCl}]$; (b) $[\text{CuL}(\text{SCPh}_3)]$. Ferrocene added as an internal standard in (a). Scan rates: (a) 0.02 V s^{-1} ; (b) 0.01 V s^{-1}

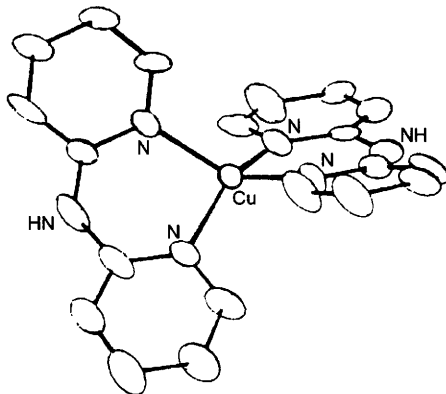


Figure 117 X-Ray structure of the dication $[Cu(dpa)_2]^{2+}$. Cu–N average bond length = 1.96 Å. Dihedral angle between the two CuN_2 planes = 55.6°

complex $[Cu(dpa)_2]^{2+}$. As can be seen, it has a distorted tetrahedral CuN_4 coordination.¹⁷⁴

In coordinating solvents, such as MeCN and dmso, $[Cu(dpa)_2]^{2+}$ binds two solvent molecules becoming hexacoordinate. In contrast in non-coordinating solvents the complex maintains its tetracoordination. Figure 118 just shows the redox behaviour of the complex in non-coordinating nitromethane solution.¹⁷⁵

It displays two successive reductions, corresponding to the sequence Cu(II)/Cu(I)/Cu(0). The first step ($E^{\circ'} = +0.19$ V) is chemically reversible ($i_{pa}/i_{pc} = 1$) but electrochemically quasireversible ($\Delta E_p = 145$ mV, at 0.2 V s^{-1}); the second step is irreversible ($E_p = -0.65$ V). The appearance of peak C in the backscan reveals, by its characteristic pointed lineshape, the presence of a process known as ‘anodic stripping’. This consists of the sudden reoxidation of the metallic copper that has been deposited on the electrode surface during the Cu(I)/Cu(0) reduction.

The corresponding Cu(I) complex, $[Cu(dpa)_2]^+$, has been isolated and its structure solved. It maintains a tetrahedral geometry, though with a few significant variations in the structural parameters (Cu–N = 2.02 Å; dihedral angle between the two CuN_2 planes = 73.3°).¹⁷⁶

If one makes the reasonable assumption that the quasireversibility of the Cu(II)/Cu(I) reduction is due to the energy barrier of the structural reorganization, one may infer that the addition of an electron causes an increase in the Cu–N bond distances by about 0.6 Å and the dihedral angle between the two CuN_2 planes approaches more closely that of a perfectly tetrahedral geometry

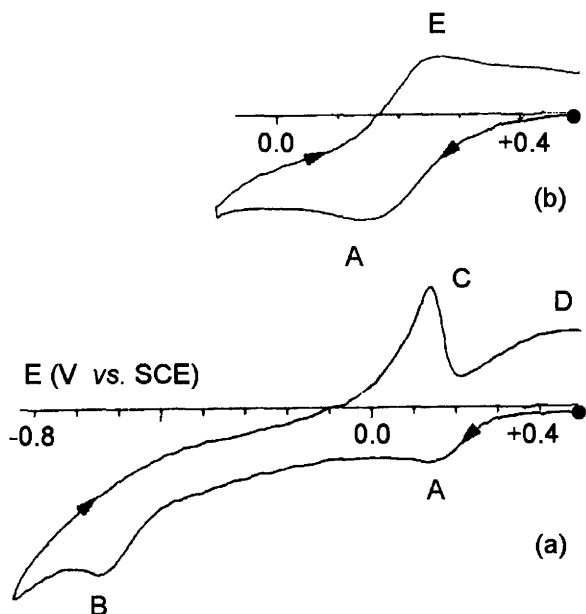
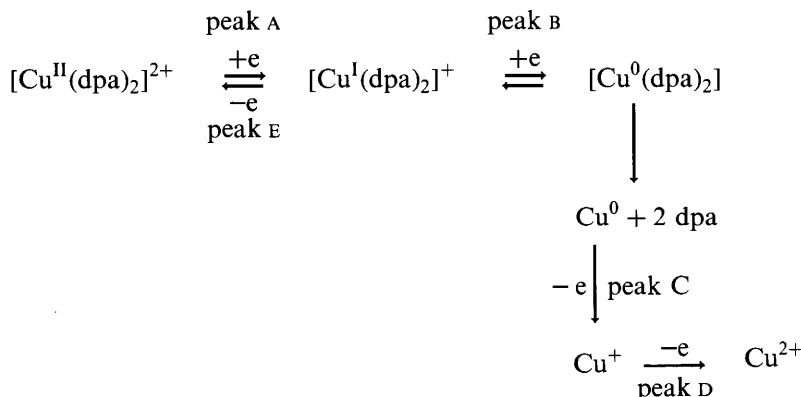


Figure 118 Cyclic voltammograms recorded at a platinum electrode in a MeNO_2 solution of $[\text{Cu}(\text{dpa})_2]\text{[ClO}_4\text{]}_2$. Scan rates: (a) 0.01 V s^{-1} ; (b) 0.02 V s^{-1}

(90°). In fact, the dihedral angle changes from 56° in the Cu(II) complex to 73° in the Cu(I) complex.

The complete reduction mechanism can be described as follows:



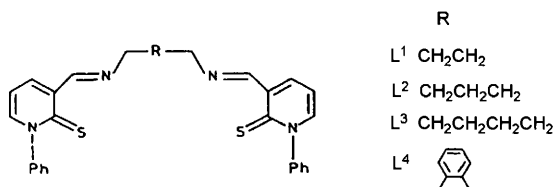
With regard to planar tetracoordinated Cu(II) complexes, we consider the usual N_2O_2 Schiff base planar complexes $[\text{Cu}^{\text{II}}(\text{salen})]$ and

$[\text{Cu}^{\text{II}}(\text{saloph})]$, the solid-state structure of which is known.^{177,178} As illustrated in Figure 119 for $[\text{Cu}(\text{saloph})]$, these complexes display a $\text{Cu}(\text{II})/\text{Cu}(\text{I})$ reduction (at about -1.1 V), the apparent chemical reversibility of which is complicated by decomposition of the instantaneously electrogenerated $\text{Cu}(\text{I})$ ion.¹⁷⁹

In fact, as deducible from the voltammogram recorded at slow scan rate (dashed line), the decomplexed $\text{Cu}(\text{I})$ ion undergoes disproportionation to $\text{Cu}(0)$, which is subsequently reoxidized at a potential corresponding to the anodic stripping peak D.

One may reasonably assume that the relative instability of the $\text{Cu}(\text{I})$ complexes of salen and saloph might be due to the relative rigidity of the $\text{Cu}^{\text{II}}\text{N}_2\text{O}_2$ planar conformation, which prevents the reorganization to the typical tetrahedral geometry of $\text{Cu}(\text{I})$ complexes.

Another related example can be found in the series of copper complexes with the bis(imino)-3-formyl-1-phenyl-pyridinethione ligands shown in Scheme 18.¹⁸⁰ Both $\text{Cu}(\text{I})$ and $\text{Cu}(\text{II})$ complexes can be prepared with this type of ligands.



Scheme 18

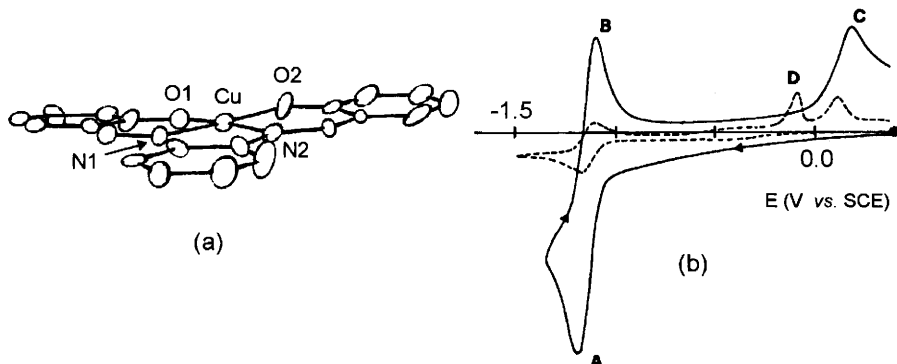


Figure 119 (a) X-Ray structure of $[\text{Cu}(\text{saloph})]$. Bond lengths: $\text{Cu}-\text{N} = 1.89 \text{ \AA}$; $\text{Cu}-\text{O} = 1.95 \text{ \AA}$. (b) Cyclic voltammograms recorded at a platinum electrode in a dmsO solution of $[\text{Cu}(\text{saloph})]$. Scan rates: (---) 0.005 V s^{-1} ; (—) 0.2 V s^{-1}

Figure 120 shows the molecular structure of complex $[\text{Cu}^{\text{II}}\text{L}^2]^{2+}$, which has a planar CuN_2S_2 coordination with a slight tetrahedral distortion.

As illustrated in Figure 121a the complex displays in MeCN solution a chemically reversible, but electrochemically quasi-reversible ($\Delta E_p = 85$ mV, at 0.2 Vs^{-1}), one-electron reduction ($E^{\circ'} = +0.01 \text{ V vs. SCE}$).

In confirmation of the chemical reversibility of such redox change, the corresponding Cu(I) complex obtained by exhaustive cathodic reduction shows a quite complementary voltammetric response, Figure 121b.

With the exception of the complex with the L^1 ligand, these complexes also display an irreversible Cu(II)/Cu(III) oxidation. In contrast, in the case of complex $[\text{Cu}^{\text{I}}\text{L}^1]^+$, both the Cu(I)/Cu(II) ($E^{\circ'} = -0.20 \text{ V}$) and Cu(II)/Cu(III) ($E^{\circ'} = +1.18 \text{ V}$) redox processes have features of chemical reversibility (in the cyclic voltammetric time scale), Figure 122.

The fact that only the L^1 ligand complex permits access to the Cu(III) complex (even if it is not indefinitely stable) agrees with the relevant structural information. In fact, one must bear in mind that the N-R-N restraint imposed by the ligand constitutes a barrier to the structural flexibility of the molecule. Therefore, when the chain connecting the two imino-nitrogen atoms is $-\text{C}_2\text{H}_4-$, it is probable that it generates sufficient rigidity to maintain the CuN_2S_2 site in planar geometry, ready to stabilize the Cu(III) complex. Conversely, the flexibility of a $-\text{C}_3\text{H}_6-$ (Figure 120), or $-\text{C}_4\text{H}_8-$ chain, producing a tetrahedral distortion, does not allow the stabilization of a planar geometry following the one-electron oxidation.

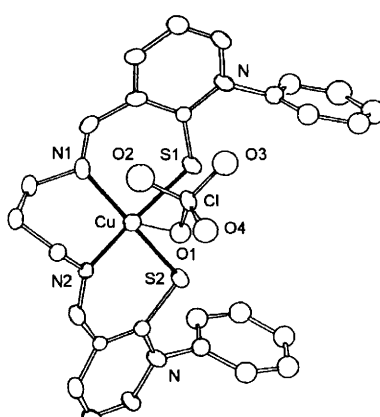


Figure 120 X-Ray structure of the dication $[\text{CuL}^2]^{2+}$. Average bond lengths: $\text{Cu}-\text{N} = 1.99 \text{ \AA}$; $\text{Cu}-\text{S} = 2.27 \text{ \AA}$; $\text{Cu}\cdots\text{O}1 = 2.64 \text{ \AA}$

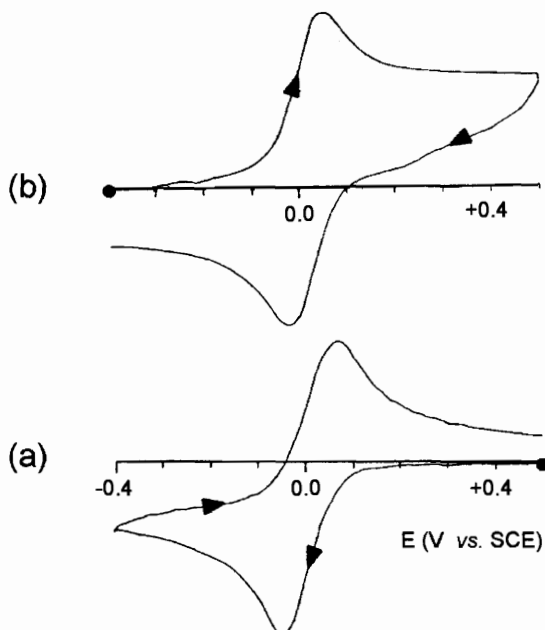


Figure 121 Cyclic voltammograms recorded at a platinum electrode in MeCN solutions of: (a) $[\text{Cu}^{\text{II}}\text{L}^2]^{\text{2}+}$; (b) $[\text{Cu}^{\text{I}}\text{L}^2]^{\text{+}}$. Scan rate 0.5 V s^{-1}

Indeed, as far as the stabilization of Cu(III) complexes is concerned, deprotonated amides proved to be suitable ligands (as has been discussed for Ni(IV) complexes). For instance, Figure 123 shows the strictly planar geometry of the oxamidate Cu(III) complex $[\text{CuL}]^-$.¹⁸¹

The ligand is able to complex copper ions either in the Cu(III), $[\text{Cu}^{\text{III}}\text{L}]^-$, or in the Cu(II), $[\text{Cu}^{\text{II}}\text{L}]^{2-}$, oxidation states. As a matter of

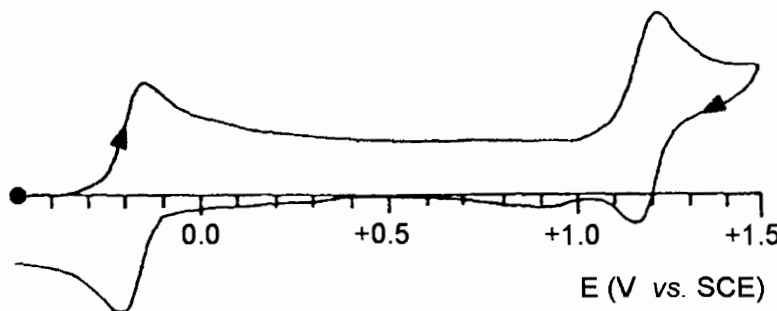


Figure 122 Cyclic voltammogram recorded at a platinum electrode in a MeCN solution of $[\text{Cu}^{\text{I}}\text{L}']^{\text{+}}$. Scan rate 0.2 V s^{-1}

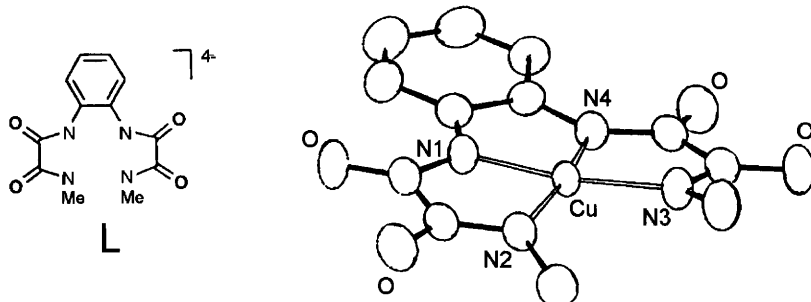


Figure 123 *X-Ray structure of the anion $[CuL]^-$. Bond lengths: $Cu-N1 = Cu-N4 = 1.84 \text{ \AA}$; $Cu-N2 = Cu-N3 = 1.88 \text{ \AA}$*

fact, the Cu(II) dianion exhibits in acetonitrile solution a reversible one-electron oxidation ($E^{\circ'} = -0.02 \text{ V}$), Figure 124.¹⁸¹

Even more educational is the case of the Cu(II) and Cu(III) complexes of N,N' -bis[2-(1-hydroxyimino-2-methyl-1-phenyl)propyl]dimethylmalondiamide (H₄mal). Figure 125 shows the molecular structure and the voltammetric behaviour of the Cu(II) form $[Cu(Hmal)]^-$.¹⁸²

As seen, the square planar complex exhibits in MeCN solution a reversible one-electron oxidation ($E^{\circ'} = -0.12 \text{ V vs. Fc/Fc}^+$; $\Delta E_p = 70 \text{ mV}$, at 0.05 V s^{-1}), which suggests the maintaining of the square planar CuN₄ coordination. In fact, as illustrated in Figure 126, the Cu(III) derivative $[Cu(Hmal)]$ is square planar.¹⁸²

The Cu(II)/Cu(III) transition involves a shortening of the Cu–N distances by 0.05 Å.

Amongst the penta- and hexacoordinate copper complexes the most didactically instructive can be found in complexes with poly-

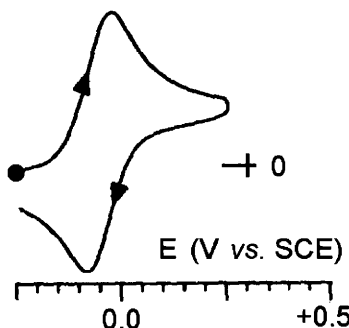


Figure 124 *Cyclic voltammogram recorded at a glassy carbon electrode in a MeCN solution of $[CuL]^{2-}$*

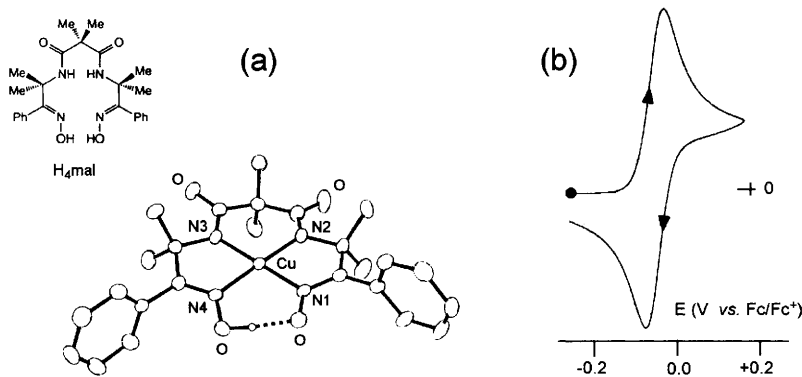


Figure 125 (a) X-Ray structure of $[Cu(Hmal)]^-$. Average bond lengths: $Cu-N1 = CuN4 = 1.95 \text{ \AA}$; $Cu-N2 = Cu-N3 = 1.91 \text{ \AA}$. (b) Cyclic voltammogram recorded at a platinum electrode in a MeCN solution of $[Cu(Hmal)]^-$. Scan rate 0.05 V s^{-1}

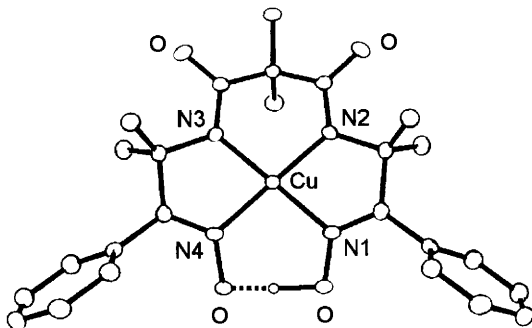
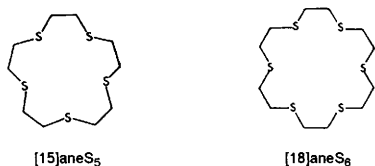


Figure 126 X-Ray structure of $[Cu(Hmal)]$. Average bond lengths: $Cu-N1 = Cu-N4 = 1.90 \text{ \AA}$; $Cu-N2 = Cu-N3 = 1.86 \text{ \AA}$

thioether macrocyclic ligands of the type $[15]\text{aneS}_5$ and $[18]\text{aneS}_6$ illustrated in Scheme 19.¹⁷²

Figure 127 shows the square pyramidal geometry of the $[Cu^{II}([15]\text{aneS}_5)]^{2+}$ dication.



Scheme 19

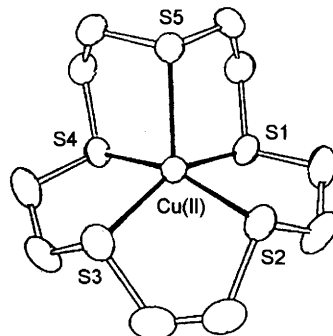


Figure 127 *X-Ray structure of the dication $[Cu([15]aneS_5)]^{2+}$. Average Cu–S bond length = 2.33 Å*

This complex, in a 80% methanol solution undergoes a quasireversible Cu(II)/Cu(I) reduction ($E^{\circ'} = + 0.61$ V vs. SCE). The molecular structure of the corresponding Cu(I) $[Cu([15]aneS_5)]^+$ monocation is reported in Figure 128.

It is evident that the central Cu(I) ion, preferring a tetrahedral geometry, abandons one of the coordinated sulfur atoms.

An analogous redox-to-structural change occurs for the redox couple $[Cu([18]aneS_6)]^{2+} / [Cu([18]aneS_6)]^+$. As illustrated in Figure 129, the $[Cu^{II}([18]aneS_6)]^{2+}$ dication has an octahedral geometry, whereas

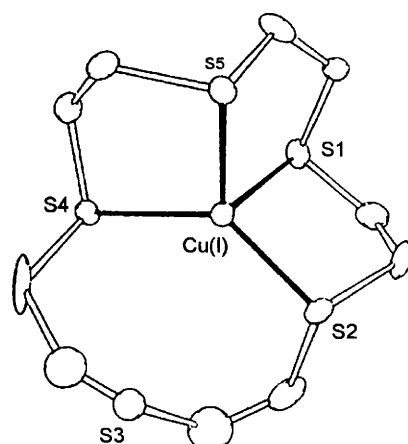


Figure 128 *X-Ray structure of the monocation $[Cu([15]aneS_5)]^+$. Average distances: Cu–S = 2.28 Å; Cu···S3 = 3.5 Å*

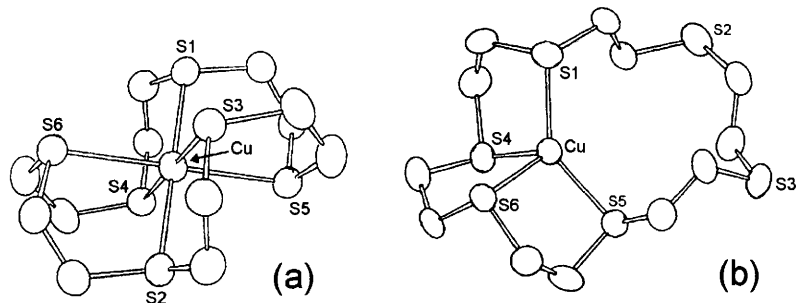


Figure 129 *X-Ray structures of: (a) $[Cu^{II}([18]\text{aneS}_6)]^{2+}$; (b) $[Cu^{II}([18]\text{aneS}_6)]^+$. Average bond lengths: (a) $Cu-S = 2.43 \text{ \AA}$; (b) $Cu-S = 2.30 \text{ \AA}$*

the corresponding monocation $[Cu^I([18]\text{aneS}_6)]^+$, upon releasing two sulfur atoms, assumes a tetrahedral geometry.

In fact, $[Cu([18]\text{aneS}_6)]^+$ in nitromethane solution exhibits a chemically reversible, but electrochemically quasireversible, oxidation ($E^\circ' = +0.72 \text{ V vs. SCE}$).

Another example (which has been already discussed in Chapter 2, Section 1.3.2) is offered by the Cu(II) complex with the oxathia crown ligand 1-oxa-4,7-dithiacyclonane $[Cu(9S_2O)_2]^{2+}$, whose Jahn–Teller distorted (axially elongated) octahedral geometry is illustrated in Figure 130.¹⁸³

As Figure 131 shows, the corresponding Cu(I) complex $[Cu(9S_2O)_2]^+$ assumes the expected tetrahedral geometry upon abandoning the coordination to the two oxygen atoms.¹⁸⁴

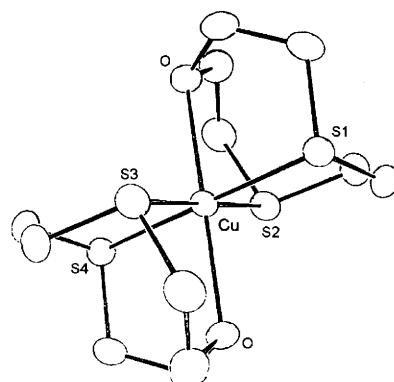


Figure 130 *X-Ray structure of the dication $[Cu(9S_2O)_2]^{2+}$. Bond lengths: $Cu-S = 2.33 \text{ \AA}$; $Cu-O = 2.36 \text{ \AA}$*

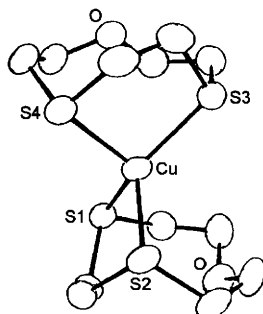


Figure 131 X-Ray structure of the monocation $[Cu(9S_2O)_2]^+$. Bond lengths: $Cu-S1 = Cu-S3 = 2.30 \text{ \AA}$; $Cu-S2 = Cu-S4 = 2.35 \text{ \AA}$

In confirmation of the significant Cu(I)/Cu(II) geometrical reorganization, $[Cu(9S_2O)_2]^+$ undergoes in acetonitrile solution a chemically reversible, but electrochemically quasireversible, oxidation ($E^{o'} = +0.61 \text{ V vs. SCE}$; $\Delta E_p = 114 \text{ mV}$, at 0.11 V s^{-1}).¹⁸⁴

As usual, we conclude with the CuN₆ coordination of polypyridine complexes. As an example, Figure 132 shows the solid state structure of $[Cu(\text{terpy})_2]^{2+}$.¹⁸⁵ The X-ray structure of $[Cu(\text{bipy})_2]^{2+}$ and $[Cu(\text{phen})_3]^{2+}$ are also available.^{186,187}

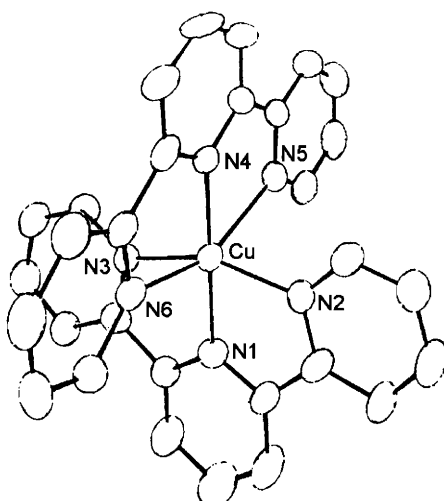


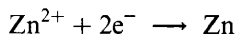
Figure 132 X-Ray structure of $[Cu(\text{terpy})_2]^{2+}$. $Cu-N1 = 1.96 \text{ \AA}$; $Cu-N2 = Cu-N3 = 2.08 \text{ \AA}$; $Cu-N4 = 2.01 \text{ \AA}$; $Cu-N5 = Cu-N6 = 2.29 \text{ \AA}$

In these cases, there is the expected tetragonal distortion due to the Jahn–Teller effect in addition to the often mentioned octahedral distortion associated with polypyridine complexes. For the terpyridine complex there is the usual difference between the distances separating the metal and nitrogen atom of the central pyridine and that of the metal and the nitrogen atom of the peripheral pyridines.

Unfortunately, there is little electrochemical information on these complexes. The only study available is concerned with $[\text{Cu}(\text{bipy})_3]^{2+}$ and $[\text{Cu}(\text{phen})_3]^{2+}$, which, in agreement with the d^9 electronic configuration, have a magnetic moment of about $1.8 \mu_B$.¹⁸⁸ The two complexes, in MeCN solution, display a Cu(II)/Cu(I) reduction at $E^\circ' = +0.04$ and $+0.03$ V (vs. SCE), respectively, which is complicated by decomposition of the electrogenerated copper(I) complexes.¹⁸⁹

8 ZINC COMPLEXES

Zinc is present in its complexes only as the Zn^{2+} ion (d^{10}). A direct consequence of the electronic saturation of the d orbitals is that zinc complexes exhibit only the two-electron reduction:



Generally, the reduction to the metallic state implies decomplexation of the bound ligands (hence, *irreversible* reduction), electrodeposition of metallic zinc on the electrode surface and consequently the anodic stripping process in the backscan.

This is the case, for example, of the complex $[\text{Zn}(\text{bipy})_3]^{2+}$, Figure 133.¹⁹⁰

As shown, this highly distorted octahedral complex¹⁹¹ in MeCN solution displays a two-electron reduction ($E_p = -1.37$ V) that in the backscan exhibits the typical ‘anodic stripping’ of the electrodeposited zinc metal. As the $\text{Zn}(\text{II})$ ion in MeCN solution (*i.e.* $[\text{Zn}(\text{MeCN})_4]^{2+}$ ion) undergoes a two-electron reduction at $E_p = -1.10$ V, it is evident that complexation renders more difficult the reduction process.¹⁹⁰

A similar behaviour is exhibited by the isostructural $[\text{Zn}(\text{phen})_3]^{2+}$.¹⁹² In MeCN solution it exhibits an irreversible reduction ($E_p = -1.40$ V vs. SCE) followed by further ligand-centred irreversible processes (we must in fact remind that polypyridines are redox active ligands).¹⁹³

Just zinc complexes bearing redox-active ligands sometimes display apparently reversible redox processes. Really, in these cases the electron transfer processes are centred on the ligand. This is, for example, the case of $[\text{Zn}(\text{papm})\text{Cl}_2]$ ($\text{papm} = 2\text{-}(p\text{-phenylazo})\text{pyrimidine}$), the (distorted) trigonal bipyramidal molecular structure of which is illustrated in Figure 134.¹⁹⁴

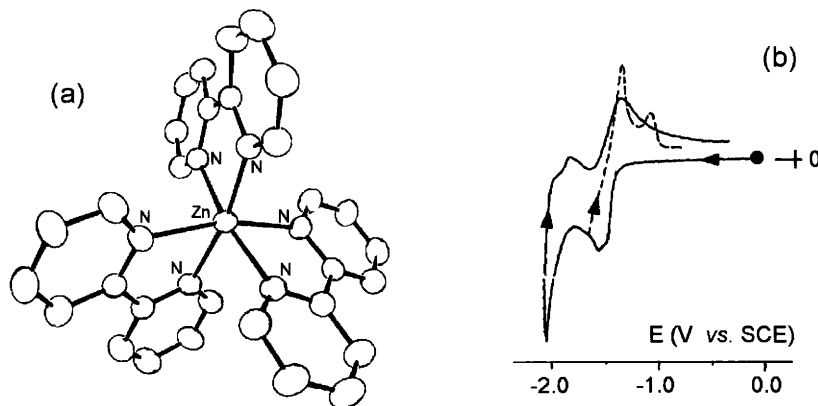


Figure 133 (a) X-Ray structure of $[Zn(bipy)_3]^{2+}$ ($[ClO_4]^-$ counteranion). Average $Zn-N$ bond length = 2.15 Å. (b) Cyclic voltammogram recorded at a glassy carbon electrode in a MeCN solution of $[Zn(bipy)_3]^{2+}$. Scan rate 0.1 V s⁻¹

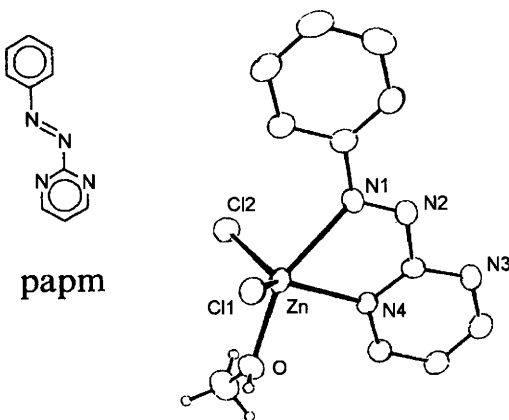


Figure 134 X-Ray structure of $[Zn(papm)Cl_2] \cdot CH_3OH$. $Zn-N1 = 2.43$ Å; $Zn-N4 = 2.10$ Å; $Zn-O = 2.15$ Å; $Zn-Cl1 = 2.24$ Å; $Zn-Cl2 = 2.22$ Å

In MeCN solution, it exhibits two quasireversible one-electron reductions ($E_{0/-}^\circ = -0.84$ V vs. SCE; $E_{-1/2}^\circ = -1.24$ V), which are centred on the azo-group according to the sequence:¹⁹⁵



Other, even more significant, examples of Zn(II) complexes with redox-active ligands will be discussed in Chapter 6, Section 5.

REFERENCES

1. N.G. Connelly and W.E. Geiger, *Adv. Organomet. Chem.*, 1984, **23**, 1.
2. N.G. Connelly and W.E. Geiger, *Chem. Rev.*, 1996, **96**, 877.
3. (a) K.H. Thompson, J.H. McNeil and C. Orvig, *Chem. Rev.*, 1999, **99**, 2561; (b) K.H. Thompson and C. Orvig, *J. Chem. Soc., Dalton Trans.*, 2000, 2885.
4. X. Wang, X.M. Zhang and H.X. Liu, *Polyhedron*, 1995, **14**, 293.
5. D. Bruins and D.L. Weaver, *Inorg. Chem.*, 1970, **9**, 130.
6. P.E. Riley, V.L. Pecoraro, C.J. Carrano, J.A. Bonadies and K.N. Raymond, *Inorg. Chem.*, 1986, **25**, 154.
7. J.A. Bonadies, W.M. Butler, V.L. Pecoraro and C.J. Carrano, *Inorg. Chem.*, 1987, **26**, 1218.
8. P. Zanello and A. Cinquantini, *Transition Met. Chem.*, 1985, **10**, 370.
9. C.J. Chang, J.A. Labinger and H.B. Gray, *Inorg. Chem.*, 1997, **36**, 5927.
10. R. Seangprasertkij and T.L. Riechel, *Inorg. Chem.*, 1984, **23**, 991.
11. D.D. Heinrich, K. Folting, J.C. Huffman, J.G. Reynolds and G. Christou, *Inorg. Chem.*, 1991, **30**, 300.
12. K. Ramesh and R. Mukherjee, *J. Chem. Soc., Dalton Trans.*, 1991, 3259.
13. M. Chatterjee, S. Ghosh and A.K. Nandi, *Polyhedron*, 1997, **16**, 2917.
14. G. Albrecht, *Z. Chem.*, 1963, **3**, 182.
15. S.S. Shah and A.W. Maverick, *Inorg. Chem.*, 1986, **25**, 1867.
16. S.S. Shah and A.W. Maverick, *Inorg. Chem.*, 1987, **26**, 1559.
17. S.R. Cooper, Y.B. Koh and K.N. Raymond, *J. Am. Chem. Soc.*, 1982, **104**, 5092.
18. J.J.R. Frausto da Silva, *Chem. Spec. Bioavail.*, 1989, **1**, 139.
19. E.M. Armstrong, R.L. Beddoes, L.J. Calviou, J.M. Charnock, D. Collison, N. Ertok, J.H. Naismith and C.D. Garner, *J. Am. Chem. Soc.*, 1993, **115**, 807.
20. M. Asri Nawi and T.L. Riechel, *Inorg. Chim. Acta*, 1987, **136**, 33.
21. M.A.A.F. de C.T. Carrondo, M.T. L.S. Duarte, J.C. Pessoa, J.A. L. Silva, J.J. R. Frausto da Silva, M.C.T.A. Vaz and L.F. Vilas-Boas, *J. Chem. Soc., Chem. Commun.*, 1988, 1158.
22. R.E. Berry, E.M. Armstrong, R.L. Beddoes, D. Collison, S.N. Ertok, M. Helliwell and C.D. Garner, *Angew. Chem. Int. Ed.*, 1999, **38**, 795.
23. S. Decurtins, H.W. Schmalle, R. Pellaux, P. Schneuwly and A. Hauser, *Inorg. Chem.*, 1996, **35**, 1451.
24. W.A. Wickramasinghe, P.H. Bird and N. Serpone, *Inorg. Chem.*, 1982, **21**, 2694.
25. M.C. Hughes and D.J. Macero, *Inorg. Chem.*, 1976, **15**, 2040.
26. N. Serpone, M.A. Jamieson, M.S. Henry, M.Z. Hoffman, F. Bolletta and M. Maestri, *J. Am. Chem. Soc.*, 1979, **101**, 2907.

27. D.M. Soignet and L.G. Hargis, *Inorg. Chem.*, 1972, **11**, 2920.
28. E.C. Constable, S.M. Elder and D.A. Tocher, *Polyhedron*, 1992, **11**, 1337.
29. P. Coggon, A.T. McPhall, F.E. Mabbs, A. Richards and A.S. Thornley, *J. Chem. Soc., (A)*, 1970, 3296.
30. D.A. Bardwell, D. Black, J.C. Jeffery, E. Schatz and M.D. Ward, *J. Chem. Soc., Dalton Trans.*, 1993, 2321.
31. F. Lloret, M. Julve, M. Mollar, I. Castro, J. Latorre, J. Faus, X. Solans and I.M. -Badarau, *J. Chem. Soc., Dalton Trans.*, 1989, 729.
32. P.V. Bernhardt, P. Comba, N.F. Curtis, T.W. Hambley, G.A. Lawrence, M. Maeder and A. Siriwardena, *Inorg. Chem.*, 1990, **29**, 3208.
33. P.V. Bernhardt, P. Comba and T.W. Hambley, *Inorg. Chem.*, 1993, **32**, 2804.
34. P. Comba, I.I. Creaser, L.R. Gahan, J. MacB. Harrowfield, G.A. Lawrence, L.L. Martin, A.W.H. Mau, A.M. Sargeson, W.H. F. Sasse and M.R. Snow, *Inorg. Chem.*, 1986, **25**, 384.
35. M.K. Chan and W.H. Armstrong, *Inorg. Chem.*, 1989, **28**, 3779.
36. X.-M. Chen, R. -Q. Wang and Z. -T. Xu, *Acta Cryst.*, C51, 1995, 820.
37. M.G.B. Drew, M. Hasan and Y. Hello, *Polyhedron*, 1989, **8**, 1853.
38. S.A. Richert, P.K.S. Tsang and D.T. Sawyer, *Inorg. Chem.*, 1989, **28**, 2471.
39. J.M. Rao, M.C. Hughes and D.J. Macero, *Inorg. Chim. Acta*, 1976, **18**, 127.
40. A.F. Jensen, Z. Su, N.K. Hansen and F.K. Larsen, *Inorg. Chem.*, 1995, **34**, 4244.
41. M. Stebler, A. Ludi and H. -B. Burgi, *Inorg. Chem.*, 1986, **25**, 4743.
42. M.M. Morrison and D.T. Sawyer, *Inorg. Chem.*, 1978, **17**, 333.
43. S.K. Chandra and A. Chakravorty, *Inorg. Chem.*, 1992, **31**, 760.
44. T.J. Hubin, J.M. McCormick, S.R. Collinson, M. Buchalova, C.M. Perkins, N.W. Alcock, P.M. Kahol, A. Raghunathan and D.H. Busch, *J. Am. Chem. Soc.*, 2000, **122**, 2512.
45. S.K. Chandra, P. Chakraborty, and A. Chakravorty, *J. Chem. Soc., Dalton Trans.*, 1993, 863.
46. S.K. Chandra, P. Basu, D. Ray, S. Pal and A. Chakravorty, *Inorg. Chem.*, 1990, **29**, 2423.
47. H. Tamura, K. Ogawa, T. Sakurai and A. Nakahara, *Inorg. Chim. Acta*, 1984, **92**, 107.
48. P. Chakraborty, S.K. Chandra and A. Chakravorty, *Inorg. Chem.*, 1993, **32**, 5349.
49. S.M. Saadeh, M.S. Lah and V.L. Pecoraro, *Inorg. Chem.*, 1991, **30**, 8.
50. G. Renger, *Angew. Chem. Int. Ed. Engl.*, 1987, **26**, 643.
51. (a) G.N. George, R.C. Prince and S.P. Cramer, *Science*, 1989, **243**, 789; (b) A. Zouni, H.-T. Witt, J. Kern, P. Fromme, N. Krauß, W. Saenger and P. Orth, *Nature*, 2001, **409**, 739.

52. (a) R.J. Debus, *Biochim. Biophys. Acta*, 1992, **1102**, 269; (b) S. Mukhopadhwany, R.J. Staples and W.H. Armstrong, *Chem. Commun.*, 2002, 864.
53. J. Messinger, J.H. Robblee, U. Bergmann, C. Fernandez, P. Glatzel, H. Visser, R.M. Cinco, K.L. McFarlane, E. Bellacchio, S.A. Pizarro, S.P. Cramer, K. Sauer, M.P. Klein and V.K. Yacandra, *J. Am. Chem. Soc.*, 2001, **123**, 7804, and references therein.
54. M. Yagi and M. Kaneko, *Chem. Rev.*, 2001, **101**, 21.
55. J.A. Gilbert, D.S. Eggleston, W.R. Murphy, Jr., D.A. Geselowitz, S.W. Gersten, D.J. Hodgson and T.J. Meyer, *J. Am. Chem. Soc.*, 1985, **107**, 3855.
56. K. Wieghardt, U. Bossek, B. Nuber, J. Weiss, J. Bonvoisin, M. Corbella, S.E. Vitols and J.J. Girerd, *J. Am. Chem. Soc.*, 1988, **110**, 7398.
57. K.S. Hagen, T.D. Westmoreland, M.J. Scott and W.H. Armstrong, *J. Am. Chem. Soc.*, 1989, **111**, 1907.
58. C.E. Dubé, D.W. Wright, S. Pal, P.J. Bonitatebus, Jr. and W.H. Armstrong, *J. Am. Chem. Soc.*, 1998, **120**, 3704.
59. S. Brooker, V. McKee and T. Metcalfe, *Inorg. Chim. Acta*, 1996, **246**, 171.
60. Q. Li, J.B. Vincent, E. Libby, H.-R. Chang, J.C. Huffman, P.D.W. Boyd, G. Christou and D.N. Hendrickson, *Angew. Chem. Int. Ed. Engl.*, 1988, **27**, 1731.
61. G. Christou and J.B. Vincent, *Biochim. Biophys. Acta*, 1987, **895**, 259.
62. S. Wang, H.-L. Tsai, E. Libby, K. Folting, W.E. Streib, D.N. Hendrickson and G. Christou, *Inorg. Chem.*, 1996, **35**, 7578.
63. G. Aromí, M.W. Wemple, S.J. Aubin, K. Folting, D.N. Hendrickson and G. Christou, *J. Am. Chem. Soc.*, 1998, **120**, 5850.
64. S. Wang, M.S. Wemple, J. Yoo, K. Folting, J.C. Huffman, K.S. Hagen, D.N. Hendrickson and G. Christou, *Inorg. Chem.*, 2000, **39**, 1501.
65. W.F. Ruettlinger, C. Campana and G.C. Dismukes, *J. Am. Chem. Soc.*, 1997, **119**, 6670.
66. J.B. Vincent, C. Christmas, H.-R. Chang, Q. Li, P.D.W. Boyd, J.C. Huffman, D.N. Hendrickson and G. Christou, *J. Am. Chem. Soc.*, 1989, **111**, 2086.
67. S.K. Chandra and A. Chakravorty, *Inorg. Chem.*, 1991, **30**, 3795.
68. S. Wang, K. Folting, W.E. Streib, E.A. Schmitt, J.K. McCusker, D.N. Hendrickson and G. Christou, *Angew. Chem. Int. Ed. Engl.*, 1991, **30**, 305.
69. E. Libby, J.K. McCusker, E.A. Schmitt, K. Folting, D.N. Hendrickson and G. Christou, *Inorg. Chem.*, 1991, **30**, 3486.
70. C. Cañada-Vilalta, J.C. Huffman and G. Christou, *Polyhedron*, 2001, **20**, 1785.

71. S. Wang, H.-L. Tsai, K.S. Hagen, D.N. Hendrickson and G. Christou, *J. Am. Chem. Soc.*, 1994, **116**, 8376.
72. C. Boskovic, K. Folting and G. Christou, *Polyhedron*, 2000, **19**, 2111.
73. M.K. Chan and W.H. Armstrong, *J. Am. Chem. Soc.*, 1989, **111**, 9121.
74. M. Suzuki, T. Sugisawa, H. Senda, H. Oshio and A. Uehara, *Chem. Lett.*, 1989, 1091.
75. M.K. Chan and W.H. Armstrong, *J. Am. Chem. Soc.*, 1990, **112**, 4985.
76. M. Suzuki, H. Senda, M. Suenaga, T. Sugisawa and A. Uehara, *Chem. Lett.*, 1990, 923.
77. S. Theil, R. Yerande, R. Chicate, F. Dahan, A. Bousseksou, S. Padhye and J.-P. Tuchagues, *Inorg. Chem.*, 1997, **36**, 6279.
78. J.C. Jeffery, P. Thornton and M.D. Ward, *Inorg. Chem.*, 1994, **33**, 3612.
79. C. Philouze, G. Blondin, S. Ménage, N. Auger, J.-J. Girerd, D. Vigner, M. Lance and M. Nierlich, *Angew. Chem. Int. Ed. Engl.*, 1992, **31**, 1629.
80. C. Philouze, G. Blondin, J.-J. Girerd, J. Guilhem, C. Pascard and D. Lexa, *J. Am. Chem. Soc.*, 1994, **116**, 8557.
81. M.K. Chan and W.H. Armstrong, *J. Am. Chem. Soc.*, 1991, **113**, 5055.
82. H. Torayama, T. Nishide, H. Asada, M. Fujiwara and T. Matsushita, *Polyhedron*, 1997, **16**, 3787.
83. M. Suzuki, Y. Hayashi, K. Muneyawa, M. Suenaga, H. Senda and A. Uehara, *Chem. Lett.*, 1991, 1929.
84. (a) M. Mikuriya, Y. Yamato and T. Tokii, *Chem. Lett.*, 1991, 1429; (b) M. Mikuriya, Y. Yamato and T. Tokii, *Bull. Chem. Soc. Jpn.*, 1992, **65**, 2624.
85. S.M.J. Aubin, Z. Sun, H.J. Eppley, E.M. Rumberger, I.A. Guzei, K. Folting, P.K. Gantzel, A.L. Rheingold, G. Christou and D.N. Hendrickson, *Polyhedron*, 2001, **20**, 1139.
86. R. Sessoli, H.-L. Tsai, A.R. Schake, S. Wang, J.B. Vincent, K. Folting, D. Gatteschi, G. Christou and D.N. Hendrickson, *J. Am. Chem. Soc.*, 1993, **115**, 1804.
87. (a) H.J. Eppley, H.-L. Tsai, N. de Vries, K. Folting, G. Christou and D.N. Hendrickson, *J. Am. Chem. Soc.*, 1995, **117**, 301; (b) T. Kuroda-Sowa, M. Lam, A.L. Rheingold, C. Frommen, W.M. Reiff, M. Nakano, J. Yoo, A.L. Maniero, L.-C. Brunel, G. Christou and D.N. Hendrickson, *Inorg. Chem.*, 2001, **40**, 6469.
88. M. Soler, S.K. Chandra, D. Ruiz, E.R. Davidson, D.N. Hendrickson and G. Christou, *Chem. Commun.*, 2000, 2417.
89. (a) S.M. J. Aubin, Z. Sun, H.J. Eppley, E.M. Rumberger, I.A. Guzei, K. Folting, P.K. Gantzel, A.L. Rheingold, G. Christou and D.N. Hendrickson, *Inorg. Chem.*, 2001, **40**, 2127; (b) M. Soler, P. Artus, K. Folting, J.C. Huffman, D.N. Hendrickson and G. Christou, *Inorg. Chem.*, 2001, **40**, 4902.

90. M. Soler, E. Rumberger, K. Folting, D.N. Hendrickson and G. Christou, *Polyhedron*, 2001, **20**, 1365.
91. J.W. Lauher and J.A. Ibers, *Inorg. Chem.*, 1975, **14**, 348.
92. K.R. Dunbar and A. Quillevéré, *Polyhedron*, 1993, **12**, 807.
93. (a) R.R. Richards and N.W. Gregory, *J. Phys. Chem.*, 1965, **69**, 239; (b) J.A. Zora, K.R. Seddon, P.B. Hitchcock, C.B. Lowe, D.P. Shum and R.L. Carlin, *Inorg. Chem.*, 1990, **29**, 3302.
94. F. Lloret, M. Julve, M. Mollar, I. Castro, J. Latorre, J. Faus, X. Solans and I.M.-Badarau, *J. Chem. Soc., Dalton Trans.*, 1989, 729.
95. P. Zanello, R. Cini and A. Cinquantini, *Polyhedron*, 1985, **4**, 1383.
96. P. Zanello, R. Cini and A. Cinquantini, *Inorg. Chim. Acta*, 1983, **74**, 89.
97. G.J.P. Britovsek, V.C. Gibson, B.S. Kimberley, P.J. Maddox, S.J. McTavish, G.A. Solan, A.J.P. White and D.J. Williams, *Chem. Commun.*, 1998, 849.
98. J.C. Dabrowiak, F.V. Lovecchio, V.L. Goedken and D.H. Busch, *J. Am. Chem. Soc.*, 1972, **94**, 5502.
99. M.C. Rakowski and D.H. Busch, *J. Am. Chem. Soc.*, 1975, **97**, 2570.
100. P.W.R. Corfield, D.P. Riley, K.S. Bowman and D.H. Busch, *J. Am. Chem. Soc.*, 1975, **97**, 5036.
101. K.B. Mertes, P.W.R. Corfield and D.H. Busch, *Inorg. Chem.*, 1977, **16**, 3226.
102. D.P. Riley, J.A. Stone and D.H. Busch, *J. Am. Chem. Soc.*, 1976, **98**, 1752.
103. P.V. Bernhardt, T. Hambley and G.A. Lawrence, *J. Chem. Soc., Chem. Commun.*, 1989, 553.
104. H. Börzel, P. Comba, H. Pritzkow and A.F. Sickmüller, *Inorg. Chem.*, 1998, **37**, 3853.
105. L.L. Koh, Y. Xu and K. Hsieh, *Acta Cryst.*, 1994, **C50**, 884.
106. P.S. Braterman, J.-I. Song and R.D. Peacock, *Inorg. Chem.*, 1992, **31**, 555.
107. J. Baker, L.M. Engelhardt, B.N. Figgis and A.H. White, *J. Chem. Soc., Dalton Trans.*, 1975, 530.
108. P.C. Healy, B.W. Skelton and A.H. White, *Austr. J. Chem.*, 1983, **36**, 2057.
109. B.N. Figgis, B.W. Skelton and A.H. White, *Austr. J. Chem.*, 1978, **31**, 57.
110. A.T. Baker and H.A. Goodwin, *Austr. J. Chem.*, 1985, **38**, 207.
111. (a) E. Pérez-Cordero, R. Buigas, N. Brady, L. Echegoyen, C. Arana and J.-M. Lehn, *Helv. Chim. Acta*, 1974, **77**, 1222; (b) E. Pérez-Cordero, C. Campana and L. Echegoyen, *Angew. Chem. Int. Ed. Engl.*, 1997, **36**, 137.
112. S. Pyo, E. Pérez-Cordero, S.G. Bott and L. Echegoyen, *Inorg. Chem.*, 1999, **38**, 3337.
113. M. Di Vaira, S. Midollini and L. Sacconi, *Inorg. Chem.*, 1981, **20**, 3430.
114. L.D. Field, A.V. George, F. Laschi, E.Y. Malouf and P. Zanello, *J. Organomet. Chem.*, 1992, **435**, 347.

115. L.D. Field, A.V. George and T. Hambley, *Polyhedron*, 1990, **17**, 2139.
116. Y. Dong, H. Fujii, M.P. Hendrich, R.A. Leising, G. Pan, C.R. Randall, E.C. Wilkinson, Y. Zang, L. Que, Jr., B.G. Fox, K. Kauffmann and E. Münck, *J. Am. Chem. Soc.*, 1995, **117**, 2778.
117. H. Zheng, S.J. Yoo, E. Münck and L. Que, Jr., *J. Am. Chem. Soc.*, 2000, **122**, 3789.
118. C. Bianchini, F. Laschi, D. Masi, F.M. Ottaviani, A. Pastor, M. Peruzzini, P. Zanello and F. Zanobini, *J. Am. Chem. Soc.*, 1993, **115**, 2723.
119. L.D. Field, A.V. George and T. Hambley, *Inorg. Chem.*, 1990, **29**, 4565.
120. R. Denis, L. Toupet, F. Paul and C. Lapinte, *Organometallics*, 2000, **19**, 4240.
121. (a) R.W. Saalfrank, S. Trummer, H. Krautscheid, V. Schünemann, A.X. Trautwein, S. Hien, C. Stadler and J. Daub, *Angew. Chem. Int. Ed. Engl.*, 1996, **35**, 2206; (b) C. Stadler, J. Daub, J. Köhler, R.W. Saalfrank, V. Coropceanu, V. Schünemann, C. Ober, A.X. Trautwein, S.F. Parker, M. Poyraz, T. Inomata and R.D. Cannon, *J. Chem. Soc., Dalton Trans.*, 2001, 3373.
122. F. Fabrizi de Biani, M. Fontani, E. Ruiz, P. Zanello, J. Monte Russell and R.N. Grimes, *Organometallics*, 2002, **21**, 4129.
123. A.H. Mahmoudkhani and V. Langer, *Acta Cryst.*, 1999, **C55**, 1631.
124. P. Zanello and M. Fontani, unpublished results.
125. E.K. Byrne and K.H. Theopold, *J. Am. Chem. Soc.*, 1989, **111**, 3887.
126. (a) N. Bresciani, M. Calligaris, P. Delise, G. Dodic, G. Nardin and L. Randaccio, *J. Chem. Soc., Dalton Trans.*, 1976, 2478; (b) W.P. Schaeffer and R.E. Marsh, *Acta Cryst.*, 1969, **B25**, 1675.
127. B.J. Kennedy, G.D. Fallon, B.M.K.C. Gatehouse and K.S. Murray, *Inorg. Chem.*, 1984, **23**, 580.
128. P. Zanello and A. Cinquantini, *Transition Met. Chem.*, 1985, **10**, 370.
129. P. Zanello, R. Cini, A. Cinquantini and P.L. Orioli, *J. Chem. Soc., Dalton Trans.*, 1983, 2159.
130. M.D. Glick, J.M. Kuszaj and J.F. Endicott, *J. Am. Chem. Soc.*, 1973, **95**, 5097.
131. N.F. Curtis, G.J. Gainsford, T.W. Hambley, G.A. Lawrence, K.R. Morgan and A. Siriwardena, *J. Chem. Soc., Chem. Commun.*, 1987, 295.
132. T.W. Hambley, G.H. Searle and M.R. Snow, *Aust. J. Chem.*, 1982, **35**, 1285.
133. K. Wieghardt, W. Schmidt, W. Herrmann and H.-J. Küppers, *Inorg. Chem.*, 1983, **22**, 2953.
134. T.W. Hambley, *Inorg. Chem.*, 1988, **27**, 2496.
135. I.I. Creaser, J. MacB. Harrowfield, A.J. Herlt, A.M. Sargeson, J. Springborg, R.J. Geue and M.R. Snow, *J. Am. Chem. Soc.*, 1977, **99**, 3181.

136. A.M. Bond, G.A. Lawrence, P.A. Lay and A.M. Sargeson, *Inorg. Chem.*, 1983, **22**, 2010.
137. S. Sahami and M.J. Weaver, *J. Electroanal. Chem.*, 1981, **122**, 171.
138. I.I. Creaser, R.J. Geue, J. MacB. Harrowfield, A.J. Herlt, A.M. Sargeson, M.R. Snow and J. Springborg, *J. Am. Chem. Soc.*, 1982, **104**, 6016.
139. D.J. Szalda, C. Creutz, D. Mahajan and N. Sutin, *Inorg. Chem.*, 1983, **22**, 2372.
140. R.M. L. Warren, L. Öhrström, G.J. Opitock, M. Shang and A.G. Lappin, *Inorg. Chim. Acta*, 1994, **225**, 75.
141. S.A. Richert, P.K.S. Tsang and D.T. Sawyer, *Inorg. Chem.*, 1989, **28**, 2471.
142. K. Yanagi, Y. Ohashi, Y. Sasada, Y. Kaizu and H. Kobayashi, *Bull. Chem. Soc. Jpn.*, 1981, **54**, 118.
143. A.R. Guadalupe, D.A. Usifer, K.T. Potts, H.C. Hurrell, A.-E. Mogstad and H.D. Abruña, *J. Am. Chem. Soc.*, 1988, **110**, 3462.
144. M.C. Hughes, D.J. Macero and J.M. Rao, *Inorg. Chim. Acta*, 1981, **49**, 241.
145. (a) E.N. Maslen, C.L. Raston and A.H. White, *J. Chem. Soc., Dalton Trans.*, 1974, 1803; (b) C.L. Raston and A.H. White, *J. Chem. Soc., Dalton Trans.*, 1976, 7; (c) W. Henke and S. Kramer, *Inorg. Chim. Acta*, 1982, **65**, L115.
146. B.N. Figgis, E.S. Kucharski and A.H. White, *Aust. J. Chem.*, 1983, **36**, 1563.
147. G.S. Hanan, D. Volkmer, U.S. Schubert, J.-M. Lehn, G. Baum and D. Fenske, *Angew. Chem. Int. Ed. Engl.*, 1997, **36**, 1842.
148. M. Ruben, E. Breuning, J.-P. Gisselbrecht and J.-M. Lehn, *Angew. Chem. Int. Ed. Engl.*, 2000, **39**, 4139.
149. A.G. Manfredotti and C. Guastini, *Acta Cryst.*, 1983, **C39**, 863.
150. A. Radha, M. Seshasayee, K. Ramalingam and G. Aravamudan, *Acta Cryst.*, 1985, **C41**, 1169.
151. P. Zanello and A. Cinquantini, *Transition Met. Chem.*, 1985, **10**, 370.
152. G. Gosden, K.P. Healy and D. Pletcher, *J. Chem. Soc., Dalton Trans.*, 1978, 972.
153. B. de Castro and C. Freire, *Inorg. Chem.*, 1990, **29**, 5113.
154. D.E. Berning, B.C. Noll and D.L. DuBois, *J. Am. Chem. Soc.*, 1999, **121**, 11432.
155. P. Zanello, A. Cinquantini, C.A. Ghilardi, S. Midollini, S. Moneti, A. Orlandini and A. Bencini, *J. Chem. Soc., Dalton Trans.*, 1990, 3761.
156. M. Di Vaira, P.L. Orioli and L. Sacconi, *Inorg. Chem.*, 1971, **10**, 553.
157. T. Ito and K. Toriumi, *Acta Cryst.*, 1981, **B37**, 88.
158. F.V. Lovecchio, E.S. Gore and D.H. Busch, *J. Am. Chem. Soc.*, 1974, **96**, 3109.
159. D.H. Busch, *Accounts Chem. Res.*, 1978, **11**, 392.
160. M. Yamashita and H. Miyamae, *Inorg. Chim. Acta*, 1989, **156**, 71.

161. N.F. Curtis, G.J. Gainsford, T.W. Hambley, G.A. Lawrence, K.R. Morgan and A. Siriwardena, *J. Chem. Soc., Chem. Commun.*, 1987, 295.
162. P.V. Bernhardt, *Acta Cryst.*, 2000, **C56**, 744.
163. (a) A. Wada, C. Katayama and J. Tanaka, *Acta Cryst.*, 1976, **B32**, 3194;
(b) E. Freire, S. Baggio, A. Mombru and R. Baggio, *Acta Cryst.*, 2000, **C56**, 541.
164. (a) B.A. Frenz and J.A. Ibers, *Inorg. Chem.*, 1972, **11**, 1109; (b) L. Suescun, A.W. Monbrú and R.A. Mariezcurrena, *Acta Cryst.*, 1999, **C55**, 1991 and references therein.
165. M.I. Arriortua, T. Rojo, J.M. Amigo, G. Germain and J.P. Declercq, *Bull. Soc. Chim. Belg.*, 1982, **91**, 337.
166. D.J. Szalda, D.H. Macartney and N. Sutin, *Inorg. Chem.*, 1984, **23**, 3473.
167. R. Prasad and D.B. Scaife, *J. Electroanal. Chem.*, 1977, **84**, 373.
168. J.C. Brodovitch, R.I. Haines and A. McAuley, *Can. J. Chem.*, 1981, **59**, 1610.
169. G. Sproul and G.D. Stucky, *Inorg. Chem.*, 1973, **12**, 2898.
170. A.K. Patra and R. Mukherjee, *Inorg. Chem.*, 1999, **38**, 1388.
171. P. Zanello, *Comments Inorg. Chem.*, 1988, **8**, 45.
172. P. Zanello, in 'Stereochemistry of Organometallic and Inorganic Compounds', I. Bernal (ed), Elsevier, Amsterdam, 1990, Vol. 4, p. 181.
173. (a) P.L. Holland and W.B. Tolman, *J. Am. Chem. Soc.*, 1999, **121**, 7270;
(b) B.A. Jazdzewski, P.L. Holland, M. Pink, V.G. Young, Jr., D.J.E. Spencer and W.B. Tolman, *Inorg. Chem.*, 2001, **40**, 6097.
174. J.E. Johnson, T.A. Beineke and R.A. Jacobson, *J. Chem. Soc. A*, 1971, 1371.
175. A. Cinquantini, G. Opronolla and P. Zanello, *J. Chem. Soc. Dalton Trans.*, 1991, 3161.
176. G.J. Pirka, R.J. Seeney and A.A. Pinkerton, *Acta Cryst.*, 1991, **C47**, 510.
177. M.M. Bhadbhade and D. Srinivas, *Inorg. Chem.*, 1993, **32**, 6122.
178. E. Suresh, M.M. Bhadbhade and D. Srinivas, *Polyhedron*, 1996, **15**, 4133.
179. P. Zanello and A. Cinquantini, *Transition Met. Chem.*, 1985, **10**, 370.
180. M. Gullotti, L. Casella, A. Pintar, E. Suardi, P. Zanello and S. Mangani, *J. Chem. Soc., Dalton Trans.*, 1989, 1979.
181. R. Ruiz, C. Surville-Barland, A. Aukauloo, E. Anxolabehere-Mallart, Y. Journaux, J. Cano and M.C. Muñoz, *J. Chem. Soc., Dalton Trans.*, 1997, 745.
182. J. Hanss, A. Beckmann and H.-J. Krüger, *Eur. J. Inorg. Chem.*, 1999, 163.
183. G.J. Grant, M.W. Jones, K.D. Loveday, D.G. VanDerveer, W.T. Pennington, C.T. Eagle and L.F. Mehne, *Inorg. Chim. Acta*, 2000, **300–302**, 250.

184. C.R. Lucas, W. Liang, D.O. Miller and J.N. Bridson, *Inorg. Chem.*, 1997, **36**, 4508.
185. R. Allmann, W. Henke and D. Reinen, *Inorg. Chem.*, 1978, **17**, 379.
186. O.P. Anderson, *J. Chem. Soc., Dalton Trans.*, 1972, 2597.
187. O.P. Anderson, *J. Chem. Soc., Dalton Trans.*, 1973, 1237.
188. R.R. Ruminski, *Inorg. Chim. Acta*, 1985, **103**, 159.
189. P. Majumdar, A.K. Ghosh, L.R. Falvello, S.-M. Peng and S. Goswami, *Inorg. Chem.*, 1998, **37**, 1651.
190. S.A. Richert, P.K.S. Tsang and D.T. Sawyer, *Inorg. Chem.*, 1989, **28**, 2471.
191. X.-M. Chen, R.-Q. Wang and X.-L. Yu, *Acta Cryst.*, 1995, **C51**, 1545.
192. A. Bencini, S. Midollini and C. Zanchini, *Inorg. Chem.*, 1989, **28**, 1963.
193. P. Zanello, unpublished results.
194. J.K. Nag, P.K. Santra, C. Sinha, F.-L. Liao and T.-H. Lu, *Polyhedron*, 2001, **20**, 2253.
195. J.L. Sadler and A.J. Bard, *J. Am. Chem. Soc.*, 1968, **90**, 1979

CHAPTER 6

Metal Complexes Containing Redox-active Ligands

This chapter will focus on compounds particularly appealing from the electrochemical viewpoint: *metal complexes containing redox-active ligands*. In fact, these complexes couple the redox aptitude of the metal centre with that of the ligand itself, giving rise to molecules possessing extended electronic mobility and hence able to afford potentially innovative materials. In the course of preceding discussions we have already faced metal complexes containing *polypyridines* (bipyridine, phenanthroline, terpyridine) and in general the most nitrogen heterocyclic ligands. As briefly discussed, it is not always easy to assign the nature of the redox changes as metal d(π) or ligand p(π) centred (spectroelectrochemical measurements can sometime help this task). In those cases in which metal-centred and ligand-centred frontier orbitals are comparable in energy, the ligands under subject are defined as redox ‘non-innocent’.¹ In addition to the above mentioned ligands, there are other common classes of redox-non-innocent ligands, such as the highly popular ferrocenes and fullerenes, or the equally well known o-dioxolenes, dithiolenes and porphyrins, all of which clearly show how problematic can be the assignment of the metal-centred or ligand-centred nature of the redox processes that their metal complexes exhibit.

1 FERROCENES AS LIGANDS IN METAL COMPLEXES

As mentioned in Chapter 4, Section 1, to date, several hundred ferrocene derivatives have been synthesized. A further increase in their number has occurred in recent years due to the use of ferrocene derivatives as ligands in metal complexes.² Since some examples of metallic centres branched by several ferrocene units have already been presented in Chapter 4, Section 1.4.2 (when dealing with dendrimers), we will limit our discussion

to a few derivatives able to depict the typical redox behaviour of this class of complex. In particular, we will give examples in which either metal fragments are appended as outer substituents to the cyclopentadienyl ring(s) of the central core ferrocene unit, or, *vice versa*, in which a central metal fragment bears ferrocene unit(s) as external ligands.

Figure 1 shows the molecular structure of the ferrocenyl-tris(pyrazolyl)borato-Mo(II) complex $[(\eta^5\text{-C}_5\text{H}_5)\text{Fe}\{\eta^5\text{-C}_5\text{H}_4\text{-(Tp)}\text{Mo}(\text{Co})_2(\text{CH}_2\text{-C(Me)=CH}_2)\}]$.³

As illustrated in Figure 2, in CH_2Cl_2 solution this complex displays two sufficiently separated one-electron oxidations with features of chemical and electrochemical reversibility ($E_{0/+}^\circ = +0.51\text{ V}$; $E_{+/2}^\circ = +0.63\text{ V}$).

Exhaustive oxidation at the first process makes the original orange solution assume an intense green colour typical of ferrocenium species. One may thus assume that the first oxidation is centred on the ferrocenyl unit and, therefore, the second process must be attributed to the Mo(II)/Mo(III) oxidation.

Figure 3 shows the voltammetric response given under the same experimental conditions by the related compound $[\text{Fe}\{\eta^5\text{-C}_5\text{H}_4\text{-(Tp)}\text{Mo}(\text{CO})_2(\text{CH}_2\text{-C(Me)=CH}_2)\}_2]$ bearing two tris(pyrazolyl)borato-Mo(II) substituents.³

Once again there are two oxidation processes but, as can be inferred from the relative peak heights, a two-electron oxidation ($E_{0/2+}^\circ = +0.60\text{ V}$) should precede a one-electron process ($E_{2+/3+}^\circ = +0.80\text{ V}$). Based on the stoichiometry of the compound, it is naively deduced that in this case the simultaneous oxidation of the two Mo(II) centres precedes the oxidation of the central ferrocene unit. This not only means that there is no electronic interaction (communication) between the two

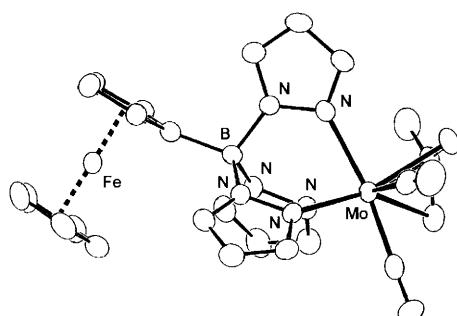


Figure 1 X-Ray structure of $[(\eta^5\text{-C}_5\text{H}_5)\text{Fe}\{\eta^5\text{-C}_5\text{H}_4\text{-(Tp)}\text{Mo}(\text{CO})_2(\text{CH}_2\text{-C(Me)=CH}_2)\}]$. Average bond lengths: $\text{Mo-N} \approx 2.24\text{ \AA}$; $\text{Mo-C}_{\text{allyl}} \approx 2.31\text{ \AA}$; $\text{B-N} \approx 1.55\text{ \AA}$; $\text{B-C} = 1.60\text{ \AA}$; $\text{Fe} \cdots \text{Mo} = 6.8\text{ \AA}$

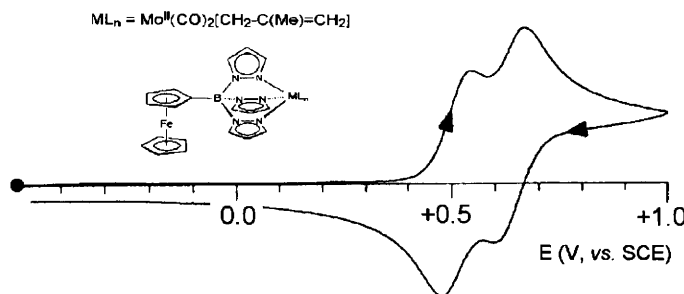


Figure 2 Cyclic voltammogram recorded at a platinum electrode in a CH_2Cl_2 solution of $[(\eta^5-C_5H_5)Fe\{\eta^5-C_5H_4-(Tp)Mo(CO)_2(CH_2-C(Me)=CH_2)\}]$. Scan rate 0.2 V s^{-1}

peripheral Mo(II) fragments (see Chapter 4, Section 1.3), but that the insertion of the two Mo(II) substituents drastically modifies the electronic distribution inside the molecule with respect to the monosubstituted species, making the oxidation of the two Mo(II) centres easier than that of the ferrocene unit.

A further example is constituted by $[Co_3(CO)_6\{\mu_2-\eta^2:\eta^1-C(C_5H_5-FeC_5H_4-C=C(PPh_2)C(O)OC(O)\}(\mu_2-PPh_2)]$, the crystal structure of which is shown in Figure 4.⁴

As illustrated in Figure 5, the complex exhibits a reversible one-electron oxidation ($E^{\circ'} = +0.36 \text{ V}$), easily assigned to the ferrocenyl unit, as well as two sequential one-electron reductions showing features of chemical reversibility, which are centred on the maleic anhydride capped tricobalt cluster.⁴

It is useful to note that the precursor $[(C_5H_5FeC_5H_4)CCo_3(CO)_9]$ also exhibits the expected ferrocenyl-centred oxidation, but only a single one-electron reduction.² This means that the actual two one-electron

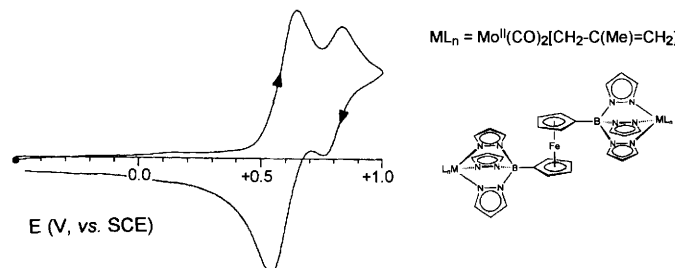


Figure 3 Cyclic voltammogram recorded at a platinum electrode in a CH_2Cl_2 solution of $[Fe\{\eta^5-C_5H_4-(Tp)Mo(CO)_2(CH_2-C(Me)=CH_2)\}_2]$. Scan rate 0.2 V s^{-1}

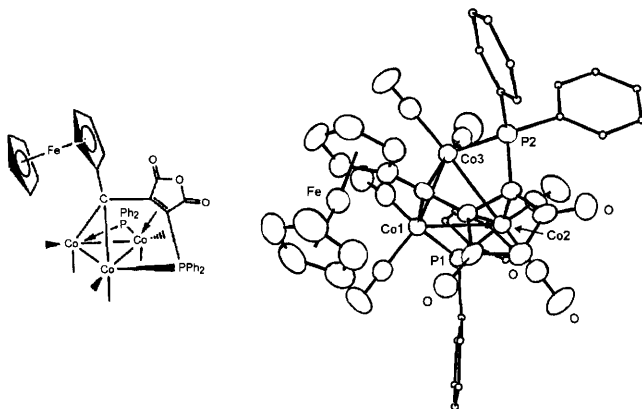


Figure 4 X-Ray structure of $[Co_3(CO)_6\{\mu_2\text{-}\eta^2\text{:}\eta^1\text{-}C(C_5H_5FeC_5H_4\text{-}C=C(PPh_2)C(O)OC(O)\}(\mu_2\text{-}PPh_2)\}]$. Bond lengths: $Co1\text{-}Co2 = 2.43 \text{ \AA}$; $Co1\text{-}Co2 = 2.57 \text{ \AA}$; $Co2\text{-}Co3 = 2.71 \text{ \AA}$; $Co1\text{-}P1 = 2.13 \text{ \AA}$; $Co2\text{-}P1 = 2.27 \text{ \AA}$; $Co3\text{-}P2 = 2.23 \text{ \AA}$

reductions arise from a cooperative interaction of the tricobalt cluster and the redox-active bis(diphenylphosphino)maleic anhydride.

Let us now consider a few complexes in which a central metal fragment is interposed between two ferrocenyl units.

Figure 6 shows the electrochemical behaviour of the diferrocenyl-bis[tris(pyrazolyl)borato]-Fe(II) derivative there schematized, strictly related to the previous complexes.³

The stoichiometry in this case again provides a clear indication that the first reversible one-electron oxidation is centred on the central Fe(II) core ($E_{0/+}^\circ = +0.06 \text{ V}$), whereas the second reversible two-electron

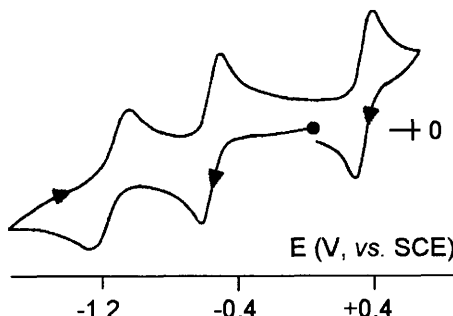


Figure 5 Cyclic voltammogram recorded at a platinum electrode in a CH_2Cl_2 solution of $[Co_3(CO)_6\{((\mu_2\text{-}\eta^2\text{:}\eta^1\text{-}C(C_5H_5FeC_5H_4\text{-}C=C(PPh_2)C(O)OC(O)})\}(\mu_2\text{-}PPh_2)\}]$. Scan rate 0.1 V s^{-1}

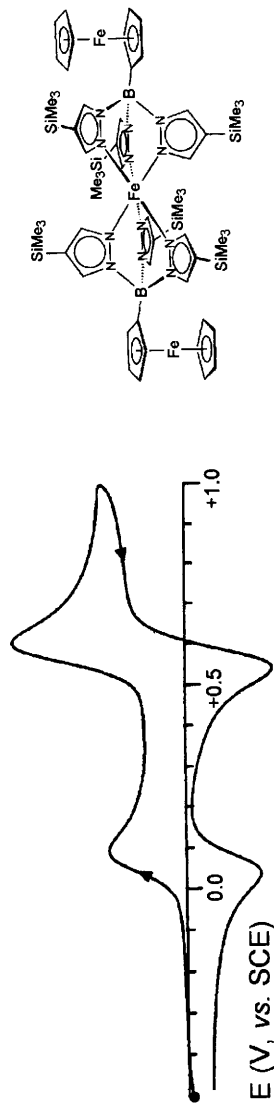


Figure 6 Cyclic voltammogram recorded at a platinum electrode in a CH_2Cl_2 solution of $[\text{Fe}^{II}\{\langle\eta^5-\text{C}_5\text{H}_5\rangle\text{Fe}(\eta^5-\text{C}_5\text{H}_5)\text{Fe}^{II}\}]_2$ ($R = \text{SiMe}_3$). Scan rate 0.2 V s^{-1}

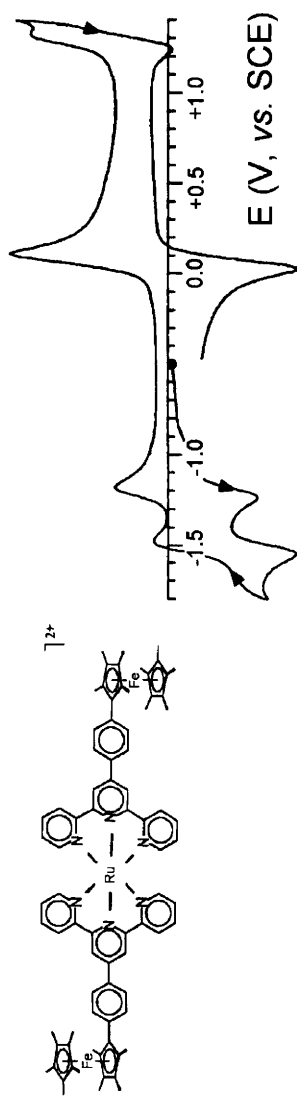


Figure 7 Cyclic voltammogram recorded at a platinum electrode in a CH_2Cl_2 solution of $[\text{Fc}^*-(\text{C}_6\text{H}_4)-\text{terpy-Ru-terpy}-(\text{C}_6\text{H}_4)-\text{Fc}^*]^2+$. Scan rate 0.2 V s^{-1} .

oxidation involves the two outer ferrocenyl substituents ($E_{+3/+}^{\circ'} = +0.57$ V), which, therefore, lack any mutual interaction.

In order to illustrate the possibly extended redox aptitude of the ferrocene complexes, Figure 7 shows the cyclic voltammetric response of the ferrocenyl-terpyridine-Ru(II) complex $[Fc^*-(C_6H_4)-\text{terpy}-\text{Ru-terpy-}(C_6H_4)-Fc^{*2+}]$ [$Fc^* = (\eta^5-\text{C}_5\text{Me}_4\text{H})\text{Fe}(\eta^5-\text{C}_5\text{Me}_4)$].

As seen, the simultaneous two-electron oxidation of the two (not communicating) ferrocenyl subunits ($E^{\circ'} = +0.07$ V) precedes the Ru(II)/Ru(III) oxidation ($E^{\circ'} = +1.25$ V). In addition, two reversible one-electron reductions appear ($E_{2+/+}^{\circ'} = -1.21$ V; $E_{+/0}^{\circ'} = -1.50$ V), which, based on the redox activity of terpyridine, are certainly contributed by such ligand.

From such examples one could infer that the presence of a metal fragment in between two ferrocene units always prevents their electronic communication. In reality, as discussed in Chapter 4, Section 1.3 (dealing with diferrocenanes), the extent of electronic interaction is dictated by the nature of the ‘spacer’ itself. This means that, as happens for diferrocenanes bearing unsaturated carbon chains as bridges, also in the case of bridges formed by proper metal fragments’ communication may be allowed. In this connection it is useful to look at the complex illustrated in Figure 8, in which a $\text{Cu}^I_3(\text{dppm})_3$ fragment [dppm = bis(diphenylphosphino)methane] is interposed between two ethynylferrocenyl units.⁶

As shown in Figure 9, in MeCN solution it exhibits two slightly separated ferrocene-centred oxidations (at about +0.15 V, vs. Ag/Ag⁺), followed by irreversible oxidation processes centred on the tricopper(I) moiety. In differential pulse polarography the two first waves are better resolved ($\Delta E^{\circ'} = 110$ mV).⁶

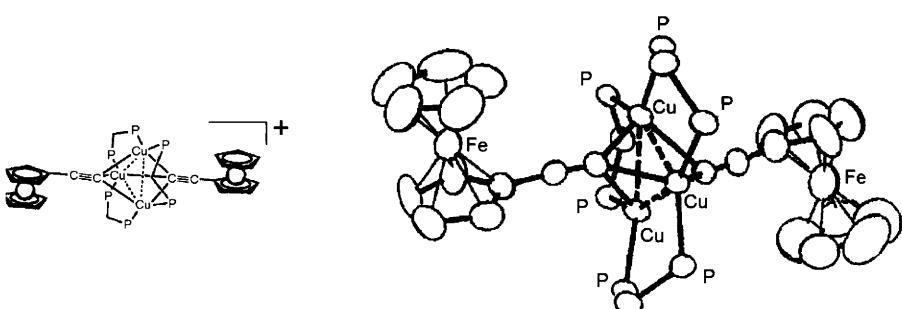


Figure 8 X-Ray structure of $[\text{Cu}^I_3(\text{dppm})_3\{\mu_3-\eta^1-[C\equiv C(C_5\text{H}_4\text{FeC}_5\text{H}_5)]\}_2]^+$. Average bond lengths: Cu-P = 2.29 Å; Cu-C ≈ 2.21 Å; Cu...Cu ≈ 2.63 Å

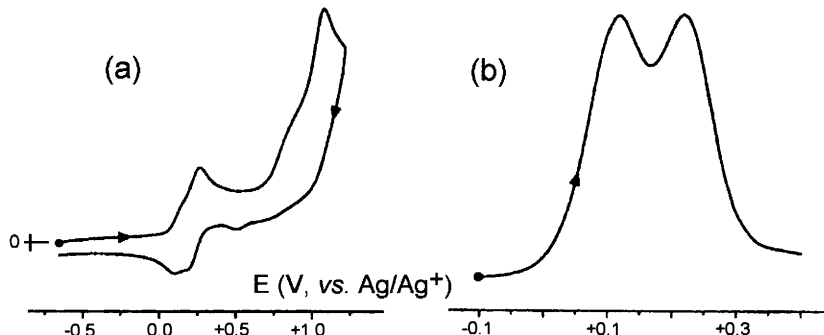


Figure 9 Cyclic (a) and differential pulse (b) voltammograms recorded at a platinum electrode in a MeCN solution of $[Cu'_{\text{3}}(\text{dppm})_{\text{3}}\{\mu_{\text{3}}\text{-}\eta'\text{-}[\text{C}\equiv\text{C}(\text{C}_5\text{H}_4\text{FeC}_5\text{H}_5)]\}_{\text{2}}]^+$. Scan rates: (a) 0.05 V s^{-1} ; (b) 0.02 V s^{-1}

The result indicates that, in spite of the great separation between the two iron centres (11.8 \AA), the electronic interaction is able to manifest.

We like to conclude the present section with an example which points out the role played by the electronic effects of ferrocene ligands in stabilizing uncommon oxidation states in metal complexes rather than their electrochemical properties. Figure 10 shows the molecular structure of the Ir(I) monocation $[\text{Ir}(\text{dppf})_2]^+$ ($\text{dppf} = 1,1'\text{-bis(diphenylphosphino)ferrocene}$)⁷ and its electrochemical behaviour in thf solution.⁸

The central Ir-P₄ core assumes a coordination intermediate between planar and tetrahedral. The cation undergoes two subsequent, chemically reversible, one-electron reductions ($E_{+/-}^{\circ} = -1.56 \text{ V}$; $E_{0/-}^{\circ} = -1.76 \text{ V}$ (vs. Ag/Ag⁺)). The corresponding Ir(0) and Ir(-I) complexes

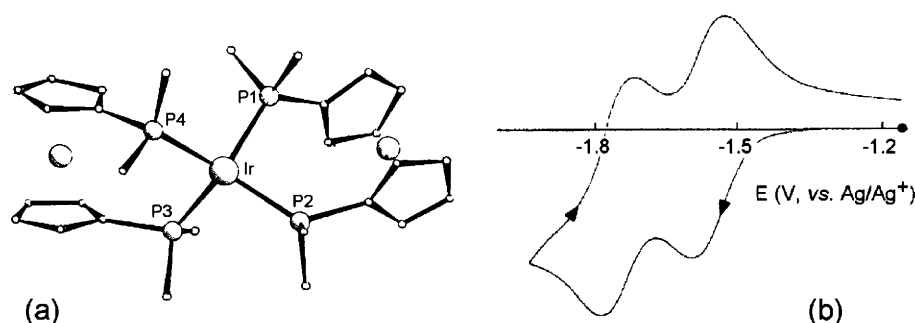


Figure 10 (a) X-Ray structure of $[\text{Ir}(\text{dppf})_2]^+$. Phenyl rings omitted. (b) Cyclic voltammetric behaviour of $[\text{Ir}(\text{dppf})_2]^+$ in thf solution. Mercury working electrode. Scan rate 0.1 V s^{-1}

have been obtained by chemical reduction in thf solution and structurally characterized, Figure 11.⁸

As a result of the stepwise addition of electrons, the tetrahedral distortion of the central Ir-P₄ fragment progressively increases, Table 1.

It is important to note that the strong electron-donating properties of diphenylphosphinoferrocene are able to stabilize the central iridium atom in the unusual 0 and -I oxidation states.

2 FULLERENES AS LIGANDS IN METAL COMPLEXES

Until 1985 the only well-characterized forms, from the structural viewpoint, of carbon were graphite and diamond. Their technological importance is well known. Graphite is used as a solid lubricant, pencil lead, moderator of neutron energy in nuclear reactors and as a strengthening material in polymer carbon products. Diamond, other than its importance in jewellery, is used in all types of industrial drilling, because of its hardness. In 1985, a very stable carbon aggregate, C₆₀, was identified spectroscopically within the vapours generated by laser excitation of graphite. This new form of carbon was proposed to have

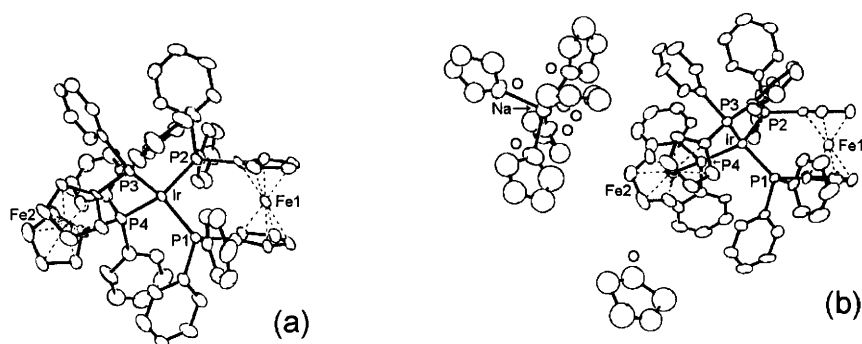


Figure 11 X-Ray structures of: (a) $[Ir(dppf)_2]^+$; (b) $[Ir(dppf)_2]^-$ in $[Na(thf)_5][Ir(dppf)_2]\cdot thf$

Table 1 (Average) structural parameters in the series $[Ir(dppf)_2]^{+/-}$

Complex	$Ir-P (\text{\AA})$	$Ir \cdots Fe (\text{\AA})$	$P1IrP2/P3IrP4 (^{\circ})^a$
$[Ir(dppf)_2]^+$	2.35	4.44	51.0
$Ir(dppf)_2$	2.31	4.37	74.7
$[Ir(dppf)_2]^-$	2.26	4.31	85.0

^aDihedral angle.

the shape of a football and was given the name *buckminsterfullerene* (in honour of the American mathematician Buckminster Fuller, 1895–1983, renown for his spherical shaped domes). From that moment began strenuous efforts to characterize these carbon superclusters and to prepare them in appreciable quantities. Their use as superconductors, when doped with alkaline metals (see Chapter 10), has definitively conferred on them technological importance.

Among the many carbon clusters identified spectroscopically (from C₄₀ to C₂₀₀), a few have been structurally characterized. For instance, Figure 12 illustrates the molecular structures of C₆₀, C₇₀, C₇₆, C₇₈, C₈₀ and C₈₂ (in their most stable isomeric forms).⁹

At present the simplest carbon cluster to prepare is the buckminsterfullerene C₆₀, the geometry of which is classified as ‘truncated icosahedral’, which belongs to the icosahedral symmetry group, I_h. As a consequence, the frontier orbitals of C₆₀ consist of a full pentadegenerate HOMO (h_u) and two triply degenerate LUMOs (t_{1u} and t_{1g}), Figure 13.

It follows that C₆₀ should be able to receive up to 12 electrons.

Dating from 1990, electrochemical studies have gradually revealed the capacity of C₆₀ to receive reversibly from 2 to 5 electrons. In 1992 low temperature studies clearly proved the ability of C₆₀ to receive 6 electrons.¹⁰ Figure 14 shows the low temperature cyclic voltammogram of C₆₀.

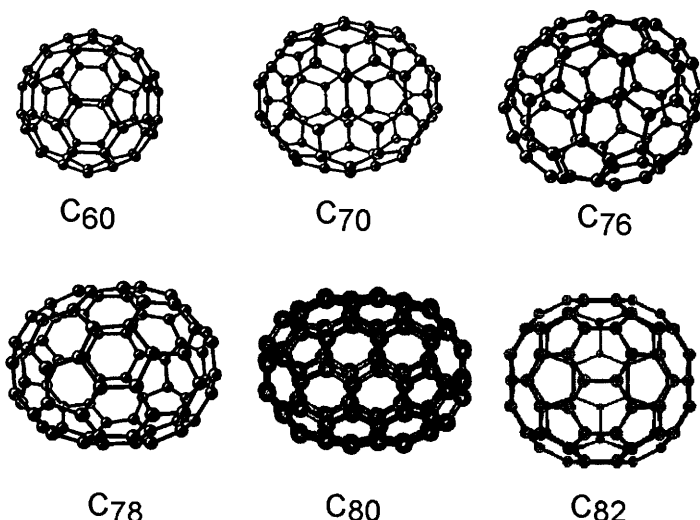


Figure 12 Molecular structures of a few fullerenes

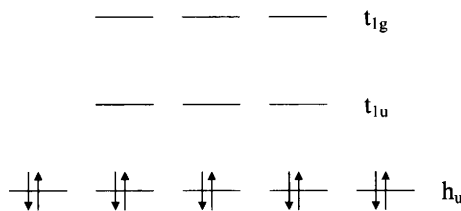


Figure 13 MO energy level diagram for the frontier orbitals of C_{60}

It must, however, be noted that under common experimental conditions one can easily detect the fourth reduction step.¹¹

As a consequence, attempts have been made to obtain a structural characterization of the corresponding fullerene anions. At present well resolved structures are available for $[C_{60}]$, $[C_{60}]^-$ and $[C_{60}]^{2-}$.¹²⁻¹⁴ The high resolution of these structures has somewhat supported the proposal that population of the LUMO t_{1u} should result in a Jahn–Teller distortion (in order to remove the orbital degeneracy). In fact, even if at the margins of statistical significance, in the monoanion a slight axial compression is present, whereas the dianion exhibits a slight axial elongation compared to the perfectly spherical shape of neutral C_{60} .

As compiled in Table 2, the sequence $C_{60} \rightarrow [C_{60}]^- \rightarrow [C_{60}]^{2-}$ displays variations in the typical C/C bond lengths which agree with the theoretical assumption that the t_{1u} orbitals are antibonding with respect to the 6:6 carbon/carbon double bonds and bonding with respect to the 5:6 carbon/carbon single bonds.

As illustrated in Figure 15, it has been found that C_{60} can also reversibly lose an electron at high potential values.¹⁵

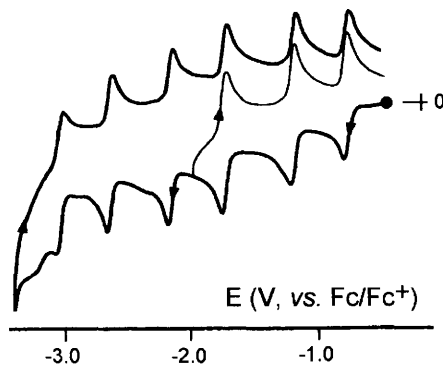
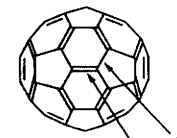


Figure 14 Cyclic voltammogram recorded at a platinum electrode in a dmf –toluene (2:3) solution of C_{60} . Scan rate 0.03 V s^{-1} . $T = 185\text{ K}$

Table 2 Variation of the C/C bond lengths (in Å) on passing from C_{60} to its anions

	C/C bond type	
	(6:6)	(5:6)
C_{60}	1.383(4)	1.453(5)
$[C_{60}]^-$	1.389(3)	1.449(3)
$[C_{60}]^{2-}$	1.399(2)	1.446(2)



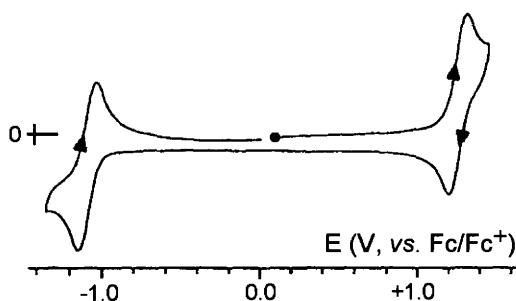
A "5-6 Ring Fusion"

It is interesting to note that the difference between the potentials of the first oxidation and the first reduction constitutes an experimental measurement of the energy separation of the HOMO/LUMO frontier orbitals. This follows that (as mentioned in the Introduction as well as in Chapter 1, Section 2.4) one assumes that in the oxidation process the electron is removed from the occupied orbital of highest energy (HOMO), whereas in the reduction process the electron is added to the unoccupied orbital of lowest energy (LUMO). In the present case, this separation is equal to $\Delta E^{\circ'} = +1.28 - (-1.04) = 2.32$ V (and hence 2.32 eV). This value is in accord with the value of 2.6 eV theoretically determined for the separation of the HOMO h_u and the LUMO t_{1u} . The relatively stable cation $[C_{60}]^+$ has been characterized in solution.¹⁶

C_{70} , which is the second easiest carbon cluster to prepare, has essentially the same redox capacity as C_{60} , Figure 16.¹⁷

C_{70} also displays a one-electron oxidation with features of chemical reversibility at a potential similar to that of C_{60} . This implies that the HOMO/LUMO separation is roughly similar in the two cases.¹⁵

In contrast, the electrochemical behaviour of C_{76} is slightly different. In fact, not only does it display four reduction processes at significantly

**Figure 15** Cyclic voltammogram recorded at a glassy carbon electrode in a 1,1,1-trichloroethane solution of C_{60} . Scan rate 0.1 V s^{-1}

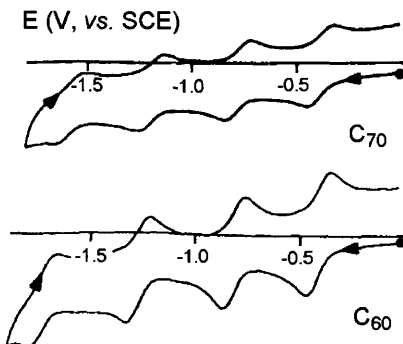


Figure 16 Cyclic voltammograms recorded at a platinum electrode in CH_2Cl_2 solutions of C_{60} (scan rate 10.0 V s^{-1}) and C_{70} (scan rate 20.0 V s^{-1}), respectively

different potentials from C_{60} , but it also exhibits an easy oxidation process (followed by further ill-defined processes), Figure 17.¹⁸

These data indicate a HOMO/LUMO separation for C_{76} of 0.4 eV , compared to the theoretical value of 1.07 eV .

The monofullerene with the highest number of carbon atoms that has been studied electrochemically is C_{84} . Figure 18 shows its cyclic voltammetric behaviour in 1,2-dichlorobenzene.¹⁹

The first three reduction processes are well formed, whereas there is some doubt concerning the fourth cathodic process, which may be due to overlapping processes or impurities of other fullerenes.

We have defined C_{84} as the highest ‘monofullerene’ electrochemically studied, but C_{60} dimers and C_{60} – C_{70} cross-dimers have been characterized also by electrochemistry (see Section 2.1).

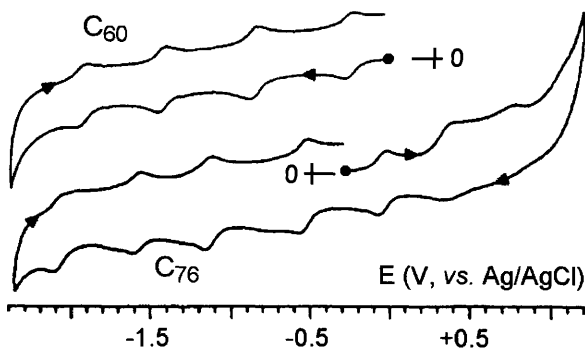


Figure 17 Cyclic voltammograms recorded at a platinum electrode in thf solutions of C_{60} and C_{76} , respectively. Scan rate 1.0 V s^{-1}

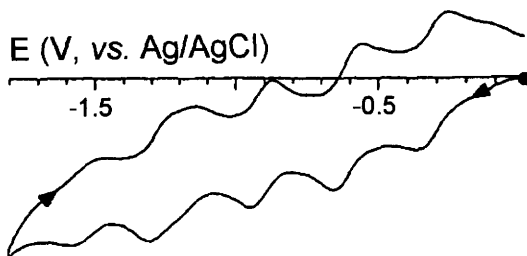


Figure 18 Cyclic voltammogram recorded at a platinum electrode in a 1,2-dichlorobenzene solution of C_{84} . Scan rate 0.2 V s^{-1}

As a last consideration on the ‘organic’ aspects of fullerenes, it must be recalled that they are poorly soluble in non-aqueous solvents. Details about their solubility can be found in the literature.²⁰

We turn our attention now to ‘inorganic’ aspects of fullerenes and, in particular, their complexes with metals.²¹ Two types of *metallafullerenes* exist:

- those in which a metal fragment is appended *outside* the spheroidal carbon cage, defined as *exohedral* metallafullerenes;
- those in which a metal(s) lies *inside* the spheroidal carbon cage, defined as *endohedral* metallafullerenes.

Crystal structures of a few fullerenes containing endohedral atoms have been recently solved (apart from the noble gas trapping $\text{Kr}@C_{60}$,^{22a} the metal atoms containing $\text{Sc}_3\text{N}@C_{78}$,^{22b} $\text{Sc}_3\text{N}@C_{80}$ and $\text{Sc}_2\text{ErN}@C_{80}$,^{22c} $\text{Y}@C_{82}$,^{22d} $\text{Sc}@C_{82}$,^{22e} $\text{Er}_2@C_{82}$,^{22f} $\text{Sc}_3@C_{82}$,^{22g} $\text{Sc}_2@C_{84}$,^{22h} $\text{Sc}_2\text{C}_2@C_{84}$,²²ⁱ)²³, but unfortunately their electrochemical behaviour is not known. Electrochemical information is also limited for those endohedral complexes which lack definitive structural characterization.

The first exohedral metallafullerene to be isolated and structurally characterized was the adduct $[(\eta^2\text{-}C_{60})\{(\kappa^2O,O)\text{-Os(O}_4)(4\text{-}tert\text{-butylpyridine)}\}]$, Figure 19.²⁴

In the C_{60} fragment all the carbon atoms are tricoordinated, except C1 and C2, which, being coordinated to an oxygen atom of the metal fragment, are tetracoordinated. As shown in Scheme 1, the sphere of carbon atoms, which has an approximate radius of 3.51 \AA , is composed of 20 six-membered rings fused with 12 five-membered rings with a repetition of the *pyracylene* building unit.

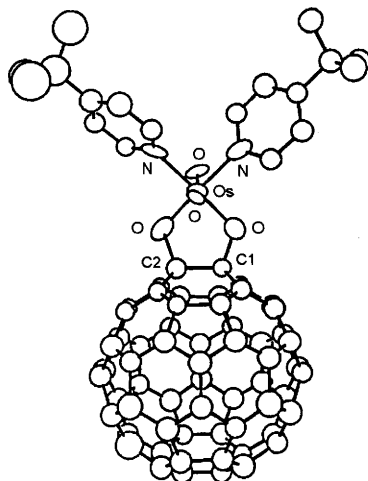
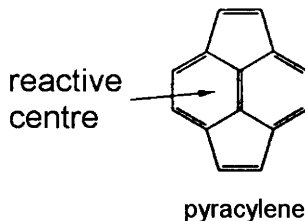


Figure 19 X-Ray structure of $[(\eta^2\text{-C}_60)\{(\kappa^2\text{O},\text{O})\text{-Os}(\text{O}_4)(4\text{-}tert\text{-butylpyridine)}\}]$. $\text{C}1\text{-C}2 = 1.62 \text{ \AA}$



Scheme 1

In fact, it is just the unsaturated central double bond of the pyracylene unit which commonly becomes the reactive site for coordination to metal fragments. This is the case not only for $[(\eta^2\text{-C}_60)\{(\kappa^2\text{O},\text{O})\text{-Os}(\text{O}_4)(4\text{-}tert\text{-butylpyridine)}\}]$, but for example also for $\text{C}_60[\text{Pt}(\text{PPh}_3)_2]^{25}$ and $[\text{Ir}(\text{CO})(\eta^2\text{-C}_60)\text{Cl}(\text{PPh}_3)_2]^{26}$. In both compounds the C1–C2 bond length ($\approx 1.50 \text{ \AA}$) is considerably longer than the value (1.38 \AA) that the 6:6 C=C bond should have in the absence of coordination (in the strictly related $[\text{Pd}(\eta^2\text{-C}_60)(\text{PPh}_3)_2]$ the C1–C2 distance is 1.45 \AA^{27}). At variance with $[(\eta^2\text{-C}_60)\{(\kappa^2\text{O},\text{O})\text{-Os}(\text{O}_4)(4\text{-}tert\text{-butylpyridine)}\}]$, in the latter cases the metal atom is directly linked to the fullerene unit.

The same unsaturation resulting from the fusion of two benzene rings is, furthermore, responsible for the coordination of several metal fragments to C_60 . At least in the solid state, this usually occurs by disposing the metal fragments symmetrically on opposite sides of the carbon sphere, as for example are the cases for example of $[\text{Ir}(\text{CO})(\eta^2\text{-C}_60)\text{Cl}(\text{PMe}_2\text{Ph})_2]_2^{28}$, $[\text{Ir}_2\text{Cl}_2(\eta^2\text{-C}_60)(1,5\text{-COD})_2]_2^{29}$ and $[\text{Pt}(\eta^2\text{-C}_60)(\text{PEt}_3)_2]_6^{30}$.

Metallocomplexes of functionalized fullerenes have been obtained, such as the mono- and di-epoxofullerenes $[\text{Ir}(\text{C}_{60}\text{O})(\text{CO})\text{Cl}(\text{AsPh}_3)_2]$ and $[\text{Ir}(\text{C}_{60}\text{O}_2)(\text{CO})\text{Cl}(\text{PPh}_3)_2]$.^{31,32}

Higher fullerenes are also able to coordinate one or more metal fragments, as is the case of the monoadducts $[\text{Ir}(\text{CO})(\eta^2\text{-C}_{70})\text{Cl}(\text{PPh}_3)_2]$, $[\text{Ir}(\text{CO})(\eta^2\text{-C}_{84})\text{Cl}(\text{PPh}_3)_2]$,^{33,34} and the diadduct $[(\eta^2\text{-C}_{70})\{\text{Ir}(\text{CO})\text{Cl}(\text{PMe}_2\text{Ph})_2\}_2]$.³⁵ Also in this case the coordination to the metal fragment occurs through the double bond of the pyracylene unit.

Let us turn our attention now to the electrochemical aspects of a few exohedral metallafullerenes.

As seen, fullerenes behave as unsaturated ligands. Hence it is expected that coordination to metal fragments might saturate (at least partially) their electron-affinity. Hence it is expected that the electron-withdrawing ability of fullerenes is lowered after complexation with respect to that in their free state.

Figure 20 shows the cyclic voltammogram exhibited by $[\text{Pt}(\eta^2\text{-C}_{60})(\text{PPh}_3)_2]$ (together with its molecular structure) in tetrahydrofuran solution, also in comparison with that of free C_{60} .³⁶

As expected, the sequential reductions of the metallafullerene (M1, M2, M3) are significantly shifted towards more negative values with respect to those of free C_{60} (F1, F2, F3). The appearance of peaks due to the C_{60} ligand itself in the voltammetric profile of the metal complex, which is particularly evident in the backscans, probably arises from the instability of the electrogenerated higher charged anions ($[\text{Pt}(\eta^2\text{-C}_{60})(\text{PPh}_3)_2]^{2-}$ and $[\text{Pt}(\eta^2\text{-C}_{60})(\text{PPh}_3)_2]^{3-}$, respectively) which tend to release the ligand. Only $[\text{Pt}(\eta^2\text{-C}_{60})(\text{PPh}_3)_2]^-$ seems to be quite stable.

Substitution of triphenylphosphine with triethylphosphine does not substantially modify the values of the redox potentials for the sequential

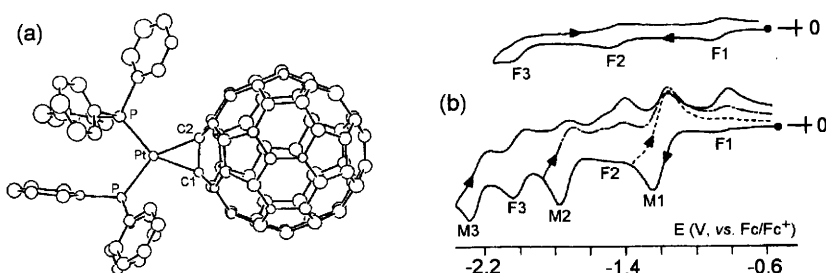


Figure 20 (a) X-Ray structure of $[\text{Pt}(\eta^2\text{-C}_{60})(\text{PPh}_3)_2]$. Bond lengths: $\text{C}1\text{-C}2 = 1.50 \text{ \AA}$; $\text{Pt}-\text{C}1 \approx \text{Pt}-\text{C}2 = 2.13 \text{ \AA}$. (b) Cyclic voltammograms recorded at a platinum electrode in THF solutions of $[\text{Pt}(\eta^2\text{-C}_{60})(\text{PPh}_3)_2]$ (bottom); (b) C_{60} (top). Scan rate 0.2 V s^{-1} .

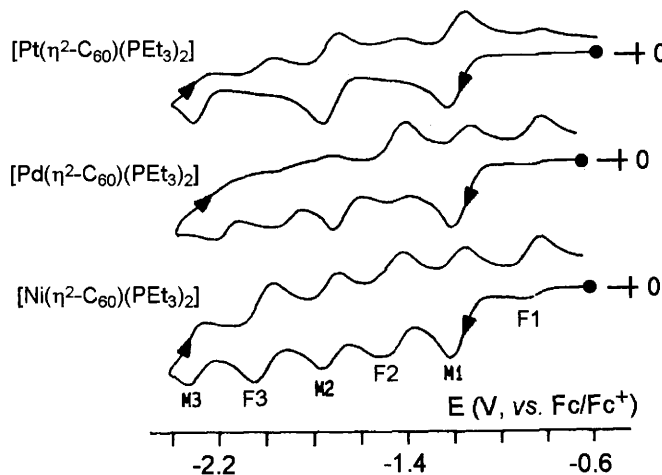


Figure 21 Cyclic voltammograms recorded at a platinum electrode in THF solutions of $[Ni(\eta^2\text{-}C_60)(PEt_3)_2]$, $[Pd(\eta^2\text{-}C_60)(PEt_3)_2]$, and $[Pt(\eta^2\text{-}C_60)(PEt_3)_2]$, respectively. Scan rate 0.2 V s^{-1} .

reduction processes, thus suggesting that the LUMO of the metal complex is essentially contributed by the C_{60} ligand. This is further supported by the observation that, as illustrated in Figure 21, substitution of Pt for Pd or Ni in $[Pd(\eta^2\text{-}C_60)(PEt_3)_2]$ and $[Ni(\eta^2\text{-}C_60)(PEt_3)_2]$, respectively, does not induce significant variations in the reduction potentials (even if the kinetic stability of the electrogenerated anions is considerably affected by the change of metal).³⁶

Table 3 compares the redox potentials for the reduction processes of C_{60} with those of the corresponding redox changes for the above mentioned metal complexes.

As deduced, the complexation of C_{60} with the different metal fragments causes a shift towards more negative potential values by about $0.3 \div 0.4\text{ V}$ with respect to free C_{60} .

Table 3 Formal electrode potentials (V , vs. SCE) for the reduction processes of complexes $[M(\eta^2\text{-}C_60)(PR_3)_2]$, in THF solution

Complex	$E_{0/-}^\circ$	$E_{-2/-}^\circ$	$E_{2-/3-}^\circ$
$[Pt(\eta^2\text{-}C_60)(PPh_3)_2]$	-0.66	-1.20	-1.68
$[Pt(\eta^2\text{-}C_60)(PEt_3)_2]$	-0.65	-1.18	-1.72
$[Pd(\eta^2\text{-}C_60)(PEt_3)_2]$	-0.63	-1.14	-1.68 ^a
$[Ni(\eta^2\text{-}C_60)(PEt_3)_2]$	-0.65	-1.19	-1.77
C_{60}	-0.31	-0.89	-1.45

^aPeak potential value for irreversible processes.

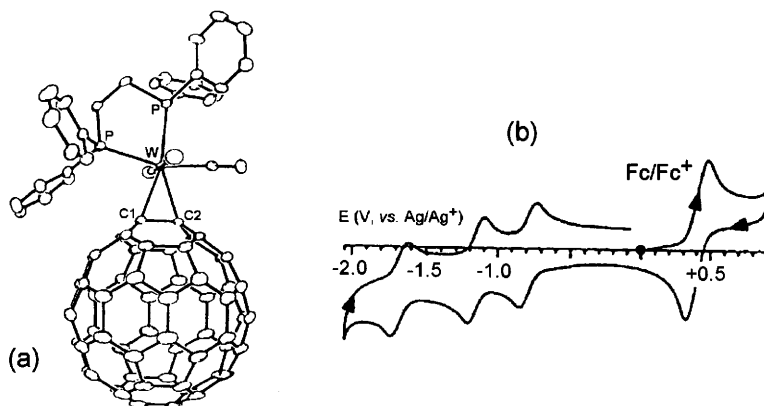


Figure 22 (a) X-Ray structure of $[W(\eta^2\text{-C}_60)(\text{CO})_3(\text{dppe})]$. Bond lengths: $C1-C2 = 1.50 \text{ \AA}$, $W-C1 \approx W-C2 = 2.29 \text{ \AA}$. (b) Cyclic voltammogram recorded at a glassy carbon electrode in a MeCN -toluene solution of $[W(\eta^2\text{-C}_60)(\text{CO})_3(\text{dppe})]$. Ferrocene added as internal standard. Scan rate 0.1 V s^{-1}

Figure 22 shows the molecular structure of $[W(\eta^2\text{-C}_60)(\text{CO})_3(\text{dppe})]$ ($\text{dppe} = 1,2\text{-diphenylphosphinoethane}$) together with its cyclic voltammetric response.³⁷

The three fullerene-centred reductions display features of chemical reversibility and are localized at potential values more negative by about 0.2 V than those of free C₆₀, Table 4. This proves that also in this case the metal fragment pushes electron density towards the fullerene.

Similar behaviour is displayed by complexes $[\text{M}(\eta^2\text{-C}_60)(\text{CO})_2(\text{phen})(\text{dbm})]$ ($\text{M} = \text{Mo}$, W : phen = 1,10-phenanthroline; dbm = dibutylmaleate).^{38a,b} Figure 23 shows the voltammetric picture exhibited by the tungsten complex.

It exhibits three sequential one-electron reductions possessing features of chemical and electrochemical reversibility, which occur at potential values more negative by about 0.15 V with respect to free C₆₀, Table 5.

As illustrated in Figure 24, the present complexes also exhibit a fourth irreversible two-electron reduction centred on the outer metal fragment, which precedes the fourth reduction of the coordinated C₆₀.

Table 4 Formal electrode potentials (V, vs. Fc/Fc^+) for the reduction processes of $[W(\eta^2\text{-C}_60)(\text{CO})_3(\text{dppe})]$ in MeCN -toluene solution

Complex	$E_{0/-}^\circ$	$E_{-1/-2}^\circ$	$E_{-2/-3}^\circ$
$[\text{W}(\eta^2\text{-C}_60)(\text{CO})_3(\text{dppe})]$	-1.19	-1.56	-2.08
C ₆₀	-0.98	-1.37	-1.87

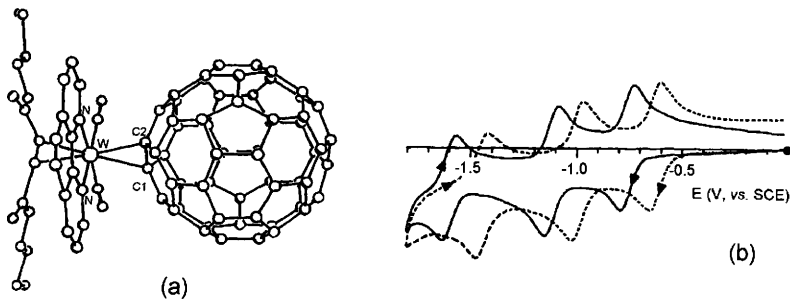
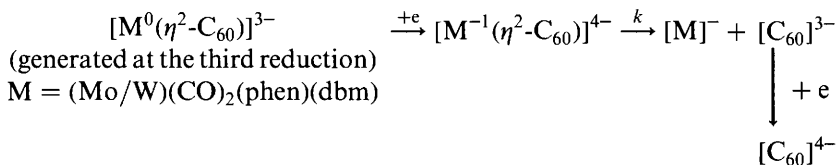


Figure 23 (a) X-Ray structure of $[W(\eta^2\text{-C}_{60})(\text{CO})_2(\text{phen})](\text{dbm})$. Bond lengths: $\text{C}_1\text{-C}_2 = 1.43 \text{ \AA}$; $\text{W-C}_1 \approx \text{W-C}_2 = 2.30 \text{ \AA}$. (b) Cyclic voltammograms recorded at a platinum electrode in CH_2Cl_2 solutions of $[W(\eta^2\text{-C}_{60})(\text{CO})_2(\text{phen})](\text{dbm})$ (—) and C_{60} (---), respectively. $T = -10^\circ \text{C}$. Scan rate 0.2 Vs^{-1}

The appearance of free fulleride reoxidations in the backscan (starred peaks) is accounted for by the following ECE mechanism:



Interestingly the related C_{70} derivative $[\text{W}(\eta^2\text{-C}_{70})(\text{CO})_2(\text{phen})](\text{dbm})$ displays a rather different electrochemical behaviour.^{38c} In fact, as illustrated in Figure 25, at variance with $[\text{W}(\eta^2\text{-C}_{60})(\text{CO})_2(\text{phen})](\text{dbm})$, the third reduction process of the C_{70} complex looks like an almost overlapped two-electron step.

Table 5 Formal electrode potentials (V , vs. SCE) and peak-to-peak separation (mV) for the fullerene-centred reductions of $[\text{M}(\text{C}_{60}/\text{C}_{70})(\text{CO})_2(\text{phen})](\text{dbm})$ in CH_2Cl_2 solution. $T = -10^\circ \text{C}$

Complex	$E_{0/-}^{\circ/}$	ΔE_p	$E_{-2/-}^{\circ/}$	ΔE_p	$E_{2/-3/-}^{\circ/}$	ΔE_p	$E_{3/-4/-}^{\circ/}$	ΔE_p
$[\text{W}(\eta^2\text{-C}_{60})(\text{CO})_2(\text{phen})](\text{dbm})$	-0.76	62	-1.17	60	-1.60	62	-	-
$[\text{Mo}(\eta^2\text{-C}_{60})(\text{CO})_2(\text{phen})](\text{dbm})$	-0.77	58	-1.13	58	-1.60	58	-	-
$[\text{Mo}(\eta^2\text{-C}_{70})(\text{CO})_2(\text{phen})](\text{dbm})$	-0.71	60	-1.09	62	-1.51 ^a	b	-1.51 ^a	b
C_{60}	-0.63	59	-1.00	60	-1.45	64	-1.9 ^c	-
C_{70}	-0.61	59	-0.98	60	-1.41	64	-1.75	62

^aAverage value for an overlapping two-electron process.

^bSee text.

^cPeak-potential value.

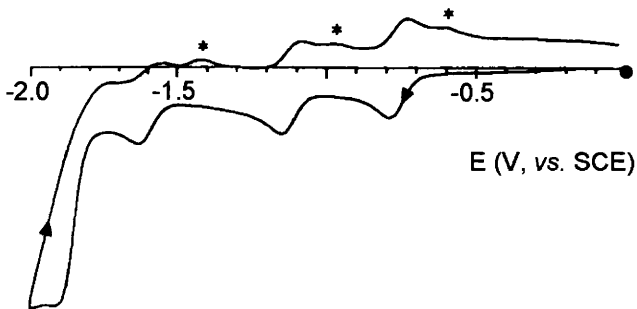


Figure 24 Cyclic voltammogram of $[W(\eta^2\text{-}C_{60})(\text{CO})_2(\text{phen})(\text{dbm})]$ recorded under the same experimental conditions of Figure 23, but extended at more negative potential values

Based on its reversibility (as well as on the fact that the $\text{Mo}(\text{CO})_2(\text{phen})(\text{dbm})$ fragment in the C_{60} complex or in the precursor $[\text{Mo}(\text{CO})_2(\text{phen})(\text{dbm})_2]$ reduces at potentials notably more negative), such a step is attributed to the almost concomitant third and fourth reductions of

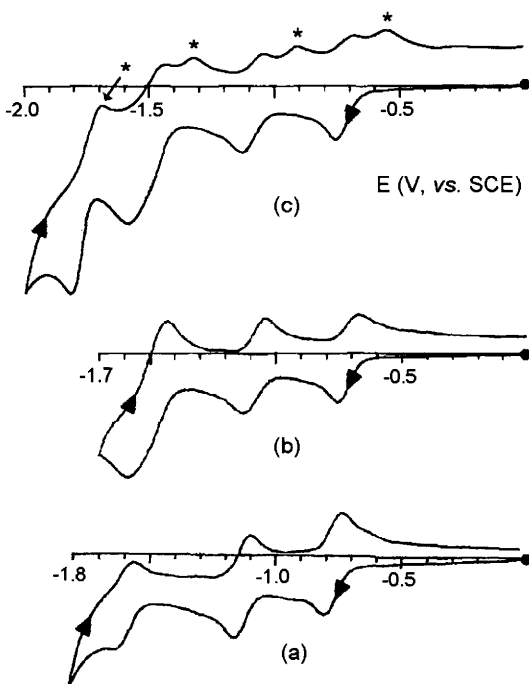
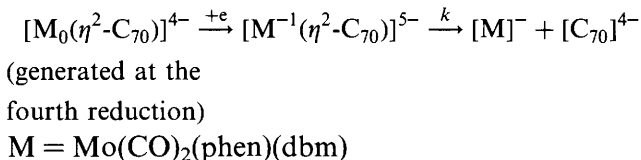


Figure 25 Cyclic voltammograms recorded at a platinum electrode in CH_2Cl_2 solutions of: (a) $[\text{Mo}(\eta^2\text{-}C_{60})(\text{CO})_2(\text{phen})(\text{dbm})]$; (b,c) $[\text{Mo}(\eta^2\text{-}C_{70})(\text{CO})_2(\text{phen})(\text{dbm})]$. $T = -10^\circ\text{C}$. Scan rate 0.2 V s^{-1}

the C₇₀ moiety. In addition, it can be seen that the fourth (metal-centred) reduction triggers decomplexation of the fulleride anions (starred peaks) as a consequence of the simple EC mechanism:



Finally, Table 5 shows that the shift of the reduction processes of the metallaccomplex towards more negative values is by 0.10 V with respect to free C₇₀. This suggests that the Mo(CO)₂(phen)(dbm) fragment saturates the coordinated C₇₀-double bond at an extent lower than C₆₀.

Figure 26 shows the molecular structure of the adduct of C₆₀ with (η^5 -bicyclo[3.2.0]hepta-1,3-dienyl)(η^4 -tetraphenylcyclobutadiene)-Co(I).³⁹ In it the metal fragment is not directly bound to C₆₀.

As shown in Figure 27 and deduced from Table 6, it also displays three reduction processes at potential values more negative by about 0.2 V with respect to free C₆₀.³⁹

Figure 28 shows the molecular structure of [Fe₂(μ -S)₂($\eta^2\text{-C}_{60}$)(CO)₆], in which again there is no direct bond between the metal(s) and the fullerene ligand.⁴⁰

At variance with the preceding derivatives, the complex displays in 1,2-dichlorobenzene solution four reduction processes (with features of chemical reversibility) at potentials slightly less negative than those of free fullerene, Table 7.⁴⁰ This indicates that, contrary to the preceding cases, the Fe₂S₂(CO)₆ fragment withdraws electron density from the coordinated fullerene.

Therefore we can conclude that the shift of the reduction potentials of the fullerene-centred reductions in metallafullerenes, with respect to free

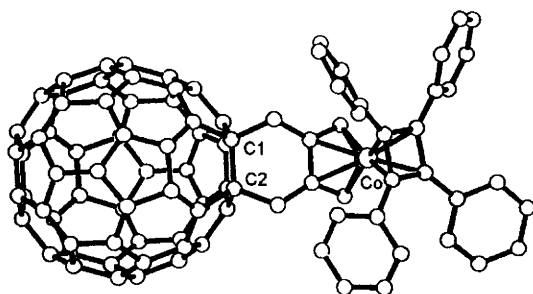


Figure 26 X-Ray structure of [Co(η^5 -bicyclo[3.2.0]hepta-1,3-dienyl)(η^4 -tetraphenylcyclobutadiene)($\eta^2\text{-C}_{60}$)]. C1–C2 = 1.59 Å

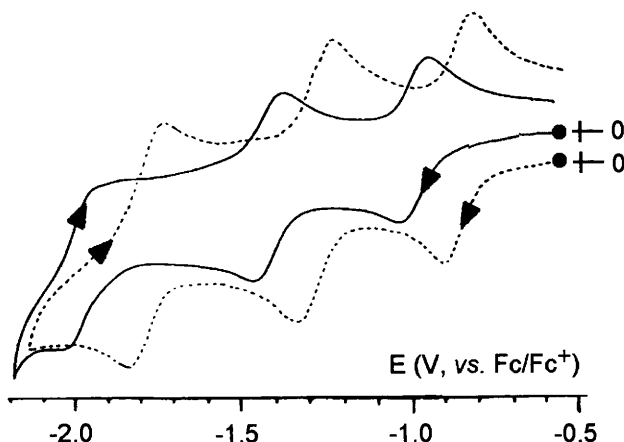


Figure 27 Comparison between the cyclic voltammogram of C_{60} (---) and that of $[Co(\eta^5\text{-bicyclo}[3.2.0]\text{hepta-1,3-dienyl})(\eta^4\text{-tetraphenyl-cyclobutadiene})(\eta^2\text{-}C_{60})]$ (—). PhCN solution

Table 6 Formal electrode potentials (V , vs. Fc/Fc^+) for the reduction processes of $[Co(\eta^5\text{-bicyclo}[3.2.0]\text{hepta-1,3-dienyl})(\eta^4\text{-tetraphenyl-cyclobutadiene})(\eta^2\text{-}C_{60})]$ in PhCN solution

Complex	$E_{0/-}^\circ$	$E_{-/2-}^\circ$	$E_{2-/3-}^\circ$
Co(I) adduct	-1.06	-1.48	-2.04
C_{60}	-0.93	-1.35	-1.84

fullerene, is governed by two not easily separable effects:

- the extent of saturation of the η^2 -coordinated carbon/carbon double-bond, which makes the reductions more difficult;
- the inductive effects exerted by the metal fragment(s), which can favour or disfavour the reduction processes.

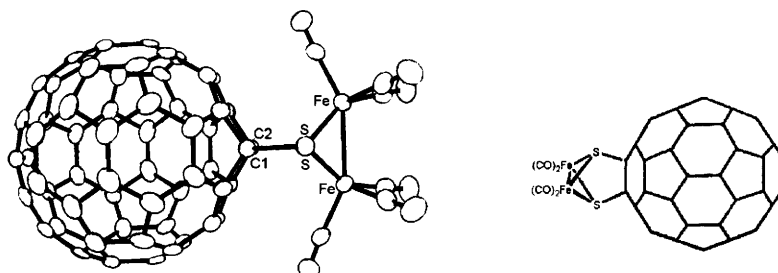


Figure 28 X-Ray structure of $[Fe_2(\mu\text{-}S)_2(\eta^2\text{-}C_{60})(CO)_6]$. $C1-C2 = 1.54 \text{ \AA}$

Table 7 Formal electrode potentials (V , vs. Ag/AgCl) for the reduction processes of $[\text{Fe}_2(\mu\text{-S})_2(\eta^2\text{-C}_{60})(\text{CO})_6]$ in 1,2-dichlorobenzene solution

Complex	$E_{0/-}^{\circ'}$	$E_{-/2-}^{\circ'}$	$E_{2-/3-}^{\circ'}$	$E_{3-/4-}^{\circ'}$
$[\text{Fe}_2(\mu\text{-S})_2(\eta^2\text{-C}_{60})(\text{CO})_6]$	-0.45	-0.83	-1.28	-1.76
C_{60}	-0.47	-0.85	-1.31	-1.78

The two effects can add or compensate each other. In this way, the measurement of the shift in redox potentials through electrochemical techniques offers a simple, but powerful tool to evaluate the overall electronic factors governing the interaction of the metal fragments with the fullerene ligands.

2.1 Intramolecular Electronic Communication in Metallobisfullerenes

As mentioned above, bisfullerenes in which the two fullerene subunits are directly linked each other have been characterized; namely, C_{120} ,⁴¹ C_{121} ,⁴² C_{120}O ,⁴³ C_{122}H_4 ⁴⁴ and the $\text{C}_{60}\text{-C}_{70}$ cross-dimer C_{130} .⁴⁵ Cyclic, differential pulse or square wave voltammetric techniques reveal that the two fullerene moieties are, at best, weakly communicating, in that the $0/-2/-3-$ sequential reductions of each subunit are essentially overlapped, the separation between reduction pairs being, at best, less than 100 mV. On the other hand, bisfullerenes in which the two C_{60} units are separated by unsaturated carbon chains do not manifest electronic interactions.^{46–48}

In this connection, quite interesting is the case of the complex $[\text{Rh}_6(\text{CO})_5(\text{dppm})(\text{CNR})(\mu_3\text{-}\eta^2,\eta^2,\eta^2\text{-C}_{60})_2]$ (dppm = diphenylphosphinomethane; R = $\text{CH}_2\text{C}_6\text{H}_5$), in which an octahedral Rh_6 cluster is interposed between two fullerene units, Figure 29.⁴⁹

One cyclohexatriene-like ring of each C_{60} unit is face-capped to one triangular face of the interposed octahedral Rh_6 cluster. As illustrated in Figure 30, the complex affords in chlorobenzene solution six, well separated, consecutive reductions, which, based on the fact that the central metal cluster is inactive in the potential window of interest, are assigned to the stepwise and pairwise three-electron additions to each C_{60} subunit.⁴⁹ Stated that such reduction processes occur at potential values more negative by more than 0.2 V with respect to free fullerene, it is noted that the separation inside the first reduction couple, which corresponds to the electron transfer sequence $([\text{C}_{60}][\text{C}_{60}])/([\text{C}_{60}][\text{C}_{60}]^-)/([\text{C}_{60}]^-\text{[C}_{60}]^-)$, is 0.19 V; the second couple $([\text{C}_{60}]^-\text{[C}_{60}]^-)/([\text{C}_{60}]^-\text{[C}_{60}]^{2-})/([\text{C}_{60}]^{2-}\text{[C}_{60}]^{2-})$ is separated by 0.24 V; the third couple $([\text{C}_{60}]^{2-}\text{[C}_{60}]^{2-})/([\text{C}_{60}]^{2-}\text{[C}_{60}]^{3-})/([\text{C}_{60}]^{3-}\text{[C}_{60}]^{3-})$ is separated by 0.29 V. Such progressive increase of the separation is assigned to increasing Coulombic repulsions.

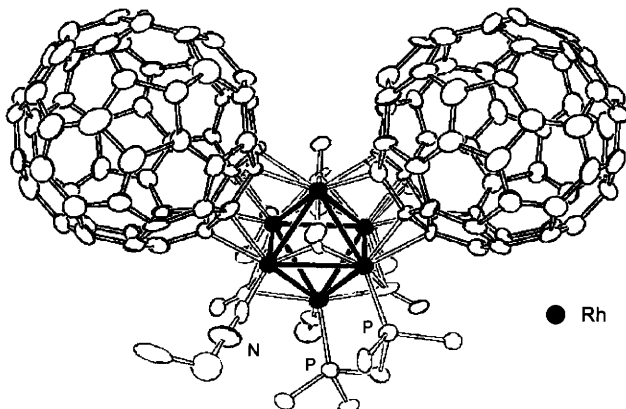


Figure 29 X-Ray structure of $[Rh_6(CO)_5(dppm)(CNR)(\eta^2-C_{60})_2]$

It is evident that the two fullerenes are strongly electronically communicating in spite of the interposed presence of the Rh_6 cluster. A partial contribution to such a strong interaction could, however, arise also from the slight unequivalence of the two C_{60} environments. In fact, one fullerene is linked to a Rh_3 triangle coordinated to a carbon atom (of one isocyanide ligand) and a phosphorus atom (of one diphosphine), respectively, whereas the other fullerene is linked to a Rh_3 triangle which coordinates two phosphorus atoms (of the two diphosphines).

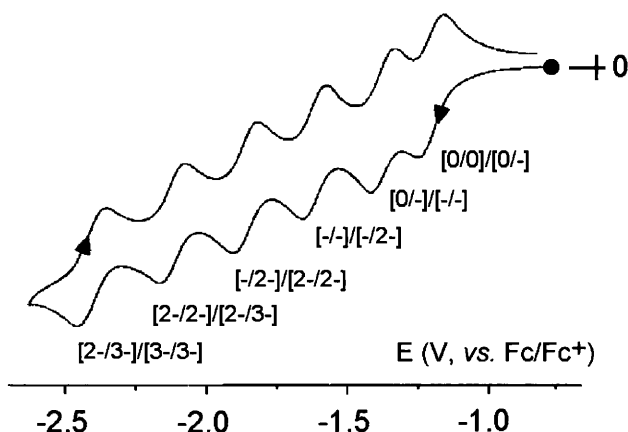
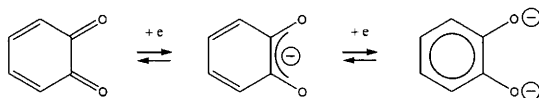


Figure 30 Cyclic voltammogram recorded at a platinum electrode in a chlorobenzene solution of $[Rh_6(CO)_5(dppm)(CNR)(\eta^2-C_{60})_2]$. Scan rate 0.01 V s^{-1}

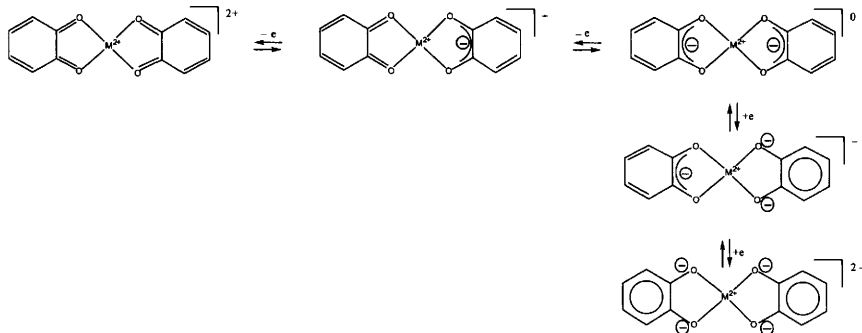
3 DIOXOLENES (AND THEIR IMINO ANALOGUES) AND DITHIOLENES AS LIGANDS IN METAL COMPLEXES

Transition metal complexes with *o*-dioxolene ligands constitute one of the most intriguing classes of complexes as far as their electrochemical behaviour is concerned, in that, as already mentioned in Chapter 5, Section 1, such ligands are able to shuttle through the oxidation states *o*-benzoquinone/*o*-benzosemiquinone/catecholate illustrated in Scheme 2⁵⁰ (a process carried out in nature by the dicopper(II)-based enzyme *catechol oxidase* through a single two-electron step; see Chapter 9, Section 1.2).



Scheme 2

This means that, for instance, assuming that the metal centre does not change its oxidation state, homoleptic bisquinoinal metal(II)-complexes, which are one of the most common classes, should theoretically exhibit the sequence illustrated in Scheme 3.



Scheme 3

Obviously, the different steps will appear more or less separated or even overlapping depending upon the degree of communication between the quinoidal subunits allowed by the central metal ion.

Indeed a limited number of monomeric $[M^{II}(\text{dioxolene})_2]^{n-}$ complexes have been structurally characterized ($M = \text{Ni}$; dioxolene = 3, 6-di-*tert*-butyl-1,2-benzosemiquinone, $n = 0$;^{51a} dioxolene = *N,N'*-bis(2, 3-dihydroxybenzoyl)-1,7-diazahexane, $n = 2$;^{51b} dioxolene = 1,2-catecholate, $n = 2$;^{51c} $M = \text{Pd}, \text{Pt}$; dioxolene = 3,5-di-*tert*-butyl-1,2-benzosemiquinone, $n = 0$ ⁵²), likely due to the fact that Ni(II) in the presence of

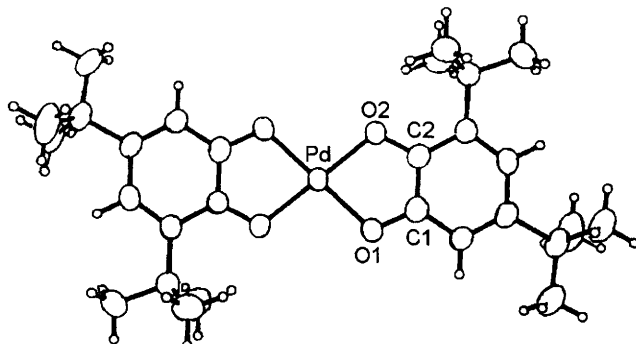


Figure 31 X-Ray structure of $[Pd(3,5\text{-di-}Bu'\text{sq})_2]$. $Pd\text{-}O = 1.98 \text{ \AA}$; $C\text{-}O = 1.30 \text{ \AA}$; $C1\text{-}C2 = 1.43 \text{ \AA}$

oxygen-containing ligands tends to be octahedrally coordinated. Thus in the absence of steric protection, they tend to form oligomers.⁵³ As illustrated in Figure 31, which refers to the semiquinonate complex $[Pd^{II}(3,5\text{-di-}Bu'\text{sq})_2]$,⁵² the cited complexes show a square planar geometry.

It is commonly accepted that the C–O distance of the quinoidal ligand is an important parameter suggestive of the charge of the ligand in metal-dioxolene complexes, namely:

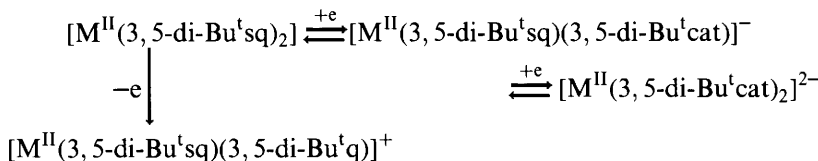
- quinone form: $C\text{-}O \approx 1.23 \text{ \AA}$;
- semiquinone form: $C\text{-}O \approx 1.29 \text{ \AA}$;
- catecholate form: $C\text{-}O \approx 1.35 \text{ \AA}$.

The actual C–O distance (1.30 \AA) does support the semiquinonic nature of the complex.

The present Pd(II) complex, as well as the isostructural Pt(II) analogue, in CH_2Cl_2 solution display two reversible reductions and an irreversible oxidation (see Table 8), which are assigned to the sequence:⁵²

Table 8 Formal electrode potentials (V , vs. Fc/Fc^+) for the redox changes exhibited by complexes $[M(3,5\text{-di-}Bu'\text{sq})_2]$ ($M = Pd, Pt$), in CH_2Cl_2 solution

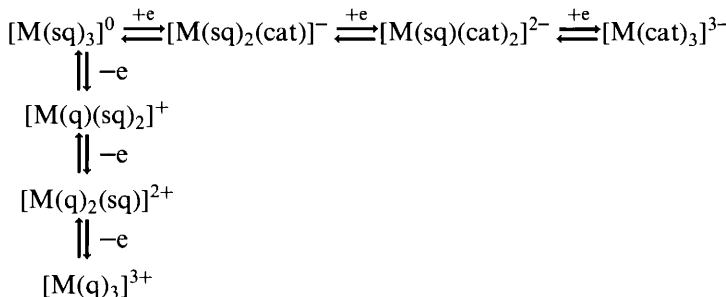
M	$E_{p+/-}$	$E_{0/-}^{o'}$	$E_{-/-2-}^{o'}$
Pd	+ 0.56	-0.24	-0.86
Pt	+ 0.69	-0.06	-0.80



Let us pass now to the wider class of homoleptic (tris)quinoidal complexes (already mentioned in Chapter 5, Section 1, speaking about the redox couple $[V(\text{cat})_3]^{2-/3-}$) starting with the neutral complex $[\text{Cr}\{\text{O}_2\text{C}_6\text{H}_2(3,5\text{-Bu}^t)_2\}_3]$, the essentially octahedral structure of which is shown in Figure 32.⁵⁴

Given the redox non-innocent character of the quinoidal ligand, the present diamagnetic complex can in principle be formulated either as $\text{Cr}(0)\text{-}(\text{quinone})_3$, or as $\text{Cr(VI)}\text{-}(\text{catechol})_3$, or as $\text{Cr(III)}\text{-}(\text{semiquinone})_3$. As a matter of fact, based also on the C–O distance, it has been preferentially assigned as $[\text{Cr}^{III}(3,5\text{-di-Bu}^t\text{sq})_3]$.⁵⁴

In agreement with the fact that tris-quinoidal-M(III) complexes, under the above-cited simplification that the oxidation state of the metal does not change, can undergo the following seven-membered redox sequence:



It exhibits in CH_2Cl_2 solution three sequential one-electron reductions and two sequential one-electron oxidations, all these processes exhibiting features of chemical reversibility, Figure 33.⁵⁵

A further educational example is offered by the neutral semiquinonate complex $[\text{Cr}(\text{O}_2\text{C}_6\text{Cl}_4)_3]$ (or $[\text{Cr}^{III}(\text{Cl}_4\text{sq})_3]$), the octahedral geometry of which is illustrated in Figure 34.⁵⁶

As illustrated in Figure 35, in CH_2Cl_2 solution it exhibits three separate one-electron reductions, which would lead to the corresponding anions $[\text{Cr}^{III}(\text{Cl}_4\text{sq})_2(\text{Cl}_4\text{cat})]^-$, $[\text{Cr}^{III}(\text{Cl}_4\text{sq})(\text{Cl}_4\text{cat})_2]^{2-}$ and $[\text{Cr}^{III}(\text{Cl}_4\text{cat})_3]^{3-}$, respectively.⁵⁵

As a matter of fact the mixed-valent mono- and di-anion congeners have been isolated and structurally characterized.⁵⁷

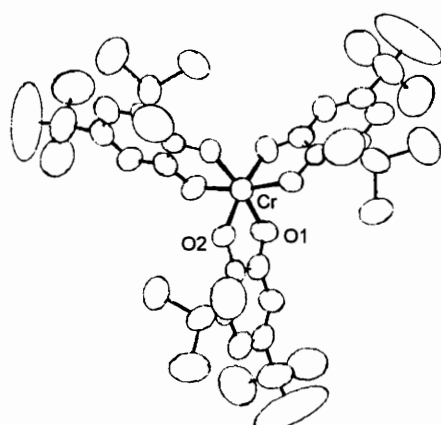


Figure 32 X-Ray structure of $[Cr\{O_2C_6H_2(Bu')_2\}_3]^0$. Average Cr–O distance = 1.93 Å; average C–O distance = 1.28 Å; O1–Cr–O2 angle = 81.4°

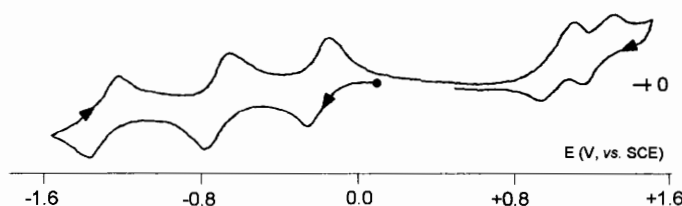


Figure 33 Cyclic voltammogram recorded at a platinum electrode in a MeCN solution of $[Cr^{III}(3,5\text{-di-}Bu'\text{sq})_3]$. Scan rate 0.05 V s⁻¹

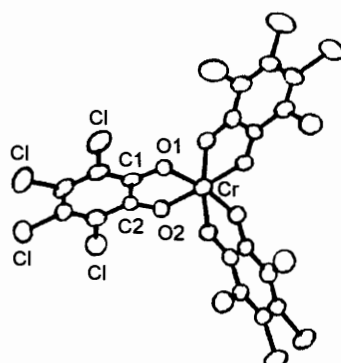


Figure 34 X-Ray structure of $[Cr^{III}(Cl_4sq)_3]$

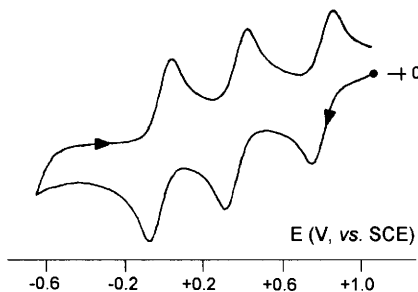


Figure 35 Cyclic voltammogram recorded at a platinum electrode in a CH_2Cl_2 solution of $[\text{Cr}^{\text{III}}(\text{Cl}_4\text{sq})_3]$. Scan rate 0.05 V s^{-1}

To account for the gradual reduction of each quinoidal ligand following the one-electron additions it is useful to look at the bond lengths collected in Table 9, that outline the structural features of the different I, II, III quinoidal $\text{O}_2\text{C}_6\text{Cl}_4$ subunits.

As seen, the variations in bond lengths are minimal, in particular as far as the Cr–O and C–C distances are concerned. From a speculative viewpoint, a significant variation (elongation by about 0.2 \AA) can be found in the C–O distance on passing from the neutral to the anionic species. This result not only supports the ligand-centred nature of the electron additions, but the homogeneity in the distances inside the three reduced ligands suggest a delocalization of the added electrons over the three centres (in agreement with the fact that separate redox changes prelude charge delocalization; see Chapter 4, Section 1.3). Further, the invariance of the Cr–O distances seems to rule out eventual changes in the oxidation state of the central metal.

Table 9 Averaged bond lengths (\AA) in the series $[\text{Cr}(\text{O}_2\text{C}_6\text{Cl}_4)_3]^0 / [\text{Cr}(\text{O}_2\text{C}_6\text{Cl}_4)_3]^- / [\text{Cr}(\text{O}_2\text{C}_6\text{Cl}_4)_3]^{2-}$

Complex	Subunit	Cr–O	C–O	C–C
$[\text{Cr}(\text{O}_2\text{C}_6\text{Cl}_4)_3]^0$	I	1.95	1.28	1.40
	II	1.95	1.27	1.40
	III	1.95	1.29	1.41
$[\text{Cr}(\text{O}_2\text{C}_6\text{Cl}_4)_3]^-$	I	1.93	1.31	1.39
	II	1.94	1.30	1.40
	III	1.96	1.29	1.40
$[\text{Cr}(\text{O}_2\text{C}_6\text{Cl}_4)_3]^{2-}$	I	1.95	1.31	1.39
	II	1.96	1.29	1.30
	III	1.96	1.30	1.40

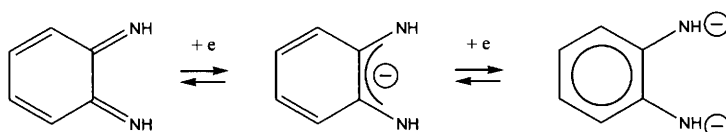
To conclude this aspect we can look at the related manganese dianion $[\text{Mn}(\text{O}_2\text{C}_6\text{H}_2(\text{Bu}^t)_2)_3]^{2-}$, which, once again, can in principle be formulated either as $[\text{Mn}^{\text{IV}}(\text{catechol})_3]^{2-}$ or alternatively as $[\text{Mn}^{\text{III}}(\text{semi-quinone})(\text{catechol})_2]^{2-}$. As the complex is EPR active (which, as mentioned in Chapter 5, Section 3, rules out a Mn(III) state) and has a magnetic moment of $3.95 \mu_{\text{B}}$, one can deduce that it is a Mn(IV) ($d^3-t_{2g}^3$) tris-catecholate complex. The Mn–O bond lengths (about 1.90 \AA) of the octahedral complex^{58a} also favour a Mn(IV) assignment, as the corresponding distances for a Mn(III) complex are generally slightly longer. On the other hand, the C–O distance agrees with a catecholate form of the dioxolene ligands.

In agreement with its catecholate nature, the complex does not display any predisposition to undergo reduction processes^{58a} (even if an irreversible metal-centred $[\text{Mn}^{\text{IV}}(3,5\text{-di-Bu}^t\text{cat})_3]^{2-}/[\text{Mn}^{\text{III}}(3,5\text{-di-Bu}^t\text{cat})_3]^-$ reduction has been reported^{58b}).

In confirmation, however, of the delicate electronic effects present in these complexes, the two-electron oxidized mixed-valent isomeric complex $[\text{Mn}^{\text{IV}}(3,6\text{-di-Bu}^t\text{cat})(3,6\text{-di-Bu}^t\text{sq})_2]$ has been isolated and structurally characterized.⁵⁹

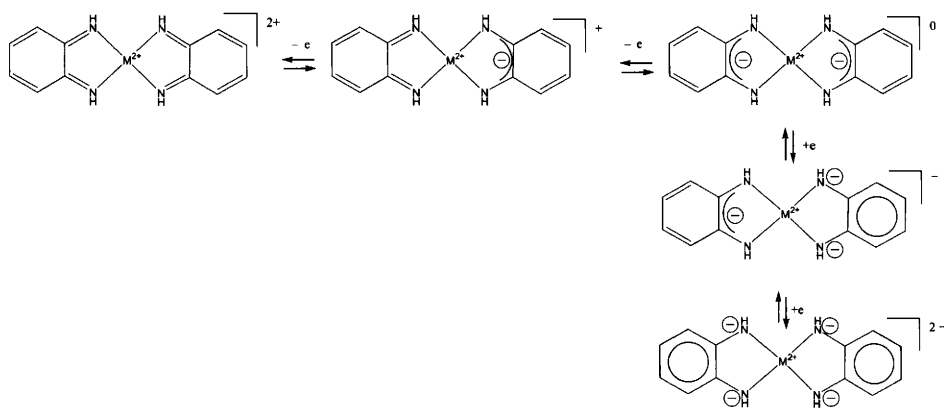
We finally point out that heteroleptic-dioxolene complexes with different redox non-innocent ligands can exhibit even further difficulty assignable redox changes.⁶⁰

Let us now illustrate some significant examples of the redox propensity of related (but less widely studied⁶¹) *quinone diimines*. As happens for 1,2-dioxolenes, such ligands also exhibit the reversible electron transfer sequence *o-benzoquinone diimine/o-benzosemiquinone diimine monoanion/o-phenylenediamine dianion* illustrated in Scheme 4.



Scheme 4

The high redox aptitude of the neutral bis-complexes $[\text{M}^{\text{II}}\{o\text{-C}_6\text{H}_4(\text{NH})_2\}_2$ ($\text{M} = \text{Co, Ni, Pd, Pt}$) is long known.⁶² Also in this case, under the assumption of the invariance of the oxidation state of the metal, such derivatives would display the redox path illustrated in Scheme 5.



Scheme 5

Accordingly, as illustrated in Figure 36 for $[\text{Pd}\{o\text{-C}_6\text{H}_4(\text{NH})_2\}_2]$, these complexes display the step-by-step reversible sequence from the dication to the dianion.⁶³

The neutral Ni^{63} and Co^{64} derivatives possess the square-planar geometry illustrated in Figure 37 for $[\text{Ni}\{o\text{-C}_6\text{H}_4(\text{NH})_2\}_2]$, which obviously corresponds to the *o*-benzosemiquinone diimine form $[\text{Ni}(\text{dsq})_2]$.

To the best of our knowledge no redox members of the above discussed series have been structurally characterized.

As in the case of *o*-dioxolenes, the diimine derivatives also form tris-complexes. Figure 38 for instance shows the molecular structure of the benzoquinone diimino dication $[\text{Os}^{\text{II}}(\text{bqdi})_3]^{2+}$.^{50c}

Such dication displays in dmso solution three separate reversible one-electron reductions ($E_{2+/+}^{\circ'} = -0.24 \text{ V vs. Fc/Fc}^+$; $E_{+/0}^{\circ'} = -0.67 \text{ V}$, $E_{0/-}^{\circ'}$

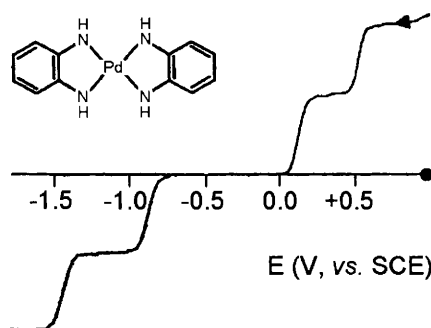


Figure 36 Polarographic profile of $[\text{Pd}\{C_6\text{H}_4(\text{NH})_2\}_2]$ in dmso solution

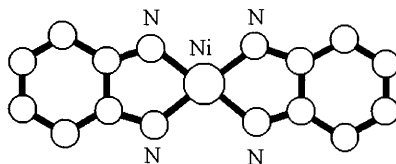


Figure 37 *X-Ray structure of $[Ni(dsq)_2]$. Average bond lengths: $Ni-N = 1.83 \text{ \AA}$; $C-N = 1.37 \text{ \AA}$; $C-C = 1.40 \text{ \AA}$*

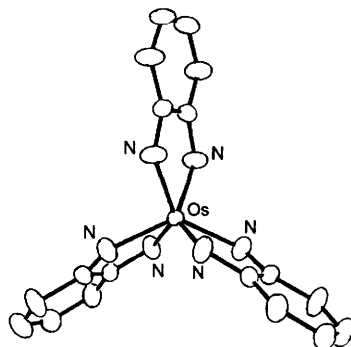


Figure 38 *X-Ray structure of $[Os(bqdi)_3]^{2+}$ ($[ClO_4]^-$ counteranion). Average bond lengths: $Os-N = 1.99 \text{ \AA}$; $C-N = 1.33 \text{ \AA}$; $C-C = 1.39 \text{ \AA}$*

$= -1.78 \text{ V}$), which have been assigned to the gradual bqdi/dsq reduction of each ligand.^{50c}

Among the other structurally characterized tris-complexes ($[Fe^{II}(bqdi)_3]^{2+}$,⁶⁴ $[Ru^{III}(bqdi)_2(opda)]^{2+}$ ⁶⁵) of known electrochemical behaviour,⁶⁶ the only case we know in which structural data are available for redox couples is concerned with $[Re\{o-C_6H_4(NH)_2\}_3]^+$ / $[Re\{o-C_6H_4(NH)_2\}_3]$.⁶⁷ Figure 39 shows the trigonal prismatic geometry of the monocation.

The corresponding neutral congener possesses a substantially similar geometry. Table 10 compiles the most significant bond lengths of the redox couple.

As seen, there is no really significant variation on the bonding distances. One could speculate that on passing from the monocation to the neutral derivative the averaged C–N distance increases from 1.34 Å to 1.36 Å, the C–C distance decreases from 1.41 Å to 1.39 Å, and the Re–N remains unvaried at 2.00 Å.

As a matter of fact, $[Re\{o-C_6H_4(NH)_2\}_3]^+$ undergoes in acetonitrile solution two reversible one-electron reductions ($E_{+/0}^{\circ'} = -0.53 \text{ V vs. Fc/Fc}^+$; $E_{0/-}^{\circ'} = -0.92 \text{ V}$).⁶⁷ The authors assign such electron additions as

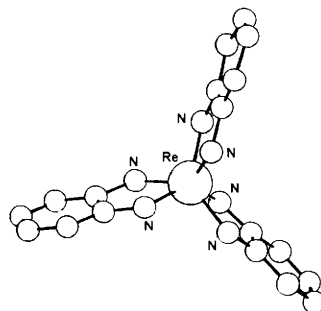


Figure 39 X-Ray structure of the cation $[Re\{o-C_6H_4(NH)_2\}_3]^+$

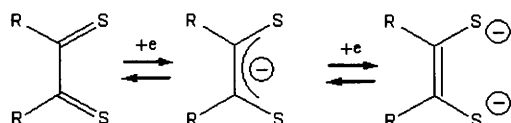
Table 10 Average bond lengths (\AA) in the series $[Re\{o-C_6H_4(NH)_2\}_3]^+ / [Re\{o-C_6H_4(NH)_2\}_3]$

Complex	Subunit	Re–N	C–N	C–C
$[Re\{o-C_6H_4(NH)_2\}_3]^+$	I	2.00	1.36	1.41
	II	1.99	1.35	1.41
	III	2.00	1.33	1.40
$[Re\{o-C_6H_4(NH)_2\}_3]$	I	2.00	1.37	1.39
	II	2.00	1.35	1.39
	III	2.01	1.36	1.38

metal-centred processes, even if they do not rule out the possibility of ligand centred processes. In particular, the first reduction is assigned to the process $[Re^{VII}(o\text{-phenylenediamine})_3]^+ / [Re^{VI}(o\text{-phenylenediamine})_3]$. The invariance of the Re–N distances and the slight variations inside the ligand in reality would seem to favour the second hypothesis.

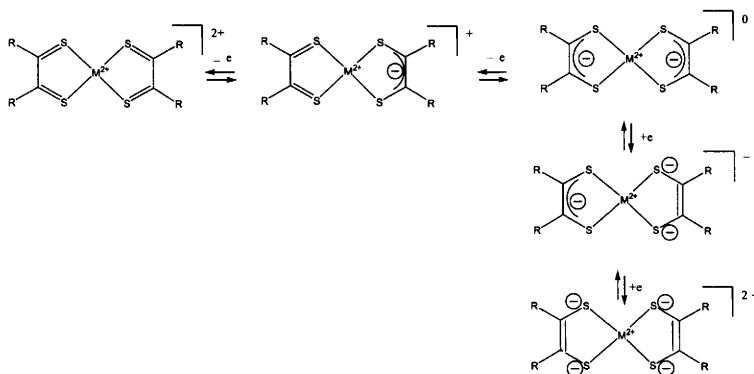
Let us now pass to metallo-dithiolene complexes, which constitute a relatively old class of compounds,⁶⁸ which are a matter of great renewed interest in the field of superconductivity just because of their extended redox propensity.⁶⁹

As happens for dioxolenes, dithiolenes can undergo the reversible sequence 1,2-dithione/1,2-dithione monoanion/ene-1,2-dithiolate illustrated in Scheme 6.



Scheme 6

Therefore the most common homoleptic bis-dithiolene metal complexes $[M^{II}(S_2C_2R_2)_2]^{n-}$ ($M = Ni, Pd, Pt$) can potentially take part in the redox sequence illustrated in Scheme 7. Once again, this has to be considered a simplified sequence in that the occurrence of internal metal-to-ligand electron transfer cannot be ruled out.



Scheme 7

As an example, Figure 40 shows the voltammetric response of the square planar dithiolate dianion $[Ni(S_2C_2Me_2)_2]^{2-}$.⁷⁰

The reversible sequence $2-/-/0$ is well visible. All the members of the series have been isolated and structurally characterized, Figure 41.⁷⁰

On passing from the neutral 1,2-dithionate to the dianionic 1,2-dithiolate, the Ni–S and C–S distances progressively increase, whereas the C–C distance decreases.

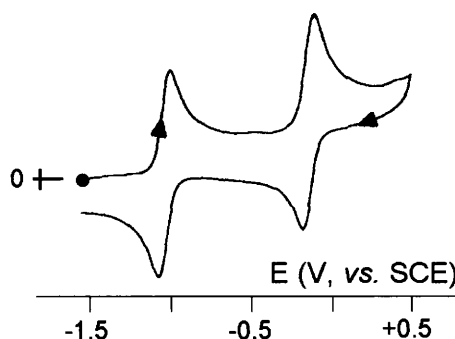


Figure 40 Cyclic voltammogram recorded at a platinum electrode in a MeCN solution of $[Ni(S_2C_2Me_2)_2]^{2-}$. Scan rate 0.1 V s^{-1}

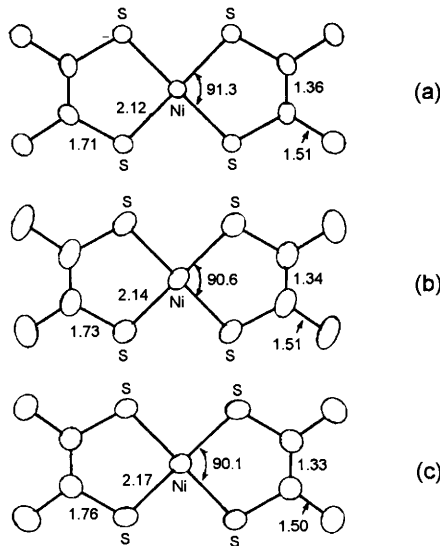


Figure 41 X-Ray structures, together with significant bond lengths, of: (a) $[\text{Ni}(\text{S}_2\text{C}_2\text{Me}_2)_2]$; (b) $[\text{Ni}(\text{S}_2\text{C}_2\text{Me}_2)_2]^-$; (c) $[\text{Ni}(\text{S}_2\text{C}_2\text{Me}_2)_2]^{2-}$

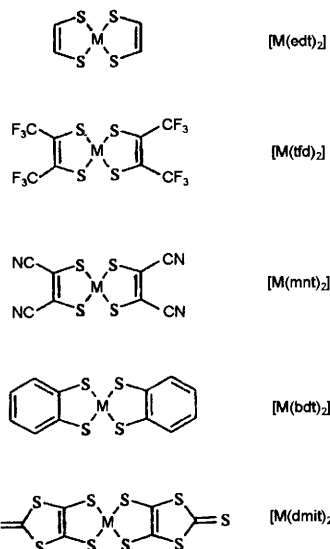
The minor but significant variation of the Ni–S distances with the electron addition/removal processes suggests that the redox processes are centred on molecular orbitals significantly contributed not only by the dithiolene ligand but also by the metal. A similar conclusion has been drawn as far as the related series $[\text{Ni}(1,2-\text{S}_2-3,5-\text{Bu}^{\text{t}}-\text{C}_6\text{H}_2)_2]^{2-/-0}$ is concerned.⁷¹

In reality, different classes of derivatives contribute the general definition of bis-dithiolene metal complexes, Scheme 8.⁷²

$\text{M}(\text{dmit})_2$ complexes ($\text{dmit} = \text{C}_3\text{S}_5^{2-} = 1,3\text{-dithiole-2-thione-4,5-dithiolate}$) constitute one of the most important subclasses. The most studied metal complexes are those of group 10 (Ni, Pd, Pt), which possess a square-planar geometry; see for instance the molecular structure of the monoanion $[\text{Ni}(\text{dmit})_2]^-$, Figure 42.⁷³

Bis(dithiolene)-metal complexes can also assume a tetrahedral geometry, for instance $[\text{Co}(\text{dmit})_2]^{2-}$,⁷⁴ $[\text{Cu}(\text{dmit})_2]^{2-}$,⁷⁵ and $[\text{Zn}(\text{dmit})_2]^{2-}$.⁷⁶ In this connection it is useful to note that $[\text{Co}(\text{edt})_2]^{2-}$ also possesses a tetrahedral geometry,⁷⁶ whereas $[\text{Co}(\text{mnt})_2]^{2-}$ is planar.^{77,78}

As illustrated in Figure 43, $[\text{Ni}(\text{dmit})_2]^-$ displays a chemically reversible $-/2-$ reduction, whereas the $-/0$ oxidation step is affected by electrode adsorption phenomena.⁷⁹



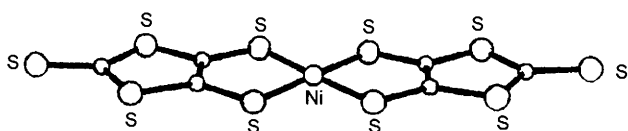
Scheme 8

All the square planar members of the series $[\text{Ni}(\text{dmit})_2]^{2-}/[\text{Ni}(\text{dmit})_2]^-/[\text{Ni}(\text{dmit})_2]^0$ have been structurally characterized and their significant bond lengths are compiled in Table 11.⁸⁰

As seen, in confirmation of the charge delocalization of the electron transfers, most distances inside the dmit ligand remain essentially unaltered. Nevertheless, the progressive shortening of the Ni–S bond suggests a non negligible contribution of the metal d orbitals to the frontier orbitals.

Dithiolenes also form tris complexes of octahedral geometry. Limiting to $\text{M}(\text{dmit})_3$ complexes we can cite as a typical example the dianion $[\text{W}(\text{dmit})_3]^{2-}$, the molecular structure of which is illustrated in Figure 44.⁸¹

As illustrated in Figure 45, this dianion undergoes two successive one-electron oxidations, the first of which is clearly chemically reversible, whereas the second is affected by electrode adsorption phenomena.⁸¹

Figure 42 X-Ray structure of the monoanion $[\text{Ni}(\text{dmit})_2]^-$

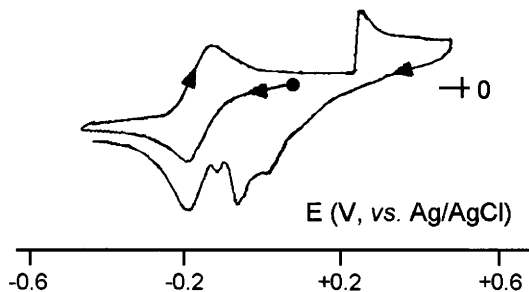


Figure 43 Cyclic voltammogram recorded at a platinum electrode in a MeCN solution of $[SMe_3][Ni(dmit)_2]$. Scan rate 0.1 V s^{-1}

Table 11 Average bond lengths (\AA) in the series $[Ni(dmit)_2]^{2-}/[Ni(dmit)_2]^-/[Ni(dmit)_2]^0$

Complex	Bond-type					
	a	b	c	d	e	f
$[Ni(dmit)_2]^{2-}$	2.22	1.75	1.72	1.74	1.68	1.39
$[Ni(dmit)_2]^-$	2.16	1.73	1.74	1.74	1.63	1.35
$[Ni(dmit)_2]^0$	2.15	1.70	1.73	1.75	1.63	1.39

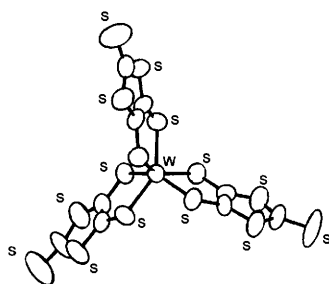


Figure 44 X-Ray structure of the dianion $[W(dmit)_3]^{2-}$

The corresponding monoanion has been isolated and structurally characterized, and Scheme 9 summarizes the averaged structural variations following the $[W(dmit)_3]^{2-}/[W(dmit)_3]^-$ redox change, which support the ligand centred nature of the oxidation process.⁸¹

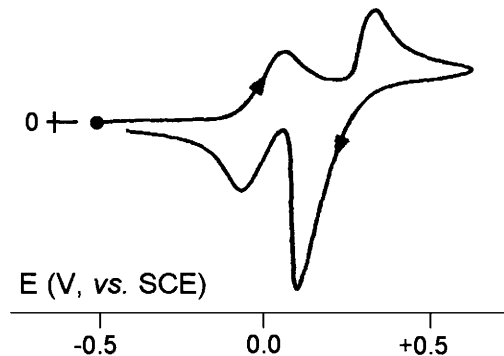
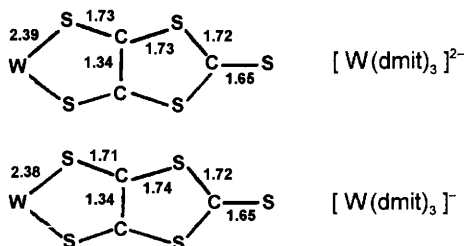


Figure 45 Cyclic voltammogram recorded at a platinum electrode in a DMF solution of $[NBu_4]_2[W(dmit)_3]$. Scan rate 0.1 V s^{-1}

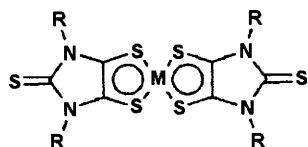


Scheme 9

It must, however, be taken into account that in some cases the electron transfers exhibited by tris(dithiolene) complexes, namely $[M(\text{dithiolene})_3]^{0/-2-}$, have been assigned as metal-centred processes. This is, for instance, the case of $[\text{Mo}(\text{S}_2\text{C}_6\text{H}_4)_3]$, which exhibits two reversible one-electron reductions at $+0.20\text{ V}$ and -0.39 V (*vs.* SCE), respectively.⁸² The crystal structures of the couple $[\text{Mo}(\text{S}_2\text{C}_6\text{H}_4)_3]^{0/-2}$ ⁸³ show that the one-electron addition causes the averaged Mo–S bonds to elongate slightly from 2.37 \AA to 2.38 \AA , whereas the S–C distance remains substantially unaltered (1.73 \AA). These data have been interpreted (but some uncertainty remains) as supporting the assignment $[\text{Mo}^{\text{VI}}(\text{S}_2\text{C}_6\text{H}_4)_3]^0$ and $[\text{Mo}^{\text{V}}(\text{S}_2\text{C}_6\text{H}_4)_3]^-$, respectively.⁸²

We will conclude the present section with a further class of metal-dithiolenes, namely $[\text{M}(\text{R}_2\text{timdt})_2]$ ($\text{R}_2\text{timdt} = 1,3\text{-dialkylimidazoline-2,4,5-trithione monoanion}$), Scheme 10.⁸⁴

At variance with the $[\text{M}(\text{dmit})_2]^{n-}$ analogues, which display the $2-/-0$ redox changes, the present derivatives also give the corresponding positively charged complexes. For instance, Figure 46 shows the cyclic voltammetric profile of $[\text{Ni}^{\text{II}}(\text{Pr}_2\text{timdt})_2]$ in CH_2Cl_2 solution.⁸⁵



Scheme 10

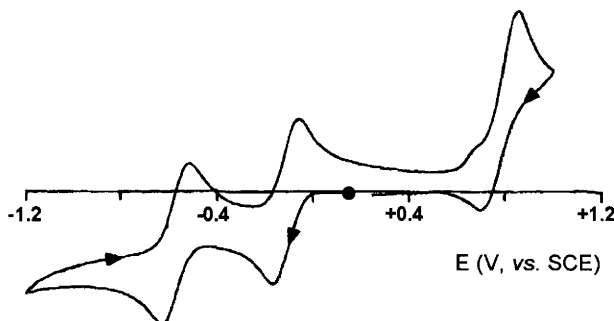


Figure 46 Cyclic voltammogram recorded at a platinum electrode in a CH_2Cl_2 solution of $[\text{Ni}^{\text{II}}(\text{Pr}^i_2\text{timdt})_2]$. Scan rate 0.1 V s^{-1}

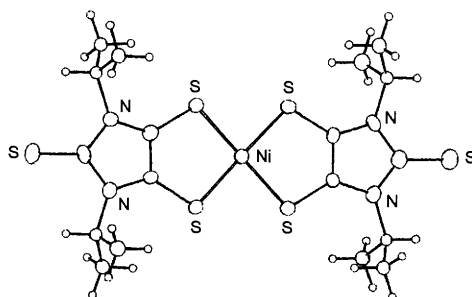


Figure 47 X-Ray structure of $[\text{Ni}^{\text{II}}(\text{Pr}^i_2\text{timdt})_2]$

In addition to the common reversible reductions $[\text{Ni}^{\text{II}}(\text{Pr}^i_2\text{timdt})_2]/[\text{Ni}^{\text{II}}(\text{Pr}^i_2\text{timdt})_2]^-$ ($E^{\circ'} = -0.12\text{ V}$) and $[\text{Ni}^{\text{II}}(\text{Pr}^i_2\text{timdt})_2]^-/[\text{Ni}^{\text{II}}(\text{Pr}^i_2\text{timdt})_2]^{2-}$ ($E^{\circ'} = -0.60\text{ V}$), it also undergoes a single (likely) two-electron oxidation ($E^{\circ'} = +0.78\text{ V}$) with features of partial chemical reversibility.

Both the neutral $[\text{Ni}^{\text{II}}(\text{Pr}^i_2\text{timdt})_2]$, Figure 47, and the corresponding monoanion $[\text{Ni}^{\text{II}}(\text{Pr}^i_2\text{timdt})_2]^-$ have been isolated and structurally characterized.^{85,86}

Table 12 Average bond lengths (\AA) in the $[\text{Ni}^{II}(\text{Pr}_2^i\text{timdt})_2]/[\text{Ni}^{II}(\text{Pr}_2^i\text{timdt})_2]^-$ couple

	$[\text{Ni}^{II}(\text{Pr}_2^i\text{timdt})_2]$	$[\text{Ni}^{II}(\text{Pr}_2^i\text{timdt})_2]^-$
Ni-S	2.16	2.16
C-S	1.69	1.70
N-C _(ring)	1.35÷1.40	1.36÷1.40
C-C _(ring)	1.38	1.35
C=S	1.65	1.66

Table 12 summarizes the relative structural parameters, which also in this case support the ligand-centred nature of the electron transfer process.

However, the related complex $[\text{Pd}^{II}(\text{Et}_2\text{timdt})_2]$ deserves a special mention, Figure 48.⁸⁷

As illustrated in Figure 49, it displays the five-membered, reversible, one-electron sequence $[\text{Pd}^{II}(\text{Et}_2\text{timdt})_2]^{2+}/[\text{Pd}^{II}(\text{Et}_2\text{timdt})_2]^+/\text{[Pd}^{II}(\text{Et}_2\text{timdt})_2]^0/\text{[Pd}^{II}(\text{Et}_2\text{timdt})_2]^-/\text{[Pd}^{II}(\text{Et}_2\text{timdt})_2]^{2-}$, according to the theoretically expected Scheme 7.⁸⁸

4 PORPHYRINS (AND TETRAAZAPORPHYRINS) AS LIGANDS IN METAL COMPLEXES

Porphyins constitute an important class of electron-transfer ligands. In nature, the biological electron-transfer conversion of light into chemical energy, known as ‘photosynthesis’, which takes place either in green plants or photosynthetic bacteria, is primarily driven by photosynthetic

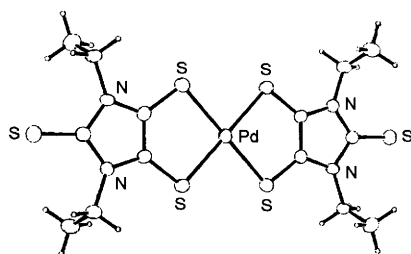


Figure 48 X-Ray structure of $[\text{Pd}^{II}(\text{Et}_2\text{timdt})_2]$. Average bond lengths: $\text{Pd}-\text{S}=2.29 \text{ \AA}$; $\text{S}-\text{C}=1.69 \text{ \AA}$; $\text{C}-\text{C}_{(\text{ring})}=1.40 \text{ \AA}$; $\text{N}-\text{C}_{(\text{ring})}=1.37 \text{ \AA}$; $\text{N}-\text{C}_{(\text{ethyl})}=1.46 \text{ \AA}$; $\text{C}=\text{S}=1.65 \text{ \AA}$

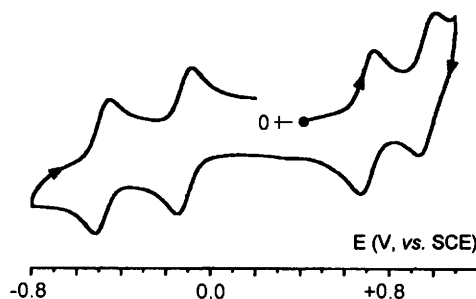


Figure 49 Cyclic voltammogram recorded at a platinum electrode in a CH_2Cl_2 solution of $[\text{Pd}(\text{Et}_2\text{imdt})_2]$. Scan rate 0.2 V s^{-1}

chromophores (light-harvesting antenna and reaction centres) which consist of special assemblies of porphyrins.⁸⁹

The electrochemical behaviour of a high number of metalloporphyrins has been reviewed some years ago.⁹⁰ We would like here to point out a few electrochemical-to-structural aspects of such derivatives.

Having previously discussed the lack of redox activity of Zn(II) derivatives (Chapter 5, Section 8), we shall start with zinc-porphyrins. Figure 50 shows the planar geometry of Zn(II)-5,10,15,20-tetraphenylporphyrinato complex, $[\text{Zn}(\text{TPP})]$.^{91,92}

One must, however, take into account that zinc porphyrin complexes have a strong tendency to coordinate axially Lewis bases, thus sometime affording pentacoordinate geometries. Figure 51 shows the example of $[\text{Zn}(\text{TPP})(\text{H}_2\text{O})]$, in which the axial coordination of the water molecule causes the zinc atom to move out of the tetrapyrrolic plane.⁹³

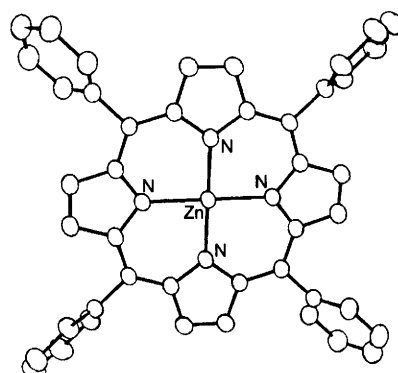


Figure 50 X-Ray structure of $[\text{Zn}(\text{TPP})]$. Average bond length: $\text{Zn}-\text{N}=2.04 \text{ \AA}$

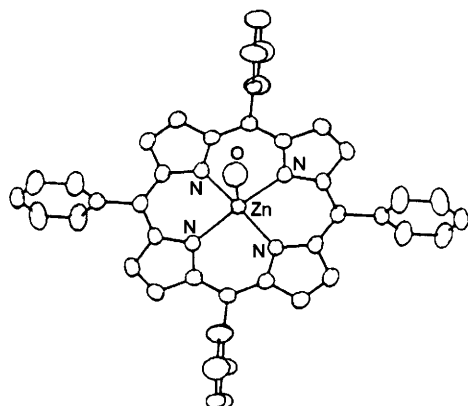


Figure 51 X-Ray structure of $[\text{Zn}(\text{TPP})(\text{H}_2\text{O})]$. Average bond lengths: $\text{Zn}-\text{N}=2.05 \text{ \AA}$; $\text{Zn}-\text{O}=2.23 \text{ \AA}$. The $\text{Zn}(\text{II})$ ion is displaced by 0.19 \AA above the tetrapyrrolic plane

$[\text{Zn}(\text{TPP})]$ in CH_2Cl_2 solution displays two separate one-electron oxidations ($E_{0/+}^{\circ'} = +0.70 \text{ V}$; $E_{+/2+}^{\circ'} = +1.07 \text{ V}$) as well as two separate one-electron reductions ($E_{0/-}^{\circ'} = -1.45 \text{ V}$; $E_{-/2-}^{\circ'} = -1.81 \text{ V}$). All have characteristics of chemical reversibility, Figure 52a.^{94–96}

In confirmation that these redox changes are centred on the porphyrin ligand, the free porphyrin (*i.e.* $[\text{H}_2\text{TPP}]$) exhibits the same electron transfer processes ($E_{0/+}^{\circ'} = +0.90 \text{ V}$; $E_{+/2+}^{\circ'} = +1.23 \text{ V}$; $E_{0/-}^{\circ'} =$

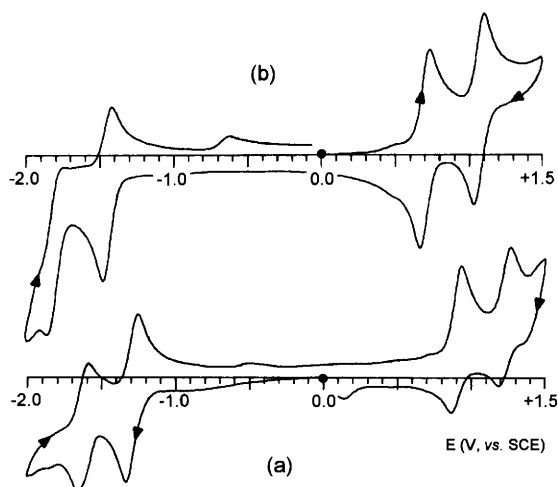


Figure 52 Cyclic voltammograms recorded at a platinum electrode in CH_2Cl_2 solutions of: (a) $[\text{Zn}(\text{TPP})]$; (b) $[\text{H}_2\text{TPP}]$. Scan rate 0.2 V s^{-1}

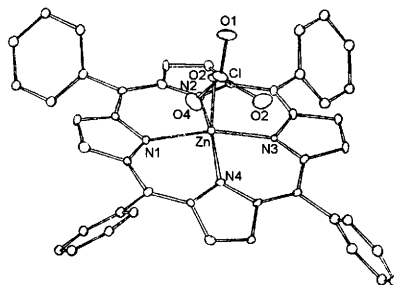


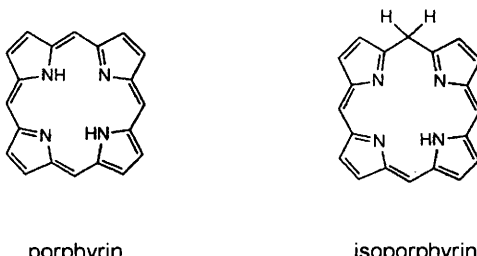
Figure 53 *X-Ray structure of [Zn(TPP)][ClO₄]. Average bond lengths: Zn–N = 2.08 Å; Zn–O = 2.08 Å. The Zn(II) ion is displaced by 0.35 Å above the tetrapyrrolic plane*

–1.29 V; $E_{-/-2}^{\circ} = -1.62$ V), Figure 52b.^{95,96} Further, the HOMO/LUMO separation for [Zn(TPP)], $\Delta E^{\circ\prime} = 1.45 - (-0.70) = 2.15$ V, is approximately equal to that of the free [H₂TPP] ligand, $\Delta E^{\circ\prime} = 0.90 - (-1.29) = 2.19$ V.

The molecular structure of the [Zn^{II}(TPP)]⁺ cation, obtained by exhaustive electrolysis at the potential of the first oxidation process (in CH₂Cl₂ solution containing [NPr₄][ClO₄] as supporting electrolyte), is shown in Figure 53.⁹⁷ In agreement with the preference for pentacoordination, Zn(II) ion coordinates axially the oxygen atom (O) of the [ClO₄]⁻ supporting electrolyte counteranion.

The subsequent exhaustive electrolysis at the potentials of the second anodic process to generate the [Zn(TPP)]²⁺ dication gives rise to important results. In fact, the electrogenerated dication is stable in the absence of nucleophilic agents, but, in the presence of nucleophilic agents (such as methanol), it transforms into zinc(II) 5'-methoxyl-5,10,15,20-tetraphenyl *isoporphyrin*, [Zn(TPiPOCH₃)]⁺.⁹⁸

'Isoporphyrins' are a tautomeric form of porphyrins in which the conjugation of the double bond in the macrocycle chain is broken, Scheme 11.



Scheme 11

The characterization of isoporphyrins is complicated by their tendency to regenerate porphyrins. One of the few isoporphyrins that has been well characterized also from a structural viewpoint is shown in Figure 54.⁹⁹

A water molecule trapped during the crystallization is axially coordinated (O_5) and induces the zinc ion to move out of the plane of the four nitrogen atoms by 0.31 \AA . It can be seen that the saturation of the carbon responsible for the break of the double bond conjugation is localized on the C5 carbon atom.

In butyronitrile, the present isoporphyrin complex exhibits an oxidation process ($E^{\circ'} = +1.09\text{ V}$, *vs.* SCE) and two consecutive reduction processes ($E^{\circ'} = -0.29\text{ V}$ and -0.61 V , respectively). As it happens for zinc porphyrins, also in this case the processes are centred on the ligands.⁹⁹ It is interesting, however, to note that the HOMO/LUMO separation is 1.38 V , which is considerably lower than that of $[\text{Zn}(\text{TPP})]$.

Let us now pass to metalloporphyrins of metal ions of higher redox propensity, such as Ni(II) or Cu(II), which obviously can afford redox changes, whose metal- or ligand-centred nature is more problematic to assess.

Figure 55 shows the cyclic voltammetric behaviour of $[\text{Ni}^{\text{II}}(\text{OEP})]$ ($\text{OEP} = 2,3,7,8,12,13,17,18\text{-octaethylporphyrin}$) in CH_2Cl_2 solution,⁹⁶ together with its solid-state molecular structure (in the planar triclinic phase).¹⁰⁰

As seen, the planar Ni(II) complex undergoes either a (one-electron) reduction ($E_{0/-}^{\circ'} = -1.55\text{ V}$; $\Delta E_p = 64\text{ mV}$, at 0.2 Vs^{-1}) or two separate (one-electron) oxidations ($E_{0/+}^{\circ'} = +0.64\text{ V}$, $\Delta E_p = 72\text{ mV}$; $E_{+/2+}^{\circ'} = +1.23\text{ V}$, $\Delta E_p = 80\text{ mV}$), all possessing features of chemical and electrochemical reversibility. Based on the fact that $[\text{H}_2\text{OEP}]$, under the same

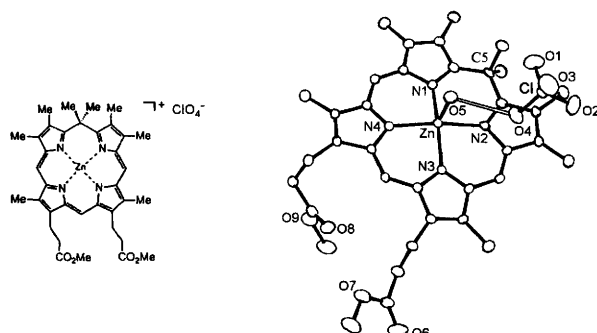


Figure 54 X-Ray structure of the schematized $\text{Zn}(\text{II})$ -isoporphyrin. Average bond lengths: $\text{Zn}-\text{N}1 \approx \text{Zn}-\text{N}2 = 2.08\text{ \AA}$; $\text{Zn}-\text{N}3 \approx \text{Zn}-\text{N}4 = 2.07\text{ \AA}$; $\text{Zn}-\text{O}5 = 2.12\text{ \AA}$

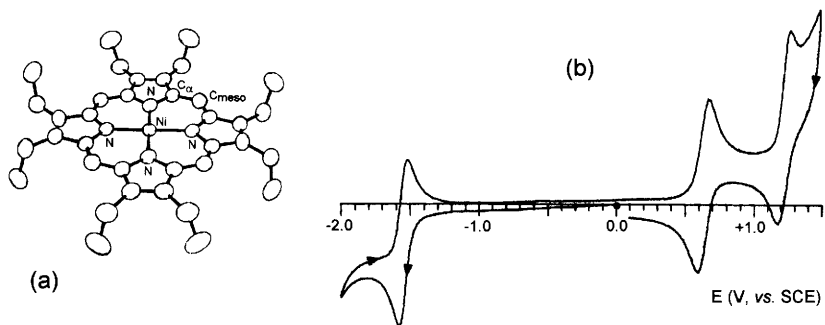


Figure 55 (a) X-Ray structure of $[Ni^{II}(OEP)]$. Average bond lengths: Ni–N = 1.95 Å; C_α–N = 1.39 Å; C_α–C_{meso} = 1.37 Å. (b) Cyclic voltammetric behaviour exhibited by $[Ni(OEP)]^+$ in CH_2Cl_2 solution. Platinum working electrode. Scan rate 0.2 V s^{-1}

experimental conditions, exhibits a substantially similar redox aptitude ($E_{0/-}^{\circ\prime} = -1.51\text{ V}$; $E_{0/+}^{\circ\prime} = +0.73\text{ V}$; $E_{+/2+}^{\circ\prime} = +1.29\text{ V}$), it does not seem too adventurous to assume that the redox processes of the porphyrinato-nickel(II) are ligand-centred. As a matter of fact, the X-ray molecular structure of the monocation $[Ni(OEP)]^+$ not only shows that it maintains the planar geometry of the neutral parent, but also the most representative bond lengths remain substantially unaltered (Ni–N = 1.95 Å; C_α–N = 1.38 Å; C_α–C_{meso} = 1.37 Å).¹⁰¹

An important class of porphyrins is that constituted by ‘conformationally distorted’ porphyrins, which mimic the non-planar geometry of the porphyrins present in photosynthetic systems.⁸⁹ Obtainment of such non-planar distortions is associated with the introduction into the macrocyclic frame of proper crowding substituents, which therefore not only cause structural distortion but also affect, through their electronic effects, the redox potentials. A typical case is that constituted by $[Cu^{II}(OETPP)]$ (OETPP = 2,3,7,8,12,13,17,18-octaethyl-5,10,15,20-tetraphenylporphyrin), the saddle-distorted molecular structure of which is illustrated in Figure 56.¹⁰²

From the electrochemical viewpoint, $[Cu(OETPP)]$ displays two reversible oxidations at potential values lower than those of $[Cu(OEP)]$ and $[Cu(TPP)]$, respectively, Table 13.

Chemical oxidation (by $AgClO_4$) affords the monocation $[Cu(OETPP)]^+$ the molecular structure of which has been solved.^{102b} An additional ruffling of the original saddle shape arises as a consequence of the one-electron removal, but the bond lengths substantially remain unvaried (Cu–N = 1.97 Å; C_α–N = 1.38 Å;

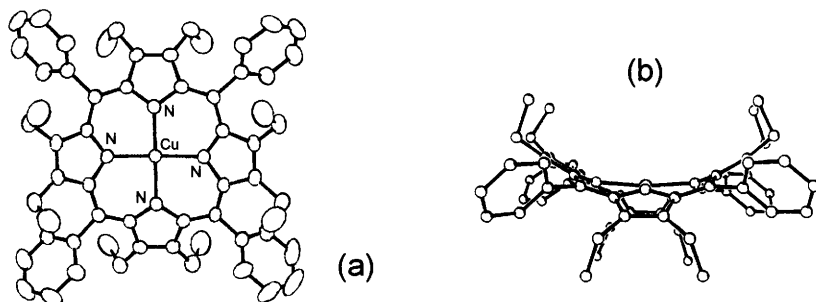


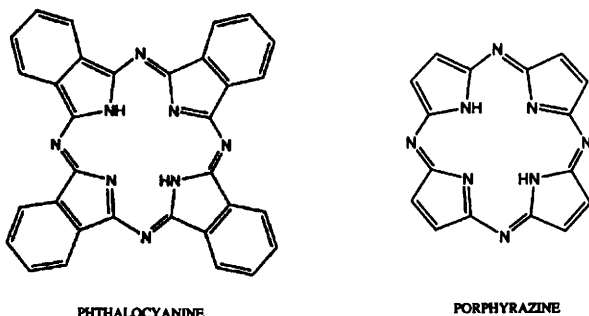
Figure 56 (a) X-Ray structure of $[Cu^{II}(OETPP)]$. (b) Side view along the $N\text{--}Cu\text{--}N$ axis. Average bond lengths: $Cu\text{--}N = 1.97 \text{ \AA}$; $C_{\alpha}\text{--}N = 1.38 \text{ \AA}$; $C_{\alpha}\text{--}C_{meso} = 1.40 \text{ \AA}$

Table 13 Formal electrode potentials (V vs. SCE) for the redox changes exhibited by $[Cu(OETPP)]$, $[Cu(OEP)]$ and $[Cu(TPP)]$, in dichloromethane solution

Complex	$E_{2+/+}^{\circ'}$	$E_{+/0}^{\circ'}$	$E_{0/-}^{\circ'}$	Ref.
$[Cu(TPP)]$	+ 1.29	+ 0.90	- 1.42	96
$[Cu(OEP)]$	+ 1.41	+ 0.63	- 1.63	96
$[Cu(OETPP)]$	+ 0.97	+ 0.38	-	102b

$C_{\alpha}\text{--}C_{meso} = 1.41 \text{ \AA}$), thus once again supporting the ligand-centred nature of the oxidation process.

Let us conclude shortly with *tetraazaporphyrins*, the most popular members of which are constituted by *phthalocyanines* and *porphrazines*, Scheme 12.



Scheme 12

Phthalocyanines are actually of great applicative interest (because of their intense blue-green colour they are used in dyes, pigments and paints, and colour photography) and up to now have been studied much more than porphyrazines.

Since the electrochemical behaviour of metallophthalocyanines has been reviewed,¹⁰³ we will simply demonstrate the ligand based nature of their redox processes. As a typical example, Figure 57 shows the redox aptitude of zinc-phthalocyanine $[\text{Zn}(\text{Pc})]$ CH_2Cl_2 in solution,⁹⁶ together with its molecular structure.¹⁰⁴

The square planar complex undergoes either two separate one-electron reductions ($E_{0/-}^{\circ} = -1.03 \text{ V}$, $\Delta E_p = 66 \text{ mV}$, at 0.2 V/s^{-1} ; $E_{-/-2}^{\circ} = -1.40 \text{ V}$), or two one-electron oxidations ($E_{0/+}^{\circ} = +0.52 \text{ V}$, $\Delta E_p = 84 \text{ mV}$, at 0.2 V/s^{-1} ; $E_{+/+2}^{\circ} = +1.4 \text{ V}$) (the second oxidation is not shown in Figure because its irreversible character masks the return peak of the first oxidation). It is easily conceivable that all the redox processes are ligand centred.

Comparison with the redox aptitude of $[\text{Zn}(\text{TPP})]$ (Figure 52) points out a minor redox flexibility of phthalocyaninates with respect to porphyrinates, in that in the former either the second reduction or the second oxidation are complicated by degradation of the corresponding congeners. We also note that the HOMO/LUMO separation for $[\text{Zn}(\text{Pc})]$ is 1.55 eV, *i.e.* lower than that of $[\text{Zn}(\text{TPP})]$ (2.15 eV).

Finally, as far as metalloporphyrazines are concerned, Scheme 13, it must be said that, in spite of their appearance in literature since about fifty years, the electrochemical ascertainment of their redox ability has been almost completely neglected for a long time.¹⁰⁵

Recently, however, the interest in their redox capacity is growing in relation to their potential use as conducting materials, thus the

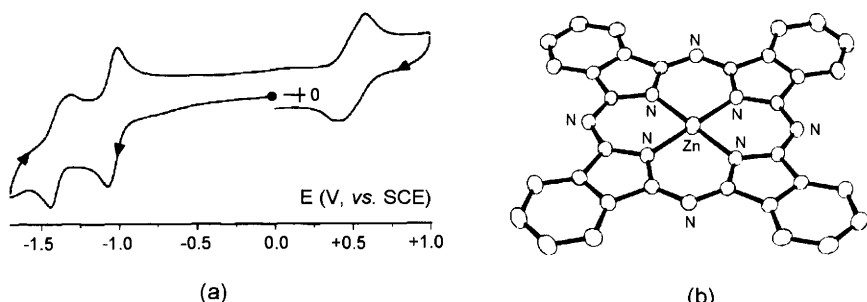
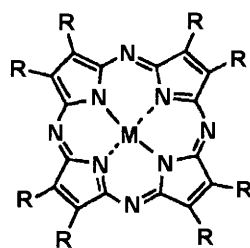


Figure 57 (a) Cyclic voltammetric behaviour of $[\text{Zn}(\text{Pc})]$ in CH_2Cl_2 solution. Platinum working electrode. Scan rate 0.2 V s^{-1} . (b) X-Ray structure of $[\text{Zn}(\text{Pc})]$. Average bond lengths: $\text{Zn}-\text{N}_p = 1.98 \text{ \AA}$; $\text{C}_x-\text{N}_p = 1.38 \text{ \AA}$; $\text{C}_x-\text{N}_m = 1.33 \text{ \AA}$



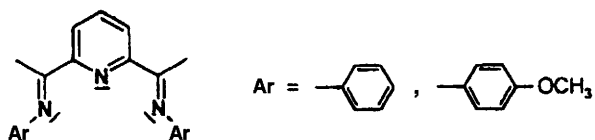
Scheme 13

ligand-based nature of the relative electron transfers has been investigated either in symmetrically or asymmetrically substituted complexes.¹⁰⁶

5 LESS KNOWN REDOX-ACTIVE LIGANDS IN METAL COMPLEXES

As briefly alluded to, there are different classes of redox-active ligands in addition to the above mentioned ones. For example, we have seen in Chapter 5, Section 8, that *azo-groups* (in particular, 2-(phenylazo)pyrimidine) are able to undergo two separate one-electron reduction processes. *Conjugated polynitriles* (mnt, tcne, tcnq) also constitute an important class of redox-active molecules and the electrochemical behaviour of their metal complexes has been reviewed.¹⁰⁷ The same holds as far as *alkyldithiocarbamates* (Rdtc) and their metal complexes are concerned,¹⁰⁸ or *nitrosyl* complexes in their possible NO^+ / NO/NO^- redox sequence.¹⁰⁹ Thus, we would like to conclude the present Chapter by discussing a few less known redox non-innocent ligands.

Let us start with the pyridine-2,6-diimine ligand (L) shown in Scheme 14.¹¹⁰



Scheme 14

Figure 58 illustrates the molecular structure and the redox propensity of the dication $[\text{Zn}(\text{L})_2]^{2+}$ ($\text{Ar} = \text{C}_6\text{H}_4-p\text{-OMe}$).^{110b}

As shown, the distorted octahedral Zn(II) complex undergoes two separated (one-electron) reductions, reversible in character,

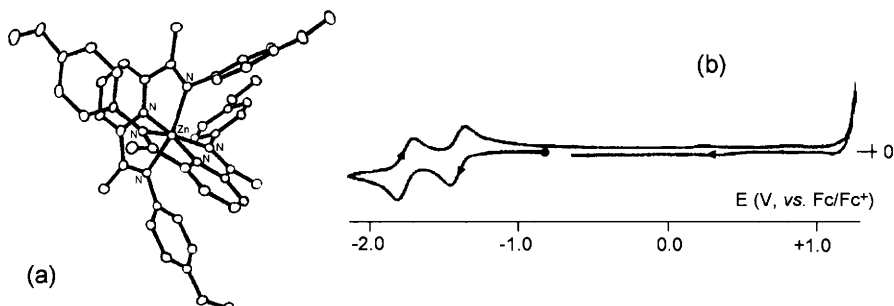
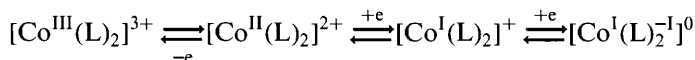


Figure 58 (a) X-Ray structure of $[Zn(L)_2]^{2+}$ ($Ar = C_6H_4-p-OMe$). Average bond lengths: $Zn-N_{py} = 2.04 \text{ \AA}$; $Zn-N_{imine} = 2.20 \text{ \AA}$; $C_{imine}-N_{imine} = 1.28 \text{ \AA}$; $C_{imine}-C_{py} = 1.50 \text{ \AA}$; $C_{py}-N_{py} = 1.34 \text{ \AA}$; $C_{py}-C_{py} = 1.39 \text{ \AA}$. (b) Cyclic voltammogram recorded at a glassy carbon electrode in a MeCN solution of $[Zn(LAr)_2][\text{PF}_6]_2$ ($Ar = C_6H_4-p-OMe$). Scan rate 0.2 V s^{-1}

($E_{2+/+}^{\circ'} = -1.39 \text{ V vs. } \text{Fc}/\text{Fc}^+$; $E_{+/0}^{\circ'} = -1.67 \text{ V}$) which are obviously centred on the pyridine-2,6-diimino ligand.

Interestingly, the isostructural Co(II) dication $[\text{Co}(L)_2]^{2+}$ ($Ar = C_6H_4-p-OMe$) displays a rather different redox behaviour. In fact, as illustrated in Figure 59, it undergoes either a one-electron oxidation ($E_{2+/3+}^{\circ'} = +0.01 \text{ V vs. } \text{Fc}/\text{Fc}^+$), or two separated one-electron reductions ($E_{2+/+}^{\circ'} = -0.93 \text{ V}$; $E_{+/0}^{\circ'} = -1.92 \text{ V}$), the first of which occurs at notably less negative potential values than the above-mentioned ligand-centred processes.^{110b}

In this case the redox processes are assigned as:



As a matter of fact, the crystal structures of the couple $[\text{Co}^{\text{II}}(L)_2]^{2+} / [\text{Co}^{\text{I}}(L)_2]^+$ have been solved and the relevant parameters are compiled in Table 14.^{110b}

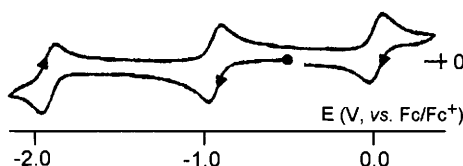


Figure 59 Cyclic voltammogram recorded at a glassy carbon electrode in a MeCN solution of $[\text{Co}(L)_2][\text{PF}_6]_2$ ($Ar = C_6H_4-p-OMe$). Scan rate 0.2 V s^{-1}

Table 14 Averaged bond lengths (\AA) in the $[\text{Co}^{\text{II}}(\text{L})_2]^{2+}$ / $[\text{Co}^{\text{I}}(\text{L})_2]^+$ ($\text{Ar} = \text{C}_6\text{H}_4\text{-p-OMe}$) couple

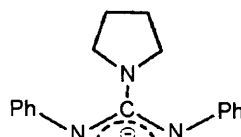
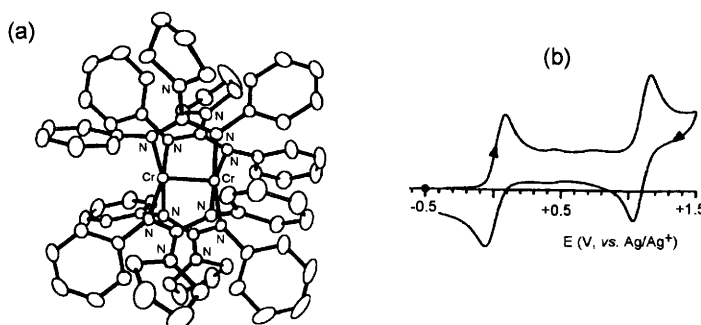
	$[\text{Co}^{\text{II}}(\text{L})_2]^{2+}$	$[\text{Co}^{\text{I}}(\text{L})_2]^+$
$\text{Co}-\text{N}_{\text{py}}$	1.92 ^a	1.99
$\text{Co}-\text{N}_{\text{imine}}$	2.09	2.15
$\text{Cimine}-\text{N}_{\text{imine}}$	1.30	1.30
$\text{Cimine}-\text{C}_{\text{py}}$	1.48	1.46
$\text{C}_{\text{py}}-\text{N}_{\text{py}}$	1.35	1.36
$\text{C}_{\text{py}}-\text{C}_{\text{py}}$	1.39	1.39

^aAveraged value between 1.85 \AA and 1.99 \AA .

As seen, the only significant structural variations are concerned with the metal-ligand bonds, thus supporting that, in this case, the first reduction is metal-centred.

As a final example let us consider the anion $[(\text{PhN})_2\text{CN}(\text{CH}_2)_4]^-$ (NN' -diphenyl-1-pyrrolidine carbodiimide anion = $[\text{DPPC}]^-$) illustrated in Scheme 15, which undergoes an irreversible oxidation at +0.8 V (vs. Ag/AgCl).¹¹¹

Figure 60 shows the molecular structure of the dichromium complex $[\text{Cr}_2(\text{DPPC})_4]$ and its electrochemical behaviour.¹¹¹

**Scheme 15****Figure 60** (a) X-Ray structure of $[\text{Cr}_2(\text{DPPC})_4]$. Average bond lengths: $\text{Cr}-\text{Cr} = 1.90 \text{ \AA}$; $\text{Cr}-\text{N} = 2.06 \text{ \AA}$. (b) Cyclic voltammetric behaviour exhibited by $[\text{Cr}_2(\text{DPPC})_4]$ in CH_2Cl_2 solution

The paddlewheel Cr_2^{4+} complex undergoes two one-electron oxidations ($E_{0/+}^{\circ\circ'} = +0.02 \text{ V}$; $E_{+/2+}^{\circ\circ'} = +1.10 \text{ V}$ vs. Ag/AgCl) featuring chemical reversibility. Based on the electrochemical behaviour of the ligand (an irreversible oxidation at high potential value), it would seem quite legitimate to assume that at least the first one-electron removal could be due to the $\text{Cr}_2^{4+}/\text{Cr}_2^{5+}$ redox step. Indeed, chemical oxidation affords the corresponding monocation $[\text{Cr}_2(\text{DPPC})_4]^+$, the X-ray structure of which is very similar to that of the neutral precursor. In fact, the relevant bond lengths ($\text{Cr}-\text{Cr} = 1.92 \text{ \AA}$; $\text{Cr}-\text{N} = 2.02 \text{ \AA}$) do not allow us to state clearly if the electron is removed from the metal or the ligand moiety.¹¹¹

REFERENCES

1. M.D. Ward and J. McCleverty, *J. Chem. Soc., Dalton Trans.*, 2002, 275.
2. P. Zanello, in *Ferrocenes*, A. Togni and T. Hayashi, eds, VCH, Weinheim, 1995, Chapter 7.
3. F. Fabrizi de Biani, F. Jäkle, M. Spiegler, M. Wagner and P. Zanello, *Inorg. Chem.*, 1997, **36**, 2103.
4. H. Shen, S.G. Bott and M.G. Richmond, *Inorg. Chim. Acta*, 1996, **250**, 195.
5. U. Siemeling, U. Vorfeld, B. Neumann, H.-G. Stammmer, P. Zanello and F. Fabrizi de Biani, *Eur. J. Inorg. Chem.*, 1999, 1.
6. J.H.K. Yip, J. Wu, K.-Y. Wong, K.-W. Yeung and J.J. Vittal, *Organometallics*, 2002, **21**, 1612.
7. U. Casellato, B. Corain, R. Graziani, B. Longato and G. Pilloni, *Inorg. Chem.*, 1990, **29**, 1193.
8. B. Longato, L. Riello, G. Bandoli and G. Pilloni, *Inorg. Chem.*, 1999, **38**, 2818.
9. (a) F. Diderich and Y. Rubin, *Angew. Chem. Int. Ed. Engl.*, 1992, **31**, 1101; (b) C.-R. Wang, T. Sugai, T. Kai, T. Tomiyama and H. Shinohara, *Chem. Commun.*, 2000, 557; (c) T. Kodama, N. Ozawa, Y. Miyake, K. Sakaguchi, H. Nishikawa, I. Ikemoto, K.-Kikuchi and Y. Achiba, *J. Am. Chem. Soc.*, 2002, **124**, 1452.
10. (a) Y. Ohsawa and T. Saji, *J. Chem. Soc., Chem. Commun.*, 1992, 781; (b) Q. Xie, E. Pérez-Cordero and L. Echegoyen, *J. Am. Chem. Soc.*, 1992, **114**, 3978.
11. D. Bubois, G. Moninot, W. Kutner, M.T. Jones and K.M. Kadish, *J. Phys. Chem.*, 1992, **96**, 7137.
12. M. Fedurco, M.M. Olmstead and W.R. Fawcett, *Inorg. Chem.*, 1995, **34**, 390.
13. W.C. Wan, X. Liu, G.M. Sweeney and W.E. Broderick, *J. Am. Chem. Soc.*, 1995, **117**, 9580.

14. P. Paul, Z. Xie, R. Bau, P.D.W. Boyd and C.A. Reed, *J. Am. Chem. Soc.*, 1994, **116**, 4145.
15. Q. Xie, F. Arias and L. Echegoyen, *J. Am. Chem. Soc.*, 1993, **115**, 9818.
16. C.A. Reed, K.-C. Kim, R.D. Bolksar and L.J. Mueller, *Science*, 2000, **289**, 101.
17. D. Bubois, K.M. Kadish, S. Flanagan, R.E. Haufler, L.P.F. Chibante and L.J. Wilson, *J. Am. Chem. Soc.*, 1991, **113**, 4364.
18. Q. Li, F. Wudl, C. Thilgen, R.L. Whetten and F. Diderich, *J. Am. Chem. Soc.*, 1992, **114**, 3994.
19. M.S. Meier, T.F. Guarr, J.P. Selegue and V.K. Vance, *J. Chem. Soc., Chem. Commun.*, 1993, 63.
20. (a) R.S. Ruoff, D.S. Tse, R. Malhotra and D.C. Lorents, *J. Phys. Chem.*, 1993, **97**, 3379; (b) W.A. Scrivens and J.M. Tours, *J. Chem. Soc., Chem. Commun.*, 1993, 1207.
21. (a) P.J. Fagan, J.C. Calabrese and B. Malone, *Acc. Chem. Res.*, 1992, **25**, 134; (b) A.L. Balch and M.M. Olmstead, *Chem. Rev.*, 1998, **98**, 2123.
22. (a) H.M. Lee, M.M. Olmstead, T. Suetsuna, H. Shimotani, N. Dragoe, R.J. Cross, K. Kitazawa and A. Balch, *Chem. Commun.*, 2002, 1352; (b) M.M. Olmstead, A. de Bettencourt-Dias, J.C. Duchamp, S. Stevenson, D. Marciu, H.C. Dorn and A.L. Balch, *Angew. Chem. Int. Ed. Engl.*, 2001, **40**, 1223; (c) M.M. Olmstead, A. de Bettencourt-Dias, J.C. Duchamp, S. Stevenson, H.C. Dorn and A.L. Balch, *J. Am. Chem. Soc.*, 2000, **122**, 12220; (d) M. Takata, B. Umeda, E. Nishihori, M. Sakata, Y. Saito, M. Ohno and H. Shinohara, *Nature*, 1995, **377**, 46; (e) E. Nishibori, M. Takata, M. Sakata, M. Inakuma and H. Shinohara, *Chem. Phys. Lett.*, 1998, **298**, 79; (f) M.M. Olmstead, A. de Bettencourt-Dias, S. Stevenson, H.C. Dorn and A.L. Balch, *J. Am. Chem. Soc.*, 2002, **124**, 4172; (g) M. Takata, E. Nishibori, M. Sakata, M. Inakuma, E. Yamamoto and H. Shinohara, *Phys. Rev. Lett.*, 1999, **83**, 2214; (h) M. Takata, E. Nishibori, B. Umeda, M. Sakata, E. Yamamoto and H. Shinohara, *Phys. Rev. Lett.*, 1997, **78**, 3330; (i) C.R. Wang, T. Kai, T. Tomiyama, T. Yoshida, Y. Kobayashi, E. Nishidori, M. Takata, M. Sakata and H. Shinohara, *Angew. Chem. Int. Ed. Engl.*, 2001, **40**, 397.
23. P. Zanello, in *Chemistry at the Beginning of the Third Millennium*, L. Fabbrizzi and A. Poggi, eds, Springer, 2000, pp. 247–278.
24. J.M. Hawkins, A. Meyer, T.A. Lewis, S. Loren and F.J. Hollander, *Science*, 1991, **252**, 312.
25. P.J. Fagan, J.C. Calabrese and B. Malone, *Science*, 1991, **252**, 1160.
26. A.L. Balch, V.J. Catalano and J.W. Lee, *Inorg. Chem.*, 1991, **30**, 3980.
27. V.V. Bashilov, P.V. Petrovskii, V.I. Sokolov, S.V. Lindeman, I.A. Guzey and Y.I. Struchkov, *Organometallics*, 1993, **12**, 991.

28. A.L. Balch, J.W. Lee, B.C. Noll and M.M. Olmstead, *J. Am. Chem. Soc.*, 1992, **114**, 10984.
29. M. Rasinkagas, T.T. Pakkanen, T.A. Pakkanen, M. Ahlgren and J. Rouvinen, *J. Am. Chem. Soc.*, 1993, **115**, 4901.
30. P.J. Fagan, J.C. Calabrese and B. Malone, *J. Am. Chem. Soc.*, 1991, **113**, 9408.
31. A.L. Balch, D.A. Costa, B.C. Noll and M.M. Olmstead, *Inorg. Chem.*, 1996, **35**, 458.
32. A.L. Balch, D.A. Costa, B.C. Noll and M.M. Olmstead, *J. Am. Chem. Soc.*, 1995, **117**, 8926.
33. A.L. Balch, V.J. Catalano, J.W. Lee, M.L. Olmstead and S.R. Parkin, *J. Am. Chem. Soc.*, 1991, **113**, 8953.
34. A.L. Balch, A.S. Ginwalla, J.W. Lee, B.C. Noll and M.L. Olmstead, *J. Am. Chem. Soc.*, 1994, **116**, 2227.
35. A.L. Balch, J.W. Lee and M.L. Olmstead, *Angew. Chem. Int. Ed. Engl.*, 1992, **31**, 1356.
36. S.A. Lerke, B.A. Parkinson, D.H. Evans and P.J. Fagan, *J. Am. Chem. Soc.*, 1992, **114**, 7807.
37. J.R. Shapley, Y. Du, H.-F. Hsu and J.J. Way, *Recent Advances in the Chemistry and Physics of Fullerenes and Related Materials*, K.M. Kadish, R.S. Ruoff, eds, The Electrochemical Society: Pennington. NJ 1994, **24**, 1255.
38. (a) K. Tang, S. Zheng, X. Jin, H. Zeng, Z. Gu, X. Zhou and Y. Tang, *J. Chem. Soc., Dalton Trans.*, 1997, 3585; (b) P. Zanello, F. Laschi, M. Fontani, C. Mealli, A. Ienco, K. Tang, X. Jin and L. Li, *J. Chem. Soc., Dalton Trans.*, (1999) 965; (c) P. Zanello, F. Laschi, A. Cinquantini, M. Fontani, K. Tang, X. Jin and L. Li, *Eur. J. Inorg. Chem.*, 2000, 1345.
39. M. Iyoda, F. Sultana, S. Sasaki and H. Butenschön, *Tetrahedron Lett.*, 1995, **36**, 579.
40. M.D. Westmeyer, T.B. Rauchfuss and A.K. Verna, *Inorg. Chem.*, 1996, **35**, 7140.
41. K. Komatsu, G.-W. Wang, Y. Murata, T. Tanaka, K. Fujiwara, K. Yamamoto and M. Saunders, *J. Org. Chem.*, 1998, **63**, 9358, and references therein.
42. N. Dragoe, H. Shimotani, J. Wang, M. Iwaya, A. de Bettencourt-Dias, A.L. Balch and K. Kitazawa, *J. Am. Chem. Soc.*, 2001, **123**, 1294.
43. A.L. Balch, D.A. Costa, R. Fawcett and K. Winkler, *J. Phys. Chem.*, 1996, **100**, 4823.
44. N. Dragoe, H. Shimotani, M. Hayashi, K. Saigo, A. de Bettencourt-Dias, A.L. Balch, Y. Miyake, Y. Achiba and K. Kitazawa, *J. Org. Chem.*, 2000, **65**, 3269.
45. K. Komatsu, K. Fujiwara and Y. Murata, *Chem. Commun.*, 2000, 1583.

46. T. Suzuki, Q. Li, K.C. Khemani and F. Wudl, *J. Am. Chem. Soc.*, 1992, **114**, 7300.
47. K. Komatsu, N. Takimoto, Y. Murata, T.S.M. Wan and T. Wong, *Tetrahedron Letters*, 1996, **37**, 6153.
48. P. Timmerman, L.E. Witschel., F. Diederich, C. Boudon, J.-P. Gisselbrecht and M. Gross, *Helv. Chim. Acta*, 1996, **79**, 6.
49. K. Lee, H. Song, B. Kim, J.T. Park and M.-G. Choi, *J. Am. Chem. Soc.*, 2002, **124**, 2872.
50. (a) C.G. Pierpont and C.W. Lange, *Progr. Inorg. Chem.*, 1994, **41**, 331, and references therein; (b) A.M. Barthram, Z.R. Reeves, J.C. Jeffery and M.D. Ward, *J. Chem. Soc., Dalton Trans.*, 2000, 3162, and references therein; (c) A.K. Ghosh, S.-M. Peng, R.L. Paul, M.D. Ward and S. Goswami, *J. Chem. Soc., Dalton Trans.*, 2001, 336, and references therein.
51. (a) G.A. Abakumov, V.K. Cherkasov, M.P. Bubnov, O.G. Ellert, Y.V. Rakitin, L.N. Zakharov, Y.T. Struchkov and Y.N. Safyanov, *Izv. Akad. Nauk. SSSR. Ser. Khim.*, 1992, 2315; (b) S.-P. Huang, K.J. Franz, M.M. Olmstead and R.H. Fish, *Inorg. Chem.*, 1995, **34**, 2820; (c) C. Brückner, D.L. Caulder and K.N. Raymond, *Inorg. Chem.*, 1998, **37**, 6759.
52. G.A. Fox and C.G. Pierpont, *Inorg. Chem.*, 1992, **31**, 3718.
53. R.M. Buchanan, B.J. Fitzgerald and C.G. Pierpont, *Inorg. Chem.*, 1979, **18**, 3439.
54. S.R. Sofen, D.C. Ware, S.R. Cooper and K.N. Raymond, *Inorg. Chem.*, 1979, **18**, 234.
55. H.H. Downs, R.M. Buchanan and C.G. Pierpont, *Inorg. Chem.*, 1979, **18**, 1736.
56. C.G. Pierpont and H.H. Downs, *J. Am. Chem. Soc.*, 1976, **98**, 4834.
57. H.-C. Chang, H. Miyasaka and S. Kitagawa, *Inorg. Chem.*, 2001, **40**, 146.
58. (a) J.R. Hartman, B.M. Foxman and S.R. Cooper, *Inorg. Chem.*, 1984, **23**, 1381; (b) D.-H. Chin, D.T. Sawyer, W.P. Schaefer and C.J. Simmons, *Inorg. Chem.*, 1983, **22**, 752.
59. A.S. Attia and C.G. Pierpont, *Inorg. Chem.*, 1998, **37**, 3051.
60. S.I. Gorelski, E.S. Dodsworth, A.B.P. Lever and A.A. Vleek, *Coord. Chem. Rev.*, 1988, **174**, 469.
61. A. Mederos, S. Domínguez, R. Hernández-Molina, J. Sanchiz and F. Brito, *Coord. Chem. Rev.*, 1999, **193–195**, 913.
62. A.L. Balch and R.H. Holm, *J. Am. Chem. Soc.*, 1966, **88**, 5201.
63. G.S. Hall and R.H. Soderberg, *Inorg. Chem.*, 1968, **7**, 2300.
64. S. Peng, C. Chen, D. Liaw, C. Chen and Y. Wang, *Inorg. Chim. Acta*, 1980, **101**, L31.
65. H. Cheng and S. Peng, *Inorg. Chim. Acta*, 1990, **169**, 23.
66. L.F. Warren, *Inorg. Chem.*, 1977, **16**, 2814.

67. A.A. Danopoulos, A.C.C. Wong, G. Wilkinson, M.B. Hursthouse and B. Hussain, *J. Chem. Soc., Dalton Trans.*, 1990, 315.
68. J.A. McCleverty, *Prog. Inorg. Chem.*, 1968, **10**, 49.
69. (a) P. Cassoux, *Coord. Chem. Rev.*, 1999, **186**, 213; (b) E. Canadell, *Coord. Chem. Rev.*, 1999, **186**, 629; (c) N. Robertson and L. Cronin, *Coord. Chem. Rev.*, 2002, **227**, 93.
70. B.S. Lim, D.V. Fomitchev and R.H. Holm, *Inorg. Chem.*, 2001, **40**, 4257.
71. D. Sellmann, H. Binder, D. Häußinger, F.W. Heinemann and J. Sutter, *Inorg. Chim. Acta*, 2000, **300–302**, 829.
72. P. Zanello and E. Grigiotti, in *New Trends in Molecular Electrochemistry*, A.J.L. Pombeiro and C. Amatore, eds, FontisMedia, SA and Marcel Dekker Inc., 2003, in press.
73. C. Handrosch, R. Dinnebier, G. Bondarenko, E. Bothe, F. Heinemann and H. Kisch, *Eur. J. Inorg. Chem.*, 1999, 1259.
74. F. Matsuda, H. Tamura and G. Matsubayashi, *Inorg. Chim. Acta*, 1999, **295**, 239.
75. G. Matsubayashi, K. Takahashi and T. Tanaka, *J. Chem. Soc., Dalton Trans.*, 1988, 967.
76. W.T.A. Harrison, R.A. Howie, J.L. Wardell, S.M.S.V. Wardell, N.M. Comerlato, L.A.S. Costa, A.C. Silvino, A.I. de Oliveira and R.M. Silva, *Polyhedron*, 2000, **19**, 821.
77. C.P. Rao, J.R. Dorfman and R.H. Holm, *Inorg. Chem.*, 1986, **25**, 428.
78. G. Schmauch, F. Knoch and H. Kish, *Chem. Ber.*, 1995, **128**, 303.
79. C. Faulmann, A. Errami, B. Donnadieu, I. Malfant, J.-P. Legros, C. Bowlas, P. Cassoux, C. Rovira and E. Canadell, *Inorg. Chem.*, 1996, **35**, 3856.
80. L. Valade, J.-P. Legros, M. Bosseau, P. Cassoux, M. Garbauskas and L.V. Interrante, *J. Chem. Soc., Dalton Trans.*, 1985, 783.
81. G. Matsubayashi, K. Douki, H. Tamura, M. Nakano and W. Mori, *Inorg. Chem.*, 1993, **32**, 5990.
82. A. Cervilla, E. Llopis, D. Marco and F. Pérez, *Inorg. Chem.*, 2001, **40**, 6525.
83. M. Cowie and M.J. Bennett, *Inorg. Chem.*, 1973, **15**, 1584.
84. F. Bigoli, P. Deplano, F.A. Devillanova, V. Lippolis, P.J. Lukes, M.L. Mercuri, M.A. Pellinghelli and E.F. Trogu, *J. Chem. Soc., Chem. Commun.*, 1995, 371.
85. F. Bigoli, P. Deplano, F.A. Devillanova, J.R. Ferraro, V. Lippolis, P.J. Lukes, M.L. Mercuri, M.A. Pellinghelli, E.F. Trogu and J.M. Williams, *Inorg. Chem.*, 1997, **36**, 1218.
86. F. Bigoli, P. Deplano, M.L. Mercuri, M.A. Pellinghelli, G. Pintus, E.F. Trogu, G. Zonnedda, H.H. Wang and J.M. Williams, *Inorg. Chim. Acta*, 1998, **273**, 175.

87. M. Arca, F. Demartin, F.A. Devillanova, A. Garau, F. Isaia, F. Lelj, V. Lippolis, S. Pedraglio and G. Verani, *J. Chem. Soc., Dalton Trans.*, 1998, 3731.
88. P. Zanello and F.A. Devillanova, work in progress.
89. (a) G. Feher, J.P. Allen, M.Y. Okamura and D.C. Rees, *Nature*, 1989, **339**, 111; (b) J. Deisenhofer and H. Michel, *Science*, 1989, **245**, 1463; (c) U. Ermler, G. Fritzsch, S.K. Buchanan and H. Michel, *Structure*, 1994, **2**, 925; (d) J. Deisenhofer, O. Epp, I. Sinning and H. Michel, *J. Mol. Biol.*, 1995, **246**, 429.
90. K.M. Kadish, *Progr. Inorg. Chem.*, 1986, **34**, 435.
91. W.R. Scheidt, M.E. Kastner and K. Hatano, *Inorg. Chem.*, 1978, **17**, 706.
92. W.R. Scheidt, J.U. Mondal, C.W. Eigenbrot, A. Adler, L.J. Radonovich and J.L. Hoard, *Inorg. Chem.*, 1986, **25**, 795.
93. A.J. Golder, D.C. Povey, J. Silver and Q.A.A. Jassim, *Acta Cryst.*, 1990, **C46**, 1210.
94. J.G. Lanese and G.S. Wilson, *J. Electrochem. Soc.*, 1972, **119**, 1039.
95. K.M. Kadish and M.M. Morrison, *Bioinorg. Chem.*, 1977, **7**, 107.
96. P. Zanello, unpublished results.
97. L.D. Spaulding, P.G. Eller, J.A. Bertrand and R.H. Felton, *J. Am. Chem. Soc.*, 1974, **96**, 982.
98. D. Dolphin, R.H. Felton, D.C. Borg and J. Fajer, *J. Am. Chem. Soc.*, 1970, **92**, 743.
99. K.M. Barkigia, M.W. Renner, H. Xie, K.M. Smith and J. Fajer, *J. Am. Chem. Soc.*, 1993, **115**, 7894.
100. (a) Meyer, E.F., Jr., *Acta Cryst.*, 1972, **B28**, 2162; (b) T.D. Brennan, W.R. Scheidt and J.A. Shelnutt, *J. Am. Chem. Soc.*, 1988, **110**, 3919.
101. K.M. Barkigia, M.W. Renner and J. Fajer, *J. Phys. Chem.*, 1997, **B101**, 8398.
102. (a) L.D. Sparks, C.J. Medforth, M.-S. Park, J.R. Chamberlain, M.R. Ondrias, M.O. Senge, K.M. Smith and J.S. Shelnutt, *J. Am. Chem. Soc.*, 1993, **115**, 581; (b) M.W. Renner, K.M. Barkigia, Y. Zhang, C.J. Medforth, K.M. Smith and J. Fajer, *J. Am. Chem. Soc.*, 1994, **116**, 8582.
103. A.B.P. Lever, E.R. Milaeva and G. Speier, in *The Phthalocyanines, Properties and Applications*, C.C. Leznoff and A.B.P. Lever, eds, VCH, New York, 1993, Vol. 3, pp. 1–69.
104. W.R. Scheidt and W. Dow, *J. Am. Chem. Soc.*, 1977, **99**, 1101.
105. L.A. Bottomley and W.J.H. Chiou, *J. Electroanal. Chem.*, 1986, **198**, 331, and references therein.
106. (a) A.G. Montalban, S.J. Lange, L.S. Beall, N.S. Mani, D.J. Williams, A.J.P. White, A.G.M. Barrett and B.M. Hoffman, *J. Org. Chem.*, 1997, **62**,

- 9284; (b) A.S. Cook, D.B.G. Williams, A.J.P. White, D.J. Williams, S.J. Lange, A.J.P. White, A.G.M. Barrett and B.M. Hoffman, *Angew. Chem. Int. Ed. Engl.*, 1997, **36**, 760; (c) H. Nie, A.G.M. Barrett and B.M. Hoffman, *J. Org. Chem.*, 1999, **64**, 6791.
107. (a) P.I. Clemenson, *Coord. Chem. Rev.*, 1990, **106**, 171; (b) W. Kaim and M. Moschersch, *Coord. Chem. Rev.*, 1994, **129**, 157.
108. A.M. Bond and R.L. Martin, *Coord. Chem. Rev.*, 1984, **54**, 23.
109. Y. Chen, F.-T. Lin and R.E. Shepherd, *Inorg. Chem.*, 1999, **38**, 973 and references therein.
110. (a) C. Arana, S. Yan, M. Keshavarz-K., K.T. Potts and H.D. Abruna, *Inorg. Chem.*, 1992, **31**, 3680; (b) Bas de Bruin, E. Bill, E. Bothe, T. Weyhermüller and K. Wieghardt, *Inorg. Chem.*, 2000, **39**, 2936.
111. F.A. Cotton, L.M. Daniels, P. Huang and C.A. Murillo, *Inorg. Chem.*, 2002, **41**, 317

CHAPTER 7

Electrochemically Induced Structural Modifications

As often underlined, one of the main targets of the electrochemical investigations on inorganic compounds is to ascertain their stability upon addition or removal of electrons. However, should the compounds undergo important molecular reorganizations as a consequence of such electron transfer processes, it is also important to ascertain the nature of such redox changes.

In this light we will now consider some examples of electrochemically detectable molecular reorganizations induced by electron transfer processes, which can be chemically more appealing than the simple variations of bond distances/angles discussed up to now.

1 GEOMETRICAL ISOMERIZATION

As happens for other physico-chemical techniques, one must first ask if an electrochemical investigation is able to distinguish geometric isomers of the type *cis/trans* or *fac/mer* metal complexes. In principle, this is possible since, as mentioned previously, the redox potential of an electron transfer is influenced also by steric effects. For instance, we have seen in Chapter 5 that some octahedral complexes of the scorpionid ‘diammac’ display different electrochemical responses, depending on whether the two outer amino groups assume *cis* or *trans* arrangements. One must keep in mind, however, that the differences in the electrochemical response of isomeric complexes can sometimes be quite small, so may escape a first examination.

The ability of electrochemistry to discriminate *cis* from *trans* isomers is exemplified in Figure 1, which shows the cyclic voltammetric responses exhibited by the *cis* and *trans* isomers of $[\text{Ru}^{\text{II}}\text{Cl}_2(\text{dppb})]$

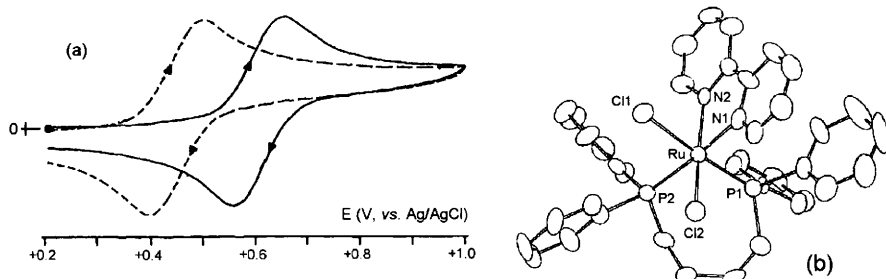


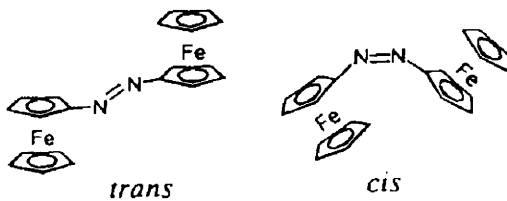
Figure 1 (a) Cyclic voltammograms recorded at a platinum electrode in CH_2Cl_2 solutions of $[\text{RuCl}_2(\text{dppb})(\text{bipy})]$: (—) cis isomer; (---) trans isomer. Scan rate 0.1 V s^{-1} . (b) X-Ray structure of cis- $[\text{RuCl}_2(\text{dppb})(\text{bipy})]$: $\text{Ru}-\text{Cl}1 = 2.48 \text{ \AA}$; $\text{Ru}-\text{Cl}2 = 2.43 \text{ \AA}$; $\text{Ru}-\text{P}1 = 2.28 \text{ \AA}$; $\text{Ru}-\text{P}2 = 2.33 \text{ \AA}$; $\text{Ru}-\text{N}1 = 2.09 \text{ \AA}$; $\text{Ru}-\text{N}2 = 2.10 \text{ \AA}$

(bipy)] [dppb = 1,4-bis (diphenylphosphino)butane; bipy = 2,2'-bipyridine], together with the octahedral geometry of the *cis* isomer.¹

Both isomers give rise to the reversible $\text{Ru}^{\text{II}}/\text{Ru}^{\text{III}}$ oxidation, but the *cis* form oxidizes at $E^{\circ'} = +0.62 \text{ V}$ (vs. Ag/AgCl), whereas the *trans* form oxidizes at $E^{\circ'} = +0.45 \text{ V}$.

Examples concerned with the simple occurrence of shifts in redox potentials for *cis/trans* complexes are not too rare. This is the case of the $\text{Fe}(\text{III})/\text{Fe}(\text{II})$ reduction of *trans/cis*- $[\text{Fe}^{\text{III}}(\text{cyclam})(\text{N}_3)_2]^+$ ($E^{\circ'} = -0.76 \text{ V}$, vs. Fc/Fc^+ , in the *trans* complex; $E^{\circ'} = -0.62 \text{ V}$, in the *cis* complex)^{2a} and the $\text{Mo}(\text{V})/\text{Mo}(\text{IV})$ reduction of *trans/cis*- $[\text{LMoOCl}_2]$ [$\text{L} = 3\text{-tert-butyl-2-hydroxy-5-methylphenyl}](\text{bis}(3,5\text{-dimethylpyrazolyl})\text{methane monoanion})$ ($E^{\circ'} = -0.93 \text{ V}$, vs. Fc/Fc^+ , in the *trans* complex; $E^{\circ'} = -1.15 \text{ V}$, in the *cis* complex).^{2b}

A further interesting example is offered by the *trans*- and *cis*-azo-bridged diferrocenyl couple illustrated in Scheme 1.³



Scheme 1

As illustrated in Figure 2a, *trans*- $[\text{Fc}-\text{N}=\text{N}-\text{Fc}]$ [$\text{Fc}=(\eta^5\text{-C}_5\text{H}_5)\text{Fe}(\eta^5\text{-C}_5\text{H}_4)$]^{3a} exhibits in benzonitrile solution two reversible, one-electron oxidations ($E^{\circ'} = +0.29 \text{ V}$ and $+0.50 \text{ V}$, vs. Ag/Ag^+ , respectively).^{3b}

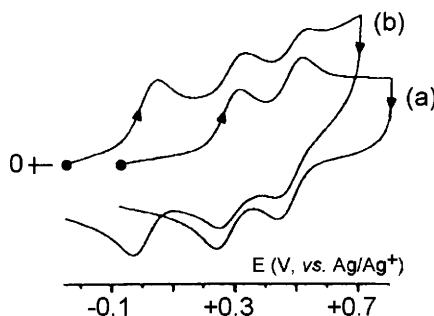
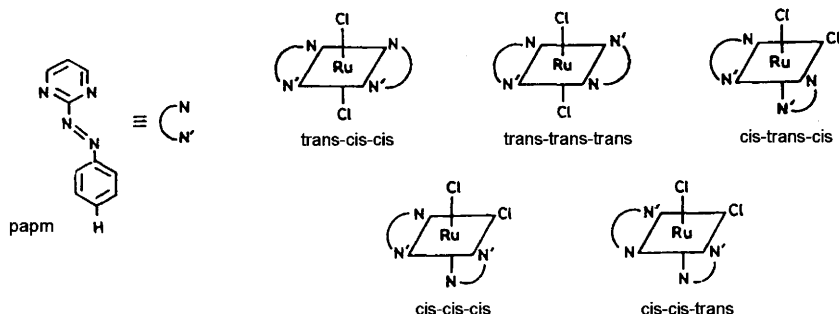


Figure 2 Cyclic voltammograms recorded at a glassy carbon electrode in PhCN solutions of: (a) trans-[Fc—N=N—Fc]; (b) after UV-photoirradiation. Scan rate 0.1 V s^{-1}

UV-photoirradiation causes *trans*-to-*cis* isomerization and the resulting solution exhibits a new voltammetric profile, Figure 2b, in which traces of the original waves are preceded by an anodic process ($E^{\circ'} = +0.03 \text{ V}$), which has been attributed to the single-stepped two-electron oxidation of *cis*-[Fc—N=N—Fc].^{3b} This suggests that the apparent simple isomerization really involves important electronic effects in that (based on the discussions in Section 1.3, Chapter 4) one must conclude that in *trans*-[Fc—N=N—Fc] the two ferrocenyl units are interacting with each other, while in *cis*-[Fc—N=N—Fc] they do not interact.

Also very interesting is the electrochemical differentiation among the multiple isomers of the complex $[\text{Ru}^{II}(\text{papm})_2\text{Cl}_2]$ (papm = 2-(phenylazo)pyrimidine). As illustrated in Scheme 2, the complex can in principle exist in five geometrical conformations.⁴



Scheme 2

Three of the five isomers have been isolated and two have been crystallographically characterized, Figure 3.⁴

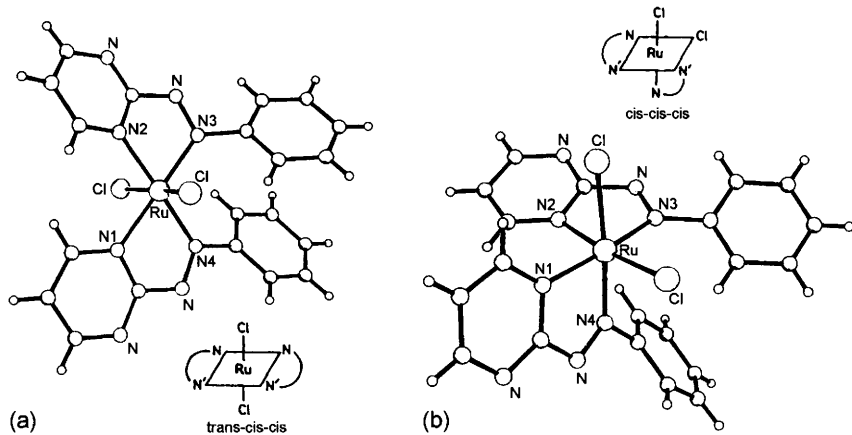


Figure 3 X-Ray structures of: (a) tcc-[Ru(papm)₂Cl₂]. Average bond lengths: Ru–Cl = 2.38 Å; Ru–N1 ≈ Ru–N2 = 2.08 Å; Ru–N3 ≈ Ru–N4 = 2.00 Å; (b) ccc-[Ru(papm)₂Cl₂]. Average bond lengths: Ru–Cl = 2.40 Å; Ru–N1 ≈ Ru–N2 = 2.04 Å; Ru–N3 = 2.01 Å; Ru–N4 1.97 Å

As illustrated in Figure 4, the three isomers undergo the $[Ru^{II}(papm)_2Cl_2]/[Ru^{III}(papm)_2Cl_2]^+$ oxidation at sufficiently different potential values ($E_{0/+}^{\circ\prime}$ (tcc) = +1.08 V; $E_{0/+}^{\circ\prime}$ (ctc) = +1.24 V; $E_{0/+}^{\circ\prime}$ (ccc) = +1.31 V).⁴

A similar behaviour holds for the geometrical isomers of the related $[Ru^{II}(pap)_2Cl_2]$ (pap = 2-(phenylazo)pyridine).⁵

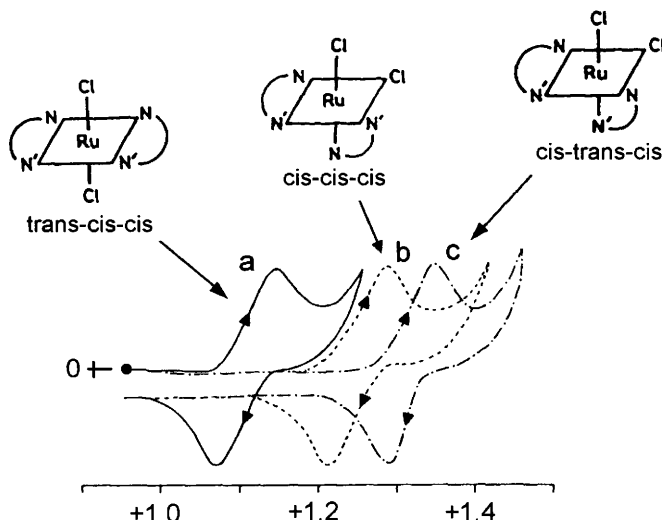


Figure 4 Cyclic voltammograms recorded at a platinum electrode on MeCN solutions of: (a) tcc-[Ru(papm)₂Cl₂]; (b) ctc-[Ru(papm)₂Cl₂]; (c) ccc-[Ru(papm)₂Cl₂]. Scan rate 0.05 V s⁻¹

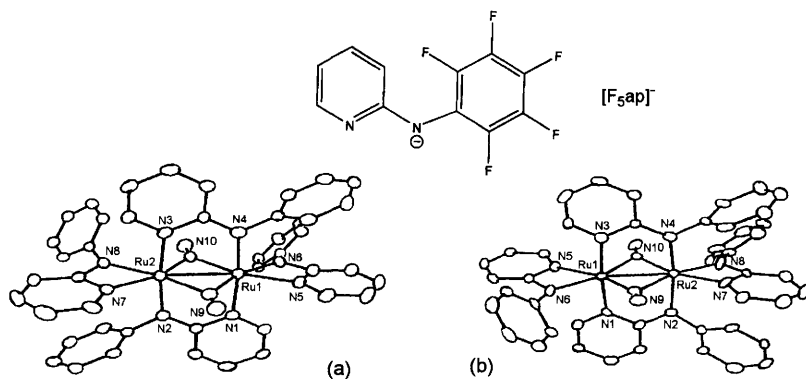


Figure 5 *X*-Ray structures of the geometric isomers of $[\text{Ru}_2(\text{Fsap})_4(\mu\text{-CN})_2]$. (a) Isomer A; (b) isomer B

Related to such type of ligands is also the behaviour of the two isomers of the diruthenium(III) complex with the (pentafluoroanilino)pyridinate anion, the molecular structures of which are illustrated in Figure 5.⁶

In isomer A each ruthenium atom is axially coordinated to one pyridine nitrogen and one aniline nitrogen; in isomer B one ruthenium atom is coordinated to two aniline nitrogens, whereas the other ruthenium atom is coordinated to two pyridine nitrogens. The Ru–Ru distance is the same (2.58 Å) in both the derivatives.

As illustrated in Figure 6, the two isomers give rise to one oxidation and two reductions, respectively.⁶

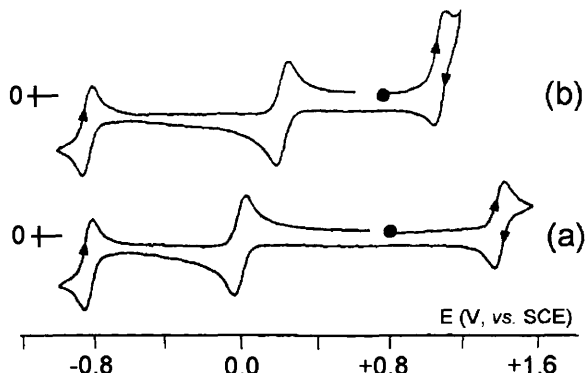


Figure 6 Cyclic voltammograms of the two isomers of $[\text{Ru}_2(\text{Fsap})_4(\mu\text{-CN})_2]$ recorded at a platinum electrode in CH_2Cl_2 solution. (a) Isomer A; (b) isomer B. Scan rate 0.1 V s^{-1}

Such processes for the two isomers occur at rather different potential values, namely:

Isomer A: $E_{\text{Ru(III)Ru(III)/Ru(III)Ru(IV)}}^{\circ'} = +1.30 \text{ V (vs. SCE)}$;

$E_{\text{Ru(III)Ru(III)/Ru(III)Ru(II)}}^{\circ'} = +0.08 \text{ V}$;

$E_{\text{Ru(III)Ru(II)/Ru(II)Ru(II)}}^{\circ'} = -0.81 \text{ V}$

Isomer B: $E_{\text{Ru(III)Ru(III)/Ru(III)Ru(IV)}}^{\circ'} = +1.10 \text{ V}$;

$E_{\text{Ru(III)Ru(III)/Ru(III)Ru(II)}}^{\circ'} = +0.22 \text{ V}$;

$E_{\text{Ru(III)Ru(II)/Ru(II)Ru(II)}}^{\circ'} = -0.82 \text{ V}$

More interesting from a dynamic viewpoint are, however, redox-induced molecular reorganizations.

One of the most illustrative examples of induced *cis* → *trans* isomerization is given by the octahedral complex *cis*-[Ru^{II}Cl₂(dppm)₂] (dppm = diphenylphosphinomethane = Ph₂PCH₂PPh₂), Figure 7a.⁷ As illustrated in Figure 7b, it undergoes in CH₂Cl₂ solution an oxidation process to the corresponding monocation *cis*-[Ru^{III}Cl₂(dppm)₂]⁺ ($E^{\circ'} = +0.79 \text{ V}$), which however is not stable and generates a secondary species that is reduced at less positive potential values ($E^{\circ'} = +0.42 \text{ V}$).⁸

As Figure 8a shows, complex *trans*-[Ru^{II}Cl₂(dppm)₂],⁷ undergoes a reversible Ru^{II}/Ru^{III} oxidation at potential values which are coincident with those of the above mentioned secondary species produced in the oxidation of *cis*-[Ru^{II}Cl₂(dppm)₂].⁸

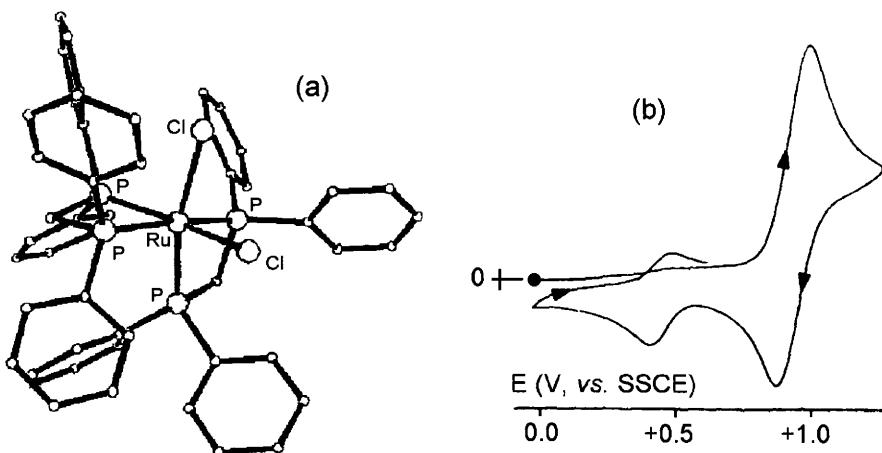


Figure 7 (a) X-Ray structure of *cis*-[Ru^{II}Cl₂(dppm)₂]. Average bond lengths: Ru-P = 2.32 Å; Ru-Cl = 2.44 Å. (b) Cyclic voltammogram recorded at a platinum electrode in a CH₂Cl₂ solution of *cis*-[Ru^{II}Cl₂(dppm)₂]

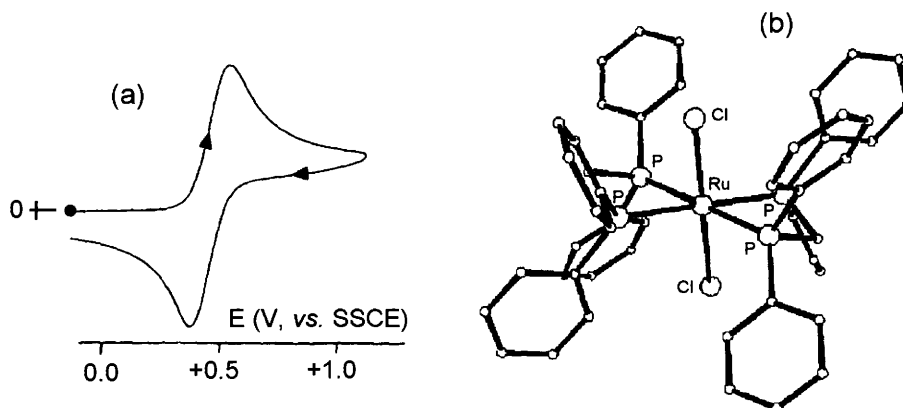


Figure 8 (a) Cyclic voltammogram recorded at a platinum electrode in a CH_2Cl_2 solution of $\text{trans-}[\text{Ru}^{\text{II}}\text{Cl}_2(\text{dppm})_2]$. (b) X-Ray structure of $\text{trans-}[\text{Ru}^{\text{II}}\text{Cl}_2(\text{dppm})_2]$. Average bond lengths: $\text{Ru-P} = 2.35 \text{ \AA}$; $\text{Ru-Cl} = 2.43 \text{ \AA}$

On the basis of the $i_{\text{pc}}/i_{\text{pa}}$ ratio of the primary oxidation $\text{cis-}[\text{Ru}^{\text{II}}\text{Cl}_2(\text{dppm})_2]/\text{cis-}[\text{Ru}^{\text{III}}\text{Cl}_2(\text{dppm})_2]^+$, one can calculate that the monocation $\text{cis-}[\text{Ru}^{\text{III}}\text{Cl}_2(\text{dppm})_2]^+$ has a half-life ($t_{1/2}$) of approximately 6 s before being isomerized to the more stable $\text{trans-}[\text{Ru}^{\text{III}}\text{Cl}_2(\text{dppm})_2]^+$.

An example of electrochemically induced $\text{trans} \rightarrow \text{cis}$ isomerization is given by the macrocyclic complex $\text{trans-}[\text{Mn}^{\text{III}}(\text{cyclam})\text{Cl}_2]^+$, the molecular structure of which is illustrated in Figure 9.⁹

As shown in Figure 10a, the cyclic voltammogram of the monocation displays an irreversible $\text{Mn}^{\text{III}} \rightarrow \text{Mn}^{\text{II}}$ reduction ($E_p = -0.17 \text{ V, vs. SCE}$), which in the reverse can generate a new peak-system at positive potential values ($E^\circ' = +0.30 \text{ V}$). Based on the electrochemical behaviour

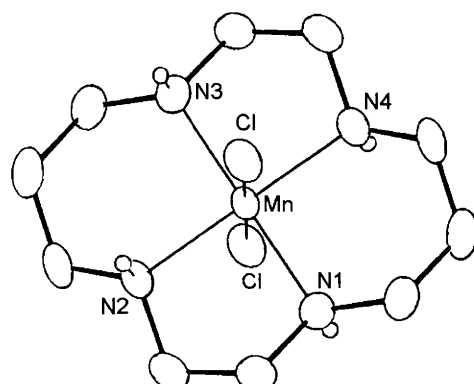


Figure 9 X-Ray structure of $\text{trans-}[\text{Mn}(\text{cyclam})\text{Cl}_2]^+$. $\text{Mn-N} = 2.04 \text{ \AA}$; $\text{Mn-Cl} = 2.53 \text{ \AA}$

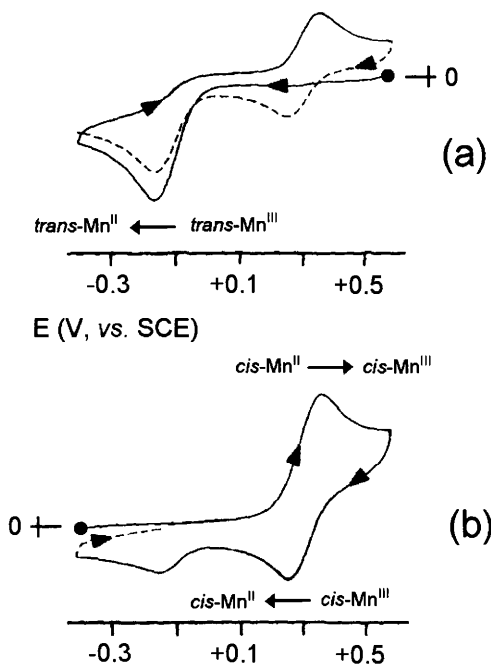
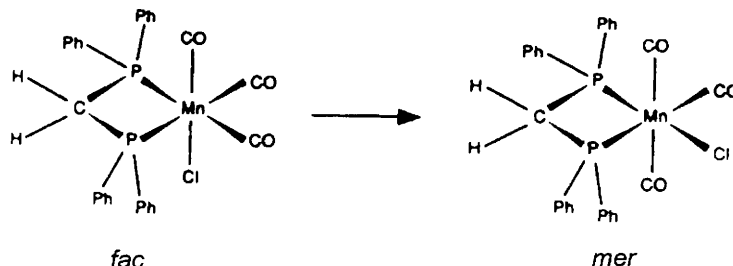


Figure 10 Cyclic voltammograms recorded at a glassy carbon electrode in *dmsol* solutions of: (a) *trans*-[Mn^{III}(cyclam)Cl₂]⁺; (b) *cis*-[Mn^{II}(cyclam)Cl₂]. Scan rate 0.1 V s⁻¹

of *cis*-[Mn^{II}(cyclam)Cl₂], Figure 10b, such new peak-system is assigned to the (partially chemically reversible) oxidation of the reorganized *cis*-[Mn^{II}(cyclam)Cl₂].⁹

This means that in the Mn(III) oxidation state the more stable form is the *trans* isomer, whereas in the Mn(II) oxidation state the more stable form is the *cis* isomer, and both the isomers convert to their respective stable forms upon changing oxidation state.



Scheme 3

As far as the *fac/mer* isomerization is concerned, the typical redox-induced conversion is that illustrated in Scheme 3 for complex $[\text{Mn}^{\text{I}}(\text{CO})_3(\text{dppm})\text{Cl}]$ ($\text{dppm} = \text{Ph}_2\text{PCH}_2\text{PPh}_2$).¹⁰

Figure 11 shows the cyclic voltammograms exhibited by *fac*- $[\text{Mn}^{\text{I}}(\text{CO})_3(\text{dppm})\text{Cl}]$ in acetonitrile solution at different temperatures.^{10a}

At room temperature it undergoes one-electron oxidation to the corresponding *fac*- Mn^{II} species through a partially chemically reversible electron transfer (peak I; $E^{\circ'} = +1.44 \text{ V}$, vs. Ag/AgCl), which in turn affords in the reverse scan a new peak-system at less positive potential values having some features of chemical reversibility too (peaks II/III; $E^{\circ'} = +0.98 \text{ V}$, vs. Ag/AgCl), Figure 11a. On the other hand, Figure 11b shows that at low temperature (-35°C), the chemical complication accompanying the *fac*- Mn^{I} /*fac*- Mn^{II} process is prevented.^{10a}

As illustrated in Figure 12, *mer*- $[\text{Mn}^{\text{I}}(\text{CO})_3(\text{dppm})\text{Cl}]$ undergoes oxidation just at the potential of the new peak-system II/III in Figure 11a.^{10a}

It is hence evident that the following electrode mechanism holds:

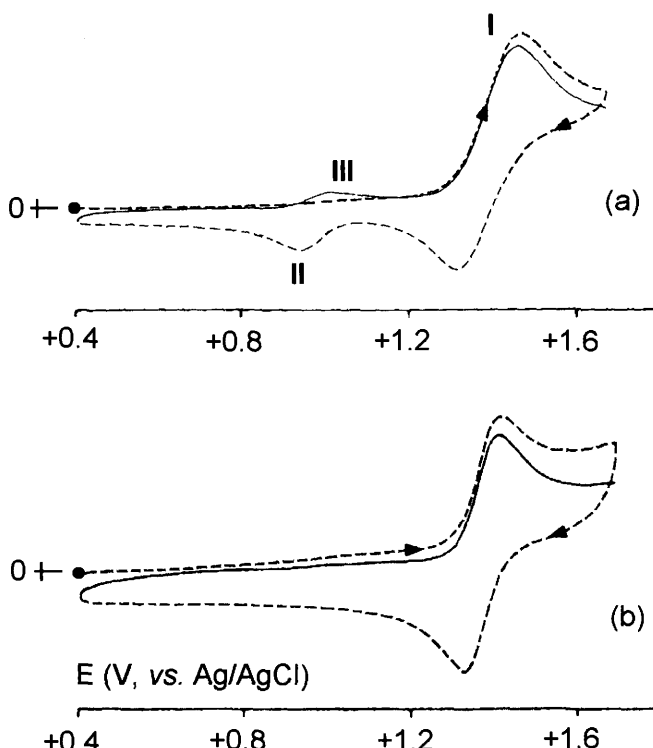


Figure 11 Cyclic voltammograms recorded at a platinum electrode in a MeCN solution of *fac*- $[\text{Mn}^{\text{I}}(\text{CO})_3(\text{dppm})\text{Cl}]$. (a) $T = 295 \text{ K}$; (b) 238 K . Scan rate 0.5 V s^{-1} . (---) First scan; (—) second scan

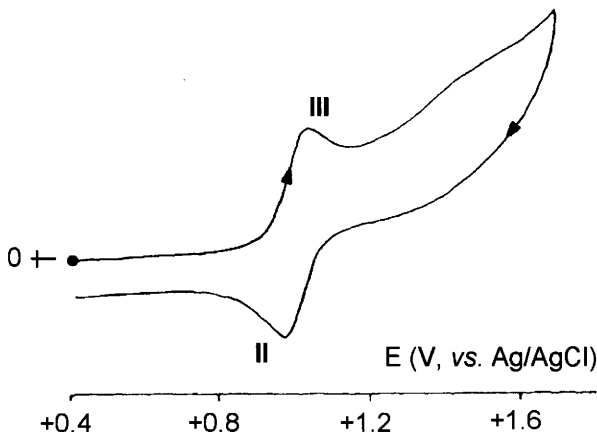
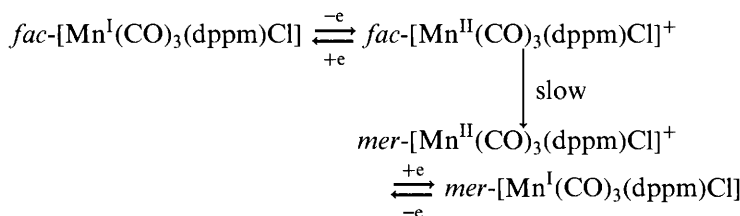
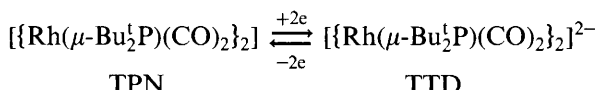


Figure 12 Cyclic voltammogram recorded at a platinum electrode in a MeCN solution of mer- $\text{Mn}^{\text{II}}(\text{CO})_3(\text{dppm})\text{Cl}$. $T = 295 \text{ K}$. Scan rate 0.5 V s^{-1}



A somewhat more complicated isomerization path is involved in the redox changes accompanying the following process:



In the neutral species $\{[\text{Rh}(\mu\text{-Bu}_2^t\text{P})(\text{CO})_2]\}_2$ the Rh1 atom has a *tetrahedral* geometry, whereas the Rh2 atom has a *planar* geometry, with respect to the Rh_2P_2 , plane (the TPN label arises from the *tetrahedral–planar* geometry of the two rhodium atoms in the *neutral* complex), Figure 13.¹¹

As shown in Figure 14 the neutral derivative undergoes a reduction process (peak I), which in the backscan generates a species which undergoes an oxidation/reduction process (peaks II/III, respectively) at less negative potential values.¹²

Exhaustive electrolysis consumes two electrons *per* molecule and generates the dianion $[\{\text{Rh}(\mu\text{-Bu}^t_2\text{P})(\text{CO})_2\}_2]^{2-}$, the molecular structure of which is shown in Figure 15.¹²

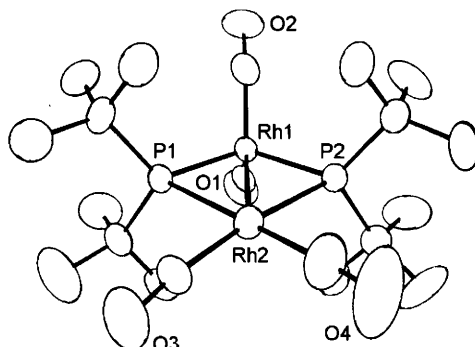


Figure 13 X-Ray structure of $\left[\{Rh(\mu\text{-}Bu'_2P)(CO)_2\}_2\right]$. Average bond lengths: $Rh-Rh = 2.76 \text{ \AA}$; $Rh1-P = 2.24 \text{ \AA}$; $Rh2-P = 2.46 \text{ \AA}$

Both the rhodium atoms assume a *tetrahedral* geometry with respect to the Rh_2P_2 plane (the TTD label derives from the *tetrahedral-tetrahedral* geometry of the two rhodium atoms in the dianion). On this basis, the overall electrode process involves the ECE mechanism illustrated in Scheme 4, where: TPA = tetrahedral-planar monoanion, TTA = tetrahedral-tetrahedral monoanion.

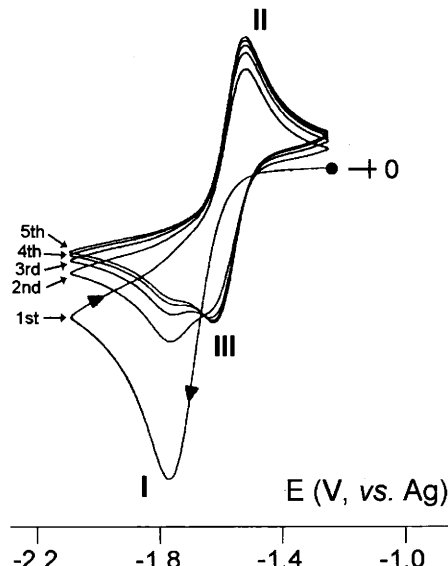


Figure 14 Multiscan cyclic voltammograms recorded at a platinum electrode in a THF solution of $\left[\{Rh(\mu\text{-}Bu'_2P)(CO)_2\}_2\right]$. Scan rate 0.2 V s^{-1}

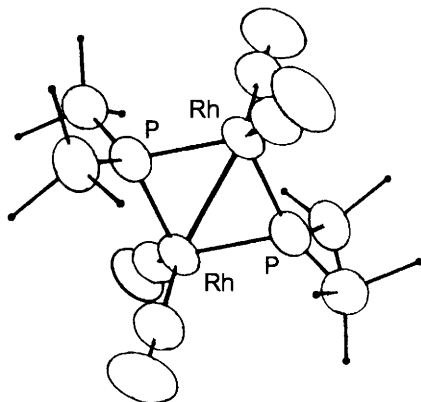
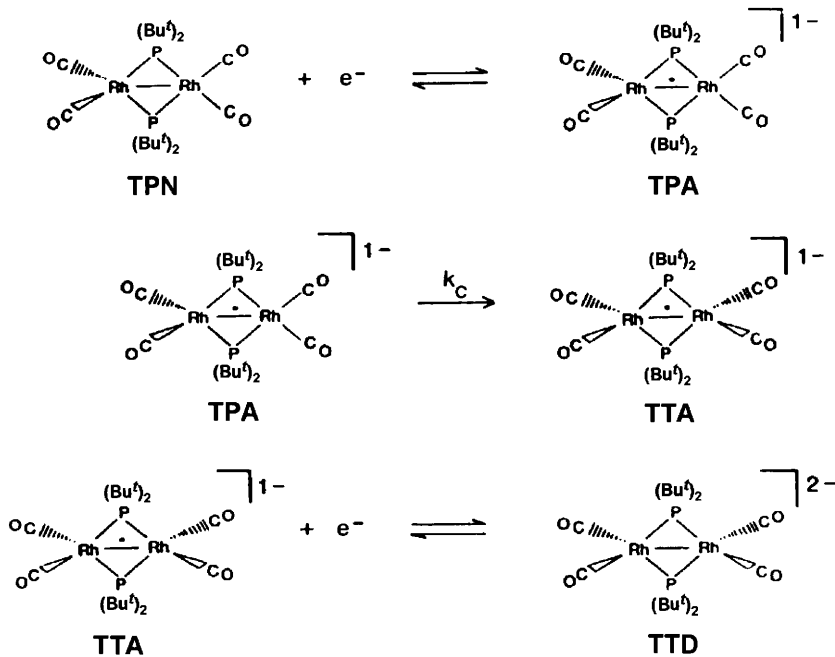


Figure 15 X-Ray structure of the dianion $[\{Rh(\mu\text{-}Bu'_2P)(CO)_2\}_2]^{2-}$. Average bond lengths: $Rh-Rh = 2.84 \text{ \AA}$; $Rh-P = 2.32 \text{ \AA}$

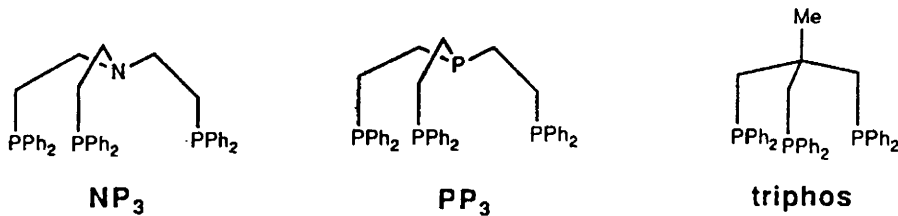


Scheme 4

2 SOME EXAMPLES OF MOLECULAR REORGANISATIONS INDUCED BY DEPROTONATION OR DEHYDROGENATION

In order to illustrate some redox-induced molecular rearrangements a little more complicated than simple isomerizations we will consider

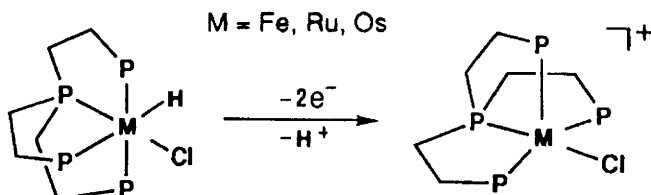
the electron transfer reactivity of a few metal complexes with the tripodal phosphines NP_3 , PP_3 and triphos represented in Scheme 5.



Scheme 5

As has already been seen for a few iron¹³ and nickel¹⁴ examples, metal complexes of these ligands generally exhibit chemically reversible redox processes, allowing, in some cases, the central metal to accede unusual oxidation states. However, sometimes these complexes undergo well-defined molecular rearrangements following irreversible redox processes.¹⁵

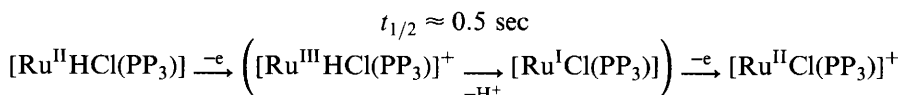
For example, conversion of the hexacoordinate (octahedral) derivatives $[\text{M}^{\text{II}}\text{HCl}(\text{PP}_3)]$ to the corresponding deprotonated pentacoordinate (trigonal-bipyramidal or square pyramidal) derivatives $[\text{M}^{\text{II}}\text{Cl}(\text{PP}_3)]^+$ ($\text{M} = \text{Fe}, \text{Ru}, \text{Os}$), Scheme 6, follows electrode mechanisms that are more or less complicated depending upon the nature of the central metal.¹⁶



Scheme 6

As a typical example, we consider the behaviour of the chloro-hydride complex $[\text{RuHCl}(\text{PP}_3)]$, which displays a rather simple conversion mechanism. In fact, Figure 16a shows that it undergoes an irreversible two-electron oxidation that generates, on the reverse scan, a voltammetric profile identical to that observed for the chloro monocation $[\text{RuCl}(\text{PP}_3)]^+$, Figure 16b.

This indicates the occurrence of the following deprotonation process:



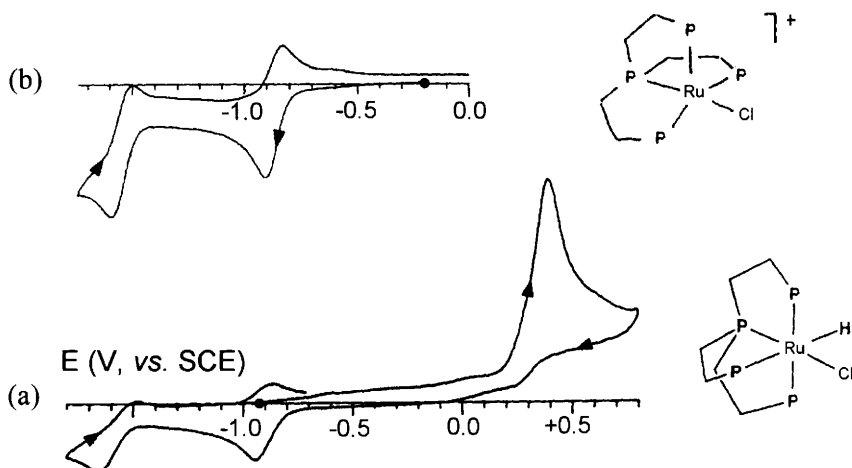
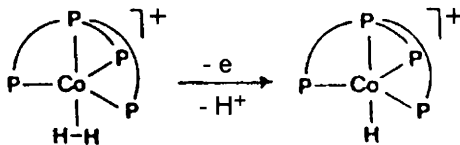


Figure 16 Cyclic voltammograms recorded at a platinum electrode in THF solutions of:
 (a) $[Ru(H)Cl(PP_3)]$; scan rate 0.5 V s^{-1} ; (b) $[RuCl(PP_3)][BPh_4]$; scan rate 0.02 V s^{-1}

Figure 17 illustrates the molecular structure of the two stable derivatives.

The octahedral/trigonal-bipyramidal reorganization induced by deprotonation leads to shortening of the Ru–Cl bond (from 2.52 \AA to 2.43 \AA), whereas the Ru–P distance (*trans* to Ru–Cl) elongates (from 2.19 \AA to 2.24 \AA).

A deprotonation process is also involved in the anodic conversion of the ‘non-classical’[#] dihydrogen-Co(I) complex $[Co(H_2)(PP_3)]^+$ to the ‘classical’ Co(II)-hydride $[CoH(PP_3)]^+$, Scheme 7.



Scheme 7

The molecular structures of the two complexes are shown in Figure 18.^{17,18}

Figure 19 shows that the irreversible (one-electron) oxidation of $[Co(H_2)(PP_3)]^+$ generates $[CoH(PP_3)]^+$. In fact, the voltammetric profile which appears in the reverse scan of Figure 19a is perfectly complementary to that of the oxidation of the neutral complex $[CoH(PP_3)]$, Figure 19b.

[#] The meaning of the term ‘non-classical’ will be discussed in Chapter 9, Section 3.

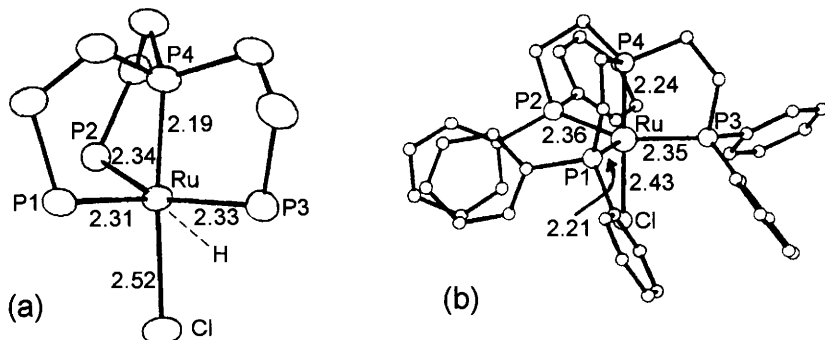


Figure 17 X-Ray structures of: (a) $[RuHCl(PP_3)]$; (b) $[RuCl(PP_3)]^+$, together with significant bond lengths

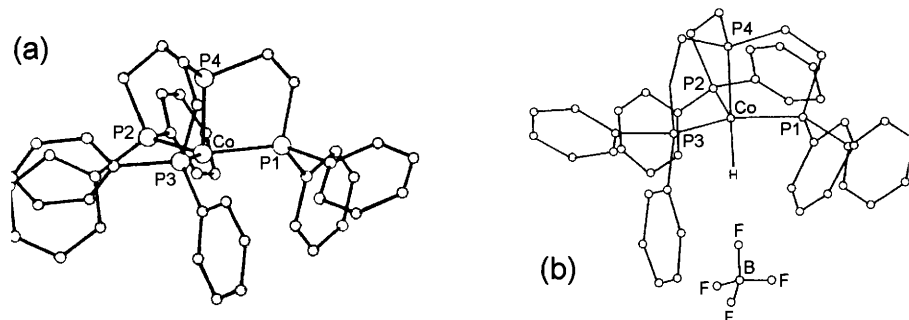


Figure 18 X-ray structures of: (a) $[Co(H_2)(PP_3)]^+$. Bond lengths: $Co-P_{(equatorial)} = 2.20 \text{ \AA}$; $Co-P_{(apical)} = 2.12 \text{ \AA}$. (b) $[CoH(PP_3)]^+$. Bond lengths: $Co-P_{(equatorial)} = 2.18 \text{ \AA}$; $Co-P_{(apical)} = 2.16 \text{ \AA}$

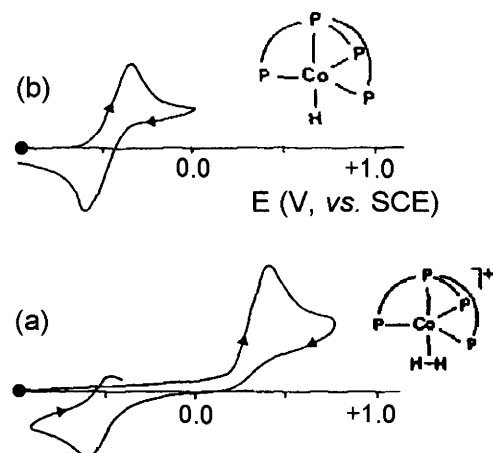


Figure 19 Cyclic voltammograms recorded at a platinum electrode in THF solutions of: (a) $[Co(H_2)(PP_3)]^+$; (b) $[CoH(PP_3)]^+$. Scan rate 0.2 V s^{-1}

Abstraction of hydrogen atoms (either as deprotonation or release of dihydrogen) is involved in the electrochemically induced conversion of the vinylidene complex $[\text{Rh}\{\text{C}=\text{CH}(\text{Ph})\}(\text{NP}_3)]^+$ to the acetylide derivatives $[\text{Rh}(\text{C}\equiv\text{CPh})(\text{NP}_3)]^{n+}$ ($n = 0, 2$). As illustrated in Figure 20, the voltammetric backscans of both the (two-electron) oxidation and the (one-electron) reduction of $[\text{Rh}\{\text{C}=\text{CH}(\text{Ph})\}(\text{NP}_3)]^+$ clearly indicate that $[\text{Rh}(\text{C}\equiv\text{CPh})(\text{NP}_3)]^{2+}$ and $[\text{Rh}(\text{C}\equiv\text{CPh})(\text{NP}_3)]$ are formed, respectively, according to the electrode mechanism indicated in Scheme 8. It is noted that there is the intermediate formation of the stable complex $[\text{Rh}(\text{C}\equiv\text{CPh})(\text{NP}_3)]^+$.

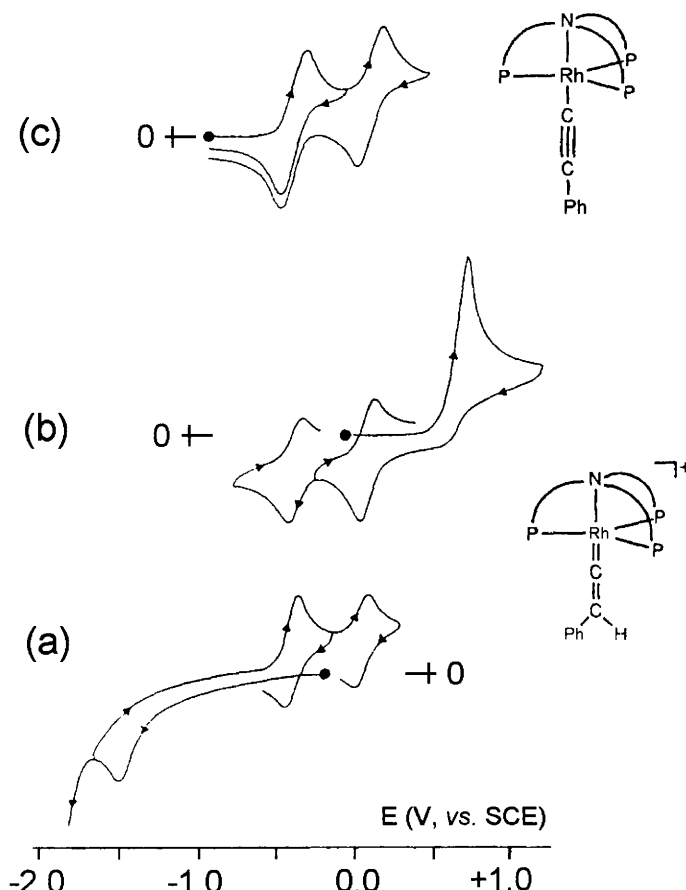
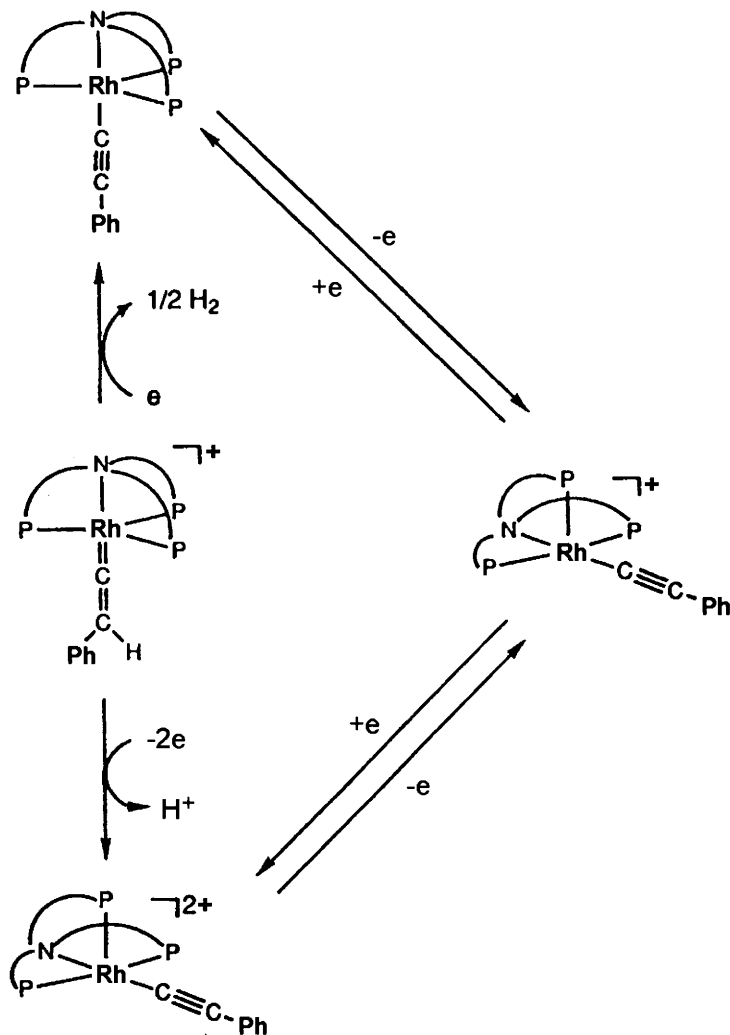


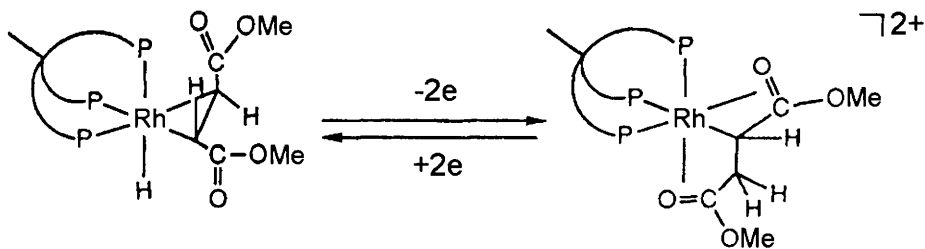
Figure 20 Cyclic voltammograms recorded at a platinum electrode in CH_2Cl_2 solutions of: (a,b) $[\text{Rh}\{\text{C}=\text{CH}(\text{Ph})\}(\text{NP}_3)]^+$; (c) $[\text{Rh}(\text{C}\equiv\text{CPh})(\text{NP}_3)]$. Scan rate 0.2 V s^{-1}



Scheme 8

3 REVERSIBLE MIGRATION OF A HYDROGEN ATOM FROM A METAL CENTRE TO A PERIPHERAL LIGAND

The reversible redox-induced transformation of the octahedral Rh(I)-dimethylfumarate complex $[\text{RhH}(\text{MeO}_2\text{CCH}=\text{CHCO}_2\text{Me})(\text{triphos})]$ to the corresponding Rh(III)-succinyl derivative $[\text{Rh}\{\text{CH}(\text{CO}_2\text{Me})\text{CH}_2(\text{CO}_2\text{Me})\}(\text{triphos})]^{2+}$, illustrated in Scheme 9, involves a mechanism more complex than simple hydrogen atom abstraction.



Scheme 9

The Rh(I)-dimethylfumarate complex undergoes an irreversible (two-electron) oxidation, that generates in the reverse scan a cathodic profile completely identical to that of the Rh(III)-succinyl derivative, Figure 21a.

In fact, the latter displays a first (one-electron) reversible reduction followed by a second irreversible reduction that in turn shows, on the reverse scan, the oxidation peak of the Rh(I)-dimethylfumarate complex, Figure 21b. The complete interconversion process is illustrated in Scheme 10.

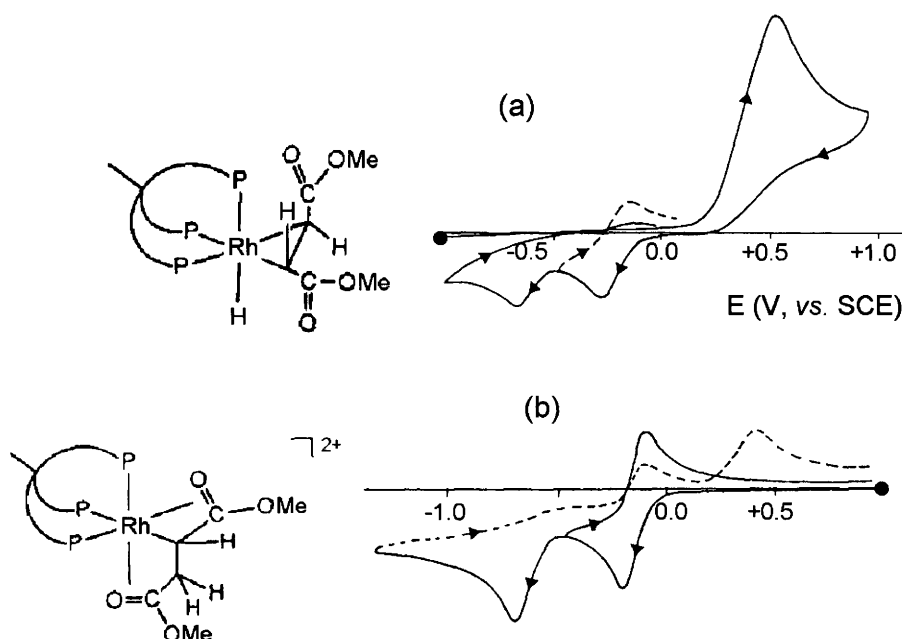
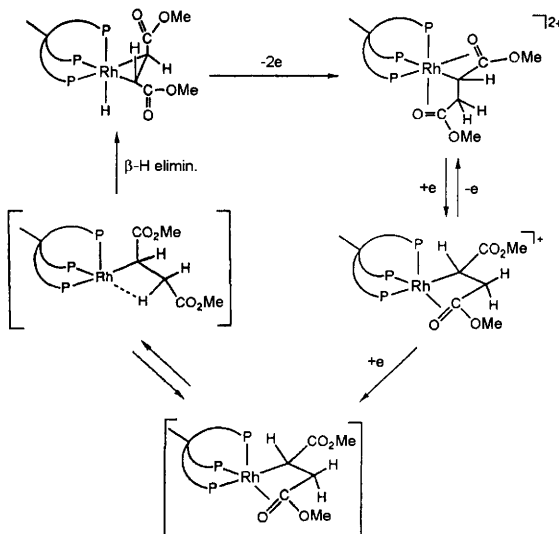


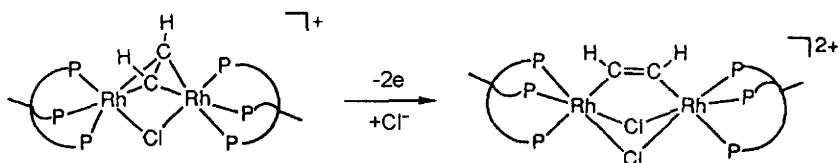
Figure 21 Cyclic voltammograms recorded at a platinum electrode in: (a) *thf* solution of $[\text{RhH}(\text{MeO}_2\text{CCH}=\text{CHCO}_2\text{Me})(\text{triphos})]$; (b) CH_2Cl_2 solution of $[\text{Rh}(\text{CH}(\text{CO}_2\text{Me})\text{CH}_2(\text{CO}_2\text{Me}))(\text{triphos})]^{2+}$. Scan rate 0.2 V s^{-1}



Scheme 10

4 REVERSIBLE ORIENTATION FROM 'PERPENDICULAR' TO 'PARALLEL' DISPOSITION OF AN ALKyne GROUP BRIDGING TWO METAL CENTRES

As a further example of redox-induced reorganisation processes we illustrate the reorientation of a μ -ethyne group bridging two metal centres from *perpendicular* to *parallel* orientation with respect to the metal centres, Scheme 11.



Scheme 11

The reorientation takes place during the oxidation of the dirhodium complex $[(\text{triphos})\text{Rh}(\mu\text{-Cl})(\mu\text{-}\eta^2,\eta^2\text{-C}_2\text{H}_2)(\text{triphos})]\text{Cl}$, the molecular structure of which is illustrated in Figure 22a, to the derivative $[(\text{triphos})\text{Rh}(\mu\text{-Cl})_2(\mu\text{-}\eta^1,\eta^1\text{-C}_2\text{H}_2)\text{Rh}(\text{triphos})]^{2+}$ (the crystal structure of such dication could not be obtained, but that of the related species $[(\text{triphos})\text{Rh}(\mu\text{-Cl})(\mu\text{-OH})(\mu\text{-}\eta^1,\eta^1\text{-C}_2\text{H}_2)\text{Rh}(\text{triphos})]^{2+}$ is shown in Figure 22b).¹⁹

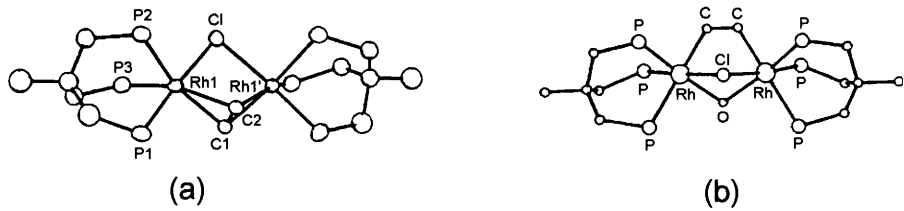


Figure 22 X-Ray structures of: (a) $[(\text{triphos})\text{Rh}(\mu\text{-Cl})(\mu\text{-}\eta^2\text{-}\eta^2\text{-C}_2\text{H}_2)\text{Rh}(\text{triphos})]^{+}$. $\text{Rh-Cl} = 2.45 \text{ \AA}$; $\text{Rh1-Cl} = \text{Rh1-C2} = 2.14 \text{ \AA}$; $\text{R1-P1} = 2.24 \text{ \AA}$; $\text{R1-P2} = \text{Rh1-P3} = 2.37 \text{ \AA}$; $\text{R1...Rh1'} = 3.31 \text{ \AA}$; (b) $[(\text{triphos})\text{Rh}(\mu\text{-Cl})(\mu\text{-OH})(\mu\text{-}\eta^1, \eta^1\text{-C}_2\text{H}_2)\text{Rh}(\text{triphos})]^{2+}$. All the hydrogen atoms and phenyl rings are omitted

Figure 23 shows that the ‘perpendicular’ monochloro cation undergoes an irreversible (two-electron) oxidation that generates a voltammetric profile coincident with that of the ‘parallel’ dichloro dication.

The overall mechanism can be described according to Scheme 12.

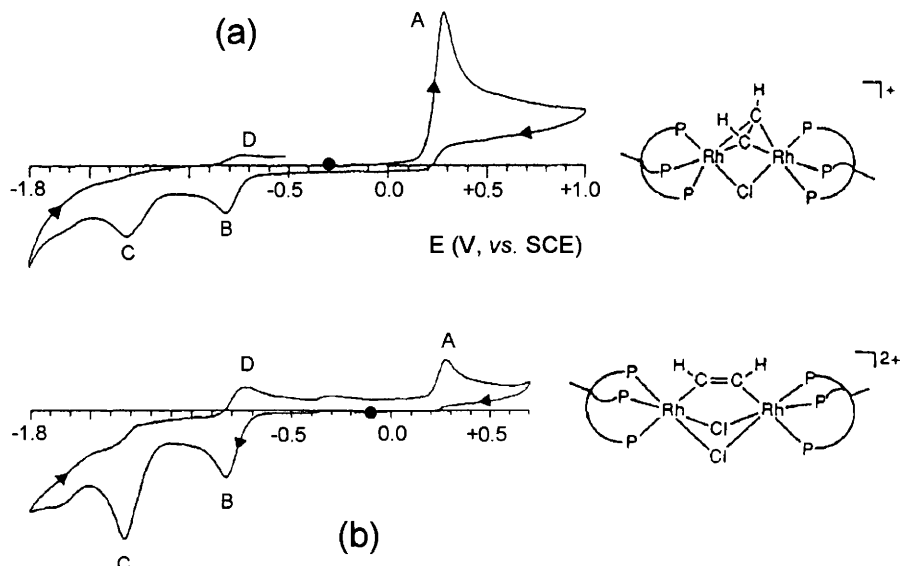
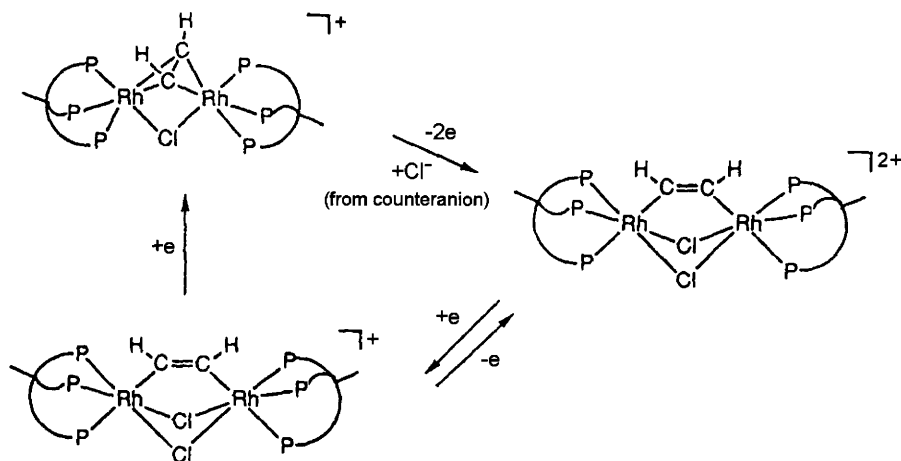
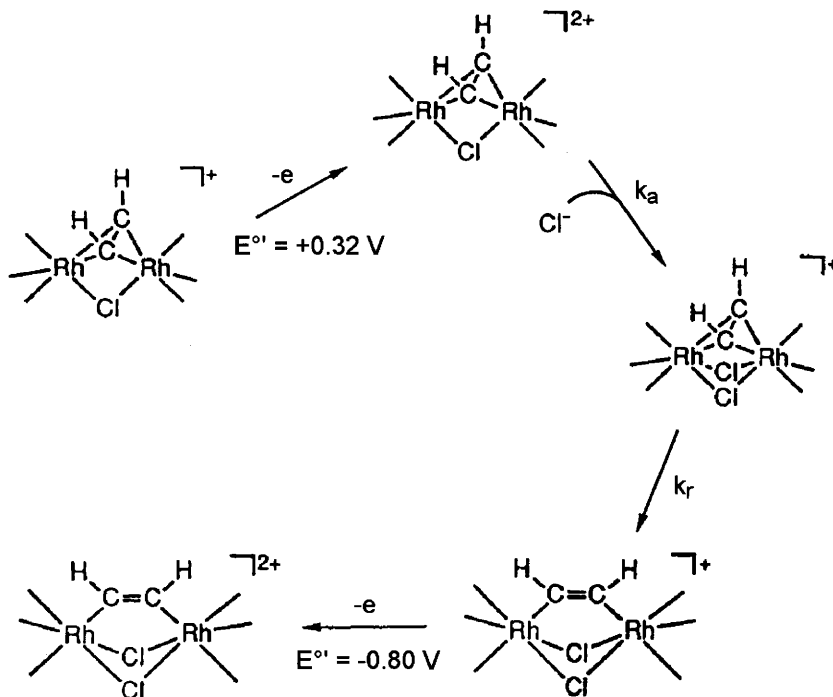


Figure 23 Cyclic voltammograms recorded at a platinum electrode on CH_2Cl_2 solutions of: (a) $[(\text{triphos})\text{Rh}(\mu\text{-Cl})(\mu\text{-}\eta^2\text{-C}_2\text{H}_2)\text{Rh}(\text{triphos})]\text{Cl}$; (b) $[(\text{triphos})\text{Rh}(\text{Cl})_2(\text{C}_2\text{H}_2)\text{Rh}(\text{triphos})](\text{ClO}_4)_2$. Scan rate 0.2 V s⁻¹



Scheme 12

Indeed, a careful assessment of the electrochemical data has enabled the process of the alkyne reorientation to be clarified according to the more detailed EC_aC_rE mechanism (C_a=chloride ion association; C_r=geometric reorganization) illustrated in Scheme 13.



Scheme 13

5 REDOX TRANSFORMATIONS FOLLOWING IRREVERSIBLE ELECTRON-TRANSFER PATHWAYS

To continue the present topic, we would like to underline that often irreversible redox processes do not cause the appearance of new, well-defined redox waves such as to induce an accurate examination of the underlying chemical complications. Nevertheless, not always irreversible redox changes lead to complete destruction of the metal complex under examination. Analysis of the products arising from irreversible processes can sometimes reveal interesting chemical pathways.

We cite as an example the oxidation of the mononuclear Au(I)-thiolate complex $[\text{Au}(\text{SC}_6\text{H}_4\text{CH}_3)(\text{PPh}_3)]$.²⁰ As illustrated in Figure 24, this complex exhibits, in CH_2Cl_2 solution, two irreversible anodic processes ($E^{\circ'} = +0.92 \text{ V}$ and $+1.6 \text{ V}$ vs. Ag/AgCl , respectively).

Controlled potential coulometry in correspondence to the first anodic process shows the consumption of a fractional charge ($n \approx 0.5$ electrons), thus confirming the occurrence of chemical complications accompanying the electron removal. Isolation of the product obtained by chemical oxidation (by ferrocenium hexafluorophosphate) showed it to consist of the tetragold complex $[\text{Au}_4(\mu-\text{SC}_6\text{H}_4\text{CH}_3)_2(\text{PPh}_3)_4](\text{PF}_6)_2$, whose molecular structure is illustrated in Figure 25.²⁰

Based on this result, the following electrode mechanism has been proposed:

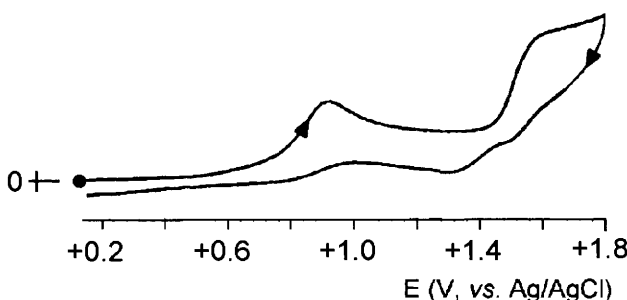
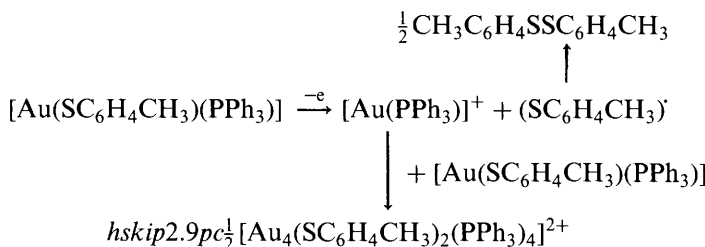


Figure 24 Cyclic voltammogram recorded at a platinum electrode in a CH_2Cl_2 solution of $[\text{Au}(\text{SC}_6\text{H}_4\text{CH}_3)(\text{PPh}_3)]$. Scan rate 0.02 V s^{-1}

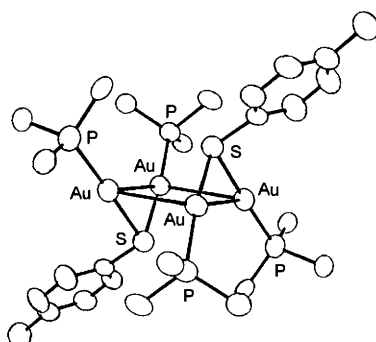
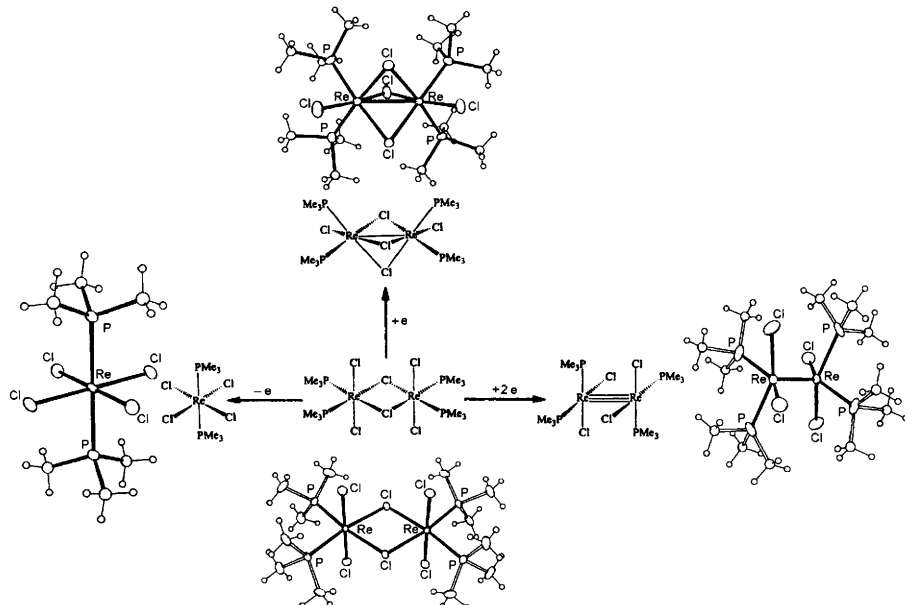


Figure 25 X-Ray structure of $[Au_4(\mu\text{-}SC_6H_4CH_3)_2(PPh_3)_4]^{2+}$. $Au-Au \approx 3.16 \text{ \AA}$; $Au\text{-}P = 2.27 \text{ \AA}$; $Au\text{-}S = 2.34 \text{ \AA}$

Even more educational is the case of the dirhenium(III) complex $[Re_2(\mu\text{-}Cl)_2Cl_4(PMe_3)_4]$.²¹ It has recently been reported that in CH_2Cl_2 solution such Re_2^{6+} species undergoes irreversible reduction and oxidation processes.²² As illustrated in Scheme 14, the use of either reducing (namely, $[KC_8]$) or oxidizing (namely, $[NOBF_4]$) chemical agents allowed to identify and structurally characterize the different complexes arising from such irreversible electron-transfer processes.^{21,22} All the new products (namely: the $Re^{III}\text{-}Re^{II}$ $[Re_2(\mu\text{-}Cl)_3Cl_2(PMe_3)_4]$, the $Re^{II}\text{-}Re^{II}$ $[Re_2Cl_4(PMe_3)_4]$; the Re^{IV} *trans*- $[ReCl_4(PMe_3)_2]$) clearly testify to more or less important fragmentations of the original molecule.



Scheme 14

6 REDOX TRANSFORMATIONS FOLLOWING QUASIREVERSIBLE ELECTRON-TRANSFER PATHWAYS

In Chapter 2, Section 1.3.2, we have already discussed about the structural consequences of a *quasireversible* electron transfer. We have thus illustrated that the molecular reorganizations can range from simple disappearance of some original bonds to severe geometrical rearrangements. To conclude the present topic we would like to mention an example of metal–metal bond formation following a *quasireversible* electron removal.

Figure 26 shows the molecular structure of the triplatinum phosphido dianion $[(C_6F_5)_2Pt(\mu-PPh_2)_2Pt(\mu-PPh_2)_2Pt(C_6F_5)_2]^{2-}$.²³

The three Pt(II) atoms have a square planar configuration and are each coordinated through bridging diphenylphosphido ligands, without any metal–metal bonding interaction.

In CH_2Cl_2 solution such a dianion undergoes a quasireversible two-electron removal to the corresponding neutral congener $[(C_6F_5)_2Pt(\mu-PPh_2)_2Pt(\mu-PPh_2)_2Pt(C_6F_5)_2]$ ($E^{\circ'} = -0.11$ V vs. SCE; $\Delta E_p = 227$ mV, at 0.1 V/s⁻¹).

As illustrated in Figure 27, the two-electron oxidation product essentially maintains the original geometry, but a new $Pt^{III}-Pt^{III}$ bond

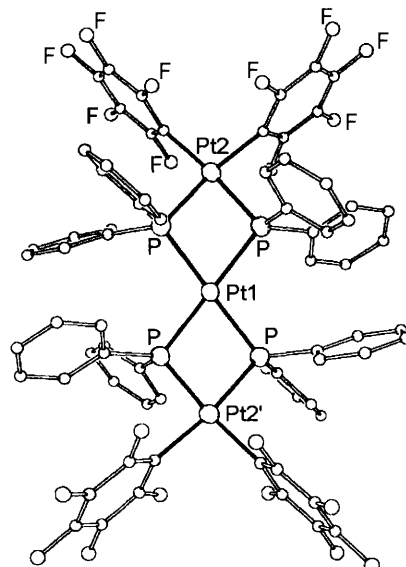


Figure 26 X-Ray structure of $[(C_6F_5)_2Pt(\mu-PPh_2)_2Pt(\mu-PPh_2)_2Pt(C_6F_5)_2]^{2-}$. $Pt2-C = 2.08 \text{ \AA}$; $Pt2-P = 2.32 \text{ \AA}$; $Pt1-P = 2.37 \text{ \AA}$; $Pt \cdots Pt = 3.59 \text{ \AA}$

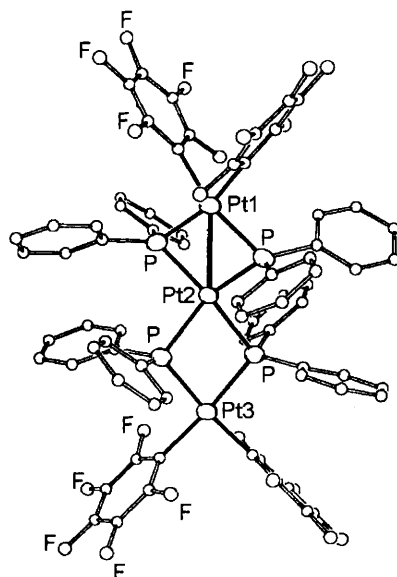


Figure 27 X-Ray structure of $[(C_6F_5)_2Pt(\mu\text{-}PPh_2)_2Pt(\mu\text{-}PPh_2)_2Pt(C_6F_5)_2]$. $Pt1-Pt2 = 2.78 \text{ \AA}$; $Pt2\ldots Pt3 = 3.67 \text{ \AA}$; $Pt1-C = 2.08 \text{ \AA}$; $Pt1-P = 2.28 \text{ \AA}$; $Pt2-P1 = 2.30 \text{ \AA}$; $Pt2-P2 = 2.38 \text{ \AA}$; $Pt3-P2 = 2.27 \text{ \AA}$; $Pt3-C = 2.05 \text{ \AA}$

forms, which obviously causes asymmetry in the intramolecular bond distances.²³

It is, however, noted that in some cases new bond formation/destruction coupled to important structural reorganizations may afford peak-to-peak separations so pronounced as to make the pertinent electron transfer apparently irreversible, in that in a limited potential range the return peak can escape detection. This is the case of the oxidation process of the monoanion $[Pt(C_6Cl_5)_4]^-$ to the neutral complex $[Pt(C_6Cl_5)_4]$ in the redox sequence $[Pt(C_6Cl_5)_4]^{2-/0}$.²⁴ In fact, as illustrated in Figure 28, the dianion $[Pt^{II}(C_6Cl_5)_4]^{2-}$ in CH_2Cl_2 solution undergoes a first chemically and electrochemically reversible one-electron oxidation ($E_{2/-}^{o'} = +0.54 \text{ V}$, vs. SCE; $\Delta E_p = 60 \text{ mV}$ at 0.1 V s^{-1}), followed by a second one-electron oxidation at high potential values ($E_p = +1.85 \text{ V}$), which exhibits a return peak ($E_p = -0.05 \text{ V}$) very far from the forward peak.

Isolation and structural characterization of the whole redox series shows that, in agreement with the electrochemical reversibility, the first one-electron removal Pt^{II}/Pt^{III} does not substantially modify the original square planar geometry (the Pt–C bond lengths elongate by less than 0.01 \AA , whereas the C–C distances remain unaltered).²⁵ By contrast, more severe are the structural consequences of the second electron

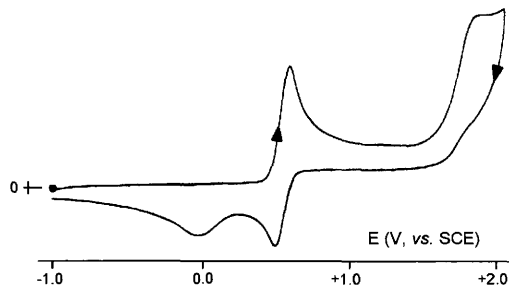


Figure 28 Cyclic voltammogram recorded at a platinum electrode in a CH_2Cl_2 solution of $[\text{Pt}(\text{C}_6\text{Cl}_5)_4]^{2-}$. Scan rate 0.2 V s^{-1}

removal $\text{Pt}^{\text{III}}/\text{Pt}^{\text{IV}}$. As shown in Figure 29, which compares the molecular structures of $[\text{Pt}^{\text{III}}(\text{C}_6\text{Cl}_5)_4]^-$ and $[\text{Pt}^{\text{IV}}(\text{C}_6\text{Cl}_5)_4]$, the neutral compound assumes a distorted octahedral geometry forcing one *ortho*-Cl atom of two of the four C_6Cl_5 rings to form bond with the platinum atom.²⁴

Confirming the assignment, an authentic sample of $[\text{Pt}^{\text{IV}}(\text{C}_6\text{Cl}_5)_4]$ exhibits in the forward scan only the apparently irreversible reduction $\text{Pt}^{\text{IV}}/\text{Pt}^{\text{III}}$, which in the backscan generates the reversible $\text{Pt}^{\text{II}}/\text{Pt}^{\text{III}}$ peak-system.

It results that in the absence of any fragmentation of the original frame, the process $[\text{Pt}(\text{C}_6\text{Cl}_5)_4]^{-/0}$ is in principle quasireversible. The large peak-to-peak separation ($\Delta E_p = 1.9 \text{ V}$, at 0.2 V s^{-1}) evidently reflects the high energy barrier required to pass from square planar tetracoordinate-Pt(III) to octahedral hexacoordinate-Pt(IV), which slows down the rate of the heterogeneous electron transfer.

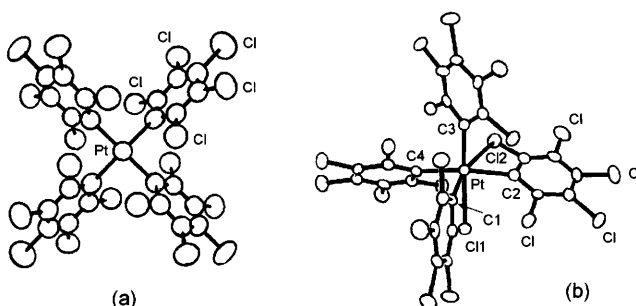


Figure 29 X-Ray crystal structures of: (a) $[\text{Pt}(\text{C}_6\text{Cl}_5)_4]^-$. Average interatomic distances: $\text{Pt}-\text{C} = 2.09 \text{ \AA}$; $\text{C}-\text{C} = 1.39 \text{ \AA}$; $\text{C}-\text{Cl} = 1.72 \text{ \AA}$; (b) $[\text{Pt}(\text{C}_6\text{Cl}_5)_4]$. Average interatomic distances: $\text{Pt}-\text{C}1 = \text{Pt}-\text{C}3 = 2.04 \text{ \AA}$; $\text{Pt}-\text{C}2 = \text{Pt}-\text{C}4 = 2.12 \text{ \AA}$; $\text{Pt}-\text{Cl}1 = 2.56 \text{ \AA}$; $\text{Pt}-\text{Cl}2 = 2.68 \text{ \AA}$; $\text{C}-\text{C} = 1.39 \text{ \AA}$; $\text{C}-\text{Cl} = 1.73 \text{ \AA}$

REFERENCES

1. S.L. Queiroz, A.A. Batista, G. Oliva, M.T.d.P. Gambardella, R.H.A. Santos, K.S. MacFarlane, S.J. Rettig and B.R. James, *Inorg. Chim. Acta*, 1998, **267**, 209.
2. (a) K. Mayer, E. Bill, B. Mienert, T. Weyhermüller and K. Wieghardt, *J. Am. Chem. Soc.*, 1999, **121**, 4859; (b) B. Kail, V.N. Nemykin, S.R. Davie, C.J. Carrano, B. Hammes and P. Basu, *Inorg. Chem.*, 2002, **41**, 1281.
3. (a) M. Kurosawa, T. Nankawa, T. Matsuda, K. Kubo, M. Kurihara and H. Nishihara, *Inorg. Chem.*, 1999, **38**, 5113; (b) M. Kurihara, T. Matsuda, A. Hirooka, T. Yutaka and H. Nishihara, *J. Am. Chem. Soc.*, 2000, **122**, 12373.
4. P.K. Santra, T.K. Misra, D. Das, C. Sinha, A.M.Z. Slawin and J.D. Woollins, *Polyhedron*, 1999, **18**, 2869.
5. G.K. Lahiri, S. Bhattacharya, S. Goswami and A. Chakravorty, *J. Chem. Soc., Dalton Trans.*, 1990, 561.
6. J.L. Bear, Y. Li, J. Cui, B. Han, E. Van Caemelbecke, T. Phan and K.M. Kadish, *Inorg. Chem.*, 2000, **39**, 857.
7. A.R. Chakravarty, F.A. Cotton and W. Schwotzer, *Inorg. Chim. Acta*, 1984, **84**, 179.
8. B.P. Sullivan and T.J. Meyer, *Inorg. Chem.*, 1982, **21**, 1037.
9. F. Létumier, G. Broeker, J.-M. Barbe, R. Guilard, D. Lucas, V. Dahaoui-Gindrey, C. Lecomte, L. Thouin and C. Amatore, *J. Chem. Soc., Dalton Trans.*, 1998, 2233.
10. (a) A.M. Bond, R. Colton and M.J. McCormick, *Inorg. Chem.*, 1977, **16**, 155; (b) A.M. Bond, B.S. Grabaric and Z. Grabaric, *Inorg. Chem.*, 1978, **17**, 1013; (c) R.G. Compton, R. Barghout, J.C. Eklund, A.C. Fisher, A.M. Bond and R. Colton, *J. Phys. Chem.*, 1993, **97**, 1661; (d) J.C. Eklund and A.M. Bond, *J. Am. Chem. Soc.*, 1999, **121**, 8306.
11. R.A. Jones, T.C. Wright, J.L. Atwood and W.E. Hunter, *Organometallics*, 1983, **2**, 470.
12. J.G. Gaudiello, T.C. Wright, R.A. Jones and A.J. Bard, *J. Am. Chem. Soc.*, 1985, **107**, 888.
13. C. Bianchini, F. Laschi, D. Masi, F.M. Ottaviani, A. Pastor, M. Peruzzini, P. Zanello and F. Zanobini, *J. Am. Chem. Soc.*, 1993, **115**, 2723.
14. P. Zanello, A. Cinquantini, C.A. Ghilardi, S. Midollini, S. Moneti, A. Orlandini and A. Bencini, *J. Chem. Soc., Dalton Trans.*, 1990, 3761.
15. P. Zanello, *Pure Appl. Chem.*, 1995, **67**, 323 and references therein.
16. C. Bianchini, M. Peruzzini, A. Ceccanti, F. Laschi and P. Zanello, *Inorg. Chim. Acta*, 1997, **259**, 61.
17. C. Bianchini, C. Mealli, M. Peruzzini and F. Zanobini, *J. Am. Chem. Soc.*, 1992, **114**, 5905.

18. A. Orlandini and L. Sacconi, *Cryst. Struct. Commun.*, 1975, **4**, 157.
19. C. Bianchini, D. Masi, A. Meli, M. Peruzzini, A. Vacca, F. Laschi and P. Zanello, *Organometallics*, 1991, **10**, 636.
20. J. Chen, T. Jiang, G. Wei, A.A. Mohamed, C. Homrighausen, J.A. Krause Bauer, A.E. Bruce and M.R.M. Bruce, *J. Am. Chem. Soc.*, 1999, **121**, 9225.
21. F.A. Cotton, E.V. Dikarev and M.A. Petrukhina, *J. Am. Chem. Soc.*, 1997, **119**, 12541.
22. F.A. Cotton, E.V. Dikarev and M.A. Petrukhina, *Inorg. Chem.*, 2001, **40**, 6825.
23. E. Alonso, J.M. Casas, J. Fourniés, C. Fortuño, A. Martín, A.G. Orpen, C.A. Tsipis and A.C. Tsipis, *Organometallics*, 2001, **20**, 5571.
24. J. Forniés, B. Menjón, R.M. Sanz-Carrillo, M. Tomás, N.G. Connelly, J.G. Crossley and A.G. Orpen, *J. Am. Chem. Soc.*, 1995, **117**, 4295.
25. R. Usón, M. Tomás, B. Menjón, R. Bau, K. Sünkel and E. Kuwabara, *Organometallics*, 1986, **5**, 1576.

CHAPTER 8

Transition Metal Clusters

A metal cluster complex is an aggregation of (more than two) metal fragments held together by ligands in a closed structure able to give rise to a series of metal–metal bonds. These compounds display a great variety of spectacular geometric arrangements and are often regarded as being capable of participating in rich series of electron transfers without changing appreciably their molecular structure. On the basis of the redox behaviour of a large number of *homo-* and *hetero-*metallic clusters,¹ one cannot generalize about the high redox activity of these derivatives.

1 METAL-SULFUR CLUSTERS

Metal-sulfur clusters probably constitute the best known class of clusters due to their considerable importance and common occurrence in the biological world, where they fulfil the role of electron carriers (see Chapter 12). This function is related to their high capacity to undergo a cascade of reversible redox processes. As an illustrative and introductory example, Figure 1 shows the redox ability of $[\text{Fe}_4(\mu_3\text{-S})_4(\eta\text{-C}_5\text{H}_5)_4]$.^{1a}

Let us consider briefly but systematically the redox properties of a few homonuclear metal–sulfur clusters in order of increasing metal atom number.

1.1 $\mathbf{M}_3\mathbf{S}_n$ ($n = 2, 4$)

There exist a number of homo metal-sulfur clusters possessing an $\mathbf{M}_3\mathbf{S}_n$ core ($\mathbf{M} = \text{Fe, Co, Ni, Mo, W}$; $n = 1\text{--}4$)^{1a}, but the most represented assemblies are $\mathbf{M}_3\mathbf{S}_2$ and $\mathbf{M}_3\mathbf{S}_4$, respectively. The latter is present in a few biological functions as an $\mathbf{Fe}_3\mathbf{S}_4$ unit² (see also Chapter 12, Section 3).

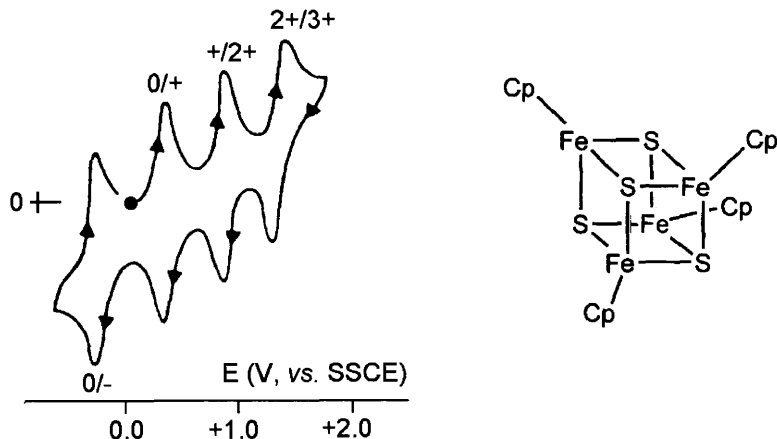


Figure 1 Cyclic voltammogram recorded at a platinum electrode in a MeCN solution of $[Fe_4(\mu_3-S)_4(\eta-C_5H_5)_4]$

As far as the M_3S_2 core is concerned, it consists of a triangle of metal atoms capped by two triply bridging sulfur atoms lying above and below the trimetallic plane, respectively. It is interesting to note that the strength of the metal–metal bonds varies with the nature of the metal. In fact, as illustrated in Figure 2, in $[Co_3(\mu_3-S)_2(\eta-C_5H_5)_3]$ the triangle is regularly closed,³ in $[Fe_3(\mu_3-S)_2(CO)_9]$ the triangle is open at one side,⁴ in $[Ni_3(\mu_3-S)_2(\eta-C_5H_5)_3]$ the Ni₃ triangle is almost completely open.⁵

As illustrated in Figure 3, the three clusters exhibit a significant electron-transfer ability according to the following sequences (V vs. Ag/AgCl):⁶

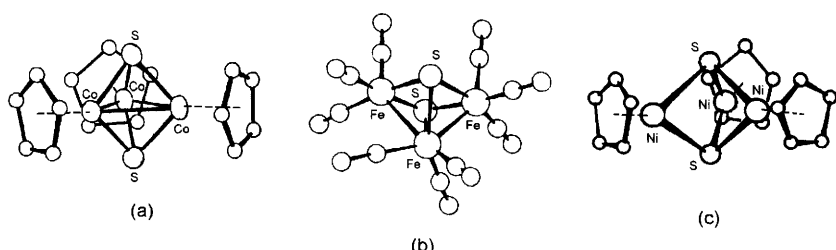


Figure 2 X-Ray structures of: (a) $[Co_3(\mu_3-S)_2(\eta-C_5H_5)_3]$: Co–Co bonding distance = 2.69 Å; (b) $[Fe_3(\mu_3-S)_2(CO)_9]$: Fe–Fe bonding distance = 2.59 Å; (c) $[Ni_3(\mu_3-S)_2(\eta-C_5H_5)_3]$: Ni · · · Ni distance = 2.80 Å

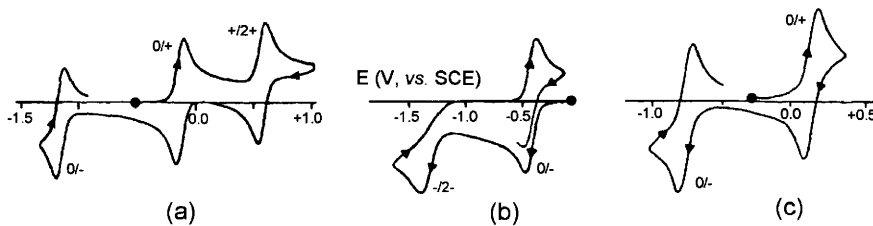
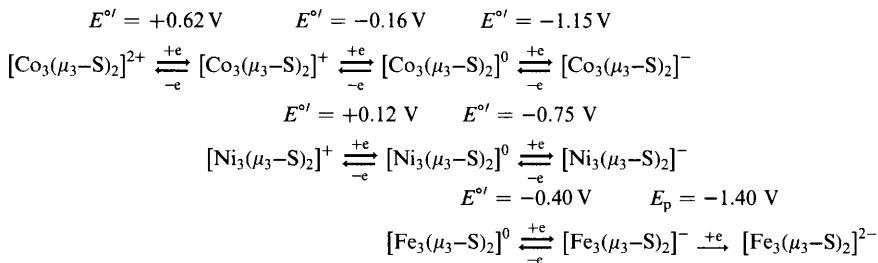
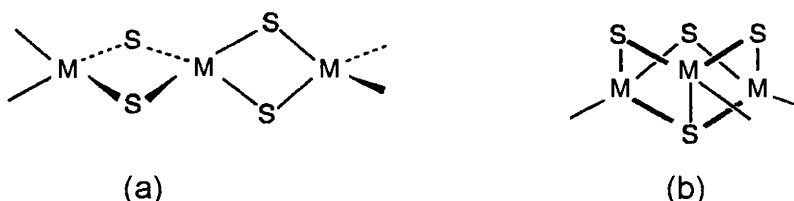


Figure 3 Cyclic voltammograms recorded at a platinum electrode in benzonitrile solutions of: (a) $[\text{Co}_3(\mu_3\text{-S})_2(\eta\text{-C}_5\text{H}_5)_3]$; (b) $[\text{Fe}_3(\mu_3\text{-S})_2(\text{CO})_9]$; (c) $[\text{Ni}_3(\mu_3\text{-S})_2(\eta\text{-C}_5\text{H}_5)_3]$. Scan rate 0.02 V s^{-1}



Most electron transfers are chemically and electrochemically reversible, thus indicating that the respective redox species are stable and substantially maintain the original molecular structure. As a matter of fact, the monocation $[\text{Co}_3(\mu_3\text{-S})_2(\eta\text{-C}_5\text{H}_5)_3]^+$ has been structurally characterized.³ Within the Co₃ triangle, two Co-Co distances remain substantially unaltered with respect to the neutral parent (Co-Co = 2.65 Å), whereas the third one shortens to 2.47 Å. This suggests that in the $[\text{Co}_3(\mu_3\text{-S})_2(\eta\text{-C}_5\text{H}_5)_3]/[\text{Co}_3(\mu_3\text{-S})_2(\eta\text{-C}_5\text{H}_5)_3]^+$ redox change the electron is removed from an antibonding orbital.

As far as the clusters containing the M₃S₄ core are concerned, there are two structural types: the *linear* (a) and the *incomplete-cubane* (b) assemblies, Scheme 1.



Scheme 1

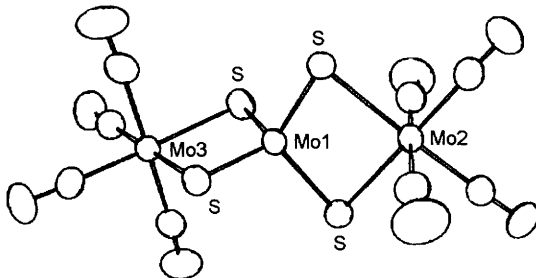


Figure 4 X-Ray structure of $[Mo_3(\mu-S)_4(CO)_8]^{2-}$. Average bond lengths: $Mo1-S = 2.22 \text{ \AA}$; $Mo2-S = Mo3-S = 2.53 \text{ \AA}$; $Mo-C = 2.00 \text{ \AA}$. $Mo \cdots Mo = 3.00 \text{ \AA}$

As an example of linear assembly one can cite the dianion $[Mo_3(\mu-S)_4(CO)_8]^{2-}$, the molecular structure of which is shown in Figure 4.⁷

The formal oxidation state of the central Mo atom is +6, whereas that of the two outer Mo atoms is 0. Such a dianion undergoes in MeCN solution a one-electron reduction ($E_{2-/3-}^\circ = -1.72 \text{ V vs. SCE}$), which is only partially chemically reversible, and an ill-defined irreversible oxidation ($E_p = +0.14 \text{ V}$).^{7a}

It has been assumed that the reduction process is centred on the central, high-valent, Mo atom, whereas the oxidation process is centred on the outer, low-valent, Mo atoms.

Similar redox behaviour is exhibited by the isostructural trianion $[Fe_3(\mu-S)_4(SPh)_4]^{3-}$.⁸

Among the incomplete-cuboidal M_3S_4 assemblies,^{1a} we can cite as an example the monocation $[Mo_3(\mu_2-S)_3(\mu_3-S)(\eta-C_5H_5)_3]^+$, the molecular structure of which is illustrated in Figure 5.⁹

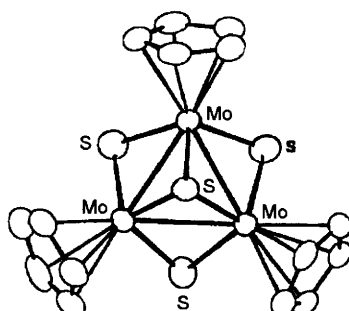


Figure 5 X-Ray structure of $[Mo_3(\mu_2-S)_3(\mu_3-S)(\eta-C_5H_5)_3]^+$. Average bond lengths: $Mo-Mo = 2.81 \text{ \AA}$; $Mo-\mu_3-S = 2.31 \text{ \AA}$; $Mo-\mu_2-S = 2.29 \text{ \AA}$; $Mo-C_5H_5(\text{centroid}) = 2.03 \text{ \AA}$

In CH_2Cl_2 solution it undergoes a chemically reversible one-electron reduction ($E_{+/-}^{\circ} = -1.04 \text{ V}$ vs. SCE) to the corresponding neutral derivative $[\text{Mo}_3(\mu_2\text{-S})_3(\mu_3\text{-S})(\eta\text{-C}_5\text{H}_5)_3]$.^{1a,9} Since theoretical calculations foresee that the electron is added to an antibonding Mo–Mo orbital, it is expected that the neutral species possesses an expanded Mo_3S_4 core. As a matter of fact, the permethylated neutral complex $[\text{Mo}_3(\mu_2\text{-S})_3(\mu_3\text{-S})(\eta\text{-C}_5\text{H}_5)_3]$ has been structurally characterized. Comparison of the relevant bond lengths of the couple quite support the theoretical revision, Table 1.¹⁰

A further useful example is given by the trianion $[\text{Fe}_3\text{S}_4(\text{LS}_3)]^{3-}$ ($\text{LS}_3 = 1,3,5\text{-tris}[(4,6\text{-dimethyl-3-mercaptophenyl})\text{thio}]\text{-2,4,6-tris}(p\text{-tolyl thio})\text{benzene(3-)}$). The molecular structure of its Fe_3S_4 core is illustrated in Figure 6.¹¹

As illustrated in Figure 7, this trianion undergoes a one-electron reduction ($E_{3-/4-}^{\circ} = -1.72 \text{ V}$ vs. SCE), and a one-electron oxidation ($E_{3-/2-}^{\circ} = -0.79 \text{ V}$), both processes having features of chemical reversibility on the cyclic voltammetric time scale.¹¹

Table 1 Average bond lengths (in Å) in $[\text{Mo}_3(\mu_2\text{-S})_3(\mu_3\text{-S})(\eta\text{-C}_5\text{H}_5)_3]^+$ and $[\text{Mo}_3(\mu_2\text{-S})_3(\mu_3\text{-S})(\eta\text{-C}_5\text{Me}_5)_3]$

Complex	Mo–Mo	Mo– $\mu_3\text{-S}$	Mo– $\mu_2\text{-S}$	Mo– C_5Me_5 (centroid)
$[\text{Mo}_3(\mu_2\text{-S})_3(\mu_3\text{-S})(\eta\text{-C}_5\text{H}_5)_3]^+$	2.81	2.31	2.29	2.03
$[\text{Mo}_3(\mu_2\text{-S})_3(\mu_3\text{-S})(\eta\text{-C}_5\text{H}_5)_3]$	2.86	2.34	2.31	2.05

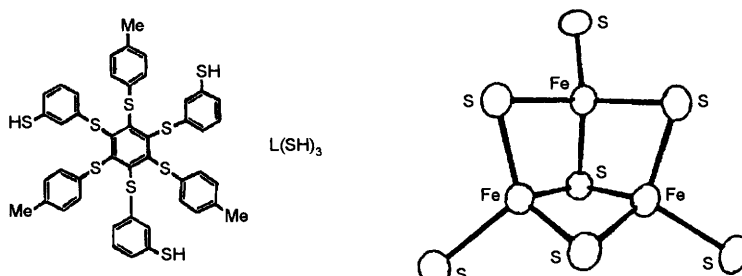


Figure 6 X-Ray structure of the $[\text{Fe}_3\text{S}_4]^0$ core of $[\text{Fe}_3\text{S}_4(\text{LS}_3)]^{3-}$. Average bond lengths: $\text{Fe}-\mu_3\text{S} = 2.31 \text{ \AA}$; $\text{Fe}-\mu_2\text{S} = 2.26 \text{ \AA}$; $\text{Fe}-\text{S} = 2.32 \text{ \AA}$; $\text{Fe} \cdots \text{Fe} = 2.70 \text{ \AA}$

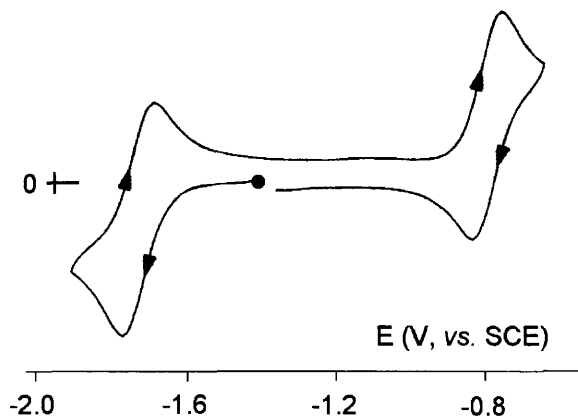


Figure 7 Cyclic voltammogram recorded at a platinum electrode in a MeCN solution of $[NEt_4]_3[Fe_3S_4(LS_3)]$. Scan rate 0.05 V s^{-1}

1.2 M_4S_n ($n = 3-6$)

Figure 8 shows the molecular structure of the monoanion $[Fe_4S_3(NO)_7]^-$,¹² a compound known as ‘the black isomer of Roussin’s salt’.

The geometry of the Fe_4S_3 core is composed of a (open base) trigonal pyramid of iron atoms with a triply bridging sulfur atom apically positioned above each face.

In MeCN solution this monoanion undergoes three reversible one-electron reductions ($E_{1/2-}^{\circ} = -0.68\text{ V}$; $E_{2/3-}^{\circ} = -1.26\text{ V}$; $E_{3/4-}^{\circ} = -1.75\text{ V}$), Figure 9.¹²

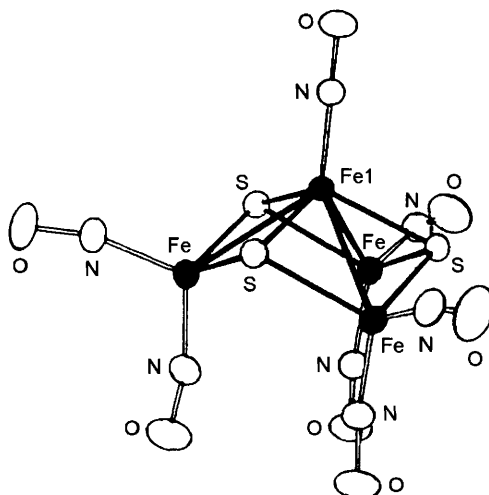


Figure 8 X-Ray structure of $[Fe_4S_3(NO)_7]^-$. Average bond lengths: $Fe1-Fe = 2.70\text{ \AA}$; $Fe1-S = 2.21\text{ \AA}$; $Fe-S = 2.26\text{ \AA}$. $Fe \cdots Fe = 3.57\text{ \AA}$

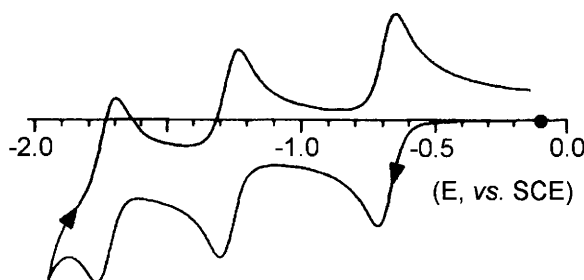
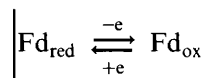
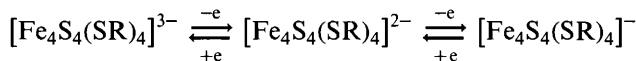


Figure 9 Cyclic voltammogram recorded at a platinum electrode in a MeCN solution of $[NEt_4][Fe_4S_3(NO)_7]$. Scan rate 0.2 V s^{-1}

The corresponding dianion $[Fe_4S_3(NO)_7]^{2-}$ has been isolated and its structure characterized. In agreement with the electrochemical reversibility of the corresponding reduction process, it maintains the structure of the monoanion precursor. Within the Fe_4S_3 core, the most significant differences in the interatomic distances involve a lengthening of the mean $Fe1-Fe$ bond lengths (by about 0.06 \AA) and a more limited lengthening of the $Fe1-S$ and $Fe-S$ distances (by about 0.02 \AA).

The best known metal–sulfur assembly is most likely the cubane M_4S_4 , because the Fe_4S_4 aggregate is widespread in biological molecules able to function as electron carriers. For example, (as we will discuss in Chapter 12, Section 3) the redox function of *ferredoxins* (Fd) and *high-potential iron proteins* (HPIP), in which the cube formed by the Fe_4S_4 atoms is bound to cysteine groups, is linked to the following chemically reversible electron transfer processes:



The important biochemical role played by this type of (non-heme) iron proteins has stimulated efforts to synthesise Fe_4S_4 complexes bound to thiolate groups. For instance, Figure 10 shows the voltammetric behaviour of two such complexes, $[Fe_4S_4(SPh)_4]^{2-}$ and $[Fe_4S_4(SBu^t)_4]^{2-}$.^{1a}

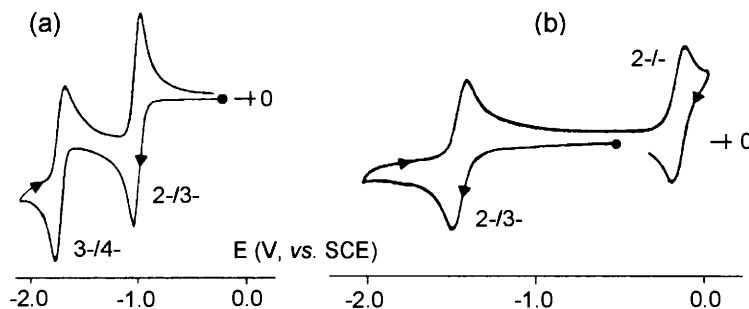
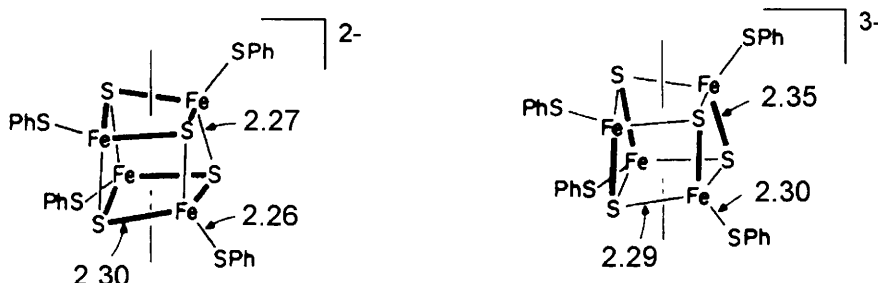


Figure 10 Cyclic voltammograms recorded in: (a) MeCN solution of $[Fe_4S_4(SPh)_4]^{2-}$; (b) dmf solution of $[Fe_4S_4(SBu')_4]^{2-}$

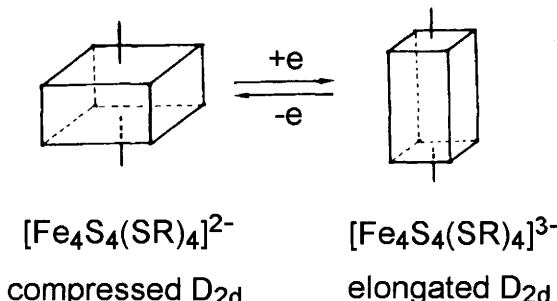
It is clear that the butyl derivative mimics the 3-/2-/1- sequence of iron proteins.

From a structural viewpoint, the Fe_4S_4 cluster can be considered to originate from the interpenetration of Fe_4 and S_4 tetrahedra. Scheme 2 depicts the molecular structures of the two redox partners $[Fe_4S_4-(S-Ph)_4]^{2-}/[Fe_4S_4(S-Ph)_4]^{3-}$.^{1a}



Scheme 2

On the basis of these data it is generally assumed that, as shown in Scheme 3, the 2-/3- redox transformation involves a structural reorganisation from a *compressed* to an *elongated* geometry.



Scheme 3

Analogous cuboidal structures are found not only for the already cited series $[Fe_4S_4(C_5H_5)_4]^n$ ($n = -1, 0, 1+, 2+, 3+$), but also for Co_4S_4 ($[Co_4S_4(C_5H_5)_4]^n$; $n = 0, 1+$), Mo_4S_4 ($[Mo_4S_4(C_5H_4-Pr^i)_4]^n$; $n = 0, 1+, 2+$),^{1a} and V_4S_4 ($[V_4S_4(C_5H_4-Me)_4]^n$, $n = 0, 1+$)¹³ derivatives.

Another four-iron sulfur assembly is Fe_4S_5 . Figure 11 illustrates the geometry of the Fe_4S_5 core of the $[Fe_4S_5(C_5H_5)_4]^{2+}$ dication.^{1a}

Compared to the most common Fe_4S_4 assembly, besides the three triply-bridging sulfur atoms, there is a disulfur group the sulfur atoms of which are also triply coordinating. This disposition leads to a structurally inequivalent arrangement and, therefore, an inequivalence in the different interatomic distances.

Figure 12 shows that also this derivative undergoes a rich series of reversible redox processes ($3+/2+/+/0$).

The monocation $[Fe_4S_5(C_5H_5)_4]^+$ has been isolated and its X-ray structure solved. As expected on the basis of the electrochemical reversibility of the $2+/+$ response, the geometry of the dication precursor is maintained, with only a slight lengthening of the bond lengths.

The last tetrairon-sulfur assembly that we consider is Fe_4S_6 . As seen in Figure 13, which refers to the cluster $[Fe_4S_6(C_5H_5)_4]$, it contains two triply bridging sulfur atoms and two disulfide groups in which one sulfur atom is triply bridging and one doubly bridging.

As illustrated in Figure 14, this derivative also undergoes three separate, reversible, one-electron redox processes ($2+/+/0/-$).

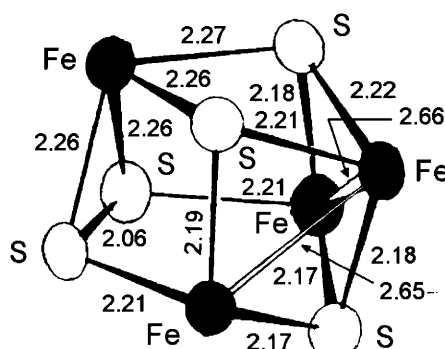


Figure 11 The geometry of the Fe_4S_5 core in $[Fe_4S_5(C_5H_5)_4]^{2+}$, together with the relevant bond lengths

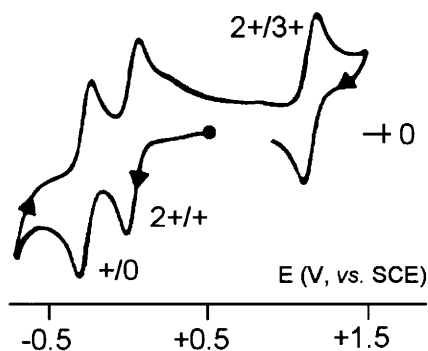


Figure 12 Cyclic voltammogram of $[Fe_4S_5(C_5H_5)_4]^{2+}$ in $MeCN$ solution

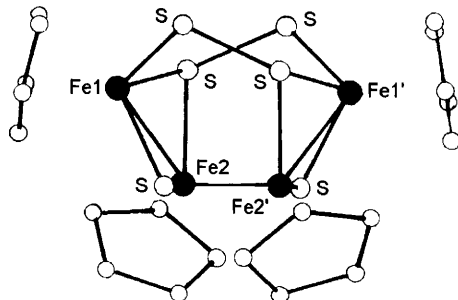


Figure 13 X-Ray structure of $[Fe_4S_6(C_5H_5)_4]$. $Fe1-Fe2 = Fe1'-Fe2' = 2.64 \text{ \AA}$; $Fe2-Fe2' = 3.41 \text{ \AA}$; $Fe1 \cdots Fe1' = 4.34 \text{ \AA}$

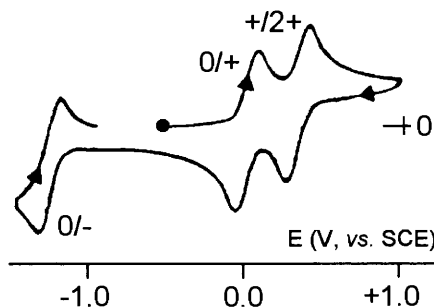


Figure 14 Cyclic voltammetric behaviour of $[Fe_4S_6(C_5H_5)_4]$ in CH_2Cl_2 solution

1.3 M_6S_n ($n = 6, 8, 9$)

The best known geometric arrangement of the M_6S_6 cluster is that of the series $[Fe_6S_6X_6]^{n-}$ (X = halides, phenolates, thiolates), called “prismanes”.^{1a} The term has its origin in the fact that these compounds, as shown in Figure 15 for the trianion $[Fe_6S_6Cl_6]^{3-}$, have a *hexagonal prismatic* geometry with alternating iron and sulfur atoms. Alternatively, it can be considered as a combination of two Fe_3S_3 cyclohexane-type ‘chair’ conformations.

These compounds do not possess a high redox flexibility in that, among the various redox changes observed, the only $[Fe_6S_6X_6]^{3-/2-}$ step is chemically reversible. For example, in the case of $[Fe_6S_6Cl_6]^{3-}$, the oxidation to $[Fe_6S_6Cl_6]^{2-}$ in CH_2Cl_2 solution occurs at +0.19 V (vs. SCE). The dianion maintains the same hexagonal prismatic geometry of the original trianion, with only fairly minor changes in the bond lengths.

Many transition metals are able to form the M_6S_8 assembly. The typical geometry is that illustrated in Figure 16 for the dication $[Fe_6S_8(PEt_3)_6]^{2+}$.^{1a,14}

The metal atoms assume an octahedral geometry. Each one of the triangular faces is apically coordinated by a triply bridging sulfur atom.

Figure 17 shows the high redox activity of this dication. It is able to support reversibly the redox sequence: $[Fe_6S_8(PEt_3)_6]^{4+/3+/2+/+/0}$ ($E_{4+/3+}^{\circ\circ} = +1.36$ V; $E_{3+/2+}^{\circ\circ} = +0.80$ V; $E_{2+/+}^{\circ\circ} = +0.06$ V; $E_{+/0}^{\circ\circ} = -1.03$ V). As a rather exceptional case, most members of such redox sequence have been isolated and structurally characterized.^{1a,14} Table 2 compiles the most significant variations in bonding lengths following the different redox changes.

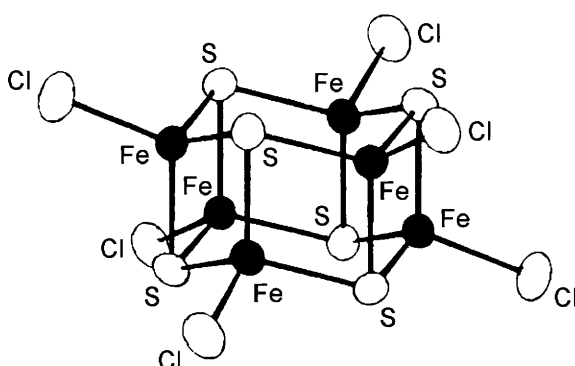


Figure 15 X-Ray structure of the trianion $[Fe_6S_6Cl_6]^{3-}$. Average distances in the Fe_3S_3 subunits: $Fe \cdots Fe = 3.79 \text{ \AA}$; $Fe-S = 2.28 \text{ \AA}$. Average distances in the perpendicular Fe_2S_2 rhomboids: $Fe \cdots Fe = 2.76 \text{ \AA}$; $Fe-S = 2.28 \text{ \AA}$

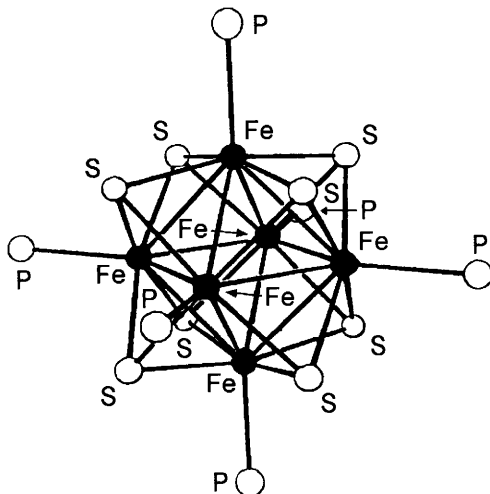


Figure 16 X-Ray structure of $[Fe_6S_8(PEt_3)_6]^{2+}$. Average bond lengths: $Fe-Fe = 2.62 \text{ \AA}$; $Fe-S = 2.25 \text{ \AA}$; $Fe-P = 2.29 \text{ \AA}$

As seen, the progressive electron additions cause a lengthening of the metal–metal bonds, which is compensated by a slight shortening of the metal–phosphorus distances, while the metal–sulfur distances remain essentially unchanged.

Table 2 Bonding distances (\AA) in the series $[Fe_6S_8(PEt_3)_6]^{3+/2+/+/0}$

Species	M–M	M–S	M–P
$[Fe_6S_8(PEt_3)_6]^{3+}$	2.58	2.24	2.30
$[Fe_6S_8(PEt_3)_6]^{2+}$	2.62	2.25	2.29
$[Fe_6S_8(PEt_3)_6]^+$	2.64	2.25	2.27
$Fe_6S_8(PEt_3)_6$	2.67	2.25	2.24

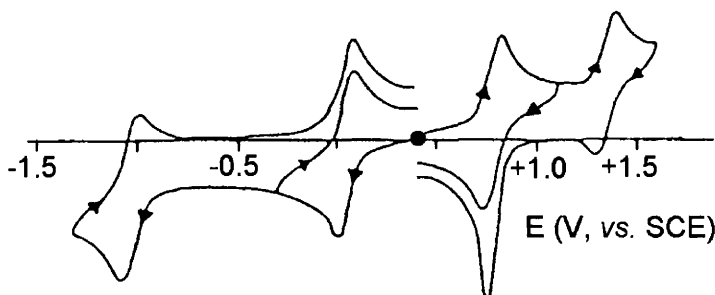


Figure 17 Cyclic voltammetric response recorded at a platinum electrode in a CH_2Cl_2 solution of $[Fe_6S_8(PEt_3)_6]^{2+}$. Scan rate 0.2 V s^{-1}

Similar behaviour has been displayed by the octahedral complexes $[\text{Co}_6\text{S}_8(\text{PEt}_3)_6]^{+}$ (which displays the reversible sequence $[\text{Co}_6\text{S}_8(\text{PEt}_3)_6]^{3+/2+/+/0/-}$),^{1a} $[\text{Mo}_6\text{S}_8(\text{PEt}_3)_6]$ (which displays the reversible sequence $[\text{Mo}_6\text{S}_8(\text{PEt}_3)_6]^{+/0/-/2-}$),¹⁵ and $[\text{Cr}_6\text{S}_8(\text{H})(\text{PEt}_3)_6]$ (which displays the reversible sequence $[\text{Cr}_6\text{S}_8(\text{H})(\text{PEt}_3)_6]^{+/0/-}$).¹⁶ In all cases at least one redox couple has been isolated and structurally characterized, and in all cases the structural rearrangements following the electron transfers are minimal.

The last six-atom metal–sulfur assembly to be considered is Fe_6S_9 , found in the thiolate derivatives $[\text{Fe}_6\text{S}_9(\text{SR})_2]^{4-}$. The rather unusual structure of one of these compounds is shown in Figure 18, which refers to $[\text{Fe}_6\text{S}_9(\text{SEt})_2]^{4-}$.^{1a}

All six iron atoms are coplanar and each one assumes a tetrahedral geometry, binding four sulfur atoms.

These compounds exhibit the chemically reversible sequence $3-/4-/5-$. However, no X-ray structure is available for the different members.

1.4 M_9S_9

To conclude this brief review of homonuclear metal–sulfur clusters we consider the Ni_9S_9 assembly present in the dication $[\text{Ni}_9\text{S}_9(\text{PEt}_3)_6]^{2+}$, which highlights the spectacular structure and high redox capacity of this cluster, Figure 19.^{1a}

The molecular structure of this cluster can be viewed either as a cofacial Ni_9 bioctahedron or as three coplanar Ni_3 triangles positioned in turn inside three coplanar S_3 triangles.

Despite the fact that it has not been possible to isolate any redox partners of this compound, it is evident that at least the monocation

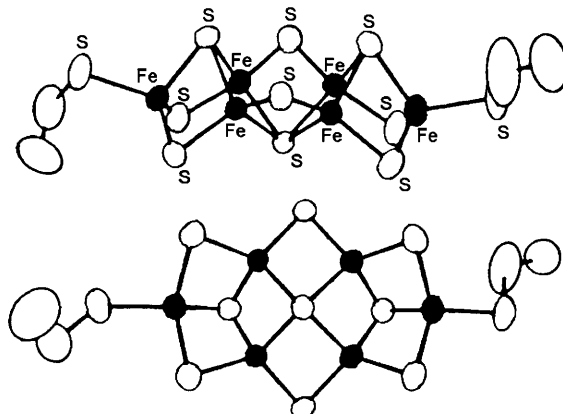


Figure 18 X-Ray structure of $[\text{Fe}_6\text{S}_9(\text{SEt})_2]^{4-}$

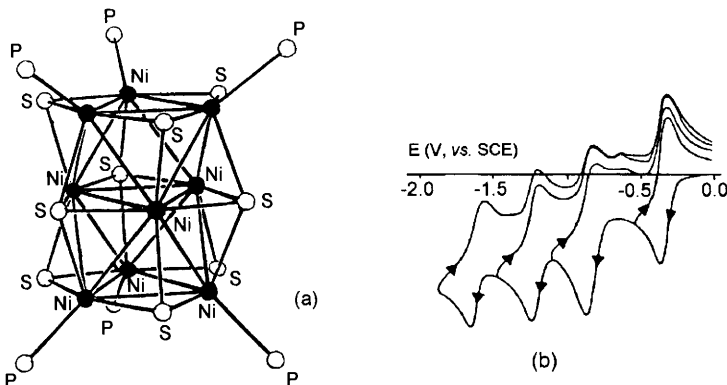


Figure 19 Cyclic voltammogram (in MeCN solution) (a) and X-ray structure (b) of $[Ni_9S_9(PEt_3)_6]^{2+}$

$[Ni_9S_9(PEt_3)_6]^{2+}$ is stable and probably has the same molecular structure of the dication precursor.

2 METAL–CARBONYL CLUSTERS

Whereas a large number of metal–sulfur clusters are present in nature, carbonyl clusters are exclusively products of chemical synthesis. They have been widely used in industrial catalytic processes¹⁷ and some of these processes are triggered by the redox aptitude of these species.^{1c–g} As for the metal–sulfur clusters, we will briefly discuss their structures and their propensity to donate/accept electrons in order of increasing nuclearity. We will consider only homonuclear and homoleptic metal–carbonyl derivatives. However, it is noted that heteronuclear derivatives are gaining considerable interest due to the synergistic effect of metal–metal bonds possessing a polar character.^{1c,1d}

2.1 $M_3(CO)_{12}$, $[M_3(CO)_{11}]^{2-}$ ($M = Fe, Ru, Os$)

Figure 20 illustrates the molecular structure of $[Fe_3(CO)_{12}]^{1d}$.

It consists of a triangle of iron atoms. Two CO molecules assume a bridging position with respect to one Fe–Fe side (Fe2–Fe3), rendering this side shorter by about 0.1 Å with respect to the other two sides bearing only terminal carbonyl groups.

In CH_2Cl_2 solution this compound displays two successive one-electron reductions, only the first of which is chemically reversible ($E'_{0/-} = -0.35$ V; $E_{p-/-2-} = -0.85$ V (vs. Ag/AgCl)). On the basis of the electrochemical quasireversibility of the $[Fe_3(CO)_{12}]/[Fe_3(CO)_{12}]^-$ process ($\Delta E_p = 110$ mV, at $0.2Vs^{-1}$), it seems reasonable to assume that

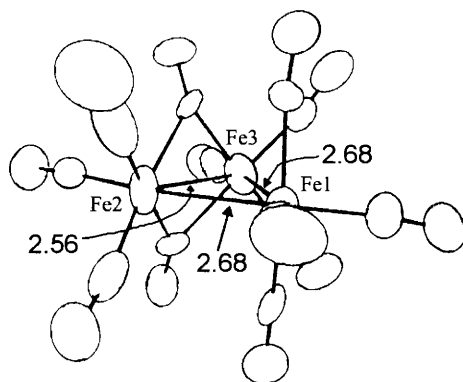


Figure 20 X-Ray structure of $[Fe_3(CO)_{12}]$ together with the relevant Fe–Fe bond lengths

the monoanion might have a slightly different geometry compared to that of the neutral precursor.

As is evident from Figure 21, the triangular $[Ru_3(CO)_{12}]$ and $[Os_3(CO)_{12}]$ display only terminal carbonyl groups.

Although these two derivatives are isoelectronic with $[Fe_3(CO)_{12}]$, both exhibit irreversible reduction processes. This observation is in agreement with the theoretical prediction that the LUMO of $[M_3(CO)_{12}]$ compounds, which are electronically saturated (48 valence electrons), is metal–metal antibonding, and the antibonding character follows the order: Os > Ru > Fe.

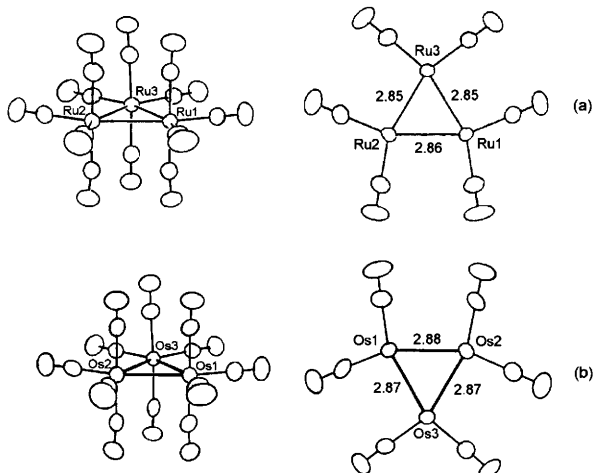


Figure 21 X-Ray structures and relevant structural parameters of: (a) $[Ru_3(CO)_{12}]$; (b) $[Os_3(CO)_{12}]$

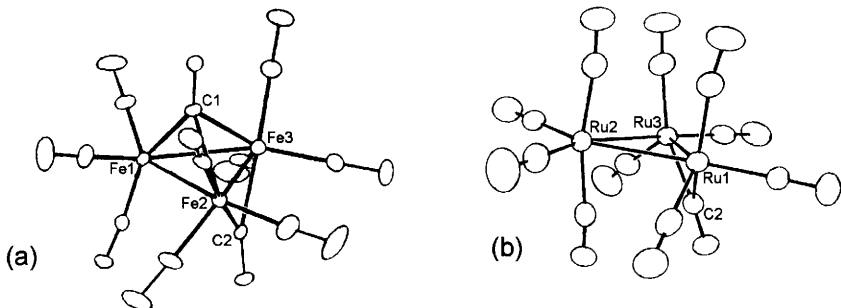


Figure 22 *X-Ray structure of: (a) $[Fe_3(CO)_{11}]^{2-}$. $Fe1-Fe = 2.60 \text{ \AA}$; $Fe1-C1 = 1.85 \text{ \AA}$; $Fe2-C1 = Fe3-C1 = 2.21 \text{ \AA}$; $Fe2-C2 = Fe3-C2 = 1.96 \text{ \AA}$; average $Fe-C_{(CO\text{-terminal})}$ distance = 1.75 \AA . (b) $[Ru_3(CO)_{11}]^{2-}$. $Ru1-Ru3 = 2.78 \text{ \AA}$; $Ru1-Ru2 = 2.88 \text{ \AA}$; $Ru2-Ru3 = 2.87 \text{ \AA}$; $Ru1-C2 = Ru3-C2 = 2.07 \text{ \AA}$; average $Ru-C_{(CO\text{-terminal})}$ distance = 1.90 \AA*

As happens for the neutral derivatives, the dianion $[Fe_3(CO)_{11}]^{2-}$ has a molecular structure different from that of the analogous $[Ru_3(CO)_{11}]^{2-}$ and $[Os_3(CO)_{11}]^{2-}$ dianions, Figure 22.

In the case of $[Fe_3(CO)_{11}]^{2-}$, a triply bridging carbonyl group is asymmetrically positioned (as deduced by the bond distances) above the Fe_3 triangle, which is not found for $[Ru_3(CO)_{11}]^{2-}$ ¹⁸ and $[Os_3(CO)_{11}]^{2-}$ ¹⁵. In all the three compounds there is a carbonyl group bridging two metal atoms.

It is found also that for the dianions $[M_3(CO)_{11}]^{2-}$ ($M = Fe, Ru, Os$), which are electronically saturated too (48 valence electrons), only $[Fe_3(CO)_{11}]^{2-}$ has a well-defined redox chemistry. In fact, in the solution, it undergoes a chemically reversible one-electron oxidation ($E^{\circ'} = -0.76 \text{ V vs. SCE}$). The molecular structure of the monoanion $[Fe_3(CO)_{11}]^-$ is reported in Figure 23.¹⁹

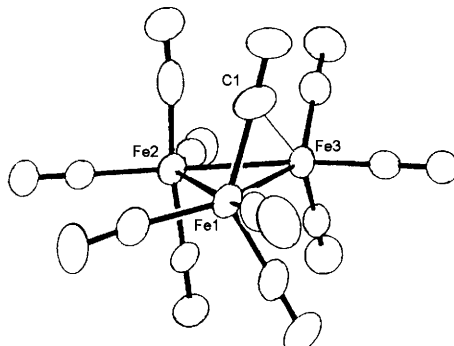


Figure 23 *X-Ray structure of $[Fe_3(CO)_{11}]^-$. $Fe1-Fe3 = 2.50 \text{ \AA}$; $Fe1-Fe2 = 2.68 \text{ \AA}$; $Fe2-Fe3 = 2.63 \text{ \AA}$; $Fe1-C1 = 1.89 \text{ \AA}$; $Fe3-C1 = 2.49 \text{ \AA}$*

Comparison with the corresponding dianion reveals important structural differences. In fact, the triply bridging apical carbonyl is no longer present and one of the bonds of the bridging carbonyl (namely, Fe₃–C1) weakens (becoming half-bonding). This asymmetric disposition of the ligand leads to an inequivalence of all the three Fe–Fe distances.

Unlike [Fe₃(CO)₁₁]²⁻, both [Ru₃(CO)₁₁]²⁻ and [Os₃(CO)₁₁]²⁻ undergo irreversible oxidations.

2.2 [Fe₄(CO)₁₃]²⁻, M₄(CO)₁₂ (M = Co, Rh, Ir)

Figure 24 shows the molecular structure of the dianion [Fe₄(CO)₁₃]²⁻.^{1d} The iron atoms are disposed in a tetrahedral arrangement and all the carbonyl groups are terminally coordinated, except the one triply bridging the Fe₃ base.

Although electronically saturated (60 valence electrons), the dianion undergoes a chemically reversible one-electron oxidation (in THF, $E^{\circ'} = -0.17$ V vs. SCE). The corresponding monoanion [Fe₄(CO)₁₃]⁻ is stable and EPR measurements indicate that it probably maintains the same geometry as the dianion precursor.

It is evident from Figure 25 that the isoelectronic [Co₄(CO)₁₂] also has a tetrahedral geometry,^{1d} but the disposition of the carbonyl groups is different from that in [Fe₄(CO)₁₃]²⁻. In fact, three are coplanar and doubly bridging the triangular Co₃ base, whereas the remaining nine groups are terminal.

As can be deduced from Figure 26, [Co₄(CO)₁₂] exhibits in dichloroethane solution a one-electron reduction ($E^{\circ'} = -0.30$ V vs. SCE) with features of chemical reversibility on the cyclic voltammetric time scale, as well as a multielectron irreversible oxidation. Nevertheless,

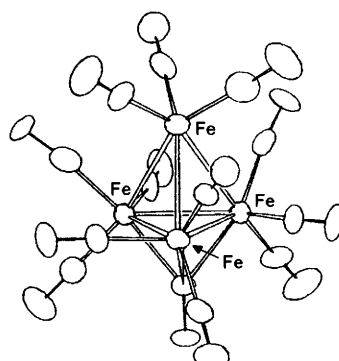


Figure 24 X-Ray structure of [Fe₄(CO)₁₃]²⁻. Average bond lengths: Fe_(basal)–Fe_(apical) = 2.61 Å; Fe_(basal)–Fe_(basal) = 2.54 Å

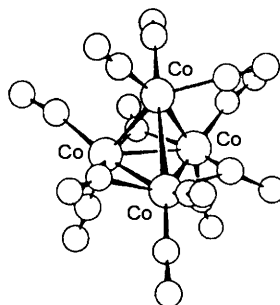


Figure 25 X-Ray structure of $[\text{Co}_4(\text{CO})_{12}]$. Average Co–Co distance = 2.49 \AA

the electrogenerated monoanion $[\text{Co}_4(\text{CO})_{12}]^-$ is unstable on the longer time of controlled potential electrolysis.

Although $[\text{Rh}_4(\text{CO})_{12}]$ is isoelectronic and isostructural with $[\text{Co}_4(\text{CO})_{12}]$ (mean Rh–Rh distance 2.78 \AA), it does not display any chemically reversible redox processes.

Finally, it is noted that no electrochemical data are available for $[\text{Ir}_4(\text{CO})_{12}]$, (which, in contrast to $[\text{Co}_4(\text{CO})_{12}]$ and $[\text{Rh}_4(\text{CO})_{12}]$, display only terminal CO groups), because of its complete insolubility in organic solvents.

In conclusion, the low redox aptitude of $[\text{M}_4(\text{CO})_{12}]$ derivatives is related to their electronic saturation (60 valence electrons).

2.3 $[\text{M}_5(\text{CO})_{15}]^{n-}$ ($\text{M} = \text{Os}$, $n = 2$; $\text{M} = \text{Rh}$, $n = 1$)

The dianion $[\text{Os}_5(\text{CO})_{15}]^{2-}$ (72 valence electrons) has a trigonal-bipyramidal structure similar to that of the monoanion $[\text{Rh}_5(\text{CO})_{15}]^-$ (76 valence electrons) illustrated in Figure 27.^{1d}

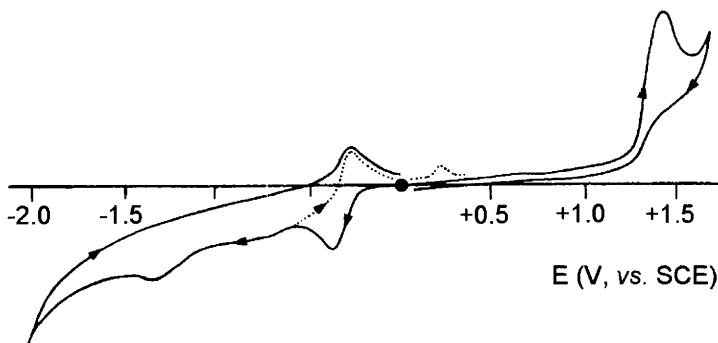


Figure 26 Cyclic voltammogram recorded at a platinum electrode in a $\text{C}_2\text{H}_4\text{Cl}_2$ solution of $[\text{Co}_4(\text{CO})_{12}]$. Scan rate 0.1 V s^{-1}

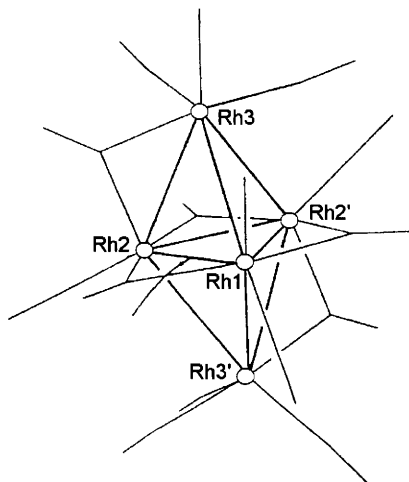


Figure 27 X-Ray structure of the monoanion $[Rh_5(CO)_{15}]^-$. Bond lengths: $Rh1-Rh2 = 2.73 \text{ \AA}$; $Rh2-Rh2' = 2.74 \text{ \AA}$; $Rh2-Rh3 = 2.92 \text{ \AA}$; $Rh1-Rh3' = 3.03 \text{ \AA}$

Both compounds are electronically saturated,²⁰ and, as such, they only exhibit irreversible redox processes.

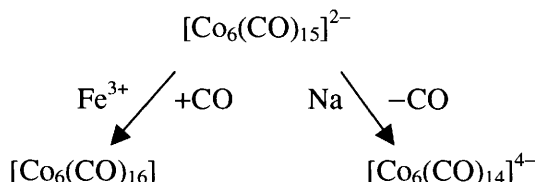
In the case of $[Os_5(CO)_{15}]^{2-}$, chemical oxidation in the presence of CO produces the trigonal-bipyramidal $[Os_5(CO)_{16}]^{1d}$.

2.4 $[M_6(CO)_{15}]^{2-}$ ($M = Co, Rh, Ir$), $[M_6(CO)_{18}]^{2-}$ ($M = Ru, Os$)

Both the series $[M_6(CO)_{15}]^{2-}$ ($M = Co, Rh, Ir$) and $[M_6(CO)_{18}]^{2-}$ ($M = Ru, Os$) are considered as electronically saturated (86 valence electrons). The two dianions $[M_6(CO)_{15}]^{2-}$ ($M = Co, Rh$) have the octahedral geometry reported in Figure 28 for $[Co_6(CO)_{15}]^{2-}$.^{1d}

The presence of three triply bridging, three doubly bridging and nine terminal carbonyl groups obviously causes inequivalence in the Co–Co bond lengths.

It is known that this compound can lose or gain carbonyl groups upon chemical reduction or oxidation according to the paths:



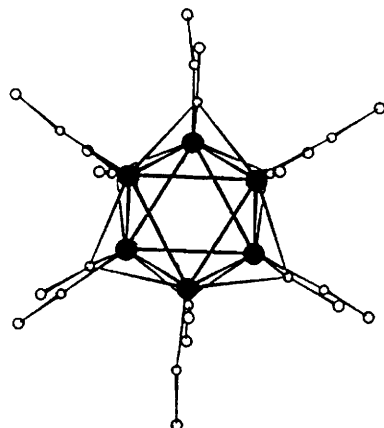


Figure 28 X-Ray structure of $[Co_6(CO)_{15}]^{2-}$. Average Co–Co bond length: 2.51 \AA

However, as shown in Figure 29, electrochemical studies showed that the intermediate monoanion $[Co_6(CO)_{15}]^-$ is a relatively stable species ($E_{2-/}^{\circ\prime} = -0.05 \text{ V}$; $\Delta E_p = 118 \text{ mV}$, at 0.2 V s^{-1}).

Conversely, the analogous rhodium complex $[Rh_6(CO)_{15}]^{2-}$ is redox inactive.

Figure 30 shows the solid-state structure of the isoelectronic dianion $[Ir_6(CO)_{15}]^{2-}$.

In support of the previous statement that iridium has a lower predisposition to form bridging carbonyl bonds compared to cobalt and rhodium, in this case, only three of the fifteen carbonyl groups assume a doubly bridging disposition whereas all the others have a terminal arrangement.

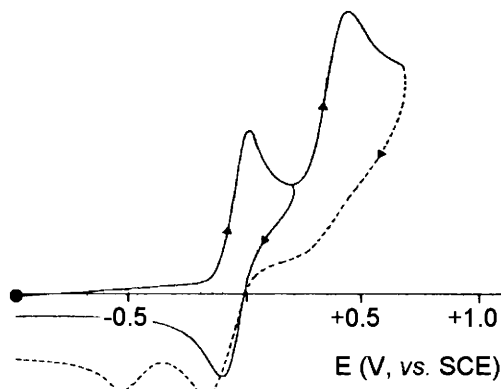


Figure 29 Cyclic voltammogram recorded at a platinum electrode in a CH_2Cl_2 solution of $[Co_6(CO)_{15}]^{2-}$. Scan rate 0.2 V s^{-1}

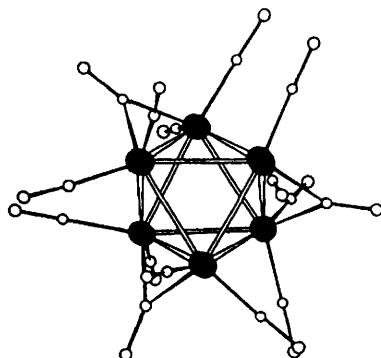


Figure 30 $X\text{-ray structure of } [\text{Ir}_6(\text{CO})_{15}]^{2-}$. Average Ir–Ir bond length: 2.77\AA

In contrast to $[\text{Co}_6(\text{CO})_{15}]^{2-}$ and $[\text{Rh}_6(\text{CO})_{15}]^{2-}$, which do not afford stable redox partners, $[\text{Ir}_6(\text{CO})_{15}]^{2-}$ generates the corresponding monoanion ($E_{2-/}^{\circ\prime} = +0.04$ V; $\Delta E_p = 96$ mV, at 0.2 V s $^{-1}$) and neutral derivative. This latter is, however, only a transient species ($E_{-/0}^{\circ\prime} = +0.36$ V), Figure 31.

Given that the redox change $[\text{Ir}_6(\text{CO})_{15}]^{2-/}$ does not depart significantly from the electrochemical reversibility, one could predict that the molecular geometry of the $[\text{Ir}_6(\text{CO})_{15}]^-$ monoanion is probably similar to that of the corresponding dianion.

Hence, it can be deduced that, despite the electronic saturation of the $[\text{M}_6(\text{CO})_{15}]^{2-}$ family, their members possess some redox propensity.

We turn our attention now to the $[\text{M}_6(\text{CO})_{18}]^{2-}$ family. In order to illustrate the redox activity of the $[\text{Ru}_6(\text{CO})_{18}]^{2-}$ and $[\text{Os}_6(\text{CO})_{18}]^{2-}$ derivatives, it is interesting to examine the redox behaviour of the neutral complex $[\text{Os}_6(\text{CO})_{18}]$ (84 valence electrons). As already discussed in

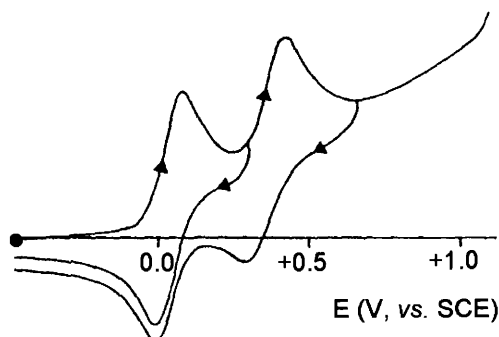


Figure 31 Cyclic voltammogram recorded at a platinum electrode in a thf solution of $[\text{Ir}_6(\text{CO})_{15}]^{2-}$. Scan rate 0.2 V s $^{-1}$

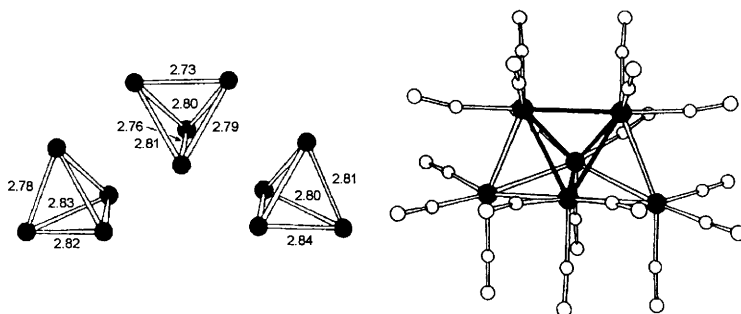


Figure 32 X-Ray structure of $[Os_6(CO)_{18}]$ together with the relevant bond lengths

Chapter 2, Section 1.3.2, it possesses a bicapped tetrahedral geometry, Figure 32.^{1d}

As shown in Figure 33, this compound undergoes a single two-electron reduction with marked characteristics of electrochemical quasireversibility ($\Delta E_p = 255$ mV, at 0.01 V s^{-1}).

The molecular structure of the corresponding dianion $[Os_6(CO)_{18}]^{2-}$ is shown in Figure 34; it has an essentially regular octahedral geometry.

One must therefore deduce that the quasireversibility of the $[Os_6(CO)_{18}]^{0/2-}$ reduction is determined by the significant molecular reorganization from bicapped-tetrahedral to octahedral geometry induced by the addition of the two electrons.

The $[Ru_6(CO)_{18}]^{2-}$ dianion also has octahedral geometry. Its electrochemical behaviour in different solvents has revealed a two-electron

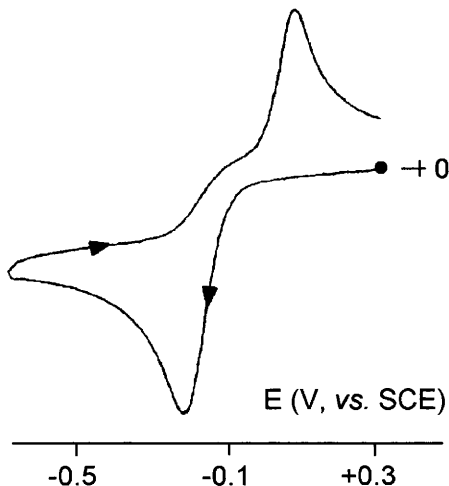


Figure 33 Cyclic voltammogram recorded at a platinum electrode in a thf solution of $[Os_6(CO)_{18}]$. Scan rate 0.04 V s^{-1}

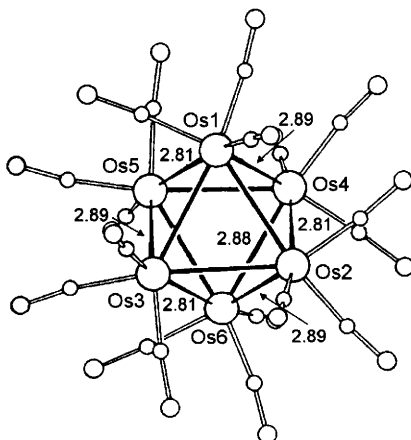


Figure 34 X-Ray structure of $[Os_6(CO)_{18}]^{2-}$ together with the relevant bond lengths

irreversible oxidation (two separate one-electron steps in acetone; a single two-electron step both in CH_2Cl_2 and thf), but in CH_2Cl_2 solution the electrogenerated $[Ru_6(CO)_{18}]$ species is short lived. By analogy with the $[Os_6(CO)_{18}]^{0/2-}$ redox couple, it seems reasonable to speculate that the transient $[Ru_6(CO)_{18}]$ species has a bicapped-tetrahedral geometry too.

2.5 Clusters of Higher Nuclearity: $[Ir_{14}(CO)_{27}]^-$, $[Pt_{19}(CO)_{22}]^{4-}$, $[Pt_{24}(CO)_{30}]^{2-}$

To conclude this brief overview of carbonyl clusters of increasing nuclearity, Figures 35–37 show the molecular structures and the relative

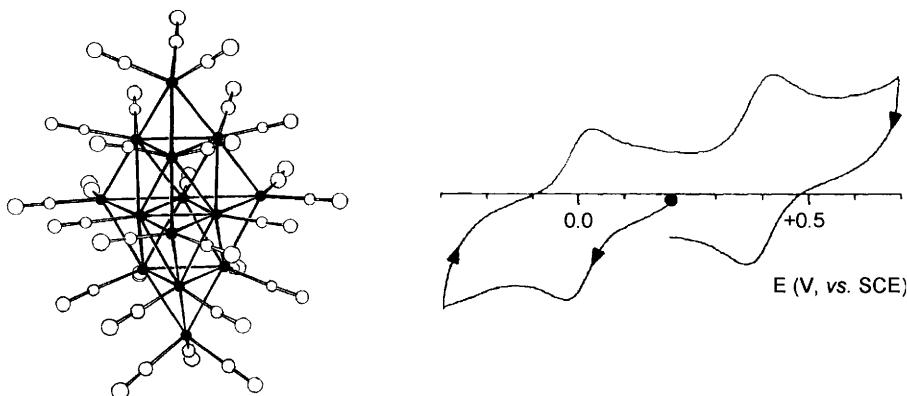


Figure 35 X-Ray structure and cyclic voltammogram (in CH_2Cl_2 solution) of $[Ir_{14}(CO)_{27}]^-$

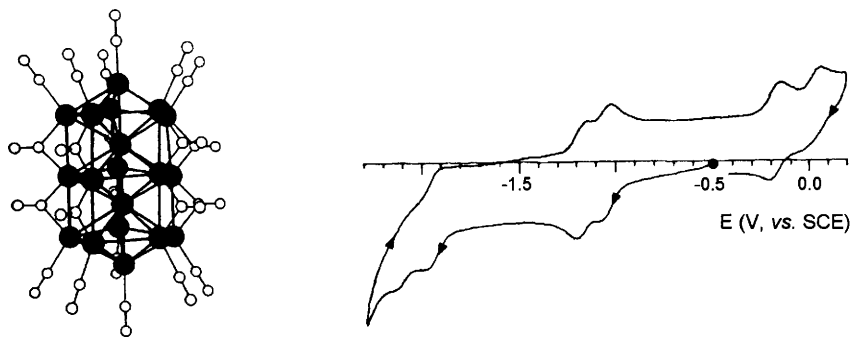


Figure 36 X-Ray structure and cyclic voltammogram (in MeCN solution) of $[Pt_{19}(CO)_{22}]^{4-}$

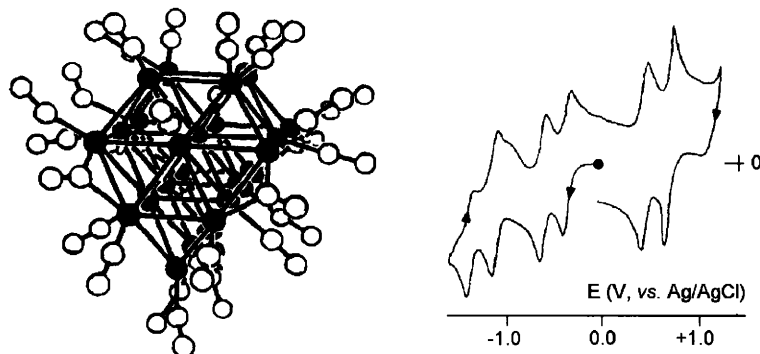


Figure 37 X-Ray structure and cyclic voltammogram (in CH_2Cl_2 solution) of $[Pt_{24}(CO)_{30}]^{2-}$

cyclic voltammograms of $[Ir_{14}(CO)_{27}]^-$, $[Pt_{19}(CO)_{22}]^{4-}$ and $[Pt_{24}(CO)_{30}]^{2-1d}$, which can be thought as ‘clusters of clusters’.

We limit the description of these compounds to highlighting simply their spectacular structures and versatility in electron transfer processes.^{1d,21} More detailed aspects can be found in the literature.^{1d,21}

3 CARBONYL CLUSTERS WITH INTERSTITIAL ATOMS

In the field of carbonyl clusters it is not rare to find compounds in which atoms such as C, N and P become trapped in interstitial or semi-interstitial positions inside the metal cage. We will briefly consider this type of compound in order of increasing encapsulation of the interstitial atom.

3.1 $[\text{Fe}_4(\text{CO})_{12}\text{C}]^{2-}$, $[\text{Fe}_4(\text{CO})_{12}\text{N}]^-$

The tetrahedral structure of the dianion $[\text{Fe}_4(\text{CO})_{13}]^{2-}$ has been described in Section 2.2. The reductive degradation of the carbonyl group apically bound to the Fe_3 basal triangle leads to the $[\text{Fe}_4(\text{CO})_{12}\text{C}]^{2-}$ carbide cluster, the molecular structure of which is shown in Figure 38.^{1d}

The tetrahedral geometry of the $[\text{Fe}_4(\text{CO})_{13}]^{2-}$ precursor is lost, being replaced by a ‘butterfly’ structure. The $\text{Fe}2\text{--Fe}3$ bond constitutes the body of the butterfly, while the $\text{Fe}1\text{Fe}2\text{Fe}3$ and $\text{Fe}4\text{Fe}2\text{Fe}3$ triangles constitute the wings. It can be seen that the carbide carbon atom is positioned half way between the tips of the two wings.

In CH_2Cl_2 solution this electronically saturated carbide dianion (62 valence electrons) displays four distinct one-electron oxidations, but only the first two processes (leading to $[\text{Fe}_4(\text{CO})_{12}\text{C}]^-$ and $[\text{Fe}_4(\text{CO})_{12}\text{C}]$, respectively) are partially chemically reversible. This result is in agreement with theoretical calculations which indicate that the HOMO of this molecule, which is centred on the $\text{Fe}2\text{--Fe}3$ body of the butterfly, is metal–metal bonding. One can, therefore, deduce that the removal of electrons causes degradation of the molecule. Nevertheless, if the oxidation is carried out in the presence of (the two-electron donor) CO the neutral compound $[\text{Fe}_4(\text{CO})_{13}\text{C}]$ (62 valence electrons) is formed, which has a structure substantially similar to that of the original dianion, but with the additional CO group bridging the $\text{Fe}2\text{--Fe}3$ bond.

As can be seen in Figure 39, the nitride monoanion $[\text{Fe}_4(\text{CO})_{12}\text{N}]^-$ has a butterfly geometry similar to that of $[\text{Fe}_4(\text{CO})_{12}\text{C}]^{2-}$, even if the wings are considerably less open.^{1d}

Despite its electronic saturation (62 valence electrons), this derivative in MeCN solution is able to add reversibly two electrons in two separate steps ($E_{-/-2}^{\circ\prime} = -1.24$ V; $E_{2-/3-}^{\circ\prime} = -1.58$ V), Figure 40.

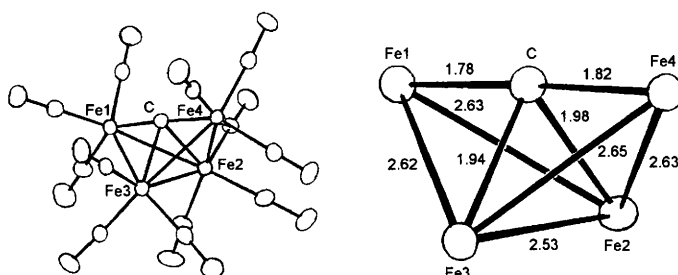


Figure 38 X-Ray structure of $[\text{Fe}_4(\text{CO})_{12}\text{C}]^{2-}$ together with the relevant bond lengths. Dihedral angle between the two triangles $\text{Fe}1\text{Fe}2\text{Fe}3/\text{Fe}4\text{Fe}2\text{Fe}3 = 102.4^\circ$

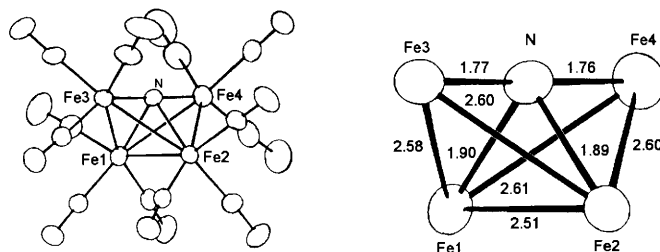


Figure 39 X-Ray structure of $[Fe_4(CO)_{12}N]^-$ together with the relevant bond lengths.
Dihedral angle between the two triangles $Fe_1Fe_2Fe_3/Fe_1Fe_2Fe_4 = 78.2^\circ$

The $[Fe_4(CO)_{12}N]^{2-}$ dianion is completely stable and, on the basis of the electrochemical reversibility of the first reduction process ($\Delta E_p = 60$ mV, at 0.1 V s $^{-1}$), it is reasonable to expect that it has a geometry similar to the monoanion precursor.

$[Fe_4(CO)_{12}N]^-$ is interesting also because it can give rise to *electrocatalytic substitution* of CO by PPh₃ (see Chapter 2, Section 1.4.4). In fact, Figure 41 shows that, in the presence of PPh₃, the cyclic voltammogram is modified compared to that reported in Figure 40, in that a new (irreversible) reduction peak ($E_p = -1.45$ V) appears in between the two original reversible reductions.

Furthermore, electrolysis at the first reduction peak ($E_w = -1.25$ V) is completed in a few seconds, consuming about 0.05 electrons per molecule. At the end of the exhaustive reduction the cyclic voltammogram displays only the irreversible peak at -1.45 V. These data unequivocally indicate the existence of the following electrocatalytic process:

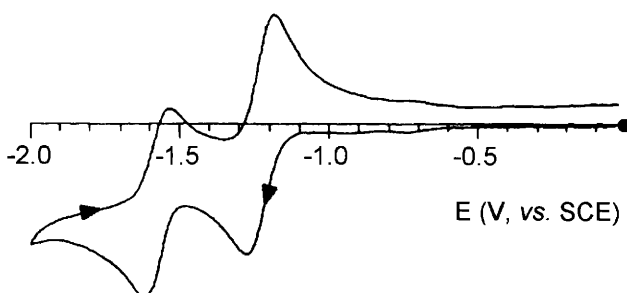


Figure 40 Cyclic voltammogram recorded at a mercury electrode in a MeCN solution of $[Fe_4(CO)_{12}N]^-$. Scan rate 0.2 V s $^{-1}$

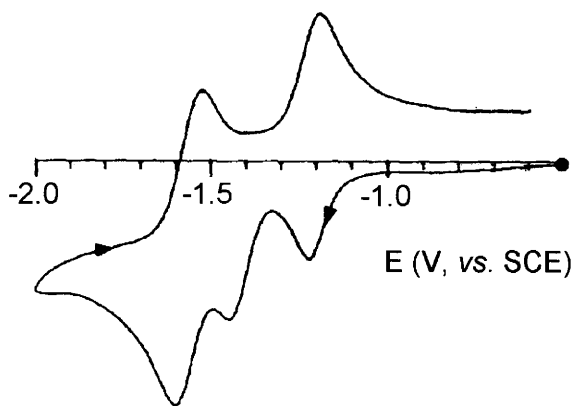
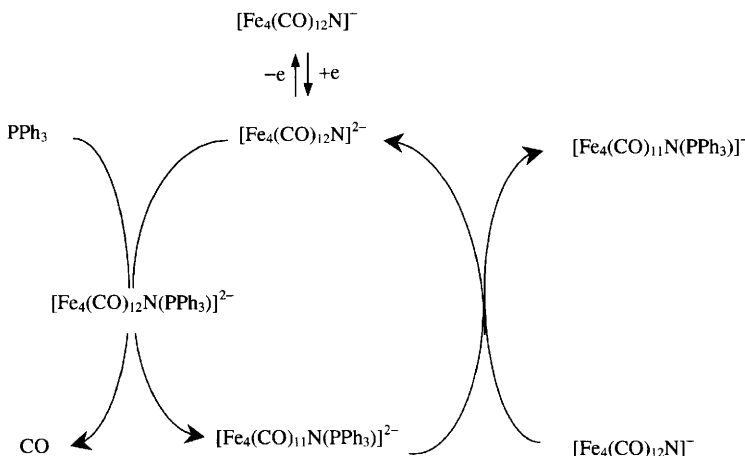


Figure 41 Cyclic voltammogram recorded at a mercury electrode in a MeCN solution of $[\text{Fe}_4(\text{CO})_{12}\text{N}]^-$ in the presence of PPh_3 . Scan rate 0.5 V s^{-1}



The driving force of this process (as measured by the difference between the pair of redox couples $[\text{Fe}_4\text{N}(\text{CO})_{12}]^-/[\text{Fe}_4\text{N}(\text{CO})_{12}]^{2-}$ and $[\text{Fe}_4\text{N}(\text{CO})_{11}(\text{PPh}_3)]^-/[\text{Fe}_4\text{N}(\text{CO})_{11}(\text{PPh}_3)]^{2-}$) is about 21 kJ mol^{-1} .

The molecular structure of the monoanion $[\text{Fe}_4\text{N}(\text{CO})_{11}(\text{PPh}_3)]^-$ is shown in Figure 42.²²

It is evident that the carbonyl group which has been substituted by the phosphine is one of those placed at the tip of one of the two ‘wings’. There are no significant differences in the bond lengths of the Fe_4N core compared to that of the $[\text{Fe}_4(\text{CO})_{12}]^-$ precursor.

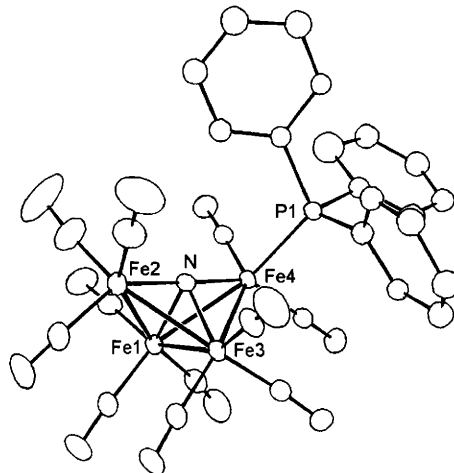


Figure 42 X-Ray structure of $[Fe_4(CO)_{11}N(PPh_3)]^-$. $Fe4-P1 = 2.22 \text{ \AA}$

3.2 $[Fe_5(CO)_{14}C]^{2-}$, $[Fe_5(CO)_{14}N]^-$

The molecular structure of the carbide dianion $[Fe_5(CO)_{14}C]^{2-}$ is shown in Figure 43.^{1d}

The five iron atoms assume a square-pyramidal geometry; the carbide atom has moved out of the basal plane by 0.18 \AA in the direction opposite to the apical iron atom. Two carbonyl groups in the basal plane are semi-bonding.

This electronically saturated derivative (74 valence electrons) undergoes in CH_2Cl_2 solution a (two-electron) reduction ($E^{\circ'} = -1.48 \text{ V}$) and a (two-electron) oxidation ($E^{\circ'} = +0.07 \text{ V}$), both processes looking like partially chemically reversible.

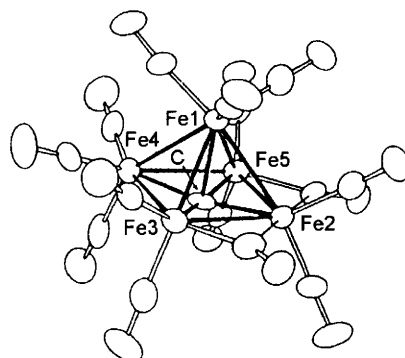


Figure 43 X-Ray structure of $[Fe_5(CO)_{14}C]^{2-}$. Average bond lengths: $Fe-Fe = 2.61 \text{ \AA}$; $Fe_{(basal)}-C = 1.89 \text{ \AA}$; $Fe_{(apical)}-C = 1.95 \text{ \AA}$

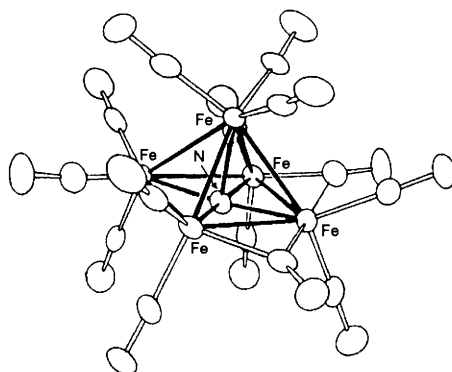


Figure 44 X-Ray structure of $[Fe_5(CO)_{14}N]^-$. Average bond lengths: $Fe-Fe = 2.60 \text{ \AA}$; $Fe_{(basal)}-N = 1.84 \text{ \AA}$; $Fe_{(apical)}-N = 1.92 \text{ \AA}$

As might be expected, the nitride monoanion $[Fe_5(CO)_{14}N]^-$ also has a square-pyramidal geometry, with the nitride atom moved out of the basal plane in a direction opposite to the apical iron atom by about 0.11 Å, Figure 44.^{1d}

Figure 45 shows that this monoanion (74 valence electrons) in MeCN solution undergoes two separate (one-electron) reductions, only the first one ($E^{\circ'} = -0.90 \text{ V}$) being chemically and electrochemically reversible.

As can be inferred from Figure 46, and confirmed by controlled potential electrolysis, in the presence of phosphines, PR_3 , $[Fe_5(CO)_{14}N]^-$ also undergoes the electrocatalytic substitution of one CO group with formation of $[Fe_5(CO)_{13}N(PR_3)]^-$.

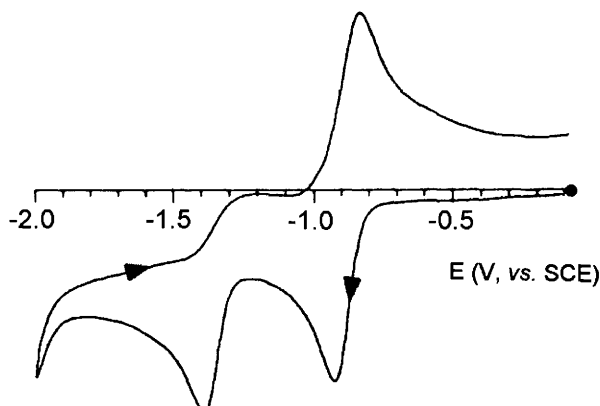


Figure 45 Cyclic voltammogram recorded at a mercury electrode in a MeCN solution of $[Fe_5(CO)_{14}N]^-$. Scan rate 0.2 V s^{-1}

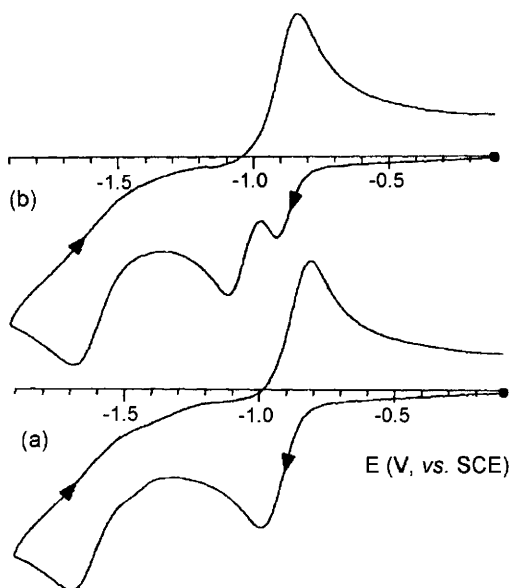


Figure 46 Cyclic voltammograms recorded at a platinum electrode in a MeCN solution of: (a) $[\text{Fe}_5(\text{CO})_{14}\text{N}]^{2-}$; (b) $[\text{Fe}_5(\text{CO})_{14}\text{N}]^{2-} + \text{PPh}_3$. Scan rate 0.2 V s^{-1}

A comparison of Figures 46 and 45 shows that the use of a different electrode materials (Pt vs. Hg) leads to a different degree of reversibility in both the reduction processes. As pointed out in Chapter 3, Section 1.1, this proves that the effect is due to surface phenomena connected with the electrode material rather than to the slow rate of the electron transfers.

3.3 $[\text{Fe}_6(\text{CO})_{16}\text{C}]^{2-}$, $[\text{Fe}_6(\text{CO})_{15}\text{N}]^{3-}$, $[\text{Os}_6(\text{CO})_{18}\text{P}]^{2-}$

In the dianion $[\text{Fe}_6(\text{CO})_{16}\text{C}]^{2-}$, the carbide atom is completely encapsulated in the octahedral metal cage. This dianion (86 valence electrons) does not exhibit any redox process with characteristics of chemical reversibility.^{1d}

The isoelectronic nitride $[\text{Fe}_6(\text{CO})_{15}\text{N}]^{3-}$ trianion possesses a similar octahedral geometry, Figure 47.²³

As illustrated in Figure 48a, this complex too has a limited redox activity, displaying three irreversible oxidations (peaks A,B,C, respectively).

However, in confirmation of the appearance of the peak-system E/F in the backscan, exhaustive three-electron oxidation in correspondence to the overall anodic process affords the cyclic voltammetric profile shown

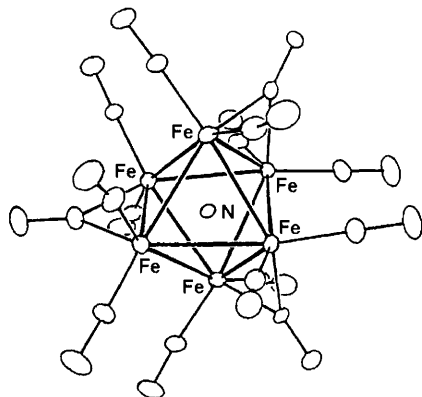


Figure 47 X-Ray structure of $[Fe_6(CO)_{15}N]^{3-}$. Average bond lengths: $Fe-Fe = 2.64 \text{ \AA}$; $Fe-N = 1.84 \text{ \AA}$

in Figure 48b, which is quite similar to that illustrated in Figure 45 for $[Fe_5(CO)_{14}N]^-$. This suggests that, as a consequence of the three-electron removal, the octahedral Fe_6 complex loses an apical $Fe(CO)_4$ group and assumes the square-pyramidal geometry of $[Fe_5(CO)_{14}N]^-$.²³

A completely different arrangement of the six metal atoms is present in the phosphide monoanion $[Os_6(CO)_{18}P]^-$. In fact, Figure 49 shows that the phosphorus atom is completely encapsulated in a trigonal-prismatic metal cage.

It has been reported that this compound (90 valence electrons) in CH_2Cl_2 solution undergoes a two-electron reduction to the corresponding trianion.^{1d}

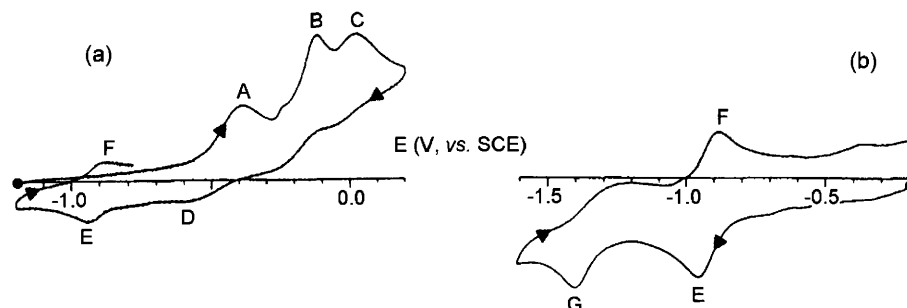


Figure 48 Cyclic voltammograms recorded at a mercury electrode in a $MeCN$ solution of $[Fe_6(CO)_{15}N]^{3-}$. (a) Original profile; (b) profile after exhaustive oxidation at $+0.2 \text{ V}$. Scan rate 0.2 V s^{-1}

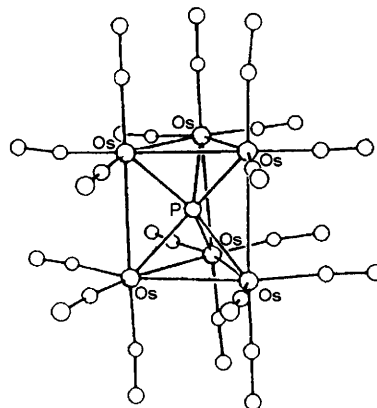


Figure 49 X-Ray structure of $[Os_6(CO)_{18}P]^-$. Average bond lengths: $Os-Os_{(basal)} = 2.93 \text{ \AA}$; $Os-Os_{(interbasal)} = 3.14 \text{ \AA}$; $Os-P = 2.31 \text{ \AA}$

3.4 $[Os_{10}(CO)_{24}C]^{2-}$

Figure 50 shows the molecular structure of the dianion $[Os_{10}(CO)_{24}C]^{2-}$.

It is constituted by a hexaosmium octahedron (encapsulating a carbon atom), four faces of which apically bear a $Os(CO)_3$ group.

The most important redox transformation of this complex (134 valence electrons) is the one-electron oxidation to the corresponding monoanion, Figure 51.

3.5 $[Co_{13}(CO)_{24}(C)_2]^{4-}$

The $[Co_{13}(CO)_{24}(C)_2]^{4-}$ tetraanion, which contains two carbide carbon atoms within its metal cage, has a rather complicated structure, Figure 52.

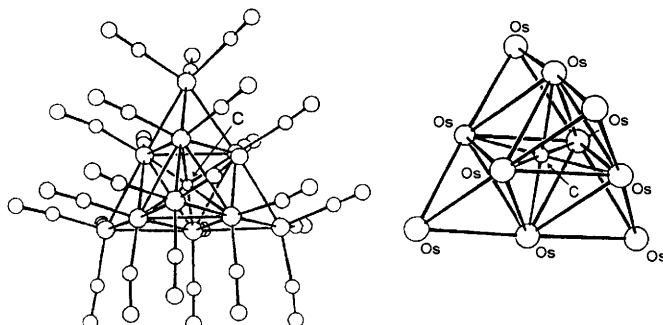


Figure 50 X-Ray structure of $[Os_{10}(CO)_{24}C]^{2-}$. Average bond lengths: $Os-Os_{(central\ octahedron)} = 2.88 \text{ \AA}$; $Os-Os_{(peripheral\ tetrahedra)} = 2.79 \text{ \AA}$; $Os-C_{(central\ octahedron)} = 2.04 \text{ \AA}$

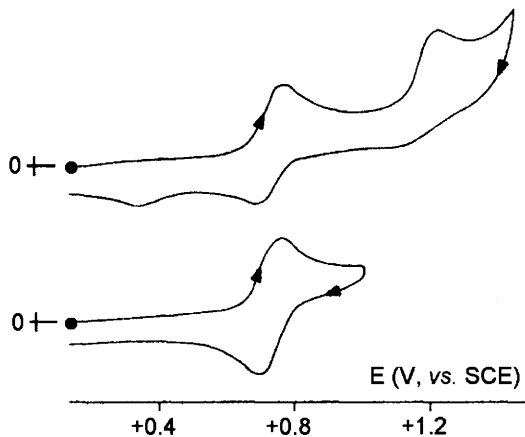


Figure 51 Cyclic voltammograms recorded at a platinum electrode in a CH_2Cl_2 solution of $[\text{Os}_{10}(\text{CO})_{24}\text{C}]^{2-}$. Scan rate 0.1 V s^{-1}

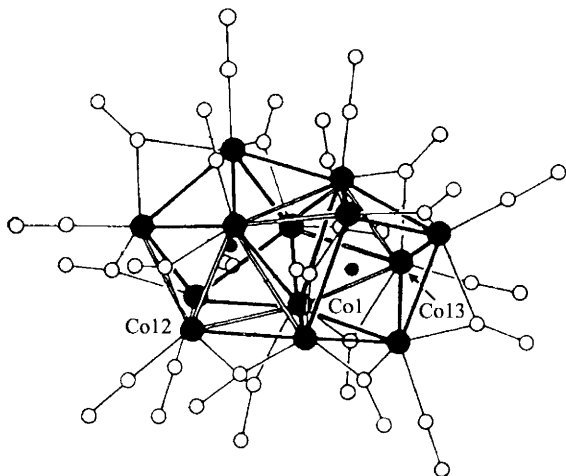


Figure 52 X-Ray structure of $[\text{Co}_{13}(\text{CO})_{24}(\text{C})_2]^{4-}$. Average bond lengths: $\text{Co}-\text{Co} = 2.57 \text{ \AA}$; $\text{Co}-\text{C}_{(\text{intraprismatic})} = 1.98 \text{ \AA}$

It can be considered to be constituted by two Co_6 prisms, each encapsulating a carbon atom, having a common apex (Co1) but rotated with respect to each other. The whole assembly is bound, on opposite sides, by a pentacoordinate cobalt atom (Co12 and Co13).^{1d} Clearly, the structural complexity results in inequivalent bond distances.

As illustrated in Figure 53, this complex (177 valence electrons) displays in CH_2Cl_2 solution a high redox activity. It is able to lose an

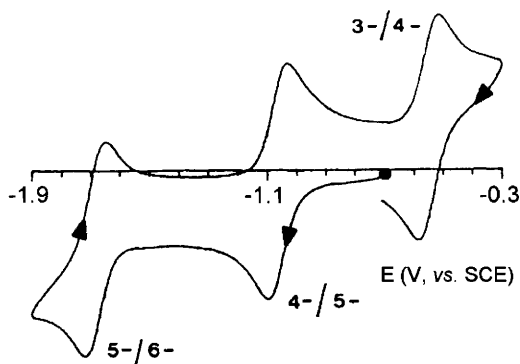


Figure 53 Cyclic voltammogram recorded at a platinum electrode in a MeCN solution of $[\text{Co}_{13}(\text{CO})_{24}(\text{C})_2]^{4-}$. Scan rate 0.2 V s^{-1}

electron reversibly $\{E^\circ ([\text{Co}_{13}(\text{CO})_{24}(\text{C})_2]^{4- / 3-}) = -0.54 \text{ V}\}$, and accept in succession two electrons $\{E^\circ ([\text{Co}_{13}(\text{CO})_{24}(\text{C})_2]^{4- / 5-}) = -1.06 \text{ V}; E^\circ ([\text{Co}_{13}(\text{CO})_{24}(\text{C})_2]^{5- / 6-}) = -1.68 \text{ V}\}$.

The trianion $[\text{Co}_{13}(\text{CO})_{24}(\text{C})_2]^{3-}$ has been isolated and its structure determined. In agreement with the electrochemical reversibility of the $[\text{Co}_{13}(\text{CO})_{24}(\text{C})_2]^{4- / 3-}$ transformation, it maintains the structure of the tetraanion and the variations in bond distances are minimal.

3.6 $[\text{Ni}_{32}(\text{CO})_{42}(\text{C})_6]^{6-}$

The last example of a cluster with interstitial atoms we will deal with is the hexaanion $[\text{Ni}_{32}(\text{CO})_{36}(\text{C})_6]^{6-}$, whose molecular structure is shown in Figure 54.²⁴

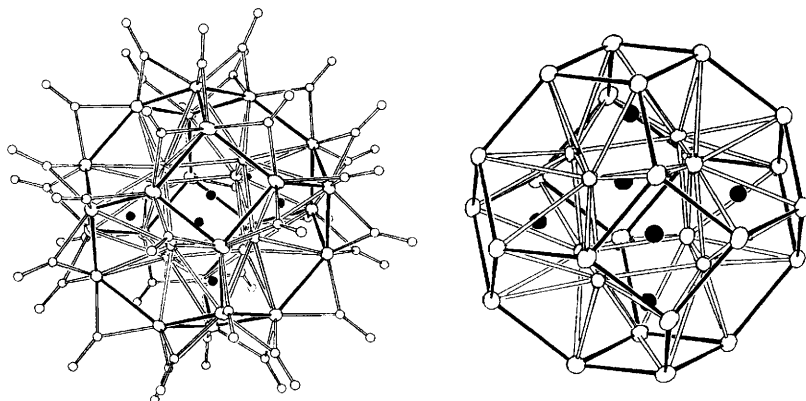


Figure 54 X-Ray structure of $[\text{Ni}_{32}(\text{CO})_{36}(\text{C})_6]^{6-}$. Average bond lengths: $\text{Ni}-\text{Ni} = 2.40 \text{ \AA}$; $\text{Ni}-\text{C}_{(\text{carbide})} = 2.06 \text{ \AA}$

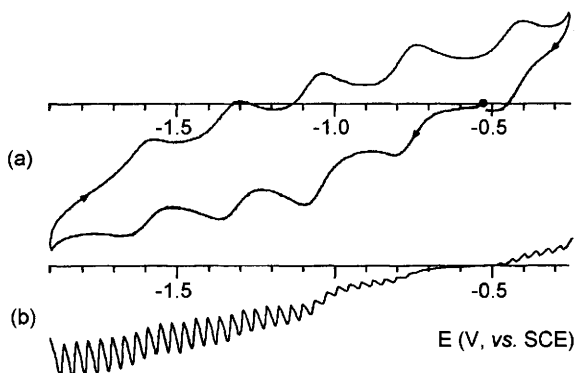


Figure 55 Cyclic (a) and hydrodynamic (or, with periodical renewal of the diffusion layer) (b) voltammograms recorded at a mercury electrode in a MeCN solution of $[Ni_{32}(CO)_{36}(C)_6]^{δ-}$. Scan rates: (a) 0.2 V s^{-1} ; (b) 0.02 V s^{-1}

This high nuclearity cluster displays an extensive redox activity, Figure 55,^{25#} in that it undergoes four successive one-electron reductions with characteristics of chemical reversibility ($E_{6-/7-}^{\circ'} = -0.77\text{ V}$; $E_{7-/8-}^{\circ'} = -1.06\text{ V}$; $E_{8-/9-}^{\circ'} = -1.33\text{ V}$; $E_{9-/10-}^{\circ'} = -1.61\text{ V}$) and a one-electron oxidation complicated by slow degradation of the corresponding pentaanion ($E_{6-/5-}^{\circ'} = -1.33\text{ V}$).

REFERENCES

1. (a) P. Zanello, *Coord. Chem. Rev.*, 1988, **83**, 199; (b) P. Zanello, *Coord. Chem. Rev.*, 1988, **87**, 1; (c) P. Zanello, *Struct. Bonding (Berlin)*, 1992, **79**, 101; (d) P. Zanello, *Stereochemistry of Organometallic and Inorganic Compounds*, P. Zanello (Ed.); Elsevier, Amsterdam, 1994, Vol. 5, 163–408; (e) P. Zanello and F. Fabrizi de Biani, *Metal Clusters in Chemistry* P. Braunstein, L.A. Oro, P.R. Raithby, eds, Wiley-VCH, Vol. 2, 1999, 1104–1136; (f) G. Longoni, C. Femoni, M.C. Iapalucci and P. Zanello, *Metal Clusters in Chemistry* P. Braunstein, L.A. Oro, P.R. Raithby, eds, Wiley-VCH, Vol. 2, 1999, 1137–1158; (g) P. Zanello, in *Unusual Structures and Physical Properties in Organometallic Chemistry*, M. Gielen, R. Willem and B. Wrackmeyer, eds, John Wiley & Sons Ltd, 2002, pp 1–49.
2. H. Beinert, R.H. Holm and E. Münck, *Science*, 1997, **277**, 653.
3. P.D. Frisch and L.F. Dahl, *J. Am. Chem. Soc.*, 1972, **94**, 5082.
4. C.H. Wey and L.F. Dahl, *Inorg. Chem.*, 1965, **4**, 493.

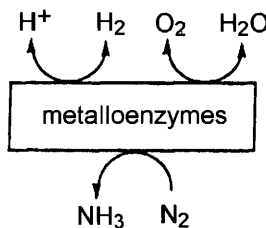
Please note the use of the hydrodynamic technique to detect the zero-current potential value needed for a correct cyclic voltammetric analysis.

5. H. Vahrenkamp, V.A. Uchtman and L.F. Dahl, *J. Am. Chem. Soc.*, 1968, **90**, 3272.
6. T. Madach and H. Vahrenkamp, *Chem. Ber.*, 1981, **114**, 505.
7. (a) B. Zhuang, P. Yu, L. Huang, L. He and J. Lu, *Polyhedron*, 1994, **13**, 125; (b) S.-P. Huang and M. Kanatzidis, *Inorg. Chim. Acta*, 1995, **230**, 9.
8. K.S. Hagen, A.D. Watson and R.H. Holm, *J. Am. Chem. Soc.*, 1983, **105**, 3905.
9. P.J. Vergamini, H. Vahrenkamp and L.F. Dahl, *J. Am. Chem. Soc.*, 1971, **93**, 6327.
10. R.E. Cramer, K. Yamada, H. Kawaguchi and K. Tatsumi, *Inorg. Chem.*, 1996, **35**, 1743.
11. J. Zhou, Z. Hu, E. Münck and R.H. Holm, *J. Am. Chem. Soc.*, 1996, **118**, 1966.
12. S. D'Addario, F. Demartin, L. Grossi, M.C. Iapalucci, F. Laschi, G. Longoni and P. Zanello, *Inorg. Chem.*, 1993, **32**, 1153.
13. J. Darkwa, J.R. Lockemeyer, P.D.W. Boyd, T.B. Rauchfuss and A.L. Rheingold, *J. Am. Chem. Soc.*, 1988, **110**, 141.
14. C.A. Goddard, J.R. Long and R.H. Holm, *Inorg. Chem.*, 1996, **35**, 4347.
15. T. Saito, N. Yamamoto, T. Nagase, T. Tsuboi, K. Kobayashi, T. Yamagata, H. Imoto and K. Unoura, *Inorg. Chem.*, 1990, **29**, 764, and references therein.
16. (a) S. Kamiguchi, H. Imoto, T. Saito and T. Chihara, *Inorg. Chem.*, 1998, **37**, 6852; (b) S. Kamiguchi, T. Saito and Z. Honda, *J. Organomet. Chem.*, 2000, **609**, 184.
17. P. Braunstein and J. Rose, in *Stereochemistry of Organometallic and Inorganic Compounds*, I. Bernal (Ed.); Elsevier, Amsterdam, 1989, Vol. 3, p. 5.
18. J. Liu, E.P. Boyd and S.G. Shore, *Acta Cryst.*, 1999, **C55**, 29.
19. F. Ragaini, D.L. Ramage, J.-S. Song and G.L. Geoffroy, *J. Am. Chem. Soc.*, 1993, **115**, 12183.
20. B.K. Teo, G. Longoni and F.R.K. Chung, *Inorg. Chem.*, 1984, **23**, 1257.
21. *Metal Clusters in Chemistry* P. Braunstein, L.A. Oro, P.R. Raithby, eds, Wiley-VCH, 1999.
22. P. Zanello, F. Laschi, A. Cinquantini, R. Della Pergola, L. Garlaschelli, M. Cucco, F. Demartin and T.R. Spalding, *Inorg. Chim. Acta*, 1994, **226**, 1.
23. R. Della Pergola, C. Bandini, F. Demartin, E. Diana, L. Garlaschelli, P.L. Stanghellini and P. Zanello, *J. Chem. Soc., Dalton Trans.*, 1996, 747.
24. F. Calderoni, F. Demartin, M.G. Iapalucci and G. Longoni, *Angew. Chem. Int. Ed. Engl.*, 1996, **35**, 2225.
25. F. Calderoni, F. Demartin, F. Fabrizi de Biani, C. Femoni, M.C. Iapalucci, G. Longoni and P. Zanello, *Eur. J. Inorg. Chem.*, 1999, 663.

CHAPTER 9

The Reactivity of Transition Metal Complexes with Small Molecules

Many transition metal complexes are able ‘to fix’ small molecules such as O₂, N₂, CO, CO₂, and SO₂. Interest in this aspect of inorganic chemistry is largely related to the role that *metalloenzymes* play in catalysing redox reactions of the type shown in Scheme 1.



Scheme 1

From an energetic viewpoint, these reactions fuel a good number of biological functions which are responsible for biochemical reactions crucial to ‘life’. In common chemical processes, these reactions require the use of heterogeneous catalytic systems and drastic reaction conditions (pressures of 100 atm and temperatures around 400°C), whereas, at a cellular level, they proceed smoothly under ambient conditions (room temperature and 1 atm pressure).

1 THE REACTIVITY OF TRANSITION METAL COMPLEXES WITH OXYGEN

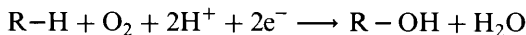
The ability of metal complexes to react with molecular oxygen is a topic of considerable interest in biochemistry. We must, however, take into

account that metal complexes can coordinate dioxygen ‘reversibly’ or ‘irreversibly’.*

1.1 Metal Complexes which React Irreversibly with Dioxygen

The ‘irreversible’ coordination of dioxygen to metal complexes is of remarkable importance in order to explain the activity of enzymes such *monooxygenases*, *dioxygenases* and *cytochrome c oxidase*.

Monooxygenases, by incorporation of a single atom of dioxygen in reactions of the type:



catalyse reactions of hydroxylation and epoxydation of organic compounds. For instance, *methane monooxygenases* are enzymes which catalyse the transformation of methane to methanol according to the reaction:

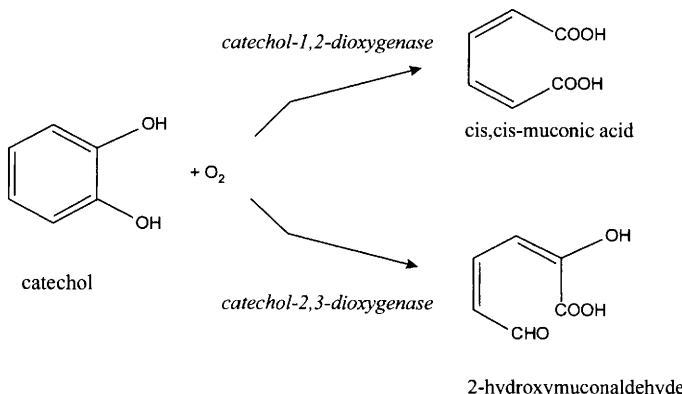


(NADH = nicotinamide adenine dinucleotide).

The molecular structure of the active site of the monooxygenase isolated from *Methylococcus capsulatus* is shown in Figure 1.¹

A dinuclear Fe(II) centre is bridged by two carboxylate and one hydroxide group. It is thought that the activation of molecular oxygen is a consequence of the ability of the active site to shuttle the Fe^{II}Fe^{II}/Fe^{II}Fe^{III}/Fe^{III} redox changes.

Dioxygenases, by incorporation of both the atoms of the dioxygen molecule, catalyse degradation reactions of aromatic derivatives according to the following mechanisms:



* With the term ‘reversible coordination’ we intend the process whereby an oxygenated complex, stable under certain conditions of partial dioxygen pressure, temperature and pH, loses the dioxygen molecule simply by changing such conditions. The simplest case of such a change in conditions is that in which bubbling a gas (e.g. dinitrogen) through a solution of the oxygenated complex liberates the coordinated dioxygen regenerating the corresponding deoxygenated complex.

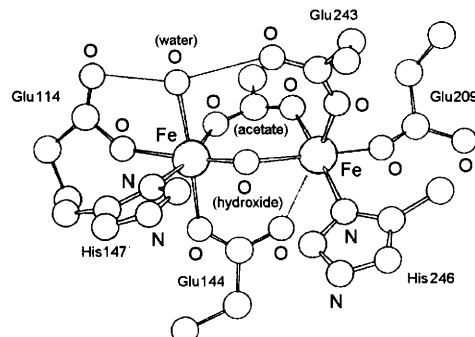


Figure 1 X-ray structure of the active site of the monooxygenase of *Methylococcus capsulatus*. $\text{Fe}\cdots\text{Fe} = 3.3 \text{ \AA}$

Dioxygenases that open the aromatic ring at the C/C bond between the *o*-diols are called *intradiol dioxygenases*. A mononuclear Fe(III) complex forms their active site. This is the case, for instance, of the active site of protocatechuate 3,4-dioxygenase of *Pseudomonas aeruginosa*, the trigonal bipyramidal geometry of which is illustrated in Figure 2.²

Dioxygenases that open the aromatic ring in the vicinal position to the *o*-diols are called *extradiol dioxygenases*. A mononuclear Fe(II) or Mn(II) complex forms their active site. This is, for instance, the case of 2,3-dihydroxybiphenyl-1,2-dioxygenase of *Pseudomonas sp. Strain KKS102*, the square pyramidal geometry of which is schematized in Figure 3.³

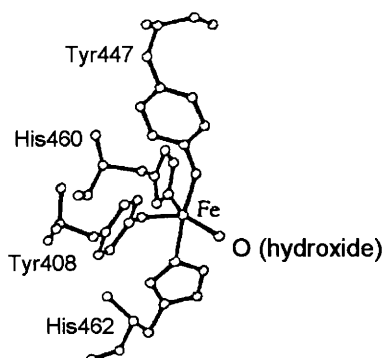


Figure 2 X-Ray structure of the site active of protocatechuate 3,4-dioxygenase from *Pseudomonas aeruginosa*

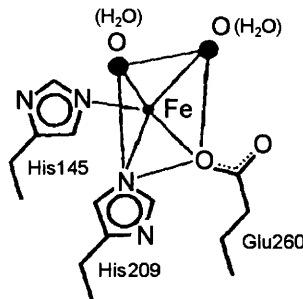
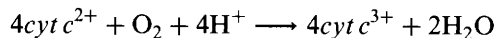


Figure 3 Schematic molecular structure of the active site of 2,3-dihydroxybiphenyl-1,2-dioxygenase

Cytochrome c oxidase is a copper protein, which, in the respiratory electron-transfer chain of mitochondria and many bacteria, catalyses the reduction of molecular oxygen to water, according to the reaction:



(which is just the reaction opposite to that occurring in the water oxidation centre of photosystem II discussed in Chapter 5, Section 3.1).

The active site of bovine heart *cytochrome c oxidase* is constituted by a multimetallic assembly (Cu , Mg , Fe , Zn),⁴ but it is thought that

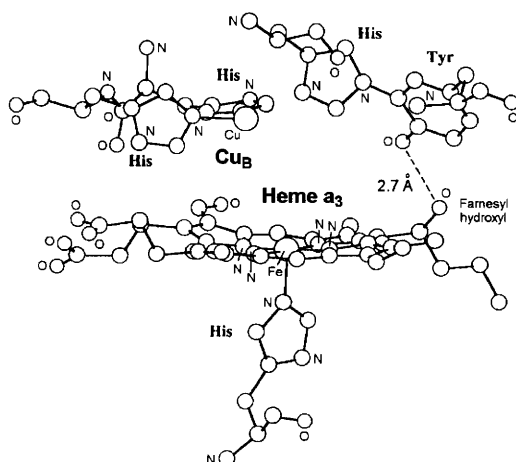


Figure 4 Structural details of the active site heme a_3 – Cu_B of cytochrome c oxidase

the fragment specifically responsible for the dioxygen reduction is the *haeme a_3 -Cu_B* site illustrated in Figure 4.

Despite the above aspects of the interaction of molecular oxygen with metal fragments, we will limit our electrochemical discussion to the reactivity of transition metal complexes with molecular oxygen in the context of modelling the dioxygen transport.

1.2 Metal Complexes which React Reversibly with Dioxygen

Three main classes of metalloproteins able to coordinate ‘reversibly’ dioxygen are known, namely:

- haemoproteins
- haemocyanins
- haemerythrin

Myoglobin and *haemoglobin* are the *haemoproteins* that govern the dioxygen transport necessary for respiration in mammals, birds and fish. A Fe(II)-porphyrin fragment forms their active site. Figure 5 shows the molecular structure of the *haeme* site of *oxymyoglobin* with its ‘end-on’ iron-dioxygen coordination according to a ‘bent’ geometry.⁵

A roughly similar Fe–O₂ arrangement has been found in human oxyhaemoglobin.⁶

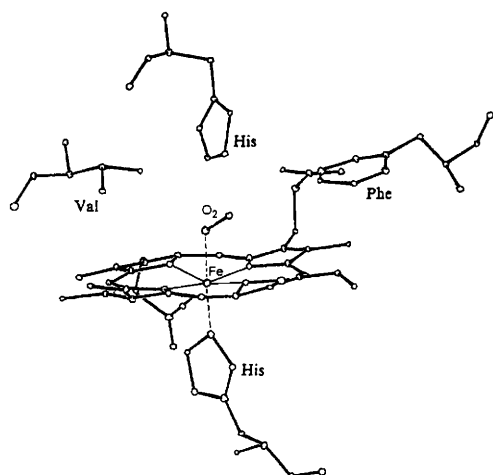


Figure 5 X-Ray structure of the heme group of oxymyoglobin. $Fe-N_{(porphyrin)} = 1.95 \text{ \AA}$; $Fe-N_{(imidazole)} = 2.07 \text{ \AA}$; $Fe-O = 1.83 \text{ \AA}$; $O-O = 1.22 \text{ \AA}$; $Fe-O-O = 115^\circ$

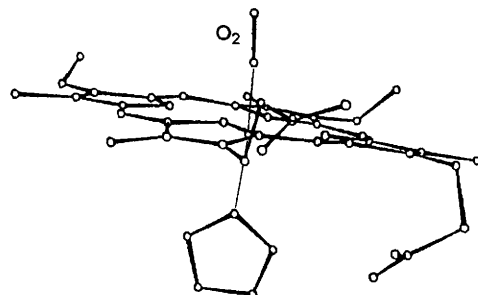


Figure 6 X-Ray structure of the heme group of oxyerithrocruorin. $\text{Fe}-\text{O} = 1.8 \text{ \AA}$; $\text{O}-\text{O} = 1.25 \text{ \AA}$; $\text{Fe}-\text{O}-\text{O} \approx 170^\circ$

For some years the exact nature of the $\text{Fe}-\text{O}_2$ bond has been under discussion: should it be viewed as $\text{Fe}^{\text{II}}-\text{O}_2^0$ or $\text{Fe}^{\text{III}}-\text{O}_2^-$? At present the $\text{Fe}^{\text{III}}-\text{O}_2^-$ form is favoured.

Considerable importance from the standpoint of the stabilization of the coordinated dioxygen is usually given to the “bent” arrangement of the $\text{Fe}-\text{O}-\text{O}$ bond. However, it must be recalled that it has been found that in *oxyerythrocytins*, a form of myoglobin found in flies, the geometry of the bond is essentially ‘linear’, Figure 6,⁷ suggesting that the bent geometry of the iron–dioxygen bond in myoglobin might not be of particular importance.

The second class of dioxygen carriers is that of *haemocyanins*. These proteins, which contain a binuclear Cu(I) site (thus in the oxidized Cu(II) *met* form they belong to the so-called ‘Type 3 copper proteins’, which contain an EPR-silent dicopper active site), regulate dioxygen transport in the respiration of arthropods and molluscs. Figures 7 and 8 show

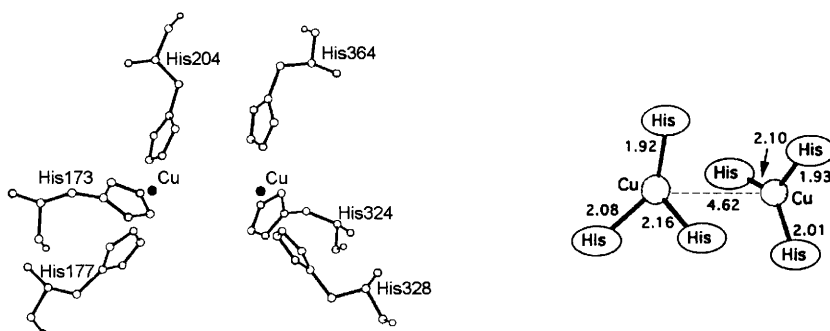


Figure 7 X-ray structure of the active site of the deoxygenated form of haemocyanin from *Limulus polyphemus*

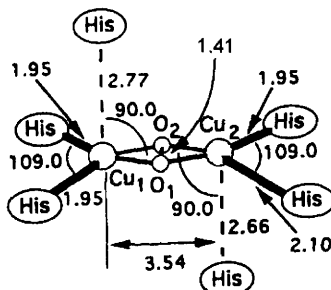


Figure 8 X-ray structural data of the active site of the oxygenated form of haemocyanin from *Limulus polyphemus*

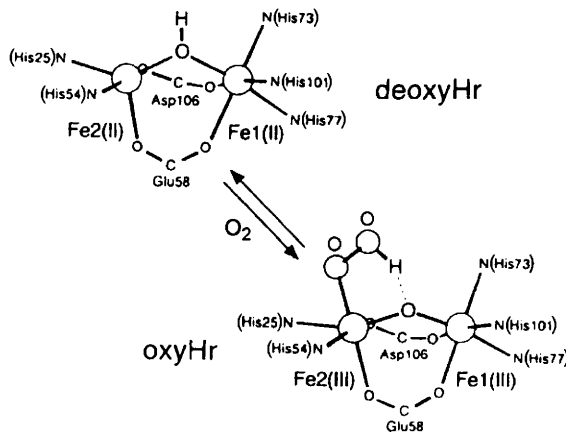
the molecular structures of the active sites of the deoxygenated and oxygenated forms, respectively, of the haemocyanin from *Limulus polyphemus*.^{8,9}

In the deoxygenated form, each Cu(I) centre is coordinated to three nitrogen atoms of three histidines. The great Cu/Cu separation (4.62 Å) foreshadows the presence of a cavity able to host a dioxygen molecule.* In fact, in the oxygenated form, the oxygen molecule is planarily positioned according to a $\mu\text{-}\eta^2\text{:}\eta^2$ peroxy coordination, and the Cu/Cu separation decreases (≈ 3.5 Å).

It is interesting to underline that there is another (plant) enzyme which possesses a coordinatively similar dicopper environment: *catechol oxidase*.¹¹ As already mentioned in Chapter 6, Section 3, such an ubiquitous enzyme catalyses the two-electron oxidation by molecular dioxygen of catechols to the corresponding quinones (the so-generated quinones in turn polymerize to form brown polyphenolic catechol melanins, which protect damaged plants from pathogens or insects).

The last class of dioxygen carriers consists of *haemerythrin*, a metalloprotein found in a few marine invertebrates.¹² Really, its reversibility in dioxygen binding is lower than that exhibited by the previous classes. As illustrated in Scheme 2, the active site of haemerythrine in the ‘deoxy’ form is constituted by two asymmetrically penta- and hexa-coordinated Fe(II) centres connected by two bridging carboxylates and one hydroxo group, whereas in the ‘oxy’ form the Fe(II) centres change to Fe(III), the μ -hydroxo bridge transforms into a μ -oxo bridge and a protonated peroxy group makes both the two iron centres hexacoordinate.

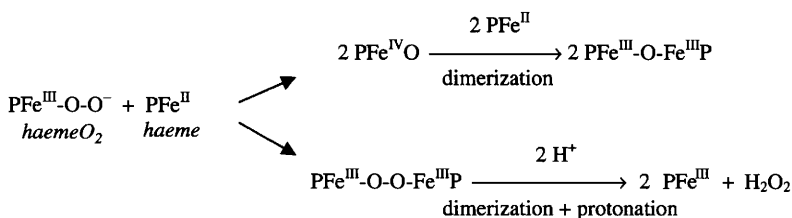
* It is noted that in the deoxygenated form of haemocyanin from *Panulirus interruptus* the Cu/Cu separation is notably shorter: 3.54 Å.¹⁰



Scheme 2

1.3 Haemoprotein-like Metal Complexes

The use of models that mimic a protein ‘active site’ is normally prompted by the desire to eliminate any influence of the polypeptide backbone surrounding the active site in real biological molecules, which may obscure its physico-chemical properties. The first attempts to synthesize metal complexes similar to the active site of haemoproteins, through the use of simple metalloporphyrin derivatives, failed. The failure was due to the fact that these complexes react irreversibly with dioxygen as a consequence of side ‘autooxidative’ reactions of the type:



P = porphyrin ring

In natural systems dimerization reactions are prevented by the location of the haeme group in a sterically protected protein pocket, which prevents another haeme group approaching and attacking the original haeme. Analogously, *protonation* reactions are limited by the fact that the haeme group lies in a hydrophobic pocket.

In order to avoid such irreversible reactions, in synthetic chemistry the following strategy has been adopted:

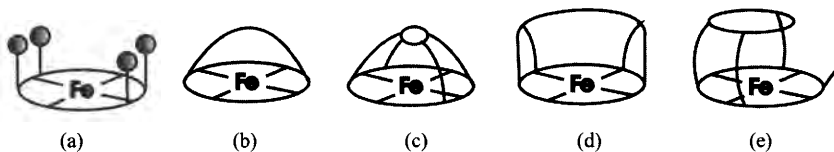


Figure 9 A few schematic examples of mononuclear $\text{Fe}(\text{II})$ -porphyrin derivatives used to prevent the irreversible oxidation to oxygen-bridged binuclear $\text{Fe}(\text{III})$ derivatives. (a) ‘Picket-fence’ complexes; (b) ‘strapped’ complexes; (c) ‘capped’ complexes; (d) ‘picnic-basket’ complexes; (e) ‘pocket’ complexes

- to prepare simple models that can sterically block bimolecular reactions;
- to test the reactivity in aprotic solvents to avoid protonation reactions.

Figure 9 shows schematically a few $\text{Fe}(\text{II})$ complexes, which model the haeme group and contain bulky groups to prevent dimerization.¹³

Particularly important in affirming this kind of investigation has been the Collman’s “picket-fence” complex illustrated in Figure 10a, in that the molecular structure of its oxygenated form has been solved, Figure 10b.¹⁴

Despite the statistical disorder, it has been found that dioxygen binds the iron centre according to a ‘bent’ geometry, as above seen for most haemoproteins.

Amongst metal complexes able to reversibly bind molecular dioxygen one should recall the previously mentioned trigonal-bipyramidal $\text{Co}(\text{II})$ complexes with bis(salicylideneimine-3-propyl)amine, $[\text{Co}(\text{R-X-saldpt})]$ (Chapter 5, Section 5), Scheme 3.

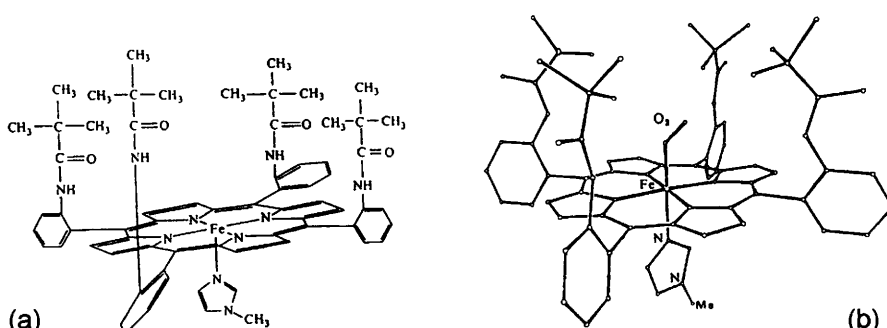
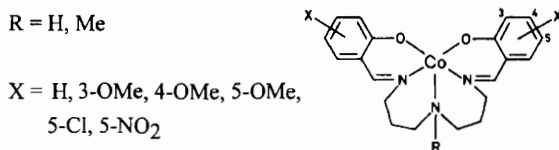


Figure 10 (a) Colmann’s ‘picket-fence’ complex; (b) X-ray structure of the corresponding oxygenated form. $\text{Fe}-\text{O} = 1.75 \text{ \AA}$; $\text{O}-\text{O} = 1.25 \text{ \AA}$; $\text{Fe}-\text{O}-\text{O} = 131^\circ$



Scheme 3

These Co(II) complexes react with molecular oxygen by a two stage mechanism: a first step with rapid formation of a 1:1 metal-dioxygen complex, followed by the slower formation of a 2:1 complex (believed to be responsible for the 'irreversible' coordination of oxygen) according to the sequence:

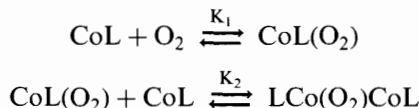


Figure 11 shows how the cyclic voltammetric shape of the reversible Co(II)/Co(III) oxidation of $[\text{Co(MeHsaldpt)}]$ changes with increasing concentration (or increasing bubbling time) of dioxygen.¹⁵

It is evident that the original reversible $\text{Co}^{II}/\text{Co}^{III}$ step ($E^{\circ'} = -0.14 \text{ V}$) is progressively substituted by an irreversible anodic process at higher potential ($E_p = +0.1 \text{ V}$), which is attributed to the oxidation of the formed oxygenated complex:

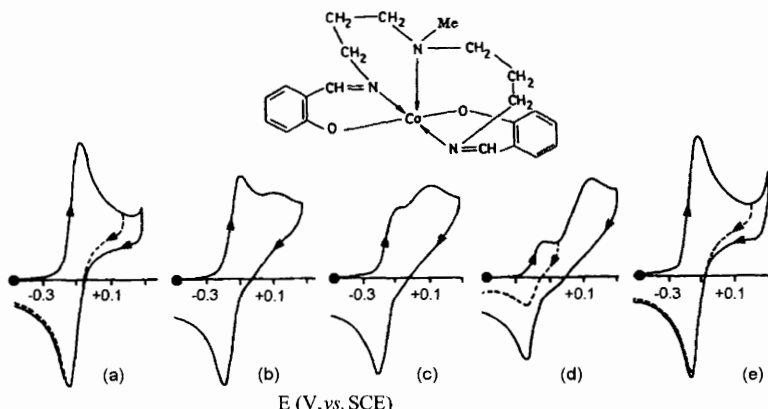
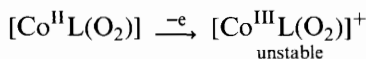


Figure 11 Anodic cyclic voltammograms recorded at a mercury electrode in a dmso solution of $[\text{Co}(\text{MeHsaldpt})]$ with the bubbling time of O_2 [$p_{\text{O}_2} = 1 \text{ atm}$]: (a) deaerated original solution; (b) after 4 min; (c) after 6 min; (d) after 30 min. (e) After bubbling again N_2 . Scan rate 0.2 V s^{-1}

This kind of electrochemical measurement enables the oxygenation equilibrium constant K_1 to be calculated by taking advantage of the fact that:

- as shown in Figure 11d, the oxygenation process does not go to completion, even for long O_2 bubbling times;
- from the height of the residual anodic process $\text{Co(II)}/\text{Co(III)}$ ($E^{\circ'} = -0.14 \text{ V}$) one can determine the concentration of the non-oxygenated complex at different oxygen partial pressures.

In the case of $[\text{Co}(\text{MeHsaldpt})]$, the constant K_1 is equal to $3 \times 10^{-3} \text{ M}^{-1}$ at 20°C .

The 1:1 oxygen complex has been isolated and its molecular structure determined. Figure 12 compares the geometries of the original deoxygenated complex (already seen in Chapter 5, Figure 85 from a different perspective) with that of the oxygenated complex.¹⁶

The oxygen molecule binds (with statistical disorder) the cobalt atom according to a ‘bent, end-on’ fashion. The insertion of the sixth peroxide ligand constrains the initially trigonal-bipyramidal complex to assume an octahedral geometry. This gives rise to significant shortening of the bond distances between the cobalt and the donor atoms of the Schiff base. The O–O bond length (1.06 Å) is unusually short for a superoxide bond that is around 1.34 Å. It is also shorter than the O–O distance of molecular oxygen (1.21 Å¹⁷). This is probably a consequence of the uncertainty in the bond length caused by statistical disorder.

The high capacity of this complex to reversibly interact with molecular oxygen (which is the characteristic of dioxygen carriers) can be inferred from Figure 11e. One can see that the simple bubbling of dinitrogen through the solution regenerates the original deoxygenated complex.

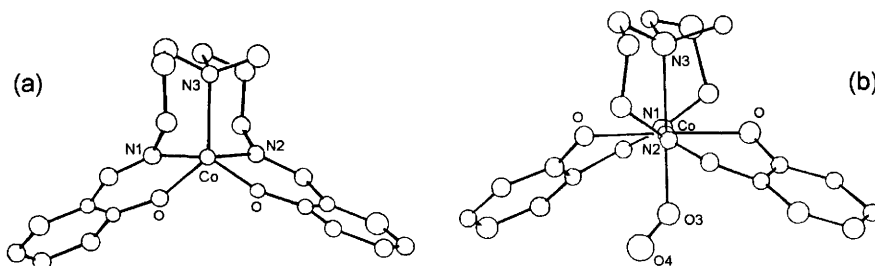


Figure 12 X-Ray structures of: (a) $[\text{Co}(\text{MeHsaldpt})]$. Bond lengths: $\text{Co}-\text{O} = 1.97 \text{ \AA}$; $\text{Co}-\text{N}3 = 2.15 \text{ \AA}$; $\text{Co}-\text{N}1 \approx \text{Co}-\text{N}2 = 2.04 \text{ \AA}$; (b) $[\text{Co}(\text{MeHsaldpt})\text{O}_2]$. Bond lengths: $\text{Co}-\text{O}_{(\text{Schiff base})} = 1.92 \text{ \AA}$; $\text{Co}-\text{O}3 = 1.88 \text{ \AA}$; $\text{Co}-\text{N}1 = 1.90 \text{ \AA}$; $\text{Co}-\text{N}2 = 2.00 \text{ \AA}$; $\text{Co}-\text{N}3 = 2.09 \text{ \AA}$; $\text{Co}-\text{O}3-\text{O}4 = 137.4^\circ$

Table 1 Formal electrode potentials (V , vs. SCE) and oxygenation constants ($l \text{ mol}^{-1}$) for the complexes $[\text{Co}(\text{R-X-salpdt})]$ in dmso solution

<i>R</i>	<i>X</i>	<i>E</i> ^o	<i>K</i> _{<i>O</i>₂}
H	H	-0.27	7×10^4
	3-OMe	-0.32	2×10^5
	4-OMe	-0.26	8×10^5
	5-OMe	-0.29	3×10^5
	5-Cl	-0.21	7×10^4
	5-NO ₂	-0.11	2×10^4
Me	H	-0.14	3×10^3
	3-OMe	-0.17	6×10^3
	4-OMe	-0.14	5×10^3
	5-OMe	-0.15	6×10^3
	5-Cl	-0.07	2×10^3
	5-NO ₂	+0.02	1×10^2

Examination of a large series of variously substituted [Co(X-R-saldp)] derivatives reveals that the electronic effects of the substituents appreciably influence the capacity of the complex to coordinate molecular oxygen, Table 1. In fact, the oxygenation constant varies in the range from 10^2 to 10^6 1 mol $^{-1}$.

The molecular structure of a Co(II) macrocycle complex that in some way mimics the strapped-type metal-porphyrin complexes is illustrated in Figure 13.^{18,19}

In de-aerated MeCN solution this complex displays a reversible Co(II)/Co(III) oxidation at about +0.2 V, Figure 14a.

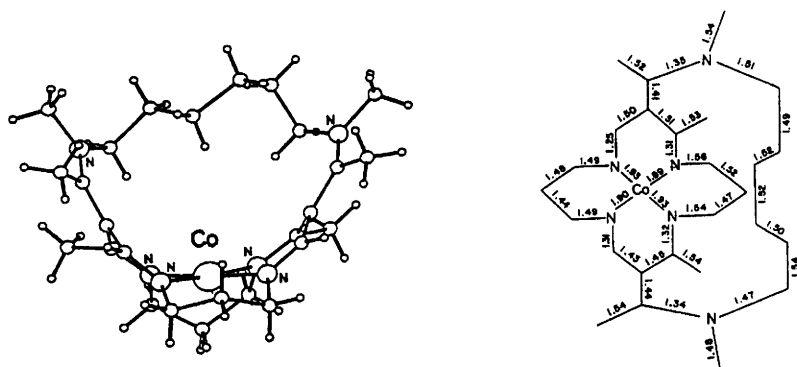


Figure 13 X-Ray structure of $[Co^{II}\{C_6Me(CH_2)\{16\}Cyd\}]$ together with the relative bond lengths

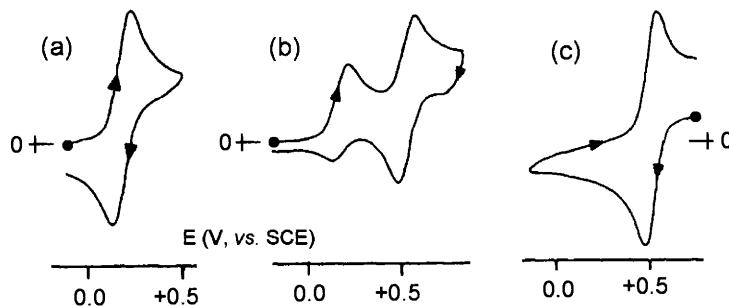


Figure 14 Cyclic voltammograms recorded at a platinum electrode in MeCN solution of $[Co^{II}\{C_6Me(CH_2)[16]Cyd\}]$. (a) Under N_2 atmosphere; (b) after air bubbling; (c) under O_2 atmosphere

Upon bubbling with air, or dioxygen, the anodic process is substituted by another reversible process at higher potentials, Figure 14b,c, which is attributed to the Co(II)/Co(III) oxidation of the oxygenated complex.²⁰ The nature of this latter species has not been clarified. In this regard, it must be borne in mind that the original complex has two possible coordination sites for the coordination of the dioxygen molecule: one inside and one outside the macrocyclic cavity. As a matter of fact, in the presence of methylimidazole, the oxygenated complex shown in Figure 15 has been isolated.^{19,21}

It can be seen that dioxygen occupies a position internal to the macrocycle and assumes a bent superoxide coordination. In this case, however, the dioxygen coordination is 'irreversible'.

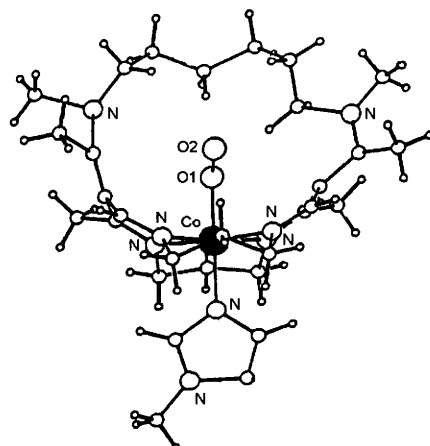


Figure 15 X-Ray structure of $[Co^{II}\{C_6Me(CH_2)[16]Cyd\}(ImO_2)]$. Bond lengths: $Co-O1 = 1.84 \text{ \AA}$; $O1-O2 = 1.32 \text{ \AA}$

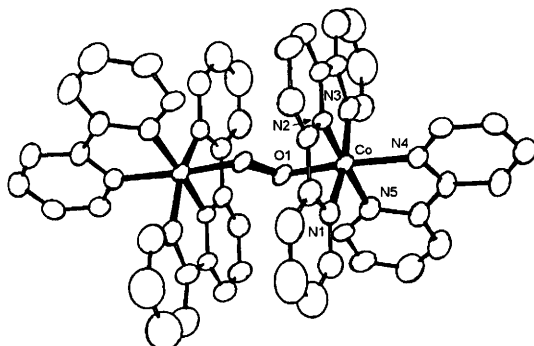


Figure 16 X-Ray structure of the tetracation $\{[Co(\text{terpy})(\text{bipy})]_2(\mu-\text{O}_2)\}^{4+}$. Bond lengths: $Co-O1 = 1.87 \text{ \AA}$; $O-O = 1.42 \text{ \AA}$; $Co-N1 \approx Co-N3 = 1.94 \text{ \AA}$; $Co-N2 = 1.86 \text{ \AA}$; $Co-N4 = 1.99 \text{ \AA}$

It has been mentioned previously that the formation of 2:1 $\text{Co}:\text{O}_2$ μ -peroxodimers is generally believed responsible for the irreversible coordination of dioxygen. In apparent contrast with this affirmation, the mixed bipyridine/terpyridine ligands complex $\{[Co(\text{terpy})(\text{bipy})]_2(\mu-\text{O}_2)\}^{4+}$, the molecular structure of which is shown in Figure 16, constitutes an example of reversible coordination of the peroxy group.²²

Such an oxygenated complex is formed by oxygenation of the dication $[Co(\text{terpy})(\text{bipy})]^{2+}$ and its formation can be followed electrochemically.²² As illustrated in Figure 17, $[Co(\text{terpy})(\text{bipy})]^{2+}$ undergoes in

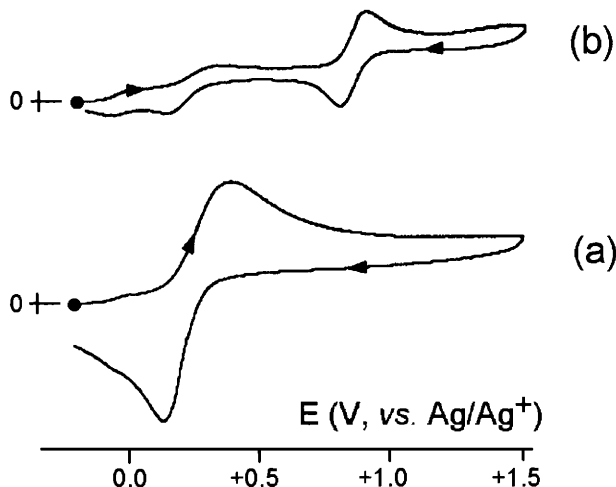
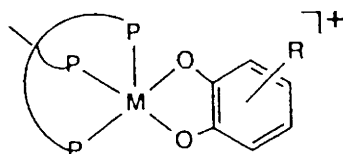


Figure 17 Cyclic voltammograms recorded at a glassy carbon electrode in a MeCN solution of $[Co(\text{terpy})(\text{bipy})]^{2+}$. (a) Under N_2 atmosphere; (b) under O_2 atmosphere. Scan rate 0.1 V s^{-1}

MeCN solution a quasireversible Co^{II/III} oxidation ($E^\circ' = +0.21\text{ V}$, vs. Ag/AgNO₃). Under dioxygen atmosphere a new anodic process is observed at more positive potentials ($E^\circ' = +0.84\text{ V}$), that is attributed to the Co^{II/III} oxidation [$\{\text{Co}(\text{terpy})(\text{bipy})\}_2(\text{O}_2)\}^{4+/5+}$ of the oxygenated dimer. Upon bubbling dinitrogen through the solution the original voltammogram is regenerated.

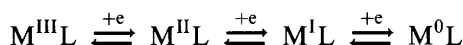
Another series of complexes able to coordinate reversibly dioxygen is constituted by the derivatives $[\text{M}(\text{triphos})(\text{catecholate})]^+$ illustrated in Scheme 4 (M = Co(III), Rh(III), Ir(III); triphos = MeC(CH₂PPh₂)₃; catecholate = 9,10-dihydroxyphenanthrene, di-*tert*-butyl-catecholate, 3,4,5,6-tetrachloro-catecholate, 4-methyl-catecholate, ethyl-3,4-dihydroxybenzoate and 1,2-dihydroxynaphthalene).²³



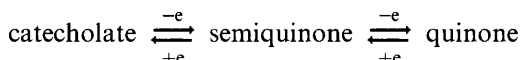
Scheme 4

These complexes combine a central metal in a high oxidation state with a redox active ligand (catechol). This combination arises from the idea that the electronic perturbation induced in the metal complex by reaction with dioxygen can discharge itself:

- on the oxidation state of the metal, that can potentially accede several oxidation states



- on the redox activity of the ligand, that (as seen in Chapter 5, Section 1 and Chapter 6, Section 3) can be oxidised according to the sequence:



All these complexes have identical spectroscopic properties; therefore, they are assigned the same square-pyramidal geometry found for $[\text{Co}(\text{triphos})(\text{DBcat})]^+$, Figure 18.²⁴

As illustrated in Figure 19, which refers to $[\text{Co}(\text{triphos})(\text{DBcat})]^+$, these complexes display both two sequential reduction processes centred on the metal ion and two sequential oxidation processes centred on the catechol ligand.

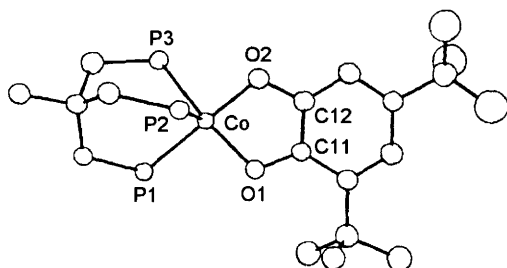


Figure 18 X-Ray structure of $[Co(\text{triphos})(\text{DBcat})]^+$. Bond lengths: $Co-P \approx 2.21 \text{ \AA}$; $Co-O1 = 1.88 \text{ \AA}$; $Co-O2 = 1.85 \text{ \AA}$; $C11-C12 = 1.40 \text{ \AA}$

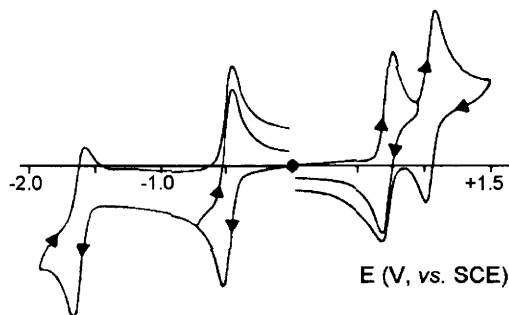


Figure 19 Cyclic voltammogram recorded at a platinum electrode in a MeCN solution of $[Co(\text{triphos})(\text{DBcat})]^+$. Scan rate 0.2 V s^{-1}

As far as the reactivity of these complexes towards molecular oxygen is concerned, it has been observed that the ligand-centred anodic processes become more informative than the metal-centred cathodic processes. This can be seen in Figure 20, which compares the responses of Ir(III)-*tert*-butyl-catecholate in the absence (a) and in the presence (b) of dioxygen.

It is evident that, in the presence of dioxygen, the cathodic part of the voltammogram becomes completely uninformative. In contrast, the anodic response, which in the absence of dioxygen displays the expected catecholate/semiquinone/quinone sequence (in correspondence of the peak-systems A/D ($E^{\circ'} = +0.25 \text{ V}$) and B/C ($E^{\circ'} = +1.10 \text{ V}$)), in the presence of oxygen, gives rise to a new irreversible oxidation process (peak H, $E_p = +1.6 \text{ V}$), which, however, in the reverse scan displays the two original peaks C and D. This indicates that the oxygenated complex, upon anodic oxidation, loses the coordinated oxygen molecule reforming the original compound (in its oxidized state).

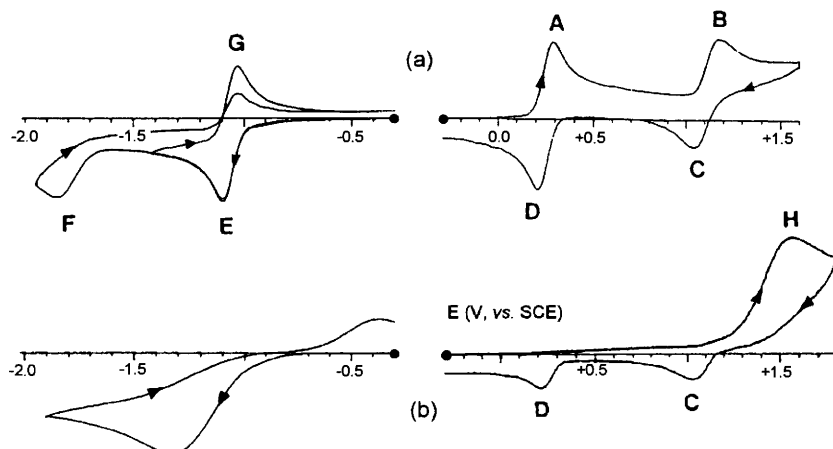


Figure 20 Cyclic voltammograms recorded at a platinum electrode in a MeCN solution of $[Ir(\text{triphos})(\text{DBcat})]^+$: (a) deaerated solution; (b) oxygenated solution. Scan rate 0.2 V s^{-1} . $T = -20^\circ\text{C}$

The molecular structure of the oxygenated form of Ir(III)-phenanthrenecatecholate complex, $[Ir(\text{triphos})(\text{Phensq})(\text{O}_2)]^+$, is shown in Figure 21.

It can be seen that inside the octahedral coordination of the Ir(III) centre an unusual peroxide bond forms between the terminal oxygen atom (O_4) of coordinated dioxygen and the carbon atom (C_7) of the semiquinone ligand. In fact, the $O-O$ distance of the oxygen molecule (1.47 \AA) is within the typical bond distance of peroxide coordination (1.49 \AA).

Confirming that the oxidation of the oxygenated complexes regenerates the initial complex in the oxidized quinone form (see Figure 20b), Figure 22 shows that the oxygenated cation $[Ir(\text{triphos})(\text{Phensq})(\text{O}_2)]^+$ is irreversibly oxidized generating in the reverse scan the reduction profiles

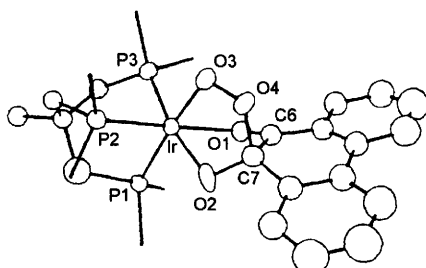


Figure 21 X-Ray structure of $[Ir(\text{triphos})(\text{Phensq})(\text{O}_2)]^+$. Bond lengths: $Ir-P \approx 2.28 \text{ \AA}$; $Ir-O1 = 2.19 \text{ \AA}$; $Ir-O2 = 2.14 \text{ \AA}$; $Ir-O3 = 1.97 \text{ \AA}$; $O3-O4 = 1.47 \text{ \AA}$; $O4-C7 = 1.54 \text{ \AA}$; $C6-C7 = 1.40 \text{ \AA}$

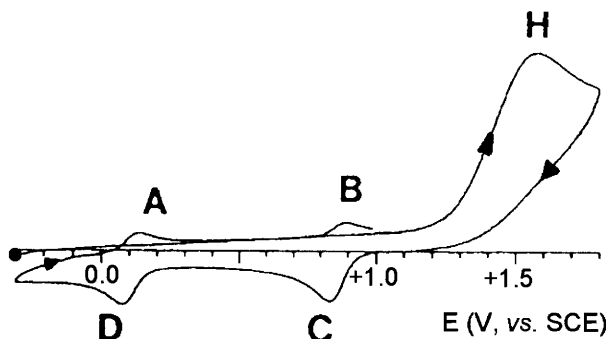
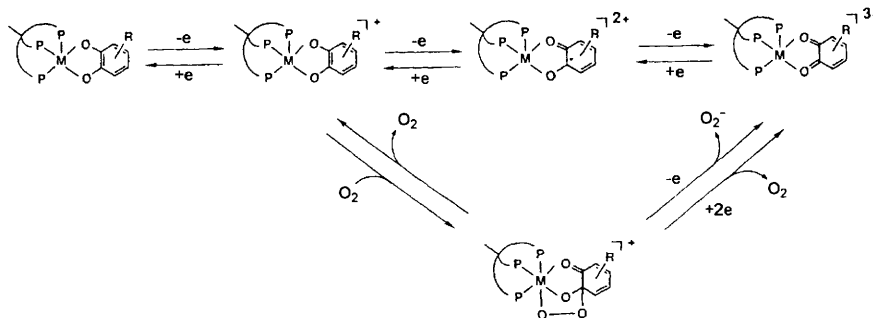


Figure 22 Cyclic voltammogram recorded at a platinum electrode in a MeCN solution of $[\text{Ir}(\text{triphos})(\text{Phensq})(\text{O}_2)]^+$. Scan rate 0.2 V s^{-1} . $T = -20^\circ\text{C}$

C/B and D/A, which correspond to the quinone/semiquinone/catecholate sequence of $[\text{Ir}(\text{triphos})(\text{Phencat})]^+$.

Really, as illustrated in Scheme 5, the irreversible oxidation of these oxygenated complexes can involve either a one-electron or a two-electron process. This depends upon the fact that the reaction of the oxygenated complex to regenerate the non-oxygenated complex can proceed through the release of a superoxide ion or an oxygen molecule.



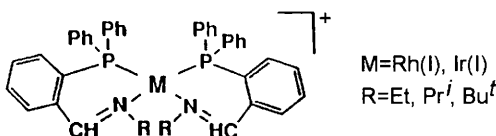
Scheme 5

As one can infer from the data summarized in Table 2, the electrochemical study has highlighted that, within each series, if the oxidation potential of the catecholate/semiquinone step is relatively low the complex is reactive towards dioxygen and the oxygenated complex regenerates the initial complex (in its quinone form) releasing molecular oxygen. Conversely, if the oxidation potential is high there is no reaction with dioxygen. Finally, for intermediate potential values, the oxygenated complex regenerates the initial complex (in its quinone form) through the release of superoxide ion.

Table 2 The reactivity of complexes $[M(\text{triphos})(\text{catecholate})]^+$ ($M = \text{Co}$, Rh , Ir) with molecular oxygen as a function of the catecholate/semiquinone oxidation potential. I = no reactivity; II = the oxygenated complex regenerates the initial complex in the quinone form by release of superoxide ion; III = the oxygenated complex regenerates the initial complex in the quinone form by release of molecular oxygen

Catechol	<i>Ir</i>	<i>Rh</i>	<i>Co</i>
9,10-dihydroxyphenanthrene	+ 0.11 (III)	+ 0.13 (III)	+ 0.66 (III)
1,2-dihydroxynaphthalene	+ 0.18 (III)	+ 0.21 (III)	+ 0.70 (I)
di- <i>tert</i> -butyl-catechol	+ 0.25 (III)	+ 0.28 (II)	+ 0.73 (I)
4-methyl-catechol	+ 0.70 (II)	+ 0.34 (II)	
ethyl-3,4-dihydroxybenzoate	+ 0.84 (I)	+ 0.79 (I)	
3,4,5,6-tetrachloro-catechol	+ 0.93 (I)		

The last class of derivatives able to mimic the haemoprotein function that we will consider is constituted by the series of square-planar $\text{Rh}(\text{I})$ and $\text{Ir}(\text{I})$ complexes with the Schiff base $\text{o-Ph}_2\text{C}_6\text{H}_4\text{CH=NR}$, Scheme 6.²⁵



Scheme 6

These complexes offer the opportunity to tune the steric hindrance around the central metal ion simply by the proper choice of the alkyl substituent R. This should clearly have some effect on the ability of dioxygen to bind the metal.

The square-planar geometry (with slight tetrahedral distortion) of these derivatives can be proved by that of the related $\text{Rh}(\text{I})$ complex with 2,2'-bis{[o-(diphenylphosphine)benzylidene]amine}-6,6'-dimethyl-diphenyl, $[\text{Rh}(\text{PPNN})]^+$, Figure 23.²⁶

In order to account for the reactivity of these complexes with dioxygen one must at first look at the cyclic voltammetric responses reported in Figure 24.

As seen, the $\text{Ir}(\text{I})$ complexes show (in addition to two one-electron reductions, of little interest with regard to the oxygenation mechanism) an oxidation process. While for derivatives with less bulky alkyl groups (Et, Pr^{i}) the oxidation involves an irreversible $\text{M}(\text{I}) \rightarrow \text{M}(\text{III})$ process, for those with the bulky group Bu^{t} it involves a reversible $\text{M}(\text{I}) \rightarrow \text{M}(\text{II})$ process.

This being stated, it must be taken into account that the derivatives with less bulky substituents (Et, Pr^{i}) react with molecular oxygen,

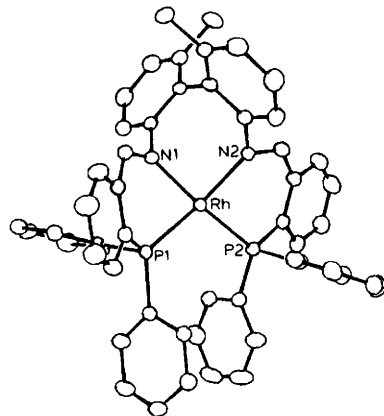


Figure 23 X-Ray structure of $[Rh(PPNN)]^+$. Average bond lengths: $Rh-P = 2.22 \text{ \AA}$; $Rh-N = 2.10 \text{ \AA}$; dihedral angle between the P_1RhN_1/P_2RhN_2 planes = 10.9°

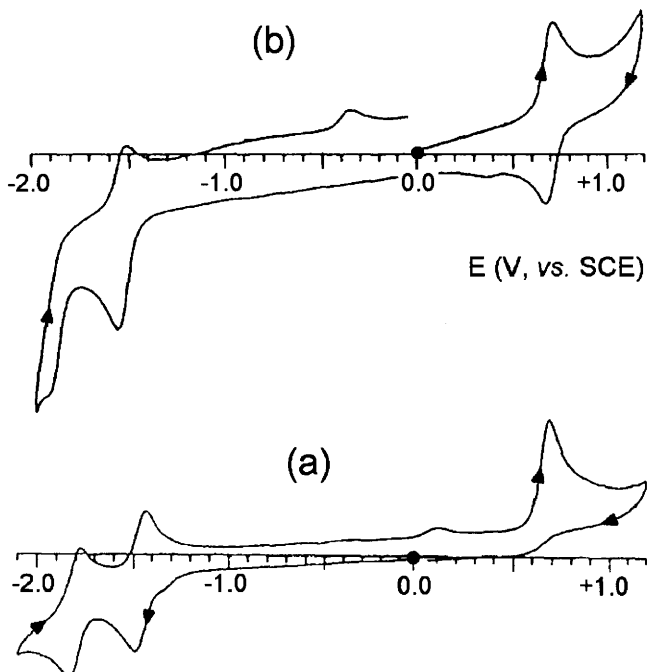


Figure 24 Cyclic voltammograms recorded at a platinum electrode in Me_2CO solutions of: (a) $[Ir(o-Ph_2PC_6H_4CH=NEt)_2]^+$; (b) $[Ir(o-Ph_2PC_6H_4CH=NBu')_2]^+$. Scan rate 0.2 V s^{-1} .

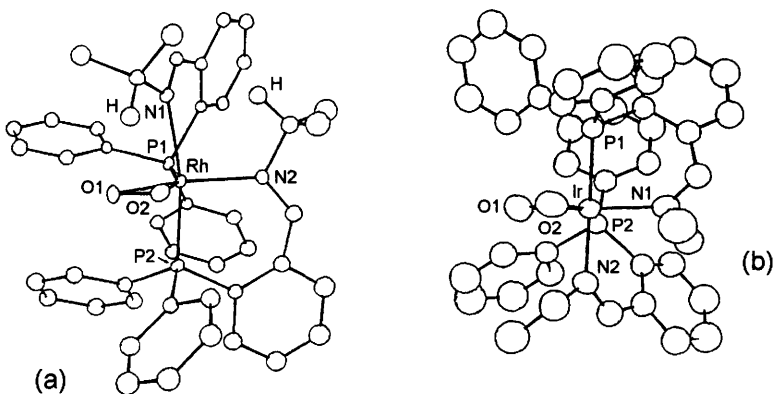


Figure 25 X-Ray structures of: (a) $[Rh(o\text{-}Ph_2PC_6H_4CH=NPri)_2]^{2+}$. Bond lengths: $Rh-P1 = 2.32 \text{ \AA}$; $Rh-P2 = 2.24 \text{ \AA}$; $Rh-N1 = 2.22 \text{ \AA}$; $Rh-N2 = 2.11 \text{ \AA}$; $Rh-O \approx 2.02 \text{ \AA}$; $O1-O2 = 1.44 \text{ \AA}$. (b) $[Ir(o\text{-}Ph_2PC_6H_4CH=NET)_2]^{2+}$. Bond lengths: $Ir-P1 = 2.26 \text{ \AA}$; $Ir-P2 = 2.29 \text{ \AA}$; $Ir-N1 = 2.10 \text{ \AA}$; $Ir-N2 = 2.16 \text{ \AA}$; $Ir-O \approx 2.01 \text{ \AA}$; $O1-O2 = 1.47 \text{ \AA}$

whereas the derivative with the bulky substituent Bu^t does not form complexes with dioxygen. In this connection, Figure 25 shows the molecular structures of the products obtained by oxygenation of the rhodium complex having the isopropyl substituent²⁷ and the iridium complex having the ethyl substituent.²⁵

In both compounds the dioxygen coordination is ‘side-on’ terminal and the O–O distance falls within the typical range of a peroxide bond coordinated to a single metal ion. In both cases the geometry can be viewed as either distorted trigonal-pyramidal or distorted octahedral, depending on whether one considers the oxygen molecule to occupy one or two positions.

In the light of the electrochemical data it seems reasonable to propose that in cases where the substituent provides effective steric protection of the central metal, dioxygen can act as a simple (outer-sphere) M(I)-to-M(II) oxidizing agent (reversible one-electron oxidation). In contrast, in those cases where the substituent offers insufficient steric protection, dioxygen can coordinate to the metal by oxidative addition forming the peroxy compound $M(III)\text{-O}_2^{2-}$ (irreversible two-electron oxidation).

Despite the apparent similarity of the Rh and Ir peroxide complexes, the rhodium complex easily loses dioxygen in solution upon bubbling through nitrogen, whereas the iridium complex is completely inert to deoxygenation. One can attempt to explain this behaviour by recalling that, generally, for a homologous series of complexes, the higher

the electron density on the metal the stronger the bond that it forms with dioxygen. Consequently, within a given family of metal complexes, metals of 3rd transition series form dioxygen complexes more stable than those of the 2nd transition series.²⁸

In conclusion, it is noted that, as an empirical rule, first row transition metal elements generally form superoxide-type dioxygen complexes, whereas elements of the second and third transition series form peroxide-type dioxygen complexes.

1.4 Haemocyanin-like Metal Complexes

As previously discussed, the binuclear Cu(I) haemocyanins constitute another important class of dioxygen carriers. The first model compound whose structure in the oxygenated form resembles most closely that of oxyhaemocyanin is the dicopper(II) complex with the tris(3,5-diisopropylpyrazolyl)borate ligand shown in Figure 26.²⁹

The O–O distance of 1.41 Å is typical of the $\mu\text{-}\eta^2\text{:}\eta^2$ - (side-on)peroxo coordination. Nevertheless, in this complex the O₂-binding is irreversible.

Another $\mu\text{-}\eta^2\text{:}\eta^2$ -peroxo compound able to bind reversibly dioxygen has been structurally characterized, namely [Cu₂O₂(L)]²⁺ (L = 1,2-bis[2-(bis(6-methyl-2-pyridyl)methyl)-6-pyridyl]ethane).³⁰

Unfortunately, no electrochemical studies have been reported either for these complexes or for the possibly related μ -1,2-(end-on) complexes.^{31,32} The only electrochemical information available is related to a few binuclear Cu(I) complexes of general formula [Cu₂(L')]²⁺ and their oxygenation products [Cu₂(O₂)(L')]²⁺, which, based on spectroscopic evidence, are likely to coordinate dioxygen in a $\mu\text{-}\eta^2\text{:}\eta^2$ -peroxo way.^{32,33}

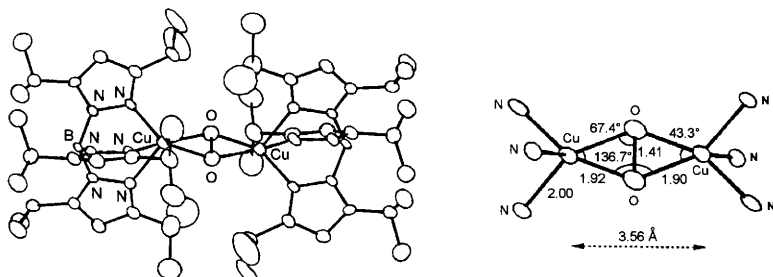
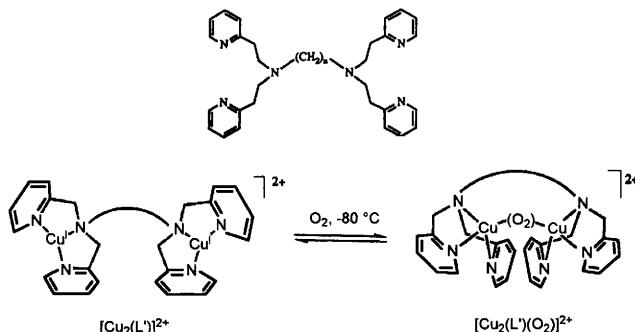


Figure 26 X-Ray structure of $[\{Cu(Tp^{iPr,iPr})\}_2(O_2)]$, together with structural parameters

As shown in Scheme 7, L' is a hydrocarbon chain of variable length having two tricoordinated bis[2-(2-pyridyl) ethyl]amine groups at its extremity.



Scheme 7

Figure 27a shows the cyclic voltammogram of the dicopper(I) complex containing the $N(CH_2)_3N$ spacer (abbreviated as $[Cu^{I}_2(N3)]^{2+}$) in CH_2Cl_2 solution.

It undergoes a single, chemically reversible, two-electron oxidation (Cu^{I}_2/Cu^{II}_2): $E^{o'} = +0.75\text{ V}$ vs. Ag/AgCl). The lack of the intermediate $Cu^{I}_2/Cu^{I}Cu^{II}$ step indicates that there is no electronic interaction (communication) between the two copper centres. After oxygenation, the voltammogram reveals an irreversible one-electron reduction ($E_p = -1.1\text{ V}$), Figure 27b, which suggests that the peroxide form is stable only in the copper(II) form $[Cu^{II}_2(N3)(O_2)]^{2+}$.

1.5 Haemerythrin-like Metal Complexes

A number of binuclear Fe(II) complexes mimicking (deoxy)haemerythrin have been characterized, but most lack electrochemical investigations, in

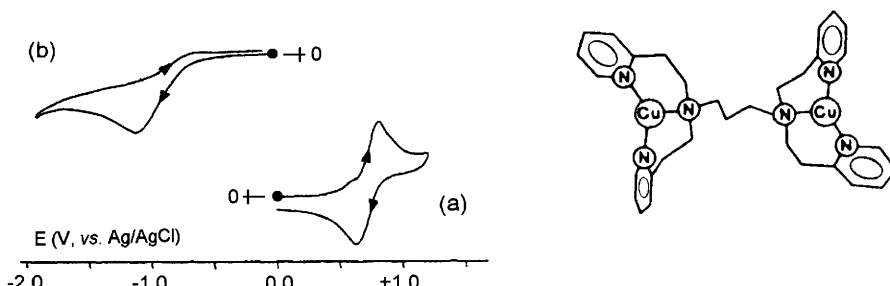


Figure 27 Cyclic voltammograms recorded at a glassy carbon electrode in a CH_2Cl_2 solution of $[Cu_2(N3)]^{2+}$: (a) under dinitrogen atmosphere; (b) after bubbling of dioxygen and subsequent bubbling of dinitrogen

spite of the fact that deoxyhaemerythrin undergoes two (potentiometrically determined) separate one-electron oxidations,^{34a} suggesting that in the O₂-induced oxidation to Fe^{III}₂ the mixed-valent Fe(II)-Fe(III) could be an important, even if not indefinitely stable,^{34b} intermediate.

One of the first electrochemically characterized models was the diiron(II) cation [Fe₂(OH)(O₂CCH₃)₂(Me₃TACN)₂]⁺, (Me₃TACN = 1,4,7-trimethyl-1,4,7-triazacyclononane), the molecular structure of which is illustrated in Figure 28.³⁵ In contrast to deoxyhaemerythrin, both the two Fe(II) centres are hexacoordinate.

The complex undergoes in dichloromethane solution a partially reversible single oxidation ($E^{\circ'} = -0.25$ V, vs. SCE), assigned as a one-electron process. This result would support the access to the corresponding mixed-valent Fe(II)Fe(III) species, the partial reversibility of the process having been attributed to deprotonation of the μ -hydroxo group.³⁵

The dication [Fe₂(Me₄-tpdp)(C₆H₅CO₂)(H₂O)]²⁺ (Me₄-tpdp = N,N,N',N'-tetrakis{(6-methyl-2-pyridyl)methyl}-1,3-diaminopropan-2-olate) illustrated in Figure 29 constitutes a further (asymmetric) binuclear Fe(II) model.³⁶

One iron atom is hexacoordinate (Fe1), the second is pentacoordinate (Fe2).

Such a complex exhibits in CH₂Cl₂ solution two separate one-electron oxidations ($E_{\text{Fe(II)Fe(II)/Fe(II)Fe(III)}}^{\circ'} = +0.60$ V, vs. SCE; $E_{\text{Fe(II)Fe(III)/Fe(III)}}^{\circ'} = +1.00$ V).³⁶

At low temperature (-35°C), in CH₂Cl₂ solution, this complex reversibly reacts with dioxygen, but nothing is reported about the electrochemical behaviour of the oxygenated complex.³⁶

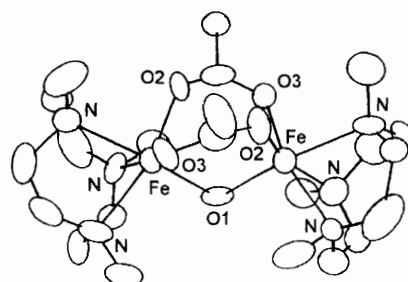


Figure 28 X-Ray structure of [Fe₂(OH)(O₂CCH₃)₂(Me₃TACN)₂]⁺. Fe-O1 = 1.99 Å; Fe-O2 = 2.14 Å; Fe-O3 = 2.12 Å; average Fe-N = 2.29 Å; Fe···Fe = 3.32 Å

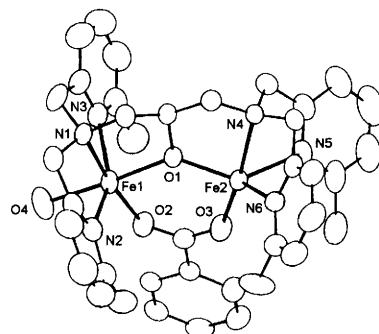
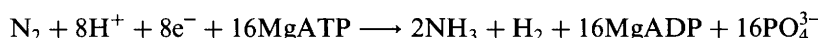


Figure 29 X-Ray structure of $[Fe_2(Me_4\text{-}tpdp)(C_6H_5CO_2)(H_2O)]^{2+}$. $Fe1-O1 = 2.06 \text{ \AA}$; $Fe1-O2 = 2.07 \text{ \AA}$; $Fe1-O4 = 2.14 \text{ \AA}$; $Fe1-N1 = 2.20 \text{ \AA}$; $Fe1-N2 = 2.29 \text{ \AA}$; $Fe1-N3 = 2.34 \text{ \AA}$; $Fe2-O1 = 1.98 \text{ \AA}$; $Fe2-O3 = 1.99 \text{ \AA}$; average $Fe2-N = 2.19 \text{ \AA}$; $Fe-Fe = 3.68 \text{ \AA}$

The same happens for the last haemerythrin model complex $[Fe_2(Htppdo)(C_6H_5CO_2)]^{3+}$ ($Htppdo = N,N,N',N'$ -tetrakis(6-pivalamido-2-pyridylmethyl)-1,3-diaminoprop-2-ol), in which one Fe(II) atom is heptacoordinate, and the other Fe(II) atom is hexacoordinate. At low temperature (-50°C), in acetone solution this complex reversibly reacts with dioxygen.³⁷ The only electrochemical information is that, in MeCN solution, the original trication exhibits two one-electron oxidations ($E_{Fe(II)Fe(II)/Fe(II)Fe(III)}^{o'} = +0.29 \text{ V vs. NHE}$; $E_{Fe(II)Fe(III)/Fe(III)Fe(III)}^{o'} = +0.79 \text{ V}$).³⁷

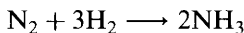
2 THE REACTIVITY OF TRANSITION METAL COMPLEXES WITH DINITROGEN

Interest in metal complexes able to bind molecular dinitrogen is mainly due to a desire to understand and reproduce in the laboratory the so-called *nitrogen fixation* reaction. This process, which in nature is catalysed by the metalloprotein *nitrogenases*, reduces the inert dinitrogen molecule to the metabolically useful NH₃:



The electrons required for this reduction process are provided *in vivo* by electron carriers such as *ferredoxins* (see Chapter 12, Section 3), whereas *in vitro* they can be provided by reducing agents such as dithionite.

To appreciate the height of the activation barrier that the biological catalysts are able to overcome one can recall that the Haber–Bosch process:



uses iron-based catalysts and requires temperatures of 300–500°C and pressures of 100 atm.

To date, three types of nitrogenases have been identified, namely *FeMo*-, *FeV*- and *FeFe*- *nitrogenases*, depending upon the metal (in addition to iron) present in their cofactor.

As shown schematically in Figure 30, the *FeMo-nitrogenase* is composed of two proteins:

- the *Fe-protein* ($\text{MW} \approx 60\,000$), which contains two identical protein subunits bridged by a Fe_4S_4 cluster;
- the *FeMo-protein* ($\text{MW} \approx 220\,000$), a tetramer containing two unique types of metal–sulfur clusters: the *P cluster* and the *FeMo cofactor* (FeMoco).^{38,39}

The *Fe-protein*, whose molecular structure is shown in Figure 31,^{40,41} acts as a one-electron donor to the *FeMo-protein*. This electron-donating ability arises from the propensity of the Fe_4S_4 cluster to undergo a one-electron oxidation.

As illustrated in Figure 32, the *FeMo-protein* (of *Azotobacter vinelandii*) incorporates the *P-cluster*, which for sake of simplicity can be thought of as composed of two cuboidal Fe_4S_4 centres each linked by a common sulfur atom, and the *FeMoco* (sometimes defined as the *M-centre*) of composition MoFe_7S_9 . A Fe_4S_3 subunit and a MoFe_3S_3 subunit form this latter centre.⁴²

Figure 33 shows in more detail the two clusters of the *FeMo-protein* and the sulfur bridges which connect the two cluster subunits.

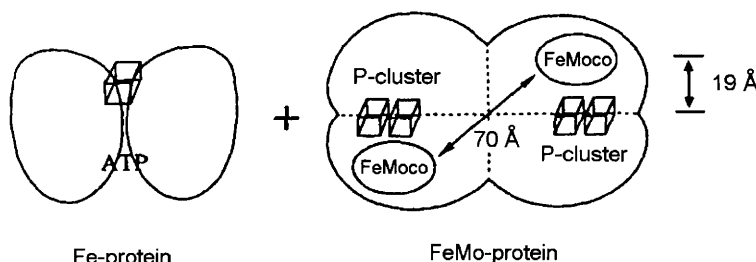


Figure 30 Schematic representation of the *FeMo* nitrogenase

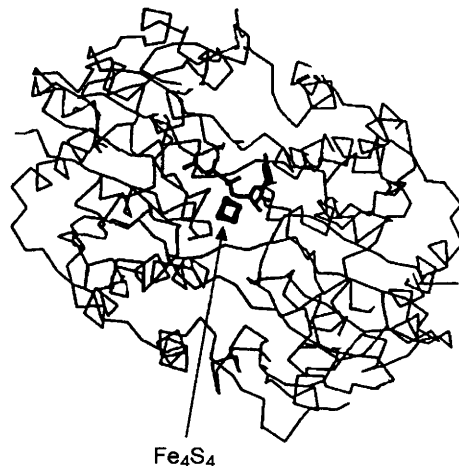


Figure 31 X-Ray structure of the active site of Fe-protein in the nitrogenase of *Azotobacter vinelandii*. Polypeptide chains surround the central Fe_4S_4 cluster

Although the role of the P-cluster is not yet clear, it is believed to act as an electron reservoir originating from the *Fe-protein* in readiness for the redox requirements of *FeMoco*.

As a matter of fact, the P-cluster exists either in the native P^{N} form (shown in Figure 33a) or in the two-electron (chemically) oxidized P^{OX} form, the molecular structures of which show significant differences at the bridging sulfur connections.^{42b,c}

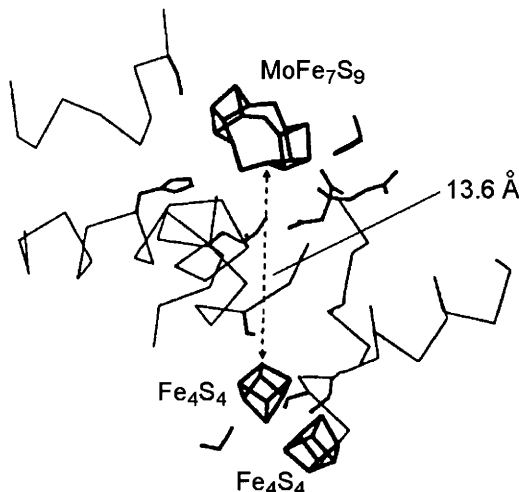


Figure 32 X-Ray structure of the active site of FeMo-protein in the nitrogenase of *Azotobacter vinelandii*

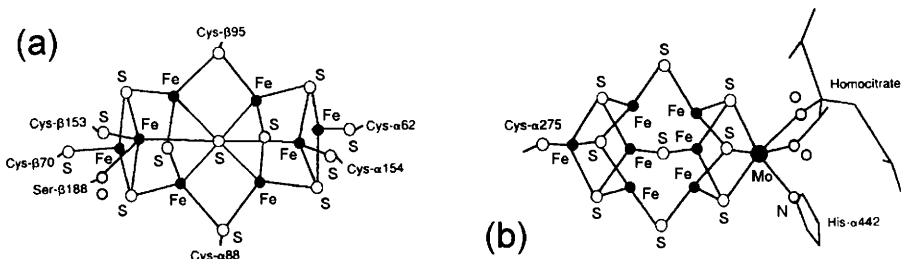


Figure 33 The molecular structures of: (a) P-cluster; (b) FeMoco

At this time we are not aware of electrochemical studies pertinent to the redox change: $P^N \rightleftharpoons P^{OX} + 2e^-$. In contrast, the redox aptitude of FeMoco has been electrochemically proved. The cyclic voltammogram of oxidized FeMoco in nmf ($HCONHCH_3$) solution is shown in Figure 34.^{43,44}

Even if the extraction of FeMoco in nmf slightly modifies the outer coordination of the $MoFe_7S_9$ cluster, in agreement with the experimental observation that the FeMo-protein can exist in the oxidized, semi-reduced and reduced forms, it exhibits two successive one-electron reductions ($E_{1st}^{o'} = -0.32$ V and $E_{2nd}^{o'} = -1.00$ V, vs. NHE). In the absence of thiophenol, the first reduction appears to be complicated by self-oxidation processes, whereas the presence of thiophenol apparently stabilizes the different oxidation states.

It is still debated if the overall oxidation state of the *FeMo cofactor* in its resting state (or, without substrate binding) has to be described as $Mo^{IV}Fe^{III}Fe_6^{II}$ or as $Mo^{IV}Fe_3^{III}Fe_4^{II}$.^{45,46}

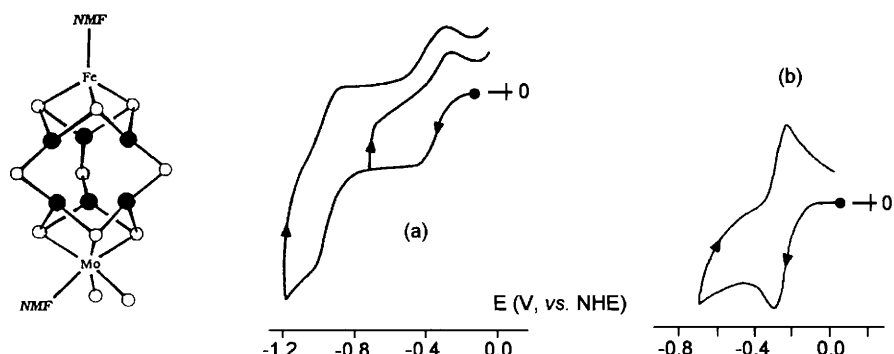


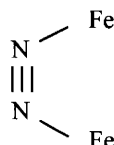
Figure 34 (a) Cyclic voltammogram recorded at a glassy carbon electrode in nmf solution of FeMoco. (b) After the addition of an excess of PhSH. Scan rate 0.1 V s^{-1}

Despite the availability of the molecular structures of the different active sites of the FeMo-nitrogenases, the mechanism of nitrogen fixation remains obscure. The interest of our discussion, however, is centred on the various modes proposed to describe how molecular nitrogen might coordinate the FeMoco. Some of the reported schemes are inspired by the type of coordination found in model compounds.

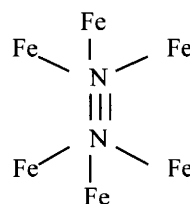
- (A) 'Side-on' coordination of the nitrogen molecule bridging two iron atoms, as if it were substituting for the sulfur atom bridging the two subunits.



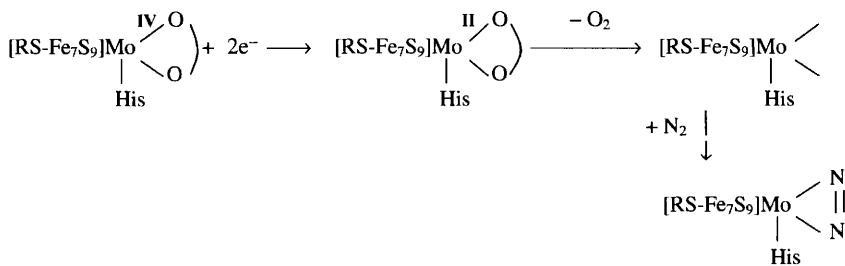
- (B) 'End-on' coordination of the nitrogen molecule between two iron atoms of the Fe₄S₄ subunits.



- (C) Penetration of the nitrogen molecule inside the P-cluster and coordination to the six iron atoms of the two Fe₄S₄ subunits.

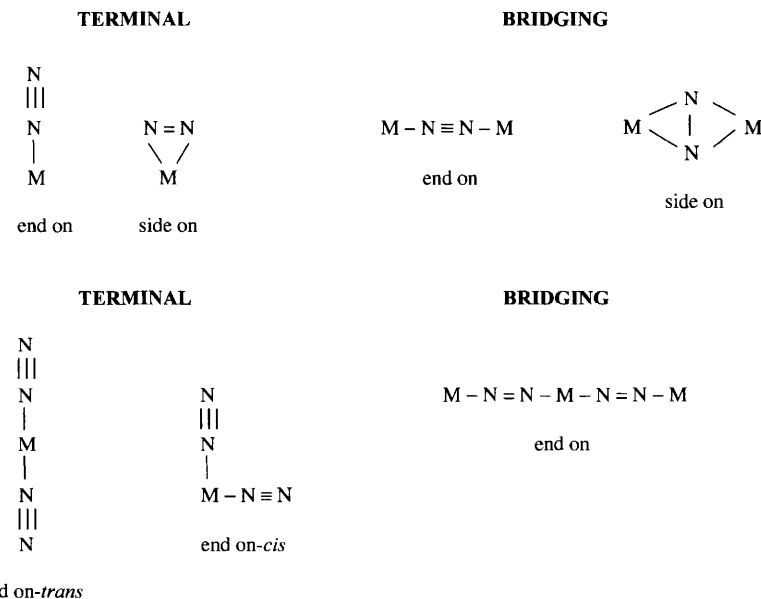


These examples would seem to indicate that the molybdenum atom, that for a long time was considered to be the specific site of dinitrogen coordination, is of little importance. It should be borne in mind, however, that the X-ray structure of the protein was obtained in the resting state. As noted, under such conditions, the Mo atom is assigned oxidation state IV and has a saturated coordination, hence not able to further coordinate nitrogen. EXAFS studies on the active protein indicate a Mo coordination different to that determined by X-ray diffraction. One hypothesis considers the dissociation of the homocitrate, induced by addition of electrons, that would leave vacant coordination sites which could then be saturated by the nitrogen molecule.



The uncertain role of the Mo atom is emphasized by the existence of the ‘alternative’ *nitrogenases*, which contain a FeV or a FeFe cofactor.

Amongst the model compounds able to coordinate dinitrogen, some can coordinate one dinitrogen and some two dinitrogen molecules. The following coordination modes have been identified for such complexes.



As usual our discussion of the model compounds will be limited to those complexes for which an electrochemical study and the corresponding molecular structure are available.

2.1 Metal Complexes with Terminal Coordination to One Dinitrogen Molecule

The first dinitrogen complex, $[\text{Ru}(\text{NH}_3)_5(\text{N}_2)]^{2+}$, was prepared in 1965.⁴⁷ Its X-ray structure⁴⁸ showed an octahedral geometry very

similar to that illustrated in Figure 35, which refers to the isostructural and isoelectronic dication $[\text{Os}(\text{NH}_3)_5(\text{N}_2)]^{2+}$.⁴⁹

The N–N distance of the linearly coordinated dinitrogen molecule (1.12 Å) is slightly longer than that of the nitrogen molecule in the gaseous state (1.10 Å).

In $\text{H}_2\text{SO}_4\text{-K}_2\text{SO}_4$ solution (pH 1.1), $[\text{Os}(\text{NH}_3)_5(\text{N}_2)]^{2+}$ displays an oxidation process to the corresponding trication $[\text{Os}(\text{NH}_3)_5(\text{N}_2)]^{2+/3+}$ ($E_{(2+/3+)}^{\circ} = +0.28$ V vs. SCE), complicated by slow degradation of the electrogenerated trication probably due to the loss of the coordinated dinitrogen molecule.⁵⁰

Under the same experimental conditions, $[\text{Ru}(\text{NH}_3)_5(\text{N}_2)]^{2+}$ gives rise to a completely irreversible oxidation ($E_p = +0.80$ V), indicating that the trication undergoes a still faster loss of the coordinated dinitrogen.⁵⁰

Figure 36 illustrates the molecular structure of $[\text{ReCl}(\text{N}_2)(\text{PMe}_2\text{Ph})_4]$.⁵¹ Also in this case the central metal atom has octahedral geometry with a linearly coordinated nitrogen molecule.

This Re(I) complex, in dichloromethane-methanol (10:1) solution, displays a reversible one-electron oxidation ($E^{\circ} = +0.05$ V vs. SCE) to the corresponding Re(II) complex $[\text{ReCl}(\text{N}_2)(\text{PMe}_2\text{Ph})_4]^+$,⁵² thus indicating the dinitrogen coordination is maintained upon the electron removal.

The same behaviour holds for the Re(I) monocation $[\text{Re}(\text{N}_2)(\text{PPh}_3)(\text{ampy})_2]^+$ [ampy = 2-(aminomethyl)pyridine], Figure 37,⁵³ which also exhibits a reversible oxidation to the corresponding Re(II) dication $[\text{Re}(\text{N}_2)(\text{PPh}_3)(\text{ampy})_2]^{2+}$ ($E^{\circ} = -0.20$ V vs. NHE, in *N,N*-dimethylacetamide).

Finally, the electrochemical behaviour of $[\text{FeH}(\text{N}_2)(\text{dppe})_2]^+$ (dppe = $\text{Ph}_2\text{PCH}_2\text{CH}_2\text{PPh}_2$) and $[\text{FeH}(\text{N}_2)(\text{depe})_2]^+$ (depe = $\text{Et}_2\text{PCH}_2\text{CH}_2\text{PEt}_2$) has been briefly studied. Both complexes undergo oxidation to the corresponding Fe(III) compounds, which are quite stable.⁵⁴ Even if

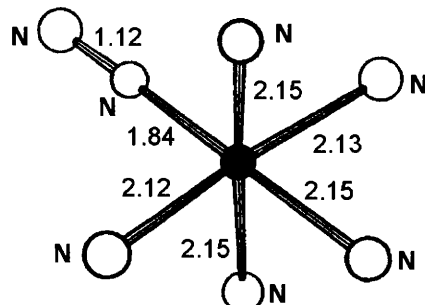


Figure 35 X-Ray structure of $[\text{Os}(\text{NH}_3)_5(\text{N}_2)]^{2+}$

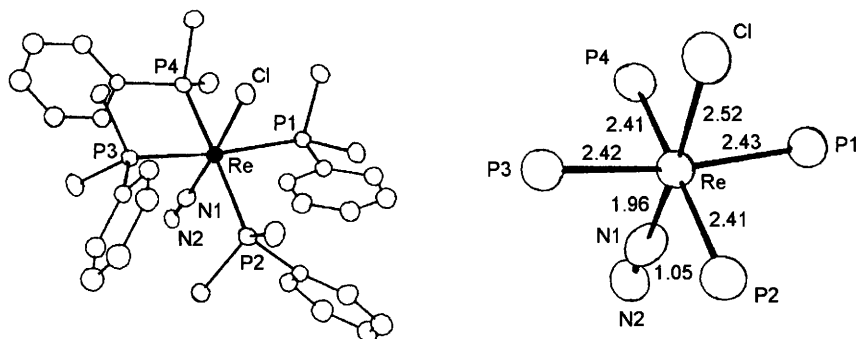


Figure 36 X-Ray structure of $[ReCl(N_2)(PMe_2Ph)_4]$

the X-ray structure of these complexes is not available, they should have the octahedral geometry exhibited by $[FeH(N_2)(dmpe)_2]^+$ ($dmpe = Me_2PCH_2CH_2PM_2$), with the linearly coordinated dinitrogen and the hydride atom occupying the axial positions (average bond lengths: $Fe-P = 2.21 \text{ \AA}$; $Fe-H = 1.33 \text{ \AA}$; $Fe-N = 1.83 \text{ \AA}$; $N-N = 1.11 \text{ \AA}$).⁵⁵

2.2 Metal Complexes with Bridging Coordination to One Dinitrogen Molecule

Figure 38 shows the molecular structure of the tetracation $[Ru_2(NH_3)_{10}(N_2)]^{4+}$,⁵⁶ the binuclear form of the previous dication $[Ru(NH_3)_5(N_2)]^{2+}$.

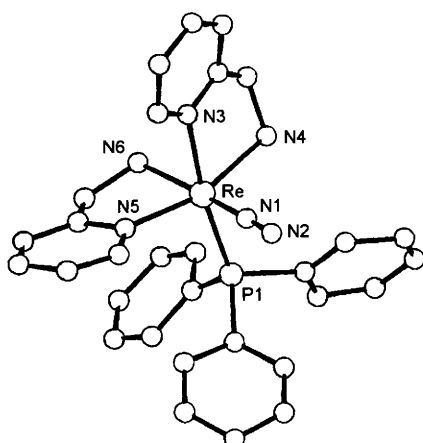


Figure 37 X-Ray structure of $[Re(N_2)(PPh_3)(ampy)_2]^+$. Bond lengths: $N1-N2 = 1.15 \text{ \AA}$, $Re-N1 = 1.85 \text{ \AA}$

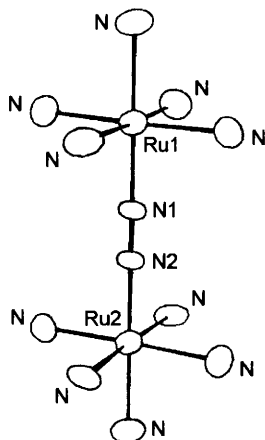
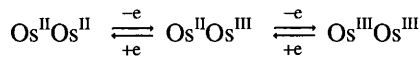


Figure 38 X-Ray structure of $[Ru_2(NH_3)_{10}(N_2)]^{4+}$. Bond lengths: Ru1–N1 = 1.93 Å; N1–N2 = 1.12 Å

Each ruthenium atom is octahedrally coordinated and the dinitrogen molecule is positioned in between the two metal centres.

The cyclic voltammogram in 0.28 M H_2SO_4 solution reveals a reversible one-electron oxidation ($E^{\circ\prime} = +0.46$ V vs. SCE). However, in the long times of macroelectrolysis, the exhaustive oxidation causes decomposition of $[Ru_2(NH_3)_{10}(N_2)]^{5+}$ to $[Ru^{II}(NH_3)_5(N_2)]^{2+}$ and $[Ru^{III}(NH_3)_5X]^{50}$. Since the complex contain two Ru(II) atoms, the lack of the second Ru^{II/III} oxidation is likely to be masked by the easy oxidation of the aqueous solvent.

In confirmation of this assumption, for instance, the binuclear complex $[(terpy)(Cl)_2Os^{II}(N_2)Os^{II}(Cl)_2(terpy)]$ (terpy = 2,2':6',2''-terpyridine) displays in dmf solution two separate oxidation processes reversible in character:⁵⁷



$$E^{\circ\prime} = +0.21 \text{ V} \quad E^{\circ\prime} = +0.77 \text{ V}$$

Figure 39 shows the molecular structure of the mixed-valent monocation $[(terpy)(Cl)_2Os^{II}(N_2)Os^{III}(Cl)_2(terpy)]^+$.⁵⁷

The Os1-N1-N2-Os2 axis is not perfectly linear. The inequality of the bond distances (which would assign the oxidation states III to the Os1 atom and II to the Os2 atom, respectively) should classify the monocation as a charge localized (Class I) mixed-valent species. Nevertheless, this result is in contrast with the electrochemical separation of the two

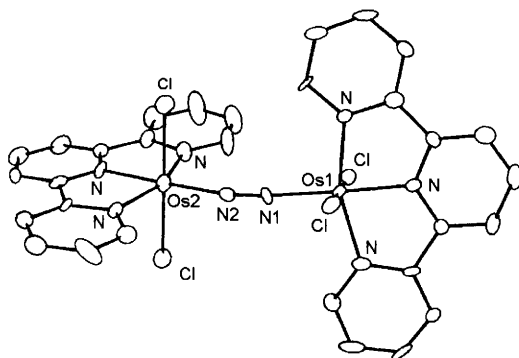


Figure 39 *X-Ray structure of the monocation $[(\text{terpy})(\text{Cl})_2\text{Os}^{\text{II}}(\text{N}_2)\text{Os}^{\text{III}}(\text{Cl})_2(\text{terpy})]^+$. Bond lengths: $\text{N1}-\text{N2} = 1.13 \text{ \AA}$; $\text{Os2}-\text{N2} = 1.91 \text{ \AA}$; $\text{Os1}-\text{N1} = 1.97 \text{ \AA}$; $\text{Os2}-\text{Cl} \approx 2.40 \text{ \AA}$; $\text{Os1}-\text{Cl} \approx 2.36 \text{ \AA}$*

oxidation processes ($\Delta E^\circ' = 0.56 \text{ V}$), which, affording a $K_{\text{com}} \approx 3 \times 10^9$, suggests a completely delocalized (Class III) mixed-valent species. Hence it has to be considered if the crystal packing may somewhat contribute to the difference in bonding lengths.

Figure 40 shows the molecular structure of $[\text{Tp}(\text{CO})_2\text{Re}^{\text{I}}(\mu\text{-N}_2)\text{Re}^{\text{I}}(\text{CO})_2\text{Tp}]$ (Tp = hydrotris(pyrazolyl)borate).⁵⁸

Such complex, in dimethylacetamide solution, also exhibits two one-electron processes, the first of which is reversible in character ($E_{\text{Re(I)Re(I)/Re(I)Re(II)}}^\circ' = +0.90 \text{ V}$, vs. NHE), whereas the second is irreversible ($E_{\text{pRe(I)Re(II)/Re(II)Re(II)}}^\circ = +1.55 \text{ V}$).

An interesting electrochemical behaviour is exhibited by the V(II) complex $[\text{V}(\text{mes})_3(\text{thf})]$ ($\text{mes} = 2,4,6\text{-Me}_3\text{C}_6\text{H}_2$) under dinitrogen atmosphere.⁵⁹ As illustrated in Figure 41a, in thf solution under argon

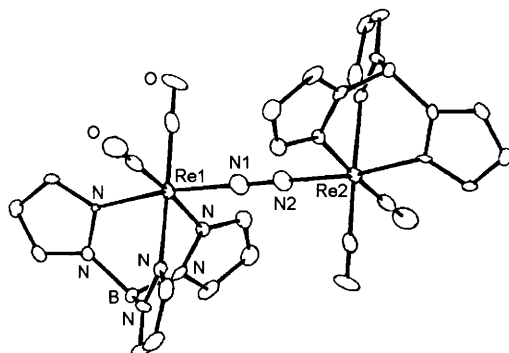


Figure 40 *X-Ray structure of $[\text{Tp}(\text{CO})_2\text{Re}(\mu\text{-N}_2)\text{Re}(\text{CO})_2\text{Tp}]$. Bond lengths: $\text{Re1}-\text{N1} = 1.98 \text{ \AA}$; $\text{N1}-\text{N2} = 1.15 \text{ \AA}$; $\text{Re}-\text{N}_{(\text{Tp})} = 2.13 \text{ \AA}$*

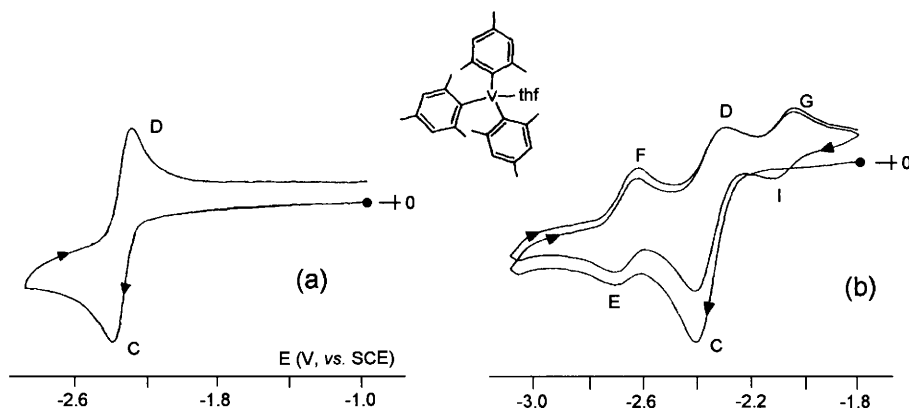
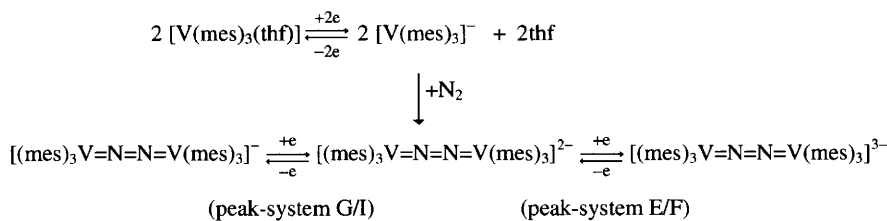


Figure 41 Cyclic voltammograms recorded at a platinum electrode in a thf solution of $[\text{V}(\text{mes})_3(\text{thf})]$ under the following experimental conditions: (a) under Ar atmosphere; (b) under N_2 atmosphere. Scan rate 0.2 V s^{-1}

atmosphere, it displays a reversible one-electron reduction (peak-system C/D, $E^{\circ'} = -2.09 \text{ V}$ vs. SCE).

Upon bubbling dinitrogen, two new peak-systems add to such a reduction step: a reduction process at the peak-system E/F ($E^{\circ'} = -2.40 \text{ V}$) and an oxidation process at the peak-system I/G ($E^{\circ'} = -1.84 \text{ V}$), respectively, Figure 41b. These results have been interpreted as due to the following electrode mechanism:



In this connection, Figure 42 shows the molecular structure of the monoanion $[\text{(mes)}_3\text{V=N=N=V(mes)}_3]^-$.⁵⁹

In confirmation of the proposed mechanism, an authentic sample of $[\text{(mes)}_3\text{V=N=N=V(mes)}_3]^-$ displays the sequential $-/2/-3-$ reductions, Figure 43.

The chemical complications following the oxidation $[\text{(mes)}_3\text{V=N=N=V(mes)}_3]^-$ occurring at peak H ($E_p = -0.95 \text{ V}$) trigger regeneration of the original mononuclear complex $[\text{V}(\text{mes})_3(\text{thf})]$, which in turn oxidizes at the peak-system A/B ($E^{\circ'} = +0.16 \text{ V}$).

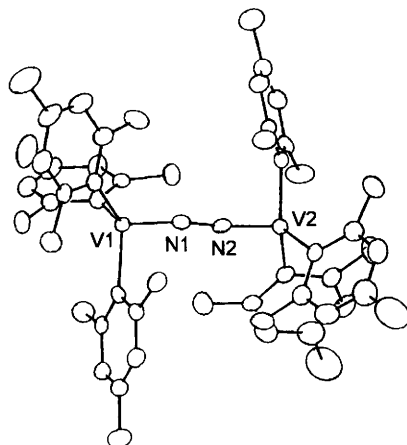


Figure 42 X-Ray structure of $\left[\left(\text{mes}\right)_3\text{V}=\text{N}=\text{N}=\text{V}\left(\text{mes}\right)_3\right]^-$. $\text{VI}-\text{NI} = 1.77 \text{ \AA}$; $\text{V2}-\text{N2} = 1.74 \text{ \AA}$; average $\text{V}-\text{C} = 2.09 \text{ \AA}$; $\text{NI}-\text{N2} = 1.22 \text{ \AA}$

A further vanadium-dinitrogen complex is represented by $\left[\{\text{V}(\text{NPt}_2^+)_3\}_2(\mu\text{-N}_2)\right]$, the molecular structure of which is illustrated in Figure 44.⁶⁰

In THF solution, it exhibits a reversible one-electron reduction ($E^\circ = -0.05 \text{ V}$, vs. SCE).⁶⁰

Figure 45 illustrates the molecular structure of complex $\left[\{\text{W}(\text{C}_5\text{Me}_5)\text{-Me}_2(\text{OC}_6\text{F}_5)\}_2(\mu\text{-N}_2)\right]$.⁶¹

The dinitrogen molecule bridges the two tungsten atoms, each of which assumes a ‘four-legged piano stool’ geometry.

In CH_2Cl_2 solution it exhibits either an irreversible oxidation ($E_p = 1.0 \text{ V}$ vs. Ag/AgCl) or an irreversible reduction ($E_p = -1.65 \text{ V}$).⁶¹

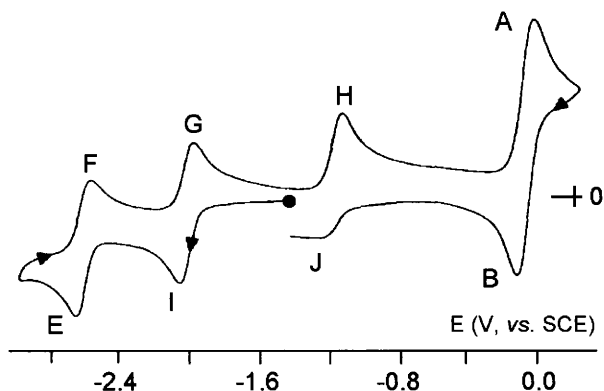


Figure 43 Cyclic voltammogram recorded at a platinum electrode in a THF solution of $\left[\left(\text{mes}\right)_3\text{V}=\text{N}=\text{N}=\text{V}\left(\text{mes}\right)_3\right]^-$, under N_2 atmosphere. Scan rate 0.2 V s^{-1}

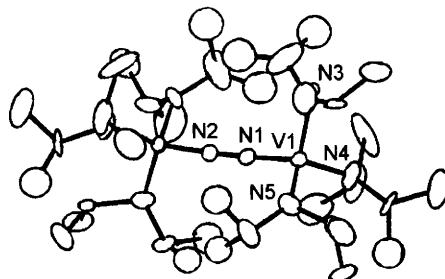


Figure 44 X-Ray structure of $\{[V(NPr^i_2)_3]_2(N_2)\}$. Bond lengths: $V1-N_{(amine)} = 1.89 \text{ \AA}$; $V1-N1 = 1.74 \text{ \AA}$; $N1-N2 = 1.27 \text{ \AA}$

We conclude with the dinitrogen complex of a three-coordinate iron complex bearing the ligand $L = 2,4\text{-bis}(2,6\text{-diisopropylphenylimido})\text{pentane anion}$, $[\{\text{FeL}\}_2(\mu\text{-N}_2)]$. The dinitrogen complex has been obtained by chemical reduction of $[\text{FeLCI}]$ (which is the analogue of complex $[\text{CuLCI}]$ illustrated in Chapter 5, Section 7) under a dinitrogen atmosphere. Its molecular structure is illustrated in Figure 46.⁶²

Even if the electrochemical behaviour of the complex is unknown, chemical two-electron reduction (by sodium or potassium metal) affords the corresponding dianion $[\text{LFe}—\text{N}=\text{N}—\text{FeL}]^{2-}$, the molecular structure of which is substantially similar to that of the neutral precursor.⁶² In the dianion, the $\text{Fe}—\text{N}_{(\text{dinitrogen})}$ distance remains essentially unaltered with respect to the neutral congener, whereas the $\text{N}=\text{N}$ distance elongates by about 0.06 \AA . Such a lengthening of the $\text{N}=\text{N}$ bond agrees with theoretical results which show that the two added electrons enter $\text{N}=\text{N}$ antibonding orbitals.

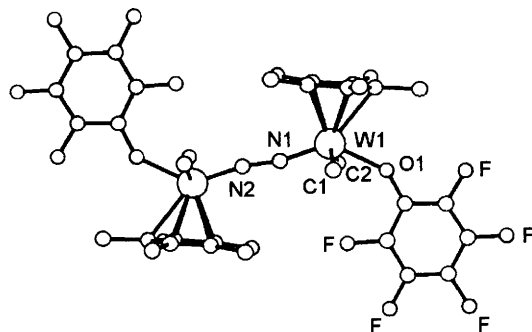


Figure 45 X-Ray structure of $\{[W(C_5Me_5)Me_2(OC_6F_5)]_2(N_2)\}$. Bond lengths: $W1-N1 = 1.77 \text{ \AA}$; $W1-C1 = 2.13 \text{ \AA}$; $W1-C2 = 2.11 \text{ \AA}$; $W1-O1 = 2.08 \text{ \AA}$; $N1-N2 = 1.26 \text{ \AA}$

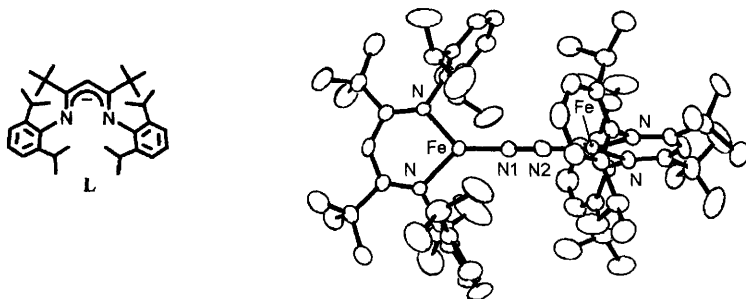


Figure 46 X-Ray structure of the iron-dinitrogen complex $[LFe-N=N-FeL]$. $Fe-N_{(imido)} = 1.87 \text{ \AA}$; $Fe-N_{(dinitrogen)} = 1.77 \text{ \AA}$; $N1-N2 = 1.18 \text{ \AA}$

2.3 Metal Complexes with Terminal Coordination to Two Dinitrogen Molecules

Figure 47 shows the octahedral geometry of $[Mo^0(N_2)_2(dppe)_2]$ ($dppe = Ph_2PCH_2CH_2PPh_2$) with the two nitrogen molecules linearly coordinated in *trans* position.⁶³

Its cyclic voltammetric behaviour in dmf solution is illustrated in Figure 48.⁶⁴

It undergoes a one-electron oxidation ($E^{o'} = -0.23 \text{ V}$), which possesses features of chemical reversibility on the time scale of cyclic voltammetry.⁶⁴ In reality, as suggested by the appearance of the minor oxidation peak after traversing the main anodic peak, the corresponding monocation $[Mo^1(N_2)_2(dppe)_2]^+$ slowly decomposes in different solvents through dinitrogen release with a lifetime of $t_{1/2} \approx 16 \text{ s}$.^{65,66}

The complex *trans*- $[W^0(N_2)_2(dppe)_2]$ displays a very similar behaviour. In thf solution it undergoes oxidation at $E^{o'} = -0.15 \text{ V}$, which is

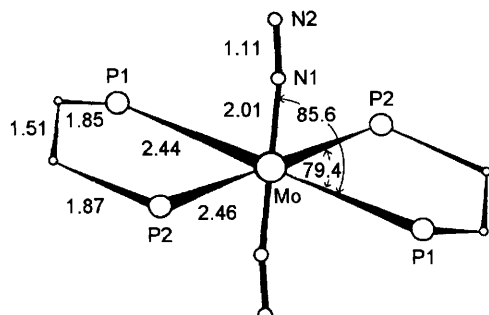


Figure 47 X-Ray structure of *trans*- $[Mo(N_2)_2(dppe)_2]$. Phenyl groups bound to the phosphorus atoms have been omitted

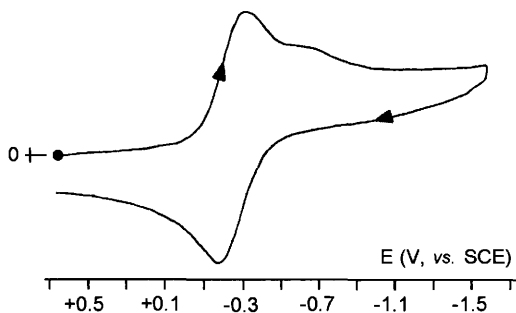


Figure 48 Cyclic voltammograms recorded at a platinum electrode in a dmso solution of *trans*-[$\text{Mo}(\text{N}_2)_2(\text{dppe})_2$]. Scan rate 10 V s^{-1}

substantially coincident with that of *trans*-[$\text{Mo}(\text{N}_2)_2(\text{PMePh}_2)_4$], which in the same solvent oxidizes at $E^{\circ\prime} = -0.16 \text{ V}$.⁶⁶

Complex *trans*-[$\text{Mo}^0(\text{N}_2)_2(\text{PMePh}_2)_4$], which is structurally similar to *trans*-[$\text{Mo}(\text{N}_2)_2(\text{dppe})_2$],⁶⁷ also displays a one-electron oxidation with features of chemical reversibility (in dmso: $E_{0/+}^{\circ\prime} = -0.53 \text{ V}$,⁶⁴ in thf: $E_{0/+}^{\circ\prime} = -0.43 \text{ V}$ ⁶⁷). Also in this case, the electrogenerated monocation $[\text{Mo}(\text{N}_2)_2(\text{PMePh}_2)_4]^+$ decomposes slowly.⁶⁴

Figure 49 shows the molecular structure of the macrocyclic complex *trans*-[$\text{Mo}^0(\text{N}_2)_2\text{Me}_8[16]\text{aneS}_4$].⁶⁸

In thf solution it exhibits an irreversible $\text{Mo}^{0/\text{I}}$ oxidation ($E_p = -0.52 \text{ V}$). This result indicates that, despite the easier oxidation compared to *trans*-[$\text{Mo}(\text{N}_2)_2(\text{dppe})_2$], in the oxidized state it loses the coordinated nitrogen much more quickly.

A final aspect which follows what is discussed in Chapter 7, Section 1, is the different electrochemical behaviour of the *cis* and *trans* isomers as a consequence of the different stability of their oxidized states.

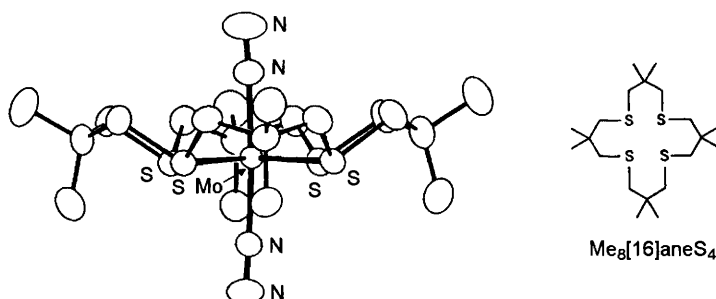


Figure 49 X-Ray structure of *trans*-[$\text{Mo}(\text{N}_2)_2(\text{Me}_8[16]\text{aneS}_4)$]. Average bond lengths: $\text{Mo}-\text{S} = 2.42 \text{ \AA}$; $\text{Mo}-\text{N} = 2.00 \text{ \AA}$; $\text{N}-\text{N} = 1.11 \text{ \AA}$

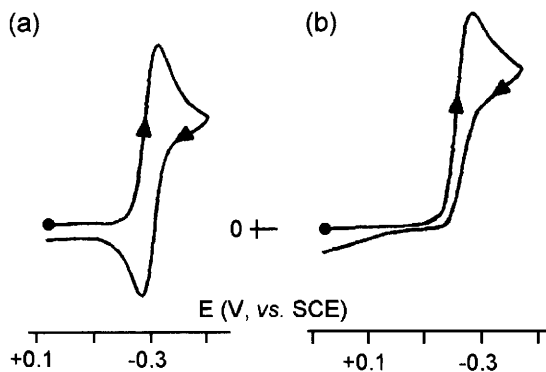


Figure 50 Cyclic voltammograms recorded at a platinum electrode in *thf* solutions of: (a) *trans*-[W(N₂)₂(PMe₂Ph)₄]; (b) *cis*-[W(N₂)₂(PMe₂Ph)₄]. Scan rate 0.1 V s⁻¹. T = 0°C

Figure 50 compares the cyclic voltammogram of *trans*-[W(N₂)₂(PMe₂Ph)₄] with that of *cis*-[W(N₂)₂(PMe₂Ph)₄], recorded in *thf* solution at 0°C.⁶⁹

It is evident that *trans*-[W(N₂)₂(PMe₂Ph)₄] gives rise to a reversible oxidation, which indicates that the W(I) congener is relatively stable (at 25°C, the chemical reversibility decreases slightly). Conversely, *cis*-[W(N₂)₂(PMe₂Ph)₄], though oxidized at the same potential, displays an irreversible oxidation, indicating rapid decomplexation of the dinitrogen.

A similar behaviour has been found for the isomers *trans*-[Mo(N₂)₂(PMe₂Ph)₄] and *cis*-[Mo(N₂)₂(PMe₂Ph)₄].⁷⁰

3 THE REACTIVITY OF TRANSITION METAL COMPLEXES WITH DIHYDROGEN

Even if hydrides of transition metals play an important role as intermediates in catalytic processes such as hydrogenation and hydroformylation of alkenes and the Fischer-Tropsch reaction,⁷¹ in order to follow with the bioinorganic subject, we refer to the interconversion process:



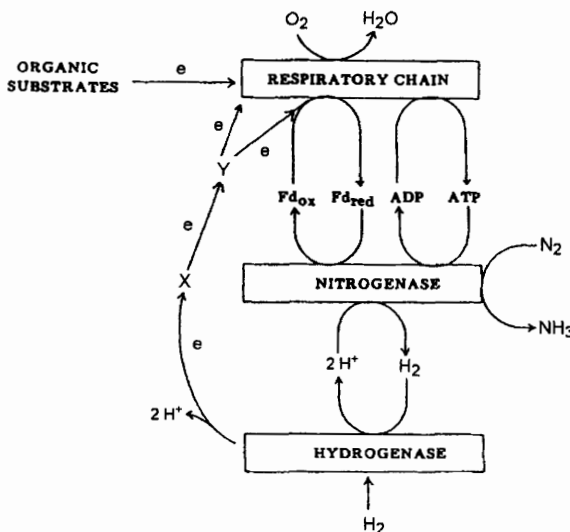
which, in nature, is catalysed by metalloproteins called *hydrogenases*.⁷² In fact, bacterial *hydrogenases* catalyse both the oxidation of molecular hydrogen and the reduction of protons. This biological function is

strictly connected to the activity of the previously discussed *nitrogenases*. In fact, the reduction of molecular dinitrogen:



produces dihydrogen, which, if not removed, inhibits the further reduction of dinitrogen.

The link between nitrogen fixation and the oxidation of hydrogen in bacterial systems is schematically summarized in Scheme 8.⁷³



Scheme 8

There are several types of hydrogenases, all of which have a metal-containing active site. In fact, they are classified as: *Fe-only hydrogenases*, *Ni–Fe hydrogenases* and *Ni–Fe–Se hydrogenases*.

At the moment, the best structurally characterized is the *Ni–Fe hydrogenase* from *Desulfovibrio* bacteria,^{74,75} even if crystallographic data from *Fe-only hydrogenases* start to be available.⁷⁶ The active site of the Ni–Fe hydrogenase contains a NiS₂Fe group, two cuboidal Fe₄S₄ clusters and one quasi-cuboidal Fe₃S₄ cluster, Figure 51.

There is evidence that in the oxidized form, an oxo or hydroxo group bridges the Ni and Fe atoms, which should be absent in the enzymatically active reduced form.

The Fe–S clusters are believed to act as electron transfer centres for external redox agents such as *cytochrome c*₃ (the high electron transfer ability of metal–sulfur clusters has been discussed in Chapter 8, Section 1, whereas the redox aptitude of cytochromes will be considered in

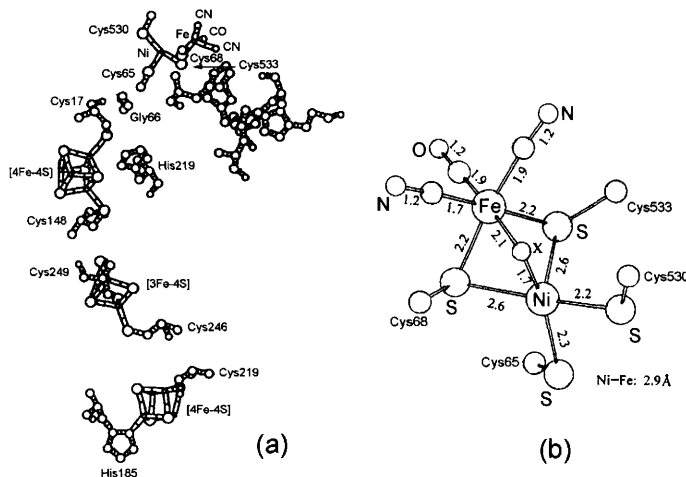


Figure 51 The chain of metal fragments forming the active site of the Ni–Fe hydrogenase of *Desulfovibrio gigas*. (a) Overall view; (b) structural details of the NiS₂Fe centre

Chapter 12, Section 2). It is generally accepted that the site responsible for the oxidation of dihydrogen and the reduction of protons is the nickel-containing assembly, possibly exploiting its capacity to shuttle between the multiple oxidation states Ni(III)/Ni(II)/Ni(I)/Ni(0).

A number of mechanisms of hydrogen coordination to the nickel fragment have been proposed, including the possibility that it coordinates as molecular dihydrogen. This suggestion is strengthened by the observation that in many metal complexes which coordinate molecular hydrogen, substitution of dihydrogen by dinitrogen is achieved simply by bubbling dinitrogen through the solution. This does not occur for the classical hydride complexes.^{77#} In addition, dihydrogen–metal complexes seem to play a promising role as diagnostic agent in medicinal chemistry.⁷⁹

The first molecular structure of a dihydrogen complex was obtained for [W(CO)₃(PPrⁱ)₂(H₂)], Figure 52.⁸⁰

The dihydrogen molecule assumes a ‘side-on’ terminal coordination. The W–H₂ distance is 1.95 Å (X-ray diffraction) or 1.89 Å (neutron diffraction). The H–H distance is 0.75 Å (X-ray diffraction) or 0.82 Å (neutron diffraction), with respect to 0.74 Å for molecular hydrogen in the gaseous state.

As shown in Figure 53, the interaction of dihydrogen with the metal centre of transition metal complexes can be described as a *two-electron*

In a few dihydrogen metal complexes also dioxygen can displace dihydrogen.⁷⁸

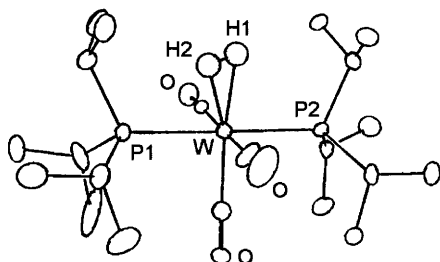


Figure 52 X-Ray structure, at -100°C , of $[\text{W}(\text{CO})_3(\text{PPr}_3)_2(\text{H}_2)]$

three-centre bond generated by electron donation from the filled σ orbital of dihydrogen to an empty d orbital of the metal, accompanied by back-donation from the filled d orbitals of the metal to the empty σ^* orbital of dihydrogen.⁸¹

It is easy to imagine that either the depopulation of the bonding orbital of dihydrogen, caused by the σ -donation, or the population of the antibonding orbital of dihydrogen, caused by the π -back-donation both lead to the weakening of the H–H bond. Therefore, there must be a delicate balance between these two interactions if a change from a ‘non-classical’ coordination (coordinated hydrogen molecule) to a ‘classical’ (hydride complex) has to be avoided.

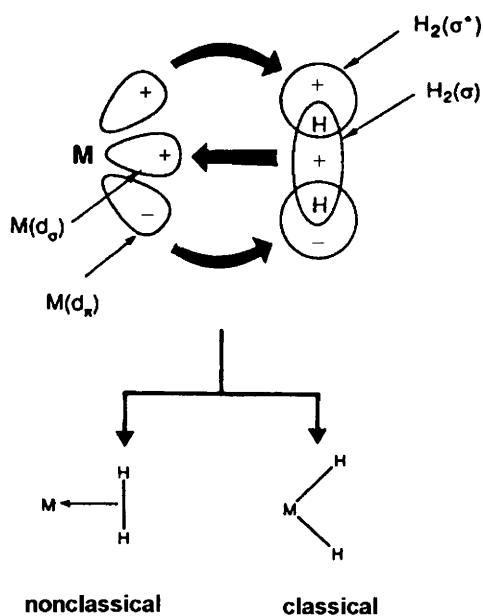
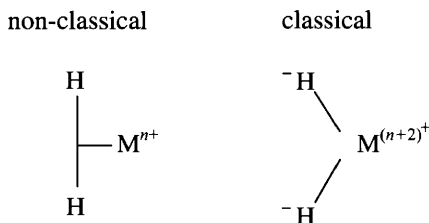


Figure 53 The mechanism of formation of the MH_2 bond

Due to localization of the electron density, Scheme 10, the oxidation state of the metal increases by two units upon passing from a *non-classical* to a *classical* coordination, which in principle offers the opportunity to use electrochemistry to discriminate between classical and non-classical hydrides.⁸¹



Scheme 10

The first attempt to use electrochemistry to solve the dilemma of classical or non-classical coordination was in the case of the polyhydride $[\text{ReH}_5(\text{PPh}_3)_3]$. Its solid-state molecular structure would correspond to that of the classical pentahydride $[\text{Re}^{\text{V}}\text{H}_5(\text{PPh}_3)_3]$, whereas solution NMR studies would indicate a non-classical hydride $[\text{Re}^{\text{III}}\text{H}_3(\text{H}_2)(\text{PPh}_3)_3]$.

As shown in Figure 54, this derivative undergoes in CH_2Cl_2 solution a reversible one-electron oxidation ($E^{\circ'} = +0.29 \text{ V}$ vs. Ag/AgCl).⁸¹

Unfortunately, as rhenium can assume all the oxidation states in the range from -1 to $+7$, such an anodic process can be attributed either to the oxidation $\text{Re(V)}/\text{Re(VI)}$, according to the classical hydride formulation $[\text{Re}^{\text{V}}\text{H}_5(\text{PPh}_3)_3]$, or to the $\text{Re(III)}/\text{Re(IV)}$ oxidation, according to the non-classical hydride formulation $[\text{Re}^{\text{III}}\text{H}_3(\text{H}_2)(\text{PPh}_3)_3]$.

In this regard a more significant determination should be obtained from a study of the polyhydride complexes $[\text{ReH}_7(\text{PR}_3)_2]$, in that: (i) if the complex is a classical hydride the rhenium atom would be in its maximum oxidation state ($+7$) and, therefore, could not undergo further oxidation processes; (ii) if the complex is a non-classical hydride, the rhenium atom would be in a lower oxidation state and, consequently, could display oxidation processes.

As shown in Figure 55, $[\text{ReH}_7(\text{PPh}_3)_2]$ exhibits an oxidation process which is localized at potential values less positive than those of the free phosphine ligand.⁸¹

This observation (coupled to NMR data) seemed to support the thesis that the complex was a non-classical hydride. (Unfortunately) the neutron diffraction structure of a few related complexes such as

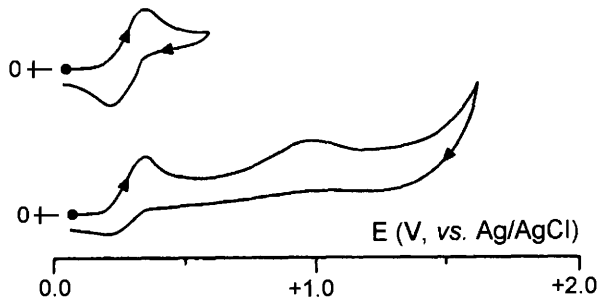


Figure 54 Cyclic voltammograms recorded at a platinum electrode in a CH_2Cl_2 solution of $[\text{ReH}_5(\text{PPh}_3)_3]$. Scan rate 0.2 V s^{-1}

$[\text{ReH}_7(\text{PMePh}_2)_2]$ and $[\text{ReH}_7(\text{PPhPr}^i)_2]$ showed that they were classical hydrides, calling into question the electrochemical and NMR interpretation on the nature of $[\text{ReH}_7(\text{PPh}_3)_2]$. Nevertheless, the subsequent resolution of the crystal structure of $[\text{ReH}_7(\text{P}\{p\text{-tolyl}\}_3)_2]$, Figure 56,⁸² showed that two of the seven hydrogen atoms were separated by 1.36 \AA ($\text{H}3\text{--H}5$), which is a distance intermediate between the value of 0.8 \AA , found for non-classical hydrides, and 1.7 \AA for classical hydrides. In a certain sense, this gave again credibility to the $[\text{Re}^{\text{V}}\text{H}_5(\text{H}_2)(\text{PPh}_3)_2]$ formulation deducible from the electrochemical behaviour of $[\text{ReH}_7(\text{PPh}_3)_2]$.

Furthermore, this demonstrated that the factors governing the equilibrium between classical and non-classical hydrides are very delicately balanced.

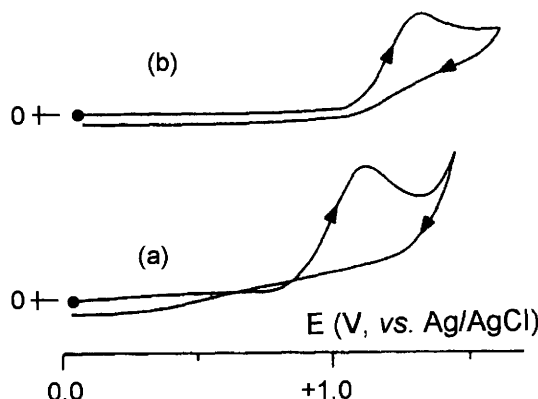


Figure 55 Cyclic voltammograms recorded at a platinum electrode in a CH_2Cl_2 solution of: (a) $[\text{ReH}_7(\text{PPh}_3)_2]$; (b) PPh_3 . Scan rate 0.2 V s^{-1}

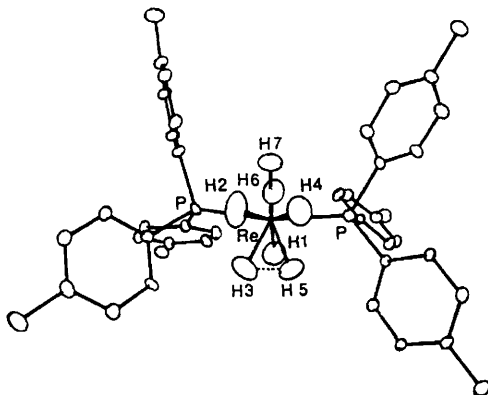


Figure 56 Neutron diffraction structure of $[ReH_7(P\{p\text{-MeC}_6\text{H}_4\}_3)_2]$

Let us now consider a few non-classical hydride complexes for which molecular structures are available.

As already mentioned in Chapter 7, Section 2 (Figures 18, 19)[#], the monocation $[\text{Co}(\text{PP}_3)(\text{H}_2)]^+$ ($\text{PP}_3 = \text{P}(\text{CH}_2\text{CH}_2\text{PPh}_2)_3$), present as non-classical hydride in $[\text{Co}(\text{PP}_3)(\text{H}_2)][\text{PF}_6]$, undergoes an irreversible oxidation (Figure 19), which generates the monocation $[\text{Co}(\text{PP}_3)\text{H}]^+$, thus suggesting that the oxidation of the dihydrogen complex simply causes deprotonation.⁸³

Figure 57 shows the octahedral geometry of the monocation $[\text{Fe}(\text{dppe})_2(\text{H}_2)(\text{H})]^+$ ($\text{dppe} = \text{Ph}_2\text{PCH}_2\text{CH}_2\text{PPh}_2$).⁸⁴

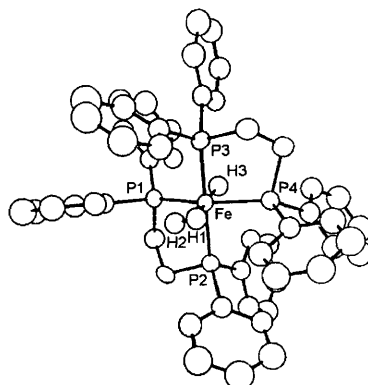


Figure 57 The molecular structure of $[\text{Fe}(\text{dppe})_2(\text{H}_2)(\text{H})]^+$. The H–H bond length is 0.82 Å at the neutron diffraction and 0.87 Å at X-ray diffraction, respectively

[#] It is useful to note that the simple substitution of the counteranion to form $[\text{Co}(\text{triphos})(\text{H}_2)][\text{BPh}_4]$ produces a classical hydride complex. This is a further demonstration of the lability which characterizes the boundary between ‘classical’ and ‘non-classical’ hydrides.

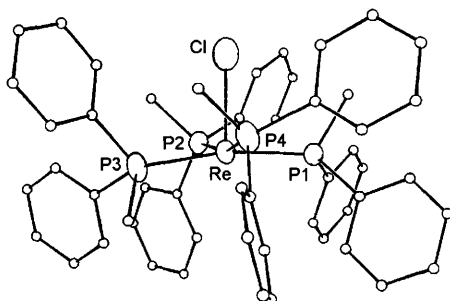


Figure 58 X-Ray structure of $[ReCl(H_2)(PMePh_2)_4]$. The hydrogen atoms have not been localized

In CH_2Cl_2 solution, this complex displays an irreversible oxidation at $E_p = +1.2 \text{ V}$ (vs. SCE).⁸⁵

The isostructural and isoelectronic complex $[\text{Os}(\text{dppe})_2(\text{H}_2)(\text{H})]^+$ ⁸⁶ also exhibits in CH_2Cl_2 solution an irreversible oxidation at $E_p = +1.5 \text{ V}$ (vs. SCE).⁸⁵ It is interesting to note that in $[\text{Os}(\text{dppe})_2(\text{H}_2)(\text{H})]^+$ the H–H distance at the neutron diffraction is 0.79 \AA , whereas in the related chloro-complex $[\text{Os}(\text{dppe})_2(\text{H}_2)(\text{Cl})]^+$ the H–H distance is 1.15 \AA at the neutron diffraction (and 1.11 \AA at the X-ray diffraction).⁸⁷ It is hence deduced that the nature of the atom *trans* to H_2 (H vs. Cl) significantly affects the H–H bond length.⁸⁸

On the basis of the foregoing discussion it thus would seem that the dihydrogen complexes decompose upon oxidation. Some complexes have been reported to show reversible oxidation.⁸¹ Amongst those for which the molecular structure is available we can, for example, mention the octahedral $[\text{ReCl}(\text{H}_2)(\text{PMePh}_2)_4]$, Figure 58.⁸⁹

In CH_2Cl_2 solution this complex displays a reversible one-electron oxidation at $E^{\circ'} = 0.0 \text{ V}$ (vs. SCE).⁹⁰ The easy oxidation agrees well with the Re(I) oxidation state in a non-classical hydride formulation, even if the calculated H–H bond distance of 1.39 \AA poses the derivative at the border of classical and non-classical hydrides.⁹¹

REFERENCES

1. A.C. Rosenzweig, C.A. Frederick, S.J. Lippard and P. Nordlund, *Nature*, 1993, **366**, 537.
2. A.M. Orville, J.D. Lipscomb and D. Ohlendorf, *Biochemistry*, 1997, **36**, 10052.
3. T. Senda, K. Sugiyama, H. Narita, T. Yamamoto, K. Kimbara, M. Fukuda, M. Sato, K. Yano and Y. Mitsui, *J. Mol. Biol.*, 1996, **255**, 735.

4. T. Tsukihara, H. Aoyama, E. Yamashita, T. Tomizaki, H. Yamaguchi, K. Shinzawa-Itoh, R. Nakashima, R. Yaono and S. Yoshikawa, *Science*, 1995, **269**, 1069.
5. (a) S.E.V. Phillips, *Nature*, 1978, **273**, 247; (b) S.E.V. Phillips, *J. Mol. Biol.*, 1980, **142**, 531.
6. B. Shaanan, *J. Mol. Biol.*, 1983, **171**, 31.
7. E. Weber, W. Steigemann, T.A. Jones and R. Huber, *J. Mol. Biol.*, 1978, **120**, 327.
8. B. Hazes, K.A. Magnus, C. Bonaventura, J. Bonaventura, Z. Dauter, K.H. Kalk and W.G.J. Hol, *Protein Sci.*, 1993, **2**, 597.
9. K.A. Magnus, B. Hazes, H. Ton-That, C. Bonaventura, J. Bonaventura and W.G.J. Hol, *Proteins: Struct. Funct. Genet.*, 1994, **19**, 302.
10. A. Volbeda and W.G.J. Hol, *J. Mol. Biol.*, 1989, **209**, 249.
11. (a) T. Klabunde, C. Eicken, J.C. Sacchettini and B. Krebs, *Nature Struct. Biol.*, 1998, **5**, 293; (b) C. Eichen, B. Krebs and J.C. Sacchettini, *Curr. Opin. Struct. Biol.*, 1999, **9**, 677,
12. R.E. Stenkamp, *Chem. Rev.*, 1994, **94**, 715.
13. P.G. Jene and J.A. Ibers, *Inorg. Chem.*, 2000, **39**, 5796, and references cited therein.
14. J.P. Collman, R.R. Gagné, C.A. Reed, T.R. Halbert, G. Lang and W.T. Robinson, *J. Am. Chem. Soc.*, 1975, **97**, 1427.
15. P. Zanello, R. Cini, A. Cinquantini and P.L. Orioli, *J. Chem. Soc., Dalton Trans.*, 1983, 2159.
16. R. Cini and P. Orioli, *J. Chem. Soc., Dalton Trans.*, 1983, 2563.
17. H. Seyeda and M. Jansen, *J. Chem. Soc., Dalton Trans.*, 1998, 875.
18. J.C. Stevens, P.J. Jackson, W.P. Shammel, G.G. Christoph and D.H. Busch, *J. Am. Chem. Soc.*, 1980, **102**, 3283.
19. N.W. Alcock, W.-K. Lin, C. Cairns, G.A. Pike and D.H. Busch, *J. Am. Chem. Soc.*, 1989, **111**, 6630.
20. M.Y. Chavan, T.J. Meade, D.H. Busch and T. Kuwana, *Inorg. Chem.*, 1986, **25**, 314.
21. D.H. Busch, P.J. Jackson, M. Kojima, P. Chmielewski, N. Matsumoto, J.C. Stevens, W. Wu, D. Nosco, N. Herron, N. Ye, P.R. Warburton, M. Masarwa, G. Christoph and N.W. Alcock, *Inorg. Chem.*, 1994, **33**, 910.
22. D. Ramprasad, A.G. Gilicinski, T.J. Markley and G.P. Pez, *Inorg. Chem.*, 1994, **33**, 2841.
23. P. Barbaro, C. Bianchini, K. Linn, C. Mealli, A. Meli, F. Vizza, F. Laschi and P. Zanello, *Inorg. Chim. Acta*, 1992, **31**, 198–200.
24. C. Bianchini, D. Masi, C. Mealli, A. Meli, G. Martini, F. Laschi, P. Zanello, *Inorg. Chem.*, 1987, **26**, 3683.
25. P. Barbaro, C. Bianchini, F. Laschi, S. Midollini, S. Moneti, G. Scapacci and P. Zanello, *Inorg. Chem.*, 1994, **33**, 3180.

26. T.L. Marxen, B.J. Johnson, P.V. Nilsson and L.H. Pignolet, *Inorg. Chem.*, 1984, **23**, 4663.
27. C.A. Ghilardi, S. Midollini, S. Moneti, A. Orlandini and G. Scapacci, *J. Chem. Soc., Dalton Trans.*, 1992, 3371.
28. J.C. Stevens, P.J. Jackson, W.P. Shammel, G.G. Christoph and D.H. Busch, *J. Am. Chem. Soc.*, 1980, **102**, 3283.
29. N. Kitajima and Y. Moro-oka, *Chem. Rev.*, 1994, **94**, 737.
30. M. Kodera, K. Katayama, Y. Tachi, K. Kano, S. Hirota, S. Fujinami and M. Suzuki, *J. Am. Chem. Soc.*, 1999, **121**, 11006.
31. W.B. Tolman, *Acc. Chem. Res.*, 1997, **30**, 227.
32. H.-C. Liang, K.D. Karlin, R. Dyson, S. Kaderli, B. Jung and A.D. Zuberbühler, *Inorg. Chem.*, 2000, **39**, 5884.
33. K.D. Karlin, Z. Tyeklár, A. Farooq, M.S. Haka, P. Ghosh, R.W. Cruse, Y. Gultneh, J.C. Hayes, P.J. Toscano and J. Zubieta, *Inorg. Chem.*, 1992, **31**, 1436.
34. (a) F.A. Armstrong, P.C. Harrington and R.G. Wilkins, *J. Inorg. Biochem.*, 1983, **18**, 83; (b) J.M. Nocek, D.M. Kurtz, Jr., R.A. Pickering and M.P. Doyle, *J. Biol. Chem.*, 1984, **259**, 12334.
35. J.A.R. Hartman, R.L. Rardin, P. Chaudhuri, K. Pohl, K. Wieghardt, B. Nuber, J. Weiss, G.C. Papaefthymiou, R.B. Frankel and S.J. Lippard, *J. Am. Chem. Soc.*, 1987, **109**, 7387.
36. Y. Hayashi, T. Kayatani, H. Sugimoto, M. Suzuki, K. Inomata, A. Uehara, Y. Mizutani, T. Kitagawa and Y. Maeda, *J. Am. Chem. Soc.*, 1995, **117**, 11220.
37. H. Arii, S. Nagatomo, T. Kitagawa, T. Miwa, K. Jitsukawa, H. Einaga and H. Masuda, *J. Inorg. Biochem.*, 2000, **82**, 153.
38. D. Sellmann, *Angew. Chem. Int. Ed. Engl.*, 1993, **32**, 64.
39. R.R. Eady and G.J. Leigh, *J. Chem. Soc., Dalton Trans.*, 1994, 2739.
40. M.M. Georgiadis, H. Komiya, P. Chakrabarti, D. Woo, J.J. Kornuc and D.C. Rees, *Science*, 1992, **257**, 1653.
41. J. Christiansen, J.M. Chan, L.C. Seefeldt and D.R. Dean, *J. Inorg. Biochem.*, 2000, **80**, 195.
42. (a) J. Kim and D.C. Rees, *Science*, 1992, **257**, 1677; (b) J.W. Peters, M.H.B. Stowell, S.M. Soltis, M.G. Finnegan, M.K. Johnson and D.C. Rees, *Biochemistry*, 1997, **36**, 1181; (c) K.B. Musgrave, H.I. Liu, L. Ma, B.K. Burgess, G. Watt, B. Hedman and K.O. Hodgson, *JBIC*, 1998, 344.
43. F.A. Schultz, S.F. Gheller, B.K. Burgess, S. Lough and W.E. Newton, *J. Am. Chem. Soc.*, 1985, **107**, 5364.
44. F.A. Schultz, B.J. Feldman, S.F. Gheller and W.E. Newton, *Inorg. Chim. Acta*, 1990, **170**, 115.
45. H.-I. Lee, B.J. Hales and B.M. Hoffman, *J. Am. Chem. Soc.*, 1997, **119**, 11395.

46. S.J. Yoo, H.C. Angove, V. Papaefthymiou, B.K. Burgess and E. Münck, *J. Am. Chem. Soc.*, 2000, **122**, 4926.
47. A.D. Allen and C.V. Senoff, *Chem. Commun.*, 1965, 621.
48. F. Bottomley and S.C. Nyburg, *Acta Cryst.*, 1968, **B24**, 1289.
49. J.E. Fergusson, J.L. Love and W.T. Robinson, *Inorg. Chem.*, 1972, **11**, 1662.
50. C.M. Elson, J. Gulens, I.J. Itzkovitch and J.A. Page, *Chem. Commun.*, 1970, 875.
51. B.R. Davis and J.A. Ibers, *Inorg. Chem.*, 1971, **10**, 578.
52. J. Chatt, C.M. Elson, N.E. Hooper and G.J. Leigh, *J. Chem. Soc., Dalton Trans.*, 1975, 2392.
53. R.M. Chin, J. Barrera, R.H. Dubois, L.E. Helberg, M. Sabat, T.Y. Bartucz, A.J. Lough, R.H. Morris and W.D. Harman, *Inorg. Chem.*, 1997, **36**, 3553.
54. R.H. Morris, *Inorg. Chem.*, 1992, **31**, 1471.
55. A. Hills, D.L. Hughes, M. Jimenez-Tenorio, G.J. Leigh and A.T. Rowley, *J. Chem. Soc., Dalton Trans.*, 1993, 3041.
56. I.M. Treitel, M.T. Flood, R.E. Marsh and H.B. Gray, *J. Am. Chem. Soc.*, 1969, **91**, 6512.
57. K.D. Demadis, T.J. Meyer and P.S. White, *Inorg. Chem.*, 1997, **36**, 5678.
58. T.B. Gunnoe, M. Sabat and W.D. Harman, *J. Am. Chem. Soc.*, 1998, **120**, 8747.
59. R. Ferguson, E. Solari, C. Floriani, D. Osella, M. Ravera, N. Re, A. Chiesi-Villa and C. Rizzoli, *J. Am. Chem. Soc.*, 1997, **119**, 10104.
60. J.-I. Song, P. Berno and S. Gambarotta, *J. Am. Chem. Soc.*, 1994, **116**, 6927.
61. M.B. O'Regan, A.H. Liu, W.C. Finch, R.R. Schrock and W.M. Davis, *J. Am. Chem. Soc.*, 1990, **112**, 4331.
62. J.M. Smith, R.J. Lachicotte, K.A. Pittard, T.R. Cundari, G. Lukat-Rodgers, K.R. Rodgers and P.L. Holland, *J. Am. Chem. Soc.*, 2001, **123**, 9222.
63. T. Uchida, Y. Uchida, M. Hidai and T. Kodama, *Acta Cryst.*, 1975, **B31**, 1197.
64. T.A. George and C.D. Seibold, *Inorg. Chem.*, 1973, **12**, 2548.
65. C.M. Elson, *Inorg. Chim. Acta*, 1976, **18**, 209.
66. G.J. Leigh and C.J. Pickett, *J. Chem. Soc., Dalton Trans.*, 1977, 1797.
67. N.J. Lazarowych, R.H. Morris and J.M. Ressner, *Inorg. Chem.*, 1986, **25**, 3926.
68. T. Yoshida, T. Adachi, M. Kaminaka and T. Ueda, *J. Am. Chem. Soc.*, 1988, **110**, 4872.
69. T.A. George, J.R.D. DeBord, B.B. Kaul, C.J. Pickett and D.J. Rose, *Inorg. Chem.*, 1992, **31**, 1295.
70. T.A. George, R.K. Hayes, M.Y. Mohammed and C.J. Pickett, *Inorg. Chem.*, 1989, **28**, 3269.

71. D.M. Heinekey and W.J. Oldham, Jr., *Chem. Rev.*, 1993, **93**, 913.
72. M.W.W. Adams, *Biochim. Biophys. Acta*, 1990, **1020**, 115.
73. M.W.W. Adams, L.E. Mortenson and J.-S. Chen, *Biochim. Biophys. Acta*, 1981, **594**, 105.
74. A. Volbeda, M.-H. Charon, C. Piras, E.C. Hatchikian, M. Frey and J.C. Fontecilla-Camps, *Nature*, 1995, **373**, 580.
75. A. Volbeda, M.-H. Charon, C. Piras, E.C. Hatchikian, M. Frey and J.C. Fontecilla-Camps, *J. Inorg. Biochem.*, 1995, **59**, 637.
76. Y. Nicolet, A.L. de Lacey, X. Vernède, V.M. Fernandez, E.C. Hatchikian and J.C. Fontecilla-Camps, *J. Am. Chem. Soc.*, 2001, **123**, 1596.
77. R.H. Crabtree, *Inorg. Chim. Acta*, 1986, **125**, L7.
78. G. Jia, W.S. Ng, H.S. Chu, W.-T. Wong, N.-T. Yu and I.D. Williams, *Organometallics*, 1999, **18**, 3597, and references therein.
79. (a) Z.-W. Li and H. Taube, *Science*, 1992, **256**, 210; (b) P. Yang, X.-L. Meng, L.-J. Yue and Y.B. Wei, *J. Inorg. Biochem.*, 2002, **89**, 248.
80. G.J. Kubas, R.R. Ryan, B.I. Swanson, P.J. Vergamini and H.J. Wasserman, *J. Am. Chem. Soc.*, 1984, **106**, 451.
81. P. Zanello, *Comments Inorg. Chem.*, 1991, **11**, 339.
82. L. Brammer, J.A.K. Howard, O. Johnson, T.F. Koetzle, J.L. Spencer and A.M. Stringer, *J. Chem. Soc., Chem. Commun.*, 1991, 241.
83. C. Bianchini, F. Laschi, M. Peruzzini, F.M. Ottaviani, A. Vacca and P. Zanello, *Inorg. Chem.*, 1990, **29**, 3394.
84. J.S. Ricci, T.F. Koetzle, M.T. Bautista, T.M. Hofstede, R.H. Morris and J.F. Sawyer, *J. Am. Chem. Soc.*, 1989, **111**, 8823.
85. M.T. Bautista, E.P. Cappellani, S.D. Drouin, R.H. Morris, C.T. Schweitzer, A. Sella and J. Zubkowski, *J. Am. Chem. Soc.*, 1991, **113**, 4876.
86. D.H. Farrar, P.A. Maltby and R.H. Morris, *Acta Cryst.*, 1992, **C48**, 28.
87. P.A. Maltby, M. Schlaf, M. Steinbeck, A.J. Lough, R.H. Morris, W.T. Klooster, T.F. Koetzle and R.C. Srivastava, *J. Am. Chem. Soc.*, 1996, **118**, 5396.
88. M.A. Esteruelas, C. Garcia-Yebra, M. Oliván, E. Oñate and M.A. Tajada, *Organometallics*, 2002, **21**, 1311, and references therein.
89. A. Cotton and R.L. Luck, *J. Chem. Soc., Chem. Commun.*, 1988, 1277.
90. A. Cotton and R.L. Luck, *Inorg. Chem.*, 1989, **28**, 2181.
91. C.A. Bayse, R.L. Luck and E.J. Schelter, *Inorg. Chem.*, 2001, **40**, 3463.

CHAPTER 10

Superconductors in Electrochemistry

In electrochemical terms, one of the expected employment of ‘superconductors’ is as electrode materials. However, before considering the eventual benefits offered to electrochemistry by such materials we must introduce the physical, physico-chemical and structural properties of superconductors.¹

1 GENERAL ASPECTS OF SUPERCONDUCTIVITY

The phenomenon of superconductivity was discovered at the beginning of the twentieth century by the Dutch physicist H. Kamerlingh Onnes, during the first attempts to liquefy helium (which at atmospheric pressure boils at 4.2 K). After refining the technique of helium liquefaction, in 1911, Onnes attempted to measure the electrical resistance of metals at these extraordinary low temperatures, and realized that at 4 K the resistance of mercury, as well as that of other metals indicated in Figure 1, became too low to be measured. This change in electrical property became the indication of the new superconductive physical state. The temperature below which materials become superconducting is defined as the *critical temperature*, T_c .

Twenty years later, in 1933, the German physicist Walter Meissner (together with his co-worker Robert Ochsenfeld) discovered that superconductors cannot be crossed by magnetic field lines. This property is today defined as the *Meissner effect*.

In the years that followed, attempts were made to exploit the technological potential of the two properties of superconductivity:

- the absence of electrical resistance
- an absolute diamagnetism

Figure 1 The elements of the Periodic Table which behave as superconductors at atmospheric pressure and at temperatures lower than 10 K

Unfortunately, there were two practical problems severely hindering possible applications:

- the achievement of the superconducting state is dependent on being able to reach very low temperatures
 - the superconducting state disappears when an external magnetic field is applied (even quite weak, as that generated by the passage of low electrical currents).

To overcome these practical problems, research aimed at the preparation of new materials exhibiting superconductivity at higher and higher temperatures and able to sustain this state even in the presence of strong magnetic fields (or, also in the presence of high electric currents).

The first objective was that of achieving critical temperatures higher than 77 K (-196°C). In this way liquid nitrogen (boiling point 77 K) could be used as the cryogenic liquid instead of the much more expensive and difficult to handle liquid helium.

Some positive steps were made in this direction through the use of niobium-based alloys. In 1973 the alloy Nb₃Ge was found to have a $T_c = 23$ K, which remained the highest attainable critical temperature until 1986. In 1986 two IBM scientists in Zurich, the German, Johannes Georg Bednorz and the Swiss, Karl Alex Müller found that a ceramic oxide based on lanthanum, barium and copper (of stoichiometry

$\text{La}_{1.85}\text{Ba}_{0.15}\text{CuO}_4$) lost its resistance at a $T_c = 30\text{--}35\text{ K}$. The observation of superconductivity in a ‘metal oxide’ at temperatures higher than those of metals themselves triggered a change in emphasis in superconductivity research towards this type of material. In 1987 two research groups, at the University of Houston and the University of Alabama, reported that the oxide of formula $\text{YBa}_2\text{Cu}_3\text{O}_{7-x}$ (commonly known as ‘1-2-3 superconductor’, from the stoichiometric ratios Y:Ba:Cu of 1:2:3) displayed a T_c of 92 K.

The great interest aroused by these new materials was also due to their easy preparation. In fact, ‘ceramics’ are inorganic materials that can be mixed and worked into the desired form at room temperature. The successive baking at high temperature renders them stable in the pre-moulded form both by agglomeration (sintering) of the crystallites and by partial fusion of the mix of raw materials. The use of these mixed ceramic oxides means that superconductivity at liquid nitrogen temperatures is no longer a problem. For example, the compound $\text{HgBa}_2\text{Ca}_2\text{Cu}_3\text{O}_{8+x}$ has a $T_c = 150\text{ K}$.

While attempts are still being made to find materials which exhibit superconductivity at temperatures as close as possible to room temperature, the main thrust of research is now directed towards superconducting materials that can withstand high current densities and are malleable and ductile (*i.e.* able to be prepared as thin sheets or wire).

1.1 Physical Properties of Superconductors

1.1.1 The Loss of Electrical Resistance. As mentioned previously, a superconductor displays an abrupt change in resistivity when it is cooled below the critical temperature.

As schematized in Figure 2, the decrease in resistance of a conductor with temperature is a general law of physics. The vibrations of the metal

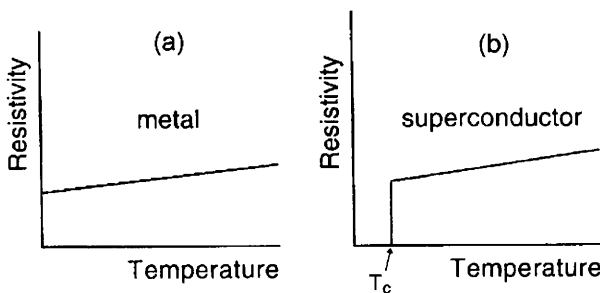


Figure 2 Comparison between the change in resistivity with temperature for a metal (a) and a superconductor (b)

atoms diminish as the temperature falls. The vibrations of the atoms favour, in fact, collisions with electrons which consequently oppose an ordered electron flow in a material subjected to a difference of electrical potential.

However, in the case of a superconductor, below the critical temperature the resistivity abruptly becomes zero. This means that a current can flow indefinitely through the material.

1.1.2 The Meissner Effect and Levitation. Besides the absence of electrical resistance, a superconducting material is characterized by perfect *diamagnetism*. The exclusion of magnetic field lines from a material when it passes from a normal state to a *superconducting* state is shown schematically in Figure 3.

Superconductors which follow this behaviour completely are classified as 'Type I'. The first superconductors to be discovered belong to this category.

Such a description is, however, only partially correct for 'Type II', which include the *1-2-3 superconductors*. In this case, the magnetic field lines arising from low intensity magnetic fields are completely excluded, but with the increasing of the magnetic field a greater and greater number of field lines penetrate the material (following a spiralling path), until at high magnetic field the material loses its superconducting characteristics.

The so-called phenomenon of *levitation* of a magnet placed above a superconductor, Figure 4, is a direct consequence of the Meissner effect.

In order to understand how the Meissner effect leads to levitation we must recall the principles of electromagnetism.

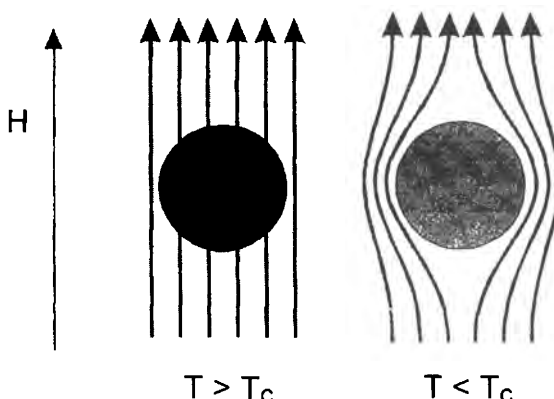


Figure 3 *The Meissner effect. A superconductor (here in a circular section) excludes the magnetic field lines when it is frozen below the critical temperature*

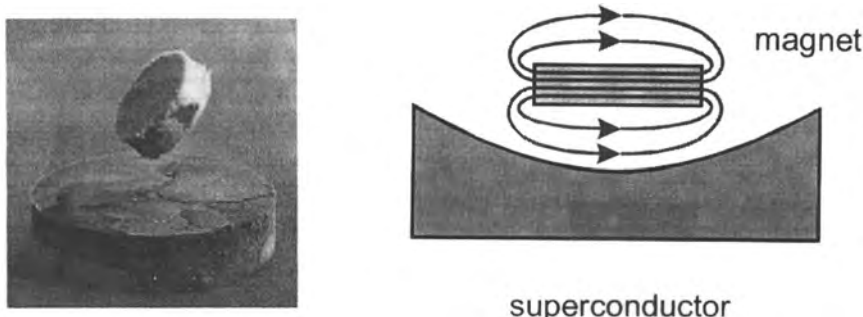


Figure 4 The levitation of a magnet placed above a small platelet of $\text{YBa}_2\text{Cu}_3\text{O}_{7-\chi}$ immersed in a liquid nitrogen bath

The generation of a magnetic field by an electric current is easily observed by placing a compass above a wire through which an electric current is flowing, Figure 5.

On this well-known effect is based the construction of modern electromagnets, which have found application in the NMR spectrometers (in particular in spectrometers used in the application of magnetic resonance in medicine). The strong magnetic field produced by a high current density flowing in superconducting materials remains indefinitely. Once installed, a current in a superconducting magnet can continue to flow for years, providing the circuit is always kept below T_c .

The opposite question of how a magnetic field generates a current in a conductor is related to the foregoing discussion and is also of some interest to us. The first observation at the beginning of the century

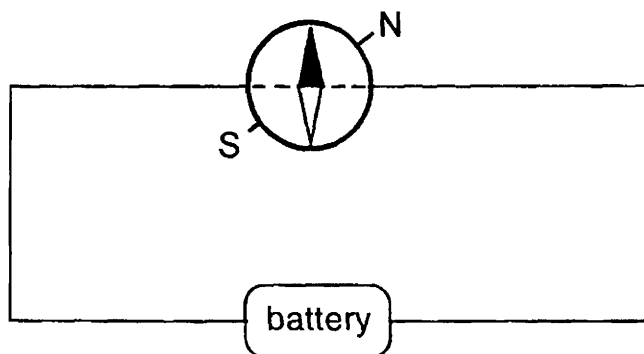


Figure 5 The needle of a compass placed upon a wire crossed by an electric current deviates from its natural N/S position arranged perpendicularly to the wire

showed that when a magnet is moved constantly inside a solenoid a current is produced in the electrical circuit, Figure 6.

In fact, many large-scale electrical generators are presently based on this principle.

The coupling of the two effects described above is responsible for the phenomenon of levitation discussed previously. This can be understood if one considers that when a magnet (or a magnetic field) approaches the superconductor a ‘supercurrent’ is generated in it. This current (which does not meet resistance in the superconductor) in turn generates a magnetic field opposite to that possessed by the magnet; this generates repulsion.

The magnetic field induced by the current cancels the magnetic field induced in the superconductor by the magnet. This is the origin of the perfect diamagnetism of Type I superconductors.

Levitation in Type I superconductors is, however, a rather ephemeral effect. The absence of restraints on the lateral motion of the magnet eventually result in the magnet falling at the side of the superconductor.

Conversely, in Type II superconductors (that are penetrated by spiralling magnetic field lines), levitation is completely stable. In fact, the magnetic field lines of the magnet, which enter the superconductor following a well-defined spiral geometry, oppose the motion of the magnet confining it to a certain position.

1.1.3 The Mechanism of Superconductivity. A satisfactory theory of superconductivity was proposed in 1957 by the American physicists John

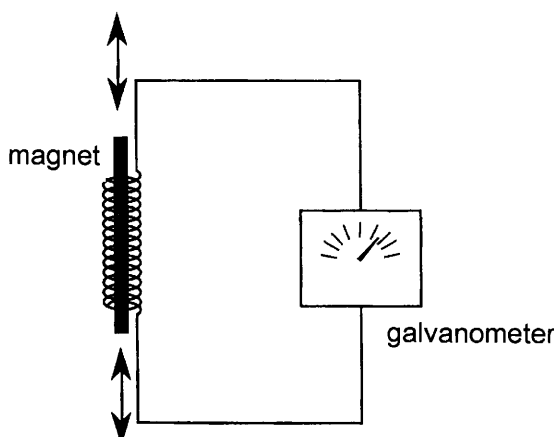


Figure 6 The periodical movement of a magnet inside a conductive solenoid generates an electrical current

Bardeen, Leon Cooper and John Robert Schrieffer, which, from their initials, was called *BCS theory*.

The fundamental concept of the theory appears at first sight paradoxical: electrons in the superconductor are mutually attracted forming so-called 'Cooper electron pairs'.

In fact, this attraction between negative charges (that violates the principles of electrostatics) is mediated by the crystal structure of the superconductor. In every metal lattice there is a reciprocal stripping of valence electrons between metal sites which results in these metal sites, fixed at lattice positions, assuming a positive charge. As shown in Figure 7, when a moving electron crosses these positive metal sites the metal ions are attracted towards the electron trajectory and disturbed from its equilibrium position.

As the positive metal ions are heavier than the electron that caused the displacement, they return to their original positions fairly slowly. The relatively long time taken to re-establish the original positions allows the displaced metal ions to attract a second electron, which, given the proximity of the just passed first electron, leads to the formation of a *Cooper pair*.

It is important to bear in mind that the pairing of the electrons results in a coupling of their spins. Consequently, an energy transfer mechanism between the electrons which collide with the vibrating atoms of the crystal (responsible for the electrical resistance) is absent. Temperature is a major factor in destroying the coupling between electrons inside the Cooper pairs and, hence, the existence of a critical temperature can be immediately anticipated. Analogously, application of strong magnetic fields (and the corresponding induced currents) can provide sufficiently

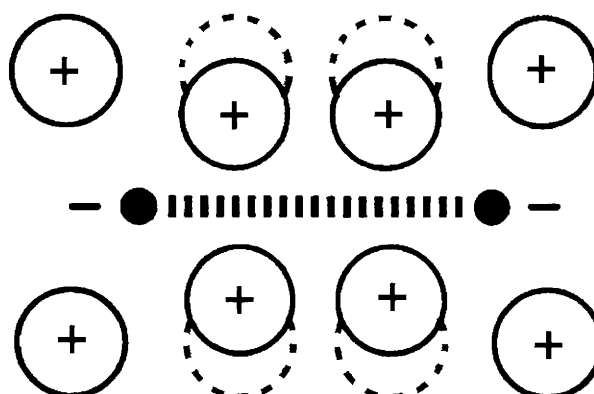


Figure 7 The coupling of electrons as Cooper pairs

high energy levels to destroy the Cooper pairs and, therefore, the superconductivity.

1.2 Chemical Properties of High T_C Superconductors

1.2.1 Synthesis and Oxidation States of 1-2-3 Superconductors. The preparation of platelets of YBa₂Cu₃O_{7-x} ($x \approx 0.1$) is relatively simple. The typical preparation involves the following steps. A mixture of Y₂O₃, BaCO₃ and CuO, according to a rough proportion of 1:2:3 in Y, Ba, Cu, is ground, then heated at 950°C for 10–12 h. During this phase the crystal structure takes shape by mutual migration of the ions, but the composition YBa₂Cu₃O_{7-x} lacks oxygen ($x \approx 0.5$). The material is then cooled to about 500°C in the presence of air for another 10–12 h. The reaction with oxygen has the effect of reducing the oxygen deficit to $x \approx 0.1$.

The non-stoichiometric amount of oxygen is a clear indication of lattice defects.

Assigning oxidation states of –2 to oxygen, +3 to yttrium and +2 to barium, one would obtain an oxidation state 7/3 for copper when $x=0$. The non-integer oxidation state of copper is interpreted as if 2/3 of the ions are present as Cu²⁺ and 1/3 as Cu³⁺. This ‘mixed-valent’ composition seems to be determinant for the occurrence of superconductivity. In fact, as noted in Table 1, all the superconducting ceramic oxides contain Cu in a non-stoichiometric composition.

It is noted that, as previously mentioned, there is a rapidly growing interest in the superconductivity of inorganic fullerene compounds.

Table 1 Superconducting materials

Species	T _c (K)
Bi ₂ Sr ₂ CuO ₆	9
La _{2-x} Sr _x CuO ₄	38
Bi ₂ (Sr,Ca) ₂ CuO ₆	80
Bi ₂ Sr _{2.7} Ln _{0.3} Cu ₂ O ₈ ^a	80
Bi ₂ Ca ₃ Sr ₂ Cu ₄ O ₁₀	90
YBa ₂ Cu ₃ O _{7-x}	95
Bi ₂ Ca ₂ Sr ₂ Cu ₃ O ₁₀	110
Tl ₂ Ba ₂ Ca ₂ Cu ₃ O ₁₀	125
Hg ₂ Ba ₂ Ca ₂ Cu ₃ O ₈	150
K ₃ C ₆₀	18
K ₂ RbC ₆₀	22
KRb ₂ C ₆₀	24
Rb ₃ C ₆₀	29

^a Ln = lanthanides.

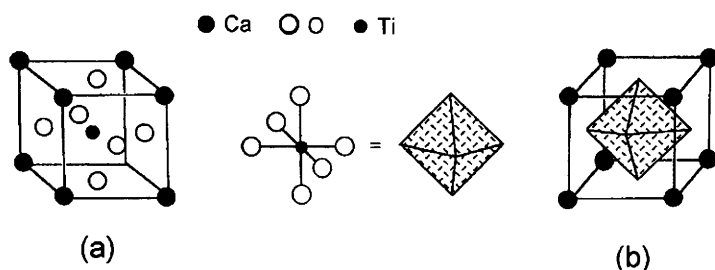


Figure 8 The elementary cell of the perovskite CaTiO_3 . (a) Common representation; (b) stereoscopic representation

1.2.2 Molecular Structure of 1-2-3 Superconductors. X-ray diffraction studies have established that 1-2-3 superconductors have a crystal structure similar to that of *perovskites*. These latter compounds typically have a ratio of two metal atoms per three oxygen atoms. Some examples are: CaTiO_3 , NaNbO_3 and LaAlO_3 . It is evident that the sum of oxidation states of the metal must be + 6, in order to balance the charge of -6 of the three oxygen atoms. As an example, Figure 8 shows the molecular structure of CaTiO_3 .

The larger Ca^{2+} ions are positioned at the corners of the cube, whereas the smaller Ti^{4+} ions are at the centre of the cube and bound to the six O^{2-} ions forming a TiO_6 group of octahedral geometry.

Another way of representing the perovskite structure is to move the origin of the coordination axes such that the Ca^{2+} ions are now at the centre of the cubic cell, Figure 9. The latter representation allows a better understanding of the structure of a superconductor such as $\text{YBa}_2\text{Cu}_3\text{O}_{7-x}$ ($x \leq 0.1$).

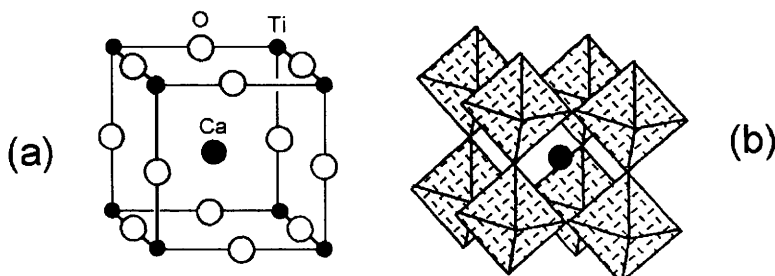


Figure 9 A second way to represent the molecular structure of CaTiO_3 . (a) Common representation; (b) stereoscopic representation. Symbols as in Figure 8

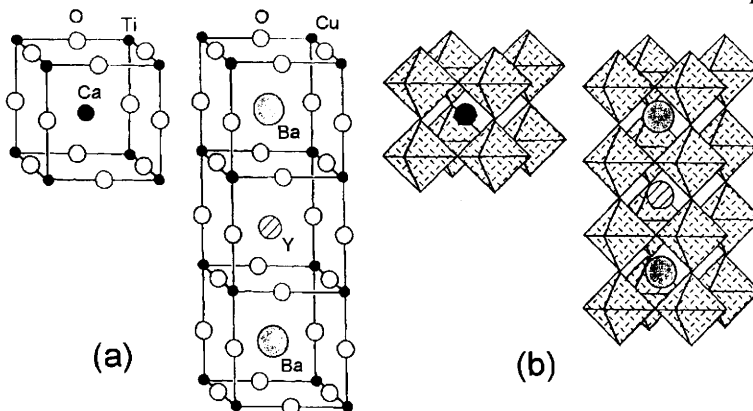


Figure 10 The first stage in the building of the molecular structure of the superconductor $\text{YBa}_2\text{Cu}_3\text{O}_{7-x}$ starting from CaTiO_3 perovskite units. The formation of $\text{YBa}_2\text{Cu}_3\text{O}_9$. (a) Common representation; (b) stereoscopic representation

In Figure 10 one begins with the structure of the perovskite and builds that of the superconductor by forming a chain of three cells, then the Ca^{2+} ion is substituted with Ba^{2+} in the first and third cell and with a Y^{3+} ion in the second cell. In addition, the Ti^{4+} ions are replaced by Cu ions forming CuO_6 octahedra. In this way one would generate the $\text{YBa}_2\text{Cu}_3\text{O}_9$ species.

The successive removal of 8 oxygen atoms placed on the edges of the cube (therefore, $8 \times 1/4 = 2$ lattice oxygen atoms) leads to the idealized structure of $\text{YBa}_2\text{Cu}_3\text{O}_7$, Figure 11.

In effect, the Y^{3+} ion loses 4 of the 12O^{2-} ions which surround it in $\text{YBa}_2\text{Cu}_3\text{O}_9$. Another 4 O^{2-} ions are lost from the bottom and top faces of the cell. These oxygen lattice ‘vacancies’ are linked to the oxidation state of the copper, in that if one decreases the oxygen content, the Cu oxidation state also decreases. In fact, since the solid must be electrically neutral, every O^{2-} ion loss must be compensated by the reduction of two Cu^{3+} ions to two Cu^{2+} ions. As can be inferred, the oxygen vacancies create sheets and chains of Cu atoms bound by oxygen bridges that play an important role in superconductivity. Moreover, this arrangement means that the physical properties of these materials, including superconductivity, are anisotropic.

2 ELECTROCHEMICAL ASPECTS OF SUPERCONDUCTORS

The recent discovery of high T_c superconductors means that applications of electrochemistry in this field are still in the initial phases

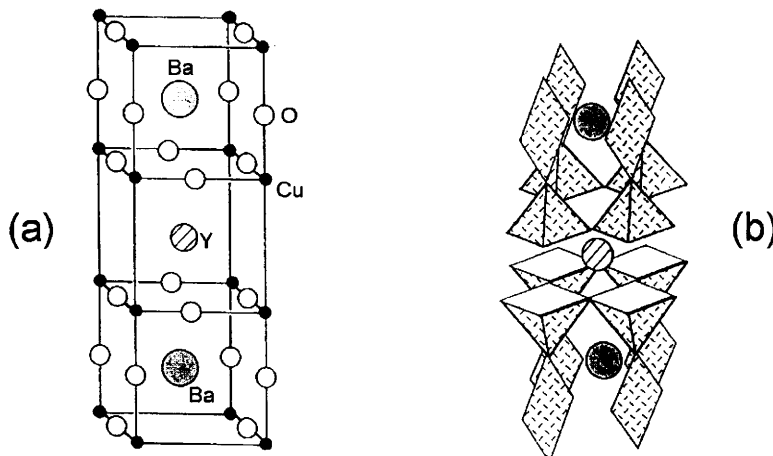


Figure 11 The second stage in the building of the molecular structure of $\text{YBa}_2\text{Cu}_3\text{O}_7$ through the removal of two oxygen atoms from $\text{YBa}_2\text{Cu}_3\text{O}_9$. (a) Common representation; (b) stereoscopic representation

of development.² Unfortunately, not only the electromagnetic properties, but also the chemical properties of the last generation superconductors (*i.e.* the copper-based ceramic oxides) make their potential applications difficult. In fact, such materials undergo chemical degradation when exposed to water, acids and carbon oxides (CO, CO₂). However, it appears that electrochemical studies of copper-based superconductors may lead to a better understanding of the essential role played by their 'mixed-valent' Cu²⁺/Cu³⁺ composition. In addition, efforts are being performed to improve the resistance of superconductors to corrosion by coating their surface with proper adsorbate molecules.³

2.1 The Preparation and Use of Electrodes of Superconducting Materials

Before studying the properties of superconductors one must have efficient 'electrodes' of these materials available. However, their fragile, porous and chemically non-inert nature makes them unsuitable in principle for use as electrodes.

Figure 12 shows a number of geometric arrangements which are used in the construction of electrodes from ceramic superconductors.

In all cases the superconducting material is inserted on an inert support (usually an epoxy resin) and the electrode surface is frequently renewed by mechanical cleaning.

The use of this type of electrode at room temperature is strongly dependent on the choice of solvent. In an aqueous medium the ceramic

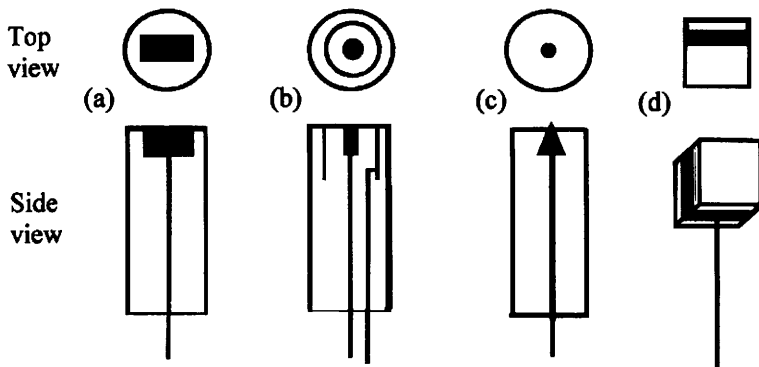


Figure 12 Schematic representation of the geometrical arrangements of electrodes of superconducting material, in the form of: (a) a small block; (b) a cylinder; (c) a micro-disk; (d) a thin film

superconductors degrade. For example, given that yttrium and barium have only a single oxidation state, the response of 1-2-3 $\text{YBa}_2\text{Cu}_3\text{O}_{7-x}$ is determined by the redox activity of Cu^{2+} ions (Cu^{3+} ion is strongly oxidising and is never observed; see the next section). Conversely, in non-aqueous solvents the ceramic superconductor (taking the proper precautions of mechanical cleaning) behaves as an inert electrode. For example, Figure 13 compares the cathodic response exhibited by tetracyanoquinodimethane (tcnq) (which undergoes the two successive one-electron sequence $[\text{tcnq}]^{0/-1/2-}$) at a platinum electrode (Figure 13a) with those obtained at different ceramic oxide materials (Figure 13b–f).

2.2 Study of the Corrosion of Ceramic Superconductors

The high reactivity of copper superconductors is a large obstacle to their practical application. Many spectroscopic studies have been devised to investigate the surface chemistry of these materials, but electrochemical investigations can also be important.

In particular, the use of hydrodynamic techniques (for example employing rotating disk and ring electrodes; see Figure 12b) has provided information on the stoichiometry of the degradation products of $\text{YBa}_2\text{Cu}_3\text{O}_{7-x}$. The use of HCl solutions in the concentration range from 10^{-3} M to 10^{-1} M (containing 1 M NaCl as supporting electrolyte) gives quantities of Y^{3+} , Ba^{2+} and Cu^{2+} in the ratio 1:2:3 typical of the original electrode material. In this pH

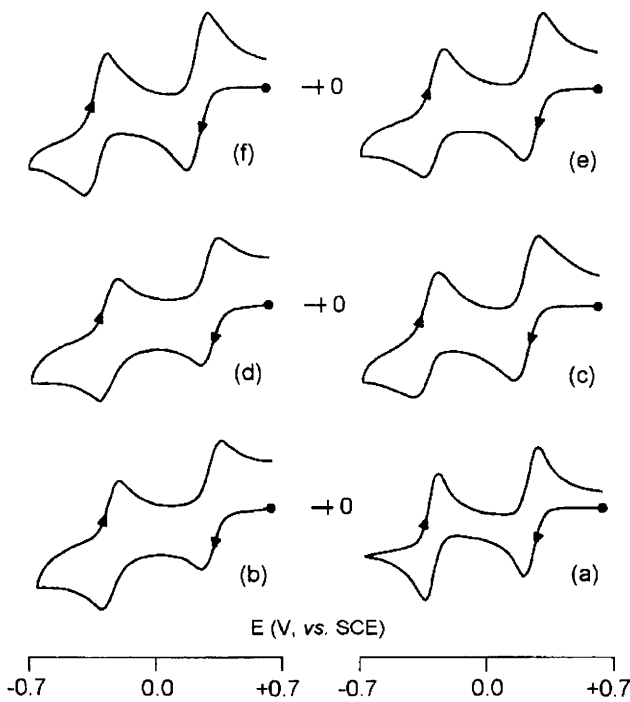
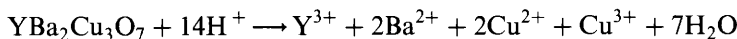
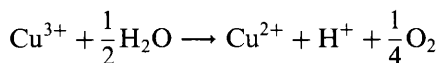


Figure 13 Cyclic voltammetric responses recorded in MeCN solutions of tcnq using the following electrode materials: (a) platinum; (b) $\text{YBa}_2\text{Cu}_3\text{O}_{7-\text{x}}$; (c) $\text{La}_{1.85}\text{Sr}_{0.15}\text{CuO}_4$; (d) $\text{La}_{1.5}\text{Ba}_{1.5}\text{Ce}_{0.15}\text{CuO}_{7.18}$; (e) $\text{Tl}_{1.5}\text{Ba}_2\text{CuO}_{5.37}$; (f) $\text{Nd}_{1.85}\text{Ce}_{0.15}\text{CuO}_4$. Scan rate 0.1 V s^{-1} . $[\text{NEt}_4][\text{BF}_4]$ (0.1 mol dm^{-3}) supporting electrolyte

range, the rate of corrosion is proportional to the concentration of H^+ ions and follows the reaction:



The presence of Cu^{3+} ions has not been directly verified, but one can infer from the observed generation of gaseous oxygen that the following reaction takes place:



Another method used to study the reactivity of ceramic superconductors is to compare the cyclic voltammetric response of a reversible redox couple (in the present case $[\text{tcnq}]^{0/-}$) at a superconductor electrode with and without corrosion. As illustrated in Figure 14, in principle, in

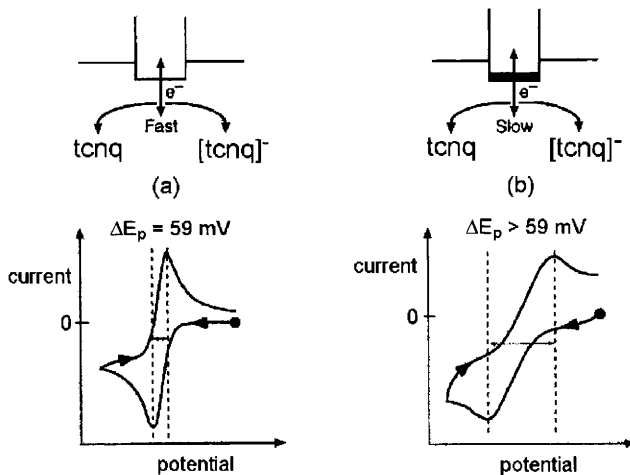
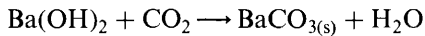
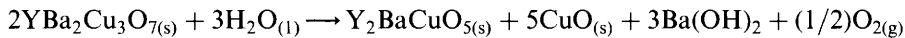


Figure 14 Cyclic voltammetric responses for a reversible one-electron process expected at: (a) a perfectly clean electrode surface; (b) an electrode surface covered by a passivating layer

the absence of corrosion the peak-to-peak separation of the reduction process would be fairly close to the theoretical value of 59 mV (Figure 14a), whereas if a thin insulating layer is deposited on the electrode surface as a consequence of corrosion, there would be a marked deviation of the peak-to-peak separation from this value.

Given that in aqueous solution $\text{YBa}_2\text{Cu}_3\text{O}_{7-x}$ undergoes the following reactions:



it is evident that, in the presence of water, the $\text{YBa}_2\text{Cu}_3\text{O}_{7-x}$ electrode would become covered by an insulating material which should alter its electrochemical response.

On this basis the cyclic voltammetric responses of the $[\text{tcnq}]^{0/-}$ process using superconducting electrodes have been studied in acetonitrile–water mixtures. Figure 15 shows the results obtained, at room temperature, at a $\text{YBa}_2\text{Cu}_3\text{O}_{7-x}$ electrode, also in comparison with the analogous responses obtained at a platinum electrode.

As can be seen, whereas the platinum electrode does not suffer significant effects from the addition of water, in the case of the $\text{YBa}_2\text{Cu}_3\text{O}_{7-x}$ electrode the greater the water content the greater the peak-to-peak separation. These results are in agreement with the decomposition reactions described

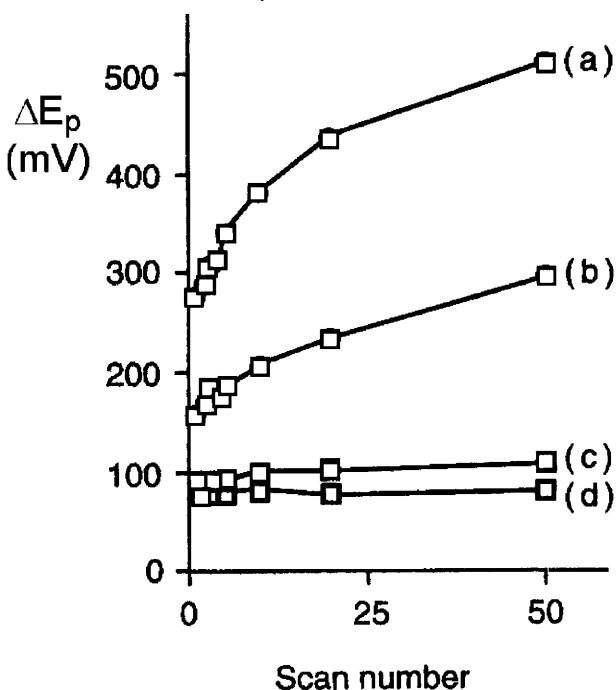


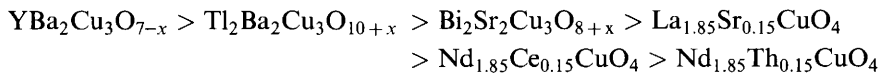
Figure 15 Peak-to-peak (ΔE_p) separations as a function of the number of reduction/reoxidation cycles recorded in a MeCN solution of tcnq ($[NBu_4][BF_4]$ 0.1 mol dm $^{-3}$) at a $YBa_2Cu_3O_{7-x}$ electrode: (a) after the addition of 250 mM H_2O ; (b) after the addition of 10 mM H_2O ; (c) without addition of H_2O . (d) Platinum electrode after the addition of 250 mM H_2O . Scan rate 0.1 V s $^{-1}$

above, which cause deposition of insulating materials on the electrode surface.

The same type of experiment has been carried out on electrodes of different superconducting materials. As deducible from Figure 16, not all of these ceramic materials undergo severe degradation in the presence of water.

The most serious corrosion effects are found for the $YBa_2Cu_3O_{7-x}$ electrode, whereas an intermediate effect is observed for $La_{1.85}Sr_{0.15}CuO_4$ and corrosion is negligible for the $Nd_{1.85}Ce_{0.15}CuO_4$ electrode.

This type of experiment has demonstrated that the surface reactivity of copper superconductors follows the order:



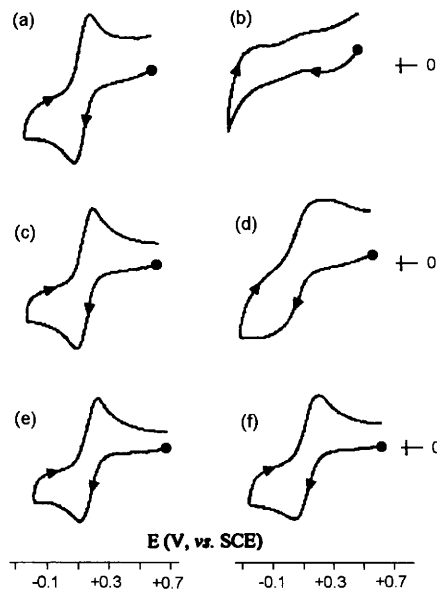


Figure 16 Cyclic voltammetric responses recorded in MeCN solutions of *tcnq* ($[NBu_4][BF_4]$ 0.1 mol dm^{-3}) without (a,c,e) and with the addition of 4.5% H_2O (b,d,f). (a,b) $YBa_2Cu_3O_{7-x}$ electrode; (c,d) $La_{1.85}Sr_{0.15}CuO_4$ electrode; (e,f) $Nd_{1.85}Ce_{0.15}CuO_4$ electrode. Scan rate 0.1 V s^{-1}

2.3 Electrochemical Synthesis of Superconductors

A potential alternative method to chemical synthesis of superconducting materials is offered by electrochemistry, particularly in view of the possibility that one has to achieve reproducible conditions.

For example, an electrodeposition method has been reported for a Tl-Ba-Ca-Cu-O based superconductor from dmso solutions containing Tl^+ , Ba^{2+} , Ca^{2+} and Cu^{2+} salts of empirically adjustable composition. The surface of the working electrode was formed by a sheet of $SrTiO_3$ (or MgO) on which a very thin layer ($\approx 500 \text{ \AA}$) of metallic silver had previously been deposited. Application of a potential of -4 V (with respect to the $Ag/AgNO_3$ reference electrode) led to the electrodeposition as metals of all the ions present in solution. This system, composed of a Tl-Ba-Ca-Cu film supported on a conducting material, was removed from the electrode and heated at $850\text{--}900^\circ\text{C}$ in order to allow crystallization and oxygenation to occur and so obtain the superconducting material. This material exhibited a T_c above 100 K, but more striking was its ability to support current densities of $5.6 \times 10^8 \text{ A m}^{-2}$ at 76 K, in the absence of a magnetic field, and of $2.0 \times 10^8 \text{ A m}^{-2}$

at 76 K in the presence of a magnetic field of 1 T. To date, from a technological viewpoint, these characteristics are amongst the best obtainable.

2.4 Electrochemistry Using Electrodes of Superconducting Materials at Temperatures Below T_c

Electrochemical studies of redox systems in solution using superconducting electrodes at temperatures below the critical temperature are still very much in their infancy.

The first necessity of such a study is the availability of an electrolytic solution able to remain liquid at the low temperatures corresponding to T_c . Figure 17 gives a general picture of the various possibilities presently available.

At this point the first investigations on electron transfer phenomena could be carried out, using electrodes able to become superconducting at sufficiently low temperature.

One of these studies, which requires sophisticated apparatus, involved the ferrocene/ferrocenium oxidation process.^{4,5} Figure 18 compares the response obtained with platinum and superconducting electrodes in the temperature range of the T_c .

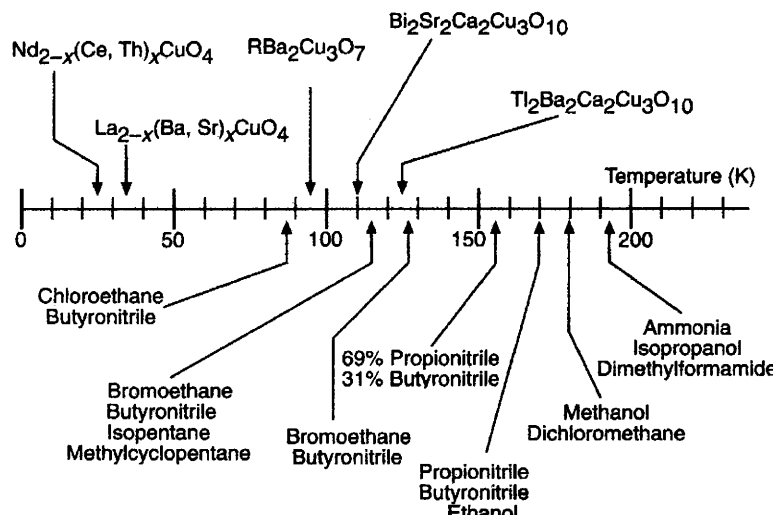


Figure 17 The temperature limits of a few electrolytic solutions in comparison with the critical temperatures of a few superconductors

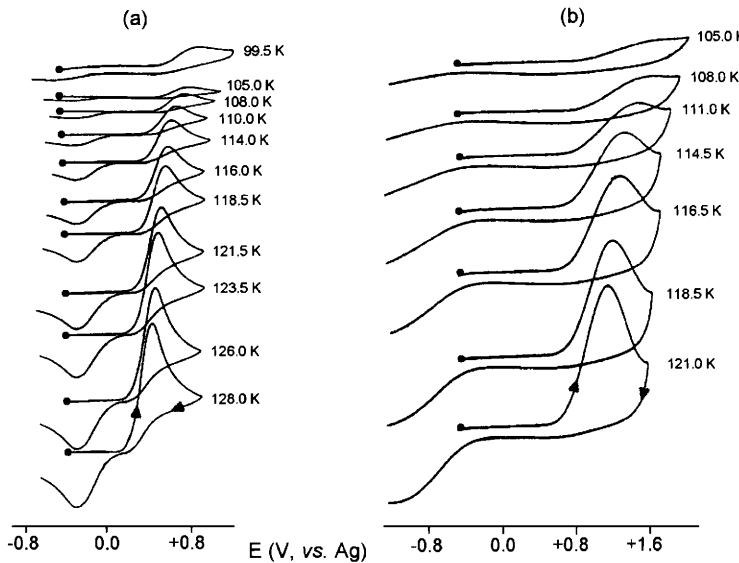


Figure 18 Cyclic voltammetric responses at different temperatures of ferrocene in a 16:17:1 chloroethane:tetrahydrofuran:2-methyl-tetrahydrofuran solution containing LiBF_4 (0.6 mol dm^{-3}) as supporting electrolyte. (a) Platinum electrode; (b) Tl 1223 ($\{\text{Tl}_{0.5}\text{Pb}_{0.5}\}\text{Sr}_2\text{Ca}_2\text{Cu}_3\text{O}_6$). Scan rate 0.025 V s^{-1} . Potential values are referred to a pseudo-reference silver wire

It is clear that the decrease of the rate of the electron transfer operated by the temperature makes the oxidation of ferrocene become quasi-reversible for both the electrode materials. Moreover, it is noted that for both types of electrode the faradaic current increases with temperature. For both the electrodes the oxidation process is governed by diffusion, since in both cases the plot of $\log(i_p)$ vs. $1/T$ is linear. Furthermore, one should note in particular that, contrary to the naive expectation, for the superconducting electrode one does not observe any abrupt change in the response upon crossing the barrier from ‘superconductor’ (that should exchange pairs of electrons) to simple ‘conductor’ (that should exchange single electrons).

REFERENCES

- (a) A.B. Ellis, M.J. Geselbracht, B.J. Johnson, G.C. Lisensky and W.R. Robinson, *Teaching General Chemistry*, American Chemical Society, Washington, DC, 1993 Chapter 9; (b) A. Simon, *Angew. Chem. Int. Ed. Engl.*, 1997, **36**, 1788–1806.
- J.T. McDewitt, D.R. Riley and S.G. Haupt, *Anal. Chem.*, 1993, **65**, 535 A.

3. K. Chen, C.A. Mirkin, R.-K. Lo, J. Zhao and J.T. McDevitt, *J. Am. Chem. Soc.*, 1995, **117**, 6374.
4. S.J. Green, D.R. Rosseinsky and M.J. Toohey, *J. Chem. Soc., Chem. Commun.*, 1994, 325.
5. S.J. Green, D.R. Rosseinsky and D.C. Sinclair, *J. Chem. Soc., Chem. Commun.*, 1994, 1421.

CHAPTER 11

Molecular Metal Wires: An Electrochemical Inspection

Materials composed by linear chain molecules constitute one of the most growing areas of research in that topical field known as “molecular electronics”,¹ *i.e.* that set of more and more extreme miniaturization processes, known as “nanotechnologies”, which would provide replacement of the different conducting or semiconducting components of the actual electronic microcircuits (wires, transistors, silicon-based microchips, *etc.*) with one or a few molecules. To have an idea of such a paradigm, one can consider that the actual level of miniaturization in computing systems allows some 100 millions of transistors (*i.e.* those tiny electrical devices able to amplify an electrical signal or to switch on/off current flows) to be put in a sliver of silicon of a few square centimeters. Representatively, if one were to scale up such a conventional microchip to occupy the present printed page, the molecular analogue would occupy the space of a period.²

The molecular wire approach is also of emerging interest in chemical sensing,³ superconductivity,⁴ magnetism (see Chapter 5, Section 3.3)⁵ and solar energy conversion.⁶

In reality, most studied derivatives linked to the above target(s) are organic polymers or conjugated organic molecules,^{1b,d,2–4,7} but a recent topic in the field is that concerned with “metal” wires, or one-dimensional arrays of inorganic molecules.⁸ These latter have, however, to be roughly subdivided in three classes:

- *pseudo-molecular wires formed by monomeric metal complexes which in the solid state give rise to unidirectional stacking interactions to form infinite chains.*

The classical example is represented by the square planar anion $[\text{Pt}(\text{CN})_4]^{2-}$, which, through the overlapping of the Pt(II)-d_{z²}

Table 1 Bond distances (\AA) and colour of $M^{\text{II}}[\text{Pt}(\text{CN})_4]$ complexes in the solid state

Complex	Colour	Pt–Pt
$\text{Sr}[\text{Pt}(\text{CN})_4] \cdot 5\text{H}_2\text{O}$	Colourless	3.60
$\text{Ca}[\text{Pt}(\text{CN})_4] \cdot 5\text{H}_2\text{O}$	Yellow	3.38
$\text{Mg}[\text{Pt}(\text{CN})_4] \cdot 4.5\text{H}_2\text{O}$	Yellow	3.36
$\text{Ba}[\text{Pt}(\text{CN})_4] \cdot 4\text{H}_2\text{O}$	Yellow-green	3.32
$\text{Be}[\text{Pt}(\text{CN})_4] \cdot 2\text{H}_2\text{O}$	Dark red	3.16
$\text{Mg}[\text{Pt}(\text{CN})_4] \cdot 7\text{H}_2\text{O}$	Dark red	3.16
$\text{Sr}[\text{Pt}(\text{CN})_4] \cdot 3\text{H}_2\text{O}$	Violet	3.09

orbitals, forms linear platinum arrays in the solid state. As illustrated in Table 1, the Pt–Pt bond length depends upon the type of crystal packing forced by the counterions, thus conditioning the colour of the different derivatives.⁹

Below the Pt–Pt distance of 3.6 \AA , the onset of a coloration testifies the formation of a solid material, whereas above such limiting distance the solid compound maintains the colourless appearance of the original monomers. As a further confirmation of the role played by crystal packing forces in this area, it must be considered that the intensely coloured solid-state complexes $[\text{Pt}(\text{CNR})_4][\text{Pt}(\text{CN})_4]$, when exposed to volatile solvents, undergo significant colour changes (a phenomenon known as “vapochromism”), just because the interstitial penetration of solvent molecules changes the lattice parameters, and hence the $\text{Pt}^{\text{II}}\text{--Pt}^{\text{II}}$ interactions.¹⁰

Other square planar Pt(II) complexes able to form infinite unidirectional chains in the solid state are known, in particular the Magnus's green salt $[\text{Pt}(\text{NH}_3)_4][\text{PtCl}_4]$,¹¹ but also Pt(I) complexes such as $[\text{Pt}(\text{bipy})_2](\text{NO}_3)_2 \cdot 2\text{H}_2\text{O}$ (obtained by electrochemical reduction of $[\text{Pt}(\text{bipy})_2](\text{NO}_3)_2 \cdot \text{H}_2\text{O}$) have recently shown linear chain crystals (Pt–Pt = 3.56 \AA).¹²

For the purposes of molecular electronics, the formation of solid-state multiple linear stacks, causing electron delocalization, favours electrical conductivity. Further, (partial) oxidation of such linear materials can produce non-stoichiometric (or mixed-valent) complexes like $\text{K}_{1.75}\text{Pt}(\text{CN})_4 \cdot 1.5\text{H}_2\text{O}$,⁹ and $\text{K}_{1.62}\text{Pt}(\text{C}_2\text{O}_4)_2 \cdot 2\text{H}_2\text{O}$,^{8b} which possess higher conductivity than their precursors.

- molecular wires formed by molecules in which metal fragments are interposed by conjugated organic spacers.¹³
- molecular wires formed by polynuclear metal complexes containing unidirectional metal–metal bonds.^{8a}

This last class, which is the subject of the present Chapter, is essentially constituted by metal complexes in which the formation of extended metal–metal bonds is favoured by the presence of coordinating bridging ligands which hold the metal centres in close proximity.

Before examining the electrochemical properties of this class of compounds (we will limit the discussion to “homonuclear” derivatives), it must be clear that the technological application of molecular wires belongs to solid-state chemistry. Nevertheless, since the main target of such new molecules is to conduct electricity, it seems useful to ascertain preliminarily their intrinsic ability towards intramolecular electron mobility by electrochemical investigations in solution, *i.e.* in the absence of intermolecular interactions.

1 PLATINUM BLUES

A rich family of intensely blue-coloured, linear platinum complexes, called “platinum blues”, has received a great body of attention in the years from 1970 to 1990, not only for their unusual physico-chemical properties, but also for their antitumor properties.¹⁴

Our interest towards such derivatives is dictated by the fact that they are mixed-valent complexes, which means that electrons may easily flow along their metal frame.

In general, such derivatives are constituted by tetraplatinum complexes having as the main ligand a wide range of bio-compatible molecules. The first, structurally characterized platinum blue complex was the α -pyridonate $[Pt_4(NH_3)_8(C_5H_4NO)_4](NO_3)_5$, Figure 1.¹⁵

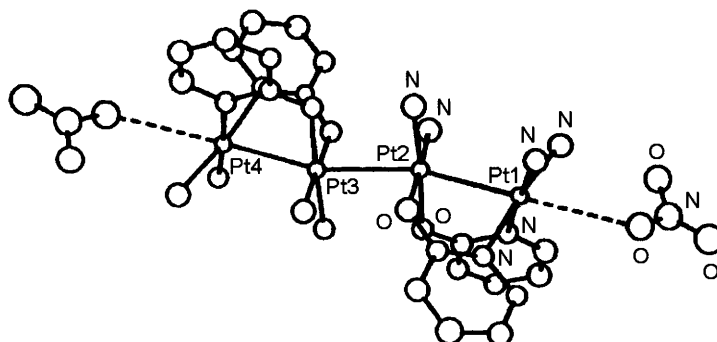
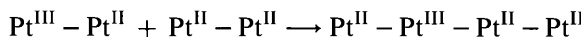


Figure 1 X-Ray crystal structure of $[Pt_4(NH_3)_8(C_5H_4NO)_4]^{5+}$ ($[NO_3]^-$ cation). Average bond lengths: $Pt1-Pt2 = 2.77 \text{ \AA}$; $Pt2-Pt3 = 2.88 \text{ \AA}$; $Pt-N_{(NH_3)} = 2.06 \text{ \AA}$; $Pt-N_{(pyridone)} = 2.05 \text{ \AA}$; $Pt-O_{(pyridone)} = 2.04 \text{ \AA}$; $Pt-O_{(NO_3)} = 3.32 \text{ \AA}$

As a consequence of the Pt^{II}–Pt^{III}–Pt^{II}–Pt^{II} assignment, the formal oxidation state of each platinum atom in the pentacation is + 2.25.

Interestingly, the one-electron reduced, yellow-green, species [Pt₄(NH₃)₈(C₅H₄NO)₄](NO₃)₄ was also structurally characterized. The tetracation has a geometry essentially identical to that of the pentacation, the main structural variation being a significant increase of the Pt–Pt distances (Pt1–Pt2 = 2.88 Å; Pt2–Pt3 = 3.13 Å), which agrees with the electronic structure Pt^{II}–Pt^{II}–Pt^{II}–Pt^{II} (or, formal oxidation state of each platinum atom: + 2.00).¹⁶

In spite of such well defined redox change, no direct electrochemical measurement was carried out to determine the redox potential of such one-electron process. It has been, however, ascertained that the Pt^{III}₂ precursor [Pt₂(NH₃)₄(C₅H₄NO)₂(H₂O)(NO₃)](NO₃)₃, in aqueous solution (pH 1), undergoes a single two-electron reduction (Pt^{III}–Pt^{III}/Pt^{III}–Pt^{II}/Pt^{II}–Pt^{II}: $E^{\circ'} = + 0.63$ V vs. SCE) coupled to chemical complications. Since macroelectrolysis experiments on the reduction process afford a blue coloured intermediate, it has been proposed¹⁷ that the blue tetraplatinum pentacation arises from the side dimerization:



A similar behaviour holds for the strictly related redox couple [Pt₄(en)₄(C₅H₄NO)₄]⁵⁺/[Pt₄(en)₄(C₅H₄NO)₄]⁴⁺. On passing from the blue Pt^{II}–Pt^{III}–Pt^{II}–Pt^{II} to the yellow Pt^{II}–Pt^{II}–Pt^{II}–Pt^{II}, the Pt–Pt distances vary from {Pt1–Pt2 = 2.83 Å, Pt2–Pt3 = 2.92 Å} to {Pt1–Pt2 = 2.99 Å, Pt2–Pt3 = 3.24 Å}.¹⁸

No redox changes have been put in evidence either for the 1-methyluracilate blue [Pt₄(NH₃)₈(C₅H₅N₂O₂)₄](NO₃)₅,¹⁸ or the yellow 1-methyhydantoinate [Pt₄(NH₃)₈(C₄H₅N₂O₂)₄](NO₃)₄ (which undergoes oxidation to a blue-green species).¹⁹ Brief (ambiguous) electrochemical data have been reported for the 3,3-dimethylglutarimidate blue [Pt₄(NH₃)₈(C₇H₁₀NO₂)₄](NO₃)₅.²⁰

Rather interesting appears the redox behaviour of the α -pyrrolidonate tan [Pt₄(NH₃)₈(C₄H₆ON)₄](NO₃)₆.²¹ The Pt–Pt distances in such Pt^{II}–Pt^{III}–Pt^{III}–Pt^{II} derivative are shorter than those found in the α -pyridonate blue [Pt₄(NH₃)₈(C₅H₄NO)₄](NO₃)₅ (see below). In 4.5 M H₂SO₄ solution, the hexacation exhibits a reversible reduction process to the (not structurally characterized) blue [Pt₄(NH₃)₈(C₄H₆ON)₄]⁵⁺ ($E^{\circ'} = + 0.53$ V vs. SCE).^{22a} Further electrochemical investigations also suggest the existence of the octacation [Pt₄(NH₃)₈(C₄H₆ON)₄]⁸⁺.^{22b,c} Few redox congeners have been structurally characterized, some of which are non-stoichiometric compounds, Table 2.

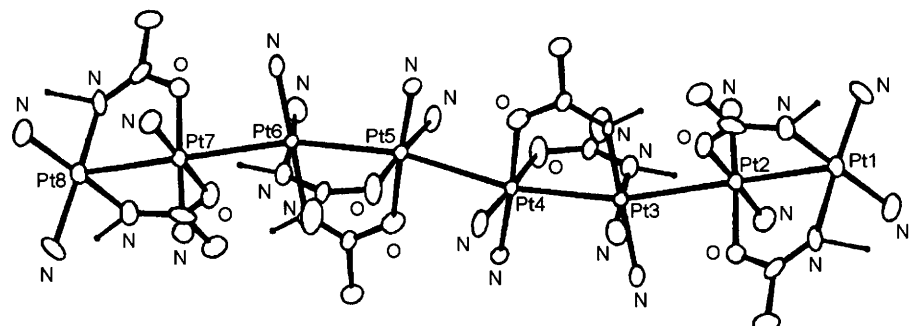
Table 2 Selected structural parameters (average distances, Å) in the family $[Pt_4(NH_3)_8(C_4H_6ON)_4]^{n+}$

Complex	Pt1–Pt2	Pt2–Pt3	Pt3–Pt4	Colour	Average Pt oxidation state	Reference
$[Pt_4(NH_3)_8(C_4H_6ON)_4]^{6+}$	2.70	2.71	2.71	dark red	2.50	21
$[Pt_4(NH_3)_8(C_4H_6ON)_4]^{5.48+}$	2.76	2.74	2.74	green	2.37	23
$[Pt_4(NH_3)_8(C_4H_6ON)_4]^{4.56+}$	2.84	2.87	2.84	violet	2.14	24
$[Pt_4(NH_3)_8(C_4H_6ON)_4]^{4+}$	3.03	3.18	3.03	yellow	2.00	22c

They prove that the platinum oxidation state can be finely varied without causing important structural changes, but for a progressive elongation of the Pt–Pt distance with the decrease of the overall charge.

We like to conclude the section with the spectacular molecular structure of the octanuclear platinum acetamidate blue $[Pt_8(NH_3)_{16}(CH_3CONH)_8]^{10+}$, Figure 2, even if no pertinent electrochemical investigation has been carried out.²⁵

The average oxidation state of each platinum atom is +2.25. An isostructural complex with a overall non-integral oxidation state is constituted by the related 2-fluoroacetamidate blue $[Pt_8(NH_3)_{16}(CH_2FCONH)_8]^{18.66+}$ (average platinum oxidation state: 2.08; Pt1–Pt2 = 2.94 Å; Pt2–Pt3 = 2.83 Å; Pt3–Pt4 = 2.98 Å; Pt4–Pt5 = 2.96 Å).²⁵

**Figure 2** X-Ray crystal structure of $[Pt_8(NH_3)_{16}(CH_3CONH)_8]^{10+}$ ($[NO_3]^-$ cation). Average bond lengths: Pt1–Pt2 = 2.88 Å; Pt2–Pt3 = 2.90 Å; Pt3–Pt4 = 2.78 Å; Pt4–Pt5 = 2.93 Å

Finally, rhodium and iridium blue complexes have been also characterized, but no electrochemical studies have been carried out, as no redox couples seem to be accessible.^{14b}

2 CHLORIDE-BRIDGED TRIRUTHENIUM COMPLEXES

A too-quickly interrupted research on redox active Ru_3Cl_n complexes appeared in literature in 1980–1990, triggered by the will to determine the nature of an elusive ruthenium “blue” complex (actually, a tetrarhodium pyrazolate blue complex has been structurally characterized: $[\text{Rh}_4(\text{C}_3\text{H}_3\text{N}_2)_4(\text{CNBu}')_8]^{2+}$).^{12b,26} The first approach led to isolation of the deep-green derivative $[\text{Ru}_3\text{Cl}_{12}]^{4-}$, which contains the linear array $\text{Ru}^{\text{III}}-\text{Ru}^{\text{II}}-\text{Ru}^{\text{III}}$.²⁷ In it, two triads of doubly-bridging chloride ligands hold together the three ruthenium atoms. Unfortunately, no pertinent electrochemical investigation has been carried out (in spite of the hypothesis that “ruthenium blue” could be the one-electron reduced product $[\text{Ru}_3\text{Cl}_{12}]^{5-}$).^{27a}

Subsequently, the new class of triruthenium compounds $[\text{Ru}_3\text{Cl}_8(\text{PR}_3)_4]$ ($\text{R} = \text{Me, Et, Bu}$) was obtained, in which four of the six terminal chloride atoms of $[\text{Ru}_3\text{Cl}_{12}]^{4-}$ are replaced by four phosphine ligands.²⁸ As a typical example, Figure 3 shows the crystal structure of the mixed-valent $\text{Ru}^{\text{III}}-\text{Ru}^{\text{II}}-\text{Ru}^{\text{III}}$ $[\text{Ru}_3\text{Cl}_8(\text{PEt}_3)_4]$.^{28b}

In CH_2Cl_2 solution, these complexes exhibit a one-electron oxidation and two separate one-electron reductions, all the processes being chemically reversible, Table 3.^{28b}

The electrode potentials well reflect the electron-donating power of the phosphine substituents.

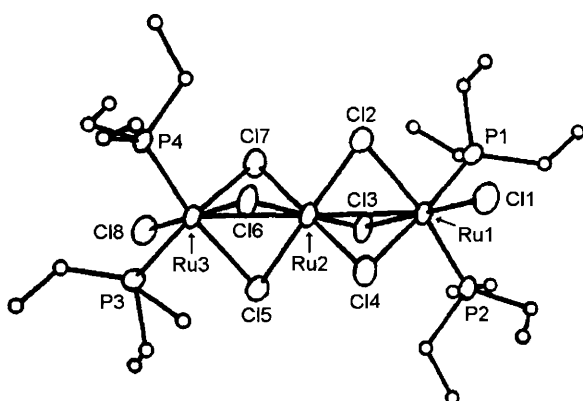


Figure 3 X-Ray crystal structure of $[\text{Ru}_3\text{Cl}_8(\text{PEt}_3)_4]$

Table 3 Formal electrode potentials (V , vs. Ag/AgCl) for the redox processes exhibited by complexes $[\text{Ru}_3\text{Cl}_8(\text{PR}_3)_4]$ in CH_2Cl_2 solution

R	$E_{+/0}^{\circ'}$	$E_{0/-}^{\circ'}$	$E_{-/2-}^{\circ'}$
Me	+ 0.84	+ 0.08	- 0.80
Et	+ 0.81	+ 0.04	- 0.82
Bu	+ 0.77	- 0.07	- 0.92

As a consequence of such a redox picture, the corresponding monocations and monoanions have been isolated; in particular, the $\text{Ru}^{\text{III}}-\text{Ru}^{\text{III}}-\text{Ru}^{\text{III}}$ monocation $[\text{Ru}_3\text{Cl}_8(\text{PEt}_3)_4]^+$ has been crystallographically characterized, Table 4.^{28b}

The main consequences of the electron removal $[\text{Ru}_3\text{Cl}_8(\text{PEt}_3)_4]^{0/+}$ reside in a slight increase of the Ru–Ru distances and a significant shortening of the axial Ru–Cl distance of the outer Ru atoms. This means that the HOMO level of $[\text{Ru}_3\text{Cl}_8(\text{PR}_3)_4]^0$ is mainly contributed by the outer metal fragments (the metal affords a non-bonding contribution, whereas the terminal chloride contributes an antibonding character).

The last series of Ru_3Cl_n family is concerned with the monocations $[\text{Ru}_3\text{Cl}_6(\text{PR}_3)_6]^+$ ($\text{R} = \text{Et}, \text{Bu}$), in which all the terminal chloride ligands of the $[\text{Ru}_3\text{Cl}_{12}]^{4-}$ precursor have been replaced by phosphines.²⁹ These complexes can be formally represented as $\text{Ru}^{\text{III}}-\text{Ru}^{\text{II}}-\text{Ru}^{\text{II}}$ arrays, but, as deducible from their typical structural parameters reported in Table 4, with respect to the $\text{Ru}^{\text{III}}-\text{Ru}^{\text{II}}-\text{Ru}^{\text{III}}$ $[\text{Ru}_3\text{Cl}_8(\text{PR}_3)_4]$ complexes, the one more electron looks like delocalized on both the two outer Ru atoms.

Table 4 Typical structural parameters (average distances, \AA) in the different families of $[\text{Ru}_3\text{Cl}_n]$ complexes (atom labelling refers to Figure 3)

Complex	$\text{Ru1}-\text{Ru2}$	$\text{Ru2}-\text{Ru3}$	$\text{Ru1}-\text{P}$	$\text{Ru1}-\text{Cl}_{(\text{terminal})}$	$\text{Ru1}-\text{Cl}_{(\text{bridging})}$	$\text{Ru2}-\text{Cl}_{(\text{bridging})}$	$\text{Ru3}-\text{Cl}_{(\text{bridging})}$	$\text{Ru3}-\text{Cl}_{(\text{terminal})}$	$\text{Ru3}-\text{P}$
$[\text{Ru}_3\text{Cl}_{12}]^{4-}$	2.80	2.80	–	2.37	2.38	2.37	2.38	2.37	–
$[\text{Ru}_3\text{Cl}_8(\text{PEt}_3)_4]$	2.86	2.86	2.33	2.34	2.45	2.37	2.45	2.34	2.33
$[\text{Ru}_3\text{Cl}_8(\text{PEt}_3)_4]^+$	2.89	2.89	2.34	2.28	2.47	2.35	2.44	2.30	2.36
$[\text{Ru}_3\text{Cl}_6(\text{PEt}_3)_6]^+$	3.08	3.08	2.31	–	2.50	2.35	2.50	–	2.31

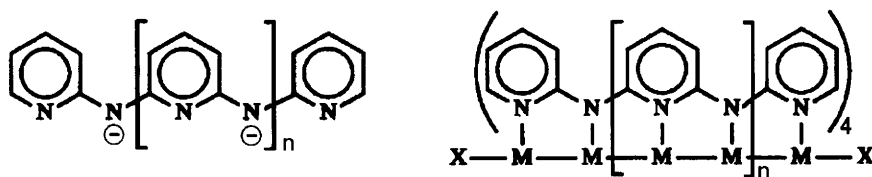
Table 5 Formal electrode potentials (V , vs. Ag/AgCl) for the redox processes exhibited by complexes $[\text{Ru}_3\text{Cl}_6(\text{PR}_3)_6]^+$ in CH_2Cl_2 solution

R	$E_{2+/+}^{\circ'}$	$E_{+/0}^{\circ'}$	$E_{0/-}^{\circ'}$
Et	+0.96	+0.74	-0.38
Bu	+1.06	+0.88	-0.47

Complementary to the redox behaviour of the series $[\text{Ru}_3\text{Cl}_8(\text{PR}_3)_4]$, the extra electron present in $[\text{Ru}_3\text{Cl}_6(\text{PR}_3)_6]^+$ causes the occurrence of two reversible one-electron oxidations and a reversible one-electron reduction, Table 5.²⁹

3 OLIGO-2-PYRIDYLAMIDES AS BRIDGING LIGANDS IN POLYNUCLEAR LINEAR COMPLEXES

(Deprotonated) dipyridylamine has been the fruitful progenitor of a series of ligands, Scheme 1, which, by increasing the number of coordinating nitrogen atoms, are able to afford (at the moment) from trinuclear to nonanuclear linear metal complexes.



$n = 0$ dpa = dipyridylamine monoanion

$n = 1$ tpda = tripyridylamine dianion

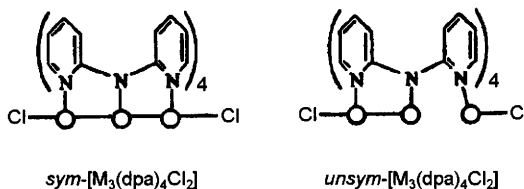
$n = 2$ tepta = tetrapyridyltriamine trianion

$n = 3$ pepta = pentapyridyltetramine tetraanion

Scheme 1

3.1 Trinuclear Complexes

Let us start our examination with the dpa-metal complexes. A series of trimetallic complexes of general formula $[\text{M}_3(\text{dpa})_4\text{Cl}_2]$ ($\text{M} = \text{Cr},^{30} \text{Ni},^{31} \text{Co},^{32} \text{Cu},^{33} \text{Ru},^{34} \text{Rh},^{34}$) have been structurally characterized. As illustrated in Scheme 2, such trinuclear complexes in the solid state can display either a “symmetrical” or an “unsymmetrical” M_3 chain, depending upon if the metal–metal bond is extended over the three metal atoms, or is localized only between two metal atoms.³⁵



Scheme 2

Representatively, Figure 4 shows the crystal structure of [Co₃(dpa)₄Cl₂]^{32g} together with its electrochemical behaviour.^{32f}

Figure 4a refers to the symmetrical isomer, but it is noted that in solution the symmetrical and unsymmetrical forms are equivalent and only contain the symmetrical isomer.^{32d,h}

As seen, [Co₃(dpa)₄Cl₂] (as well as the analogues bearing different axial fragments) undergoes two one-electron oxidations displaying features of chemical reversibility in the cyclic voltammetric time scale, Table 6.

As discussed in Chapter 4, Section 1.3, the appearance of two sequential oxidations allows a preliminary determination of the extent of charge delocalization in the mixed-valent monocations [Co₃(dpa)₄X₂]⁺. The separation of 0.8–0.9 V between the two anodic processes leads to K_{com} values of the order of 10¹⁸, which should imply that the monocation belongs to the completely delocalized mixed-valent Class III. As a matter of fact, chemical oxidation (by NOBF₄) allowed isolation of the monocation [Co₃(dpa)₄Cl₂]⁺.^{32f} In agreement with the electrochemical reversibility of the first anodic step, it shows an (almost) symmetric Co₃ chain substantially similar to that of the original (symmetric) precursor, Table 7. In agreement with the likely extended charge delocalization, the variation in Co–Co bond lengths are minimal, if any, but a significant shortening of the axial Co–Cl distances occurs. These data suggest that also in this case the HOMO of the neutral complex has a chlorine antibonding and a metal nonbonding character.^{32f}

Somewhat different are the structural and electrochemical aspects of [Cr₃(dpa)₄Cl₂]. Like [Co₃(dpa)₄Cl₂], the linear Cr₃ complex can adopt either the symmetric, or the unsymmetric geometry.^{30a–c} In CH₂Cl₂ solution [Cr₃(dpa)₄Cl₂] undergoes two one-electron oxidations ($E_{0/+}^{\circ\circ'} = +0.07$ V; $E_{+/-}^{\circ\circ'} = +0.83$ V, vs. Fc/Fc⁺) and a one-electron reduction ($E_{0/-}^{\circ\circ'} = -0.51$ V), all the processes displaying features of chemical reversibility.^{30c} Chemical oxidation allowed also in this case the obtainment of the monocation [Cr₃(dpa)₄Cl₂]⁺, but in contrast to [Co₃(dpa)₄Cl₂]⁺, it has been found that it prefers the unsymmetrical geometry, Table 8.

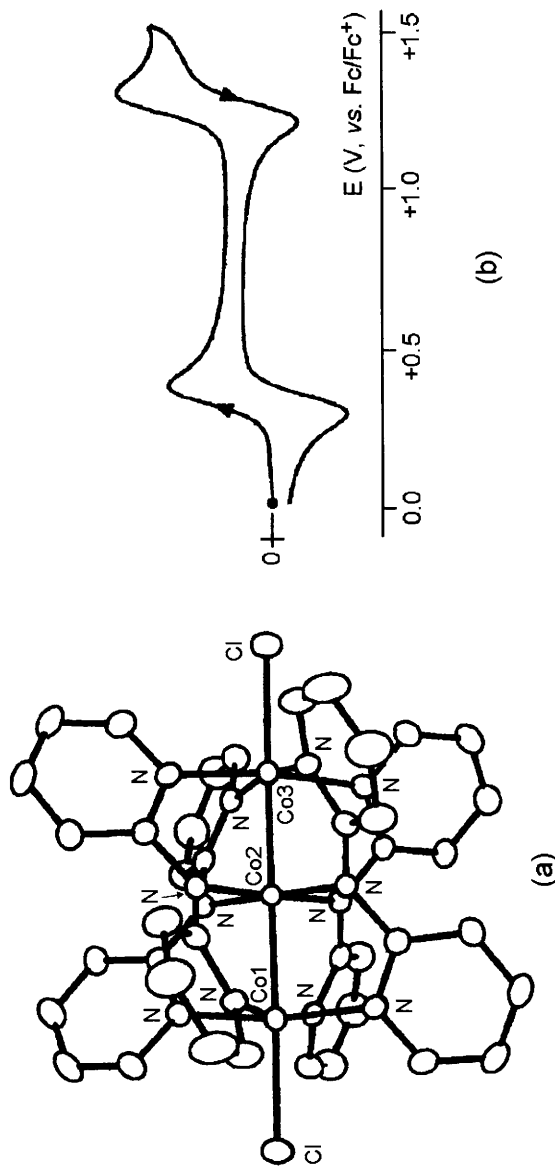


Figure 4 (a) X-Ray crystal structure and (b) cyclic voltammogram (CH_2Cl_2 solution; Pt working electrode) of $[Co_3(dpa)_4Cl_2]$

Table 6 Formal electrode potentials (V vs. Fc/Fc^+) for the redox processes exhibited by complexes $[Co_3(dpa)_4X_2]$ in CH_2Cl_2 solution

Complex	$E_{2+/+}^{o'}$	$E_{+/0}^{o'}$	Reference
$[Co_3(dpa)_4Cl_2]$	+ 1.24	+ 0.32	32f
$[Co_3(dpa)_4Br_2]$	+ 1.25	+ 0.35	32i
$[Co_3(dpa)_4(CN)_2]$	+ 1.01	+ 0.28	32l

Table 7 Selected structural parameters (average distances, \AA) for the redox couple $[Co_3(dpa)_4Cl_2]^{0/+}$ (atom labelling refers to Figure 4)

Complex	$Co1-Co2$	$Co2-Co3$	$Co1-Cl$	$Co3-Cl$	Reference
$sym-[Co_3(dpa)_4Cl_2]^a$	2.34	2.34	2.49	2.49	32g
$unsym-[Co_3(dpa)_4Cl_2]^a$	2.30	2.47	2.43	2.36	32g
$[Co_3(dpa)_4Cl_2]^{+a}$	2.33	2.34	2.36	2.37	32f

^a Crystallographic data at room temperature.

Such behaviour has been interpreted assuming that in this case the electron removal is localized on one of the two outer Cr atoms, and hence $[Cr_3(dpa)_4Cl_2]^+$ can be viewed as possessing the authentic $Cr(1)^{II}-Cr(2)^{II}-Cr(3)^{III}$ electronic configuration.^{30d}

The last trinuclear dpa complex we will consider is $[Ni_3(dpa)_4Cl_2]$, the electrochemical behaviour of which is known.³¹ In fact, complexes such as $[M_3(dpa)_4Cl_2]$ ($M = Cu, Ru, Rh$) have been structurally characterized,^{33,34} but nothing has been reported on their redox activity.

In contrast with the Co and Cr analogues, $[Ni_3(dpa)_4Cl_2]$ has been, up to now, crystallized only in the symmetrical geometry (Ni—Ni bonding,^{31a} or, alternatively, Ni—Ni nonbonding^{31b} distances of 2.43 \AA , and Ni—Cl

Table 8 Selected structural parameters (average distances, \AA) for the redox couple $[Cr_3(dpa)_4Cl_2]^{0/+}$ (atom labelling is related to Figure 4)

Complex	$Cr1-Cr2$	$Cr2-Cr3$	$Cr1-Cl$	$Cr3-Cl$	Counteranion	Reference
$sym-[Cr_3(dpa)_4Cl_2]^{a,b}$	2.37	2.37	2.55	2.55	—	30c
$sym-[Cr_3(dpa)_4Cl_2]^{c,d}$	2.37	2.37	2.56	2.56	—	30c
$unsym-[Cr_3(dpa)_4Cl_2]^{a,b}$	2.01	2.61	2.54	2.53	—	30c
$unsym-[Cr_3(dpa)_4Cl_2]^{a,e}$	2.35	2.37	2.56	2.55	—	30c
$[Cr_3(dpa)_4Cl_2]^{+a,b}$	2.01	2.55	2.44	2.27	$[AlCl_4]^-$	30d
	2.01	2.56	2.45	2.28	$[FeCl_4]^-$	30d
	2.09	2.48	f	f	$[PF_6]^-$	30d

^a Crystallographic data at 213 K; ^b CH_2Cl_2 interstitial solvent; ^c crystallographic data at 295 K; ^d thf interstitial solvent; ^e toluene interstitial solvent; ^f unresolved.

of 2.34 Å). Such a neutral complex, in CH₂Cl₂ solution, only exhibits a chemically reversible one-electron oxidation ($E_{0/+}^{\circ\circ'} = +0.91$ V, vs. Ag/AgCl).^{31c} Unfortunately, oxidation with AgPF₆ afforded [Ni₃(dpa)₄](PF₆)₃,^{31c} which does not allow a direct evaluation of the structural consequences of the electron removal.

To conclude the section, we recall that ligands somewhat related to dpa also give rise to linear trinuclear complexes. This is the case of 2,6-bis(phenylamino)pyridine,³⁶ 2,6-bis(phenylamino)piperidine,³⁷ and bis(2-pyridyl)formamidine.³⁸ At the moment, however, no (significant) electrochemical investigation has been carried out on their metal complexes.

3.2 Tetranuclear Complexes

A few linear tetranuclear complexes of ligands related to dpa have been structurally characterised, namely [Ni₄(phdpda)₄] (phdpda = dianion of N-phenyldipyridylamine),³⁹ [Cu₄(dphip)₄]²⁺ (dphip = anion of 2,6-bis(phenylamino)piperidine),^{37b} and [Cr₄(dpf)₄Cl₂]²⁺ (dpf = anion of bis(2-pyridyl)formamidine),³⁸ but no pertinent electrochemical investigation is available.

3.3 Pentanuclear Complexes

Figure 5 shows the crystal structure of [Co₅(tpda)₄(NCS)₂].⁴⁰

All the Co atoms are co-linear and are separated from each other by metal–metal like bond distances (really, theoretical calculation assigns Co–Co bond order of 0.5^{41a}). At variance with the trinuclear

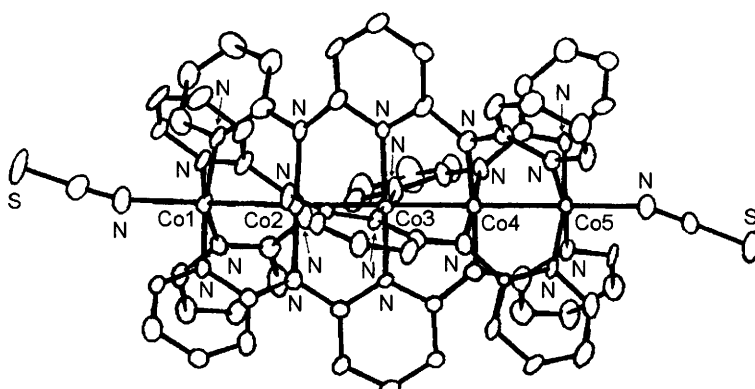


Figure 5 (a) X-Ray crystal structure of [Co₅(tpda)₄(NCS)₂]

complexes, they have a substantially symmetric geometry. The same structural features are exhibited by complexes bearing different axial ligands $[\text{Co}_5(\text{tpda})_4(\text{X})_2]$ ($\text{X} = \text{Cl}, \text{N}_3, \text{CN}, \text{SO}_3\text{CF}_3$).^{40b}

As illustrated in Figure 6, all the pentacobalt complexes display at least two chemically reversible one-electron oxidations at about +0.35 V and +0.85 V, respectively, and a one-electron reduction at -0.50 V, which in some cases is partially chemically reversible.^{40b}

The separation between the first two electron oxidations ($\Delta E^\circ \approx 0.5$ V) affords K_{com} values of about 3×10^8 , which suggests that also in this case the corresponding monocations $[\text{Co}_5(\text{tpda})_4(\text{X})_2]^+$ should belong to the completely delocalised mixed-valent Class III. As a matter of fact, oxidation by silver salts allowed the corresponding monocations to be isolated and crystallographically characterized.^{40b} As Table 9 shows, all the Co-Co distances undergo a slight elongation, which agrees with the charge delocalization. As in the case of the trinuclear analogues, the axial Co-X distances slight decrease, indicating the antibonding character of the axial substituents in the neutral species.

The quite similar series $[\text{Ni}_5(\text{tpda})_4(\text{X})_2]$ ($\text{X} = \text{Cl}, \text{N}_3, \text{CN}, \text{NCS}$) has been structurally characterized.^{40a,41a} Although also in this case

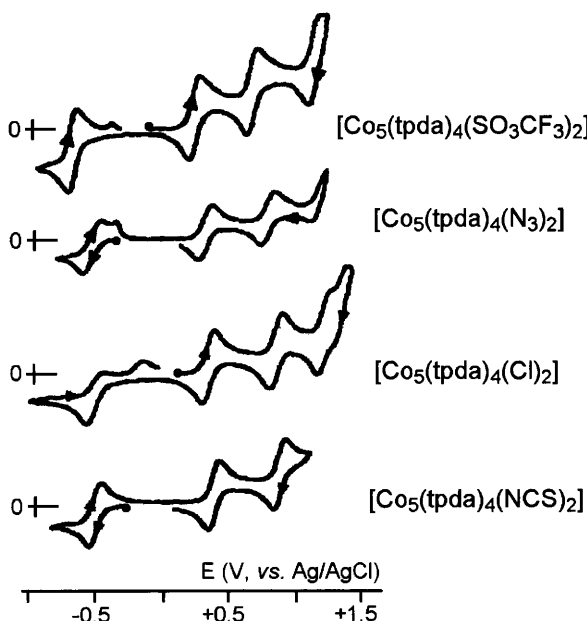


Figure 6 Cyclic voltammograms recorded in CH_2Cl_2 solutions of complexes $[\text{Co}_5(\text{tpda})_4(\text{X})_2]$

Table 9 Selected interatomic distances (\AA) for the redox couples $[\text{Co}_5(\text{tpda})_4(\text{X})_2]^{0/+}$ (atom labelling refers to Figure 5)

Complex	<i>Co1–Co2</i>	<i>Co2–Co3</i>	<i>Co3–Co4</i>	<i>Co4–Co5</i>	<i>Co1–X</i>	<i>Co5–X</i>
$[\text{Co}_5(\text{tpda})_4(\text{Cl})_2]$	2.28	2.23	2.23	2.28	2.44	2.44
$[\text{Co}_5(\text{tpda})_4(\text{Cl})_2]^+$	2.30	2.25	2.24	2.28	2.42	2.41
$[\text{Co}_5(\text{tpda})_4(\text{NCS})_2]$	2.28	2.23	2.23	2.27	2.08	2.07
$[\text{Co}_5(\text{tpda})_4(\text{NCS})_2]^+$	2.29	2.24	2.24	2.28	2.08	2.04
$[\text{Co}_5(\text{tpda})_4(\text{SO}_3\text{CF}_3)_2]$	2.25	2.22	2.22	2.25	2.24	2.24
$[\text{Co}_5(\text{tpda})_4(\text{SO}_3\text{CF}_3)_2]^+$	2.28	2.25	2.24	2.29	2.19	2.21

the Ni/Ni distances fall within apparent bonding lengths, theoretical calculation leads to Ni–Ni bond order of 0.^{41a} In contrast to $[\text{Co}_5(\text{tpda})_4(\text{X})_2]$, the outer Ni–Ni distances are significantly longer (by about 0.1 \AA) than the inner ones. In addition, in spite of the lacking electrochemical information, the monocation $[\text{Ni}_5(\text{tpda})_4(\text{SO}_3\text{CF}_3)_2]^+$ has been isolated.^{41b} Interestingly, here all the Ni–Ni distances are slightly shorter than those of the neutral complexes, thus suggesting that the one-electron removal induces direct Ni–Ni bonding interactions.

We finally mention that $[\text{Cr}_5(\text{tpda})_4(\text{Cl})_2]$ has been also structurally characterized.^{42a,b} The five Ni^{II} atoms are assumed to form alternating Ni–Ni bonds, or Ni–Ni···Ni–Ni···Ni.^{42c} Such a bonding situation is even more evident in the monocation $[\text{Cr}_5(\text{tpda})_4(\text{F})_2]^+$.^{42b} Also in this case the oxidation process $[\text{Cr}_5(\text{tpda})_4(\text{X})_2]^{0/+}$ has not been electrochemically followed.

3.4 Higher Nuclearity Complexes

It is hoped that, exploiting the coordinating ability of oligo- α -pyridylamines with more and more nitrogen atoms, longer and longer metal string complexes will become available.

Actually, the heptanuclear complexes $[\text{M}_7(\text{teptra})_4(\text{X})_2]$ ($\text{M} = \text{Cr}$, $\text{X} = \text{Cl}$;⁴³ $\text{M} = \text{Ni}$, $\text{X} = \text{Cl}$, NCS^{39,44}) have been structurally characterized, but no electrochemical information is available. The same (unfortunately) holds for the highly spectacular nonanuclear complex $[\text{Ni}_9(\text{peptea})_4(\text{Cl})_2]$ illustrated in Figure 7.⁴⁵

Scheme 3 gives an overall picture of the Ni/Ni distances (in \AA) on passing from $[\text{Ni}_5(\text{tpda})_4(\text{Cl})_2]$ to $[\text{Ni}_7(\text{teptra})_4(\text{Cl})_2]$ to $[\text{Ni}_9(\text{peptea})_4(\text{Cl})_2]$.⁴⁵

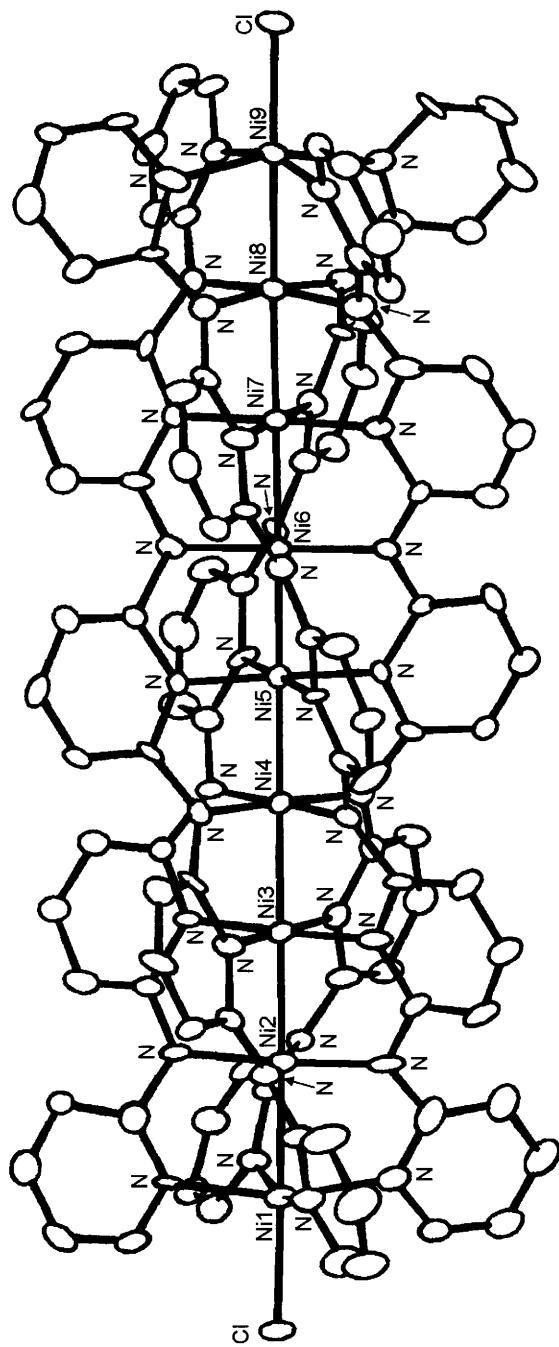
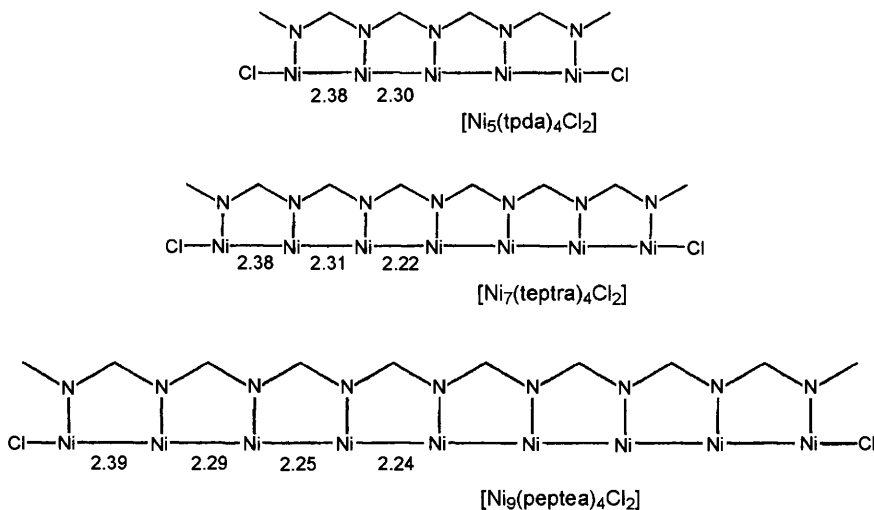


Figure 7 X-Ray crystal structure of $[Ni_9(peptea)_4(Cl)_2]$



Scheme 3

As seen, they maintain the trend: the closer to the middle the Ni atoms, the shorter are the intermetallic distances.

4 ISOCYANIDES AND NITRILE LIGANDS IN POLYNUCLEAR LINEAR COMPLEXES

Isocyanides are long known as ligands able to afford linear polynuclear complexes. This is, for example, the case of the trinuclear $[\text{Rh}_3(\text{C}_6\text{H}_5\text{CH}_2\text{NC})_{12}\text{I}_2]^{3+}$,⁴⁶ and tetranuclear $[\text{Rh}_4\{\text{NC}(\text{CH}_2)_3\text{NC}\}_8\text{Cl}]^{5+}$,⁴⁷ complexes, the electrochemical behaviour of which is, however, unknown.

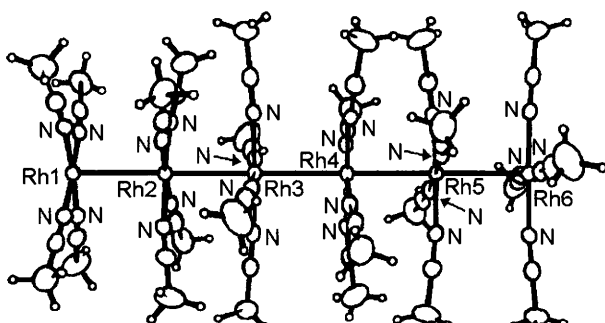


Figure 8 $X\text{-Ray crystal structure of the } [\text{Rh}_6(\text{MeCN})_{24}]^{9+} \text{ unit of } [\text{Rh}(\text{MeCN})_4(\text{BF}_4)^{1.5}]_n$. Average interatomic distances: $\text{Rh}_2\text{--Rh}_3 = 2.84 \text{ \AA}$; $\text{Rh}_3\text{--Rh}_4 = 2.93 \text{ \AA}$

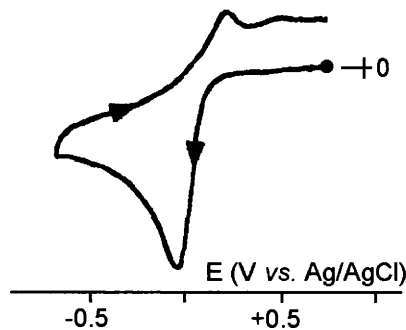


Figure 9 Cyclic voltammogram recorded at a platinum electrode on a MeCN solution of $[\text{Rh}_2^{\text{II}}(\text{MeCN})_{10}]^{4+}$

An interesting electrochemical behaviour is linked to the hexanuclear motif $[\text{Rh}_6(\text{MeCN})_{24}]^{9+}$ illustrated in Figure 8, which constitutes the repeating unit of the polymer $[\text{Rh}(\text{MeCN})_4(\text{BF}_4)_{1.5}]_n$.⁴⁸

Such a polymer is generated by cathodic electrocrystallization of a MeCN solution of $[\text{Rh}^{\text{II}}_2(\text{MeCN})_{10}]^{4+}$.⁴⁸ In fact, as shown in Figure 9, the tetracation undergoes in MeCN solution a one-electron reduction to the unstable trication $[\text{Rh}^{\text{II}}\text{Rh}^{\text{I}}(\text{MeCN})_{10}]^{3+}$ ($E_p = -0.05 \text{ V vs. Ag/AgCl}$), which in turn evidently polymerizes to the mixed-valent polymer $[\text{Rh}^{\text{II},\text{I}}(\text{MeCN})_4(\text{BF}_4)_{1.5}]_n$.⁴⁸ The assembly of Rh(I) and Rh(II) centres could be responsible for the two types of Rh–Rh bond lengths (both them, however, being longer than the Rh–Rh distance of 2.62 Å in $[\text{Rh}_2^{\text{II}}(\text{MeCN})_{10}]^{4+}$).⁴⁸

Polymeric mixed-valent Rh(I)–Rh(II) complexes of the type $[\text{Rh}_2(\text{MeCO}_2)(\text{N–N})_2(\text{anion})]_n$ ($\text{N–N} = \text{bipy, phen}$; anion = BF_4^- , PF_6^-) have been also structurally characterized,⁴⁹ but no electrochemical intervention has been occurred in their preparation.

Finally, we point out that further structural assemblies exist in the construction of linear “metallic” frames (such as: Au_3 and Au_5 ,⁵⁰ Pd_3 and Pd_4 ,⁵¹ Ir_4 ,²⁶), but no pertinent electrochemical investigations on their electron transfer ability have been carried out.

REFERENCES

1. (a) A. Aviram and M. Ratner, *Molecular Electronics: Science and Technology*, *Ann. NY Acad. Sci.*, Vol. 852, 1998; (b) M.C. Petty, M.R. Brice and D. Bloor, eds, *Introduction to Molecular Electronics*, Oxford University Press, New York, 1995; (c) D. Astruc, *Electron Transfer and Radical Processes in Transition Metal Complexes*, Wiley-VCH, New York, 1995, Ch. 4; (d) R.R. Birge, ed, *Advances in Chemistry*, Series 240,

- Molecular and Biomolecular Electronics*, American Chemical Society, 1994; (e) M. Metzger, P. Day and G.C. Papavassiliou, Eds., *Lower-Dimensional Systems and Molecular Electronics*, Plenum Press, New York, 1990; (f) P. Monceau, Ed., *Electronic Properties of Quasi-One Dimensional Compounds*, D. Reidel Publishing Co., Dordrecht, 1985.
2. (a) M.A. Reed and J.M. Tour, *Sci. Am.*, 2000, **282**, 86; (b) J.M. Tour, *Acc. Chem. Res.*, 2000, **33**, 791.
 3. T.M. Swager, *Acc. Chem. Res.*, 1998, **31**, 201.
 4. (a) D. Jérôme and K. Bechgaard, *Nature*, 2001, **410**, 162; (b) J.H. Schön, A. Dodabalapur, Z. Bao, Ch. Kloc, O. Schenker and B. Batlogg, *Nature*, 2001, **410**, 189.
 5. D. Gatteschi and R. Sessoli, *Angew. Chem. Int. Ed.*, 2003, **42**, 268.
 6. (a) V.H. Houlding and A.J. Frank, *Homogeneous and Heterogeneous Photocatalysis*, E. Pelizzetti and N. Serpone, eds, NATO ASI Ser., Ser. C., 1986; (b) R. Palmans and A.J. Frank, *J. Phys. Chem.*, 1991, **95**, 9438; (c) R. Palmans, A.J. Frank, V.H. Houlding and V.M. Miskowski, *J. Mol. Catal.*, 1993, **80**, 327.
 7. (a) J. Lehn, *Angew. Chem. Int. Ed.*, 1988, **27**, 89; (b) L.A. Bumm, J.J. Arnold, M.T. Cygan, T.D. Dunber, T.P. Burgin, L. Jones II, D.L. Allara, J.M. Tour and P.S. Weiss, *Science*, 1996, **271**, 1705; (c) W.B. Davis, W.A. Svec, M.A. Ratner and M.R. Wasiliewski, *Nature*, 1998, **396**, 60; (d) B. Jiang, S.W. Yang, S.L. Bailey, L.G. Hermans, R.A. Niver, M.A. Bolcar and W.E. Jones, Jr, *Coord. Chem. Rev.*, 1998, **171**, 365; (e) S. Yamaguchi and K. Tamao, *Silicon Containing Polymers: The Science and Technology of Their Synthesis and Applications*, D. Jones, W. Ando and J. Chojnowski, eds, Kluwer Academic Publishers, Dordrecht, The Netherlands, 2000, pp. 461–498; (f) J.M. Tour, A.M. Rawlett, M. Kozaki, Y. Yao, R.C. Jagessar, S.M. Dirk, D.W. Price, M.A. Reed, C.-W. Zhou, W. Wang and I. Campbell, *Chem. Eur. J.*, 2001, **7**, 5118.
 8. (a) J. Heinze and P. Tschunko, *Electronic Materials: The Oligomer Approach*, K. Müllen and G. Wegner, eds, Wiley-VCH, New York, 1998, pp. 479–514; (b) P. Cassoux and L. Valade, *Inorganic Materials*, D.W. Bruce and D. O’Hare, eds, Wiley, Chichester, 1999, p. 3; (c) N. Kimizuka, *Adv. Mater.*, 2000, **12**, 1461; (d) J.K. Bera and K.R. Dunbar, *Angew. Chem. Int. Ed.*, 2002, **41**, 4453.
 9. K. Krogmann, *Angew. Chem. Int. Ed.*, 1969, **8**, 35.
 10. (a) C.A. Daws, C.L. Exstrom, J.R. Sowa, Jr and K.R. Mann, *Chem. Mater.*, 1997, **9**, 363, and references therein; (b) J.W. Grate, L.K. Moore, D.E. Janzen, D.J. Veltkamp, S. Kaganove, S.M. Drew and K.R. Mann, *Chem. Mater.*, 2002, **14**, 1058, and references therein.
 11. P.D. Fleischauer, *Concepts of Inorganic Photochemistry*, A.W. Adamson and P.D. Fleischauer, eds, John Wiley, New York, 1975, p. 398.

12. R. Palmans, D.B. MacQueen, C.G. Pierpont and A.J. Frank, *J. Am. Chem. Soc.*, 1996, **118**, 12647.
13. (a) L.M. Tolbert, X. Zhao, Y. Ding and L.A. Bottomley, *J. Am. Chem. Soc.*, 1995, **117**, 12891; (b) V. Grosshenny, A. Harriman and R. Ziessel, *Angew. Chem. Int. Ed.*, 1995, **34**, 2705; (c) F. Paul and C. Lapinte, *Coord. Chem. Rev.*, 1998, **178–180**, 431; (d) S. Creager, C.J. Yu, C. Bamdad, S. O'Connor, T. MacLean, E. Lam, Y. Chong, G.T. Olsen, J. Luo, M. Gozin, and J.F. Kayyem, *J. Am. Chem. Soc.*, 1999, **121**, 1059; (e) F. Barigelletti and L. Flamigni, *Chem. Soc. Rev.*, 2000, **29**, 1; (f) D. Holten, D.F. Bocian and J.S. Lindsey, *Acc. Chem. Res.*, 2002, **35**, 57; (g) E. Iengo, E. Zangrando, R. Minatel and E. Alessio, *J. Am. Chem. Soc.*, 2002, **124**, 1003.
14. (a) B. Lippert, *Coord. Chem. Rev.*, 1999, **182**, 263; (b) C. Tejel, M.A. Ciriano and L.A. Oro, *Chem. Eur. J.*, 1999, **5**, 1131.
15. A.P. Ginsberg, T.V. O'Halloran, P.E. Fanwick, L.S. Hollis and S.J. Lippard, *J. Am. Chem. Soc.*, 1984, **106**, 5430, and references therein.
16. L.S. Hollis and S.J. Lippard, *J. Am. Chem. Soc.*, 1983, **105**, 3494, and references therein.
17. L.S. Hollis and S.J. Lippard, *Inorg. Chem.*, 1983, **22**, 2605, and references therein.
18. T.V. O'Halloran, P.K. Mascharak, I.D. Williams, M.M. Roberts and S.J. Lippard, *Inorg. Chem.*, 1987, **26**, 1261, and references therein.
19. J.-P. Laurent, P. Lepage and F. Dahan, *J. Am. Chem. Soc.*, 1982, **104**, 7335.
20. (a) K. Matsumoto, J. Matsunami and H. Urata, *Chem. Lett.*, 1993, 597; (b) J. Matsunami, H. Urata and K. Matsumoto, *Inorg. Chem.*, 1995, **34**, 202.
21. (a) K. Matsumoto and K. Fuwa, *J. Am. Chem. Soc.*, 1982, **104**, 897; (b) K. Matsumoto, H. Takahashi and K. Fuwa, *Inorg. Chem.*, 1983, **22**, 4086.
22. (a) K. Matsumoto and M. Matoba, *Inorg. Chim. Acta*, 1986, **120**, L1; (b) K. Matsumoto and M. Matoba, *Inorg. Chim. Acta*, 1988, **142**, 59; (c) K. Matsumoto, H. Miyamae and H. Moriyama, *Inorg. Chem.*, 1989, **28**, 2959.
23. K. Matsumoto, H. Takahashi and K. Fuwa, *J. Am. Chem. Soc.*, 1984, **106**, 2049.
24. K. Matsumoto, *Bull. Chem. Soc. Jpn.*, 1985, **58**, 651.
25. K. Matsumoto, K. Sakai, K. Nishio, Y. Tokisue, R. Ito, T. Nishide and Y. Shichi, *J. Am. Chem. Soc.*, 1992, **114**, 8110.
26. C. Tejel, M.A. Ciriano, J.A. López, F.J. Lohoz and L.A. Oro, *Angew. Chem. Int. Ed.*, 1998, **37**, 1542.
27. (a) A. Bino and F.A. Cotton, *J. Am. Chem. Soc.*, 1980, **102**, 608; (b) B.E. Bursten, F.A. Cotton and A. Fang, *Inorg. Chem.*, 1983, **22**, 2127.
28. (a) F.A. Cotton, M. Matusz and R.C. Torralba, *Inorg. Chem.*, 1989, **28**, 1516; (b) F.A. Cotton and R.C. Torralba, *Inorg. Chem.*, 1991, **30**, 3293.
29. F.A. Cotton and R.C. Torralba, *Inorg. Chem.*, 1991, **30**, 4386.

30. (a) F.A. Cotton, L.M. Daniels, C.A. Murillo and I. Pascual, *J. Am. Chem. Soc.*, 1997, **119**, 10223; (b) F.A. Cotton, L.M. Daniels, C.A. Murillo and I. Pascual, *Inorg. Chem. Commun.*, 1998, **1**, 1; (c) R. Clérac, F.A. Cotton, L.M. Daniels, K.R. Dunbar, C.A. Murillo and I. Pascual, *Inorg. Chem.*, 2000, **39**, 748; (d) R. Clérac, F.A. Cotton, L.M. Daniels, K.R. Dunbar, C.A. Murillo and I. Pascual, *Inorg. Chem.*, 2000, **39**, 752.
31. (a) S. Aduldecha and B. Hathaway, *J. Chem. Soc., Dalton Trans.*, 1991, 993; (b) R. Clérac, F.A. Cotton, K.R. Dunbar, C.A. Murillo, I. Pascual and X. Wang, *Inorg. Chem.*, 1999, **38**, 2655; (c) J.F. Berry, F.A. Cotton, L.M. Daniels and C.A. Murillo, *J. Am. Chem. Soc.*, 2002, **124**, 3212.
32. (a) E.-C. Yang, M.-C. Cheng, M.-S. Tsai and S.-M. Peng, *J. Chem. Soc., Chem. Commun.*, 1994, 2377; (b) F.A. Cotton, L.M. Daniels, G.T. Jordan, IV, and C.A. Murillo, *J. Am. Chem. Soc.*, 1997, **119**, 10377; (c) F.A. Cotton, L.M. Daniels and G.T. Jordan, IV, *Chem. Commun.*, 1997, 421; (d) F.A. Cotton, C.A. Murillo and X. Wang, *Inorg. Chem.*, 1999, **38**, 6294; (e) F.A. Cotton, C.A. Murillo and X. Wang, *J. Chem. Soc., Dalton Trans.*, 1999, 3327; (f) R. Clérac, F.A. Cotton, K.R. Dunbar, T. Lu, C.A. Murillo and X. Wang, *J. Am. Chem. Soc.*, 2000, **122**, 2272; (g) R. Clérac, F.A. Cotton, L.M. Daniels, K.R. Dunbar, K. Kirschbaum, C.A. Murillo, A.A. Pinkerton, A.J. Schultz and X. Wang, *J. Am. Chem. Soc.*, 2000, **122**, 6226; (h) R. Clérac, F.A. Cotton, L.M. Daniels, K.R. Dunbar, C.A. Murillo and X. Wang, *J. Chem. Soc., Dalton Trans.*, 2001, 386; (i) R. Clérac, F.A. Cotton, S.P. Jeffery, C.A. Murillo and X. Wang, *Inorg. Chem.*, 2001, **40**, 1265.
33. (a) L.-P. Wu, P. Field, T. Morissey, C. Murphy, P. Nagle, B. Hathaway, C. Simmons and P. Thornton, *J. Chem. Soc., Dalton Trans.*, 1990, 3835; (b) G.J. Pyrka, M. El-Mekki and A. Pinkerton, *J. Chem. Soc., Chem. Commun.*, 1991, 84; J.F. Berry, F.A. Cotton, P. Lei and C.A. Murillo, *Inorg. Chem.*, 2003, **42**, 377.
34. J.-T. Sheu, C.-C. Lin, I. Chao, C.-C. Wang and S.-M. Peng, *Chem. Commun.*, 1996, 315.
35. F.A. Cotton, *Inorg. Chem.*, 1998, **37**, 5710.
36. F.A. Cotton, L.M. Daniels, P. Lei, C.A. Murillo and X. Wang, *Inorg. Chem.*, 2001, **40**, 2778.
37. (a) R. Clérac, F.A. Cotton, L.M. Daniels, K.R. Dunbar, C.A. Murillo and H.-C. Zhou, *Inorg. Chem.*, 2000, **39**, 3414; (b) R. Clérac, F.A. Cotton, L.M. Daniels, J. Gu, C.A. Murillo and H.-C. Zhou, *Inorg. Chem.*, 2000, **39**, 4488.
38. F.A. Cotton, L.M. Daniels, C.A. Murillo and X. Wang, *Chem. Commun.*, 1998, 39.
39. S.-Y. Lai, T.-W. Lin, Y.-H. Chen, C.-C. Wang, G.-H. Lee, M. Yang, M. Leung and S.-M. Peng, *J. Am. Chem. Soc.*, 1999, **121**, 250.

40. (a) S.-J. Shieh, C.-C. Chou, G.H. Lee, C.-C. Wang and S.-M. Peng, *Angew. Chem. Int. Ed.*, 1997, **36**, 56; (b) C.-Y. Yeh, C.-C. Chou, K.-C. Pan, C.-C. Wang, G.H. Lee, Y.O. Su and S.-M. Peng, *J. Chem. Soc., Dalton Trans.*, 2002, 2670.
41. (a) C.-C. Wang, W.-C. Lo, C.-C. Chou, G.-H. Lee, J.-M. Chen and S.-M. Peng, *Inorg. Chem.*, 1998, **37**, 4059; (b) C.-Y. Yeh, Y.-L. Chiang, G.-H. Lee and S.-M. Peng, *Inorg. Chem.*, 2002, **41**, 4096.
42. (a) F.A. Cotton, L.M. Daniels, T. Lu, C.A. Murillo and X. Wang, *J. Chem. Soc., Dalton Trans.*, 1999, 517; (b) H.-C. Chang, J.-T. Li, C.-C. Wang, T.-W. Lin, H.-C. Lee, G.-H. Lee, and S.-M. Peng, *Eur. J. Inorg. Chem.*, 1999, 1243; (c) F.A. Cotton, L.M. Daniels, C.A. Murillo and X. Wang, *Chem. Commun.*, 1999, 2461.
43. Y.-H. Chen, C.-C. Lee, C.-C. Wang, G.-H. Lee, S.-Y. Lai, F.-Y. Li, C.-Y. Mou and S.-M. Peng, *Chem. Commun.*, 1999, 1667.
44. S.-Y. Lai, Y.-H. Chen, C.-C. Lee, Y.-H. Liu and S.-M. Peng, *J. Chin. Chem. Soc.*, 1999, **46**, 477.
45. S.-M. Peng, C.-C. Wang, Y.-L. Jang, Y.-H. Chen, F.-Y. Li, C.-Y. Mou and M.K. Leung, *J. Magn. Magn. Mater.*, 2000, **209**, 80.
46. A.L. Balch and M.M. Olmstead, *J. Am. Chem. Soc.*, 1979, **101**, 3128.
47. K.R. Mann, M.J. DiPietro and T.P. Gill, *J. Am. Chem. Soc.*, 1980, **102**, 3965.
48. (a) G.M. Finniss, E. Canadell, C. Campana and K.R. Dunbar, *Angew. Chem. Int. Ed.*, 1996, **35**, 2772; (b) M.E. Prater, L.E. Pence, R. Clérac, G.M. Finniss, C. Campana, P. Auban-Senzier, D. Jérôme, E. Canadell and K.R. Dunbar, *J. Am. Chem. Soc.*, 1999, **121**, 8005.
49. (a) F.P. Pruchnik, P. Jakimowicz, Z. Ciunik, K. Stanislawek, L.A. Oro, C. Tejel and M.A. Ciriano, *Inorg. Chem. Commun.*, 2001, **4**, 19; (b) F. P. Pruchnik, P. Jakimowicz and Z. Ciunik, *Inorg. Chem. Commun.*, 2001, **4**, 726.
50. (a) R. Usón, A. Laguna, M. Laguna, M.T. Tartón and P.G. Jones, *J. Chem. Soc., Chem. Commun.*, 1988, 748; (b) R. Usón, A. Laguna, M. Laguna, J. Jiménez and P.G. Jones, *Angew. Chem. Int. Ed.*, 1991, **30**, 198.
51. (a) S. Kannan, A.J. James and P.R. Sharp, *J. Am. Chem. Soc.*, 1998, **120**, 215; (b) T. Murahashi, E. Mochizuchi, Y. Kai and H. Kurosawa, *J. Am. Chem. Soc.*, 1999, **121**, 10660.

CHAPTER 12

The ‘Direct’ Electrochemistry of Redox-active Proteins

1 INTRODUCTION

The term ‘direct’ electrochemistry of proteins means the possibility to detect the ‘direct’ exchange of electrons between the active site(s) of a protein and a (metallic or inert material) electrode without the help of redox mediators, which might favour an ‘indirect’ interaction between the electrode and the protein (see the discussion on *Electrocatalysis* in Chapter 2, Section 1.4.4). This aspect of electrochemistry is not yet as widely explored as it deserves, but the relevant results are now analysed in a rather comprehensive fashion.^{1–4}

Most mechanisms which control biological functions, such as cell respiration and photosynthesis (already discussed in Chapter 5, Section 3.1), are based on redox processes. In particular, as shown again in Figure 1, it is evident that, based on their physiological redox potentials, in photosynthesis a chain of electron carriers (*e.g.* iron–sulfur proteins, cytochromes and blue copper proteins) provides a means of electron transport which is triggered by the absorption of light.

Other biological redox processes are for instance important in the bacterial degradation of chemical products found in the soil (such as the *oxygenases* illustrated in Chapter 9, Section 1.1).

As electrochemistry is particularly suitable for studying electron transfer events, its application to biological redox processes appears reasonable. Unfortunately, the difficulties encountered and the few results obtained until the beginning of the 1980s meant that it became firmly believed that it would not be possible to use this technique to study the direct electron transfers activated by proteins. The basis of this scepticism were the following:

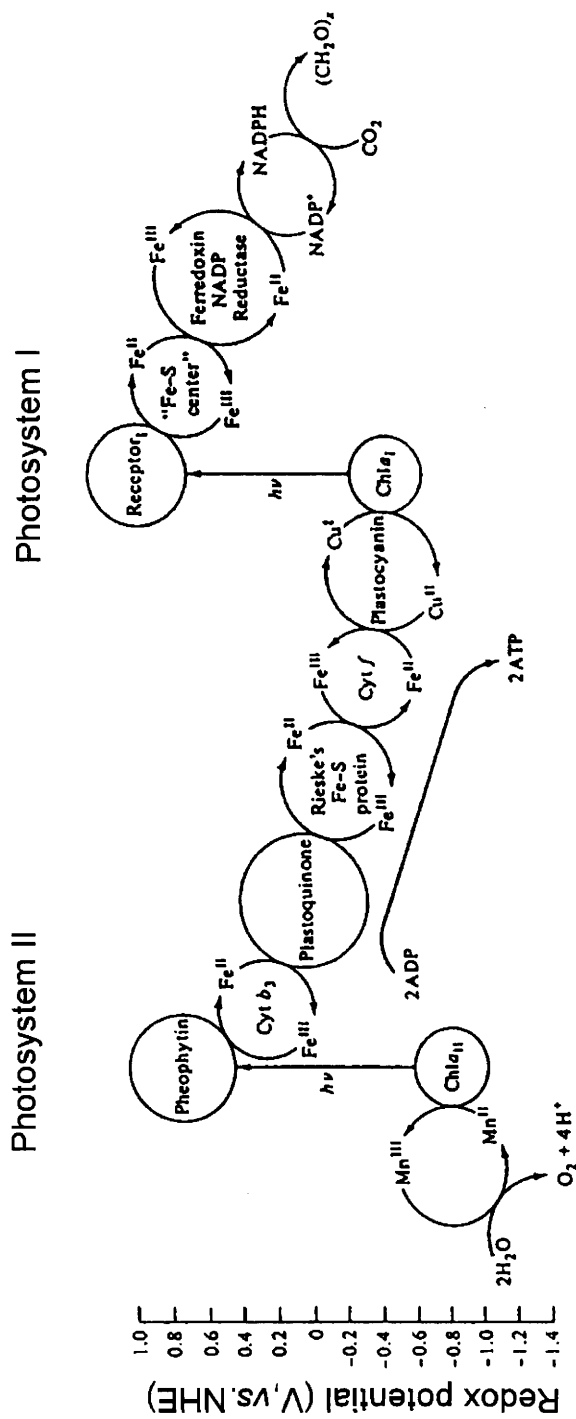


Figure 1 Redox sequences active in Photosynthesis

- the slow rate of diffusion of biological molecules (due to their high molecular weight) resulted in very low faradaic currents;
- as the electroactive site is buried within the protein chain, direct electron exchange with the electrode is considerably impaired;
- the first results using a mercury electrode indicated that even when a direct interaction between electrode and redox active site could be established, it caused denaturation of the protein;
- the easy adsorption of proteins onto the electrode can cause severe poisoning of the electrode surface.

In biological systems the movement of an electron from a donor to an acceptor site is a quite common and apparently simple event. In reality, however, electron transfers over distances greater than 10 Å are frequently necessary, which means that the electron transfer can be a slow process. In fact, according to the *Marcus theory*, the rate constant for electron transfer between two redox sites, k_{et} (s^{-1}), is given by:⁵

$$k_{\text{et}} = \frac{10^{13}}{e^{\beta \cdot (d-3)}} \cdot \frac{1}{e^{\frac{(\lambda + \Delta G^\circ)^2}{4 \cdot \lambda \cdot R \cdot T}}}$$

where:

λ = structural reorganization energy (eV) necessary such that the donor and acceptor sites have geometrical arrangements able to favour the electron transfer;

ΔG° = change in the free energy (eV) that accompanies the redox process;

d = the separation (Å) between the two redox sites;

β = a constant (\AA^{-1}) which measures how quickly the rate of the electron transfer decreases with distance; normally about 1 Å⁻¹.

When the electron-transfer sites are well separated ($d \gg 3$ Å) the last term of the above expression approximates to 1. Hence, it reduces to:

$$k_{\text{et}} \approx \frac{10^{13}}{e^{\beta \cdot d}}$$

This relationship, which shows that the rate of an electron transfer process decreases exponentially with the separation, is usually used to evaluate the separation between redox sites when it is possible to measure k_{et} .

For some years the distance between redox centres was considered as the rate determining step of electron transfer processes. However,

it is now recognized to be only one of the different factors which raise the energy barrier of electron transfer (such as structural changes concomitant with the electron transfer, spatial disposition of the protein with respect to the electrode surface, and other factors we will now examine). In this regard, it has been calculated that if the distance between the point of contact on the electrode surface and the active site is less than 10 Å, one can have fast reversible electron transfer.

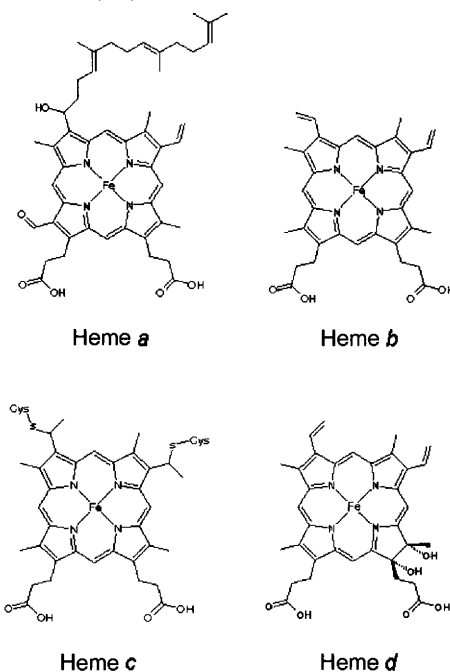
The points which render the redox processes of proteins occurring at an electrode different from those which proceed *via* chemical routes are the following:

- at the electrode–solution interface there is the double layer region of molecular dimensions that is organised in function of the charge imposed to the electrode by the applied potential;
- proteins are also charged, but, contrary to electrodes, they have an asymmetric rather than a symmetric charge distribution.

Consequently, electrostatic interactions at the electrode–solution interface between electrodes and proteins can occur at all potential values, independent of the sign of the overall protein charge. Hence, the asymmetric distribution of charge on the protein, due to the presence of positive and negative protein sites, means that irrespective of the global charge the protein can be adsorbed onto the electrode surface for any value and sign of the electrode potential. Therefore, with respect to an electrode, proteins can be active either by a simple electrostatic adsorption taking place at any potential value, or by diffusion triggered by an electron exchange occurring at the standard potential value of the specific redox process. One should thus always keep in mind that upon employing voltammetric techniques there exists the possibility that protein adsorption on the electrode surface can occur. Furthermore, it is possible that in extreme cases a protein is oxidized or reduced only when it is adsorbed on the electrode surface.

2 ELECTROCHEMISTRY OF CYTOCHROMES

Cytochromes are iron-porphyrin based (hemo)proteins ubiquitous both in the animal and plant kingdom specifically deputed to electron transport processes. As represented in Scheme 1, there are four main classes of cytochromes: *a*, *b*, *c*, *d*, respectively, depending upon the heme type they contain.⁶



Scheme 1

Further classifications among cytochromes belonging to the same class are made using symbols related to the order of their participation in electron-transfer chains or to the wavelength of their maximum absorbance.

The different cytochromes display rather similar redox activity, *i.e.* the reversible $\text{Fe(III)} \rightleftharpoons \text{Fe(II)}$ process, but their redox potentials change with the peripheral substituents of the Fe(III)-porphyrin (particularly, as a function of the axially coordinated groups).

As an initial example let us consider the chemical reduction of cytochrome c (FW = 12 400), a protein which plays a series of important roles in living organisms. The structural effects of the $\text{Fe(III)}/\text{Fe(II)}$ redox process are known from crystallographic data, Figure 2.^{7a,b,c}

As can be seen, the addition of one electron, corresponding to the $\text{Fe(III)}/\text{Fe(II)}$ reduction, does not cause significant structural changes in the octahedral coordination sphere of the iron centre. Rather, structural variations are concerned with a series of hydrogen bridges which destroy and form in the peripheral zone (between residues 40–80), as a consequence of protonation/deprotonation processes triggered by the electron transfer. Indeed, the coupling of electron transfer to proton transfer is fairly common in biochemical processes⁸ (in general reduction

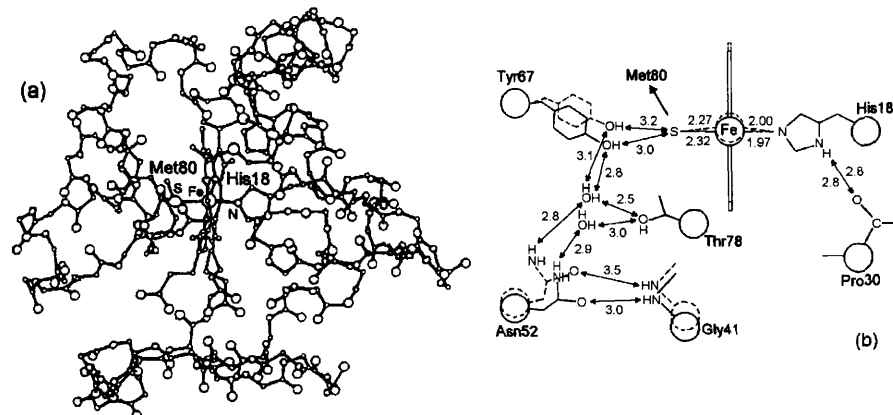


Figure 2 (a) X-ray structure of the active site of the tuna fish cytochrome c. (b) The most significant structural changes caused by the Fe(III)/Fe(II) reduction. Solid lines represent the reduced state; dashed lines represent the oxidized state

is associated with protonation, whereas oxidation is associated with deprotonation), and has its origin in the different capacity of protons to penetrate the molecular frame of the oxidized cytochrome c compared to that of the reduced cytochrome c.

One may deduce that, based on the absence of significant structural changes at the active site, the electron transfer process should be fast (which means *electrochemically reversible*).

When using electrochemistry to monitor directly the Fe(III)/Fe(II) reduction it is important to keep in mind that cytochrome c, at pH 7, in the oxidised state has an overall charge of + 7.5, whereas in the reduced state it has a charge of + 6.5.[#]

Figure 3 shows the cyclic voltammograms of cytochrome c recorded in aqueous solution either when the protein is adsorbed (or immobilized) on the electrode (SnO_2) surface (a), or when it diffuses to a gold electrode pretreated by adsorption of 4,4'-bipyridyl (b).

Apart from the general appearance and the different current densities, it is evident that the reduction process is really reversible ($E^{\circ'} = + 0.26 \text{ V}$ vs. NHE, $\Delta E_p \approx 60 \text{ mV}$ at the different scan rates) for both experimental conditions. As one might expect, in the case of adsorption (Figure 3a)

[#] Such overall charges are calculated on the basis of the amino acid composition. In other words, it is determined by the number of negative charges due to the COO^- groups of glutamate, aspartate and cysteinate and the number of positive charges due to the NH_3^+ groups of lysine, arginine and histidine and those of the metal ion itself.

However, the knowledge of the *isoelectric point* (*pI*) is immediately sufficient to allow one to know if the overall charge of a protein is positive or negative, in that a *pI* higher than 7 means that at pH 7 the protein is positively charged, whereas a *pI* lower than 7 means that at pH 7 the protein is negatively charged. Accordingly, the isoelectric point of cytochrome c is 10.2.

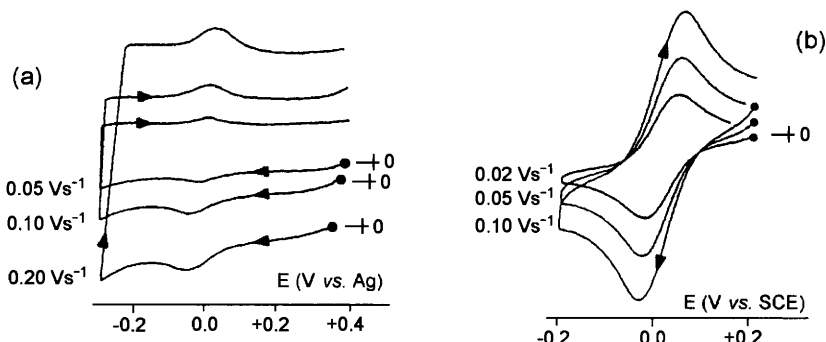


Figure 3 Cyclic voltammograms recorded at different scan rates in aqueous solution ($\text{pH } 7$) of cytochrome c , under the following experimental conditions: (a) protein adsorbed on the SnO_2 electrode surface; (b) Au electrode pretreated with bipyridyl; protein in solution

the current increases linearly with the scan rate, whereas in the case of simple diffusion (Figure 3b) the current increases linearly with the square root of the scan rate.

From hereafter, we will neglect the electrochemical aspects of redox processes of 'adsorbed' proteins, in order to consider in more detail redox processes governed by diffusion of the protein in solution. As mentioned in Chapter 2, Section 1.6, the case of adsorbed species is in some ways easier to treat, given the absence of the mathematical laws of mass transport, but in some cases it may be complicated by anomalous currents or electrode poisoning.

It is immediately evident from Figure 3b that 'pre-treatment' of the electrode surface is essential for a 'direct' electrochemical study of proteins. The reason for the success achieved using an electrode on which 4,4'-bipyridyl has been pre-adsorbed is shown in Figure 4.

Since oxidized cytochrome c , at pH 7, has an overall positive charge of + 7.5, it means that it bears an excess of NH_3^+ groups. Hence, the activated complex formed through hydrogen bonds between the lysine groups of the protein and the pyridyl nitrogen atoms adsorbed on the electrode surface, is thought to provide a good route for the rapid exchange of electrons. This hypothesis is supported by the observation that if the process is recorded at pH 4, where the pyridyl nitrogen atoms are already protonated, the electrochemical activity disappears.

The investigation on the use of molecules suitable for modifying the electrode surface so as to favour electron transfers with proteins (so-called *promoters*, which are non-redox active molecules and therefore unable to act as redox mediators) has determined that they must be bifunctional molecules $X-\backslash\diagup\diagdown-Y$, in which X is a group able to

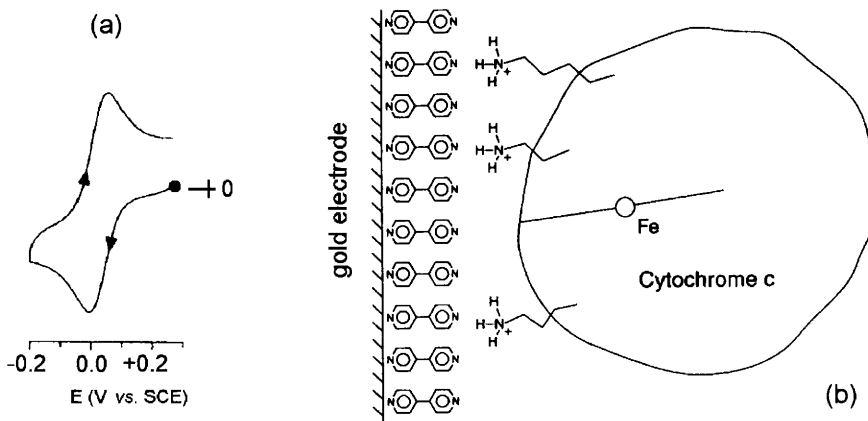


Figure 4 (a) Typical cyclic voltammogram of cytochrome c recorded at a gold electrode the surface of which has been modified by bipyridyl (pH 7). (b) The hypothesis of the interaction between the electrode surface and the protein

produce an almost irreversible adsorption with the electrode surface, Y is the functional group able to electrostatically interact with the protein and the spacer — $\backslash\backslash$ — can be either an aliphatic or an aromatic chain.

Usually X is a group able to act either as σ -donor, or as π -acceptor, such as 4-pyridyl-N, -SH, -S-S-, or -PR_x.

The effectiveness of the Y groups can be divided into two classes:

- neutral groups, such as 4-pyridyl-N, anilines Ar-NH₂, which are slightly basic, hence able to form hydrogen bonds with the lysine residues -NH₃⁺;
- anions such as carboxylates, sulfonates, phosphonates, phosphates, which can interact with the -NH₃⁺ residues either through hydrogen bond formation, or through salt reaction.

Within the promoter there can be subtle structural differences that influence the polar interaction with the protein. For example, Figure 5 illustrates the cyclic voltammograms of cytochrome c obtained at a gold electrode modified with isomers of pyridine-carboxylaldehyde-thiosemicarbazone (PATS).

As seen, the shift of the pyridyl nitrogen atom from *para* (PATS-4) to *ortho* (PATS-3), to *meta* position (PATS-2), making more and more difficult the hydrogen bond formation with the -NH₃⁺ residues of the protein, progressively worsens the voltammetric response.

Recently, an inorganic promoter as [Ru(CN)₅(Spy)]⁴⁻ (Spy = 4-thiopyridine) adsorbed on a gold electrode surface also proved to be very effective in the direct electrochemistry of cytochrome c; the tetraanion not

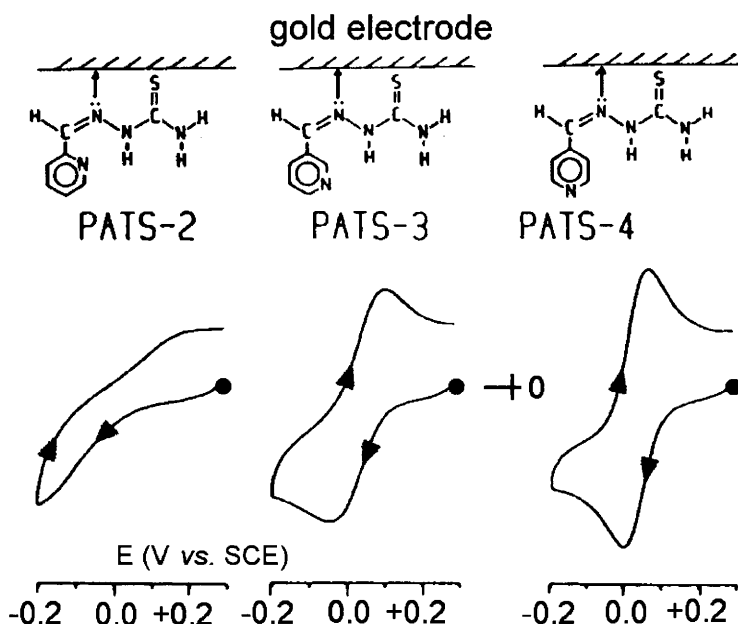


Figure 5 Cyclic voltammograms of cytochrome c recorded at gold electrodes modified with different isomers of PATS

only strengthens the stability of the adsorbed layer, but its negative charge also provides a favourable electrostatic interaction with the protein.⁹

The selective pretreatment of electrodes also has the advantage of preventing the occasional adsorption of other molecules, which is very probable when working with biological materials.

However, modification of the electrode surface is not the only way in which one can facilitate reversible electron transfer between an electrode and a protein site. The indispensable condition is that the electrode surface is electrostatically compatible with the protein surface.

An example is represented by the reduction of cytochrome c using a pyrolytic graphite electrode suitably prepared. In fact, as schematised in Figure 6, this type of carbon material (briefly alluded to in Chapter 3, Section 1.1) has a solid state structure fairly close to the ideal structure of graphite.

In the electrode construction, this anisotropic material can be cut either 'parallel' to the basal benzenoid-like carbon planes formed by C/C covalent bonds (plane *ab*), or 'perpendicular' to the carbon layers where the C/C bonds are van der Waals type (planes *ac* and *bc*).

Figure 7 shows the cyclic voltammetric responses of cytochrome c obtained at pyrolytic graphite electrodes treated in various ways.

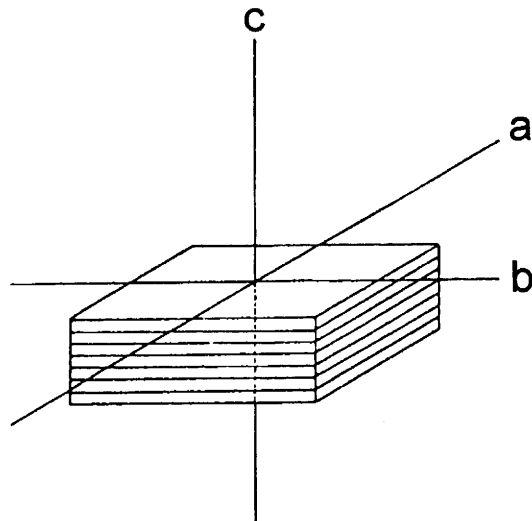


Figure 6 Schematic representation of the layered structure of pyrolytic graphite

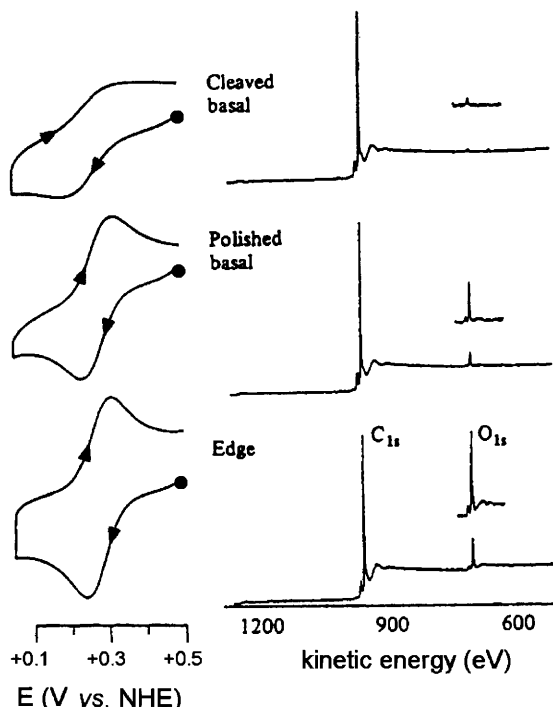


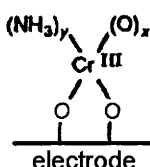
Figure 7 Cyclic voltammograms of cytochrome *c* recorded at different types of pyrolytic graphite electrodes. Also shown are the relative ESCA spectral patterns which show the O/C ratio in the different treated electrode material (a scale enlargement ($\times 3$) is shown for the O_{1s} peak)

As one can see, at an electrode freshly cut along the *basal plane* the response is fairly poorly defined, whereas if the electrode is cut along the *edge planes* (*i.e.* perpendicular to the carbon layers) the response becomes reversible. As can be inferred from the ESCA (electron spectroscopy for chemical analysis) data, the explanation of this behaviour is that when the cut is made in the basal plane a quasi-metallic, hydrophobic surface is formed with the carbon valencies almost saturated ($O/C \approx 0.02$). Conversely, when the cut is made in the edge plane an unsaturated surface is created which can generate a high number of C–O functional groups, such as carbonyl, phenol, carboxylic ($O/C \approx 0.33$). These groups impart to the electrode surface a hydrophilic, and hence a *negative* character in neutral or basic solutions. This favours the electrostatic interaction with those proteins that have a *positive* charge.

It is also evident that polishing (with alumina) the surface cut parallel to the basal planes can improve the response. In fact, the mechanical action breaks the covalent C/C bonds, which then reform binding oxygen from the air ($O/C \approx 0.11$).

It is noted that the glassy carbon electrode behaves as the perpendicularly cut pyrolytic graphite electrode.

In support of the explanation presented above, using perpendicularly cut pyrolytic graphite in solutions containing agents (such as amino-Cr(III) salts or Mg^{2+} ions) which neutralize the negatively charged functional C/O groups, Scheme 2 (with consequent weakening of the electrostatic interaction with the protein), the redox activity is significantly reduced, Figure 8.



Scheme 2

In summary, the overall successful effect has been assigned to the fact that any pretreatment of either the electrode surface (use of promoters, use of specific carbon electrodes, with the eventual generation of functional COO^- groups) or the solutions (addition of multicharged cationic species, proper choice of pH) creates at the bare electroinactive surface more and more specific microscopic active sites able to favour the exchange of electrons with proteins.¹⁰ This means that, in the absence of proper pretreatments, the electrode surface does not possess specific sites

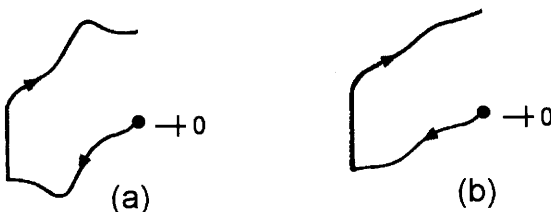


Figure 8 Cyclic voltammograms of cytochrome c recorded at an edge-oriented pyrolytic graphite electrode. In the absence (a) and in the presence (b) of $[Cr(NH_3)_6]^{3+}$

to favour the electron transfer, and the cyclic voltammogram is quite flat (for instance, Figure 8b). As soon as the pretreatment is started, the number of specific sites begins to increase and the cyclic voltammetric response improves more and more (for instance, Figure 8a).

As illustrated in Figure 9, a single specific microscopic active site created at the electrode surface is sufficient to afford a ‘sigmoidal’ curve, in that the mass transport is governed by radial diffusion (see Chapter 2, Section 1.1.1.1), even if in this case relatively low faradaic currents are generated at the microsized active electrode. Upon increasing the number of specific sites through the proper prefunctionalization of the electrode surface, the mass transport, because of the overlap of the multiple radial diffusion layers, becomes governed by linear diffusion and the voltammogram assumes the typical ‘peak-shaped’ profile, giving rise to relatively high faradaic currents.

Let us pass to other cytochromes. *Cytochrome f* (or cytochrome c₅₅₂) (FW = 15 000), the crystal structure of which is known,¹¹ is an electron carrier present in the photosynthetic chain and also possesses a positive overall charge. It exhibits a reversible Fe(III)/Fe(II) reduction at a gold electrode modified with 4,4'-dithiopyridine,¹² Figure 10.

The process occurs at potential values slightly more positive (by about 20 mV) than those of cytochrome c.

It is also interesting to look at the electrochemical behaviour of bovine liver cytochrome b₅ (FW = 16 000), a microsomal protein of known crystal structure,¹³ which forms a complex with cytochrome c and possesses a negative overall charge. As illustrated in Figure 11, such protein affords a reversible Fe(III)/Fe(II) reduction ($E^{\circ'} = +0.01$ V vs. NHE) at a gold electrode modified using as promoter a cysteine-lysine-cysteine peptide. In fact, as shown, it is assumed that the modified electrode surface exposes a positive charge to the negatively charged protein.¹⁴

Similar results have been obtained at a gold electrode modified using β -thiopropionate as promoter.¹⁵

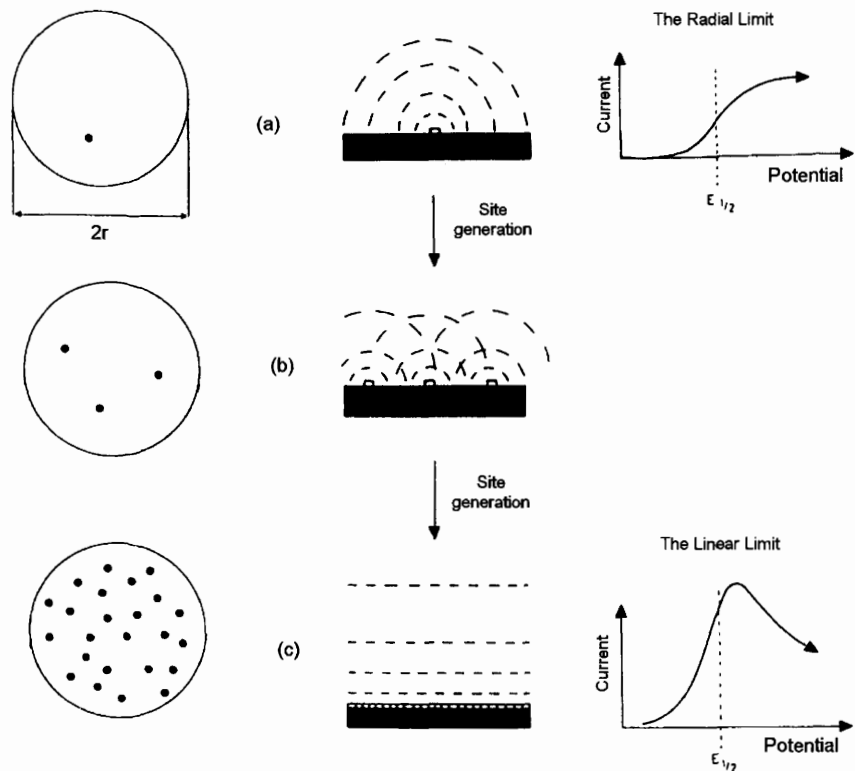


Figure 9 Schematic representation of the conversion of the diffusive movement of a species towards the electrode from radial to linear with the increase of the number of microscopic sites present at the electrode surface. Electrode of radius r

It is interesting to note that the outer mitochondrial membrane cytochrome b_5 , which is isostructural with the microsomal cytochrome b_5 ,¹⁶ reduces, under the same experimental conditions, at slightly more negative potential values ($E^{\circ'} = -0.05$ V vs. NHE),¹⁷ suggesting the presence of minor structural differences.

We consider now the electrochemical behaviour of an unusual cytochrome, namely cytochrome c_3 . This protein (FW $\approx 14\,000$), which was first found in anaerobic sulfate reducing *Desulfovibrio* bacteria and then in the facultative anaerobic *Shewanella putrefaciens*, is one of the few (at the moment) proteins containing more than one heme group¹⁸ (for instance, the crystal structures of the diheme cytochrome c_4 ,¹⁹ the triheme cytochrome c_7 ,²⁰ the octaheme cytochrome cc_3 ,²¹ the nonaheme cytochrome 9Hcc,²² up to the 24-heme hydroxylamine oxidoreductase²³ are known). As illustrated in Figure 12, cytochrome c_3 from *Desulfovibrio vulgaris* is a tetraheme cytochrome²⁴

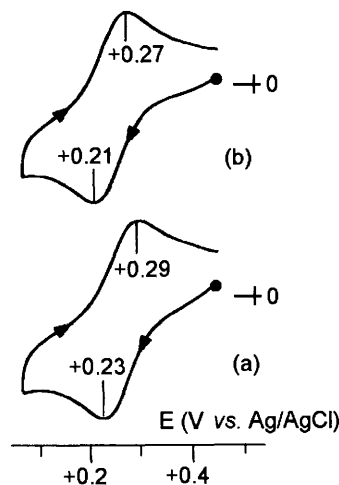


Figure 10 Cyclic voltammograms at a modified gold electrode (see text) of: (a) cytochrome c; (b) cytochrome f. Aqueous solution buffered at pH 7.3

(some structural differences exist with respect to the heme core of *Shewanella* bacteria²⁵).

Cytochrome c_3 has a positive charge ($pI = 10.5$) and displays problems of adsorption at a mercury electrode. However, these problems are avoided using a glassy carbon electrode, Figure 13,²⁶ in that, as said above, such a material behaves as a negatively charged surface.

In spite of the presence of four Fe(III)-porphyrin groups, the reduction process in cyclic voltammetry substantially appears as a single

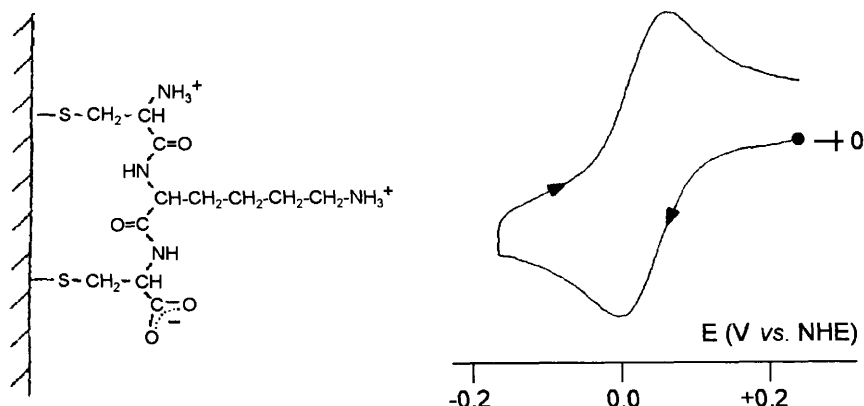


Figure 11 Cyclic voltammogram of cytochrome b_5 recorded at a gold electrode pretreated with Cys-Lys-Cys. Aqueous solution at pH 7.0 ($KCl 0.1 \text{ mol dm}^{-3}$). Scan rate 0.005 V s^{-1}

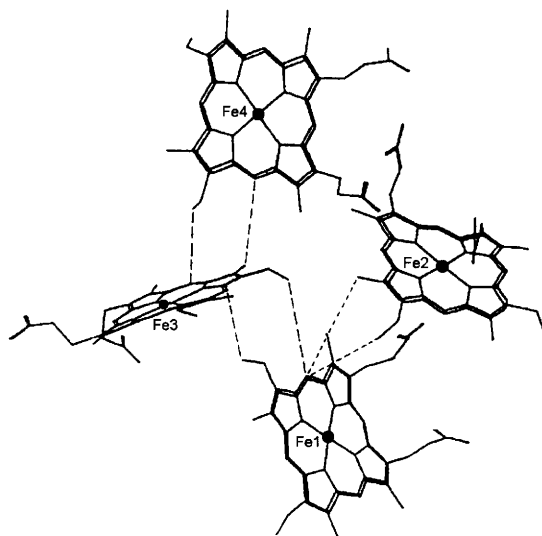


Figure 12 X-Ray structure of the active site of cytochrome c_3

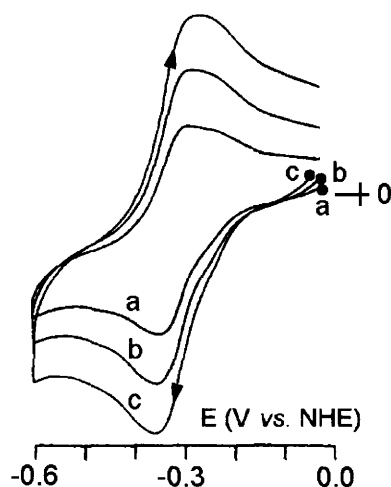


Figure 13 Cyclic voltammograms recorded at a glassy carbon electrode in an aqueous solution (pH 7) of cytochrome c_3 . Scan rates: 0.002, 0.004, 0.007 V s⁻¹

reversible four-electron process ($E^{\circ'} = -0.32$ V vs. NHE), due to essentially overlapping processes. Even if potentiometric measurements reveal four microscopic separate electron additions (in the range from -0.29 V to -0.37 V vs. NHE²⁷), it can be stated that the four electrons are added at essentially the same potential value, which implies that there is very little electronic communication among the four heme groups.

Before leaving our discussion of cytochromes, it is instructive to examine the voltammetric response of cytochrome c at a gold electrode modified by hydroxoalkanethiol carbon chains of variable length, Figure 14.²⁸

As can be seen, the increase in separation between the electrode surface and the redox-active site operated by the variable-in-length carbon chain {from $(\text{CH}_2)_3$ to $(\text{CH}_2)_{11}$ } makes the process change from electrochemically reversible to irreversible. In fact, in agreement with the (simplified) Marcus equation, $k_{\text{et}} = 10^{13}/e^{\beta d}$, the rate of the electron transfer is considerably reduced with the distance d .

The modification of electrode surfaces by adsorbates can be related to a further successful way to obtain direct electrochemical responses from enzymes.²⁹ In particular, application of films mimicking biomembranes (which are structurally constituted by assemblies of both phospholipids and proteins) allowed to achieve positive electrochemical results from enzymes, the direct redox behaviour of which escaped the above mentioned methodologies. The rationale is that most enzymes are naturally active when bound to membranes.³⁰ In this connection, biomembrane-like films are obtained by mixing surfactants and proteins, spreading the liquid mixture on the electrode surface and drying. As a typical example, Figure 15 shows the cyclic voltammetric behaviour in aqueous solution of a cytochrome P450_{cam}-DMPC film at a basal-plane pyrolytic graphite electrode (the phospholipid DMPC is dimyristoylphosphatidylcholine).³⁰ The reversibility of the Fe(III)/Fe(II) reduction is evident.

A short introduction to cytochrome P450_{cam} is needed. The term P450 historically refers to the pigment obtained by reduction of the involved

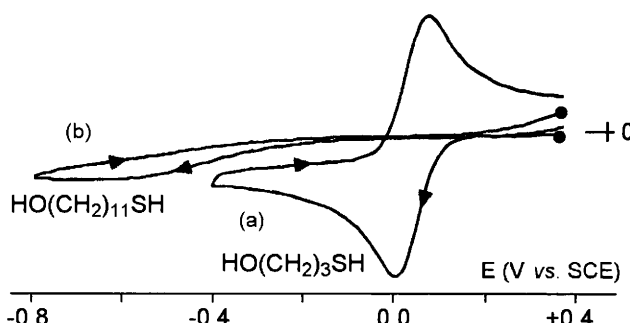


Figure 14 Cyclic voltammograms recorded in an aqueous solution of cytochrome c ($\text{pH } 7.1$) at gold electrodes modified by: (a) 3-hydroxy-1-propanthiol; (b) 11-hydroxy-1-undecanethiol. Scan rate 0.5 V s^{-1} . $T = 0^\circ\text{C}$

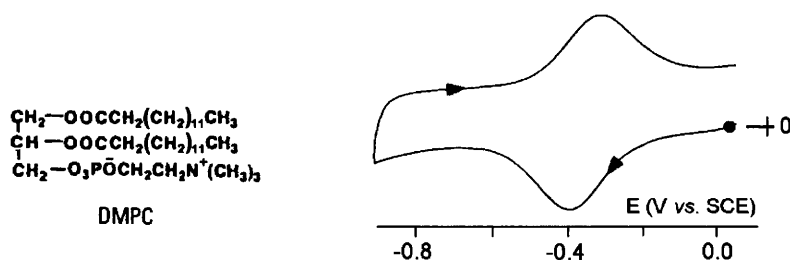


Figure 15 Cyclic voltammogram recorded in a aqueous solution ($\text{pH}=7$) of a cytochrome $\text{P}450_{\text{cam}}$ -DMPC thin film at a basal plane pyrolytic graphite electrode. Scan rate 0.1 V s^{-1}

biological system under CO atmosphere; it absorbs at 450 nm. Cytochromes P450 are ubiquitous *b*-type heme proteins containing a cysteine thiolate in axial position which catalyze hydroxylation of a wide number of aromatic or aliphatic substrates (they hence act as monooxygenases, see Chapter 9, Section 1.1).³¹ In particular, cytochrome $\text{P}450_{\text{cam}}$ catalyses the hydroxylation of camphor to isobutyrate and acetate in the soil bacterium *Pseudomonas putida*; the molecular structure of its heme core in the camphor-free form is shown in Figure 16.³²

It must be taken into account that the redox potential of protein films slightly depend on the nature of the surfactants themselves and

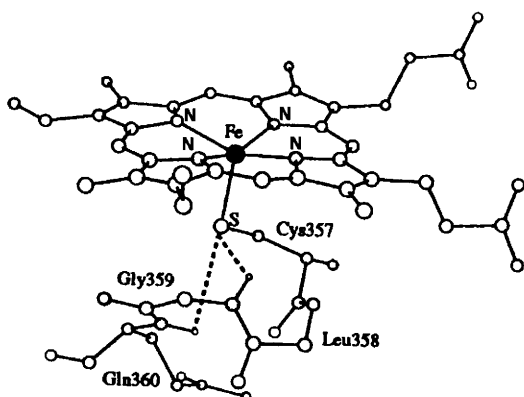


Figure 16 X-Ray structure of the active site of cytochrome $\text{P}450_{\text{cam}}$. In the camphor-bound form the bond distances are: $\text{Fe-S} \approx 2.20 \text{ \AA}$; $\text{Fe-N} \approx 2.05 \text{ \AA}$. The heme geometry of the camphor-free form is substantially similar to that of the camphor-bound form; the only difference is that the iron atom is displaced from the tetrapyrrole plane towards the axial sulfur atom by 0.30 \AA in the camphor-free form, and by 0.44 \AA in the camphor-bound form³³

Table 1 Formal electrode potentials (V vs. NHE) for the one-electron reduction of substrate-free cytochrome P450_{cam} under different experimental conditions

pH aqueous solution	7.0	7.0	7.4
film forming surfactant	DMPC	DDAB ^a	—
type of pyrolytic graphite electrode	basal plane	basal plane	edge plane
temperature	ambient	ambient	6°C
E°'	-0.12	+0.02	-0.28
reference	30	30	34

^a DDAB = didodecyldimethylammonium bromide.

also slightly differ from those obtained from proteins in solution, see Table 1.

It is interesting to note that despite the overall negative charge of cytochrome P450_{cam} ($pI = 4.55$) at pH 7, it gives a successful voltammetric response at the negatively charged edge-plane electrode. This has been attributed to the fact that a specific positive charge pattern is most likely present at the protein surface, such as to favour a local electrostatic interaction.³⁴ It is also interesting to know that the camphor-bound cytochrome P450_{cam}, the molecular structure of which is known,³³ reduces at potential values less negative than the substrate-free congener by about 0.14 V,³⁴ whereas, under CO atmosphere, it reduces at potential values less negative by about 0.06 V.³⁰

3 ELECTROCHEMISTRY OF IRON-SULFUR PROTEINS

Iron-sulfur proteins are non-heme electron carriers present in a wide range of living organisms and are known to cover different and important roles in biological processes. They will be treated here in order of their increasing iron content.

The simplest of these proteins are rubredoxins, which are bacterial proteins having a characteristic red colour (from which their name is derived) containing an FeS₄ assembly, consisting of an Fe(III) ion coordinated to four cysteine groups. The typical tetrahedral structure of this group is illustrated in Figure 17 for the rubredoxin isolated from *Clostridium pasteurianum* (FW ≈ 6100).³⁵

One obviously expects that these Fe(III) compounds exhibit a Fe(III)/Fe(II) reduction. However, since the protein has a total negative charge of -13 at pH 7 ($pI \approx 3$), a situation which is electrostatically opposite to that of cytochrome c, it is fairly intuitive that the use of a perpendicularly

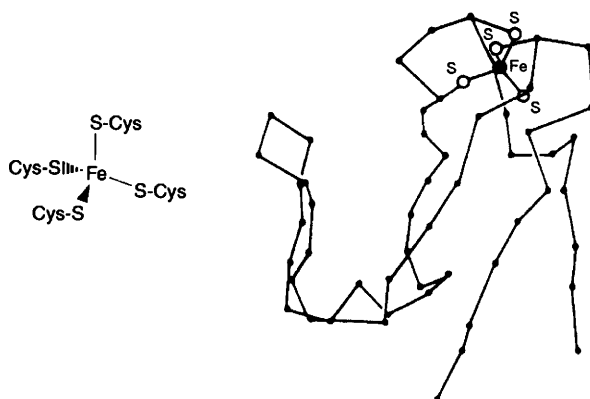


Figure 17 *X-Ray structure of the active site of the rubredoxin from Clostridium pasteurianum*

cut pyrolytic graphite electrode does not favour the electrostatic interaction between the electrode surface and the protein. As discussed above, this can be overcome by the use of positively charged additives (Mg^{2+} salts, $[Cr(NH_3)_6]^{3+}$, $[Pt(NH_3)_6]^{4+}$), which compensate the negative charge of the electrode. Figure 18 shows that through the use of such an artefact one obtains well-shaped voltammetric responses ($E^{\circ\prime} = -0.07$ V vs. NHE).³

Similar well-shaped responses have been obtained at a gold electrode using the aminoglycoside neomycin (neomycin sulfate), which is a positively charged promoter favouring the electrostatic interaction with negatively charged proteins.³⁶

Rubredoxins have $E^{\circ\prime}$ values for the Fe(III)/Fe(II) reduction which range from +0.05 V to -0.05 V vs. NHE.³⁷

The second class of iron–sulfur proteins contains an 2Fe–2S core. The first subclass of such proteins is that of 2Fe ferredoxins. These are proteins from plants or algae containing an Fe_2S_2 core formed by two Fe(III) ions linked by two sulfide bridges, each Fe(III) ion being in turn bound to two cysteinyl thiolate residues, according to the formula $[(Cys)_2Fe^{III}(\mu_2-S)_2Fe^{III}(Cys)_2]^{2-}$. Figure 19, for example, shows the molecular structure of the ferredoxin from *Spirulina platensis*.³⁸

These proteins ($FW \approx 11\,000$) bear a strongly negative charge (-18 in the oxidised state; -19 in the reduced state). It is therefore expected that treating a ‘perpendicular’ pyrolytic graphite electrode with positive additives will afford good results. In effect, under those conditions

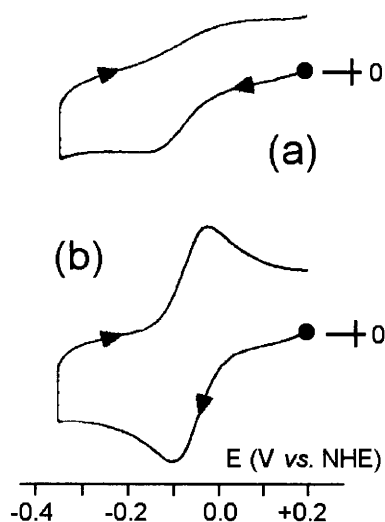


Figure 18 Cyclic voltammograms recorded at an edge-oriented pyrolytic graphite electrode in an aqueous solution ($pH\ 8$) of the rubredoxin from *Clostridium pasteurianum*. In the absence (a) and in the presence (b) of $[Cr(NH_3)_6]^{3+}$. Scan rate $0.02\ V\ s^{-1}$.

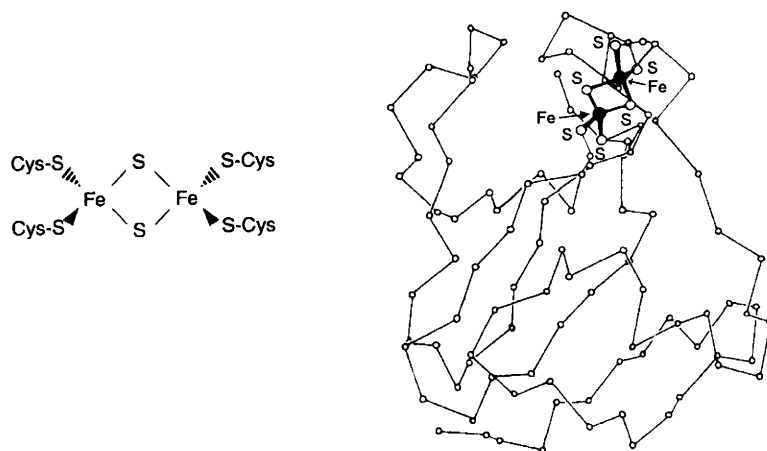


Figure 19 X-Ray structure of the active site of the 2Fe ferredoxin of *Spirulina platensis*

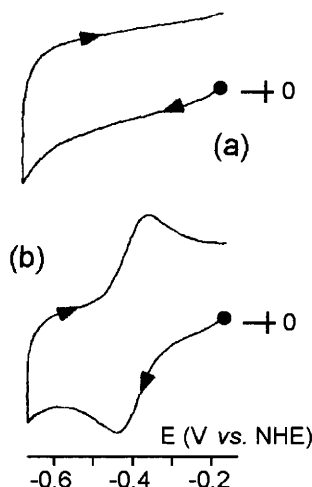
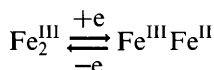


Figure 20 Cyclic voltammograms recorded at an edge-oriented pyrolytic graphite electrode in an aqueous solution ($\text{pH } 8$) of spinach ferredoxin. In the absence (a) and in the presence (b) of $[\text{Cr}(\text{NH}_3)_6]^{3+}$. Scan rate 0.02 V s^{-1}

one obtains a reversible one-electron reduction ($E^{\circ'} = -0.40 \text{ V vs. NHE}$), Figure 20.³

Concerning the 2Fe ferredoxins, the reduction process $[2\text{Fe}-2\text{S}]^{2+/+}$, which corresponds to the redox change:



occurs at potentials between -0.43 V and -0.24 V (vs. NHE).³⁷ On this basis they are classified as 'low potential' iron–sulfur proteins.

The other subclass of 2Fe–2S electron carrier proteins is constituted by the *Rieske-type iron–sulfur clusters*, or Rieske ferredoxins. This class of proteins in turn divides in two subclasses: (i) those which are active in the respiratory or photosynthetic chains (Figure 1) of eukaryotes and prokaryotes; (ii) those present in a few aromatic ring-dihydroxylating dioxygenases. Like 2Fe ferredoxins, the iron–sulfur core of these proteins is formed by two Fe(III) ions linked by two sulfide bridges, but, in contrast with the former proteins, one of the two iron centres is linked to two histidine ligands (rather than to two thiolates), according to the formula $[(\text{Cys})_2\text{Fe}^{\text{III}}(\mu_2-\text{S})_2\text{Fe}^{\text{III}}(\text{His})_2]^0$. Figure 21, which refers to the iron–sulfur assembly of the respiratory bc_1 complex,³⁹ exemplifies the molecular structure of the Rieske ferredoxins.

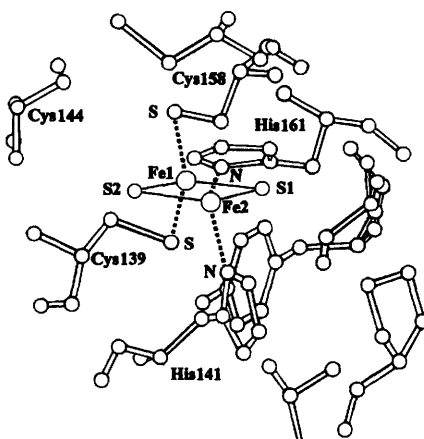


Figure 21 X-Ray structure of the Rieske ferredoxin of bovine heart mitochondrial bc₁ complex. Fe1–S ≈ 2.25 Å; Fe2–N ≈ 2.15 Å; Fe1···Fe2 = 2.71 Å; SFe1S = 105.6°; NFe2N = 90.8°

Crystal structures of the Rieske centres in photosynthetic components (namely the *b*₆*f* complex)⁴⁰ or in biphenyl dioxygenase⁴¹ display substantially similar geometrical features. It is important to consider that either in the respiratory/photosynthetic subclass or in the bacterial dioxygenase subclass the Rieske centres lie near the protein surface.^{40–42} Such common peripheral location is in some way connected with the redox aptitude of these proteins. In fact, like the 2Fe ferredoxins, the Rieske ferredoxins undergo reversible Fe₂^{III}/Fe₂^{III}–Fe^{II} one-electron reduction; in the case of the membrane-associated complexes the formal electrode potential of such a redox step markedly varies with pH, whereas in dioxygenases it is independent of pH. An earlier explanation proposed that in the respiratory/photosynthetic complexes the dependence of the potential from pH likely arose from the solvent exposure of the Fe₂S₂ cluster, which causes protonation/deprotonation of the histidinyl ligands; in contrast, the pH-independent potential of dioxygenase-type Fe₂S₂ clusters was attributed to the fact that the iron–sulfur assembly was probably buried inside the protein loops and hence inaccessible to solvent effects. In reality, the structural findings that in all cases the Rieske centres are located close to the protein surface, make rather complex the explanation of the dependence of the redox potential from pH on the basis of macroscopic structural parameters.^{41–42}

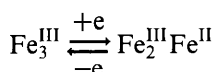
This being stated, what is really striking is the difference in redox potentials between the two Rieske subclasses. In fact,

in membrane-associated complexes the $\text{Fe}_2^{\text{III}}/\text{Fe}^{\text{III}}\text{Fe}^{\text{II}}$ reduction occurs in the range from +0.3 V⁴² to +0.15 V⁴³ (vs. NHE), at pH ≈ 7.0, whereas in dioxygenase complexes it occurs at -0.15 V (vs. NHE).^{44,45} In this connection, Figure 22 compares the cyclic voltammetric profiles exhibited by the 2Fe–2S cluster present in *bc*₁ complex⁴⁵ and that present in biphenyl-dioxygenase ferredoxin⁴² in aqueous solution, at pH ≈ 7.0.

More simple is to account for the difference between the relatively high redox potentials of Rieske ferredoxins and the low potential values of plant 2Fe ferredoxins. In fact, the dianionic form of plant ferredoxins $[(\text{Cys})_2\text{Fe}^{\text{III}}(\mu_2\text{-S})_2\text{Fe}^{\text{III}}(\text{Cys})_2]^{2-}$ certainly electrostatically disfavours electron addition with respect to the neutral charge of Rieske ferredoxins $[(\text{Cys})_2\text{Fe}^{\text{III}}(\mu_2\text{-S})_2\text{Fe}^{\text{III}}(\text{His})_2]^0$.

The next class of iron–sulfur proteins contains Fe_3S_4 clusters. The commonest example of such proteins is that of *3Fe ferredoxins*, which are found in bacteria. As shown in Figure 23, in these proteins the Fe_3S_4 cluster belongs to the class previously defined as having an ‘incomplete’ cuboidal geometry (Chapter 8, Section 1.1).⁴⁶

Potentiometric data assign to the $[\text{3Fe}-4\text{S}]^{+0}$ process:



potential values of about -0.15 V (vs. NHE).³⁷ In this connection, however, it is interesting to discuss aconitase, an enzyme which catalyses the citrate/isocitrate interconversion in the Krebs cycle. In fact, in its catalytically inactive form, it possesses a cubane-like $[\text{3Fe}-4\text{S}]^+$ core^{47a}

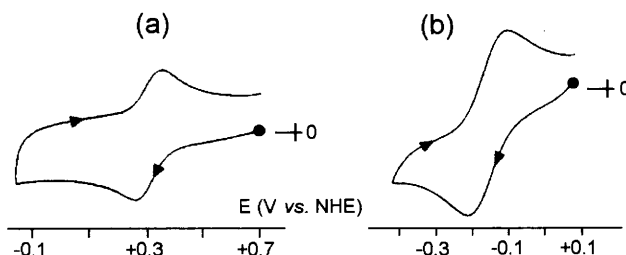


Figure 22 Cyclic voltammograms recorded in aqueous solutions of Rieske fragments from: (a) *bc*₁ complex; glassy carbon working electrode; pH 7.2; (b) (recombinant) biphenyldioxygenase; (basal) pyrolytic graphite working electrode (in the presence of the positively charged additive neomycin); pH 7.0. Scan rate 0.01 V s⁻¹

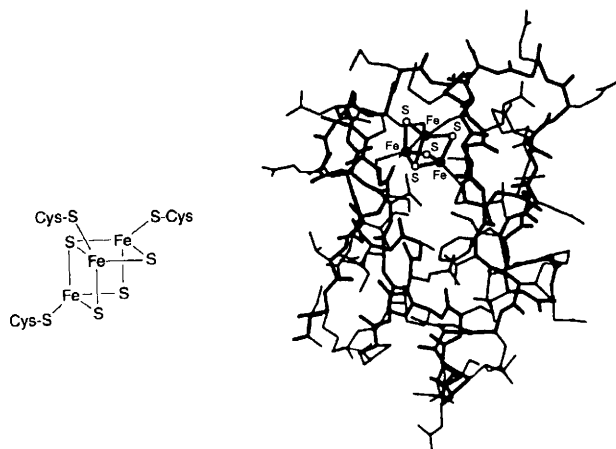


Figure 23 X-Ray structure of the active site of the 3Fe ferredoxin of *Desulfovibrio gigas*

(which can physiologically convert to the catalytically active cuboidal $[4\text{Fe}-4\text{S}]^{2+}$ form^{47b} discussed below). As illustrated in Figure 24, such an $[3\text{Fe}-4\text{S}]^+$ pseudo-cuboidal form exhibits a reversible one-electron reduction at an edge-plane pyrolytic graphite electrode ($E^\circ = -0.27$ V vs. NHE, at pH 7.4).

It is, however, evident that either the electrode potential linearly shifts towards more negative values, or the current decreases, with pH.⁴⁸

The fact that aconitase is positively charged ($pI = 8.5$), not only agrees with the successful response at the negatively charged edge-plane

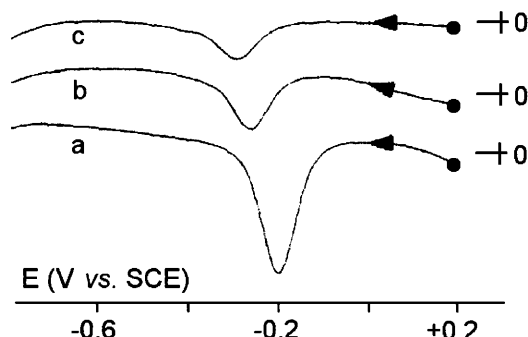


Figure 24 Square wave voltammograms recorded at an edge-oriented pyrolytic graphite electrode in buffered aqueous solutions of $[3\text{Fe}-4\text{S}]$ aconitase. (a) pH 6.2; (b) pH 7.5; (c) pH 8.2. Scan rate 0.1 V s^{-1}

pyrolytic graphite electrode, but also explains the progressive decrease of the current. In fact the increase of pH, attenuating the positive charge of the protein disfavours the electrostatic electrode–protein interaction. On the other hand, the shift of the potential with pH indicates that electron transfer is coupled to a concomitant proton transfer.⁴⁸

A further interesting aspect is given by the fact that the cuboidal Fe_3S_4 cluster of aconitase at $\text{pH} \geq 9.5$ assumes the linear Fe_3S_4 assembly discussed in Chapter 8, Section 1.1. As a matter of fact, under the experimental conditions of Figure 24, but at $\text{pH } 9.5$, the $[\text{3Fe}-4\text{S}]^{+0}$ reduction occurs at $E^{\circ'} = -0.28 \text{ V}$, or at a potential value less negative than the value of -0.35 V expected on the basis of the above cited linear cathodic shift with pH if the Fe_3S_4 would have maintained its incomplete cuboidal geometry.⁴⁸

Recently, another protein, which would possess a linear Fe_3S_4 core, has been characterized, but electrochemical data are not available.⁴⁹

Let us now pass to the proteins containing the 'complete' cuboidal Fe_4S_4 unit, already mentioned in Chapter 8, Section 1.2. They can be divided into two distinct classes:

- the so-called 'high potential' proteins (HiPIP) ($\text{FW} \approx 9800$);
- the 'low potential' 4*Fe* ferredoxins ($\text{FW} \approx 5500$).

The molecular structure of a member of each class is shown in Figure 25.^{50,51}

Potentiometric results indicate that:

- the 'high potential' proteins undergo an *oxidation* process $[\text{4Fe}-4\text{S}]^{2+/3+}$, which corresponds to the sequence:

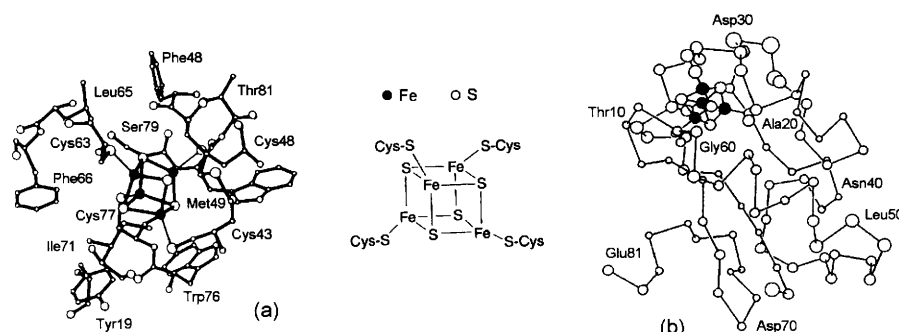
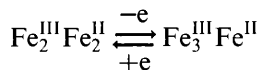
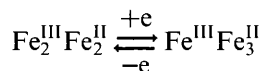


Figure 25 X-Ray structure of the active sites of the 4*Fe* proteins: (a) HiPIP *Chromatium vinosum*; (b) *Bacillus thermoproteolyticus*



characterized by potential values in the range from +0.1 V to +0.46 V (vs. NHE).³⁷

- the low potential *4Fe ferredoxins* undergo a *reduction* process [4F–4S]^{2+/+}, which is described as:



characterized by potential values in the range from -0.42 V to -0.28 V (vs. NHE).³⁷

Directly related to the single Fe₄S₄ proteins are the bacterial *8Fe ferredoxins*, which contain two Fe₄S₄ units (FW ≈ 6000), Figure 26.⁵²

These ferredoxins also possess an overall negative charge (-12 in the oxidized state). In fact, as Figure 27 shows, the use of a ‘perpendicular’ pyrolytic graphite electrode in the presence of positively charged additives (actually, decamethonium bromide = DM²⁺ = Me₃N(CH₂)₁₀NMe₃²⁺) reveals a single two-electron reduction with features of reversibility ($E^{\circ'} = -0.38$ V vs. NHE).³

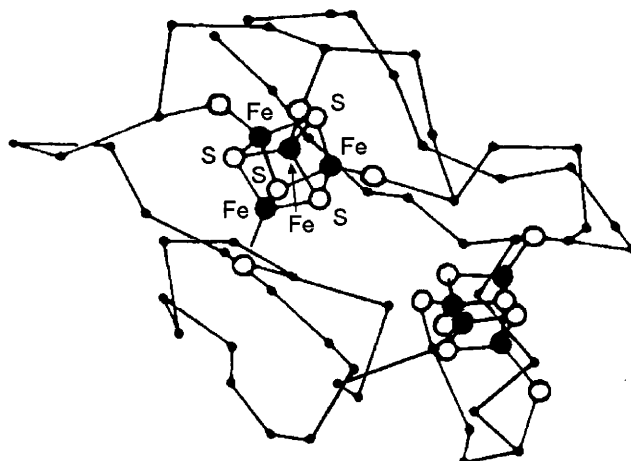


Figure 26 X-Ray structure of the active site of the 8Fe ferredoxin of *Peptococcus aerogenes*

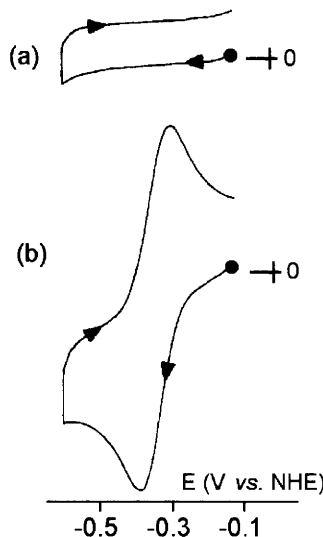
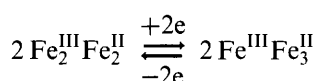


Figure 27 Cyclic voltammograms recorded at an edge-oriented pyrolytic graphite electrode in an aqueous solution ($\text{pH } 8$) of the 8Fe ferredoxin of *Clostridium Pasteurianum* in the absence (a) and in the presence (b) of DM^{2+} . Scan rate 0.02 V s^{-1}

The addition of one electron by each Fe_4S_4 cluster at the same potential indicates that there is no electronic interaction between the two iron–sulfur clusters.

For these proteins, the reduction process $[\text{2(4Fe–4S)}]^{4+/2+}$ is described as:



The process occurs at potentials of about -0.45 V (vs. NHE).³⁷

The last class of iron–sulfur proteins to be considered is that of the bacterial 7Fe ferredoxins, which contain both an Fe_3S_4 and an Fe_4S_4 cluster. Figure 28 shows the molecular structure of that from *Azotobacter vinelandii* (FW $\approx 12\,700$).⁵³

Since these proteins have a negative charge, one can expect that their voltammetric behaviour may be studied using a ‘perpendicular’ pyrolytic graphite electrode in the presence of positively charged additives. In fact, the 7Fe ferredoxin from *Sulfolabus acidocaldarius*, which has an overall negative charge of -22 , displays a well defined voltammetric response at

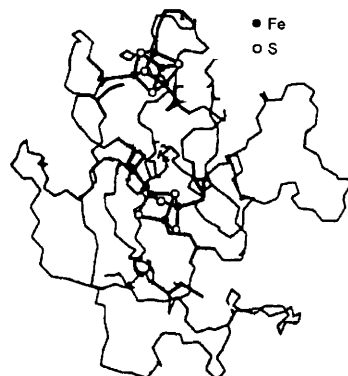


Figure 28 X-Ray structure of the active site of the 7Fe ferredoxin of *Azotobacter vinelandii*

a perpendicular graphite electrode in the presence of the positively charged additive neomycin, Figure 29.⁵⁴

As expected on the basis of the presence of an Fe_3S_4 and an Fe_4S_4 cluster the response displays multiple redox processes. As a matter of fact there are three consecutive reduction processes, namely A, B and C, with characteristics of chemical reversibility. The processes A and B involve one-electron additions, whereas process C is a two-electron step. Processes A and C are assigned to the Fe_3S_4 -centred reductions $[\text{3Fe}-4\text{S}]^{+/-}$ and $[\text{3Fe}-4\text{S}]^{0/2-}$, whereas the central system B is assigned to the Fe_4S_4 -centred reduction $[\text{4Fe}-4\text{S}]^{2+/+}$. The redox potentials (*vs.* NHE) for these processes are:

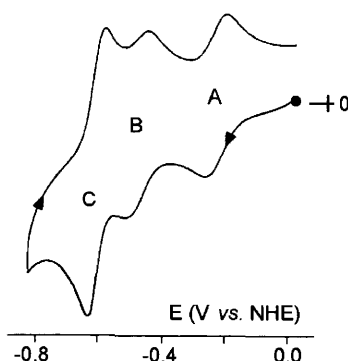
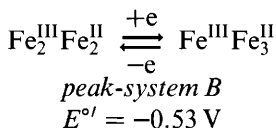
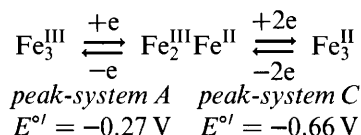


Figure 29 Cyclic voltammogram recorded at an edge-oriented pyrolytic graphite electrode in an aqueous solution ($\text{pH } 6.4$) of the 7Fe ferredoxin of *Sulfolobus acidocaldarius* in the presence of neomicin sulfate



In confirmation of the chemical and electrochemical reversibility of these processes, the one-electron reduced complex of the 7Fe ferredoxin of *Azotobacter vinelandii* has been structurally characterized. The Fe_3S_4 cluster, on which the first reduction is centred, maintains a quasi-cuboidal geometry essentially unaltered with respect to the oxidized form; some minor structural variation is observed on the peripheral amino acids.⁵⁵

It is recalled that in Chapter 9, Section 2, the electrochemical behaviour of the FeMo cofactor from FeMo-nitrogenase, was reported. It possesses a heteronuclear iron–molybdenum–sulfur (MoFe_7S_9) cluster, which has similarities with the above discussed iron–sulfur proteins.

4 ELECTROCHEMISTRY OF BLUE COPPER PROTEINS

Blue (or ‘type 1’) copper proteins (or cupredoxins) are important components of biological electron transfer processes in many organisms ranging from bacteria to animals, from fungi to plants.⁵⁶ They are characterized by:

- a very strong absorption band at ≈ 600 nm, with an extinction coefficient ($\epsilon \approx 4 \times 10^3 \text{ M}^{-1} \text{ cm}^{-1}$) 10 to 100-fold greater than most Cu(II) complexes, which imparts their blue coloration;
- an EPR spectrum characterized by small hyperfine coupling constants ($A_{\parallel} = \approx 5 \text{ mT}$) in the g_{\parallel} region;
- a Cu(II)/Cu(I) redox potential considerably higher than that of the $\text{Cu}^{2+/+}$ couple in aqueous solution (+ 0.16 V vs. NHE).

Let us start our examination with the prototypical blue protein plastocyanin, found in the thylacoid membrane of chloroplasts, where it acts as an electron carrier in photosynthesis (see Figure 1). As Figure 30 illustrates, the active site of plastocyanin is formed of a Cu(II) ion (pseudo)tetrahedrally coordinated to two histidine nitrogen atoms and

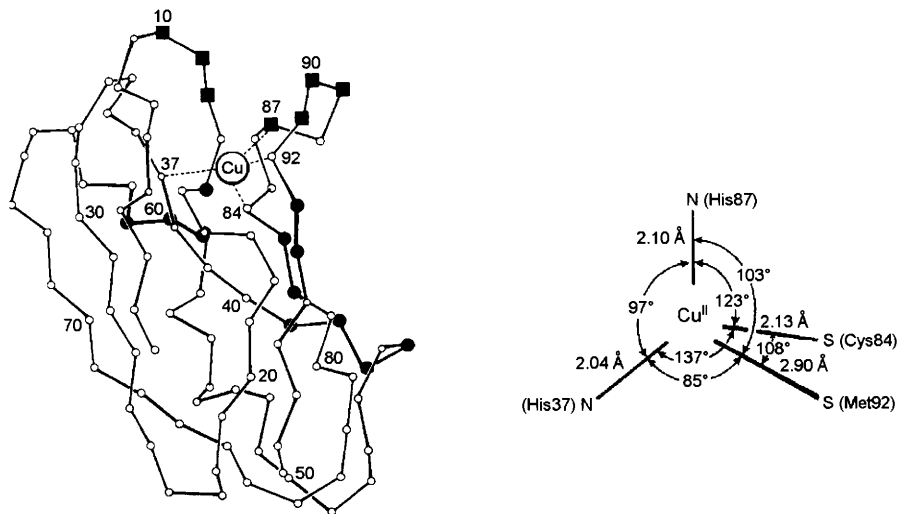


Figure 30 X-Ray structure of the active site of poplar plastocyanin

two sulfur atoms, one from a methionine and one from a cysteine residue.⁵⁷ In fact, the coordination can be typically seen as a nearly trigonal planar $(\text{His})_2\text{Cu}(\text{Cys})$ centre bound to a more remote Met ligand.

The protein ($\text{FW} = 10\,500$) has an overall negative charge ($\text{pI} = 4.2$). In particular: -8 in the oxidized state; -9 in the reduced state). It is, therefore, expected that in order to have a good voltammetric response for the $\text{Cu}(\text{II})/\text{Cu}(\text{I})$ reduction using a ‘edge-plane’ pyrolytic graphite electrode, a positively charged additive (e.g. $[\text{Pt}(\text{NH}_3)_6]^{4+}$) is necessary, Figure 31.³

The electrochemical reversibility of the $\text{Cu}(\text{II})/\text{Cu}(\text{I})$ process ($E^{\circ'} = +0.36\text{ V}$ vs. NHE) is in agreement with the X-ray structure of reduced plastocyanin, which shows that the active site maintains its trigonally distorted tetrahedral geometry with a slight lengthening (of about 0.1 \AA) of the $\text{Cu}-\text{N}$ distances.

It is interesting to note that the plastocyanin from the alga *Anabaena variabilis* has a similar structure to that isolated from poplar, while having a different amino acid sequence.⁵⁸ This results in an overall positive charge of $+2$. Thus, as shown in Figure 32a, it affords a well-shaped response for the $\text{Cu}(\text{II})/\text{Cu}(\text{I})$ reduction ($E^{\circ'} = +0.32\text{ V}$ vs. NHE) using a ‘perpendicular’ pyrolytic graphite electrode, without the presence of additives.

In confirmation of such an electrostatic interaction, the addition of positively charged additives compromises the response, Figure 32b.⁵⁹

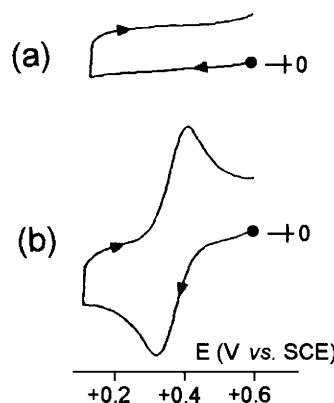


Figure 31 Cyclic voltammograms recorded at an edge-oriented pyrolytic graphite electrode in an aqueous solution ($\text{pH } 6$) of spinach plastocyanin. In the absence (a) and in the presence (b) of $[\text{Pt}(\text{NH}_3)_6]^{4+}$. Scan rate 0.02 V s^{-1}

The molecular structure of another blue protein, the 'phytocyanin' (phytocyanins are electron carriers found in the non-photosynthetic part of plants) *cucumber basic protein* ($\text{FW} = 10\,100$), also known as *plantacyanin*, is shown in Figure 33.⁶⁰

In this case also, the Cu(II) ion is coordinated to two histidine nitrogen atoms, a cysteine sulfur atom and a methionine sulfur atom with a distorted tetrahedral geometry. Since this protein has an overall positive charge ($\text{pI} = 10.6$), it gives a well formed response for the Cu(II)/Cu(I) reduction ($E^{\circ'} = +0.32 \text{ V vs. NHE}$) simply using a glassy carbon

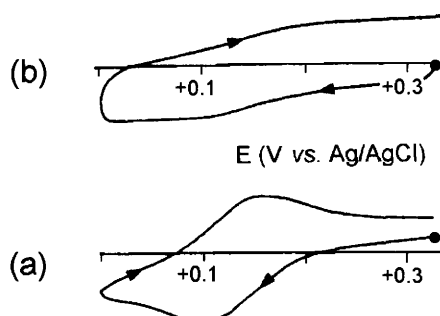


Figure 32 Cyclic voltammograms recorded at an edge-oriented pyrolytic graphite electrode in an aqueous solution ($\text{pH } 7.0$) of plastocyanin from *Anabaena variabilis*. In the absence (a) and in the presence (a) of $\text{Mg}(\text{II})$ salts. Scan rate 0.01 V s^{-1}

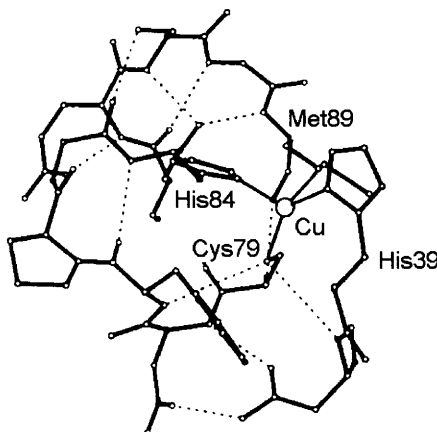


Figure 33 *X-Ray structure of the active site of plantacyanin from *Cucumis sativus* (cucumber). Bond lengths: $\text{Cu}-\text{N}_{(\text{His}39)} = 1.93 \text{ \AA}$; $\text{Cu}-\text{N}_{(\text{His}84)} = 1.95 \text{ \AA}$; $\text{Cu}-\text{S}_{(\text{Cys}79)} = 2.16 \text{ \AA}$; $\text{Cu}-\text{S}_{(\text{Met}89)} = 2.16 \text{ \AA}$*

electrode, Figure 34,⁶¹ which, as previously mentioned, behaves as the negatively charged ‘perpendicular’ pyrolytic graphite electrode.

As illustrated in Figure 35, the same redox behaviour is exhibited by the positively charged blue protein *pseudoazurin* (FW = 13 400; pI = 8.9), a class of proteins devoted to reduction of NO_2^- to NO in denitrifying bacteria.

In agreement with the electrochemical reversibility of the Cu(II)/Cu(I) reduction ($\Delta E_p = 60 \text{ mV}$ at 0.001 Vs^{-1} ; $E^{\circ'} = +0.28 \text{ V vs. NHE}$),⁶¹ which preludes a substantial maintenance of the original molecular

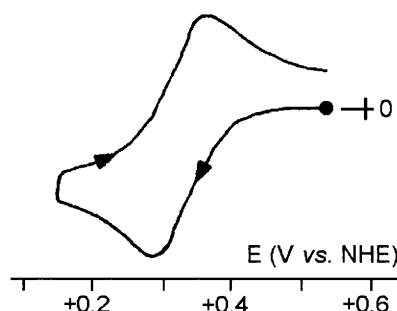


Figure 34 *Cyclic voltammogram recorded at a glassy carbon electrode in an aqueous solution (pH 6.0) of *Cucumis sativus* plantacyanin. Scan rate 0.001 V s^{-1}*

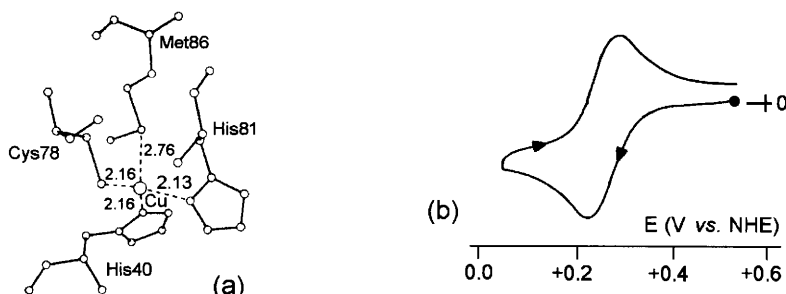


Figure 35 (a) X-Ray structure of pseudoazurin (from *Alcaligenes faecalis*). (b) Cyclic voltammogram recorded at a glassy carbon electrode in an aqueous solution ($\text{pH } 8.0$) of pseudoazurin (from *Achromobacter cyclostases*). Scan rate 0.001 V s^{-1}

structure,⁶² the reduced Cu(I) protein (crystallized at pH 7.8) maintains the pseudotetrahedral geometry of the Cu(II) congener.⁶³ In particular, as a consequence of the one-electron addition, the Cu–N(His81) elongates from 2.13 Å to 2.29 Å, the Cu–N(His40) remains unaltered at 2.16 Å, the Cu–S(Cys78) passes from 2.16 Å to 2.17 Å, and the Cu–S(Met86) elongates from 2.76 Å to 2.91 Å.

Another interesting blue protein is *stellacyanin* ($\text{FW} = 20\,000$) from the Japanese lacquer tree *Rhus vernicifera*, in which, with respect to the other cupredoxins, glutamine replaces the methionine ligand.⁶⁴ *Stellacyanin* also bears an overall positive charge ($\text{pI} = 9.9$). It, therefore, gives a reversible Cu(II)/Cu(I) response at a glassy carbon electrode in aqueous solution ($\text{pH } 7.6$).⁶¹ The formal electrode potential of the Cu(II)/Cu(I) reduction ($E^{\circ'} = +0.18 \text{ V vs. NHE}$) is the lowest among cupredoxins.

In this last connection we must mention the copper protein with the highest Cu(II)/Cu(I) potential, namely *rusticyanin*, a blue copper protein ($\text{FW} = 16\,500$) highly stable in acid solution ($\text{pH} \approx 2$), which, through its Cu(II)/Cu(I) cycling, contributes to maintaining the Fe(II)/Fe(III) respiratory chain of the gram-negative bacterium *Thiobacillus ferrooxidans*.⁶⁵ Oxidized rusticyanin possesses the typical distorted trigonal planar geometry of the other blue Cu(II) proteins, even if the weakest Cu–S(Met) bond is here even weaker ($\text{Cu–S(Met148)} \approx 2.9 \text{ \AA}$), Figure 36.⁶⁶

Since rusticyanin is positively charged ($\text{pI} = 9.1$), its electrochemical response should be tested at negatively charged electrodes (namely, edge-plane pyrolytic graphite or glassy carbon electrodes). As a matter of fact, no positive response is obtained at a carbon paste electrode, but in the presence of a promoter such as 4,4'-bipyridyl a sufficiently resolved cyclic voltammetric response is obtained, Figure 37.⁶⁷

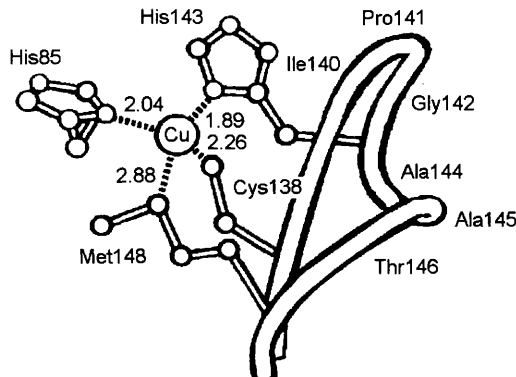


Figure 36 X-Ray structure of rusticyanin

The Cu(II)/Cu(I) reduction occurs at $E^{\circ'} = +0.47$ V vs. Ag/AgCl ($E^{\circ'} = +0.67$ V vs. NHE), the highest potential found in blue copper proteins. Attempts have been made to correlate such a potential value with the presence of the abnormally weak axial Cu-S bond. Nevertheless, more complicated structural factors seem to be responsible.⁶⁸

In agreement with the chemical reversibility of the Cu(II)/Cu(I) reduction, the reduced form of *rusticyanin* possesses a copper coordination quite similar to that of the oxidized form.⁶⁹

A further cupredoxin we consider is *mavicyanin* from green zucchini peelings (FW = 12 700),⁷⁰ a positively charged *phytocyanin* ($pI = 8.85$) the copper site of which is very similar to that of the above discussed

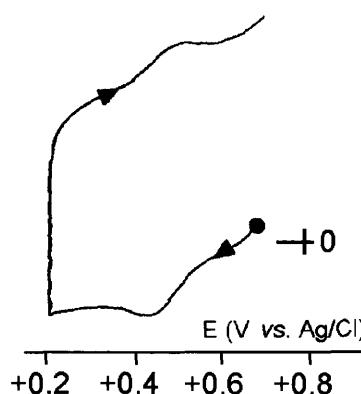


Figure 37 Cyclic voltammogram recorded at a carbon paste electrode pretreated with 4,4'-bipyridyl in an aqueous solution ($pH 2.2$) of rusticyanin

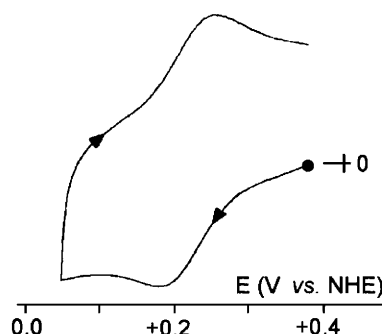


Figure 38 Cyclic voltammogram recorded at a pyrolytic graphite electrode in an aqueous solution ($pH\ 6.0$) of Zucchini mavicyanin. Scan rate $0.02\ V\ s^{-1}$

plantacyanin. Figure 38 shows the cyclic voltammogram recorded at a pyrolytic graphite electrode.⁷¹

It undergoes a reversible Cu(II)/Cu(I) reduction ($E^{\circ'} = +0.22\ V$ vs. NHE). Quite similar behaviour has been obtained using a gold electrode using bis(4-pyridyl)disulfide as promoter.⁷²

Finally, we examine *azurin*, a blue protein (FW = 14 000) devoted to bacterial electron transport, the copper centre of which has a penta-coordinate trigonal bipyramidal geometry, at variance with all the other cupredoxins, Figure 39.⁷³

In fact, in addition to the usual strong N_2CuS in-plane coordination [$Cu-N(His46)$; $Cu-N(His117)$; $Cu-S(Cys112)$], in axial positions there are either the usual weak fourth Cu–S bond [$Cu-S(Met121)$], or an

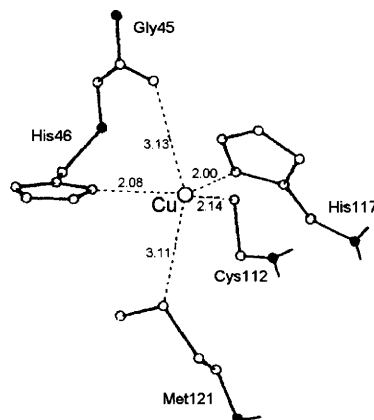


Figure 39 X-Ray structure of the copper centre in azurin from *Pseudomonas Aeruginosa*

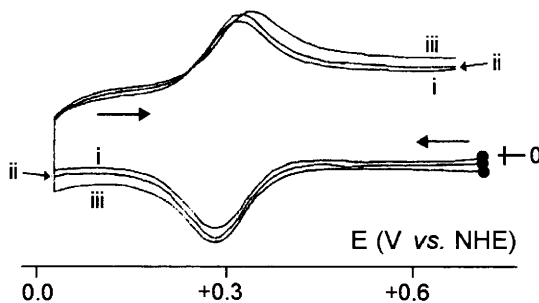


Figure 40 Cyclic voltammograms recorded at a carbon paste electrode pretreated with 4,4'-bipyridyl in an aqueous solution of azurin (from *Pseudomonas Aeruginosa*) buffered at pH 7.0. Scans at different times: (i) after 4 min; (ii) after 13 min; (iii) after 85 min

unusual fifth weak bond with the carbonyl group of a glycine residue [$\text{Cu}=\text{O}(\text{Gly}45)$].

As shown in Figure 40, azurin, which is negatively charged ($\text{pI} = 5.4$), affords a reversible $\text{Cu(II)}/\text{Cu(I)}$ reduction ($E^{\circ\prime} = +0.31 \text{ V}$ vs. NHE) at a carbon paste electrode pretreated with 4,4'-bipyridyl.⁷⁴

The slight variations of the voltammetric profile with time are due to slight absorption of the protein on the carbon electrode.

Once again electron addition causes a general elongation of the copper-to-ligand bonds [$\text{Cu}-\text{N}(\text{His}46)$: from 2.10 \AA to 2.14 \AA ; $\text{Cu}-\text{N}(\text{His}117)$: from 2.03 \AA to 2.12 \AA ; $\text{Cu}-\text{S}(\text{Cys}112)$: from 2.25 \AA to 2.28 \AA ; $\text{Cu}-\text{S}(\text{Met}121)$: from 3.13 \AA to 3.21 \AA ; $\text{Cu}-\text{O}(\text{Gly}45)$: from 2.96 \AA to 3.06 \AA][#] while maintaining the distorted trigonal bipyramidal geometry of the copper centre.^{56b}

REFERENCES

1. F.A. Armstrong, H.A.O. Hill and N.J. Walton, *Quart. Rev. Biophys.*, 1986, **18**, 261.
2. J.E. Frew, H.A. Hill, *Eur. J. Biochem.*, 1988, **172**, 261.
3. F.A. Armstrong, H.A.O. Hill and N.J. Walton, *Acc. Chem. Res.*, 1988, **21**, 407.
4. A.M. Bond, *Inorg. Chim. Acta.*, 1994, **226**, 293.
5. (a) R.A. Marcus and N. Sutin, *Biochim. Biophys. Acta.*, 1985, **811**, 265;
(b) A.W. Axup, M. Albin, S.L. Mayo, R.J. Crutchley and H.B. Gray, *J. Am. Chem. Soc.*, 1988, **110**, 435.

[#] Averaged values of the distances observed at pH 5.5 and pH 9.0, respectively.

6. G. Palmer and J. Reedijk, *Eur. J. Biochem.*, 1991, **200**, 599.
7. (a) L. Banci, I. Bertini, A. Rosato and G. Varani, *JBIC*, 1999, **4**, 824, references therein; (b) T. Takano and R.E. Dickerson, *J. Mol. Biol.*, 1981, **153**, 79; (c) T. Takano and R.E. Dickerson, *J. Mol. Biol.*, 1981, **153**, 95.
8. See for instance: (a) M.S. Graige, M.L. Paddock, J.M. Bruce, G. Feher and M.Y. Okamura, *J. Am. Chem. Soc.*, 1996, **118**, 9005; (b) A. Kannt, R.D. Lancaster and H. Michel, *Biophys. J.*, 1998, **74**, 708; (c) B. Rabenstein, G.M. Ullmann and E.W. Knapp, *Biochemistry*, 1998, **37**, 2488; (d) G.M. Ullmann, *J. Phys. Chem.*, 2000, **104**, 6293.
9. I.C.N. Diógenes, F.C. Nart, M.L.A. Temperini and Í.S. Moreira, *Inorg. Chem.*, 2001, **40**, 4884.
10. (a) F.A. Armstrong, A.M. Bond, H.A.O. Hill, B.N. Oliver and I.S. Psalti, *J. Am. Chem. Soc.*, 1989, **111**, 9185; (b) F.A. Armstrong, A.M. Bond, H.A.O. Hill, I.S.M. Psalti and C.G. Zoski, *J. Phys. Chem.*, 1989, **93**, 6485.
11. Y.-I. Chi, L.-S. Huang, Z. Zhang, J.G. Fernández-Velasco and E.A. Berry, *Biochemistry*, 2000, **39**, 7689.
12. S. Hirota, M. Endo, K. Hayamizu, T. Tsukazaki, T. Takabe, T. Kohzuma and O. Yamauchi, *J. Am. Chem. Soc.*, 1999, **121**, 849.
13. R.C.E. Durley and S. Mathews, *Acta Cryst.*, 1996, **D52**, 65.
14. S. Bagby, P.D. Barker, K. Di Gleria, H.A.O. Hill and V.J. Lowe, *Biochem. Soc. Trans.*, 1988, **16**, 958.
15. M. Rivera, R. Seetharaman, D. Girdhar, M. Wirtz, X. Zhang, X. Wang and S. White, *Biochemistry*, 1998, **37**, 1485.
16. M.J. Rodríguez-Marañón, F. Qiu, R.E. Stark, S.P. White, X. Zhang, S. Foundling, V. Rodríguez, C.L. Schilling, III, R.A. Bunce and M. Rivera, *Biochemistry*, 1996, **35**, 16378.
17. M. Rivera, M.A. Wells and F.A. Walker, *Biochemistry*, 1994, **33**, 2161.
18. I.A.C. Pereira, M. Teixeira and A.V. Xavier, *Structure and Bonding*, 1998, **91**, 65.
19. A. Kadziola and S. Larsen, *Structure*, 1997, **5**, 203.
20. (a) M. Assfalg, L. Banci, I. Bertini, M. Bruschi and P. Turano, *Eur. J. Biochem.*, 1998, **256**, 261; (b) M. Assfalg, L. Banci, I. Bertini, M. Bruschi, M.T. Giudici-Orticoni and P. Turano, *Eur. J. Biochem.*, 1999, **266**, 634.
21. M. Czjzek, F. Guerlesquin, M. Bruschi and R. Haser, *Structure*, 1996, **4**, 395.
22. P.M. Matias, L.M. Saraiva, C.M. Soares, A.V. Coelho, J. Le Gall and M.A. Carrondo, *JBIC*, 1999, **4**, 478.
23. N. Igarashi, H. Moriyama, T. Fujiwara, Y. Fukumori and N. Tanaka, *Nat. Struct. Biol.*, 1997, **4**, 276.
24. D.L. Turner, C.A. Salgueiro, J. LeGall and A.V. Xavier *Eur. J. Biochem.*, 1992, **210**, 931.

25. M. Pessanha, L. Brennan, A.V. Xavier, P.M. Cuthbertson, G.A. Reid, S.K. Chapman, D.L. Turner and C.A. Salgueiro, *FEBS Letter*, 2001, **489**, 8.
26. W.R. Hagen, *Eur. J. Biochem.*, 1989, **182**, 523.
27. M. Bruschi, M. Loufti, P. Bianco and J. Haladjian, *Biochem. Biophys. Res. Comm.*, 1984, **120**, 384.
28. S. Terrettaz, J. Cheng and C.J. Miller, *J. Am. Chem. Soc.*, 1996, **118**, 7857.
29. F.A. Armstrong, *J. Chem. Soc., Dalton Trans.*, 2002, **661**; and references therein.
30. J.F. Rusling, *Acc. Chem. Res.*, 1998, **31**, 363; and references therein.
31. Ortiz de Montellano, ed., *Cytochrome P450: Structure, Mechanism, Biochemistry*, 2nd edn, Plenum Publ. Corp., 1995.
32. T.L. Poulos, B.C. Finzel and A.J. Howard, *Biochemistry*, 1986, **25**, 5314.
33. T.L. Poulos, B.C. Finzel and A.J. Howard, *J. Mol. Biol.*, 1987, **195**, 687.
34. J. Kazlauskaitė, A.C.G. Westlake, L.-L. Wong and H. Allen O. Hill, *Chem. Commun.*, 1996, **2189**.
35. K. Watenpaugh, L.C. Sieker and L.H. Jensen, *J. Mol. Biol.*, 1980, **138**, 615.
36. M.M. Correia dos Santos, P.M. Paes de Sousa, M.L. Simões Gonçalves, C. Ascenso, I. Moura and J.J.G. Moura, *J. Electroanal. Chem.*, 2001, **501**, 173.
37. F. Capozzi, S. Ciurli and C. Luchinat, *Struct. Bonding*, 1998, **90**, 127.
38. K. Fukuyama, T. Hase, S. Matsumoto, T. Tsukihara, Y. Katsube, N. Tanaka, M. Kakudo, K. Wada and H. Matsubara, *Nature*, 1980, **286**, 522.
39. S. Iwata, M. Saynovits, T.A. Link and H. Michel, *Structure*, 1996, **4**, 567.
40. C.J. Carrell, H. Zhang, W.A. Cramer and J.L. Smith, *Structure*, 1997, **5**, 1613.
41. C.L. Colbert, M.M.-J. Couture, L.D. Eltis and J.T. Bolin, *Structure*, 2000, **8**, 1267.
42. M.M.-J. Couture, C.L. Colbert, E. Babini, F.I. Rosell, A.G. Mauk, J.T. Bolin and L.D. Eltis, *Biochemistry*, 2001, **40**, 84.
43. Y. Zu, J.A. Fee and J. Hirst, *J. Am. Chem. Soc.*, 2001, **123**, 9906.
44. T.A. Link, O.M. Hatzfeld, P. Unalkat, J.K. Shergill, R. Cammack and J. Mason, *Biochemistry*, 1996, **35**, 7546.
45. T.A. Link, W.R. Hagen, A.J. Pierik, C. Assman and G. von Jagow, *Eur. J. Biochem.*, 1992, **208**, 685.
46. C.R. Kissinger, L.C. Sieker, E.T. Adman and L.H. Jensen, *J. Mol. Biol.*, 1991, **219**, 693.
47. (a) A.H. Robbins and C.D. Stout, *Proteins*, 1989, **5**, 289; (b) A.H. Robbins and C.D. Stout, *Proc. Natl. Acad. Sci. USA.*, 1989, **86**, 3639.
48. J. Tong and B.A. Feiberg, *J. Biol. Chem.*, 1994, **269**, 24920.
49. J. Gailer, G.N. George, I.J. Pickering, R.C. Prince, P. Kohlhepp, D. Zhang, F.A. Walker and J.J. Winzerling, *J. Am. Chem. Soc.*, 2001, **123**, 10121.

50. (a) C.W. Carter, Jr., J. Kraut, S.T. Freer and R.A. Alden, *J. Biol. Chem.*, 1974, **249**, 6339; (b) E. Parisini, F. Capozzi, P. Lubini, V. Lamzin, C. Luchinat and G.M. Sheldrick, *Acta Cryst.*, 1999, **D55**, 1773.
51. K. Fukuyama, Y. Matsubara, T. Tsukihara and Y. Katsume, *J. Mol. Biol.*, 1989, **210**, 383.
52. Z. Dauter, K.S. Wilson, L.C. Sieker, J. Meyer and J.-M. Moulis, *Biochemistry*, 1997, **36**, 16065.
53. C.D. Stout, *J. Mol. Biol.*, 1989, **205**, 545.
54. J.L.C. Duff, J.L.J. Breton, J.N. Butt, F.A. Armstrong and A.J. Thomson, *J. Am. Chem. Soc.*, 1996, **118**, 8593.
55. C.D. Stout, *J. Biol. Chem.*, 1993, **268**, 25920.
56. (a) H.B. Gray and E.I. Solomon, in 'Copper Proteins', T.G. Spiro, ed., Wiley, New York, 1981; (b) A. Messerschmidt, *Struct. Bonding*, 1998, **90**, 37.
57. (a) J.M. Guss and H.C. Freeman, *J. Mol. Biol.*, 1983, **169**, 521; (b) Y. Xue, M. Ökvist, Ö. Hansson and S. Young, *Protein Sci.*, 1998, **7**, 2099; (c) T. Inoue, H. Sugawara, S. Hamanaka, H. Tsukui, E. Suzuki, T. Kohzuma and Y. Kai, *Biochemistry*, 1999, **38**, 6063.
58. U. Badsberg, A.M.M. Jorgensen, H. Gesmar, J.J. Led, J.M. Hammerstad, L.-L. Jespersen and J. Ulstrup, *Biochemistry*, 1996, **35**, 7021.
59. D.D.N. McLeod, H.C. Freeman, I. Harvey, P.A. Lay and A.M. Bond, *Inorg. Chem.*, 1996, **35**, 7156.
60. (a) J.M. Guss, E.A. Merritt, R.P. Phizackerley, B. Hedman, M. Murata, K.O. Hodgson and H.C. Freeman, *Science*, 1988, **241**, 806; (b) J.M. Guss, E.A. Merritt, R.P. Phizackerley and H.C. Freeman, *J. Mol. Biol.*, 1996, **262**, 686.
61. T. Sakurai, O. Ikeda and S. Suzuki, *Inorg. Chem.*, 1990, **29**, 4715.
62. K. Petratos, Z. Dauter and K.S. Wilson, *Acta Cryst.*, 1988, **B44**, 628.
63. E. Vakoufari, K.S. Wilson and K. Petratos, *FEBS Lett.*, 1994, **347**, 203.
64. (a) B.A. Fields, J.M. Guss and H.C. Freeman, *J. Mol. Biol.*, 1991, **222**, 1053; (b) P.J. Hart, A.M. Nersessian, R.G. Herrmann, R.M. Nalbandyan, J.S. Valentine and D. Eisenberg, *Protein Sci.*, 1996, **5**, 2175.
65. W.J. Ingledew and J.G. Cobley, *Biochim. Biophys. Acta.*, 1980, **590**, 141.
66. R.L. Walter, S.E. Ealick, A.M. Friedman, R.C. Blake II, P. Proctor and M. Shoham, *J. Mol. Biol.*, 1996, **263**, 730.
67. A.G. Lappin, C.A. Lewis and W.J. Ingledew, *Inorg. Chem.*, 1985, **24**, 1446.
68. A. Donaire, B. Jiménez, J.M. Moratal, J.F. Hall and S.S. Hasnain, *Biochemistry*, 2001, **40**, 837.
69. M.V. Botuyan, A. Toy-Palmer, J. Chung, R.C. Blake II, P. Beroza, D.A. Case and H.J. Dyson, *J. Mol. Biol.*, 1996, **263**, 752.
70. S. Maritano, A. Marchesini and S. Suzuki, *JBIC*, 1997, **2**, 177.

71. G. Battistuzzi, M. Borsari, L. Loschi, A. Ranieri, M. Sola, B. Mondoví and A. Marchesini, *J. Inorg. Biochem.*, 2001, **83**, 223.
72. K. Kataoka, M. Nakai, K. Yamaguchi and S. Suzuki, *Biochem. Biophys. Res. Commun.*, 1998, **250**, 409.
73. H. Nar, A. Messerschmidt, R. Huber, M. Vandekamp and G.W. Canters, *J. Mol. Biol.*, 1991, **221**, 765.
74. R. Dhesi, T.M. Cotton and R. Timkovich, *J. Electroanal. Chem.*, 1983, **154**, 129.

CHAPTER 13

Linear Correlations Between the Redox Potential and Other Chemical and Physico-chemical Parameters

The redox potential of an electron transfer process involving a metal complex is influenced by various factors; typically, in addition to the many times cited inductive effects of the ligands (together with the eventual substituents of the ligands themselves) and the stereochemistry of the redox couples, the degree of solvation of the complex and the temperature also play an important role. In an attempt to rationalize the effects of these factors on the redox potential, as well as the relationship between the redox potential and the spectroscopic properties of the complex, linear correlations between redox potential and widely differing chemical and physico-chemical properties have been investigated.

Since such correlations belong to a series of treatments which are commonly identified as *Linear Free Energy Relationships* (LFER), and as only the *standard potential* is an electrochemical quantity directly linked with *free energy* ($\Delta G^\circ = -n \cdot F \cdot \Delta E^\circ$), one can make use of these mathematical treatments only in cases of *electrochemically reversible* redox processes (or in the limit of *quasireversibility*). Only in these cases does the measured redox potential have thermodynamic significance.

1 REDOX POTENTIAL AND ELECTRONIC EFFECTS OF THE LIGANDS

The electronic effects that ligands can have on the redox potential of a metal complex have been considered in the following way:

- *electron-donating* ligands render oxidation *easier* and reduction *more difficult*
- *electron-withdrawing* ligands render oxidation *more difficult* and reduction *easier*.

In order to put the discussion on a more quantitative basis we consider one of the more traditional and conceptually simpler methods. Obviously, when speaking about 'ligands' one must take into account that a ligand can bear different substituents. To correlate the variation of the redox potential of a metal complex with the electronic effects played by the substituents of an *aromatic ring* ligand one uses the *Hammett equation* in its electrochemical form:

$$\Delta E^{\circ'} = \rho \cdot \sigma$$

where:

$\Delta E^{\circ'}$ = the difference between the redox potential of the complex containing the substituted ligand and that of the complex containing the unsubstituted ligand

ρ = constant which measures the sensitivity of the redox potential to the electronic effects of the substituents

σ = Hammett parameter which assigns a numerical value to the electronic effects of the substituents

The values of the Hammett 'constant', σ , normally refer to the *inductive* electronic effects of the substituents in *meta* (σ_m) or *para* (σ_p) positions of aromatic rings.

Electron-withdrawing groups have *positive* σ values, whereas *electron-donating* groups have *negative* σ values.

When the substituent groups enter resonance with the reaction centre through π bonds, it may be necessary to modify the values of the σ constants on the basis of either the inductive or resonance effects. In this case the situation becomes complicated and will not be treated further here.¹

Values of the constants σ_m and σ_p for a number of substituents are reported in Table 1. A more extensive list of substituents can be found in the literature.¹

The Hammett equation has been further extended to include substituents of aliphatic systems too. In this case the constants that quantify the inductive effects, which are represented as σ^* , have different values compared to those concerned with aromatic systems and are defined as *Taft constants*. Some values of these latter are also reported in Table 1.

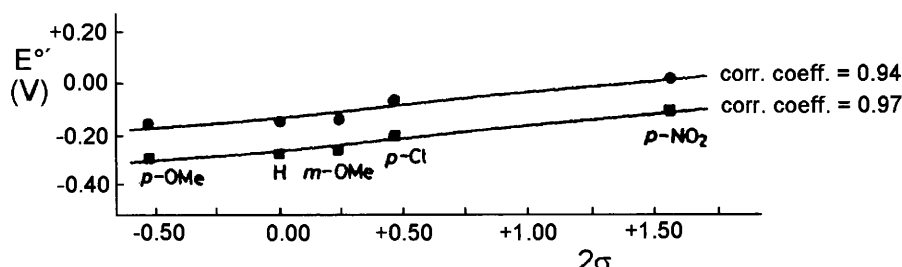
As an example of the application of this method we can consider the cobalt complexes of bis(salicyldeneamine-3-propyl)amine,

Table 1 σ (for substituents of aromatic rings) and σ^* (for substituents of aliphatic groups) values for common substituents

Substituent	σ_m	σ_p	σ^*
H	0.00	0.00	+0.49
CH ₃	-0.07	-0.17	0.00
CF ₃	+0.43	+0.54	
CH ₃ CH ₂	-0.07	-0.15	-0.10
CH=CH ₂	+0.06	-0.04	
C≡CH	+0.21	+0.23	
CH ₃ CH ₂ CH ₂	-0.06	-0.13	-0.11
(CH ₃) ₂ CH	-0.04	-0.15	-0.19
CH ₃ CH ₂ CH ₂ CH ₂	-0.08	-0.16	-0.13
(CH ₃) ₂ CHCH ₂	-0.07	-0.12	-0.12
(CH ₃) ₃ C	-0.10	-0.20	-0.30
CH ₃ O	+0.12	-0.27	-0.22
CH ₃ S	+0.15	0.00	
CH ₃ CH ₂ O	+0.10	-0.24	-0.18
CHO	+0.35	+0.42	
COOCH ₃	+0.37	+0.45	+2.00
C ₆ H ₅	+0.06	-0.01	+0.60
N(CH ₃) ₂	-0.16	-0.83	
NH ₂	-0.16	-0.66	
NO ₂	+0.71	+0.78	+0.97
F	+0.34	+0.06	+0.41
Cl	+0.37	+0.23	+0.37
Br	+0.39	+0.23	+0.38
I	+0.35	+0.18	+0.38

[Co(R-X-Saldpt)] (already mentioned in Chapter 5, Section 5, and Chapter 9, Section 1.3). The values of the Co(II)/Co(III) oxidation potential for different substituents are compiled in Chapter 9, Table 1.

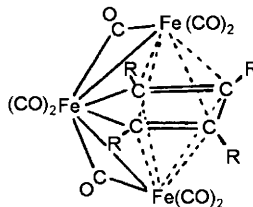
As Figure 1 shows, there is a linear relationship between the redox potentials and the electronic effects of the substituents for the two series

**Figure 1** Dependence of the formal electrode potentials of the Co(II)/Co(III) oxidation for [Co(R-X-Saldpt)] derivatives on the electronic effects of the substituents (■) $R=H$; (●) $R=Me$

of derivatives ($R=H, Me$) if the substituents are considered to be in a *meta* or *para* position with respect to the phenolic oxygen. In contrast, if one prepares an analogous plot considering the substituents in *meta* or *para* position with respect to the $CH=N$ group, a linear relationship is not obtained.

This implies that the path by which the substituents drive electron density towards, or attract electron density from, the cobalt atom passes through the $XC_6H_4-O-Co-O-C_6H_4X$ bonds. It is noted that the molecules under study have two aromatic rings. Therefore, the parameter 2σ is reported along the x -axis.

To illustrate an example of substituents on aliphatic ligands, let us consider the case of a few triferric-metallacycle clusters of general formula $[Fe_3(CO)_8(RC_2R)_2]$, Scheme 1.



Scheme 1

These complexes undergo two consecutive one-electron reductions with features of chemical and electrochemical reversibility both in $MeCN$ and CH_2Cl_2 solution.² Table 2 summarizes the formal electrode potentials for the first reduction process and the sums of the Taft constants of the various substituents for each complex.

Table 2 *Formal electrode potentials (V vs. SCE) for the first reduction process of $[Fe_3(CO)_8(RC_2R)_2]$ complexes together with the relative Taft constants*

Complex	$E^{\circ'}$		
	$MeCN$	CH_2Cl_2	$\Sigma \sigma^*$
$[Fe_3(CO)_8(PhC_2Ph)_2]$	-0.66	-0.75	+ 2.40
$[Fe_3(CO)_8(EtC_2Et)_2]$	-0.81	-0.94	-0.40
$[Fe_3(CO)_8(PhC_2Ph)(EtC_2Et)]$	-0.76	-0.83	+ 1.00
$[Fe_3(CO)_8(PhC_2Ph)(HC_2H)]$	-0.70	-0.74	+ 2.18
$[Fe_3(CO)_8(EtC_2Et)(HC_2H)]$	-0.81	-0.86	+ 0.78
$[Fe_3(CO)_8(MeC_2Ph)(HC_2H)]$	-0.74	-0.83	+ 1.58
$[Fe_3(CO)_8(PhC_2Me)(HC_2H)]$	-0.73	-0.79	+ 1.58
$[Fe_3(CO)_8(MeC_2Ph)(PhC_2Ph)]$	-0.73	-0.80	+ 1.80
$[Fe_3(CO)_8(PhC_2Me)(PhC_2Ph)]$	-0.72	-0.78	+ 1.80

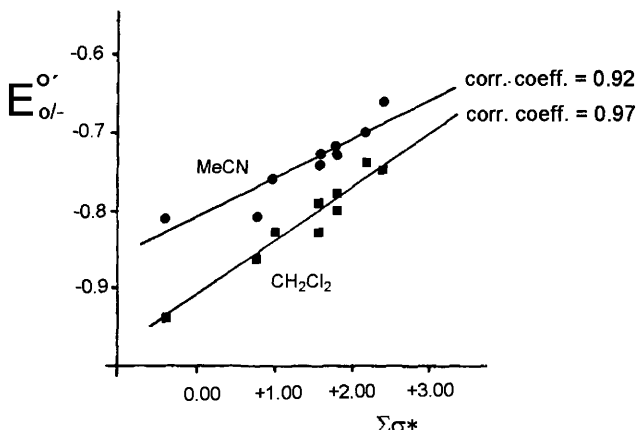


Figure 2 The dependence of the reduction potential of the series $[\text{Fe}_3(\text{CO})_8(\text{RC}_2\text{R})_2]$ on the sum of the Taft constants of the different substituents

As illustrated in Figure 2, there is a good linear correlation between $E^{\circ'}$ and $\Sigma\sigma^*$ in both solvents.

The linear dependence of the sum of the four substituents' Taft constants suggests that the electron density due to the substituents is delocalized along the entire butadiene system.

As already mentioned, in order to evaluate the electronic effects of the ligands on the redox activity of a metal complex one can also use spectroscopic data (usually, IR or NMR). As an example we again consider the complexes $[\text{Fe}_3(\text{CO})_8(\text{RC}_2\text{R})_2]$ for which IR and NMR data have been reported, Table 3.²

Table 3 Formal electrode potentials (V vs. SCE) for the first reduction process of complexes $[\text{Fe}_3(\text{CO})_8(\text{RC}_2\text{R})_2]$ and relative IR and NMR spectroscopic parameters

Complex	$E^{\circ'}$		v_{CO}^a (cm^{-1})	$\delta^{(13)\text{CO}}$ (ppm)
	MeCN	CH_2Cl_2		
$[\text{Fe}_3(\text{CO})_8(\text{PhC}_2\text{Ph})_2]$	-0.66	-0.75	2005	203.0
$[\text{Fe}_3(\text{CO})_8(\text{EtC}_2\text{Et})_2]$	-0.81	-0.94	1990	205.9
$[\text{Fe}_3(\text{CO})_8(\text{PhC}_2\text{Ph})(\text{EtC}_2\text{Et})]$	-0.76	-0.83	1999	204.2 ^b
$[\text{Fe}_3(\text{CO})_8(\text{PhC}_2\text{Ph})(\text{HC}_2\text{H})]$	-0.70	-0.74	2004	203.8 ^b
$[\text{Fe}_3(\text{CO})_8(\text{EtC}_2\text{Et})(\text{HC}_2\text{H})]$	-0.81	-0.86	1996	204.8 ^b
$[\text{Fe}_3(\text{CO})_8(\text{MeC}_2\text{Ph})(\text{HC}_2\text{H})]$	-0.74	-0.83	1998	204.1 ^b
$[\text{Fe}_3(\text{CO})_8(\text{PhC}_2\text{Me})(\text{HC}_2\text{H})]$	-0.73	-0.79	2001	204.1 ^b
$[\text{Fe}_3(\text{CO})_8(\text{MeC}_2\text{Ph})(\text{PhC}_2\text{Ph})]$	-0.73	-0.80	2005	203.9 ^b
$[\text{Fe}_3(\text{CO})_8(\text{PhC}_2\text{Me})(\text{PhC}_2\text{Ph})]$	-0.72	-0.78	2003	203.8

^a The most intense CO band sensitive to electronic variation; ^b average value.

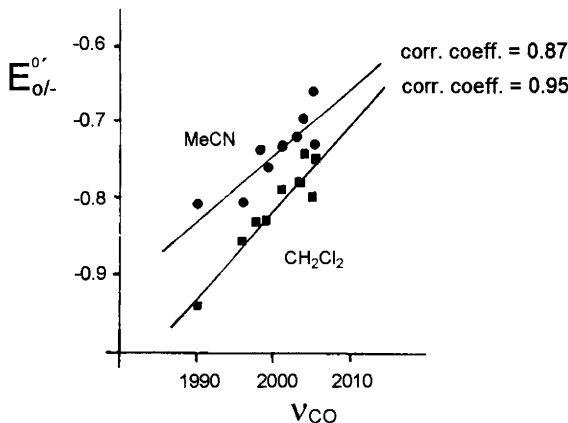


Figure 3 The dependence of the reduction potential of $[Fe_3(CO)_8(RC_2R)_2]$ on the ν_{CO} of the sharp band more sensitive to electronic variation

Figures 3 and 4 show the trend of the redox potential as a function of the stretching frequency and the chemical shift of the CO group, respectively.

In both cases there is a good linear correlation.

As a general conclusion, one may state that in a homologous series of complexes a linear correlation exists between the redox potential and the spectroscopic parameters when the variation of both parameters are dictated purely by the *electronic effects* of the substituents. If these effects are present concomitant with *steric effects* induced by the substituents,

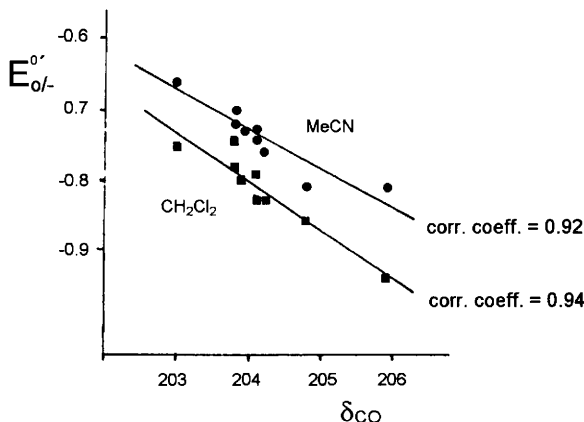


Figure 4 The dependence of the reduction potential of $[Fe_3(CO)_8(RC_2R)_2]$ on the average ^{13}C chemical shift of the CO groups

it may happen that one does not observe a linear relationship, unless other parameters are introduced (through the use of multi-parameter equations) into the correlation equation which take into account the steric effects.

More recent approaches to the effects of the ligands on the redox activity of metal complexes are based upon the assumption that the electrode potential of a redox change involving a metal complex is determined by the additivity of the electronic contribution of all the ligands linked to the metal centre, or to the overall balance between the σ -donor and the π -acceptor capability of each ligand.³ In particular two ligand electrochemical parameters have gained popularity:

- the so-called 'Pickett-Pletcher' parameter, P_L ,^{4a}
- the so-called 'Lever' parameter, E_L .^{4b}

Since the two parameters are related each other by the empirical relationship:^{4b}

$$P_L = 1.17 \cdot E_L - 0.86$$

it is possible to pass from one scale to the other.

Both treatments are essentially concerned with octahedral metal complexes (even if these are recent attempts to apply it to other geometrical assemblies).⁵

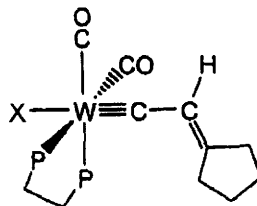
The numerical value of P_L assigned to each ligand reflects the net difference between its π -acceptor and its σ -donor ability. Table 4 compiles a list of P_L (and E_L) values for some common ligands.

Table 4 P_L and E_L values (in V) for a few common ligands

Substituent	P_L	E_L	Substituent	P_L	E_L
Br^-	-1.17	-0.22	N_2	-0.07	+0.68
$-\text{CH}=\text{CH}_2$	-	+0.76	N_3^-	-1.26	-0.30
CO	0.00	+0.99	NH_3^+	-0.77	+0.07
$(\text{COO})_2^-$	-	-0.17	NO_3^+	+1.40	-
$\text{C}_6\text{H}_5\text{N}$	-0.59	+0.25	NO_2^-	-	+0.02
CN^-	-1.00	+0.02	NO_3^-	-	-0.11
Cl^-	-1.19	-0.24	OCN^-	-1.16	-0.25
ClO_4^-	-	+0.06	OH^-	-1.55	-0.59
F ⁻	-	-0.42	PMe_3	-	+0.33
H_2O	-	+0.04	$\text{P}(\text{OPh}_3)$	-0.18	+0.58
I ⁻	-1.15	-0.24	PPh_3	-0.35	+0.39
MeCN	-0.58	+0.34	SCN^-	-0.88	-0.06

Obviously, those ligands which have weak π -acceptor character (which favours oxidation) and strong σ -donor character (which also favours oxidation) will display a low P_L and will contribute to a decrease in the oxidation potential (or an increase in the reduction potential). The opposite happens for strong π -acceptors and weak σ -donors.

Let us start with an example of the Pickett–Pletcher treatment. Consider the series of the octahedral alkenylcarbyne tungsten complexes represented in Scheme 2.⁶



Scheme 2

These derivatives undergo an irreversible oxidation process. Assuming that such electron removal involves an electrochemically reversible process complicated by fast chemical reactions, a thermodynamic meaning can be assigned to the different peak potential values.

Table 5 compiles the oxidation potentials of a few members of the series and Figure 5 shows the relative plot of the oxidation potentials vs. the respective P_L parameters.⁶

The plot is linear and obeys the equation:

$$E_P = 0.80 \cdot P_L + 1.80$$

Table 5 *Electrochemical parameters for the oxidation of the complexes $[W(X)(CO)_2(dppe)(CCH=R)]$ ($dppe = PPh_2CH_2CH_2PPh_2$; $R = C_5H_4$) in MeCN or thf solution*

X	E_p (V, vs. SCE)	P_L (V, vs. NHE)
CO ^a	+ 1.78	0.00
CN	+ 1.07	-1.00
Cl	+ 0.82	-1.19
MeCN ^b	+ 1.34	-0.58
OCN	+ 0.85	-1.16
Pme ₃	+ 1.45	-0.47 ^c
SCN	+ 1.04	-0.88

^a *cis* isomer; ^b monocation; ^c estimated from E_L .

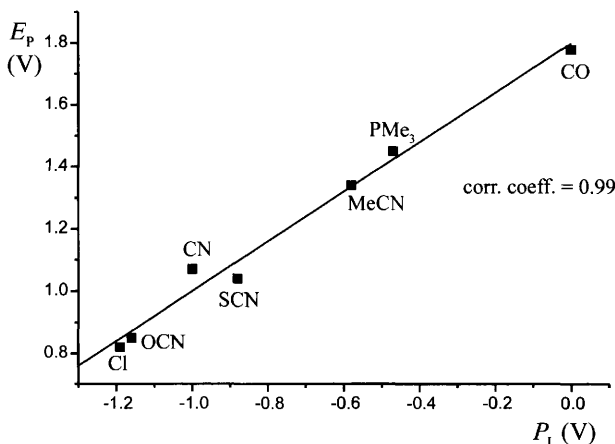


Figure 5 Plot of the peak potential for the oxidation of $[W(X)(CO)_2(dppe)]$ ($CCH=R$) vs. P_L

According to the theory of the ligand additivity, the oxidation potentials of a series of complexes having a common metal fragment M_S are governed by either the electronic effects of the variable L ligand (the net π -acceptor minus σ -donor capability), P_L , or the electron richness of the metal fragment itself, E_S , (the higher E_S , the lower the electron richness):

$$E_{\text{ox}}\{M_S L\} = \beta \cdot P_L\{L\} + E_S$$

where β is a measure of the sensitivity of the redox potential to the electronic effects of the ligands or the polarizability of the metal site (the lower β , the lower the polarizability).

This means that in the present series the richness of the $[W(X)(CO)_2(dppe)(CCH=R)]$ fragment E_S is 1.80 and the sensitivity β is 0.80.

Comparison of E_S and β values for different families of complexes can account for, or allows one to predict their reactivity.^{4a,6}

In conclusion, the present treatment offers the opportunity to evaluate the electronic effects played on completely changing one of the ligands present in a certain metal complex (in contrast to the Hammett or Taft treatment, which make reference to the substituents of the same ligand).

The Lever treatment is of wider application in that it can be extended to (six-coordinate) complexes which have only the same central metal ion in common but totally different ligands. Consider the series of iron(II) complexes in Table 6.^{4b}

Table 6 Formal electrode potentials (V , vs. NHE) for the $\text{Fe(II)}/\text{Fe(III)}$ redox change of a series of iron complexes in non-aqueous solvents and sum of the electrochemical E_L parameters (V , vs. NHE) of all the ligands

Complex	$E^{\circ'}$	ΣE_L
$[\text{Fe}(\text{NCMe})_6]^{2+}$ (1)	+2.64	2.74
$[\text{Fe}(\text{phen})_3]^{2+}$ (2)	+1.41	1.56
$[\text{Fe}(\text{bipy})_3]^{2+}$ (3)	+1.27	1.55
$[\text{Fe}(\text{terpy})_3]^{2+}$ (4)	+1.33	1.49
$[\text{Fe}(\text{phendione})_3]^{2+}$ (5)	+1.6	1.68
$[\text{Fe}(\text{bipy})_2(\text{CN})_2]^{2+}$ (6)	+0.71	1.08
$[\text{Fe}(\text{phen})_2(\text{MeCN})_2]^{2+}$ (7)	+1.79	1.98
$[\text{Fe}(\text{CN})_6]^{4-}$ (8)	-0.31	0.12

As Figure 6 shows there is a good linear correlation between the formal electrode potentials and the sum of the ligand parameters. Such a linear trend obeys the expression:

$$E^{\circ'} = 1.14 \cdot \Sigma E_L - 0.43$$

In this connection, it must be considered that according to the theory,^{4b} the following relationship holds:

$$E_{\text{obs}} = S_M \cdot \Sigma E_L + I_M$$

which means that the experimental electrode potential is a linear function of ΣE_L and the slope S_M reflects the sensitivity of the metal core towards

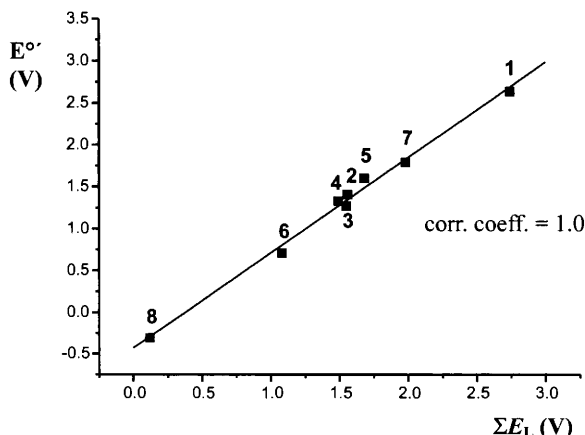


Figure 6 Plot of the $\text{Fe(II)}/\text{Fe(III)}$ electrode potential and the overall ligand contribution ΣE_L for a series of iron(II) complexes

the ligands. In this connection, note that an S_M value of 1 for a series of metal complexes implies that the dependence of the electrode potential from the ligands is of the same order of that which the same ligands would exert towards the Ru(III)/Ru(II) reference couple: the lower S_M , the lower such dependence. Importantly, different series of complexes exhibiting the same S_M value are likely to possess the same stereochemistry, and spin state. The intercept I_M in turn essentially depends on the access to low or high oxidation states of the metal under study.

It must be taken into account that the Lever equation also allows one to predict reliably the formal electrode potential of a redox process for those complexes which are eventually so sensitive to the working conditions to make difficult the relative experimental measurement.

Finally, a further refinement of the Lever equation^{4c} allows one, in applying the treatment of ligand electrochemical parameters E_L , to account for the presence of eventual aromatic or aliphatic ligands bearing different substituents, *i.e.* to take into account the Hammett, or Taft, substituent parameters σ (above discussed) for a certain ligand. The expression is:

$$E_{\text{obs}} = S_M \cdot \Sigma E_L + 2.303 \frac{R \cdot T}{n \cdot F} \rho \cdot \Sigma \sigma + I_M$$

Here, ρ measures the sensitivity of the redox potential to substitution at a ligand L, and $\Sigma \sigma$ is the sum of the Hammett, or Taft, parameters of the substituents attached to L. The symbols R, T, n, F have their usual meaning.

2 REDOX POTENTIAL AND SOLVENT EFFECTS

The data of Table 2 have already effectively shown that the solvent induces appreciable variations in the formal electrode potential of redox processes. Furthermore, such an effect was described during the discussion of ferrocene oxidation in Chapter 4, Section 1.1.

When one tries to rationalize the effect of the solvent on any type of chemical reactivity, considerable problems are encountered due to the multiple factors responsible for the solute/solvent interaction.⁷ One of the common ways to take into account the solvent effect is to consider it in terms of polarity (or polarizability) of the solvent. However, this concept is vague and difficult to define precisely. A first tentative

explanation was given in terms of electrostatic models of solvation which essentially take into account:

- the *dielectric constant* of the solvent
- the *dipole moment* of the solvent.

The dielectric constant is a measure of the variation of the intensity of the electric field observed between the plates of a capacitor when it is taken from vacuum into the solvent.

An electric field induces a dipole moment in non-polar solvent molecules and consequently these molecules become electrostatically aligned with the electric field according to the field polarity. Hence, the dielectric constant describes the capacity of a solvent to separate the electric charges of a solute through an appropriate orientation of its molecules.

The solute/solvent interaction is, however, a much more complex physical effect than the simple creation of dipole moments in solvent molecules and their subsequent reorientation operated by the charges of the salts forming the solute. In fact, one can consider:

- the electrostatic interactions due either to inductive effects, or to instantaneous dispersion forces (*i.e.* van der Waals bonds), or to formation of hydrogen bonds,
- the interactions between Lewis bases and Lewis acids (electron pairs, donor and acceptor atoms)
- the solvophobic interactions.

Therefore, one must accept that the description of the solvent effect is rather complex and cannot be simplistically made on the basis of single physical parameters. A large number of parameters (including empirical parameters) must be considered which derive from thermodynamic calculations (equilibrium constant) and kinetic calculations (rate constants) performed on a large number of chemical reactions.

Consequently, it is also apparent that the solvent effect can be described on the basis of mathematical relationships between parameters which fall within the relationships defined as *free energy correlations*. In fact, the more parameters that are included in the mathematical treatment (multi-parameter equations), the better the description of the solvent effect that results. However, we will consider here only those parameters which take into account the solvent effect on redox potentials.

The empirical parameters most frequently encountered in the description of the solvent effect (still in non-SI units) are:⁷

- (i) the Dimroth–Reichardt parameter $E_T(30)$ (kcal mol $^{-1}$)
- (ii) Gutmann donor number DN (kcal mole $^{-1}$)
- (iii) Gutmann acceptor number AN (dimensionless)
- (iv) Kosower value Z (kcal mol $^{-1}$)
- (v) Brooker parameters χ_R and χ_B (kcal mol $^{-1}$)
- (vi) the Knauer–Napier parameter A_N (G)
- (vii) Brownstein parameter S (dimensionless)
- (viii) the Kamlet–Taft solvatochromic parameters α , β , π^* (cm $^{-1}$)
- (ix) the Koppel–Palm parameter B (cm $^{-1}$)
- (x) the Kagiya electron donor and electron acceptor power $\Delta\nu_D$, $\Delta\nu_A$ (cm $^{-1}$)

The measurement units of each parameter give a preliminary indication of the nature of these parameters, but for a more precise idea of their chemical and physical significance the reader is referred to the literature^{7–9}. In the present context it is sufficient to bear in mind that most of these empirical parameters can be subdivided into parameters which measure the *Lewis acidity* (hence, the electrophilic power) and *Lewis basicity* (hence, the nucleophilic power) of a solvent.

Table 7 reports a few of these empirical parameters for those solvents used most frequently in electrochemistry, together with dielectric constants (ϵ) and dipole moments (μ , in Debye).

Table 7 Empirical parameters for solvents commonly used in electrochemical studies

Solvent	(acidity)			(basicity)		(polarity)		
	$E_T(30)$	AN	α	DN	β	π^*	ϵ	μ
MeCN	45.6	19.3	0.19	14.1	0.31	0.75	36.0	3.96
PhCN	41.5	15.5	0.00	11.9	0.41	0.90	25.2	3.9
thf	37.4	8.0	0.00	20.0	0.55	0.58	7.4	1.7
CH_2Cl_2	40.7	20.4	0.30	0.0	0.00	0.82	8.9	1.5
1,2-C ₂ H ₄ Cl ₂	41.3	16.7	0.00	0.0	0.00	0.81	10.4	1.75
Me ₂ CO	42.2	12.5	0.08	17.0	0.48	0.68	20.7	2.86
dmf	43.2	16.0	0.00	26.6	0.69	0.88	36.7	3.86
dmso	45.1	19.3	0.00	29.8	0.76	1.00	46.7	3.90
MeNO ₂	46.3	20.5	0.22	2.7	—	0.85	36.7	3.57
py	40.5	14.2	0.00	33.1	0.64	0.87	12.3	2.2
EtOH	51.9	37.1	0.83	21.0	0.77	0.54	24.3	1.70
PC ^a	46.0	18.3	0.00	15.1	0.40	0.83	65.0	4.98
HCONH ₂	55.8	39.8	0.71	23.0	—	0.97	109.5	3.4

^a Propylene carbonate.

As indicated, the parameters $E_T(30)$, AN and α measure the acidity, whereas the parameters DN and β measure the basicity of the solvents. The parameter π^* is not correlated with the acid–base properties, but with the capacity of the solvent to act as an electric dipole.

It should be kept in mind that the terms ‘acidity’ and ‘basicity’ of the solvent have to be intended not only according to the Lewis concept (electrophilic *vs.* nucleophilic properties), but also according to the Brönsted concept (proton donor *vs.* proton acceptors), or to the hydrogen bonding capacity (hydrogen bond donor *vs.* hydrogen bond acceptor).

As an example, the variation of the redox potential of the ferrocene/ferrocenium oxidation with solvent is considered. This has already been cited in Chapter 4, Table 2, and is now more extensively reported in Table 8.

Among the reported parameters the only one which shows some degree of linear correlation with the redox potential is the acidity parameter $E_T(30)$, Figure 7.

This suggests that the effect of the solvent on the oxidation process of ferrocene is essentially dependent on the electrophilic properties of the solvent.

A more complex example can be found in the oxidation of the dinuclear complex $[\text{Rh}_2(\text{form})_4]$ (form = *N,N'*-di-*p*-tolylformamidinate). Its lantern-like structure is shown schematically in Scheme 3.¹⁰

Table 8 Formal electrode potentials (V vs. SCE) for the one-electron oxidation of ferrocene in different solvents

Solvent	Supporting electrolyte (0.2 M)	$E^\circ/$
HCONH ₂	[NBu ₄][ClO ₄]	+ 0.25
PC ^a	[NEt ₄][ClO ₄]	+ 0.32
MeCN	[NEt ₄][ClO ₄]	+ 0.38
PhCN	[NBu ₄][ClO ₄]	+ 0.38
thf	[NBu ₄][ClO ₄]	+ 0.54
CH ₂ Cl ₂	[NBu ₄][ClO ₄]	+ 0.45
1,2-C ₂ H ₄ Cl ₂	[NBu ₄][ClO ₄]	+ 0.46
Me ₂ CO	[NBu ₄][ClO ₄]	+ 0.46
dmf	[NEt ₄][ClO ₄]	+ 0.49
dmso	[NEt ₄][ClO ₄]	+ 0.40
MeNO ₂	[NBu ₄][ClO ₄]	+ 0.31
py	[NBu ₄][ClO ₄]	+ 0.50
EtOH	[NBu ₄][ClO ₄]	+ 0.33

^a Propylene carbonate.

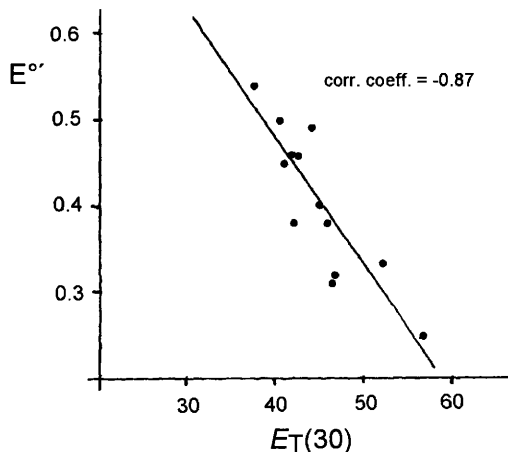
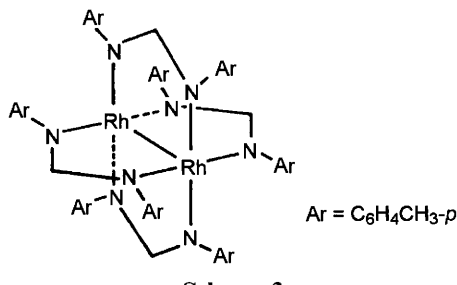


Figure 7 The dependence of the oxidation potential of ferrocene upon $E_T(30)$



Scheme 3

Table 9 shows that the electrode potential of the reversible, one-electron oxidation exhibited by such a derivative [which corresponds to the redox change $\text{Rh(II)}\text{Rh(II)} / \text{Rh(II)}\text{Rh(III)}$], is very dependent on the solvent. In the same table the values of the empirical parameters for the basicity (DN), acidity ($E_T(30)$) and polarizability (π^*) of the solvents used are also reported.¹⁰

Table 9 Formal electrode potentials (V vs. Fc/Fc^+) for the one-electron oxidation of $[\text{Rh}_2(\text{form})_4]$ in different solvents and pertinent empirical parameters

Solvent	$E_{0'/+}^\circ$	DN	$E_T(30)$	π^*
MeCN	-0.36	14.1	45.6	0.75
thf	-0.24	20.0	37.4	0.58
CH_2Cl_2	-0.23	0.0	40.7	0.82
dmf	-0.40	26.6	43.2	0.88
py	-0.39	33.1	40.5	0.87

One does not gain a clear indication of the dominance of any of the empirical parameters of the solvent from an examination of the dependence of the redox potential on those parameters, as the coefficients of the linear correlation are: 0.72 (DN), 0.57 ($E_T(30)$) and 0.69 (π^*), respectively. However, using equations which take simultaneously into account the acidity, basicity and polarizability of the solvent,¹¹ one can obtain, for example, a linear variation of the redox potential according to the following equation:

$$E^{\circ'} = -0.0047\ DN - 0.0108\ E_T(30) - 0.2006\ \pi^* - 16.5186$$

This result confirms that in order to have an adequate treatment of the effect of solvation on the redox potential, one should make use of multi-parameter equations which take into account, on a case by case basis, the acid, basic and electrostatic character of the solvent, thus allowing evaluation of their respective contributions.

3 REDOX POTENTIAL AND TEMPERATURE

In general, the study of the variation of the formal electrode potential of a redox process with temperature has thermodynamic implications. Hence, one is interested in the measurement of ΔG° , ΔS° and ΔH° for the electron transfer process. It is recalled from thermodynamics that, under standard conditions, ΔE° is directly proportional to the free energy of the redox reaction according to the equation:

$$\Delta G^\circ = -n \cdot F \cdot \Delta E^\circ$$

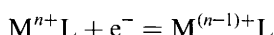
where:

n = the number of electrons involved in the redox reaction

F = the Faraday constant (96500 Coulomb)

$$\Delta E^\circ = E_{\text{cathode}}^\circ - E_{\text{anode}}^\circ$$

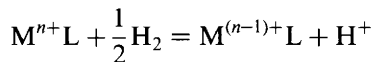
To adapt this fundamental relationship to the case of voltammetric investigations on redox processes of metal complexes, let us assume that the reversible reduction of any complex:



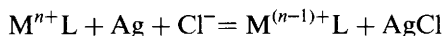
takes place at a potential of $E'_{(\text{M}^{n+}\text{L}/\text{M}^{(n-1)+}\text{L})}$. The value of $\Delta E'^\circ$ which should be used in the preceding thermodynamic relationship is

the difference between the potential value $E_{(M^{n+}L/M^{(n-1)+}L)}^{\circ'}$ and the electrode potential of the reference electrode.

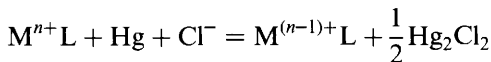
Therefore, if a normal hydrogen electrode (NHE) is used as reference electrode, one can describe the reaction in the electrochemical cell as:



If a Ag/AgCl electrode is used as reference electrode, the reaction occurring in the electrochemical cell can be described as:

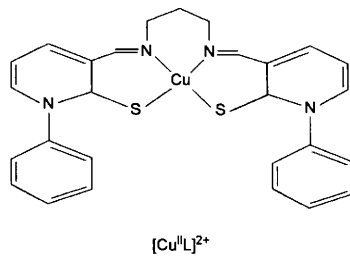


Finally, the use of a saturated calomel electrode as reference electrode would generate a reaction which can be described as:



Nevertheless, since in thermodynamics the values of the standard potentials are normally referred to the NHE electrode, when one wishes to obtain thermodynamic data from electrochemical experiments it is usual to transform the redox potentials obtained employing other reference electrodes into values with respect to the NHE, according to the scales given in Chapter 3, Section 1.2.

As an example of thermodynamic treatment of electrochemical data, we can consider the case of the planar (with slight tetrahedral distortion) Cu(II) complex, $[CuL]^{2+}$ shown in Scheme 4 (already mentioned in Chapter 5, Section 7).¹²



Scheme 4

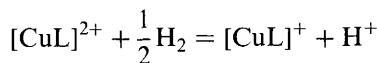
As previously discussed, this complex in MeCN solution undergoes an essentially (both chemically and electrochemically) reversible Cu(II)/Cu(I) reduction. At 20°C, the formal electrode potential of the reduction process is:

$$E^{\circ'} = +0.01 \text{ V, vs. SCE}$$

which corresponds to:

$$E^{\circ'} = +0.25 \text{ V, vs. NHE}$$

This means that at 20°C the standard free energy variation for the reaction:



is given by:

$$\begin{aligned}\Delta G^\circ &= -n \cdot F \cdot \Delta E^\circ = -1.96500 \cdot (E_{\text{cat}}^{\circ'} - E_{\text{an}}^{\circ'}) = -96500 \cdot (+0.25 - 0.00) \\ &= -24125 \text{ J mol}^{-1} = -24.1 \text{ kJ mol}^{-1}\end{aligned}$$

The use of a *non-isothermal* electrochemical cell (see Chapter 3, Section 2.1) enables one to calculate the entropy variation for the redox couple $[\text{CuL}]^{2+}/[\text{CuL}]^+$, $\Delta S_{\text{rc}}^\circ = S_{\text{red}}^\circ - S_{\text{ox}}^\circ$, by measuring the redox potential as a function of temperature (in K), and using the relationship:¹³

$$\Delta S_{\text{rc}}^\circ = S_{\text{red}}^\circ - S_{\text{ox}}^\circ = n \cdot F \cdot \left(\frac{dE^{\circ'}}{dT} \right)_{\text{ni}}$$

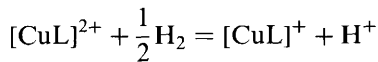
where the symbols rc and ni indicate *redox couple* and *non-isothermal* conditions, respectively.

For the case in question, the variation in redox potential of the couple Cu(II)/Cu(I) in the temperature range from -20 to +20°C follows a linear trend with a correlation coefficient of 0.97, Figure 8.

The positive slope of the line (0.00137 VK^{-1}), which represents the temperature coefficient ($dE^{\circ'}/dT$) in the above relationship, enables one to determine:

$$\Delta S_{\text{rc}}^\circ = S_{([\text{CuL}]^+)}^\circ - S_{([\text{CuL}]^{2+})}^\circ = 1.96500 \cdot 0.00137 = 133.2 \text{ J K}^{-1} \text{ mol}^{-1}$$

Considering the general reaction:



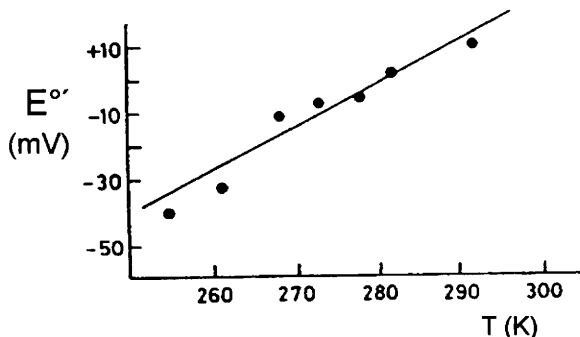


Figure 8 Variation of the formal electrode potential for the one-electron reduction of $[CuL]^{2+}$ with temperature, in MeCN solution

the entropy variation is given by:

$$\begin{aligned}\Delta S^\circ &= S_{([CuL]^+)}^\circ + S_{(H^+)}^\circ - S_{([CuL]^{2+})}^\circ - \frac{1}{2} S_{(H_2)}^\circ \\ &= [S_{([CuL]^+)}^\circ - S_{([CuL]^{2+})}^\circ] - [\frac{1}{2} S_{(H_2)}^\circ - S_{(H^+)}^\circ] = \Delta S_{rc}^\circ - [\frac{1}{2} S_{(H_2)}^\circ - S_{(H^+)}^\circ]\end{aligned}$$

Since it is commonly accepted that:¹⁴

$$[\frac{1}{2} S_{(H_2)}^\circ - S_{(H^+)}^\circ] = 65.2 \text{ J K}^{-1} \text{ mol}^{-1}$$

it follows that:

$$\Delta S^\circ = 133.2 - 65.2 = 68.0 \text{ J K}^{-1} \text{ mol}^{-1}$$

Knowing this value, from the relationship:

$$\Delta G^\circ = \Delta H^\circ - T\Delta S^\circ$$

one can calculate that at 20 °C the variation in enthalpy of the reaction is:

$$\begin{aligned}\Delta H^\circ &= -24125(\text{J mol}^{-1}) + 293(\text{K}) \cdot 68.0(\text{J K}^{-1} \text{ mol}^{-1}) = -4201 \text{ J mol}^{-1} \\ &= -4.2 \text{ kJ mol}^{-1}\end{aligned}$$

Coming back to the factor ΔS_{rc}° , besides the determination of the thermodynamic parameters which accompany a redox reaction, it also

presents some interest with respect to the *structural reorganizations* which accompany a redox process, a theme central to the electrochemical study of inorganic complexes. In fact, by determining the parameter ΔS_{rc}° makes possible to draw (semi-quantitative) conclusions not only on the *metal-ligand* structural reorganization (first coordination sphere; ‘inner sphere’ entropy) following a redox process, but also on the *metal complex-solvent* reorganization (second coordination sphere; ‘outer-sphere’ entropy) accompanying the redox process.

This interpretation is based on the fact that the variation of the overall charge which occurs when the metal complex undergoes a redox process influences the number of solvent molecules surrounding the complex (which are hence electrostatically orientated), as well as the number of solvent molecules which form hydrogen bonds with the complex. The change in the number of solvent molecules near the metal complex can be translated into an increase or decrease of the molecular order of the entire system and, hence, into an increase or decrease of entropy.

In the case of the $[\text{CuL}]^{2+}$ complex discussed previously, it is likely that the positive value of ΔS_{rc}° ($+133.2 \text{ J K}^{-1} \text{ mol}^{-1}$) might result as a consequence of the charge decrease that occurs on passing from $[\text{CuL}]^{2+}$ to $[\text{CuL}]^+$, which causes a release of solvent molecules (acetonitrile) towards the mass of the solution, *i.e.* part of those molecules which were ordered by the dipole interaction around the metal complex become disordered.

An opposite case is found, for example, in the reduction of Cu(III) complexes with some deprotonated peptides. For example, Figure 9 illustrates the molecular structure of the trideprotonated Cu(II) tetraglycine $[\text{Cu}^{\text{II}}(\text{H}_3\text{G}_4)]^{2-}$

As may be expected, the planar geometry of the $\text{Cu}^{\text{II}}\text{N}_4$ coordination enables access and stabilization of the corresponding complex

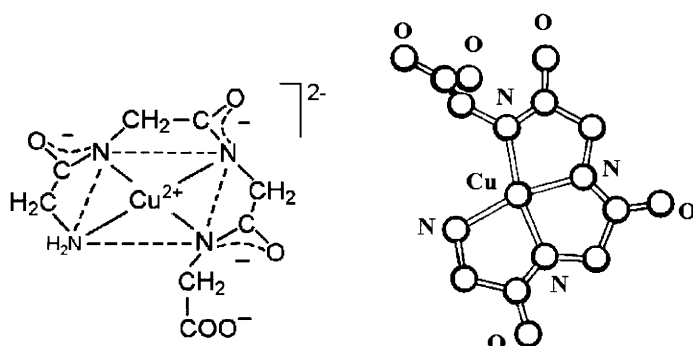


Figure 9. *X-Ray structure of $[\text{Cu}^{\text{II}}(\text{H}_3\text{G}_4)]^{2-}$*

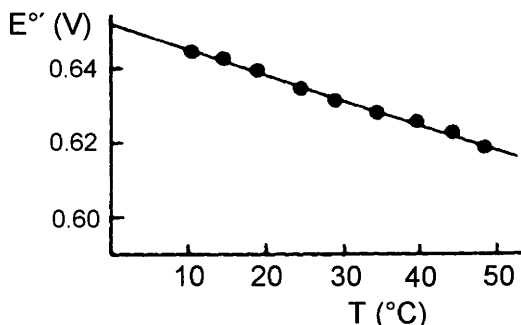


Figure 10 Variation of the formal electrode potential for the one-electron reduction of $[\text{Cu}^{\text{III}}(\text{H}_3\text{G}_4)]^-$ with temperature, in aqueous solution ($\text{pH} = 9.5$)

$[\text{Cu}^{\text{III}}(\text{H}_3\text{G}_4)]^-$. The reversible Cu(III)/Cu(II) reduction of the complex in aqueous solution at several temperatures demonstrates that the redox potential decreases linearly with temperature, Figure 10.¹⁶

Calculation of the entropy variation of the $[\text{Cu}^{\text{III}}(\text{H}_3\text{G}_4)]^-/\text{[Cu}^{\text{II}}(\text{H}_3\text{G}_4)\text{]}^{2-}$ redox couple from the negative slope of the linear trend gives:

$$\Delta S_{\text{rc}}^\circ = -82.8 \text{ J K}^{-1} \text{ mol}^{-1}$$

In this case, the decrease in entropy of the redox couple (*i.e.* a decrease of the molecular disorder) is proposed to be due to the passage of the complex from the $\text{Cu}^{\text{III}}\text{N}_4$ square planar geometry to the usual octahedral geometry of Cu(II) complexes which requires the axial coordination of two solvent molecules (water). This reduces the disorder of the solvent molecules around the complex.

Negative values for redox couple entropy have also been obtained for the Cu(II)/Cu(I) reduction, in aqueous medium, of the blue copper proteins stellacyanin, plastocyanin and azurin.¹⁴ The decrease in molecular disorder has been attributed in this case to the fact that the charge neutralization of the redox site (from +1 to 0) favours the formation of hydrogen bonds between the solvent (water) and the copper centre.¹⁷

It should be kept in mind that this type of study, treated here in terms of single complexes, acquires greater importance when carried out on a series of homologous complexes. This allows one to evaluate how the electronic and/or structural variations of the ligand influence the reorganization processes of the solvent molecules. In fact, such a comparison has recently led to a reinterpretation of the $\Delta S_{\text{rc}}^\circ$ parameter also in terms of the structural reorganisations of the first coordination sphere.^{18,19} For example, if one compares the $\Delta S_{\text{rc}}^\circ$ values for

the isostructural couples $[\text{Fe}(\text{bipy})_3]^{3+/2+}$ and $[\text{Co}(\text{bipy})_3]^{3+/2+}$, one finds in aqueous solution:

$$[\text{Fe}(\text{bipy})_3]^{3+/2+} \quad \Delta S_{\text{rc}}^\circ = 8.4 \text{ J K}^{-1} \text{ mol}^{-1}$$

$$[\text{Co}(\text{bipy})_3]^{3+/2+} \quad \Delta S_{\text{rc}}^\circ = 92.0 \text{ J K}^{-1} \text{ mol}^{-1}$$

About the same difference holds for the couple $[\text{Fe}(\text{phen})_3]^{3+/2+}$ vs. $[\text{Co}(\text{phen})_3]^{3+/2+}$.¹³

Since the difference in entropy between the two redox couples is difficult to ascribe to different complex–solvent interactions, as the charges of the complexes are identical in the two cases, other causes of the entropy difference must be considered.

In the case of the iron complex, the Fe–N stretching frequencies are essentially identical in both the Fe(III) and Fe(II) oxidation states. This agrees with the fact that, as mentioned in Chapter 5, Section 4, the averaged Fe–N bond length is essentially the same in the two cases (1.96 Å). However, in the case of the cobalt complex, the Co–N stretching frequencies of the Co(III) complex are higher by about 130 cm⁻¹ than for the Co(II) complex. As a matter of fact, as seen in Chapter 5, Section 5, the averaged Co^{III}–N distance (1.93 Å) is significantly shorter than the Co^{II}–N distance (2.13 Å). This implies that a good part of the entropy difference (about 84 J K⁻¹ mol⁻¹) between the two redox couples results from entropy effects of the intramolecular vibrational motion (due to the lengthening of the bonds which accompanies the Co(III)/Co(II) reduction), or, it can be ascribed to structural factors concerned with the first coordination sphere.

To conclude, a related thermodynamic treatment has been extended to the calculation of the enthalpic variation for redox couples, $\Delta H_{\text{rc}}^\circ = H_{\text{red}}^\circ - H_{\text{ox}}^\circ$. Such a treatment is useful to understand how enthalpic or entropic factors may influence the magnitude and sign of the free energy, or the electrode potential, of a redox change.²⁰ In fact, one must consider that:

$$E_{(\text{vs. NHE})}^{\circ'} = -\frac{\Delta H_{\text{rc}}^\circ}{n \cdot F} + \frac{T \cdot \Delta S_{\text{rc}}^\circ}{n \cdot F}$$

The determination of $\Delta H_{\text{rc}}^\circ$ is based on the Gibbs–Helmholtz equation:

$$\Delta H_{\text{rc}}^\circ = -n \cdot F \cdot \frac{(dE^{\circ'}/dT)_{\text{ni}}}{d(1/T)}$$

In this case also the slope of the temperature coefficient $dE^{\circ'}/dT$, under *non-isothermal* conditions, as a function of $1/T$ affords $\Delta H_{\text{rc}}^\circ$.

For example, in Chapter 12, Section 4, we have examined the electrochemical response of *azurin* (from *Pseudomonas aeruginosa*), the only cupredoxin in which the copper(II) ion is pentacoordinate. Its reversible Cu(II)/Cu(I) reduction occurs at $E^{\circ'} = +0.31$ V, vs. NHE, at 25°C. Measurements of the variation of the formal electrode potential with temperature in a *non-isothermic* electrochemical cell gives the two diagrams illustrated in Figure 11.²⁰

From the negative slope of the plot $E^{\circ'} \text{ vs. } T$ ($-0.00068 \text{ V K}^{-1}$) we can calculate that:

$$\Delta S_{rc}^{\circ} = S_{(\text{azurin red})}^{\circ} - S_{(\text{azurin ox})}^{\circ} = -1.96500 \cdot 0.00068 = -65.6 \text{ J K}^{-1} \text{ mol}^{-1}$$

From the positive slope of the plot $E^{\circ'}/T \text{ vs. } 1/T$ (0.5 V) we can calculate that:

$$\begin{aligned}\Delta H_{rc}^{\circ} &= H_{(\text{azurin red})}^{\circ} - H_{(\text{azurin ox})}^{\circ} = -1.96500 \cdot 0.5 = -48250 \text{ J mol}^{-1} \\ &= -48.2 \text{ kJ mol}^{-1}\end{aligned}$$

Simple thermodynamic considerations state that the reduction process is favoured (*i.e.* more positive $E_{\text{Cu(II)/Cu(I)}}^{\circ'}$ potential values are obtained) if the electron transfer is exothermic (ΔH° negative) and if the molecular disorder increases (ΔS° positive). It is therefore evident that the positive potential value for the reduction of *azurin* (as well as that of the most blue copper proteins) is favoured by the enthalpic factor. This means that the metal-to-ligand interactions inside the first coordination sphere (which favour the stability of the reduced form over the oxidized form) prevail over the metal complex-to-solvent interactions inside the second

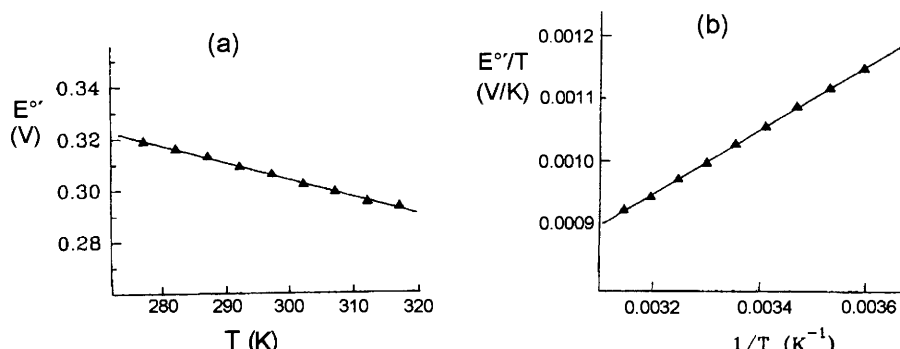


Figure 11 (a) Variation of the formal electrode potential for the one-electron reduction of *azurin* with temperature; (b) variation of the $E^{\circ'}/T$ parameter as a function of $1/T$. Gold working electrode pretreated with 4-thiopyridine. Phosphate buffer aqueous solution ($pH = 7.0$)

coordination sphere (namely, the release of ordered water molecules as a consequence of charge neutralization, see above¹⁴).

REFERENCES

1. C. Hansch, A. Leo and R.W. Taft, *Chem. Rev.*, 1991, **91**, 165.
2. D. Osella, G. Arman, M. Botta, R. Gobetto, F. Laschi and P. Zanello, *Organometallics*, 1989, **8**, 620.
3. B.E. Bursten and M.R. Green, *Progr. Inorg. Chem.*, 1989, **36**, 393.
4. (a) J. Chatt, C.T. Kan, G.J. Leigh, C.J. Pickett and D.R. Stanley, *J. Chem. Soc., Dalton Trans.*, 1980, 2032; (b) A.B.P. Lever, *Inorg. Chem.*, 1990, **29**, 1271; (c) H. Masui and A.B.P. Lever, *Inorg. Chem.*, 1993, **32**, 2199.
5. M.F.C. Guedes da Silva, A.M. Trzeciak, J.J. Ziolkowski and A.J.L. Pombeiro, *J. Organomet. Chem.*, 2001, **620**, 174.
6. (a) L. Zhang, M.P. Gamasa, J. Gimeno, R.J. Carbajo, F. López-Ortiz, M.F.C. Guedes da Silva and A.J.L. Pombeiro, *Eur. J. Inorg. Chem.*, 2000, 341; (b) L. Zhang, M.P. Gamasa, J. Gimeno, M.F.C. Guedes da Silva, A.J.L. Pombeiro, C. Graiff, M. Lanfranchi and A. Tiripicchio, *Eur. J. Inorg. Chem.*, 2000, 1707; (c) L. Zhang, M.F.C. Guedes da Silva, M.L. Kuznetsov, M.P. Gamasa, J. Gimeno, J.J.R. Frausto da Silva and A.J.L. Pombeiro, *Organometallics*, 2001, **20**, 2782.
7. C. Reichardt, *Angew. Chem. Int. Ed. Engl.*, 1979, **18**, 98.
8. M.J. Kamlet, J.L.M. Abboud and R.W. Taft, *Progr. Phys. Org. Chem.*, 1980, **13**, 485.
9. T. Kagiya, Y. Sumida and T. Inoue, *Bull. Chem. Soc. Jpn.*, 1968, **41**, 767.
10. P. Piraino, G. Bruno, S. Lo Schiavo, F. Laschi and P. Zanello, *Inorg. Chem.*, 1987, **26**, 2205.
11. R. Seeber, P. Piu, P. Piraino P. Zanello, *Inorg. Chim. Acta*, 1989, **155**, 27.
12. M. Gullotti, L. Casella, A. Pintar, E. Suardi, P. Zanello and S. Mangani, *J. Chem. Soc., Dalton Trans.*, 1989, 1979.
13. E.L. Yee, R.J. Cave, K.L. Guyer, P.D. Tyma, M.J. Weaver, *J. Am. Chem. Soc.*, 1979, **101**, 1131.
14. V.T. Taniguchi, N. Sailasuta-Scott, F.C. Anson and H.B. Gray, *Pure & Appl. Chem.*, 1980, **52**, 2275.
15. H.C. Freeman and M.R. Taylor, *Acta Cryst.*, 1965, **18**, 939.
16. M.P. Youngblood and D.W. Margerum, *Inorg. Chem.*, 1980, **19**, 3068.
17. N. Sailasuta, F.C. Anson and H.B. Gray, *J. Am. Chem. Soc.*, 1979, **101**, 455.
18. D.E. Richardson and P. Sharpe, *Inorg. Chem.*, 1993, **32**, 1809.
19. P.W. Crawford and F.A. Schultz, *Inorg. Chem.*, 1994, **33**, 4344.
20. G. Battistuzzi, M. Borsari, L. Loschi, F. Righi and M. Sola, *J. Am. Chem. Soc.*, 1999, **121**, 501, and references therein.

Appendices

PHYSICAL CONSTANTS

Name	Symbol	Value
Avogadro's constant	N	6.0221×10^{23}
Bohr's magneton	BM	$9.2740 \times 10^{-24} \text{ J T}^{-1}$
Boltzmann's constant	k	$1.3807 \times 10^{-23} \text{ J K}^{-1}$
elementary charge	e	$1.6022 \times 10^{-19} \text{ C}$
Faraday's constant	F	96485 C mol ⁻¹
gas constant	R	$8.3145 \text{ J K}^{-1} \text{ mol}^{-1}$
gravitational acceleration	g	9.8066 m s^{-2}
speed of light	c	$2.9979 \times 10^8 \text{ m s}^{-1}$
standard temperature	T	25° C

SI BASE UNITS

Base Quantity	Unit	Symbol
length	metre	m
mass	kilogram	kg
time	second	s
electric current	ampere	A
thermodynamic temperature	kelvin	K
luminous intensity	candela	cd
amount of substance	mole	mol

DERIVED SI UNITS

Quantity	Unit	Symbol	Dimensions	
capacitance	farad	F	C V ⁻¹	kg ⁻¹ m ⁻² s ⁴ A ²
Celsius temperature	degree Celsius	°C		
energy	joule	J	N m	kg m ² s ⁻²
electric charge	coulomb	C	A s	
electric conductance	siemens	S	A V ⁻¹	kg ⁻¹ m ⁻² s ³ A ²

(continued)

<i>Quantity</i>	<i>Unit</i>	<i>Symbol</i>	<i>Dimensions</i>	
electric potential difference	volt	V	W A^{-1}	$\text{kg m}^2 \text{s}^{-3} \text{A}^{-1}$
electric resistance	ohm	Ω	V A^{-1}	$\text{kg m}^2 \text{s}^{-3} \text{A}^{-2}$
force	newton	N	Kg m s^{-2}	
frequency	hertz	Hz	s^{-1}	
inductance	henry	H	Wb A^{-1}	$\text{kg m}^2 \text{s}^{-2} \text{A}^{-2}$
magnetic flux	weber	Wb	V s	$\text{kg m}^2 \text{s}^{-2} \text{A}^{-1}$
magnetic flux density	tesla	T	Wb m^{-2}	$\text{kg s}^{-2} \text{A}^{-1}$
power	watt	W	J s^{-1}	$\text{kg m}^2 \text{s}^{-3}$
pressure	pascal	Pa	N m^{-2}	$\text{kg m}^{-1} \text{s}^{-2}$

SI PREFIXES

<i>Factor</i>	<i>Prefix</i>	<i>Symbol</i>	<i>Factor</i>	<i>Prefix</i>	<i>Symbol</i>
10^1	deka	da	10^{-1}	deci	d
10^2	hecto	h	10^{-2}	centi	c
10^3	kilo	k	10^{-3}	milli	m
10^6	mega	M	10^{-6}	micro	μ
10^9	giga	G	10^{-9}	nano	n
10^{12}	tera	T	10^{-12}	pico	p
10^{15}	petra	P	10^{-15}	femto	f
10^{18}	exa	E	10^{-18}	atto	a
10^{21}	zetta	Z	10^{-21}	zepto	z
10^{24}	yotta	Y	10^{-24}	yocto	y

CONVERSION FACTORS

- $1 \text{ Pa} = 9.869 \times 10^{-6} \text{ atm} = 10 \text{ dyn cm}^{-2} = 7.501 \times 10^{-4} \text{ cmHg}$
 $1 \text{ electronvolt (eV)} = 1.6022 \times 10^{-19} \text{ J} = 3.827 \times 10^{-20} \text{ cal} = 8065.5 \text{ cm}^{-1}$
 $1 \text{ J} = 10^7 \text{ erg} = 6.2420 \times 10^{18} \text{ eV} = 0.2389 \text{ cal} = 1 \text{ kg cm}^2 \text{ s}^{-2}$
 $= 1 \text{ V C} = 2.778 \times 10^{-7} \text{ kWh}$
 $1 \text{ cal} = 4.186 \text{ J} = 2.613 \times 10^{19} \text{ eV} = 1.163 \times 10^{-6} \text{ kWh}$
 $1 \text{ eV/molecola} = 23.060 \text{ kcal mol}^{-1} = 96485 \text{ J mol}^{-1}$
 $1 \text{ kilowattora (kWh)} = 3.6 \times 10^6 \text{ J} = 2.247 \times 10^{25} \text{ eV}$
 $1 \text{ watt (W)} = 0.2389 \text{ cal s}^{-1}$
 $R \cdot T = 2.479 \text{ kJ mol}^{-1}$
 $R \cdot T/F = 0.02569 \text{ V}$
 $2.303 \cdot R \cdot T/F = 0.05916 \text{ V}$
 $1/F = 0.010364 \text{ V [1/(kJ mol}^{-1}\text{)]}$

$$F/R \cdot T = 38.92 \text{ V}^{-1}$$

$$^{\circ}\text{C} = 5 (\text{ }^{\circ}\text{F} - 32)/9 \quad \text{ }^{\circ}\text{F} = 9 (\text{ }^{\circ}\text{C})/5 - 32 \quad \text{K} = \text{ }^{\circ}\text{C} + 273.15$$

$$1 \text{ tesla (T)} = 1 \text{ weber metro}^{-2} (\text{Wb m}^{-2}) = 10^4 \text{ gauss (G)}$$

$$1 \text{ Wb} = 10^8 \text{ maxwell (Mx)}$$

THE GREEK ALPHABET (TOGETHER WITH THE EQUIVALENT ENGLISH LETTERS)

α	A	alpha	(a)	ι	I	iota	(i)	ρ	P	rho	(r)
β	B	beta	(b)	κ	K	kappa	(k)	σ, ς	Σ	sigma	(s)
γ	Γ	gamma	(g)	λ	Λ	lambda	(l)	τ	T	tau	(t)
δ	Δ	delta	(d)	μ	M	mu	(m)	ν	Y	upsilon	(u)
ε	E	epsilon	(e)	ν	N	nu	(n)	ϕ	Φ	phi	(f)
ζ	Z	zêta	(z)	ξ	Ξ	xi	(ks)	χ	X	chi	(ch)
η	H	êta	(ê)	\o	O	omicron	(o)	ψ	Ψ	psi	(ps)
θ	Θ	thêta	(th)	π	Π	pi	(p)	ω	Ω	omega	(ô)

Subject Index

- α , Kamlet–Taft solvatochromic parameter, (table) 591
transfer coefficient, 26–28
- A_N , Knauer–Napier parameter, 591
- AN , Gutman acceptor number, (table)
- aconitase, 561
- activated complex, 23
- activation barrier, symmetry of, 28, 29, 57, 62
- adsorption, 13, 104
 isotherm, 107
 processes, 104
- Amavadin, 228
- amperometric sensors, 193–196
- anodic stripping, 100, 304, 306, 313
- antenna, 196
 light-harvesting, 364
- auxiliary electrode, 19, 20, 139, 147
- azurin, 573, 599, 601
- β , sensitivity of E°' to electronic effects, 587
 sensitivity of electron transfer rate to distance, 541
 Kamlet–Taft solvatochromic parameter, (table) 591
- B , Koppel–Palm parameter, 591
- Bardeen–Cooper–Schrieffer (BCS) theory, 503
- biosensors, 194
- blue copper proteins, 302, 450, 567–577
- Brooker parameters, 591
- Brownstein parameter, 591
- Butler–Volmer equation, 26, 30, 34, 47
- χ , Brooker parameters, 591
calomel, electrode, 18, 19, 141–143
capacitive currents, 43, 44, 47, 108, 110, 111, 113, 144
- capacitor, 43, 44, 143, 144
- carbon electrodes, 121, 140
 carbon nanotube, 140
 carbon paste, 140
 glassy carbon, 140, 141
 pyrolytic graphite, 140, 547–549
- catalytic regeneration of the reagent, 83, 128, 194, 196
 diagnostic criteria, 86, 87
- catechol oxidase, 348, 451
- CE mechanisms, 68
- cell, voltage, 17, 20
 time constant, 144
- cells, electrochemical, 16, 19, 44, 142–149
 for controlled potential coulometry, 147–149
 for cyclic voltammetry, 146, 147
 non-isothermal, 147
- chemical reactions, coupled, 13, 67–99, 126

- following, 13, 67, 74–87, 127–130
 interposed, 88–93, 130–133
 preceding, 13, 67, 68–74, 126, 127
 chromium complexes, 230–236
 molecular wires, 525, 530
 chromocene, 205, 206
 chronoamperometry, 123–133
 double potential step, 124
 single potential step, 123
 classical hydrides, 487–491
 clusters, transition metal,
 carbonyl, 422–444
 with interstitial atoms, 432–443
 sulfur, 409–422
 cobalt complexes, 276–289
 molecular wires, 525, 528
 cobaltocene, 208, 209
 coefficient, diffusion, 37
 transfer, 26
 compact layer, 46
 comproportionation, 101
 constant, 101, 174
 concentration, gradient, 35, 36, 51
 profiles, 38–41, 51, 52
 consecutive electron transfers, 99
 diagnostic criteria, 104
 controlled potential, electrolysis, 97,
 117–123, 147
 diagnostic criteria in, (table), 122
 microelectrolysis, 123
 voltammetry, 123
 convection, 35, 126
 Cooper electron pairs, 503
 copper, complexes, 301–313
 proteins, 302, 450, 567–577
 Cottrell equation, 38, 40, 123, 124,
 128, 133
 coulometry, controlled potential,
 117–123
 counter electrode, 14, 16, 139, 146
 coupled chemical reactions, 13,
 67–99
 critical temperature, superconductivity 497, 504
 current, 14
 and potential, 16
 capacitive, 43, 44, 47, 108, 110,
 111, 113
 charging, 45
 exchange, 30, 31
 faradaic, 15, 30, 45, 110, 115, 144
 non-faradaic, 15
 residual, 45
 cyclic voltammetry, 49–110, 115
 cytochromes, electrochemistry,
 542–556
 cytochrome *b*₅, 551, 552
 cytochrome *c*, 543–551, 553, 554
 cytochrome *c*₃, 552, 553
 cytochrome *f*, 551
 cytochrome *P450*, 554
 ΔE_p , 56, 64
 ΔG° , 23, 24, 27–29, 255, 541, 579,
 594, 596, 597
 ΔH° , 594, 597
 ΔH_{rc}° , 600–602
 Δv , Kagiya electron donor/acceptor
 power, 591
 ΔS° , 591
 ΔS_{rc}° , 596–601
 D, diffusion coefficient, 37
 DN, Gutmann donor number,
 (table) 591
 delocalization of charge, 104, 173,
 174
 dendrimers, 186–193
 diagnostic criteria for,
 consecutive electron transfers, 99,
 122
 following chemical reactions,
 first-order, 76, 79, 86, 87, 122
 catalytic regeneration of the
 reagent, 86, 87, 122
 second-order,
 dimerization, 81, 82, 122
 disproportionation, 83
 interposed chemical reactions, 93,
 122
 irreversible processes, 60–62, 122

- preceding chemical reactions,
first order, 72, 74, 122
quasireversible processes, 64–66
reversible processes, 56, 57, 122
dielectric constant of solvents,
(table) 150, 590
differential pulse voltammetry,
110–113
diffusion, 35, 36, 39, 40, 104, 126
coefficient, 37
layer, 11, 46
electrode with periodical
renewal of the, 116, 117
thickness of, 39, 40, 115, 120
linear, 36, 41, 51, 59, 139, 146,
550, 551
radial (spherical), 38, 41, 58, 59,
139, 146, 550
dihydrogen metal complexes,
484–491
dimerization, 79
diagnostic criteria, 81, 122
Dimroth–Reichardt parameter
($E_T(30)$), (table) 591
dinitrogen metal complexes, 474–484
dioxolene ligands, 227, 348–353
dioxygenases, 446–448, 560
dioxygen metal complexes, 449–469
dipole moment of solvents, 590,
(table) 591
direct electrochemistry of proteins,
blue copper, 567–577
cytochromes, 542–556
iron–sulfur, 556–567
disproportionation, 82
diagnostic criteria, 83
dithiolene ligands, 348, 356–363
double layer, 11, 43–47
dropping mercury electrode, 38, 45,
47, 112, 117, 140
- ϵ , dielectric constant, (tables) 150,
591
- E_L , Lever parameter, (table) 585, 587
- E_S , electron richness, 587
- $E_T(30)$, (table) 591
EC, mechanisms, 74
ECE, mechanisms, 88, 122, 130
EE, mechanisms, 99
electrocapillary curves, 47
electrocatalysis, 93, 96, 434–438
catalytic efficiency, 98
driving force, 98, 435
electrochemical, cells, 16, 19–22, 44,
142–149, 596, 601
irreversibility, 42, 59
reversibility, 42, 51, 56, 57
potential, 46
sensors, 193–198
electrochemically induced structural
modifications, 381–408
electrode, 11, 139–142
 Ag/Ag^+ , 141, 142
auxiliary, 19, 20, 139, 147
carbon, 121, 140
glassy, 140, 141, 549
nanotube, 140
paste, 140
pyrolytic graphite, 140, 547–549
counter, 14, 16, 139, 146
energy of electrons inside, 15
enzymatic, 194
formal potential, 25, 27, 57
gold, 121, 140
indicator (working), 139–141
interface, 11, 17, 43–45, 145
mercury, 38, 45, 47, 112, 117, 140,
438
normal (standard) hydrogen
(NHE), 19, 141, 595
planar, 36, 139
diffusion at, 36
platinum, 121, 140, 438
poisoning, 121, 545
potential, 17
formal, 25
windows, (table) 140
pretreatment, 547
reactions, 12, 14
rate of, 14

- reference, 19, 20, 139, 141, 146, 147
 rotating disk, 116, 281
 saturated calomel, 18, 19, 141–143, 146, 149, 595
 silver–silver chloride, 141, 142, 146, 149, 595
 spherical, 38, 59, 139
 standard potential, 25
 superconductors, 140, 507, 508
 with periodical renewal of the diffusion layer, 116, 117, 443
 working, 14, 17, 20, 27, 115, 139–141, 145–147
- electrococrystallization, 123
- electrolysis, 97
 cell for, 148
 controlled potential, 117–123
 reversal, 122
- electrolyte, supporting, 36, 123, 140, 149–154
- electron carriers, 539
- electron-donating effects, 165, 166, 284, 580
- electron carriers, 539
- electron transfer, 7, 12, 22, 42, 46, 51, 59, 62, 543
 catalytic chain, 93, 96
 coupled to proton transfer, 543, 563
 kinetics, 22, 24, 46
 reactions, 7
- electroneutrality, 11, 12, 17
- electronic communication, 102, 173, 185, 274, 346
 delocalization, 173
 effects and redox potential, 579–589
- electron-withdrawing effects, 166, 170, 580
- electrostatic potential, 46, 47
- empirical parameters of solvents, 591
- energy, of electrons, 15
 reorganization, 283, 284, 541
- enthalpy, 597
 redox couple, 600–602
 entropy, 597,
 redox couple, 596–601
 enzymatic electrodes, 194
 equation, Butler–Volmer, 26, 30, 34, 47
 Cottrell, 38, 40, 123, 124, 128, 133
 Gibbs–Helmholtz, 600
 Hammett, 580
 Nernst, 18, 24, 25, 30, 32, 52
 Randles–Sevcik, 54, 100, 118, 133
 equivalent circuit, 44, 142, 144, 145
 error function, 39
 complement, 39, 126
 ETC catalysis, 93, 96
 exchange current, 30, 31, 46
 density, 31
- Faradaic current, 15, 30, 45, 110, 115, 144, 147
 impedance, 144
- Faraday, constant of, 14, 118
 law of, 14, 15, 118, 121
- Fe-protein (nitrogenase), 470
- FeMo cofactor (nitrogenase), 470
- FeMo protein (nitrogenase), 470
- Fermi level, 15, 16
- ferredoxins, 415, 558, 561, 562, 564, 565
 Rieske, 558–560
- ferrocenes, electrochemical behavior, 3, 57, 58, 159–204
 as electrochemical sensors, 193–198
 as ligands in metal-complexes, 325–332
 as materials for non-linear optical properties, 198–204
 molecular orbital diagram, 2, 3, 159
 monoferrocenes, 160–167
 multiferrocenes, 171–193
 oligoferrocenes, 171–182
 polymers, 182–193
 linear, 182–185

- branched, 186–193
ferrocenophanes, 167–171
Fick, first law, 37, 38, 52
 second law, 37–40, 53, 54, 59
films mimicking biomembranes, 554–556
flux, 37
following chemical reactions, 67, 74–87, 127–130
 first-order, 74–79, 83, 127, 128
 diagnostic criteria, 76, 79, 86, 87
 second-order, 79, 83
 diagnostic criteria, 81, 83
formal electrode potential, 25, 27, 57
Fourier theorem, 201
free energy, 23, 27, 541, 579
 relationships, 579–602
Frumkin correction, 46
fullerene ligands, 332–347, 504
- Gibbs–Helmholtz equation, 600
glassy carbon electrode, 140, 141, 549
glucose, dosage of, 194
Gouy–Chapman–Stern double layer, 45
Gutmann, acceptor number (AN), (table) 591
 donor number (DN), (table) 591
- haemerythrin, 449, 451
haemerythrin-like complexes, 467–469
haemocyanins, 449, 450
haemocyanin-like complexes, 466, 467
haemoglobin, 449
haemoproteins, 449
haemoprotein-like complexes, 452–466
Hammett, constant, 580, (table) 581
 equation, 580
Helmholtz, internal plane, 46
 outer plane, 46
- heterogeneous, reactions, 13
 standard rate constant, 26
high-potential iron proteins, 415, 563
HOMO, level, 1, 15
HOMO–LUMO separation, 335, 366, 367, 370
homogeneous, reactions, 13
hydrides, classical, 487–491
 non-classical, 487–490
hydrodynamic techniques, 115–117
hydrogenases, 484–486
- i_0 , exchange current, 31, 32, 46
 I_M , Lever parameter,
indicator electrodes, 139–141
inductive effects, 166, 302, 579
inner sphere, entropy, 598
 reactions, 8–10
 mechanism, 8–10, 12
interface, electrode, 11, 17, 43–45, 145
 potential, 46
internal layer, 46
interposed chemical reactions, 88–93, 130–133
 diagnostic criteria, 93
interstitial atoms, clusters with, 432–446
iR drop, 17, 20–22
iron complexes, 263–276
iron–sulfur proteins, 556–567
irreversibility, electrochemical, 42, 59, 62
 chemical meaning, 62
 diagnostic criteria, 60
irreversible processes, 59–62
isoelectric point, 544
isoporphyrins, 366
IUPAC convention, 55, 162
- K_{com} , 101, 102, 174, 175, 248, 525, 529
 k° , standard rate constant, 26, 31, 32, 42, 46, 47, 61, 62, 64

- k_{et} , electron transfer rate constant, 541
 Kagiya parameters, 591
 Kamlet–Taft parameters (α , β , π^*), (table) 591
 Knauer–Napier parameter, 591
 Kok cycle, 248
 Koppel–Palm parameter, 591
 Kosower's value, 591
- Langmuir isotherm, 107, 182
 Laplace transformation, 39, 54
 Laser light, 198, 199
 law of, Faraday, 14, 15, 118, 121
 Fick, 37, 38
 mass transport, 37
 layer, compact, 46
 diffusion, 11, 46
 double, 11, 43–47
 internal, 46
 Lever parameter, (table) 585, 587
 levitation, 500–502
 ligand, additivity, 585, 587
 exchange, 97
 redox-active, 225, 227, 314, 325,
 332, 348, 364, 368, 370
 redox non-innocent, 325
 linear, diffusion, 36, 41, 51, 59, 139,
 146
 free energy relationships, 579–602
 low-potential iron–sulfur proteins, 559
 Luggin capillary, 20, 146, 147
 LUMO, level, 1, 15
- μ , dipole moment, (table) 591
 macrocyclic effect, 233
 manganese complexes, 236–263
 in material science, 262, 263
 in photosynthesis, 244–250
 manganocenes, 207, 208
 Marcus theory, 541
 mass transport, 12, 33, 34, 42, 51, 59,
 62, 115, 120
 law of, 37
 rate of, 37
 mavicyanin, 572
 Meissner effect, 497, 500
 mercury, electrode, 38, 45, 47,
 112, 117, 140
 amalgam, 140
 metallocenes, 159–215
 metal–carbonyl, clusters, 422–443
 metal–sulfur, clusters, 409–422
 metal wire complexes, electrochemistry, 517–537
 microelectrode, 59
 migration, 35, 47
 mixed-valent derivatives, 173, 238,
 478, 518, 519, 525, 529
 modifications, electrochemically
 induced, 381–408
 molecularity, 22
 monooxygenases, 446, 555
 myoglobin, 449
- nanoscale magnets, 262
 nanotube carbon electrodes, 140
 Nernst equation, 18, 24, 25, 30, 32,
 52
 nickel complexes, 290–301
 molecular wires, 527, 529
 nickelocenes, 210, 211
 nitrogenases, 469–472
 nitrogen fixation, 469, 485
 non-classical hydrides, 487, 488, 490
 non-faradaic, currents, 15, 43
 non-isothermal cells, 147, 596, 601
 non-linear optical properties,
 198–204
 nucleophilicity, 152
 number of electrons involved
 in a redox process, 26
 determination of, 117, 118, 133
- ohmic drop, 17, 19, 20, 147
 Osteryoung square wave
 voltammetry, 113–115
 outer sphere, entropy, 598
 reactions, 8, 9

- mechanism, 8–10, 12
Overvoltage, 32, 34
Oxidizing agents, 217, (table) 218
Oxidation, 14, 15, 23
oxyerythrocytins, 450
oxyhaemoglobin, 449
oxymyoglobin, 449
- π^* , Kamlet–Taft solvatochromic parameter, (table) 591
 P_L , Pickett–Pletcher parameter, (table) 585, 586
P cluster (nitrogenase), 470–472
peak-to-peak separation, 56, 57
phase, electrostatic potential, 46
formation, 13
photosynthesis, 244–250, 363
photosynthetic water oxidation, 236,
244–250
phthalocyanines, 369, 370
phytocyanin, 569, 572
Pickett–Pletcher parameter, (table)
585, 586
plantacyanin, 569
plastocyanin, 567–569
platinum, electrode, 121, 140, 438
blues, 519–522
polarity (polarisability), of solvents,
149, 589, 591
polarography at solid electrodes, 117
porphyrazine ligands, 368, 370
porphyrin ligands, 363–370
potential, 15, 16
and current, 16
difference of, 17, 20
electrochemical, 46
electrostatic, 46, 47
standard, 15, 16, 25
potentiometric sensors, 193,
196–198
preceding chemical reactions, 13, 67,
68–74, 126, 127
diagnostic criteria, 72, 74
profiles, concentration, 38–41, 51, 52
promoters, 545, 546, 550, 557, 571
- proteins, electrochemistry of,
539–577
proton transfer, 543, 563
pseudoazurin, 570
pulse amplitude, 110
pulse period, 111
pulse width, 110
pulsed voltammetric techniques,
110–115
pyrolytic graphite electrode, 140,
547–549
- quasireversibility, electrochemical,
62
chemical meaning, 66
diagnostic criteria, 64–66
quasireversible processes, 62–67
quinone diimine ligands, 353–356
- radial diffusion, 58, 59
Randles–Sevcik, equation, 54, 100,
118, 133
- rate, of reaction, 14
constant, 26
standard constant, 26
- reaction, coordinate, 23, 27–29
order, 22
- redox-active ligands, 325–379
azopyrimidine, 288, 314
dioxolenes, 227, 348
dithiolenes, 348
ferrocenes, 325
fullerenes, 332
polypyridines, 225
porphyrins, 363
quinone diimines, 348
tetraazaporphyrins, 369
- redox non-innocent ligands, 325
- redox, catalysis, 93, 95
mediators, 95, 96, 194, 539
potential, 28
and electronic effects, 579–589
and solvent, 589–594
and temperature, 594–602
- reducing agents, 217, (table) 218
- reduction, 14, 15, 24

- reference electrode, 19, 20, 139, 141, 146
 reorganization, energy, 283, 284, 541
 metal-ligand, 598
 resistance of solutions, 17, 21, 22, 44, 143
 reversal electrolysis, 122
 reversibility, chemical, 55, 161
 electrochemical, 42, 51, 56, 57, 62
 diagnostic criteria, 56, 57
 meaning of, 57
 reversible processes, 51–59
 rhodium molecular wires, 532
 Rieske ferredoxins, 558–560
 Robin–Day classification, 173, 174, 238
 rotating disk electrode, 116, 281
 rubredoxins, 556
 rusticyanin, 571
 ruthenium molecular wires, 522–524
- σ , Hammett constant, 580, (table) 581
 σ^* , Taft constant, 580, (table) 581
 S , Brownstein parameter, 591
 S_M , sensitivity towards ligands, 588
 sample width, 111
 sarcophagine, 235
 Saturated Calomel Electrode, 18, 19, 141–143, 146, 149, 595
 scorpions, 234
 sensors, electrochemical, 193–198
 amperometric, 193–196
 anionic, 197
 cationic, 197
 potentiometric, 193, 196–198
 sepulcrands, 284
 silver–silver chloride electrode, 141, 142, 146, 149, 595
 simultaneous electron transfers, 100
 single sweep voltammetry, 50
 solution resistance, 17, 21, 22, 44, 143
 non-compensated, 21, 142
 solutions for electrochemical studies, 149–154, 513
- solvent effects and redox potential, 589–594
 solvents, 140, 144, 149
 acidity, 591
 basicity, 591
 dielectric constant of, (table) 150, 590, (table) 591
 dipole moment of, 590, (table) 591
 empirical parameters of, 591
 polarity of, 589, (table) 591
 viscosity, 150
 spherical, diffusion, 38, 58
 electrodes, 38
 square wave voltammetry, 110
 Osteryoung, 113–115
 standard, hydrogen electrode, 19, 141, 143, 595
 potential, 15, 16, 25, 218
 rate constant, 26
 stationary conditions, 50
 stellacyanin, 570, 599
 structural modifications, 381–408
 induced by deprotonation
 or dehydrogenation, 392–397
 isomerization, 381–392, 484
 migration of hydrogen atoms, 397–399
 reorientation of alkyne groups, 399, 401
 structural reorganizations, 284, 598
 following irreversible processes, 62, 393, 402
 following quasireversible processes, 66, 67, 404
 following reversible processes, 57, 58
 superconductivity, 497
 mechanism of, 502–504
 superconductors, 140, 497–515
 chemical properties, 504–506
 electrochemistry, 506–514
 physical properties, 499–504
 supporting electrolytes, 36, 123, (table) 140, 149–154, (table) 150

- Taft constant, 580, (table) 581
temperature, and redox potential,
594–602
critical, 497, 504
tetraazaporphyrins, 369
phthalocyanines, 369, 370
porphrazines, 369
thickness of diffusion layer, 39, 40,
115, 120
transducer, 196
transfer coefficient, 26
transition metal clusters, 409–444
transition metal complexes, 217–325,
325–379
metallocenes, 159
electrochemical behaviour,
159–215
reactivity with small molecules,
445–495
dihydrogen, 484–491
dinitrogen, 474–484
dioxygen, 445, 449–469
haemerythrin-like, 467–469
haemocyanin-like, 466, 467
haemoprotein-like, 452–466
- vanadium, complexes, 219–229
nitrogenases,
- vanadocenes, 204, 205
vapochromism, 518
viscosity, solvents, 150
voltage, cell, 17, 20
voltammetry, cyclic, 49–110, 115
pulsed, 110
differential pulse, 110–113
square wave, 110, 113–115
single sweep, 50
- wires, molecular, 517–537
working, curves, $\Delta E'_p/\Delta E^\circ$, 103
 $\Delta E_p/\Psi$, 65
 $(i_a/i_c)/(k_f \tau)$, 78, 129
 $(i_{pII}/i_{pI})/\log(k_f/v)$, 90
 $(i_{pr}/i_{pf})/\sqrt{n \cdot F \cdot v / R \cdot T (k_f + k_b)}$
· 1/K, 72
 $(i_{pr}/i_{pf})/\log(k_2 C_{ox}^* \cdot \tau)$, 80, 83
 $(i_k/i_d)/\sqrt{(k_f \cdot R \cdot T) / (n \cdot F \cdot v)}$, 86
 $(i_k/i_d)/\sqrt{(k_f \cdot K \cdot t)}$, 127
 $(i_k/i_{kf=0})/\sqrt{(k_f \cdot t)}$, 130
electrode, 14, 16, 17, 20, 27, 115,
139–141, 145–147
potential, 120
- z, Kosower value, 591
zero current condition, 49, 115
zinc complexes, 314, 315

E

lectrochemistry can be an elegant and essential support to synthetic inorganic chemistry. However, it is often perceived as a difficult technique. This book aims to introduce inorganic chemists to electrochemical investigations in as straightforward a way as possible.

First, the reader is introduced to the theory of electron transfer processes, how they can be studied by various electrochemical techniques, and the practical procedures required. The book then goes on to look extensively, and with numerous illustrations, at the application of the techniques in the multiple fields of inorganic chemistry (including organometallics, coordination compounds, bioinorganics/biomimetics and materials science). Topics covered include: metallocenes; organometallic and coordination complexes; metal complexes of redox active ligands; metal-carbonyl clusters; superconductors; molecular wires; and proteins. Throughout, special attention is paid to the structural effects accompanying the electron transfer processes.

This unique book bridges the gap between undergraduate and research-level electrochemistry books, and will be welcomed as an introduction to electrochemical applications within inorganic chemistry.

Head of the Department of Chemistry at the University of Siena since 1996, Professor Piero Zanello has more than 20 years' experience in electrochemistry of organometallic and coordination compounds. He has been part of numerous national and international research groups, and is a well-known lecturer and author of scientific papers.

ISBN 0-85404-661-5



9 780854 046614